Controls on shallow plumbing systems inferred from the spatial analysis of pockmark arrays

Ana Raquel Diogo Maia

Submitted in partial fulfilment of the requirements
for the degree of Doctor of Philosophy at Cardiff University

June 2017

DECLARATION

This work has not been submitted in substance for any other degree or award at this or any other university or place of learning, nor is being submitted concurrently in candidature for any degree or other award.

Signed ..... (candidate) Date .....

STATEMENT 1

This thesis is being submitted in partial fulfillment of the requirements for the degree of PhD.

Signed ..... (candidate) Date .....

STATEMENT 2

This thesis is the result of my own independent work/investigation, except where otherwise stated. Other sources are acknowledged by explicit references. The views expressed are my own.

Signed ..... (candidate) Date .....

STATEMENT 3

I hereby give consent for my thesis, if accepted, to be available online in the University's Open Access repository and for inter-library loan, and for the title and summary to be made available to outside organisations.

Signed ..... (candidate) Date .....

STATEMENT 4: PREVIOUSLY APPROVED BAR ON ACCESS

I hereby give consent for my thesis, if accepted, to be available for photocopying and for inter-library loans **after expiry of a bar on access previously approved by the Academic Standards & Quality Committee.**

Signed ..... (candidate) Date .....

To Davide and Pedro,
my home.

Author note and status of publications

The results Chapter 4 presented in this thesis has been prepared as scientific papers for publication in international journals. The present status of publication is as follows:

Chapter 4 was published as Maia, A. R., Cartwright, J., Andersen, E., 2016, Shallow plumbing systems inferred from spatial analysis of pockmark arrays: Marine and Petroleum Geology, v. 77, p. 865-881.

Although the article is jointly co-authored with the project supervisors, the work presented in the publication is that of the lead author, Ana Maia. Editorial work was provided by the project supervisors in accordance with a normal thesis chapter.

Acknowledgements

The conclusion of this thesis would not be possible without the support of a great number of people who, directly or indirectly, helped me during this research, and one of most important and difficult periods of my life.

First and foremost, I would like to thank my family for their unconditional love and support, for believing in me and shaping me into the person I am today. Thank you, Mamã, my grandparents Avó Raquel and Zé, my silly brothers Diogo and Eduardo, my little sister Inês, my parents-in-law Rosa and Zé Gamboa, and my cousins Mena, Carlos, Paula and Rita. To our family dogs, Ginguba and Chiquito, a big thank you for all the cuddles and smiles.

I am eternally grateful to my supervisor, Joseph Cartwright, for all his guidance, help, and support, and for all I have learnt throughout these years. His knowledge and good ideas made this experience more productive and stimulating. Most importantly, I thank him for the support on all other non-PhD matters.

I must thank Fundação para a Ciência e Tecnologia (Portugal) for funding of the SFRH/BD/68286/2010 PHD grant that allowed me to undertake this project. Statoil, PGS, and Espen Andersen are thanked for providing the 3D seismic data. Schlumberger is acknowledged for the provision of seismic interpretation software.

A sincere thank you goes to my pastoral supervisor, Richard Lisle, for all the help and support he provided, and for all that I have learnt from him. Tiago Alves and Gwen Pettigrew is thanked for the indispensable support in the 3D Seismic Lab. A big thank you to Martino Foschi for all his geophysical knowledge, and for helping me with statistical tests. Annabel Cartwright is thanked for the help on spatial statistics. Many thanks to Margherita Sau for helping me with seismic interpretations. David James, Dan Morgan and Dan Carruthers are thanked for the many useful discussions. Thank you to all present and past Cardiff University students I met for the knowledge and good

moments shared: Ana and Ricardo, Cristina, Duarte, Huiyu Alessia, Aggie, Paola, Iqbal, Ben, Aldina, Chris. amongst others. Thank you so much to my dearest friends Rita and Renato (and my lovely nephews, Rai and Ria), Ruben and Carla, Tania and João, Mafalda, Emilie, Nélia, and Cristina – thank you for your friendship and all the good times shared outside the university life.

A special acknowledgement goes to the medical professionals that have been helping me cope with the health issues that are part of my everyday life. I am in a better place now thanks to them. Also, thank you to all the teachers I had the pleasure to encounter in schools and universities (both in Portugal and in the UK) – I am a better scientist because of you.

Finally, my deepest gratitude goes to my best friend and husband, Davide Gamboa. There are not enough words or gestures to thank him for everything he has done for me. I am grateful for his unconditional love and support, for being by my side in every moment, good or bad. His patience and belief are invaluable to overcome the grey days. His smile and “witty jokes” (a.k.a. “dad humour”) are always the highlight of my day. Without him, none of this would have been possible. Thank you. And thank you for giving me the best gift ever, our little Pedro. (I still want a dog.)

Ana Maia

Controls on shallow plumbing systems inferred from the spatial analysis of pockmark arrays

Abstract

In marine geological settings, pockmarks are evidence of highly focused fluid expulsion at the seabed. The modern seafloor of the Lower Congo Basin (LCB, offshore West Africa) is covered by densely packed arrays of thousands of pockmarks, whose distribution reflects in part the spatial organization of underlying seal bypass features. This study describes and analyses the variable distributions of seabed pockmarks using 3D seismic and spatial statistics, in order to infer sub-surface processes that control the fluid migration routes and understand the overall shallow plumbing system of the area. The 3D seismic visualization of feeding conduits (pipes) allowed the identification of the source interval for the fluids expelled during pockmark formation. Pockmark formation may be linked to gas hydrate dissociation and/or expulsion of free gas beneath the GHSZ. Spatial statistics were used to show the relationship between underlying discontinuities and seabed pockmarks distributions, and revealed that pockmark occurrence is not considered to be random. Several different types of geo-mechanical controls were recognised and divided into 1) stratigraphic or depositional controls, 2) strati-structural controls, and 3) structural controls, corresponding to increasing stages of deformation affecting basin sediments. Furthermore, from the wide variability of pockmark sizes present in the area and the local geomorphology, it is possible to conclude that pockmark size is related 1) to the sub-surface depth at which the fluid source interval occurs and 2) to lateral variations of the degree of overpressure.

The results of this study are relevant for the understanding of shallow fluid plumbing systems in offshore settings, with implications on our current knowledge of overall fluid flow systems in hydrocarbon-rich continental margins. This is relevant for the understanding of shallow fluid plumbing systems in offshore settings and overall fluid flow systems in hydrocarbon-rich continental margins.

Keywords: pockmark distributions; shallow plumbing systems; spatial statistics; stratigraphic controls; structural controls; seal breaching; Lower Congo Basin.

Table of Contents

Chapter 1

FLUID FLOW IN SEDIMENTARY BASINS - AN OVERVIEW

THESIS INTRODUCTION

1. Fluid flow in sedimentary basins – an overview

1.1. Rationale

For several decades, much has been discussed about the geological controls on fluid plumbing systems in sedimentary basins. Much emphasis has been given to fault discontinuities, their properties, and their ability to act either as barriers or conduits for fluid migration. Both scenarios are extensively documented in literature. Although the mechanisms and processes by which faults aid in or inhibit fluid flow are well constrained, a better understanding of their role on fluid distribution in sedimentary basins is necessary. Questions remain about the complexity and variability of these structures affect flow rates for both primary and secondary hydrocarbon migration, whether or not faults can be semi-permanently open pathways, how complex are the geometries of deep and shallow plumbing system, and what can seafloor expressions of fluid seepage – such as pockmark arrays – tell us about the subsurface drainage geometry.

The distribution of seabed pockmark arrays and associated subsurface fluid flow networks depend on factors such as physical and geo-mechanical properties of existing faults, hosting lithologies and fluids involved. Ultimately it depends on the overall geological setting and regional stress, as it is the result of the geological history of the area in focus. It is also time dependant. This continuous evolution is often imprinted as a series of past indicators of fluid

venting to the seabed which may or may not have been perpetuated to recent times.

Several different structural and stratigraphic processes may be involved to explain fault-fluid interaction. Understanding these mechanisms is of extreme importance, especially for the hydrocarbon exploration industry and carbon capture, as they may cause reservoir leakage. However, the complexity of the subsurface drainage networks changes throughout the vertical succession existing between deep reservoirs and the seabed. Conduits at deeper levels, where pressure is higher, tend to be narrower and more focused, but upon reaching shallow levels it is common for their complexity to increase. This is expressed by widened areas with branching conduits.

The key aim of this thesis is to understand the geometry of shallow plumbing systems, and how this influences distribution the distribution patterns and morphology of seafloor pockmarks.

1.2. Seabed fluid flow systems on continental margins

The seepage of fluids from the seafloor into the ocean water column is a widespread phenomenon on continental margins worldwide (Berndt, 2005; Huuse et al., 2010; Judd and Hovland, 2007) (fig. 1.1), and has also been increasingly recognised and characterised in lacustrine systems (Reusch et al., 2015). These seepage phenomena occur due to the presence of fluids in the subsurface that, under the right physical conditions (namely pressure and temperature) and geological setting, can migrate up through the stratigraphic

successions and reach the seabed (fig. 1.1). Fluid plumbing systems and the associated seabed seepage have a deep impact on the geological, chemical and biological cycles of marine environments, and also influence the atmospheric composition (Judd and Hovland, 2007). The term “fluid flow system” implies a suite of spatial features and processes involved in the migration, accumulation and leakage of fluid in sedimentary basins (Cartwright et al., 2007; Talukder, 2012). The organisation of the system comprises an arrangement of permeable strata able to store fluid in reservoirs at variable depths. These are connected by sub-vertical fluid migration paths, usually associated with faults and fractures, and/or sub-horizontal high-permeability beds. The fluids can be supplied to the flow system by migrating from deeply buried source rocks, or be generated locally. Fluids escaping from the subsurface system lead to the development of expulsion features on the seabed, such as pockmarks (Berndt, 2005; Cartwright et al., 2007; Judd and Hovland, 2007; Løseth et al., 2009; Pilcher and Argent, 2007).

The types of fluids emanating from seepage structures are associated with their tectonic setting (Etiope, 2015; Judd and Hovland, 2007; Talukder, 2012). Magmatic active settings, like divergent oceanic ridges or island-arc margins, have active hydrothermal fields with fluids circulating in the subsurface at very high temperatures (often over 300°C), and carry high concentrations of elements dissolved from the host rocks. When reaching the seafloor, these fluids are released through diffusion, along hot vents such as white and black smokers, or as sporadic plumes. The first two types of emissions can last for continuous periods of time, up to years or decades.

Cold seep venting is largely more common and a ubiquitous phenomenon on active or passive continental margins, occurring at depths up to 3000m. These systems consist of low-temperature gaseous or hydrocarbon-rich aqueous solutions, water and/or sediment emanating from the seafloor (Etiope, 2015; Judd and Hovland, 2007; Talukder, 2012). Cold seeps occur in settings where thick sedimentary successions and abundant organic material accumulate, and are often associated with active petroleum systems. Methane is the main contributor for seafloor seepage fluids, alongside minor volumes of hydrocarbon gases and CO_2. Seafloor seeps can also emanate carbonated water, or even fresh water, in carbonate successions or coastal settings. Sediment remobilised from overpressured mud units can be expelled to the surface and create mud volcanoes (Davies and Stewart, 2005; Dimitrov, 2002; Loncke et al., 2004). Viscous material such as bitumen can also migrate and be expelled at the seafloor forming tar seeps, such as the ones identified in the Gulf of Mexico (Brüning et al., 2010).

Cold seep systems are more complex than just their seabed expression, comprising the three main elements of subsurface fluid flow systems: source, plumbing system and vents at or near the seabed. Of these, the plumbing system is the most complex and often the least known and understood (Cartwright et al., 2007; Talukder, 2012). Importantly, recognising the plumbing systems and their architecture is an indicator for the 3D location of weak or overpressured domains on offshore stratigraphic successions. The geometry of the cold seep plumbing system is linked to the regional tectonic stress of where it occurs, with far more complex systems being present at

convergent active margins when compared to passive settings (Saffer and Tobin, 2011).

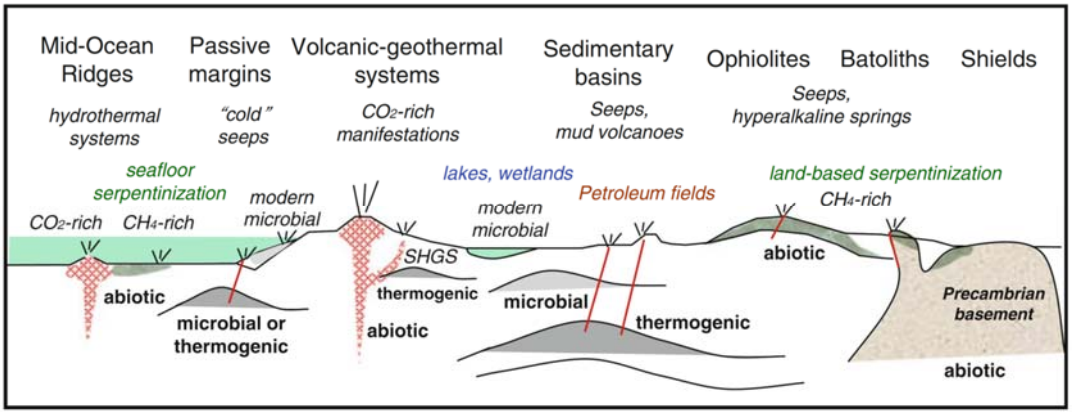

Figure 1.1. Schematic diagram of the various geological environments for microbial, thermogenic and abiotic methane production on Earth (from Etiope, 2015)

1.2.1. Methane genesis and expulsion

Methane is generated in the subsurface if abundant volumes of organic matter are available in buried stratigraphic units. Methane in marine sediments can be generated through microbial activity in the subsurface or through thermogenic decomposition of organic matter.

Thermogenic fluids are generated in kerogen-rich source rocks with TOC contents over 2%, buried beyond the zone of diagenesis. The production of hydrocarbons occurs through the "cracking" of kerogen molecules at high temperatures (typically up to 200°C), and the genesis of simpler molecules in which methane is included (Giavarini and Hester, 2011; Judd and Hovland, 2007). Methane is the shortest of the hydrocarbon molecules, and it is formed towards the end of the oil and gas window, after more complex molecules have been broken down. Local factors such as the type of organic matter, length of time of burial and geothermal gradients influence the duration and depth of

the thermogenic processes. In addition to the "biotic" origin of thermogenic gas derived from the breakdown of organic matter, abiotic gas can also be generated in the subsurface. This gas derives from chemical reactions that do not require organic matter, typical of magmatic or metamorphic processes (Etiope, 2015; Giavarini and Hester, 2011).

Biogenic methane is resultant from the activity of microbe-degrading organisms at shallow depths, at relatively low temperatures and pressures. This process is undertaken by strictly anaerobic methanogenic archaea that live in a wide range of temperatures, typically up to 60-80° C (Etiope, 2015). Seven key conditions have been established for microbial methano-genesis to occur in marine sediments (Rice, 1992): 1) the presence of an anoxic environment; 2) low sulphate concentrations; 3) low temperatures between 35 and 45° C; 4) abundant organic matter; 5) type and preservation of the organic matter; 6) adequate pore space for the microbes to function; 7) and a favourable rate of deposition to maintain the sediment at the optimum temperature zone. The shallowest conditions for methano-genesis can be as shallow as two metres to hundreds of metres, depending on the temperature gradient. Biogenic gas is generally very dry, constituting almost entirely of methane, and this composition is typically characteristic of shallow gas sources and reservoirs (Etiope, 2015).

Regardless of their genesis, recently generated methane accumulations will tend to migrate to the shallow subsurface driven by buoyancy forces. The methane can be dissolved in gas-saturated water, which is lighter than normal water, or as highly buoyant free gas bubbles formed due to vertical pressure decrease. Overpressure at depth created by excessive accumulation and/or

compaction is also an important driver for fluid migration. Overpressure is primarily related to quick tectonic events and/or increased sedimentation rates, which result in a perturbation of compaction equilibrium. Under normal conditions, pore water expulsion during compaction leads to increasing pore pressure with depth following a normal hydrostatic gradient. In overpressure conditions, the dewatering is hindered and pressure will increase above the hydrostatic levels (Talukder, 2012). The deeper the fluid bearing lithologies are buried, the less efficient is the mechanical compaction, thus increasing the potential for sources for upward injected fluid. Overpressure tends to prevail in mudstones and thick clays due to their low permeability. It can also develop due to lateral permeability contrasts between permeable and impermeable lithologies in combination with sealing faults, which can lead to overpressured subsurface compartments. Compaction perturbation alone will not exceed the lithostatic pressure limit, but overpressure can be enhanced by temperature-driven processes such as the genesis of hydrocarbons from buried sediments enriched in organic matter (Hedberg, 1974; Talukder, 2012). These will drive a large increase in trapped fluid volume, significantly adding to the system pressure. Gas exsolution during upward migration can also induce secondary overpressure or modify the main overpressure gradient.

The movement of hydrocarbons from their source rocks to the overlying stratigraphic units is sub-divided into primary, secondary and tertiary migration (Gluyas and Swarbrick, 2013; Weimer and Slatt, 2004). While the primary and secondary migrations describe the flow of methane from the source into trapping structures, the tertiary migration refers to the flow of methane from a reservoir structure towards the seepage point at the

subsurface. As previously mentioned, the spatial complexity of the migration route depends on the architecture of the fluid flow system, especially when fault networks are present. The route complexity and migration time are more significant in ascending thermogenic methane, while shallow plumbing systems of microbially produced methane will be shorter but not necessarily less complex.

1.3. Faults and diapirs – pathways for fluid migration

1.3.1. Faults

Faults are a key component identified in deep and shallow plumbing systems (Andresen and Huuse, 2011; Cartwright et al., 2007; Gay et al., 2007; Sibson, 1995; Sibson, 1996). Faults play a major role in fluid flow plumbing systems as they increase the effective permeability, breach baffles and barriers, and sequester gas and fluids from within the rocks. One key issue is their dual behaviour as either a sealing or leaking structure for fluid migration – fluids may flow free is faults are held open, or be retained if faults are closed under stress (Cartwright et al., 2007; Jolley et al., 2007; Sibson, 1995; Smith, 1980).

In essence, a fault is a discontinuity zone on a rock volume along which there has been a significant displacement. It consists of an inner region where most of the displacement takes place – the fault core – and a surrounding damage zone that accommodates strain (fig. 1.2) (Knipe et al., 1998; Zhang et al., 2010). Slip surfaces, fault gouge, breccias and cataclasites can be found at the fault core, whereas subsidiary faults and fractures characterise the damage zone.

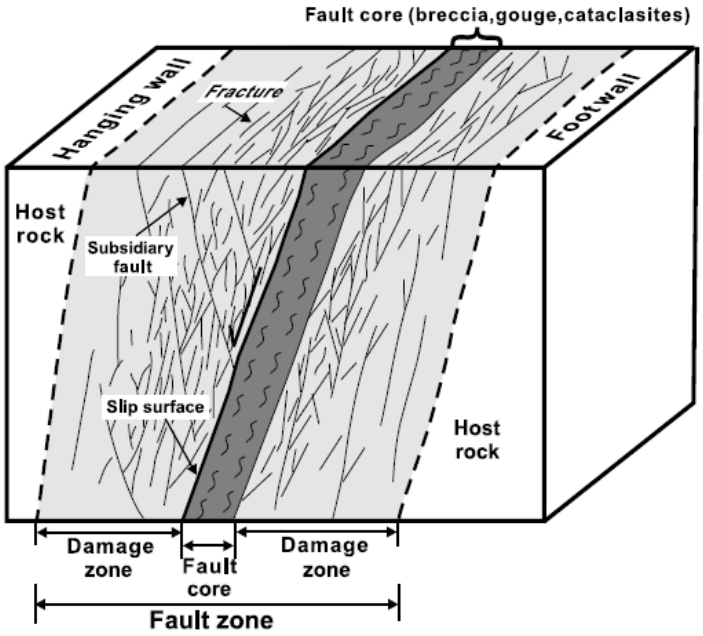

Figure 1.2. Conceptual model of elements in a fault zone (from Zhang et al., 2010).

The definition above is crucial for any fluid flow analysis. Damage zones record a history of strain accumulation and are therefore generally very complex structures. The multi-scale (micro to macro) analysis of fracture arrays and populations of offset faults are of extreme importance for fluid analysis, as these influence the rock permeability and limit fluid migration. The orientation and distribution of these features strongly depend on the stress orientation of the faulting regime and lithological contrasts (hard/brittle deformation vs. soft deformation) (Hickman et al., 1995).

Normal faults accommodate extension in the Earth's crust (Fossen, 2016; National Research Council, 1996). Normal fault systems generally present arrays of high-angle extension/dilatation fractures (figs. 1.3, 1.4 and 1.5) (Sibson, 1994). Inter-seismic extensional strain can maintain these fractures opened, whereas co-seismic compressional elastic rebound of the

regions surrounding the normal fault may reduce crustal permeability, leading to post-seismic expulsion of fluids that may be stored in fractures (Muir Wood, 1994). Normal faults are characteristic of passive margins, and upslope domains of salt and gravity tectonics. Extensional faults also associate with doming or crestal grabens resultant from rising salt walls and diapirs (Stewart, 2006; Vendeville and Jackson, 1992b).

Reverse or thrust faults are characteristic of compressional tectonic environments and tend to form very complex fault systems. Typically these systems form a series of imbricated faults that emerge from a sub-horizontal detachment fault at depth (Fossen, 2016; National Research Council, 1996). As a result, sub-horizontal fractures or veins may occur on either side of the fault zone (figs. 1.3 and 1.5) (Sibson, 1994). If steeply dipping fractures occur, they tend to be closed in inter-seismic periods (inter-seismic compression) but may be opened during fault rupture due to extensional elastic rebound (Muir Wood, 1994). The transport of fluids along reverse faults systems has been widely evidenced in active compressive or transcurrent tectonic environments, from submarine accretionary prisms to thrust sheets in mountain ranges (National Research Council, 1996). Shallow plumbing in thrust systems can be complex as fluid escape paths may develop not along the main compressive faults but on local extensional faults created by the crestal collapse of thrust anticlines ((Talukder, 2012; Von Huene et al., 2004).

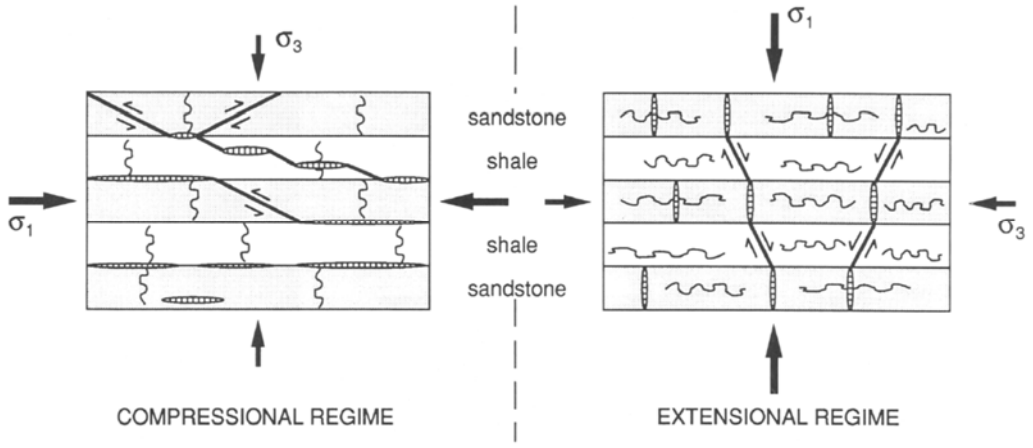

Figure 1.3. Schematic representation of stress-control of permeability by "brittle" structures (faults, extension fractures (hachured), and stylolites (wavy lines)) affecting an anisotropic, sandstone-shale sequence in compressional and extensional stress regimes (from Sibson, 1994).

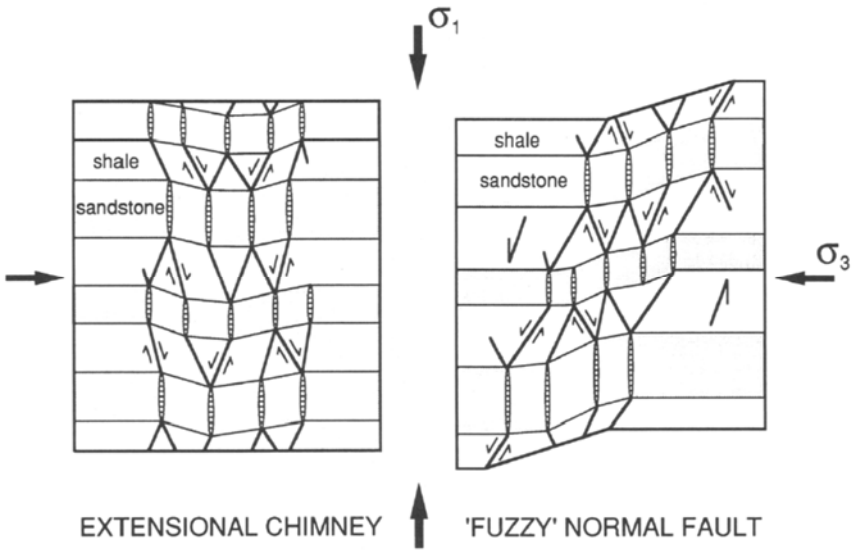

Figure 1.4. Fault/fracture meshes acting as fluid conduits within an extensional stress regime, either as extensional chimneys or "fuzzy" normal faults. Note that the passage of large fluid volumes leads to increased disorganisation and brecciation within the fault/fracture mesh (from Sibson, 1994).

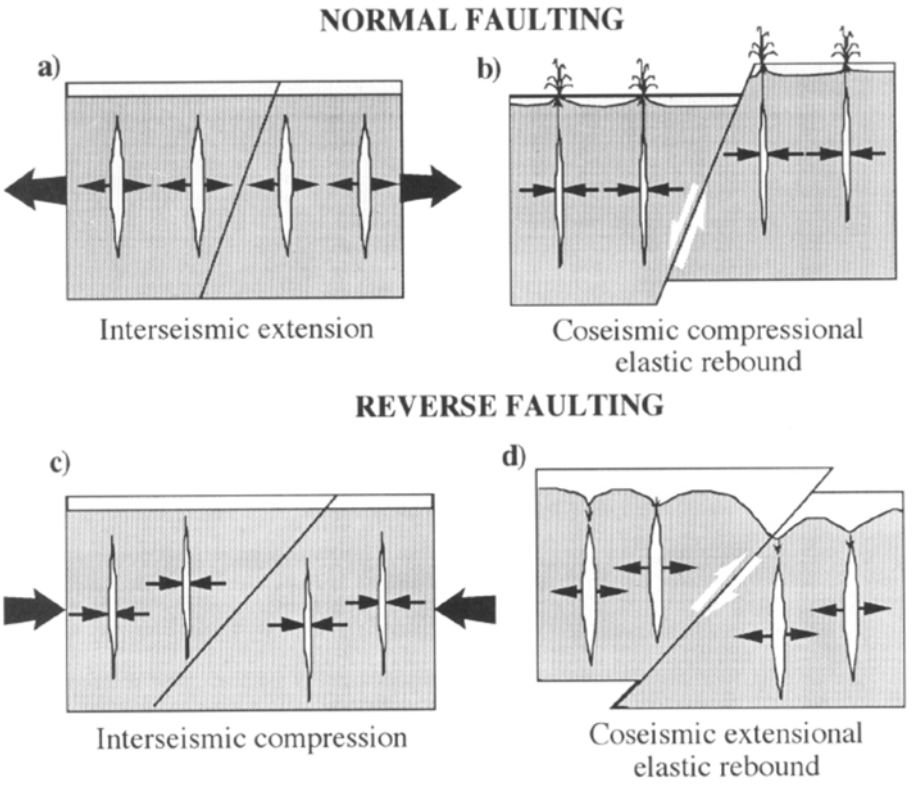

Figure 1.5. For extensional faulting the inter-seismic period **(A)** is associated with crack opening and increase of effective porosity. At the time of the earthquake **(B)** cracks close and fluids are expelled. For compressional faulting the inter-seismic period **(C)** is associated with crack closure and the expulsion of fluids. At the time of the earthquake **(D)** cracks open and fluids are drawn in (from Muir Wood, 1994).

Growth or syn-depositional faults have been reported for their relative importance to fluid accumulation and migration. They are *"normal faults which are active at the same time as sediment accumulation"* (Hooper, 1991), creating a thicker downthrown section when compared to the foot-wall (fig. 1.6). Rapid sediment deposition and fast burial rates, alongside poor formation dewatering, bury low to moderately consolidated sediments charged with fluids. While compacting these sediments, fluid pressure will build up, generating enough driving forces for the fluids to migrate upwards along the fault (Hooper, 1991; Talukder, 2012). Fluid leakage may be related to rupture events. Large listric faults in offshore settings with mobile substrates typically

show growth fault geometries, with very significant thickening on their hanging-walls when compared to the foot-wall counterpart (Fort et al., 2004; Hudec and Jackson, 2007).

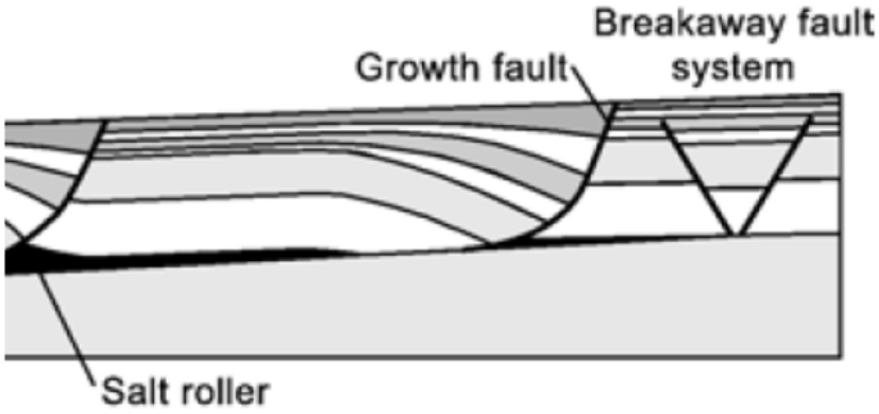

Figure 1.6. Schematic representation of a listric growth fault typically associated with salt rollers. Significant thickening of individual beds on the hanging-wall occurs near the fault and rollover anticline (modified from Hudec and Jackson, 2007).

Polygonal fault systems are a common occurrence in offshore settings (Cartwright, 2011). First described with 3D seismic technology in 19993/1994, these consist of laterally extensive arrays of layer-bounder extensional faults that exhibit a diverse range of fault strikes that partially or fully intersect, creating a range of polygonal patterns on map view of non-tectonic origin (Cartwright, 2011; Cartwright and Dewhurst, 1998; Cartwright et al., 2003). Polygonal faults are exclusively normal and dominated by dip-slip. The shape of the faults is planar in thinner tiers (below 300m). Polygonal faults become gently listric in thick tiers due to compacting by increasing vertical stress, but these involve a discrete detachment at the tier base (Cartwright, 2011). Fault geometry is associated to the geometry of the whole polygonal fault tier. Tiers of constant thickness tend to have equal numbers of faults dipping on opposite

directions, while wedge-shaped tiers show the large majority of faults dipping towards the thin edge of the tier (up-dip) (Cartwright, 2011; Mandl, 1988). Mixed tier geometries may occur, characterised by larger master faults transecting the whole tier alongside smaller ones with shorter height (Cartwright, 2011).

Several genetic mechanisms have been suggested for the origin of polygonal faults, including syneresis, diageneticaly-induced shear failure, silica diagenesis, differential compaction, density inversion and low coefficients of friction (Morgan et al., 2015 and references therein). Although their origin is still poorly understood, they are considered to be seal bypass features promoting fluid migration across sealing sequences during slip events (Cartwright et al., 2007; Gay and Berndt, 2007). Some studies suggest significant fluid leakage is associated with polygonaly faulted sequences, including pockmark trails and stacked gas anomalies (Gay et al., 2007; Gay et al., 2006a), while others argue that these faults are dominantly sealing features (Andresen et al., 2011). In Chapter 4, the sealing capacity of the polygonal faults in the study area is addressed and their control imposed on fluid migration pathways is discussed.

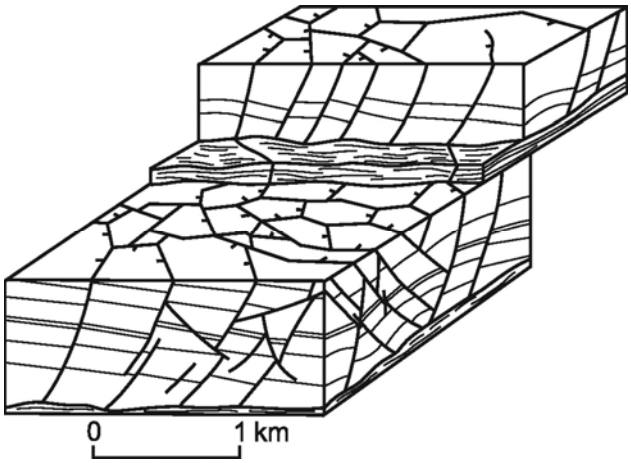

Figure 1.7. Schematic 3D diagram of two polygonal fault tiers, evidencing the planform polygonal pattern created by intersecting faults (modified from Cartwright et al., 2003).

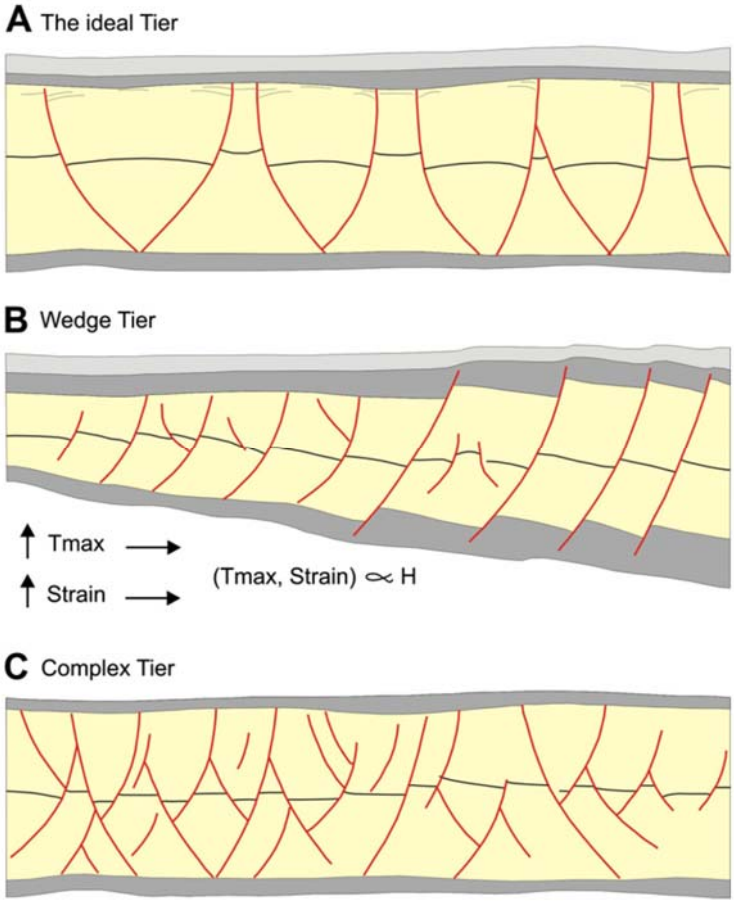

Figure 1.8. Schematic diagram of the different polygonal fault tiers. **(A)** Ideal tear with identical opposite-dipping faults. **(B)** Wedge-shaped tier with fault dipping towards the thin end of it. **(C)** Complex tier, with master fault intersecting the full thickness of tier (from Cartwright, 2011).

1.3.2. Salt diapirs

Salt diapirs in offshore settings are intrinsically linked to subsurface fluid flow and focused venting at the seafloor. Diapirism on continental margins is a result of gravity-driven thin-skinned tectonics, where ductile lithologies like evaporites flow and rise from an originally flat unit that deforms into variably complex structures (Hudec and Jackson, 2007; Jackson et al., 1994). Different salt architectures are observed along passive continental margins (fig. 1.6). At the upper slope regions, extensional processes prevail, creating salt rollers attached to large listric faults (fig. 1.6). Salt diapirs and salt walls are present at mid-slope transitional domains. A compressive domain is present on distal slope, forcing the active growth of salt structures like salt-cored anticlines, salt ridges, thrusts and canopies. Their development often leads to intense deformation of the seafloor (Brun and Fort, 2011; Fort et al., 2004; Jackson et al., 1994; Jackson and Vendeville, 1994; Leyden et al., 1976). Salt also has a very high thermal conductivity and impacts on the basin geothermal gradient. This hinders the thermal maturation of organic matter, leading to later generation and escape of hydrocarbons. Positive heat-flow anomalies developed along the salt structure can also induce fluid convection in the surrounding strata, triggering fluid migration and escape (Hudec and Jackson, 2007; Talukder, 2012).

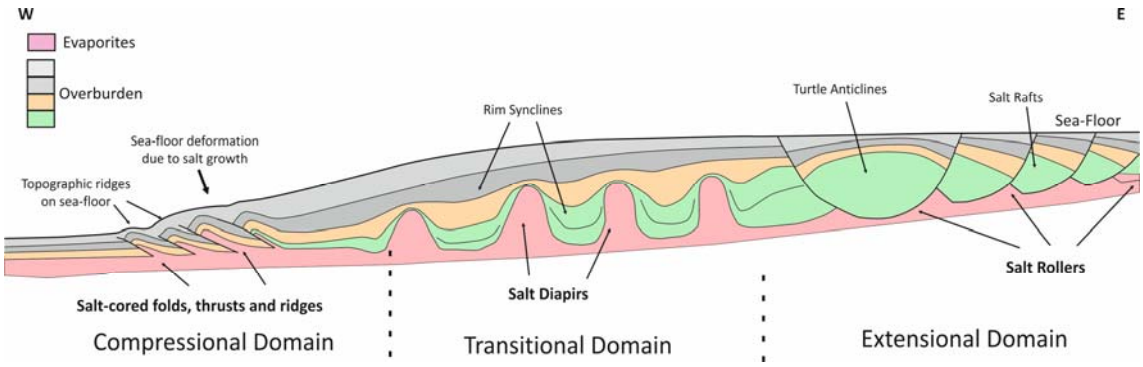

Figure 1.9. General architecture of offshore salt basins, with an extensional upslope domain with salt rollers and listric faults, a transitional diapir domain, and distal compressional domains with thrusts and ridges. Diagram follows the orientation of the west African margin, with the shore to the east.

Deformation structures created by salt movement play important roles on the shaping of subsurface plumbing systems from the seafloor down to the evaporite source layer, usually at depths of a few kilometres. Folded and upturned flanks around the salt structures focus fluid flow towards them, often leading to significant accumulations of hydrocarbons of high economic value.

Faulting is a crucial element associated with salt movement (fig. 1.10) (Stewart, 2006; Vendeville, 2005). Faults play important roles on fluid seepage across the whole margin affected by salt tectonics (Lerche, 2013; Pichel et al., 2016; Serié et al., 2017). Radial faults develop perpendicularly to diapirs or salt ridges (fig. 1.10). These radial structures are associated with the local stress created by salt rise, altering the regional fault patterns. This has been exemplified for the North Sea, where evenly spaced radial faults around salt diapirs imposed over the regional polygonal fault pattern (Carruthers et al., 2013; Davison et al., 2000b). Faults parallel to the structure are commonly formed during the extensional phase, associated with subsidence and withdrawal on the flank of the salt structures (Hudec and Jackson, 2007; Vendeville, 2002; Vendeville and Jackson, 1992a).

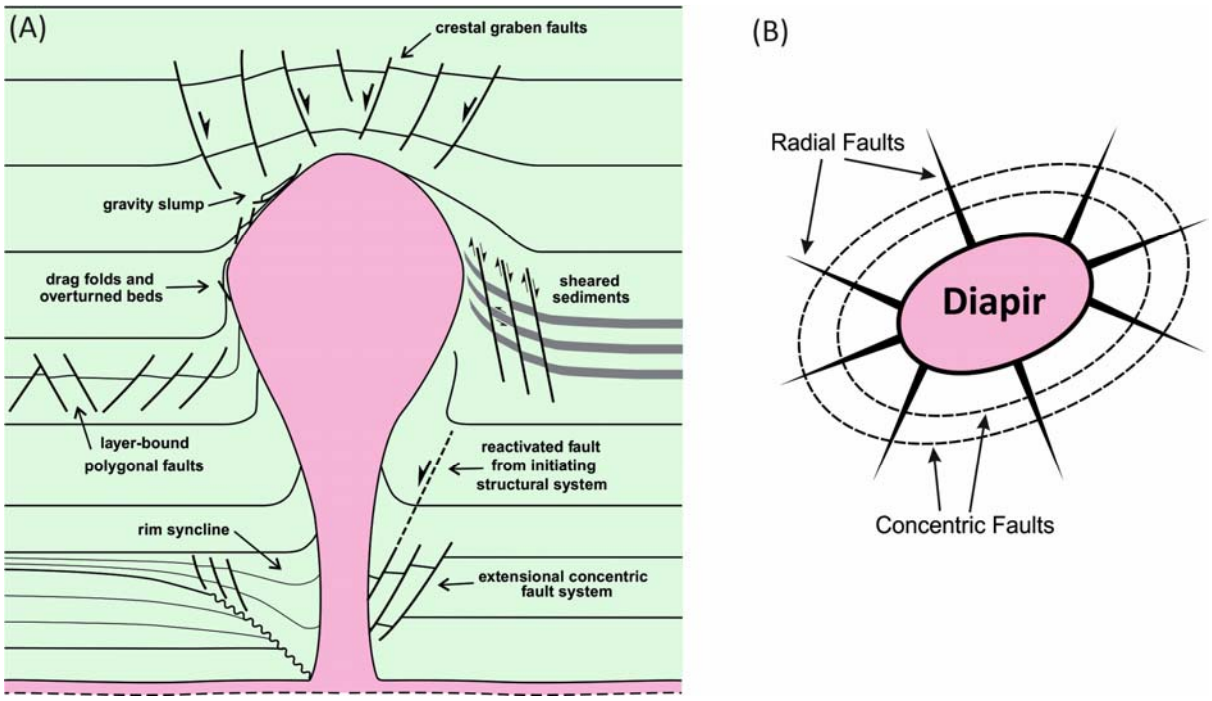

Figure 1.10. (A) Representation of the deformation structures that can develop during diapir piercement. **(B)** Plan view of radial faults perpendicular to rising salt bodies, and concentric faults parallel to them (modified from Stewart, 2006).

Crestal faults and grabens over salt structures are important for focused fluid flow on sedimentary basins. These faults often have complex arrangements and can exhibit normal or inverse behaviour (Dooley et al., 2009). The most common process is through regional extension, inducing salt rise through reactive diapirism. Salt structures created by this process are commonly triangular in cross-sections (Hudec and Jackson, 2011; Vendeville and Jackson, 1992b). Crestal grabens also develop from diapir deflation by later extension, and salt dissolution of fluid escape. Inverse crestal faults are driven by active diapirism resultant from the squeezing of salt bodies that forcedly pierce the overburden (Dooley et al., 2009). Crestal faults may have a higher proportion of open interconnected networks when compared to the diapir flanks (Davison et al., 2000a).

The rise and flow of the salt bodies creates important flow paths along the salt-sediment interface. Scaly fabrics of interconnected faults and breccias develop along this interface, which can be either open (thus favouring continued fluid rise), or cemented by evaporitic or other minerals. Cemented fractures are themselves a proof of enhanced fluid flow during the rise of salt structures. (Alsop et al., 2000; Davison et al., 2000a; Talukder, 2012).

The dynamics of salt structures vary through time, modifying the plumbing systems. One direct impact is the change of the salt body geometry. Deflating salt creates new deformation structures and induce the burial of sediments to deeper depth than their original deposition. Diapirs can also be rejuvenated under regional extension or compression, changing their geometry, piercement style, and surrounding deformation structures (Hudec and Jackson, 2011). Deeper overpressured strata can also be uplifted under compressive stresses, triggering faulting and fluid escape. These dynamic pulses impact the subsurface drainage and can lead to episodes of enhanced fluid transport and venting (Talukder, 2012).

1.4. Fault-related fluid flow mechanisms

The most straightforward mechanism for fluids to move across and along fault planes is by the juxtaposition of sands (“sand-on-sand” contacts). Similarly, when sands are placed in contact with impermeable lithologies like shales, a simple yet effective barrier for fluid migration is formed (James, 1997; Jolley et al., 2007). However, this lateral connectivity approach assumes

a zero-thickness for the fault core, which doesn't correspond to reality in most cases.

As the displacement takes place along irregular surfaces of a fault, voids will be created and cancelled from mismatching topographies, resulting in complex anastomosing conduits for fluid flow (Ligtenberg, 2005). This is particularly evident in faults that intersect competent lithologies of variable angles of internal friction (fig. 1.11). Mineralised veins, fractures and faults often occur in competent, low permeability and over-consolidated rocks, proving the viability of this type of conduits.

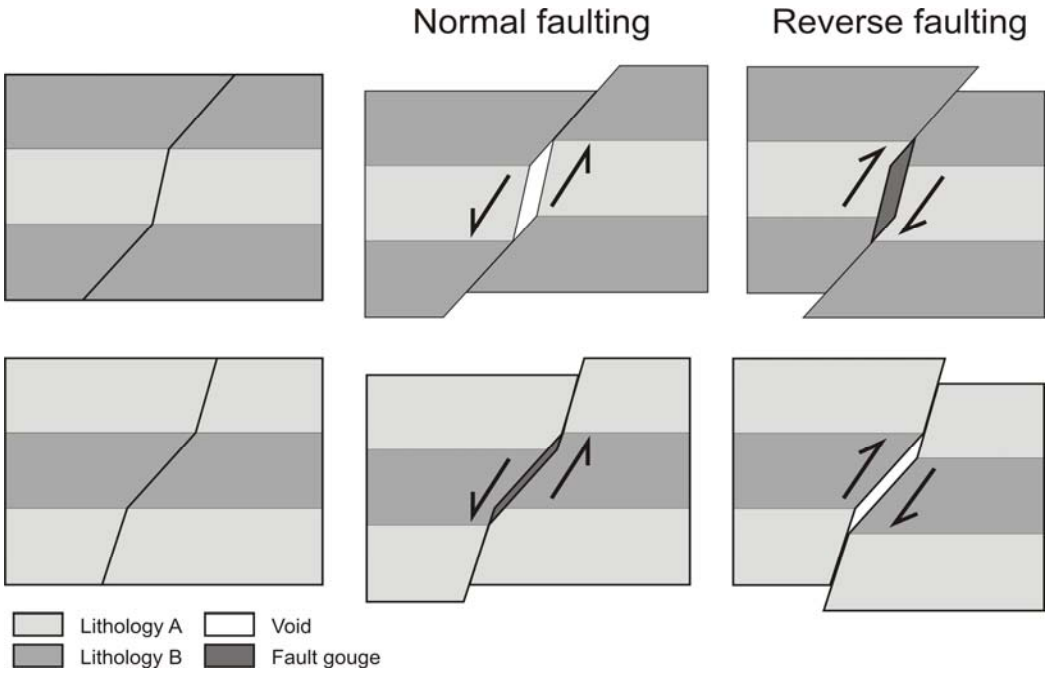

Figure 1.11. Faulting in sequence of lithologies with different lithologies (A and B) with creation of voids or fault gouge, depending on fault motion and dip of fault segments.

The roughness of the fault surface affects its shear strength and fault gouge production (Ligtenberg, 2005). The permeability of the fault core

strongly depends on the physical properties of the fault gouge. Shale smears, mainly composed of impermeable clay-rich material, prevent leakage of fluids across or along the fault plane, whereas smears of sand may significantly increase fault permeability (Hooper, 1991). The distribution of shale and sand smears may not be continuous along the gouge, as discussed by James (1997). In cases of interlayered shale and sand sequences hosting growth faults, episodic fault movement develops smear lenses of both shale and sand, producing complex permeable routes for fluid migration (fig. 1.12). Even when a fault ceases its activity, these pathways may still be open for fluid flow, establishing a semi-permanent conduit.

Cataclasites are deformation bands that commonly occur in large faults intersecting porous sandstones (Tueckmantel et al., 2010). Contrary to sand smears, cataclasitic bands show reduction of several orders of magnitude in porosity and permeability when compared to the surrounding host rock (Antonellini and Aydin, 1995). They result from grain crushing and compaction during fault movement, decreasing the grain size and promoting more grain contact surfaces. In some cases, friction between grains may even cause cementation, if rocks are buried deep enough and if mineral dissolution temperatures are reached (grain-contact quartz dissolution processes begin at 80°C (Walderhaug, 1996)). Being so, cataclastises may form barriers for fluid migration. However, porosity and permeability may be increased in zones parallel to these deformations bands, as noted by Fowles & Burley .

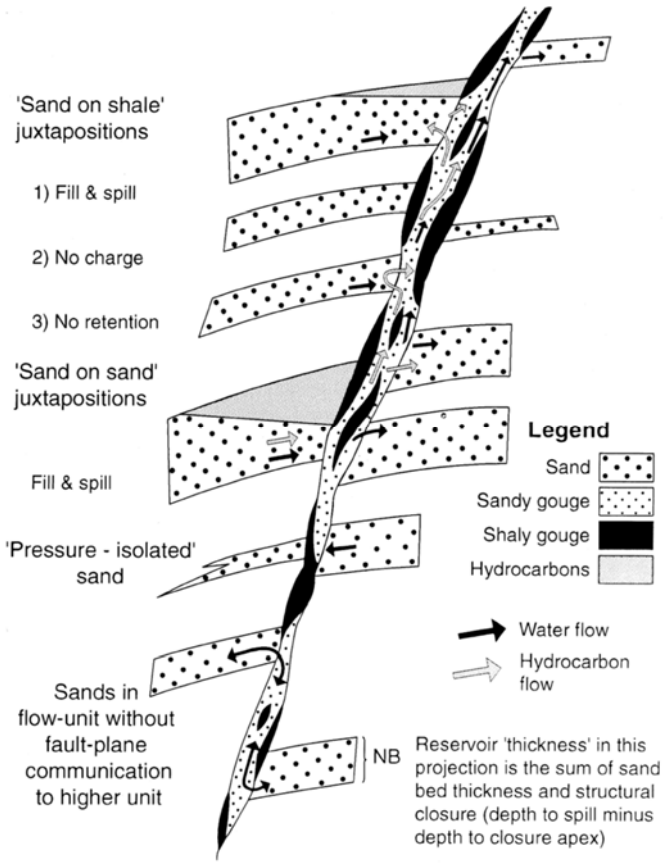

Figure 1.12. Fluid flow in fault zones, the effects of shingled gouge lenses. Shale lithology is in black (from James, 1996).

Brecciation at the fault core enhances permeability, while the space between the clasts is maintained open. Once mineral precipitation begins in these voids, progressive cementation of the fault breccias occurs and fluid flow is restricted. In any case, this mineralisation is proof that fluid migration was concentrated along these faults at some point in the past.

New rupture events may break up and re-arrange pre-existing fault gouges and damage zones, and re-open pathways for fluid flow. This episodic flow is the base idea for 1) the seismic pumping and fault-valve hypothesis discussed by Sibson et al. (1975) and Sibson (1990; 1994), 2) Hooper's (1991) periodic flow theory, and 3) Muir Wood's (1994) studies on seismic strain-

cycling flow. Several other authors proposed more mechanisms that complement the episodic flow cycle theory, including 4) pre-earthquake episodic fluid flow/compartment rupture (Byerlee, 1990, 1993), 5) creep-induced transiently increased fault fluid pressure (Blanpied et al., 1992), and 6) shear heating (Lachenbruch, 1980). Matthäi and Roberts (1997) discuss the ideas from the authors mentioned previously, and summarise them in a diagram of cause-and-effect chains, highlighting the interdependency of the physical properties that describe fluid flow in faults. As these properties are non-linear, the models above may apply simultaneously along different sections of a fault zone. An adapted version of Matthäi and Roberts diagram is shown in Figure 1.13.

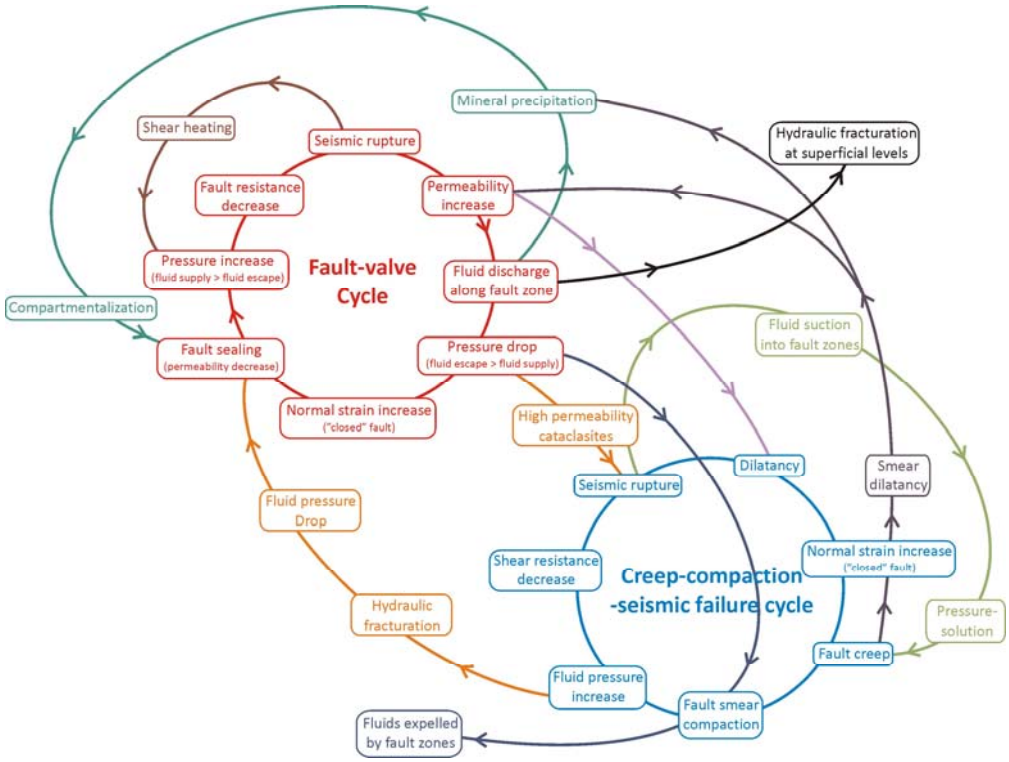

Figure 1.13. Potential "cause-and-effect" chains for hydro-mechanical processes associated with fault development and fluid flow (adapted from Matthäi and Roberts, 1997).

Fracture dilatancy accompanying strain-cycling play a major role in fault-related fluid flow as it increases the overall rock permeability, either by re-fracturing mineralized or sealed zones of a fault or by creating new open-spaces (Hooper, 1991; Sibson et al., 1975). Dilatancy may occur prior to a seismic event, following the seismic pumping model, or during failure, as described by suction pumping (Sibson, 1985).

Fluid pressure is one of the most important driving-forces in the cycles mentioned above. It is the key factor for the fault-valve behaviour described by Sibson(1994) (1994): *"Fault valve action occurs whenever ruptures transect supra-hydrostatic gradients in fluid pressure and breach impermeable barriers, leading to upwards fluid discharge along the transient permeability of the fault zone (...)"*. The discharge continues until hydrostatic pressure gradients are obtained. Once the rupture zone is sealed either by mineral precipitation or fault rock, fluid pressures may build up again, completing the cycle. Furthermore, overpressurisation of fluids may lead to hydraulic fracturing and seismic failure. According to Muir Wood (1994), *"seismic strain-cycling is akin to the function of the lungs in breathing"* (fig. 1.14). Regarding hydrocarbon mobilisation, the author highlights that capillary resistance to primary migration may be avoided by strain-cycle (open-close) response of micro-fractures in the rocks in which hydrocarbons can accumulate and repeatedly be pumped out of the matrix into larger fracture systems or highly permeable formations (fig. 1.14). By following the chains of "cause-and-effect", fault-fluid flow systems may be sustained for long periods of time. This cyclicity is particularly relevant for margins dominated by salt

tectonics, which tend to be very dynamic and induce multiple fluid expulsion episodes.

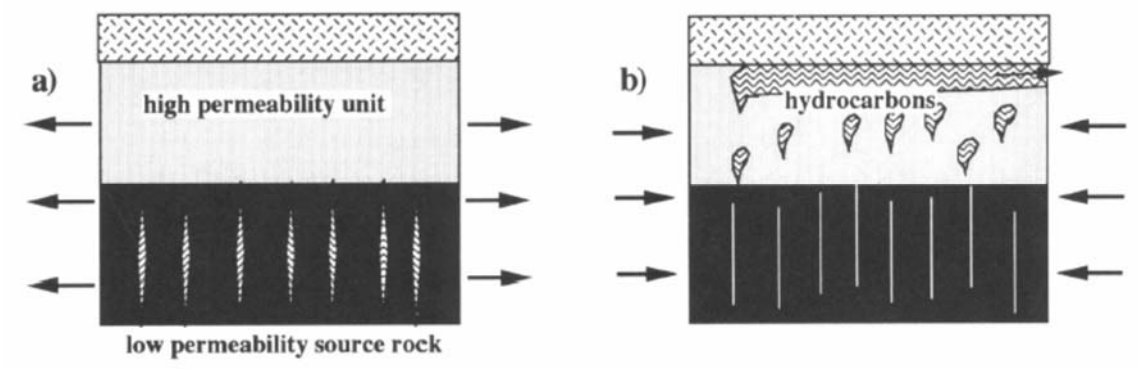

Figure 1.14. Seismic strain-cycling. **(A)** During positive (dilational) strain, fluids are drawn into widening micro-fractures accomplishing primary migration; **(B)** during negative (compressional) strain, hydrocarbon fluids are pumped from micro-fractures into high-permeability channels to accomplish secondary migration (from Muir Wood, 1994).

Fault intersections are considered important migration pathways for fluids in sedimentary basins (Gartrell et al., 2004). At the intersection of faults, a zone of high dilatation with very low shear strain is created, reducing fault gouge production. Small-scale open fractures and subsidiary faults are also concentrated in these intersection regions, making them viable and long-lived conduits for fluid flow (Gartrell et al., 2004, Ligtenberg, 2005). Some examples of hydrocarbon leakage in fault intersections are documented in the Timor Sea, Australia (Gartrell et al., 2004), and in the Mount Parnassus, Greece (de Boer et al., 2001), both from tectonic extensional settings.

In his neural network studies for fluid detection, Ligtenberg (2005) noted there are cases where fluids tend to migrate along the fault zone in *"columnar patterns, (...) instead of faults leaking along its entire length as a "curtain" of fluids"*. Not surprisingly, these columns of fluids moving upwards

following the fault orientation were directly linked to pockmarks at the seabed, spaced at regular intervals (fig. 1.15). Ligtenberg proposes a diapiric mechanism for this kind of episodic fluid leakage, explaining the correspondence between pockmarks or hydrocarbon-related diagenetic zones (HRDZs) and faults. This process is described and illustrated in Figure 1.15.

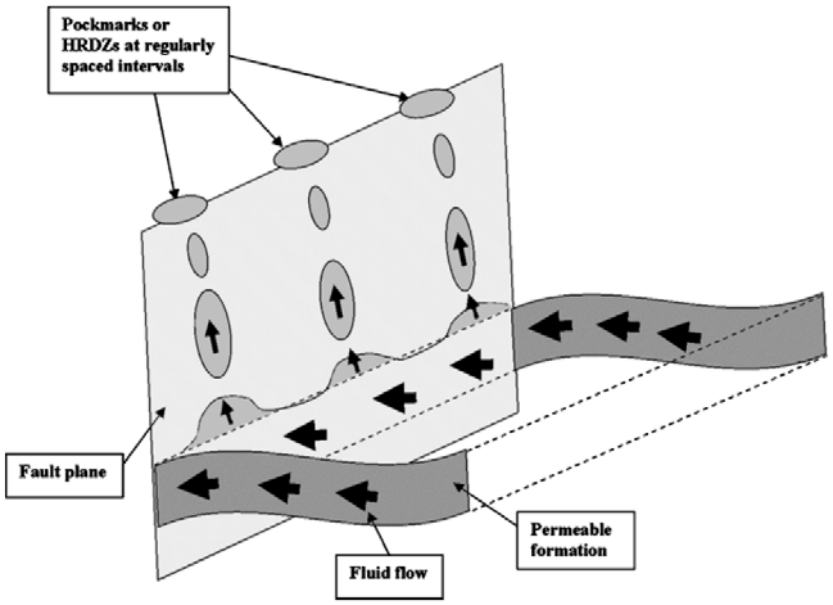

Figure 1.15. Schematic illustration of diapiric fluid flow along faults: fluids migrate through a permeable formation towards the fault zone. Differences in fluid character (such as viscosity and density) results in diapiric fluid migration, causing pulses of fluid flow and creating pockmarks or HRDZs at regular spaced intervals along the fault strike (from Ligtenberg, 2005).

To summarise, there are several different processes that promote fluid migration along and across faults. These can be grouped in mechanisms associated with constant or episodic flow. Constant flow is more likely to be promoted by geo-mechanical processes associated with fault complexities, plane irregularities and fault intersections. Episodic flow may be related to cycles of 1) fault activity, 2) overpressurisation and hydraulic fracturing, or 3)

diapirism. All these mechanisms do not exclude each other and may be working in conjunction, increasing the complexity of the analysis of fault-controlled flow.

1.5. Evidence of fault-controlled fluid flow

The most direct and visible evidences for fault-related fluid flow come from outcropping mineralised features associated with faults. Ore deposits are often related to precipitation of economically important minerals in fault-hosted veins, fractures or fault planes themselves, or result from the hydrothermal alteration of rocks by hot brines percolating along faults and fractures, generally involving significant volumes of fluids (Sibson et al., 1975).

On continental margin settings, the detection of subsurface fluids (which are not formation water) migrating along fault-controlled systems is only possible to observe by indirect methods through the use of seismic reflection data. Fluid flow features on seismic data are often recognised by amplitude anomalies or anomalous response patterns, as fluids may locally increase or decrease seismic reflection amplitudes (Berndt, 2005; Huuse et al., 2010; Judd and Hovland, 2007; Løseth et al., 2009). Tables 1.1 and 1.2 summarise the different types of anomalies generally observed on seismic data that might be related to fluids within the sediments. The analysis of the shape and spatial distribution of amplitude anomalies must be integrated with any existing geological features related to fluid migration to confidently interpret them as due to the presence of fluids. These structures can be also imaged on

3D seismic data, making this technology a powerful tool for the study of fluid flow in sedimentary basins.

Table 1.1 Descriptive amplitude anomaly terms (from Løseth et al., 2009).

Term	Definition
Brights, bright spot or high amplitude anomaly	Local increase in positive or negative amplitude along a reflection for any reason.
Dim spot (or dim zone)	Local decrease in positive or negative amplitude along a reflection or in a zone for any reason.
V-shaped bright	High amplitude V-shaped reflection in vertical section that is discordant to reflections from depositional surfaces. Seldom more that 2–3 km wide.
Flat spot	Relatively flat seismic reflection with an angle to the stratigraphic reflections.
Phase reversal	Phase shift of 180° along a continuous reflection, so that a peak becomes a trough and vice versa.
AVO	Amplitude variation with offset.
Reduced continuity	Local reduction of continuity of a seismic event.
Increased continuity	Local increase of continuity of a seismic event.
Reduced frequency	Local decrease of frequency.
Bottom simulating reflectors (BSR)	High amplitude reflection that often is parallel to seabed.

Table 1.2 Description of anomalous patterns on seismic data (from Løseth et al., 2009).

Term	Definition
Vertical wipe-out zone	The area on a seismic section where the reflections from the stratigraphic layers are deteriorated so the primary reflections either are absent or very weak.
Vertical dim zone	The area on a seismic section where the reflections from the stratigraphic layers are visible but have lower continuity and amplitude than in adjacent areas.
Vertical high amplitude or bright zone	The area on a seismic section where several high amplitude reflection anomalies occur that naturally can be grouped together.
Discontinuity zone	The area on a seismic section where the reflections from the stratigraphic layers are more discontinuous than in adjacent areas.
Chaotic reflection zone	The area on a seismic section where the reflection pattern is chaotic compared to adjacent areas.
Local depression features	Negative real down-bending or sag of a seismic reflection. The underlying reflections can be truncated, be parallel to the described structure or they can have any type of reflection pattern (e.g., chaotic).
Mounds	Positive structure of any shape rising above the normal top of a reflection. The reflection pattern below the mound can be of any type.
Push down	Apparent down-bending produced by a local, shallower low-velocity region.
Pull up	Apparent uplift produced by a local, shallower high-velocity region.

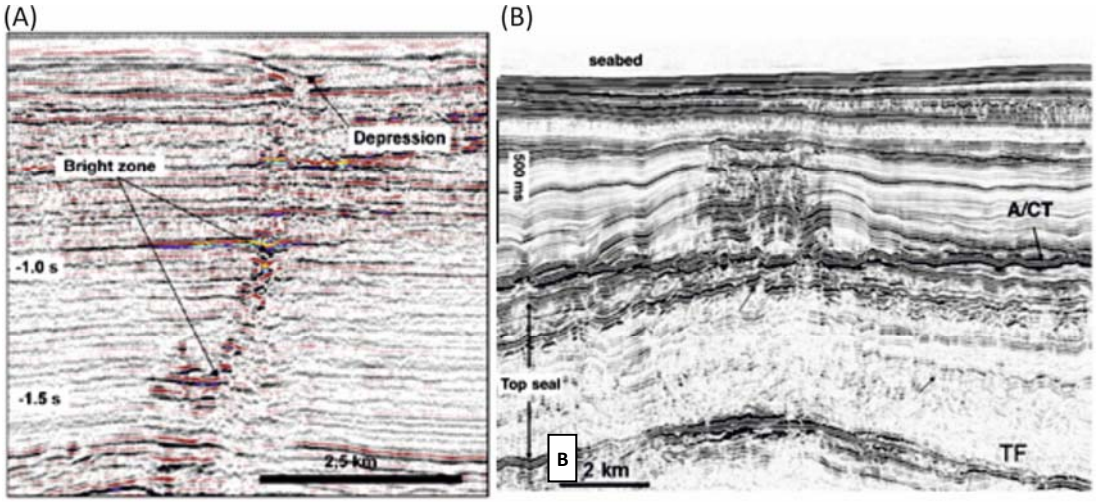

Figure 1.16. **(A)** High amplitude anomalies defining vertical bright zone in the hanging-wall of a fault, indicating gas leakage along the fault (from Løseth et al., 2009). **(B)** Extensive leakage of gas from a large anticlinal trap. Sandstone reservoir top sealed by polygonaly faulted claystone. The polygonal faults are implicated indirectly in the leakage process.

Fluidised sands at depth may be mobilised to upper levels of a sedimentary basin. These unlithified overpressured sediments can fill fractures forming intrusions such as sand sills, dikes or massive bodies (Cartwright et al., 2007; Huuse et al., 2010). If these sands reach the surface, they are expelled as sand volcanoes (Løseth et al., 2009). Due to their high permeability, **sand intrusions** may constitute effective conduits for fluid migration across otherwise sealing lithologies (Cartwright et al., 2007).

The leakage and migration of hydrocarbons into sands, followed by their biodegradation are the main processes for the formation of **hydrocarbon-related diagenetic zones** (HRDZ). The biological oxidation of hydrocarbons liberates carbon dioxide which is incorporated in carbonate cements (Løseth et al., 2009, Ligtenberg, 2005). This cementation tends to be localised and very intense, producing a strong positive seismic response due to an increase in acoustic impedance (O'Brien and Woods, 2005). Often fault leakage, especially along fault intersections, is related to the formation of HRDZs (O'Brien et al., 2002). A good outcropping example of cementation related to hydrocarbon leakage is discussed by Boles et al. (2004). The Refugio-Carneros fault zone is extensively cemented by calcite, interpreted as a result of leakage and oxidation of methane in Santa Barbara basin (fig. 1.17). Hydrocarbons were mixed with hot basinal fluids and were expelled during episodes of faulting.

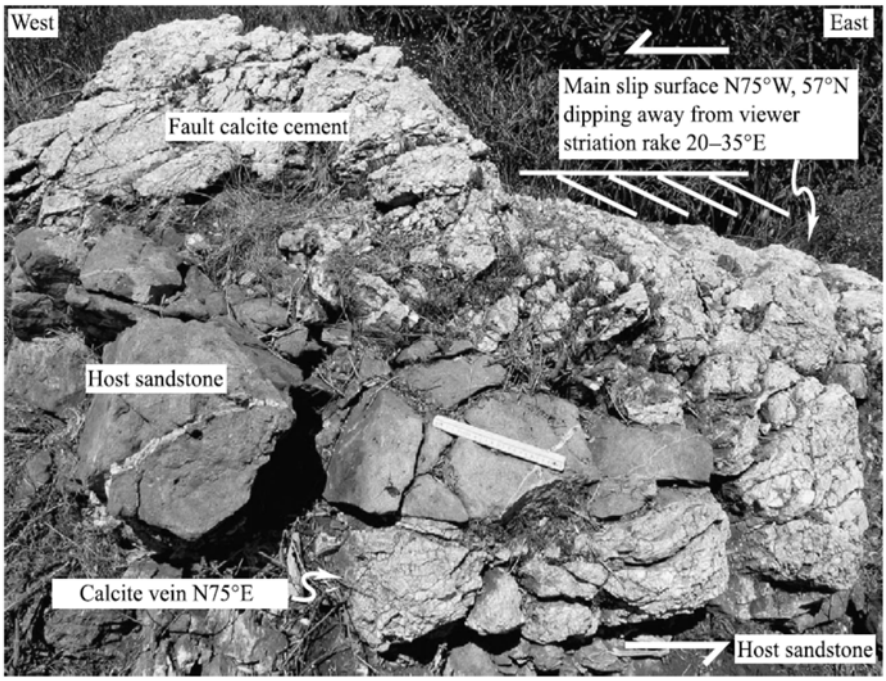

Figure 1.17. Fault calcite cement and a calcite-cemented vein in Refugio-Carneros fault (Santa Barbara basin), intersecting sandstones (from Boles et al., 2004).

Cases of biological activity increase related to hydrocarbon leakage at the seabed have been observed (Giavarini and Hester, 2011; Hovland and Judd, 1988). Hydrocarbons act as nutrients sustaining large masses of organisms and the accumulation of shells of benthic fauna (bioherm) may form **carbonate mounds** or carbonate build-ups (Løseth et al., 2009). As mentioned for the above structures, these mounds may be buried and can be identified on seismic by high amplitude anomalies (Heggland, 1998).

Other less direct evidences for fluid migration come from anomalous measurements observed either by other geophysical survey methods or in well data. As geothermal gradients may be disturbed by fluid flowing, **temperature anomalies** can be used to predict sections of fluid migration (Hooper, 1991). Hot, overpressured fluids flowing upwards along faults have been extensively documented, especially in ore geology where they are

interpreted to be the main process for mineralisation and hydrothermal alteration on both fault zones and surrounding rocks (Kumar, 1977).

Fault-related fluid flow may also be evidenced by **salinity anomalies**, but the processes involved are still poorly understood as the source for fluids in sedimentary basins is very complex (Hooper, 1991). These anomalies can either result from leakage of high-salinity brines or low-salinity fluids, depending on the geological setting, fault size and periods of activity.

If fluids are flowing upwards along fault zones, a decrease in the fluid potential is expected around the faulted areas. This reduction of fluid potential is known as **drawdown** and examples of this effect are discussed by Hooper (1991) as evidences for leaking faults.

In hydrocarbon seepage environments, oil and gas may induce alteration of magnetic minerals and iron-bearing minerals within the sediments, producing **magnetic anomalies** that can be detected by high-resolution magnetic surveys (Venkatachalapathy et al., 2010). Magnetic methods have been increasingly used in the discovery of oil and gas reservoirs, providing valuable knowledge in petroleum exploration industry (Ivakhnenko and Potter, 2004).

Losses of circulation while drilling through fault zones can indicate high permeabilities or empty spaces along these structures. It is true that losses of circulation associated with faults can also be induced by mechanical damage or hydraulic fracturing while drilling. Nevertheless, it highlights the importance of understanding fault permeabilities and their sealing/conduit potential, as they may constitute a drilling hazard.

1.6. Seabed and subsurface expression of offshore fluid flow systems

The geometry of the plumbing system may change significantly from the deep source levels towards shallow storage and source strata (fig. 1.1). If at depth the conduits tend to be focused along major paths such as large faults, at shallower levels there is an increasing influence of diffuse flow through the sediments, as pressure and consolidation decreases and lateral changes in the sediment properties occur. This will impact the distribution patterns of seafloor vents and result in mixed patterns between vertically focused clusters and/or less organised distributions (Talukder, 2012).

On the seafloor, the subsurface fluid and sediment flow is commonly expressed by mud volcanoes and pockmarks (Dimitrov, 2002; Hovland, 2003; Hovland and Judd, 1988; Loncke et al., 2004). **Mud volcanoes** are sub-aerial or seabed conical positive topographic structures that result from the expulsion of a mixture of water, gases and sediments, remobilised from deeper levels of a sedimentary sequence (fig. 1.18) (Dimitrov, 2002; Kopf, 2002; Reed et al., 1990). The size of the cone varies from 400m high and 3-4km in diameter to small metre-wide outlets (Løseth et al., 2009). These features are associated to high fluid and sediment flux in basins with high subsidence and sedimentation rates. The feeder zone is generally characterised by chaotic seismic reflections below the cone. Mud volcanoes may be related to overpressured shales or fed by fluidised material moving upwards along faults or fractures (Ligtenberg, 2005). The mixture is expelled as continuous or episodic eruptions, forming sequences of mud flows deposited at the base of the cone. Paleo-mud volcanoes can be identified in seismic data, buried under

continuous sediment layers or even below present day volcanoes, indicating intermittent flow activity (Graue, 2000; Kopf, 2002). However, studying the feeding conduits of mud volcanoes is challenging due to their poor visualisation on subsurface data due to intense attenuation (Davies and Stewart, 2005; Talukder, 2012).

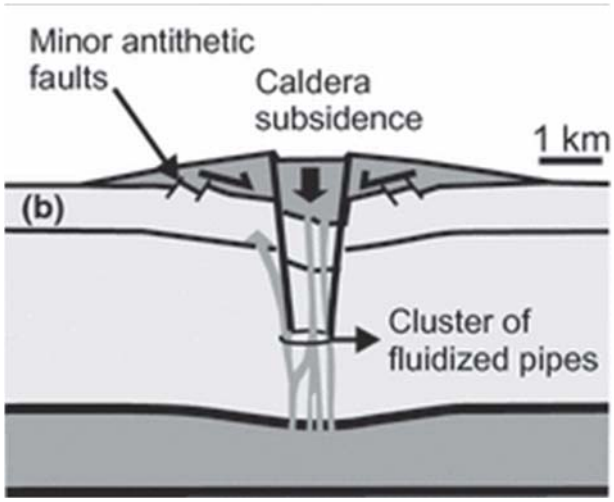

Figure 1.18. Simplified diagram of a mud volcano and subsurface feeding conduits (modified from Talukder, 2012).

Pockmarks are one of the most identified seabed seepage features on every marine environment, occurring at water depths ranging from 30m to over 3000m (Ercilla, 1996; Gay et al., 2007; Hovland and Judd, 1988; Judd and Hovland, 2007; Pilcher and Argent, 2007). First identified by King and McLean (1970), pockmarks are expressed as seabed conical depressions related to focused fluid flow. Since then, numerous studies have focused on their morphometry, distribution and origin with increasing detail (Andresen, 2012; Andresen and Huuse, 2011; Gay et al., 2006b; Gay et al., 2006c; Judd and Hovland, 2007; Moss and Cartwright, 2010), mostly due to technical advances in seafloor mapping and 3D seismic technology (Cartwright, 2007;

Cartwright and Huuse, 2005; Huuse et al., 2010). Pockmarks are commonly formed in soft, fine-grained sediments with low permeability, and are characterised by their circular to elliptical shape. Their size ranges from <5m to several hundreds of metres in diameter, and can reach up to 45m in depth (Hovland et al., 2002). Their morphology has been described as standard circular or elliptical, composite when individual pockmarks are merged, assymetric, or elongated pockmarks (Judd and Hovland, 2007). Judd and Hovland (2007) classified unit pockmarks as features usually less than 5m deep, and giant pockmarks as abnormally larger ones that can be 500m across and over 20m deep. Despite the size contrast, unit and giant pockmarks are frequently observed alongside each other. Pockmark strings (or alignments) composed of numerous relatively small pockmarks occurring at regularly spaced intervals are usually associated with fluid leakage along faults (fig. 1.19), or along buried channels (Deptuck et al., 2007; Gay et al., 2007; Ligtenberg, 2005; Pilcher and Argent, 2007). These alignments can include pockmarks of variable sizes. Pockmark distributions have been increasingly analysed using spatial statistics. Results show a variety of patterns, from high dispersion to clustering, and their association with pockmark morphometry may be a clue for the geometry of the subsurface plumbing system (Cartwrigth et al., 2011; Hammer et al., 2009; Moss and Cartwright, 2010).

The presence of pockmarks and buried paleo-pockmarks is diagnostic for present or past overpressure build-up and the occurrence of single or multiple fluid escape events, particularly when these can be identified on the subsurface through the use of 3D seismic data (Andresen, 2012). Seismic-resoluble pockmarks on the seabed often lie vertically above zones of disturbed

seismic reflections or high amplitude anomalies, indicating hydrocarbon leakage (Ligtenberg, 2005; Løseth et al., 2009; Moss and Cartwright, 2010).

When fluid leakage is focused along vertical to sub-vertical columns of stacked amplitude anomalies, pockmarks are interpreted as the seabed expression of pipes (fig. 1.19b) (Moss and Cartwright, 2010). **Pipes** are represented on seismic data either through high or low amplitude anomalies, but prior to their adequate characterisation on 3D seismic data these features were disregarded and considered as seismic artefacts (Cartwright, 2007; Løseth et al., 2010; Cartwright and Santamarina, 2015). However, pipes are crucial for the understanding of the plumbing system history of a sedimentary basin, as they constitute an important seal bypass feature that allows vertical cross-strata fluid flow through low permeability lithofacies towards the seabed (Cartwright et al., 2007). Cartwright et al. (2007) describe the classification of dissolution pipes, hydrothermal pipes, blowout pipes and seepage pipes according to their origin. In addition, pipes comprised of stacked pockmarks are representative of continuous fluid seepage through time, and intensive brecciation zones may be caused by hydro-fracturing. The amplitude anomalies characteristic of pipes may either indicate the presence of trapped gas in the pipe or the presence of cementation zones (Cartwright et al., 2007; Cartwright and Santamarina, 2015). The vertical extent of pipes is varied, commonly at least 100-300m of height, but there may be cases exceeding 1000m. Pipe width is typically below 300m. These features tend to have circular cross-sections, although there are cases of elliptical-shaped planforms related to pre-existing discontinuities (Cartwright et al., 2007; Løseth et al., 2009; Moss and Cartwright, 2010). Gas chimneys are features observed on

seismic data that may draw some resemblance to pipes. However, these tend to be very wide (<5km) and be represented by chaotic reflections with dim amplitudes, thus being fairly straightforward to distinguish chimneys from pipes (Løseth et al., 2009).

Pockmarks and pipes are the main fluid flow features identified in the study area. Their distributions and the controls on their spatial arrangement are the focus of Chapters 4, 5, 6, and 7 of this thesis.

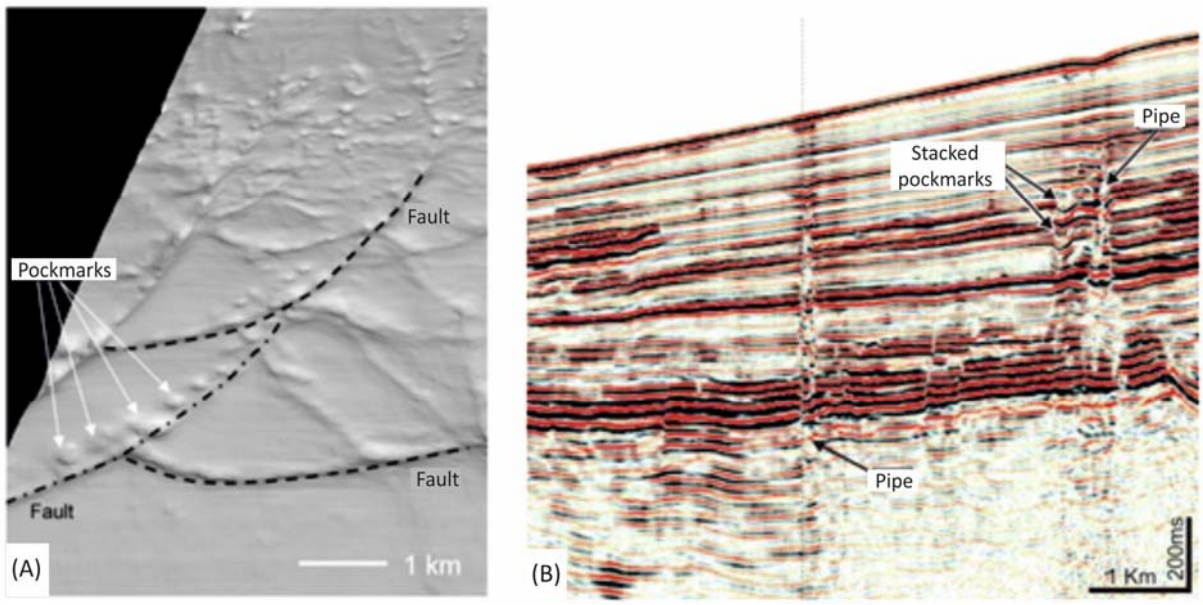

Figure 1.19. (A) Pockmarks at seabed (offshore West Africa) regularly spaced above and along leaking faults (from Ligtenberg, 2005). **(B)** Blowout pipes and stacked pockmarks from offshore Namibia (from Cartwright, 2007).

Bottom-simulating reflectors (BSRs) are often observed in association with pipes and seabed pockmarks visualised on seismic data, and their occurrence is an indicator of the presence of free gas and gas hydrates in the subsurface (Crutchley et al.; Cunningham and Lindholm, 2000; Løseth et al., 2009). Gas hydrates consist of crystalline compounds created when water or ice contacts small gas molecules – the hydrate guest –, under a certain range

of pressure and temperature. Gas hydrates tend to be stable at higher pressures and low temperatures, being formed as water freezes and creates a lattice that traps the gas molecules, but without creating chemical bonds between the host water and the guest particle (Giavarini and Hester, 2011). The guest particles can be of various origins, but methane and CO_2 have been the ones of particular interest. Hydrates form within the gas hydrate stability zone (GSHZ), confined to a limited depth range, which must meet the right properties in terms of sufficient gas supply and concentration, ideal P-T conditions, depth below the seafloor, and geothermal gradient (Giavarini and Hester, 2011; Judd and Hovland, 2007). Sediment properties such as porosity, pore size and permeability play a key role on the locus of hydrate development.

Biogenic gas is the main source of natural hydrates, and gas concentration must be higher than its solubility in water. For this to be maintained, hydrates only form in basins where high organic content is available for methano-genesis. Thermogenic gas is rarer to be found in hydrates, but when it occurs generally implies a deep source and the presence of a plumbing network for it to migrate to the shallow levels (Giavarini and Hester, 2011). Importantly, the genesis of hydrates leads to a significant decrease of permeability and the whole hydrate front acts as a laterally spread sealing interface (Taylor et al., 2000). Thus, the presence of high reflectivity, reverse polarity BSR reflections on seismic data represent the abrupt acoustic change created by the higher density of the hydrate layer. BSRs lie at a constant depth below the seafloor and follow its morphology, also cross-cutting subsurface strata if their geometry is not parallel to it (fig. 1.20) (Cunningham and Lindholm, 2000; Giavarini and Hester, 2011; Løseth et al., 2009; Serié et

al., 2017). BSRs typically mark the hydrate top of the GHSZ, but free gas can be present below it, as the hydrate becomes unstable and dissociates at deeper levels. Although BSRs on seismic data commonly imply the presence of hydrates, the reciprocal is not always valid as the lack of a seismically visible BSR does not mean that hydrates are not present at the subsurface (Giavarini and Hester, 2011).

The presence of BSRs in the study area is discussed in Chapters 4 and 5.

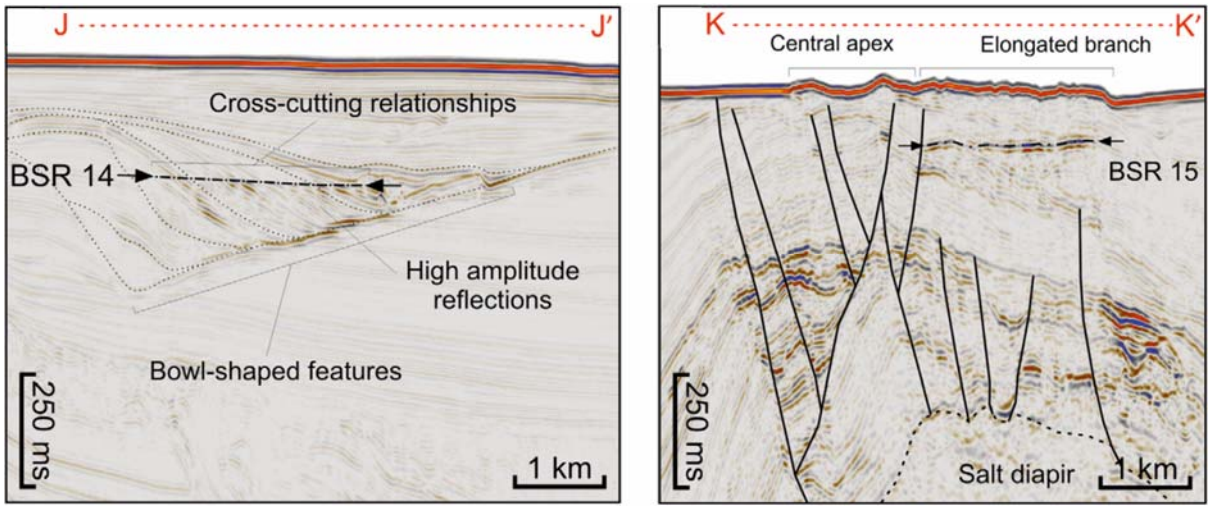

Figure 1.20. Seismic sections with examples of BSRs, showing them as parallel to the seabed and cross-cutting the geometry of the surrounding dipping strata (modified from Serié et al., 2016).

1.7. Aims of the research

The key aim of this thesis is to understand the workings of the shallow plumbing system of the Lower Congo Basin, and its influence on distribution of the seal bypass features responsible for the spatial arrangement and

morphology of seafloor pockmarks. The research presented in this thesis attempts to answer the following questions:

1) What are the controls on seal breaching and pockmark distribution?

2) What impacts do seal bypass features formed during early burial have on potential caprocks?

Understanding how seal bypass features (especially associated to structural deformation of slope sediments, i.e. faults and fractures) affect fluid flow pathways is crucial in hydrocarbon exploration and more recently in CO_2 sequestration, as these compromise the integrity of caprocks and may cause reservoir leakage. The results of this study also have a significant impact in the assessment of submarine geo-hazards.

1.8. Thesis layout

This thesis is divided into nine chapters. An introduction and overview of the previously published studies on the main topics covered in this research has been presented in the preceding sections of Chapter 1. A description of the 3D seismic dataset and methodologies used in all results chapters is given in Chapter 2, including key principles of seismic interpretation and spatial statistical methods. The geological setting of the Lower Congo Basin and a more localised geological context of the study area are described in Chapter 3. The research presented in Chapters 4, 5, and 6 form the main results chapters of this thesis. Chapter 4 analyses the spatial distribution of seabed pockmarks and their relationship to local patterns of polygonal faulting. Chapter 5

discusses the association between seabed pockmarks and mass-transport deposits in the study area. Chapter 6 is a case study focused on the distribution of a particular set of seabed pockmarks, and explain how they are linked to a shallow creep process. In this chapter, the relationship between pockmark size and the subsurface depth of the fluid source interval is also discussed. The findings of these chapters are integrated and discussed in Chapter 7, where all the control mechanisms on the spatial distribution and morphology of pockmarks are listed. The implications of this research for the general shallow plumbing system of the Lower Congo Basin are also featured here. The main conclusions of the thesis are drawn in Chapter 8, and Chapter 9 lists all bibliographic references used.

Chapter 2

DATASET AND METHODS

2. Dataset and methods

The results presented in this work are based on the interpretation of 3D seismic data and the quantitative and statistical analysis of geological features of interest. This chapter provides a brief overview of 2.1) 3D seismic acquisition and interpretation, 2.2) the dataset and 2.3) statistical methods used in this thesis.

2.1. 3D Seismic

The principle of 3D seismic is the acquisition of closely-spaced seismic-reflection data, providing detailed information of the subsurface both in horizontal and vertical directions (Bacon et al., 2003). This allows improved spatial and volumetric interpretations of the subsurface geological features when compared to 2D seismic data, particularly in areas of complex 3D structural and stratigraphic geological features (Hart, 1999; Kearey et al., 2002; Posamentier et al., 2007, Yilmaz, 2001). Marine 3D seismic data is acquired using an array of seismic sources (usually an array of airguns), and a series of hydrophone streamers towed behind the acquisition vessel (fig. 2.1). The shooting direction is called the inline direction, being coincident with the vessel track and orientation of the hydrophone arrays. Perpendicular to this direction is the crossline direction. Trace spacing in 3D surveys are commonly 12.5 to 25m for inlines and 25 to 50m for crosslines, thus an accurate knowledge of the shot and receiver locations is required to provide the best quality data (Yilmaz, 2001).

The acquisition seismic reflection data is primarily focused on the detection of compressional P-waves reflected at subsurface geological interfaces (Kearey et al., 2002; Sheriff and Geldart, 1995). In marine environments, 3D seismic surveys comprise the acquisition of data generated by the energy sources below the sea surface, which are designed to concentrate downward energy pulses. The sum of the signals fired simultaneously from each airgun provides a far-field wavelet which has a range of frequency components. The wavelets propagate through the water column to reflect off the seafloor and through underlying geological layers to provide reflection signals. The energy reflected is detected by hydrophones towed behind the vessel that record the two-way travel time (TWT) that the P-wave reflections take to travel from the source until their return to the surface (fig. 2.1).

Two important parameters of the seismic P-waves are their velocity and frequency. The P-wave velocity is variable with depth and directly controlled by the lithological composition, porosity, density, texture, pressure, compaction, elastic modulus and fluid content of the stratigraphic successions. Seismic velocity tends to increase with depth as rocks become more compacted and effective pressure increases (Brown, 2004; Kearey et al., 2002). In contrast, acoustic frequency consists in the number of wave cycles passing by one point per second. Frequency tends to decrease with depth as the higher frequencies preferentially attenuate while travelling through the rock substrate. This has a direct influence on the spatial resolution of the seismic data, decreasing as deeper stratigraphic levels are reached (Brown, 2004).

The final 3D seismic cube is obtained after data processing through the deconvolution, stacking, and migration processes. Deconvolution improves

temporal resolution by compressing the seismic wavelet. The stacking process includes CMP (common-midpoint) sorting, velocity analysis, statics correction, and stacking. CMP sorting combines individual traces into a common-cell gather (or bin), typically coincident with a CMP gather, which tend to have cell sizes of 12.5 x 25m (Yilmaz, 2001). Once the data are sorted, velocity analysis and statics corrections are performed to increase the signal-to-noise ratio. Stacking is done by summing all traces from each CMP gather along the offset axis. Next, the data have to be migrated to provide the correct location and geometry of the seismic reflectors. The migration process collapses the diffraction patterns produced by subsurface features, greatly improving the quality of the wavelet shaping (deconvolution, phase correction) and seismic image provided (Yilmaz, 2001).

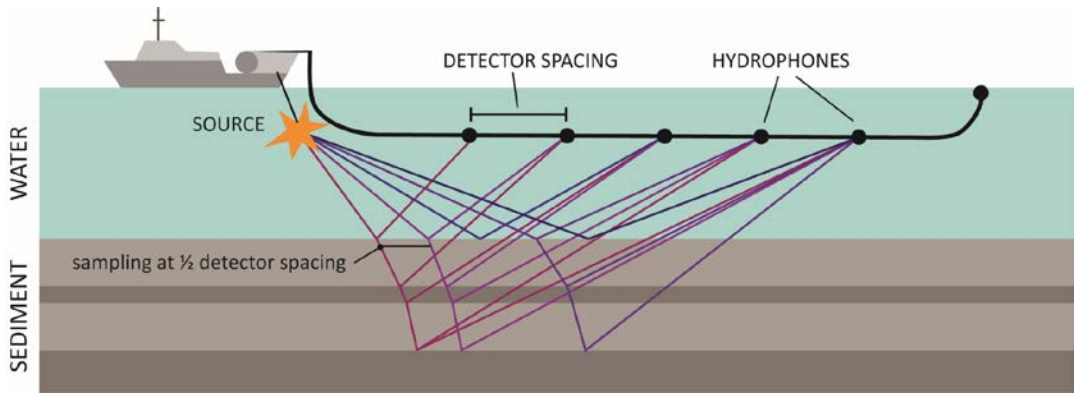

Figure 2.1. Schematic representation of 3D marine seismic surveys. A towed acoustic source near the surface emits a sound wave that travels through the water. When the acoustic properties of the rock change, the P-waves reflected to the surface are detected by hydrophones mounted in a long cable towed behind the vessel. The hydrophone spacing partly controls the horizontal resolution of the seismic data (modified from Bacon et al. 2003).

The interpretation of the processed data is based on the graphic representation of variable-strength seismic reflections detected in the subsurface. These strength variations express the contrast in physical properties across various geological interfaces and depend on the acoustic impedance (Z) between two different lithologies. This parameter is defined as the product of the rock density (ρ) and seismic velocity (v) (Brown, 2004; Kearey et al., 2002; Veeken, 2007).

Equation 2.1.

$$Z = \rho v$$

The representation of acoustic impedance contrasts on seismic data is traditionally represented in distinct colours according to the SEG (Society of Exploration Geophysicists) polarity classification (Brown, 2004) (fig. 2.2). SEG normal polarity displays 'peaks' on the seismic wavelet created by increasing acoustic impedance as positive amplitudes, while decreasing amplitudes are considered as negative amplitudes or 'troughs' (fig. 2.2a). Contrastingly, data can be represented as SEG reverse polarity where increases in acoustic impedance are represented as negative 'troughs' (fig. 2.2b) (Kearey et al., 2002; Sheriff and Geldart, 1995). A typical example of downward-increasing acoustic impedance is the representation of the seafloor reflection where the wavelet passes from the water to the higher density sediments. The 3D seismic datasets used in this thesis are represented in SEG reverse polarity (fig. 2.3).

Data phase is also part of the data classification. The surveys can be maximum, minimum and zero phase, but nowadays the latter type has gained

the preference of seismic interpreters utilizing workstations (Brown, 2004). The zero-phase data means that the wavelet is symmetrical and the majority of energy is coincident with its peak corresponding to the acoustic impedance contrast (this has a great advantage on seismic stratigraphic interpretations, as the centre of the wavelet is coincident with the geological interface creating the reflections) (fig. 2.2).

2.1.1. Seismic resolution

The key objective of any 3D seismic acquisition campaign is to provide high-resolution data of the subsurface, but this tends to decrease with depth as the rocks get increasingly more compacted (Brown, 2004). The resolution is related to the minimum proximity of two points that can still be identified as individual elements in the seismic data, with both vertical and lateral resolution being taken into account (Yilmaz, 2001).

Vertical resolution is mainly restricted by the dominant wavelength (λ), defined by the wave velocity (v) divided by the dominant frequency (f):

Equation 2.2.

$$\lambda = \frac{v}{f}$$

Typical exploration seismic wavelengths vary between 40 to 250 metres and tend to increase with depth, thus the deeper features must be thicker to be identifiable in the seismic data (Yilmaz, 2001). The vertical resolution is

marked by the limit of visibility, which is typically ¼ of the dominant seismic wavelength. This defines the potential to distinguish individual layers in the seismic data (fig. 2.4). If the layers are too closely spaced, i.e. less than the limit of visibility, the reflected seismic energy creates variable interference patterns (Veeken, 2007). Constructive interference, or tuning, occurs when positive reflections overlap and the signal amplitude is boosted as the rock layer thins (Sheriff and Geldart, 1995; Veeken, 2007). As layers become thinner, they get attenuated until invisible. Nevertheless, in some cases it is possible to detect layers within resolutions of $\lambda/30$, although their true thickness is not possible to determine (Sheriff and Geldart, 1995) (fig. 2.4). As such, despite the limitations of the seismic data, in certain circumstances it is possible to observe geological features below the resolution of the data.

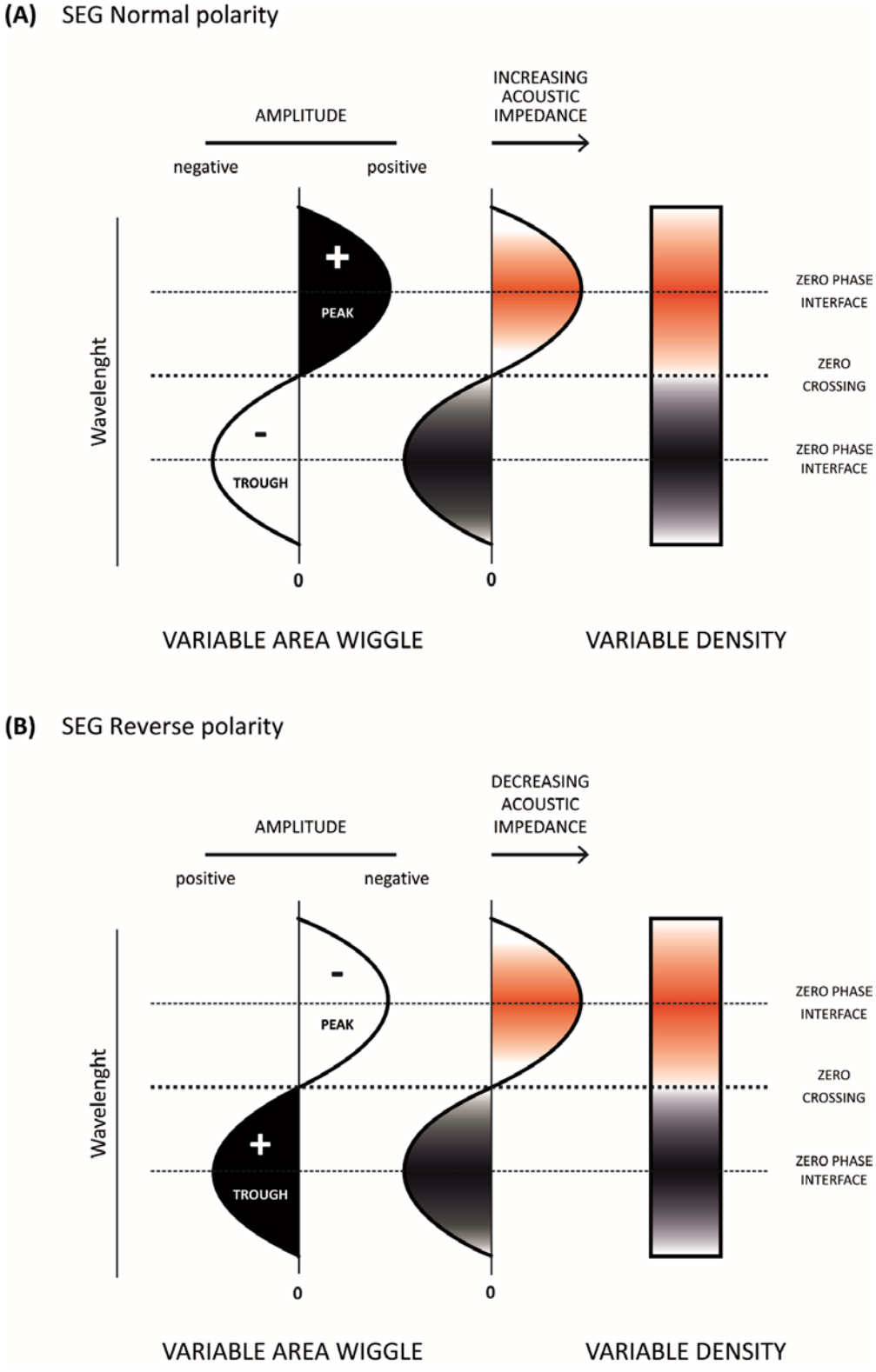

Figure 2.2. (A) Schematic representation of the seismic wavelet in SEG normal polarity zero-phased data. In variable area wiggle display, peaks are displayed in black and troughs in white. In variable density display, individual traces are represented as colour-coded voxels indicative of their amplitude. **(B)** Representation in SEG reverse polarity of zero-phase data (modified from Hart, 1999).

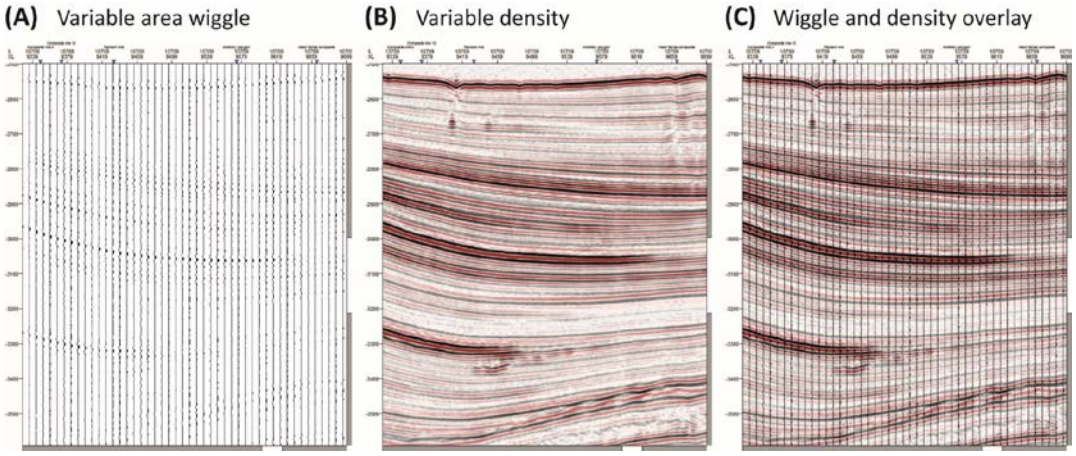

Figure 2.3. Examples of a seismic section both in variable area wiggle and variable density displays, with the latter type providing a clearer visualisation of data. Note the seafloor as a 'peak' of negative amplitude values characteristic of the SEG reverse polarity (seafloor is the first strong reflection detected, in black). (Seismic courtesy of PGS.)

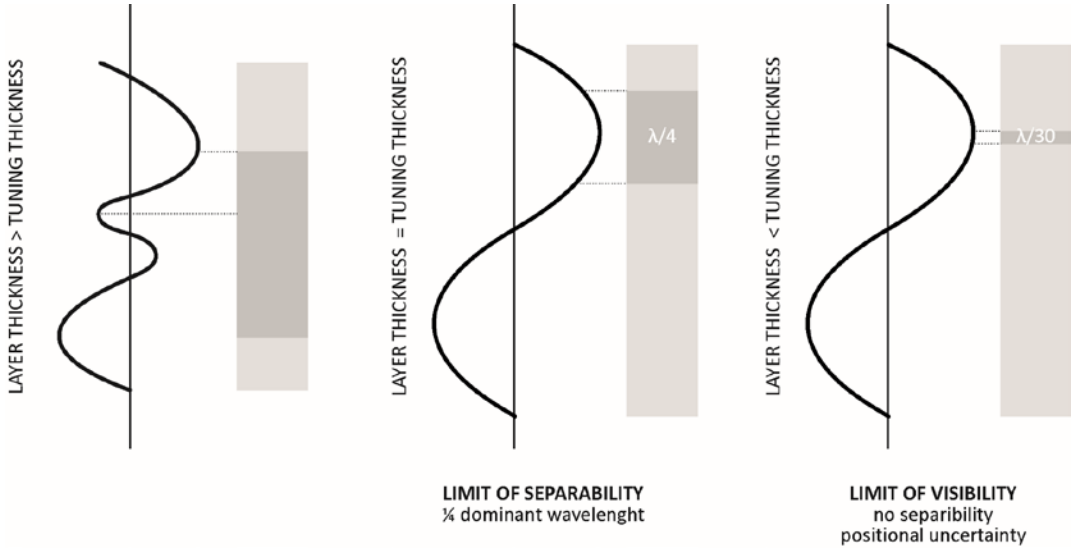

Figure 2.4. Effect of vertical resolution and tuning thickness. The resolution of the reflections from the top and bottom of a rock layer is dependant of the interaction between closely spaced wavelets (adapted from Brown, 2004).

The horizontal resolution refers to the minimal lateral proximity between two points still recognized as individual points rather than one (Yilmaz, 2001). Determining the horizontal resolution is complex due to the areal component involved in 3D seismic and has two main controls: the detector spacing and the intrinsic physical processes of the reflection (Kearey et al., 2002). The trace spacing normally ranges between 12.5 and 50 metres and influences the spacing of the individual depth estimates from which the reflector geometry is reconstructed (Kearey et al., 2002; Veeken, 2007). The other limiting control of the horizontal resolution is the size of the Fresnel Zone (fig. 2.5). The Fresnel Zone is a circular area defined by the energy returned to the hydrophone, within half a wavelength of the one initially reflected, that arrives in phase and interferes constructively to build up the signal at the reflection point (Bacon et al., 2003; Kearey et al., 2002). This depends on the depth of the reflector, the velocity above the reflector and the dominant frequency (Yilmaz, 2001). To improve the horizontal resolution of a seismic volume, data have to be migrated to correct the spatial location of the reflectors and focus the energy spread over the Fresnel Zone (Bacon et al., 2003; Brown, 2004). Smaller areas mean increased spatial resolution (Yilmaz, 2001). In perfect 3D migration, the Fresnelzone is reduced to a small circle with a radius of a quarter of the wavelength, but in practice the radius is only reduced to half of the wavelength (Brown, 2004).

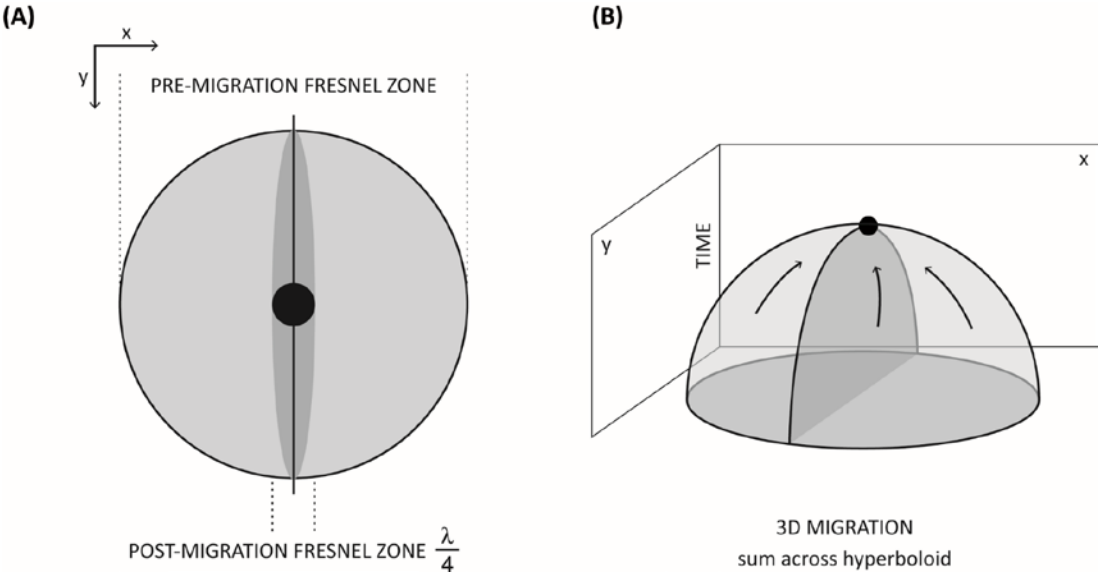

Figure 2.5. (A) Pre- and post-migration area of the Fresnel zone. In 3D seismic, the initial large circle is reduced to a smaller one with a radius of ¼ of the wavelength, represented by the black dot in the centre (modified from Brown, 2004). **(B)** Representation of data summation paths in 3D seismic processing (modified from Bacon et al., 2003).

2.1.2. 3D seismic volume visualisation and interpretation

A 3D seismic survey is a volume of data that represents the reflection coverage of each subsurface reflector within a certain surveyed area (Kearey et al., 2002). Each volume is made by a series of voxels that consist of smaller cubic units with specific dimensions (*x*, *y*, and *z*) and attribute values (Hart, 1999; Veeken, 2007). The 3D volumes can be manipulated in various ways by using interpretation workstations with high graphical processing capacity. Data can be visualised as seismic wavelets depicted as a series of continuous curves defining the amplitude peaks and troughs (fig. 2.3a). This has limitations in terms of its general overview and ease of interpretation. To overcome this limitation the data can be displayed in variable intensity mode, where each trace is displayed as a column of colour-coded voxels to display particular amplitude samples (fig. 2.3b) (Bacon et al., 2003). The data can be

visualised as 2D vertical sections following the survey's inline or crossline directions, or along any arbitrary path through the volume (fig. 2.6). Horizontal time-slices can also be obtained to display the patterns of reflections intersected by any time plane of constant two-way travel time (Hart, 1999; Kearey et al., 2002). Current seismic interpretation software packages allow an improved and simplified 3D display of the seismic data and interpreted data manipulation, greatly improving the understanding of the geological features represented.

The seismic interpretation process is fundamentally based on the manual and automatic pick of relevant reflections. In its early stages, seismic interpretation should be based on the definition of the structural and stratigraphic framework of the region by mapping major structures, unconformities and unit boundaries of the depositional sequences (Hart, 1999; Mitchum et al., 1977). The next step is the detailed analysis of seismic facies in relevant intervals based on the configuration, continuity and amplitude of the seismic reflections (Mitchum et al., 1977; Posamentier et al., 2007).

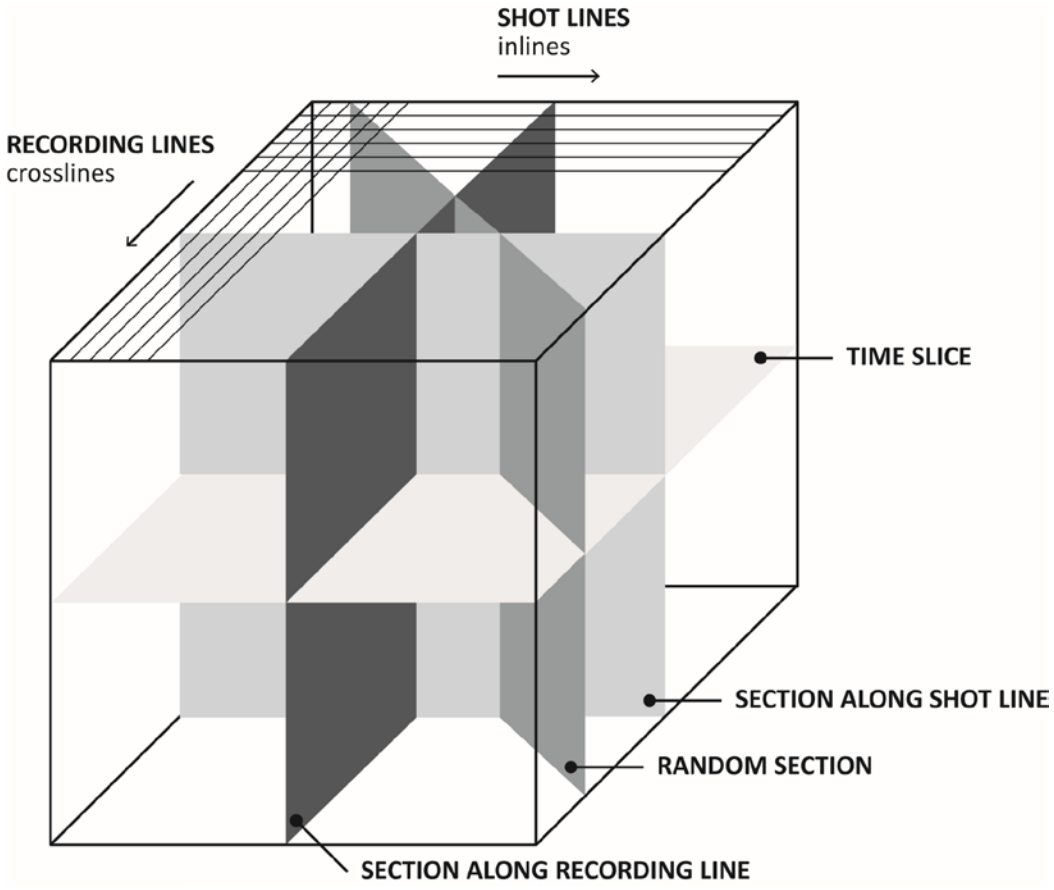

Figure 2.6. Diagram illustrative of a data volume. Vertical seismic sections can be taken through the volume in any desired direction, and (horizontal) time slices can be taken at any desired time depth (modified from Kearey et al., 2002).

The interpretation of the 3D seismic volume used in this thesis was made using Schlumberger's Petrel software. Horizon interpretation was based on picking reflections representative of stratigraphic interfaces. The initial mapping procedure consisted on a combined use of manual and 3D automatic tracking (autotracking) to pick reflections of interest in the seismic data. Manual horizon picking is started usually following the original inline and crossline directions to obtain a grid that covers its full area extent. 3D seismic data also allows the interpretation on specific line orientations defined by the user. The line spacing is defined by the interpreter and should be adapted to the complexity of the target reflection and the scale of the features of interest.

Automated tracking methods offer rapid interpretation results by picking reflection across the seismic survey from a user-defined seed point (fig. 2.7). This consists in a series of algorithm operations that automatically attempt to identify the seismic events with phase and amplitude identical to the manual seed points. This process is continued until no additional picks are identified or the user interrupts the process. The quality of the autotracking depends on data quality, geological complexity, and user-defined parameters and is prone to errors. It is imperative that the automatically obtained data is checked by the user and edited accordingly (see Hart, 1999).

Given the high-quality of the data available for this study, very reliable autotracked picks were obtained from initial stages of interpretation. After checking the quality of the automatic operation, manual picking was used to cover areas that needed careful interpretation or where the seismic signal did not allow autotracking. Manual interpretation was also the only method to map irregular surfaces in detail, such as the ones created by erosional processes. Surfaces were created from the interpreted horizons.

Surfaces create a grid populated with data points which is very useful to fill small data gaps or interpolate areas where autotracking is not suitable. Surface grids are based on the connection between the seed points following a choice of interpolation algorithms, disregarding any phase or amplitude properties. Surface objects have the advantage of being easier to manipulate and visualise, and are more versatile as inputs for models.

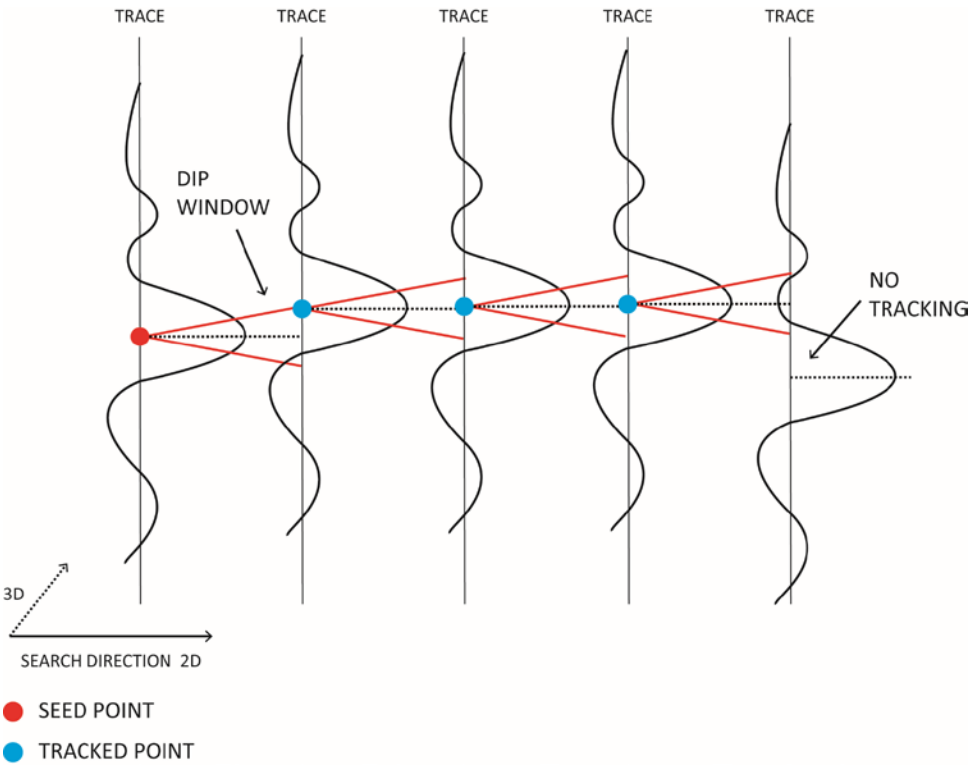

Figure 2.7. Diagram of the autotracking operation. The initial seed point sets the properties that the tracking algorithm will look for in the neighbouring trace. If a track point is found, it follows to the next trace. This operation works in 2 and 3 dimensions.

2.1.2.1. Interpretation of seismic facies

The interpretation of the stratigraphic features on the 3D seismic data is based on the grouping of reflection patterns with similar character. The analysis of the reflection termination patterns and their continuity allows the delimitation of discontinuities bounding individual seismic sequences and facies. Their geometry provides good indicators of the depositional processes that occurred in the studied basin (Mitchum et al., 1977; Posamentier et al., 2007). The features recognized on the 3D seismic dataset studied in this thesis show characteristic reflection geometries associated to specific seismic facies (fig. 2.8).

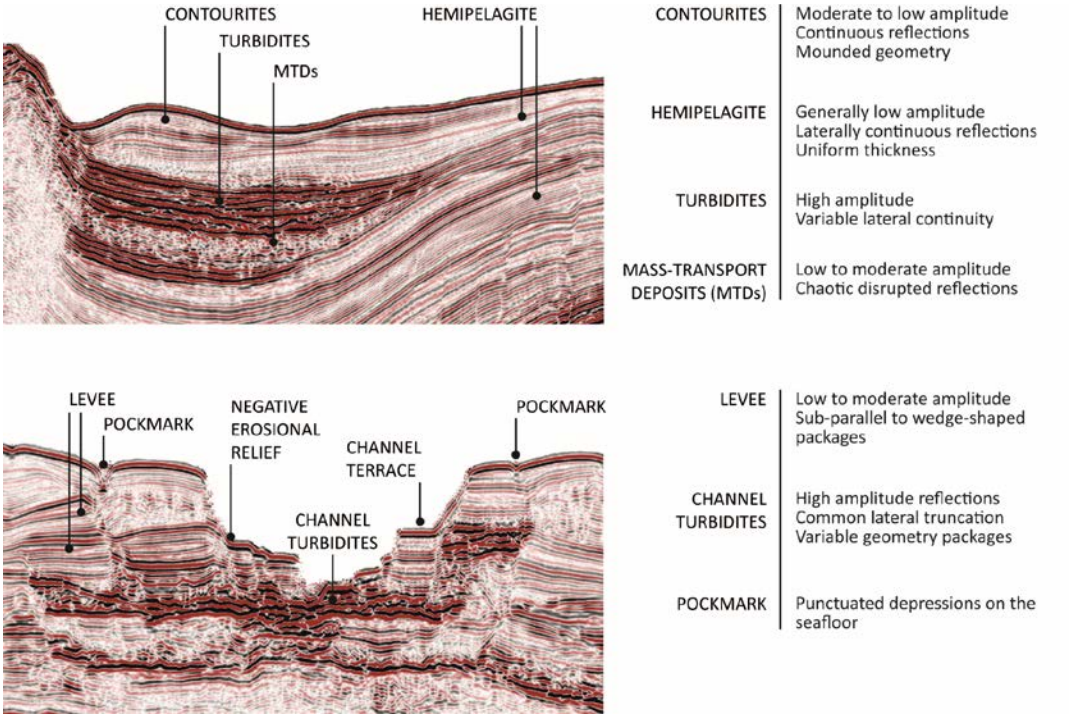

Figure 2.8. Seismic sections (SEG reverse polarity) showing examples of seismic facies observed in the study area. Description of typical seismic characters for each type of sedimentary deposit is on the right-hand side. Note that negative amplitude values are shown as red reflections in these profiles. (Seismic courtesy of PGS.)

Fine-grained sediments deposited on continental slopes commonly correspond to hemipelagites and contourites. These are characterised by seismic facies with laterally continuous, parallel to sub-parallel reflections with low to moderate amplitudes, occasionally high amplitudes (fig. 2.8). **Hemipelagites** tend to form deposits of relatively uniform thickness and high lateral extents that drape pre-existing morphologies (Stow et al., 1984). **Contourite deposits** show identical amplitude features to hemipelagites, but have characteristic mounded geometries (Hernández-Molina et al., 2008). Steeper angles and/or truncation of the reflectors and thicker accumulations are commonly observed closer to the focus of the bottom current (fig. 2.8.)

On seismic data, **turbidites** deposited in submarine lobes and fans are recognised by packages of laterally continuous, generally high amplitude

reflections (fig. 2.8). The termination of seismic packages representative of such deposits can be marked either by lateral thinning and pinch-out, or have abrupt terminations resultant from interactions with geomorphological structures or erosive flows (Weimer and Slatt, 2004).

Submarine canyons and **channels** are identified on seismic data by identifying V or U shaped erosional features (Mayall et al., 2006; Mitchum et al., 1977). The seismic facies of channel-fill deposits can be varied, but these are commonly characterised as moderate to high-amplitude reflections that onlap onto the channel margins (fig. 2.8) (Abreu et al., 2003; Clark and Cartwright, 2011; Mayall et al., 2006; Weimer and Slatt, 2004). Channel overbank deposits typically exhibit lower amplitudes, associated with the deposition of finer sediments (Deptuck et al., 2003; Mayall et al., 2006).

Mass-transport deposits (MTDs) can present various types of reflection configurations on 3D seismic data, bounded by top and base surfaces (Bull et al. 2009; Frey-Martínez et al, 2005). Regardless of their internal character, MTDs are underlain by a variable basal surface that can be planar, have irregular relief and/or present a stepped morphology. On map sections, these basal surfaces can show elongated scours of variable sizes (Gee et al., 2005; Weimer and Slatt, 2004). The MTD upper surface if generally irregular, but this aspect can be altered by the later erosion and reworking of sediment by channels or contour currents (Weimer and Slatt, 2004).

2.1.3. Seismic Attributes

Seismic attributes ate defined as quantitative measures of a seismic characteristic that provides additional information to the interpreter for better visualisation and quantification of relevant features on the seismic data (Chopra and Marfut, 2005). Seismic attributes are of great value when interpreting 3D seismic data as they provide increased detail of the stratigraphic and structural features. Several types of attributes are available in interpretation software packages. Attributes can be extracted from the seismic data either over defined time intervals or defined intervals within the volume. Time windows are created on flat levels based on a start and end time (or depth, in depth-converted volumes) value. Interval windows can be established based on a constant interval relative to a specific horizon or surface, or based on irregular intervals bound by two horizons (Brown, 2004).

There is a myriad of attributes available, each with specified appropriateness to the interpreters interest on structural, stratigraphic or rock properties (Brown, 2004). The attributes used in this thesis consisted of time-dip, amplitude, RMS amplitude and variance. The **time-dip** magnitude is a geometrical time-derived attribute that measures the horizon gradient changes by comparing the time value between adjacent points. The resultant dip maps are good indicators of the seismic horizon morphology, often highlighting subtle features at the limit of seismic resolution. The detailed morphology provided by time-dip maps aids on pockmark data collection from the horizons of interest.

Seismic amplitude is a fundamental attribute used in this research. It represents the positive or negative value measured at the crest of the reflection wavelet. On map view, the horizon amplitude patterns are prone to change due to lateral variations in acoustic impedance, which are ultimately related to changes in the lithological properties or fluid content along the horizon (Brown, 2004). Amplitude maps are extremely useful to identify stratigraphic facies variations, fluid-related amplitude anomalies and detect the distribution of faults. The amplitude extraction can be set to extract the minimum, average or maximum values within defined intervals (Brown, 2004). The **root-mean-square (RMS) amplitude** attribute shows the square root of average squared amplitude values from individual amplitude samples within a defined time interval (Brown, 2004). Common to amplitude attributes is the extraction of arbitrary time windows above or below a reference horizon within the stratigraphic interval of interest. Windows defined between two reference horizons have the advantage of constraining the analysis to the delimited interval without the interference of outside amplitude values.

Variance is an attribute calculated by comparing the dissimilarity between adjacent waveforms in a volume of continuity (normal reflections), converting it into a volume of discontinuity. The generated time-sliced volumes allows the visualization of geological discontinuities such as faults in great detail on map sections. These are often free of interpretation bias as the use of mapped horizons is not a requirement (Brown, 2004). The variance volumes are often computed and sliced using a flattened interpreted horizon as a reference. This has the advantage that all the features identified in the

variance slices are guaranteed to be at identical time gaps from the fixed datum, limiting the crossing of stratigraphic boundaries. Alternatively, variance attributes can be extracted along the original geometry of the horizon and within defined intervals. Variance attributes are crucial to assess the features and internal architecture of the stratigraphic units identified in the interpreted seismic dataset.

The use of the attributes described above is also complemented by **TWT-thickness maps**. These illustrate the time difference between the two reference horizons, providing detailed information on the thickness variation and lateral extent of specific intervals or features. TWT-thickness maps can be converted to true thickness maps when velocity information is available. The depth of specific reflections can be calculated through the equation below (eq. 2.3) when boreholes or seismic velocity functions are available. This can also be applied to limited intervals, as converting TWT-thickness maps to depth-thickness maps.

Equation 2.3.

$$D\ (m) = \frac{TWT\ (s)}{2}.V(m/s)$$

2.2. Dataset

The dataset for this study comprises a 3D seismic reflection survey from offshore Angola (West Africa), covering an area of approximately 9100km^2 in water depths ranging from 1400m to 2440m. Bin spacing is 12.5m in both inline and crossline directions. The near stack volume used to study the

subsurface displays an increase in acoustic impedance (hard reflection; negative amplitude) as black (fig. 2.3), whereas positive amplitudes characterise a decrease in acoustic impedance (soft reflections; red). Seafloor depth conversions are computed using a seismic velocity of 1500m/s for seawater. An average seismic velocity of 1680m/s was assumed for the shallow sediments (Bolli et al., 1978). The horizontal resolution is 25m (2x bin spacing).

The vertical resolution of the seismic data is estimated through the seismic velocities and the computed dominant frequency. Considering that the limit of detection resolution is about ¼ of the wavelength λ (Sheriff and Geldart, 1995; Veeken, 2007), a seismic velocity of 1680m/s for Unit 3 and average frequencies of 44Hz (seafloor) to 49Hz (horizon C4), vertical resolutions of circa 11 metres are estimated near the seafloor to 12 metres near the base of Unit 3. However, in certain circumstances it is possible to observe geological features below the resolution of the data.

Well data were not available from the study area. The lithological and chronostratigraphic framework of the region was based on information provided by ODP Leg 175 sites 1075-1077 (Pufahl et al., 1998), and by published works on the stratigraphy of the Lower Congo Basin (Andresen and Huuse, 2011; Anka et al., 2013; Gay et al., 2007; Hempton et al., 1990).

2.3. Quantitative analysis and spatial statistics

A significant part of this thesis presents quantitative data for the thousands of pockmarks and other geological features identified in the study area. The data acquisition was achieved through the combined use of Petrel, ArcGIS, and PAST software packages. Petrel was used for the seismic interpretation, primary identification of relevant features and data quantification. ArcGIS was used to acquire locations and morphological measurements of pipes and pockmarks, map faults (based on attribute maps exported to ArcGIS), and to perform statistical analysis of pipe and pockmark spatial distributions.

Two main types of pockmarks are observed in the study area: 1) seabed pockmarks, and 2) 'bulls-eye' pockmarks. Examples of these on seismic data are shown in figure 2.9. A detailed description of both types is done in Chapter 4. The method used to measure and assess pockmark morphology is shown in figure 2.10.

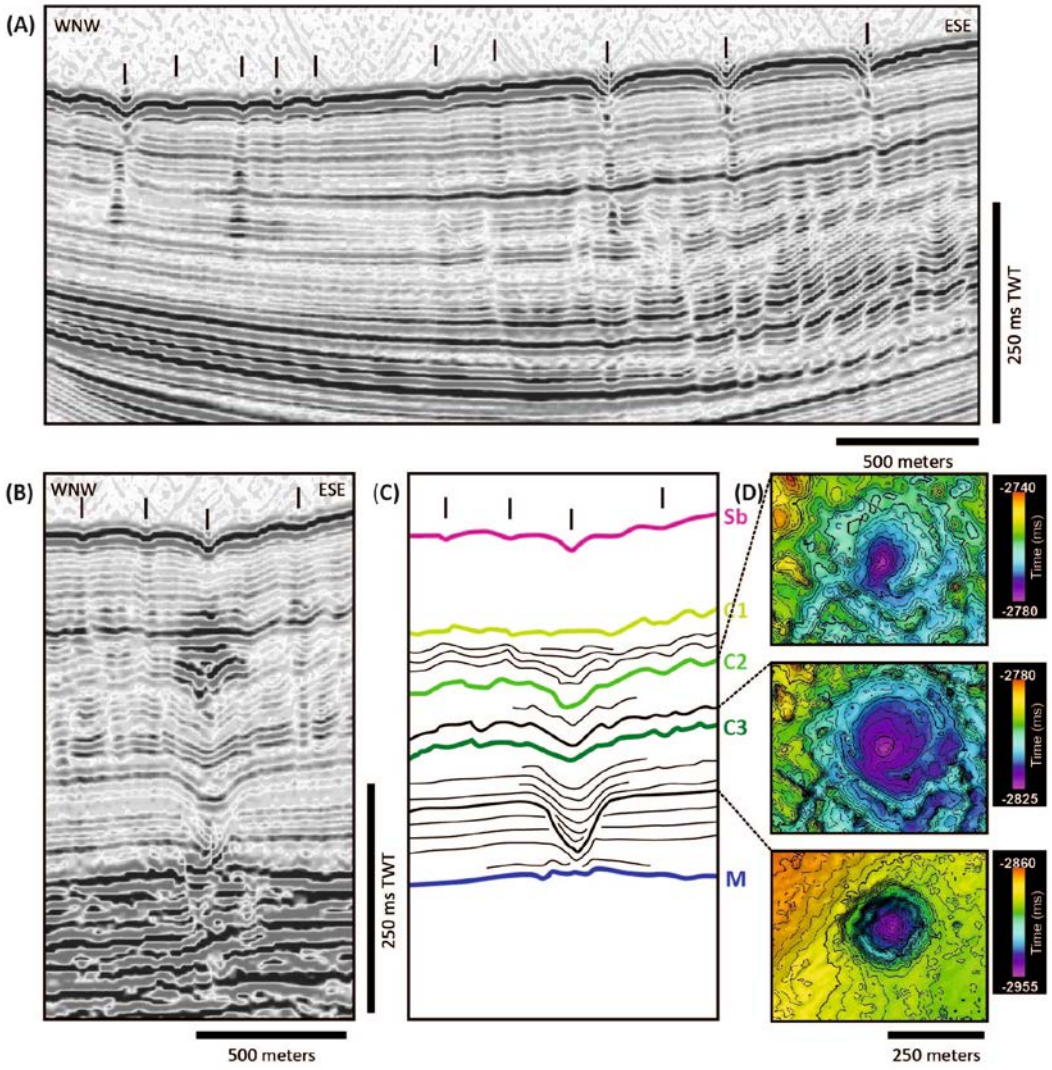

Figure 2.9. Seabed pockmarks and subsurface 'bulls-eye pockmarks' – seismic profiles and maps at event reflections. **(A)** Seismic section across mini-basin MB7, showing seabed pockmarks, feeding pipes and the polygonal fault system within Unit 3. Arrows point to seabed pockmarks. Within the pockmark depression, the seabed surface truncates underlying reflections, indicating erosion and sediment remobilisation that occurred during fluid expulsion. Location of seismic section is in figue 4.1A. **(B)** Seismic section intersecting a sub-surface 'bulls-eye' pockmark and several seabed pockmarks (black arrows) in mini-basin MB6. **(C)** Interpretation of seismic section shown in (B). Different events of fluid expulsion are represented by several distinct horizons truncating underlying reflections, which were posteriorly infilled by sediments, forming a vertically stacked array of pockmarks. **(D)** Maps of reflections within the 'bulls-eye' pockmark, showing its internal structure and variation with depth. (Seismic courtesy of PGS.)

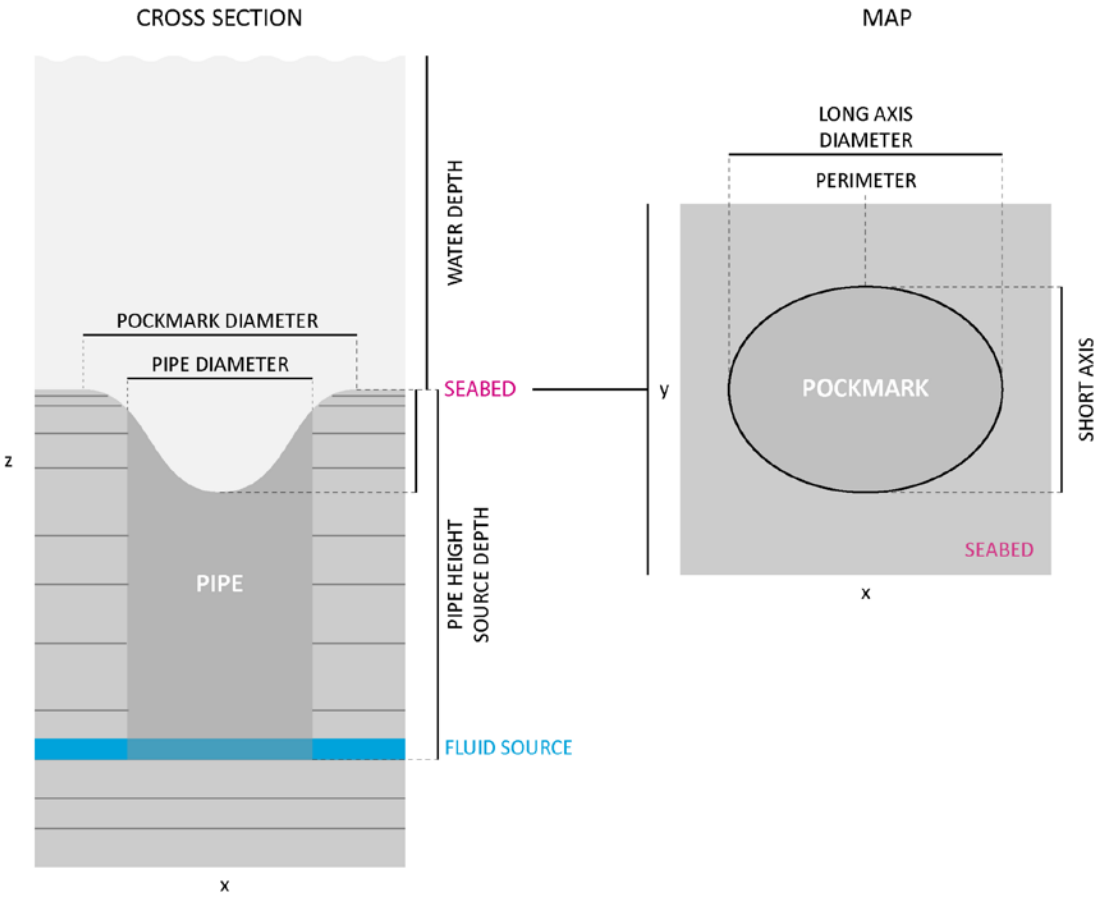

Figure 2.10. Diagram showing the morphological elements of seabed pockmarks and pipes that were measured for their quantitative analysis and spatial statistics

For all the spatial analysis presented in this work, the location of the centre of pipes and pockmarks is considered as a point with coordinates (x, y), which is a more convenient way to calculate statistics related to their patterns and to investigate what geological controls may be influencing their distributions. The distribution of points on a surface or map may be classified into three categories: uniform, random, and clustered (Davies, 2002). A pattern of points is said to be **uniform** if the density of points in any sub-area is equal to the density of points in all other sub-areas of the same size and shape (fig. 2.11a). The pattern is regular if the spacing between points repeats, as on

a grid. A **random** pattern can be created if any sub-area is as likely to contain a point as any other subarea of the same size, regardless of the sub-area's location, and the position of a point has no influence on the position of any other point (fig. 2.11b). In a **clustered** distribution the probability of occurrence of a point varies in some inverse manner with distances to pre-existing points (fig. 2.11c).

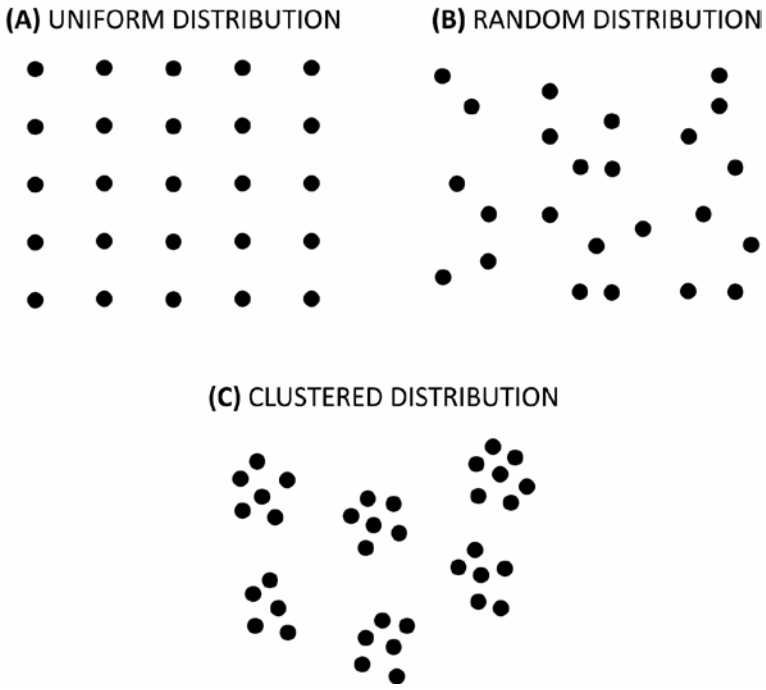

Figure 2.11. Representation of spatial distribution patterns. (**A**) Uniform distribution. (**B**) Random distribution. (**C**) Clustered distribution.

The spatial statistical significance of these distributions was analysed using the following univariate spatial autocorrelation statistical methods: 1) Average Nearest Neighbour (*Rn*), 2) Anselin Local Moran's I cluster and outlier analysis (I_i), 3) Ripley's K Multi-distance Spatial Cluster Analysis (*Ld*), and 4) Density.

The **Average Nearest Neighbour (*Rn*)** measures the ratio of the observed average distance between each feature centroid and its nearest neighbour's centroid location ($\overline{D}_{Obs}$) to the expected average distance based on a hypothetical random distribution with the same number of features covering the same total area. This method was used in Chapters 4, 5, and 6. The Average Nearest Neighbour ratio (Rn) is given as:

Equation 2.4.

$$Rn = \frac{\overline{D}_{Obs}}{0.5\sqrt{\frac{a}{n}}}$$

where $\overline{D}_{Obs}$ is the mean observed nearest neighbour distance, n is the number of pipes or pockmarks, and a is the areal extent of pipe or pockmark coverage in the study area.

If the average nearest neighbour ratio is less than 1, the distribution exhibits clustering (the nearer to 0, the more clustered the distribution). If the ratio is greater than 1, the pattern trends towards dispersion. A random distribution yields a ratio of 1. To reject the null hypothesis that there is no pattern of pipe or pockmark distribution, the Z score is calculated. The Z score is a test of statistical significance that evaluates the standard deviation away from the mean for a normal distribution of the nearest neighbour distances (Rn):

Equation 2.5.

$$Z = \frac{\overline{D}_{Obs} - 0.5\sqrt{\frac{a}{n}}}{SE}$$

Equation 2.6.

$$SE = \frac{0.26136}{\sqrt{n^2/A}}$$

SE is the standard error, and A is the areal extent of pipe or pockmark coverage in the study area. Very high or very low Z scores are found in the tails of the normal distribution, which indicates it is very unlikely that the observed spatial pattern is there by chance.

The **Anselin Local Moran's I cluster and outlier analysis (I_i)** uses a set of weighted data points to identify spatial clusters of points with attribute values similar in magnitude, and to detect spatial outliers. It is used in Chapter 4 to measure the spatial autocorrelation of pipe source intervals, i.e. whether pipes of a particular source are preferentially surrounded by pipes sourced either from the same or from a different interval. The Local Moran's I (Ii) statistic of spatial association is given as:

Equation 2.7.

$$Ii = \frac{n\sum_i \sum_j w_{ij}(x_i - \bar{x})(x_j - \bar{x})}{\sum_i \sum_j w_{ij} \sum_i (x_i - \bar{x})^2}$$

where n is the number of pipes indexed by i and j, x is the variable of interest or pipe source, $\bar{x}$ is the mean of x, and w_{ij} is a matrix of spatial weights. Pipes that are considered statistically significant outliers (pipes that have a statistically significant different source value from their neighbours) and clusters (pipes surrounded by others with a statistically similar source) have a local Moran's I (Ii) Z scores <-2 or >2, respectively. Pipes that are not statistically significant (i.e., that there is no spatial clustering of pipe source at the 95% confidence level) hold Ii Z scores between -1 and 1.

The **Multi-Distance Spatial Cluster Analysis** based on **Ripley's K-function** is a second order statistic that evaluates the spatial dependence (clustering or dispersion) of point data over a range of distances. This analysis was used in Chapters 4 and 6. The K function includes all neighbour points occurring within a given distance, rather than the distance to each point's single nearest neighbour. The analysis presented here implemented a transformation of the K-function referred to as *L(d)*:

Equation 2.8.

$$L(d) = \sqrt{\frac{A \sum_{i=1}^{n} \sum_{j=1, j \neq i}^{n} k_{i,j}}{\pi n (n-1)}}$$

where *d* is the distance, *n* is equal to the number of features, *A* represents the total area of the features and $k_{i,j}$ is a weight (either 1 if the neighbouring point is within the distance of the target point, or 0 if it is not). The *L(d)* method states that, given a random distribution of points, the expected value for any distance is the distance *(d)* itself (Mitchell, 2005). At any given distance, if the observed *L(d)* values are above the expected values, the distribution is more clustered than expected for a random distribution (fig. 2.12). Lower and upper confidence envelopes for a random distribution are generated to indicate a statistically significant clustered pattern at any given distance.

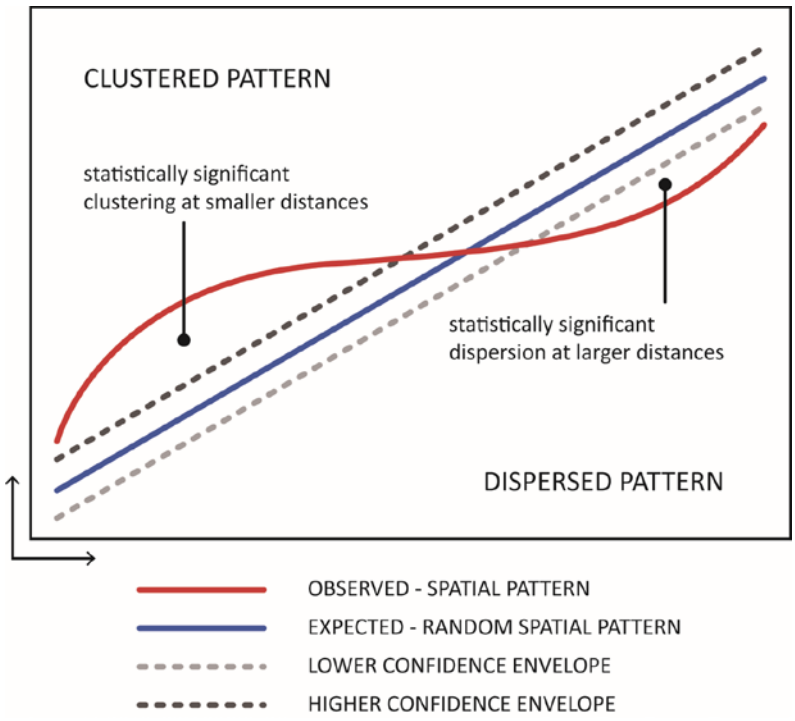

Figure 2.12. Measure of spatial clustering/dispersion over a range of distances (Ripleys's K-function).

To investigate the influence of linear geological features such as discontinuities, faults, and fractures on the distribution of pipes and pockmarks, it is crucial to identify the presence of linear patterns. For the detection of alignments, the method used in this thesis is built in the PAST software package (Hammer et al., 2001). PAST detects linear point alignments in 2D point patterns using the "continuous sector" method and tests their significance using the Rayleigh test for circular-uniform distribution. More detail on this method can be found in Hammer (2009). This method produces directional data that can be visualized on maps and plotted as rose-diagrams.

PAST software was used to detect pockmark alignments (in Chapters 4, 5, and 6), and to perform directional statistics for one (Rayleigh's test for uniform distribution) and two samples (Watson-Williams (equal mean)) and Mardia-Watson-Wheeler (equal distribution) tests). The Rayleigh's test for

uniform distribution calculates the value of the mean resultant length R using:

Equation 2.9.

$$\bar{R} = \sqrt{\left(\sum_{i=1}^{n} \cos\theta_i{}^2\right) + \left(\sum_{i=1}^{n} \sin\theta_i{}^2\right)}/n\,.$$

R is further tested against a random distribution using Rayleigh's test for directional data (Davis, 1986). Note that this procedure assumes evenly or unimodally (von Mises) distributed data; the test is not appropriate for e.g. bimodal data. The p values are approximated according to Mardia (1972):

Equation 2.10.

$$K = n\bar{R}^2$$

Equation 2.11.

$$p = e^{-K}\left(1 + \frac{2K - K^2}{4n} - \frac{24K - 132K^2 + 76K^3 - 9K^4}{288n^2}\right)$$

The Watson-Williams test examines the equal mean in two samples and is a robust parametric test. The concentration parameter K should be larger than 1 for test accuracy. The test also assumes similar angular variances (R values). The two samples φ and θ have *n1* and *n2* values. Rayleigh's spread R is calculated for each sample and for the combined sample:

Equation 2.12.

$$R_1 = \sqrt{\left(\sum_{i=1}^{n_1} \cos\emptyset_i\right)^2 + \left(\sum_{i=1}^{n_1} \sin\emptyset_i\right)^2}$$

$$R_2 = \sqrt{\left(\sum_{i=1}^{n_2} \cos\theta_i\right)^2 + \left(\sum_{i=1}^{n_2} \sin\theta_i\right)^2}$$

$$R = \sqrt{\left(\sum_{i=1}^{n_1} \cos\emptyset_i + \sum_{i=1}^{n_2} \cos\theta_i\right)^2 + \left(\sum_{i=1}^{n_1} \sin\emptyset_i + \sum_{i=1}^{n_2} \sin\theta_i\right)^2}$$

The test statistic U is computed as

Equation 2.13.

$$U = (n-2)\frac{R_1 + R_2 - R}{n - (R_1 + R_2)}$$

The significance is computed by first correcting U

Equation 2.14.

$$U = \begin{cases} \dfrac{U}{1 - \dfrac{K^2}{8} + \dfrac{1}{nk^2}} & R/n < 0.45 \\ \left(1 + \dfrac{3}{8k}\right)U & R/n < 0.95 \end{cases}$$

where $n = n_1 + n_2$. The p value is then given by the F distribution with 1 and n-2 degrees of freedom. The combined concentration parameter κ is the maximum-likelihood.

For a more detailed description and explanation of the methods of statistical analysis used in this thesis, the reader is referred to the user manuals of the software programmes ArcGIS (Esri) and PAST (Hammer et al., 2001).

Chapter 3

GEOLOGICAL SETTING AND SEISMIC CHARACTERISATION
LOWER CONGO BASIN, WEST AFRICA

3. Geological setting and seismic characterisation – Lower Congo Basin, West Africa

This chapter is divided into two sections: 3.1 Tectono-stratigraphic evolution of the Lower Congo Basin; and 3.2 Local geological setting. In section 3.1, it is summarised the general geological setting of the Lower Congo Basin. A more localised geological context of the study area is presented in section 3.2, combining information obtained from published literature and initial seismic interpretations (seismic stratigraphy and mini-basin structure). These interpretations are solely based on seismic data (see methods presented in section 2.1.2), as borehole data from the study area was not available for the work presented in this thesis. The case studies featured in the following chapters 4, 5, 6, and 7, are based on the interpreted seismic stratigraphy described here.

3.1 Tectono-stratigraphic evolution of the Lower Congo Basin

The Lower Congo basin is located on the West African passive margin (fig. 3.1) and developed from the Gondwana Breakup and opening of the South Atlantic Ocean.

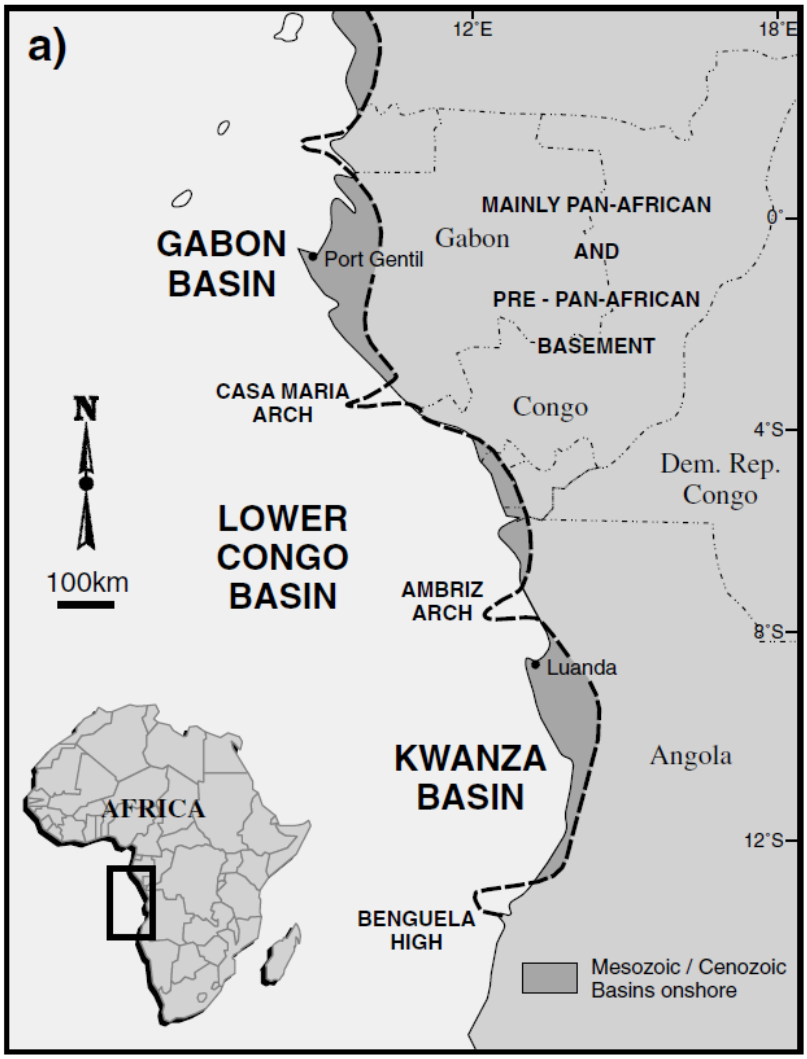

Figure 3.1. Generalised regional map showing the main basins offshore Angola (from Anderson et al., 2000).

The evolution of the West African margin initiated with early continental rifting during the Jurassic-Early Cretaceous which was followed by the onset of rifting and continental spreading during the Early Cretaceous (Brownfield and Charpentier, 2006; Hempton et al., 1990; Jolivet et al., 1984; Moulin et al., 2005). The syn-rift was marked by intense tectonic activity and formation of rift basins associated with the movement of the African and South American plates (Brownfield and Charpentier, 2006; Lentini et al., 2010). Early syn-rift rocks consist of fluvial and lacustrine sandstones and shales

deposited on a low-relief basin. Rift-related normal faulting led to increased lacustrine sedimentation within fault-controlled basins. These filled with continental conglomerates and sandstones; and lacustrine shales, limestones and marls (Brownfield and Charpentier, 2006; Evans, 1978). The extreme anoxic conditions in these lacustrine settings allowed the preservation of organic matter in extensive shale units (fig. 3.2), which constitute major source intervals for hydrocarbons, including the Bucomazi Formation (Burwood, 1999).

The syn-rift was followed by an Aptian transitional phase coincident with tectonic quiescence and cessation of fault movement, leading to a generalised smoothing of the margin. This event is marked by the bypass of the topographic barrier created by the Walvis Ridge and the supply of marine water to evaporitic basins in the rift valleys during the late Aptian (fig. 3.2) (Brownfield and Charpentier, 2006; Hempton et al., 1991). Massive salt units over 1000 m thick- the Loeme Salt- deposited in the Lower Congo Basin during four recognised evaporitic cycles (Anderson et al., 2000; Brownfield and Charpentier, 2006).

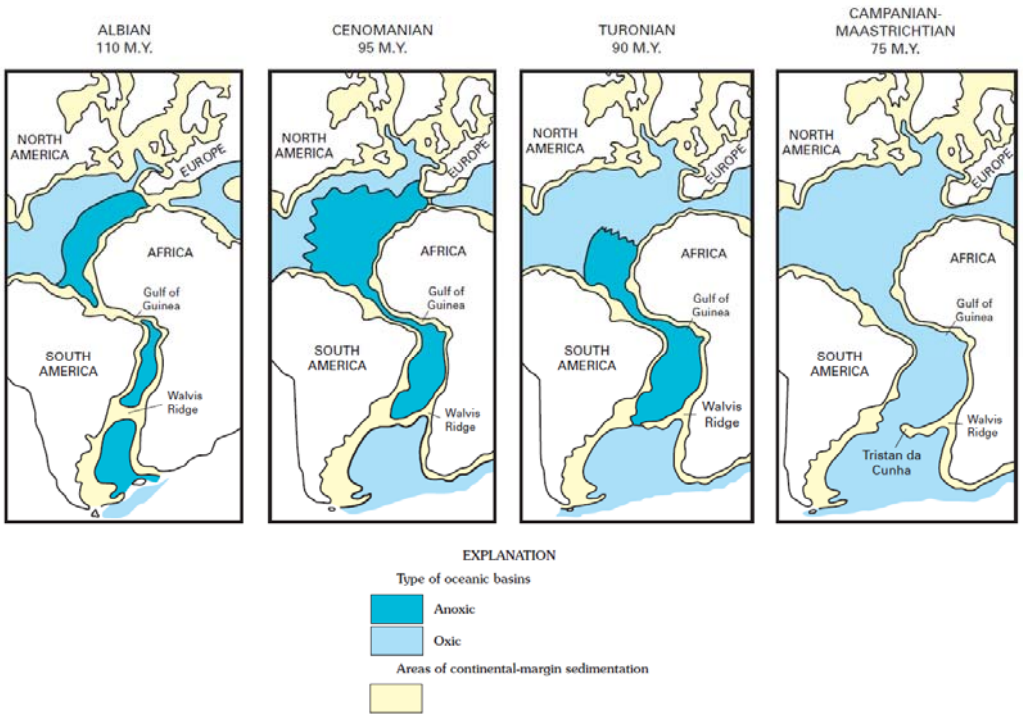

Figure 3.2 Evolution of the South Atlantic Ocean and separation of the African and South American Plates (from Brownfield and Charpentier, 2006).

Near the top of the evaporites the salt grades into regionally-extensive dolomites representative of fresh-water incursions in the basin resultant from changes in ocean circulation and climate (fig. 3.3). Thick ramp and shelf carbonates of the Pinda Formation were deposited along the margin during the Albian to Turonian time, overlaying the salt formations along the Angola margin (Duval et al., 1992; Fort et al., 2004). Thus, the basin exhibits a thin-skinned tectonic deformation style (fig. 3.4). Upslope domains are characterised by extensional Cretaceous rafts resultant from the fragmentation and movement of the carbonate platform over the salt units. Progressive raft extension and development of normal fault systems led to the development of roll0vers and extensional diapirs (Duval et al., 1992; Fort et al., 2004; Jackson, 1995; Rouby et al., 2005). The transitional domain is characterised by features such as passive diapirs that later were reactivated or included in the thrust

belts (Fort et al., 2004; Jackson et al., 1994). The distal slope is dominated by the compressional domain where elongated salt walls and canopies, fold-and-trust belts and compressional diapirs develop. The thick salt build-ups of the Angola Escarpment occur at the compressional domain, resultant from the late Cretaceous-Cenozoic salt 'squeezing' and downslope-flow driven by gravity and sediment loading (Brun and Fort, 2011; Hudec and Jackson, 2007; Jackson et al., 1994). The study area is located in the transition zone between these domains – the diapir domain – and it is characterised by salt walls or ridges of compressional geometry (Broucke et al., 2004), which define several NNE-oriented salt withdrawal mini-basins (fig. 3.5).

Post-Cretaceous sediments consist of a siliciclastic ramp that aggraded until the Early Oligocene in response to a stable hot climate with low-amplitude/high-frequency seal level changes (greenhouse period) (Rouby et al., 2003; Séranne, 1999). Within this post-salt interval, the deep marine mudstones and black shales of Upper Cretaceous and Paleogene ages (Iabe and Landana formations, respectively) are thermogenic oil and gas generating source rocks (fig. 3.3) (Burwood, 1999; Cole et al., 2000).

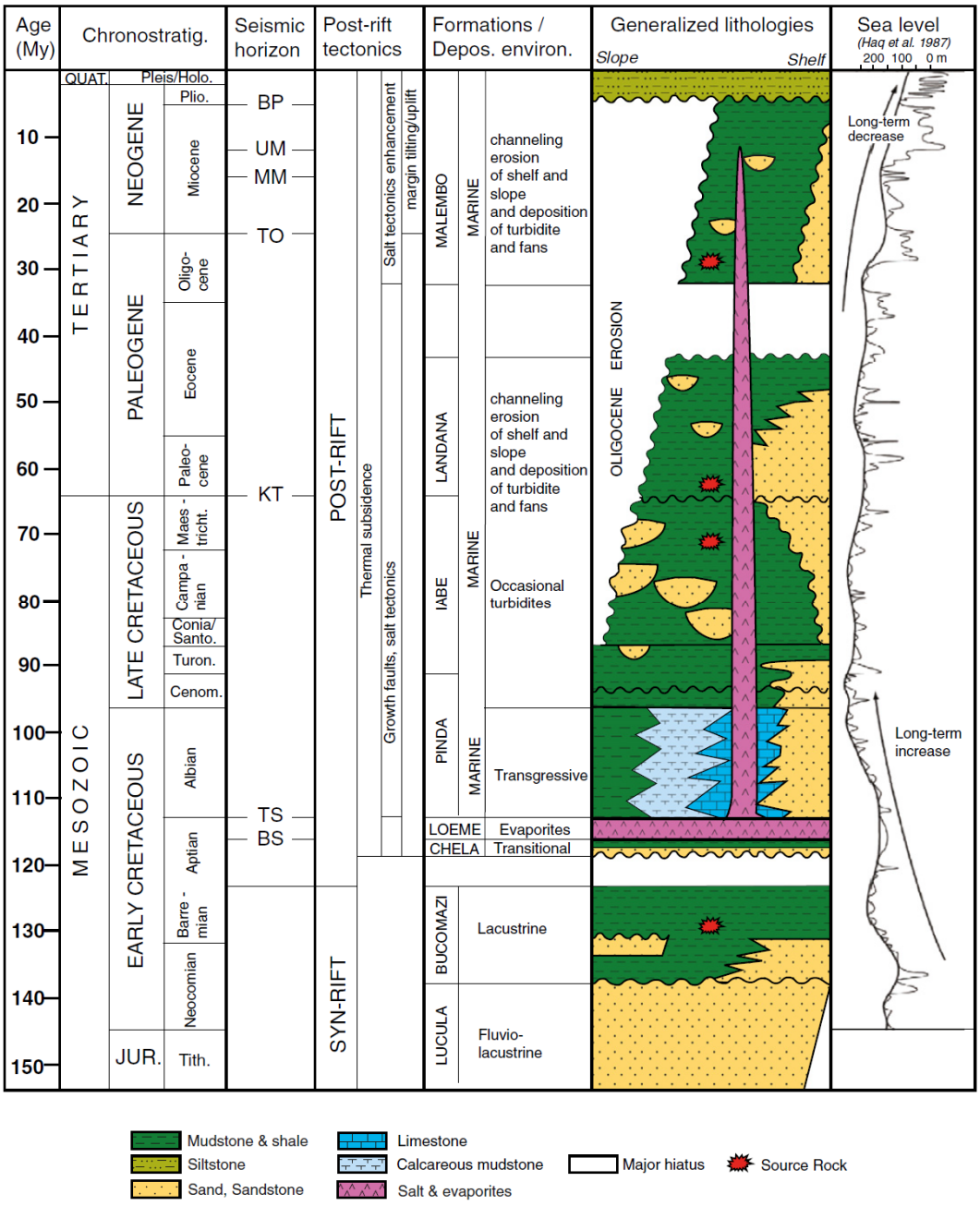

Figure 3.3 Stratigraphic column of the Angola margin (from Anka et al., 2009).

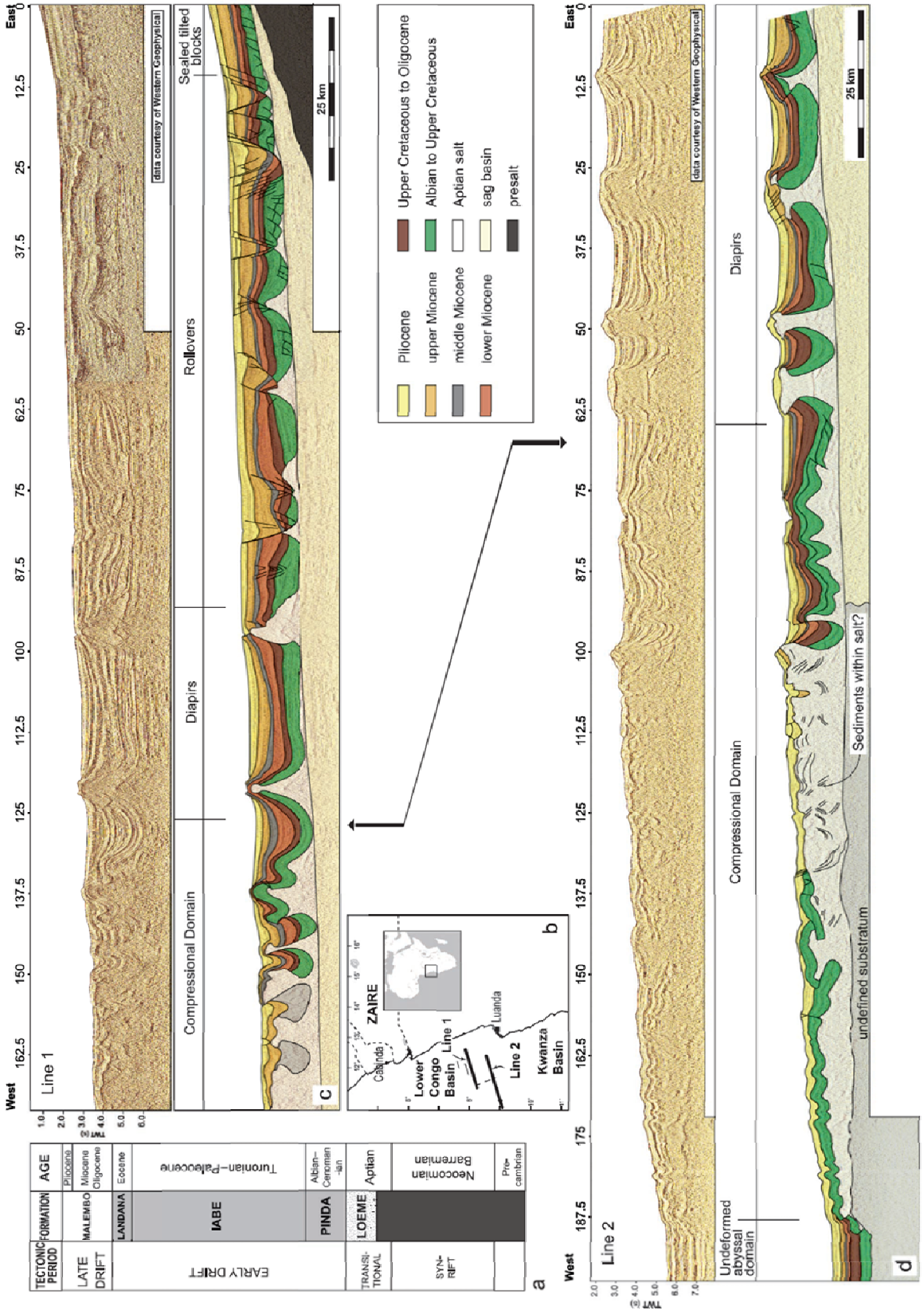

Figure 3.4. Regional sections of the Angola margin representing the three main salt domains and structural styles of each one (from Fort *et al.*, 2004).

The onset of the Antarctic glaciations and consequent global sea level fall produced the Early Oligocene erosional surface, with incision of deep canyons and submarine erosion of the slope (Séranne, 1999; Valle et al., 2001). Overlying this unconformity, a westward-prograding terrigenous wedge was developed during the Oligocene to Holocene, a period of alternating dry and wet climatic conditions and high-amplitude/high-frequency sea level changes (icehouse period). Enhanced continental erosion associated with margin uplift and westward tilting supplied clastic material for the deposition of the extensive Oligocene and Miocene turbiditic fan systems (Malembo formation), which constitute reservoirs for important oil and gas discoveries in the Lower Congo basin (Broucke et al., 2004; Brownfield and Charpentier, 2006; Cole et al., 2000; Coward et al., 1999).

Uplift of the West African margin occurred in the Early Miocene and was synchronous to rafting and tectonic processes. These strongly controlled sediment delivery and distribution in the deeper regions of the Lower Congo Basin, shifting the sediment depocentres northwards (Anderson et al., 2000; Anka et al., 2009; Kolla et al., 2001). Turbiditic mass flows were focused into local grabens, whereas mud-dominated intervals were deposited elsewhere (Anderson et al., 2000). Continued margin tilting led to the incision of the large Congo Canyon and gradual shift of its fan system towards the deep-sea (Anka and Séranne, 2004; Anka et al., 2009; Broucke et al., 2004). From the Early Pliocene onwards, the deeply-incised Congo Canyon confined and bypassed most of the coarse fraction of the sediments supplied to the slope. Consequently, the Pliocene to Holocene proximal succession in the Lower Congo basin (Cirques Formation, of Burwood et al., 1990) is characterised by

fine-grained hemipelagic sedimentation, generally considered as a sealing unit to the Oligocene-Miocene turbiditic interval.

Cores of the Early Pliocene-Holocene sequence retrieved at the Ocean Drilling Program Leg 175 (sites 1075-1079) and Deep Sea Drilling Project Sites 364 and 365 (drill sites closest to the study area) document enhanced biological productivity related to upwelling conditions (Berger et al., 1998; Bolli et al., 1978). These were established with the onset of the Benguela Current (Late Miocene – Pliocene) on the southwest African margin. The sediments are described as diatom- and nannofossil-rich clays and oozes from rain-out of suspended clays and pelagic settling of biogenic debris (Pufahl et al., 1998). Gas analysis from the cored sediments revealed high concentrations of microbial methane and carbon dioxide (10^3-10^5ppmv and 10^4-10^5ppmv, respectively), with no evidence of migration of deep thermogenic hydrocarbon gases (high C_1/C_2 ratios and absence of higher molecular weight hydrocarbons) (Meyers, 1998). High total organic carbon (TOC) concentrations (between 0.9 and 5.3wt%, average TOC ~2.5wt%) are interpreted to result from the combination of elevated palaeo-productivities and high sedimentation rates (between 10 and 60cm/m.y.), which improve preservation of the organic matter (Berger et al., 1998; Pufahl et al., 1998).

The Pliocene unit is pervasively affected by polygonal faults (Cartwright, 2011; Cartwright and Dewhurst, 1998). The formation of ubiquitous seabed pockmarks and furrows offshore Angola has been previously linked to these faults, and some authors consider that these discontinuities acted as fluid migration conduits (Gay et al., 2007; Gay et al., 2006). In some cases initial fluid expulsion episodes and pockmark genesis is

interpreted to precede the polygonal faulting process ('bulls-eye' pockmarks; Andresen & Huuse, 2011).

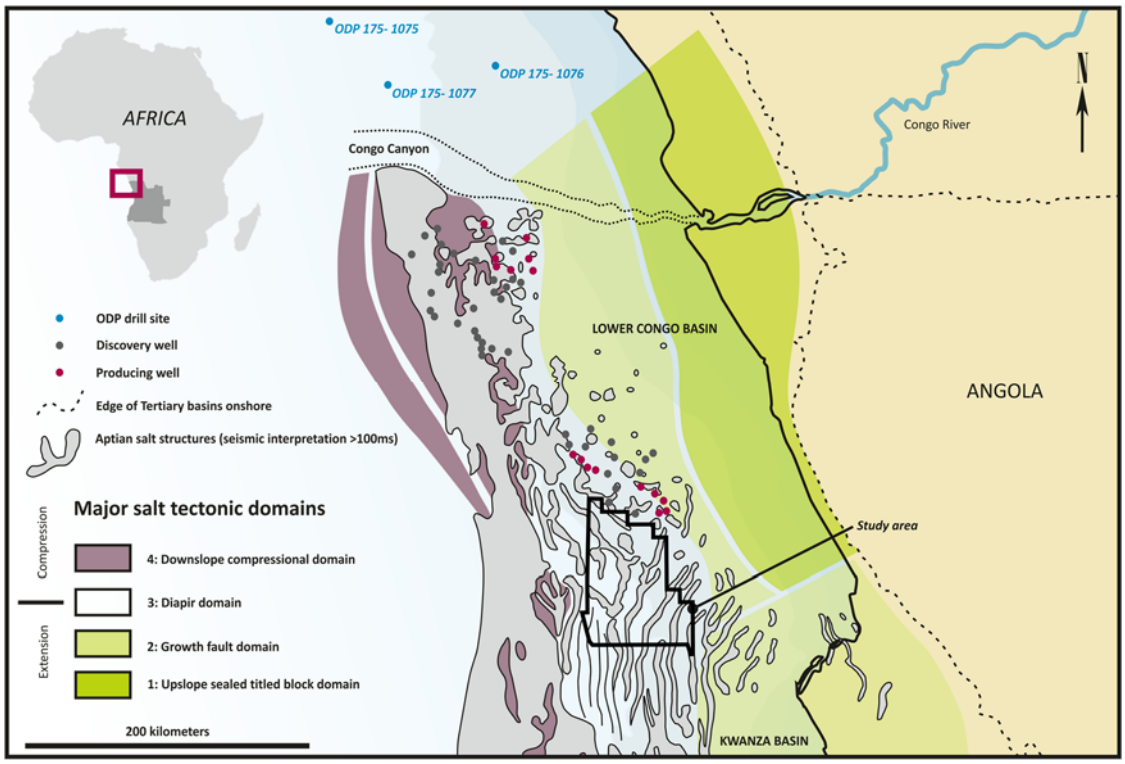

Figure 3.5. Regional map of the Lower Congo Basin and the Northern Kwanza Basin, depicting the main domains of salt tectonic deformation offshore Angola, ODP drill sites, and the location of known wells for the hydrocarbon exploration industry.

3.2. Local geological setting

3.2.1. General overview

The study area is located in the Lower Congo Basin, in the ultra-deep offshore of Angola, West Africa. Due to the confidentiality of the seismic data provided at the time of thesis submission, the author is not allowed to disclose the exact location of the survey. The surveyed region covers an area of c. 9100km^2, with water depths increasing from 1400m to 2440m depth following

a general southwest direction. Structurally, it is situated in the southern limit of the diapir domain of the Lower Congo Basin, correspondent to the transition zone between the upslope extensional and the downslope compressional domains described above (fig. 3.5). The area is characterised by extensive salt walls or ridges, which delimit numerous salt-withdrawal mini-basins (figs. 3.6 and 3.7). The orientation and geometry of the salt-withdrawal mini-basins is controlled by the flanking salt structures, and these constitute the major fairways for sediment transported to the lower slope. The seafloor expression of the salt structures is quite contrasting between the northern and southern areas (fig. 3.6). To the north, these have limited expression on the seafloor, consisting of a series of discontinuous diapirs and deep salt-cored anticlines that lead to the development of NW-SE oriented faults and localised grabens (fig. 3.6 section B). In contrast, the seafloor of the southern area shows very significant topography relief created by NE-SW oriented, continuous salt ridges bounding the mini-basins (fig. 3.6 section C).

The seafloor of the surveyed region covered with pockmarks, with at least 15167 observed on structural and dip maps of the area (fig. 3.6 and 3.8). Seabed pockmarks occur within a wide range of water depths (1600m to 2280m below sea-level). They are recognised as circular to elongated depressions related to erosion of underlying reflections, as seabed sediments are remobilised during pockmark formation. Pockmarks mostly occur within the salt mini-basins, but they can be also associated with salt structures (fig. 3.8. Pockmark frequency and density generally decrease as water depths increase (following a northeast-southwest trend), occurring sparsely in the southwest sector of the area (fig. 3.9). Pockmarks numbers associated with salt

and faults are markedly higher on the northern area over buried structures, contrasting with the low numbers occurring over the prominent ridges to the south. The seabed pockmarks and furrows generally lack seismically resolvable sediment onlap or infill.

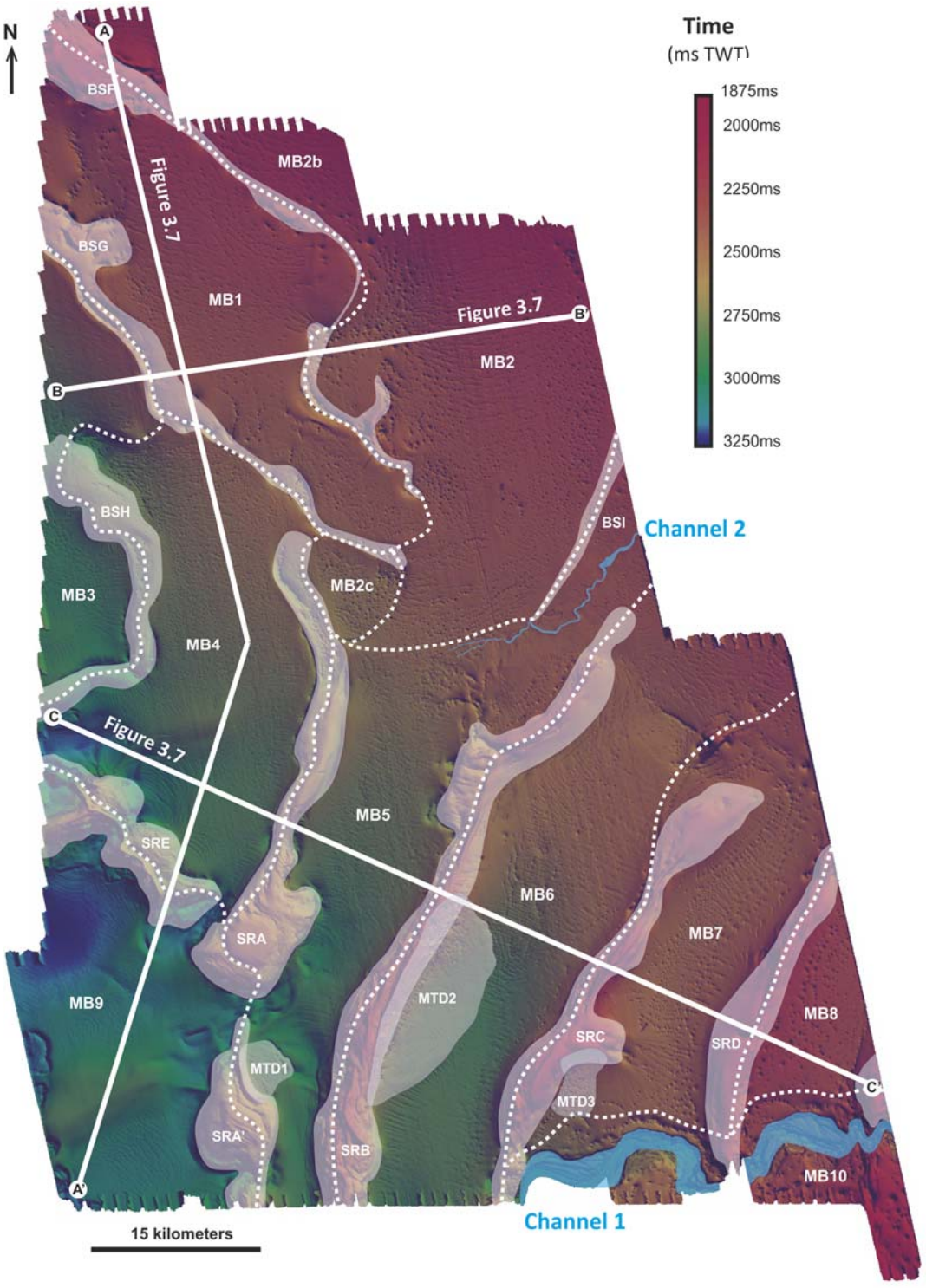

Figure 3.6. Time-structure map of the seafloor of the study area, highlighting the salt structures (white shadows) (SR = salt ridge; BS = buried salt structure) and limits of the mini-basins (dashed white lines; MB = mini-basin).

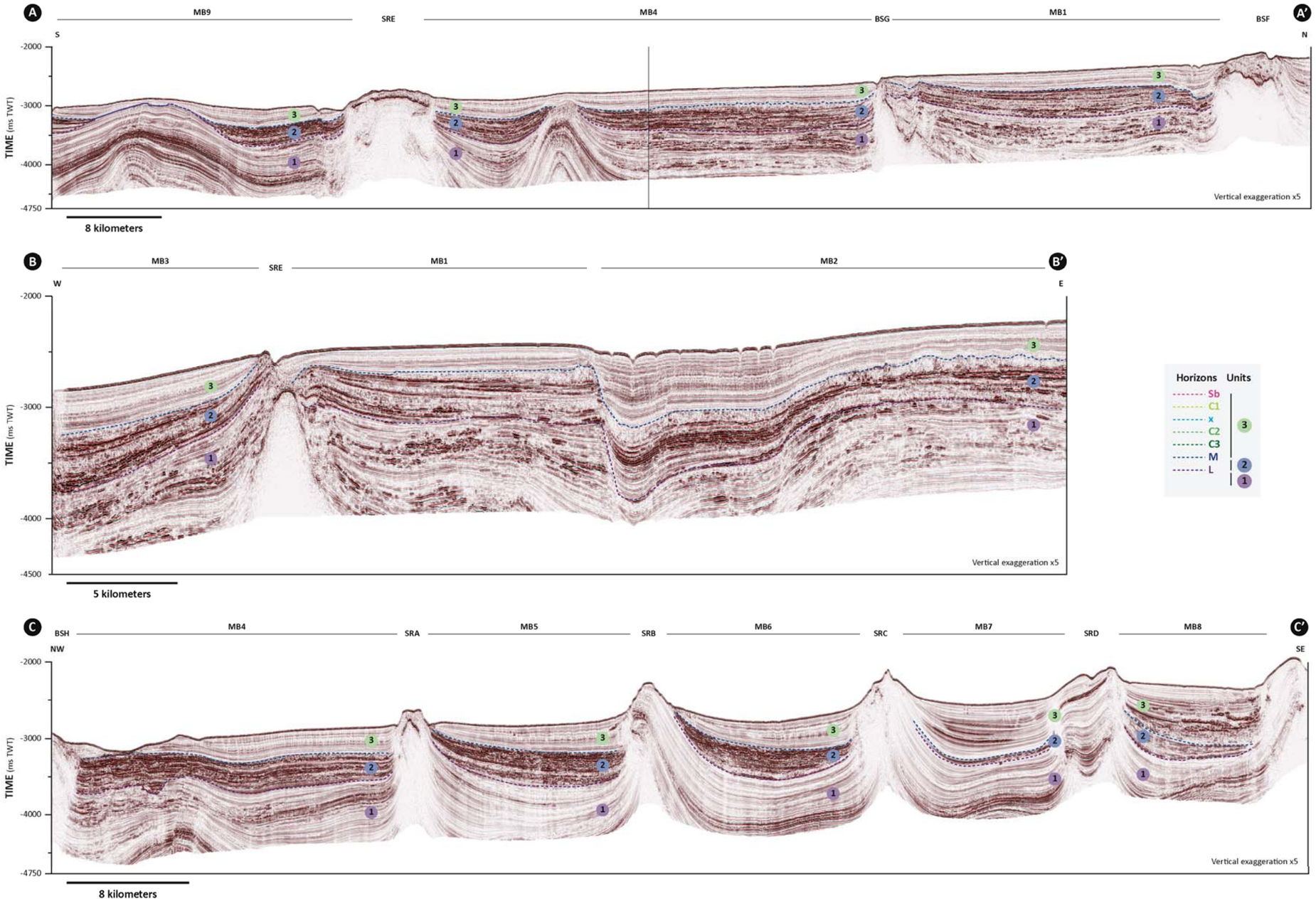

Figure 3.7. Regional seismic sections along and across the slope within the area covered by the seismic data. Cross-sections locations are shown in figure 3.6. The effect of rising salt ridges on the seafloor is well evidenced on section C. MB = mini-basin; SR = salt ridge; BS = buried salt structure; SD = salt diapir. Seismic sections locations in figure 3.6. (Seismic courtesy of PGS.)

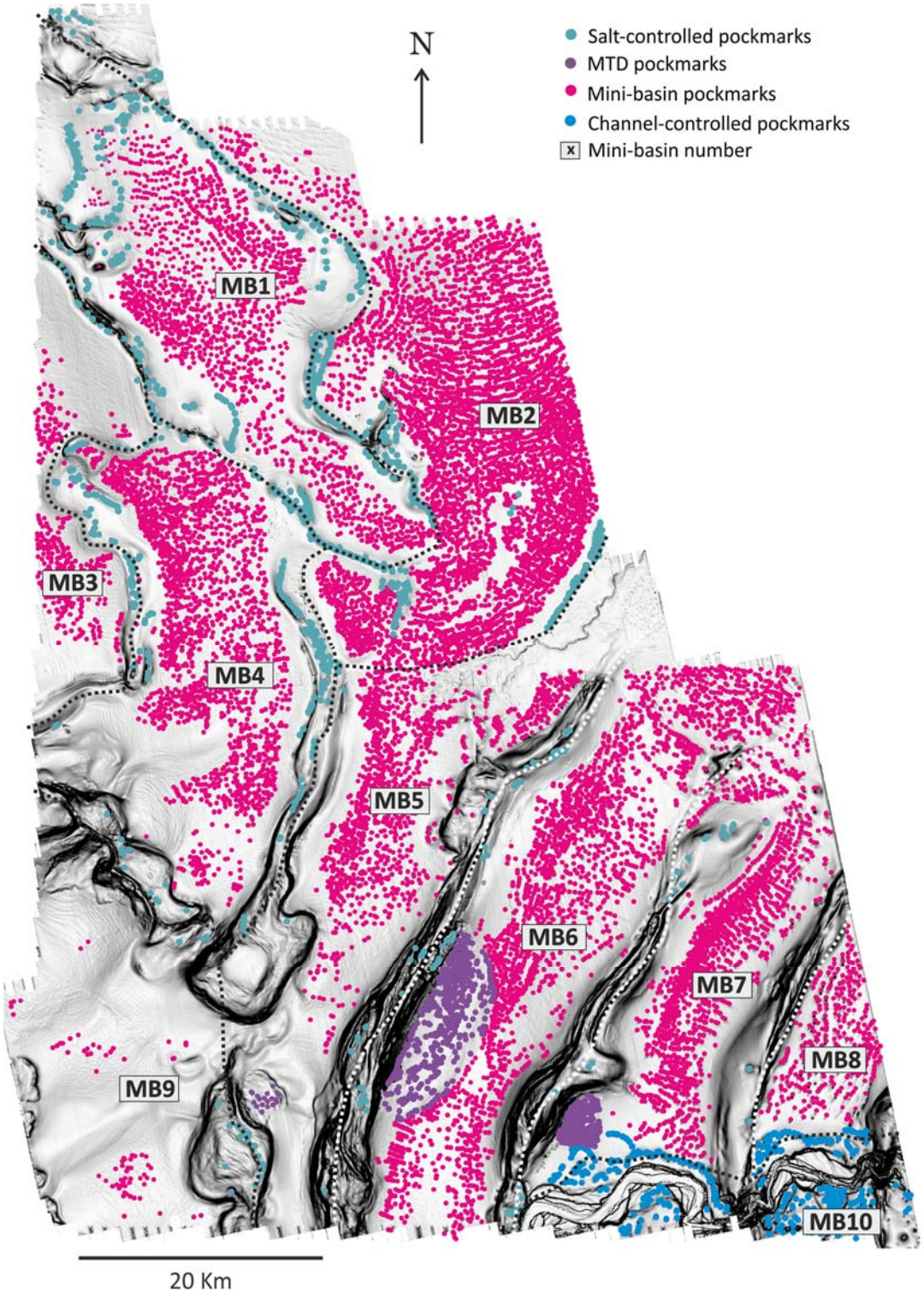

Figure 3.8. Seafloor dip map overlain with the locations of seafloor pockmarks identified in the area. Salt-controlled pockmarks = seabed pockmarks occurring above salt structures (not the focus of this thesis; described in Chapter 7); MTD pockmarks = seabed pockmarks occurring above mass-transport deposits (discussed in Chapter 5); mini-basin pockmarks = seabed pockmarks occurring within salt-withdrawal mini-basins (the main focus of this thesis; described in Chapters 4, 5, 6, and 7 for mini-basins MB2, MB6, and MB7); channel-controlled pockmarks = seabed pockmarks occurring above buried submarine channels (not the focus of this thesis; described in Chapter 7).

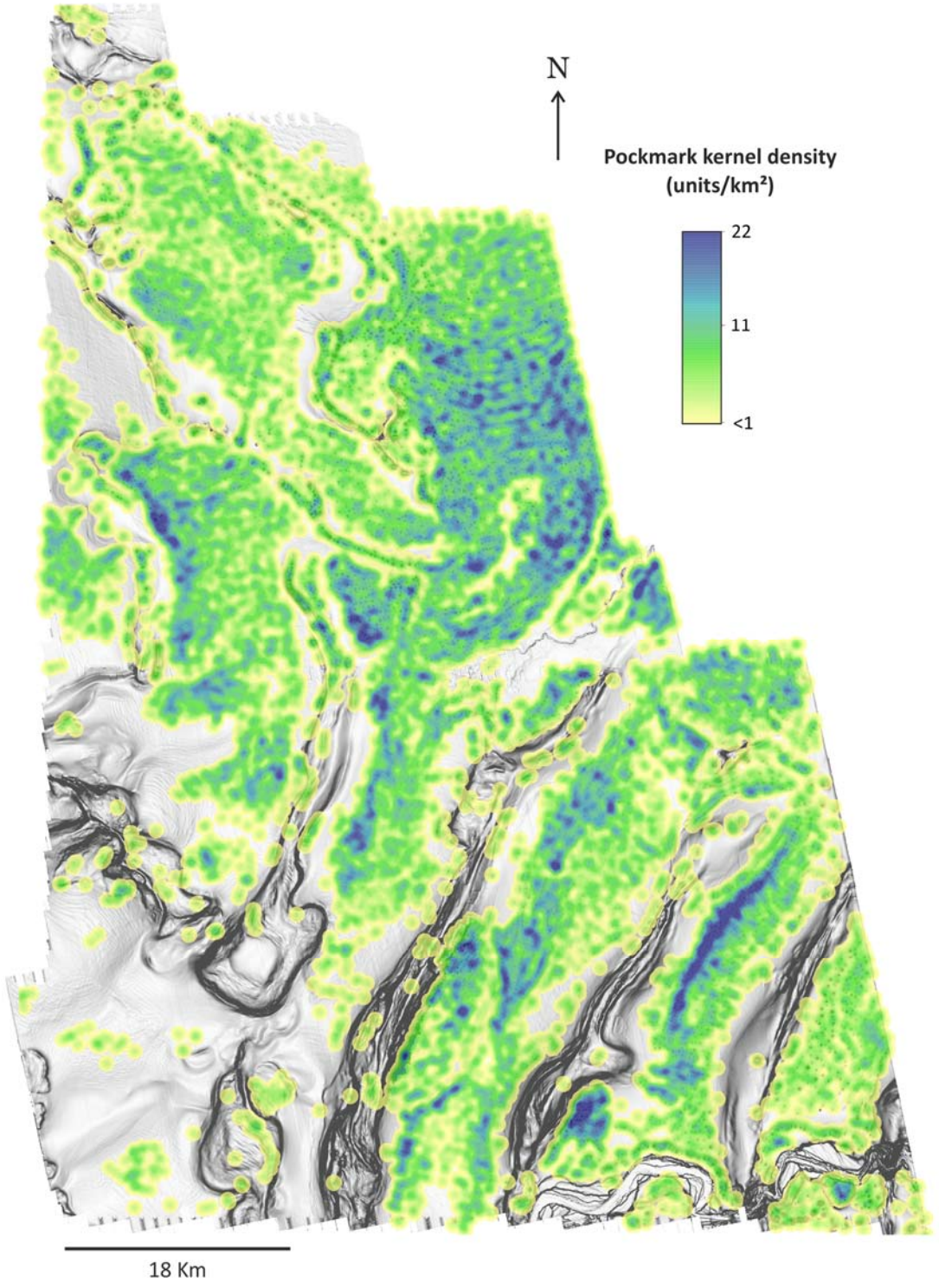

Figure 3.9. Density map of pockmark distribution in the mini-basins, overlaid on dip map of the seafloor.

Modern sedimentary features include mass wasting deposits, known here as mass-transport deposits (MTDs), flanking salt walls in the southern area, associated with slope failure due to salt growth. Two submarine channels are also identified on the present-day seafloor. The larger and more complex one (Channel 1, fig. 3.6) is located on the southeast-most corner of the surveyed area and flows along an east-west meandering path. This markedly erosive feature is about 200 to 300ms TWT deep (168 to 252m) and the most recent incision is 1000 to 2000m wide, bordered by a series of modern and buried terraces that form a wider channel belt exceeding 7000m. The smaller and younger unconfined submarine channel (Channel 2, fig. 3.6) is aggradational and is located in the central-east sector of the study area. It is levee-confined towards the northeast until it intersects the salt structure BSI, which forces a marked shift in its path. Downstream of this, the channel terminates as an unconfined frontal splay in mini-basin MB5 that variably interacts with, and infill some seafloor pockmarks. The morphology and path of both channels is strongly controlled by the topography imposed by the salt structures.

Due to its extensive size, the study area was sub-divided into ten sub-areas identified as MB1 to MB10 (fig. 3.6), according to salt mini-basin limits and distinct sedimentary domains. This sub-division allows a more detailed characterisation and geological interpretation of each sub-area.

3.2.2. Seismic stratigraphy

Sediment transfer to the lower slope is mainly focused along the salt-withdrawal mini-basins. The seismic stratigraphy of the study area is divided into three main seismic-stratigraphic Units: 1, 2, and 3 (fig. 3.10). The

stratigraphic interval of interest for this thesis covers the two shallowest seismic Units 2 and 3 (fig. 3.10), as the sedimentary and structural features embedded in these are interpreted control the distribution of the pockmarks and pipes that occur within the salt-withdrawal mini-basins and that are described in this thesis. The analysis presented in Chapters 4, 5, 6, and 7 is focused on the sediments <500m below the seabed. Thus, the term 'shallow' refers to stratigraphic levels and structures that occur in the upper 500m below the seafloor.

Units 2 and 3 correlate with the Oligocene – Miocene turbiditic sequence and the Pliocene – Holocene age, respectively. These units overlie deep marine sediments of Upper Cretaceous – Paleocene age (Unit 1). TheThe contact between the three seismo-stratigraphic units is commonly expressed by strong vertical variations on seismic amplitude and reflection geometry (figs. 3.7 and 3.10). The boundaries often correlate to erosive unconformities associated with different stratigraphic architectures, but in place these are less obvious and show as paraconformities on the seismic data. This is more obvious in MB7 where the lack of high-amplitude reflections from Unit 2 reflects the impact of salt structures on sediment routing in the study area (Oluboyo et al., 2012).

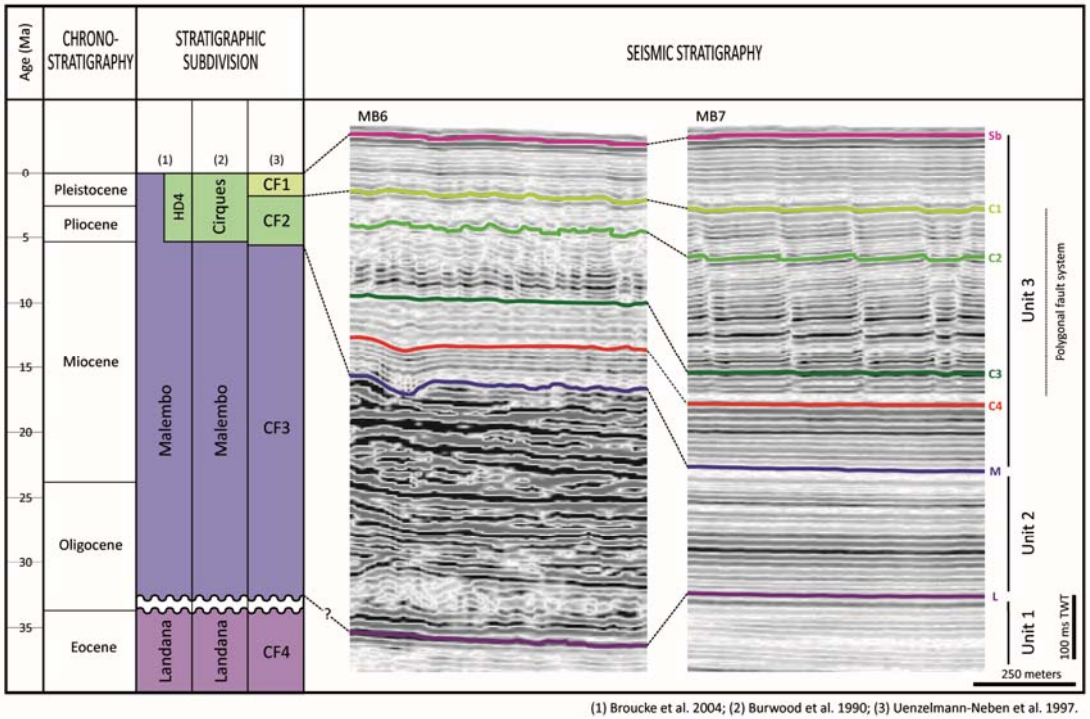

Figure 3.10. Seismic stratigraphic diagram with the relative age and seismic character of interpreted Units. (Seismic courtesy of PGS.)

Unit 1

Unit 1 is characterised by lateral continuous, sub-parallel to parallel reflectors of very low to moderate amplitude (figs. 3.7 and 3.10), which is mostly associated with fine-grained deposits. Occasional reflectors of higher amplitude may indicate deposition of coarser sediments. Local wavy reflectors of low sinuosity represent sediment waves with upslope migration. This unit is interpreted to comprise hemipelagic deposits intercalated with minor turbiditic lobes and spare contourite drifts, confined within the mini-basins. The contact with Unit 2 above is an erosional unconformity.

Unit 2

Unit 2 corresponds to the Malembo Formation and it is estimated to be Oligocene to Miocene in age (figs. 3.7 and 3.10). It sits unconformably above the Upper Cretaceous to Paleocene unit, and its top coincides with the middle

Miocene unconformity (Brownfield and Charpentier, 2006; Hempton et al., 1991). Seismically, Unit 2 is characterised by sub-parallel to chaotic reflections of moderate to very high amplitude. It is generally thicker along basin depocentres/axis, thinning and onlapping towards the flanking salt structures (fig. 3.7). Moderate to low amplitude chaotic reflections present at the bottom of this unit are associated with mass-transport deposits which are intercalated with thin laterally continuous turbidites (high amplitude reflections). The top succession of Unit 2 exhibits continuous high to very high amplitude reflections related to axial submarine channels and less confined clastic deposition (including channel levees), interbedded with hemipelagic intervals (fig. 3.7).

Unit 3

The shallowest Unit 3 contrasts significantly to Unit 2 described above. Its base is inferred to be late Miocene to early Pliocene in age (Brownfield and Charpentier, 2006) and its top coincides with the present-day seafloor. Unit 3 is characterised by laterally continuous and parallel reflections of very low (often transparent) to moderate amplitude, representative of predominant fine-grained hemipelagic deposition (fig. 3.7). Reflections of slightly higher amplitude in this succession may be associated with deposition of coarser grain size material (Gay et al., 2007), possibly related to laterally continuous turbidites and local channels. Four key horizons were mapped within Unit 3 (**C1**, **C2**, **C3** and **C4**; see fig. 3.10) for the analysis undertaken in this thesis (figs. 3.11 to 3.14). These highlight variable geological features, of which tectonic and polygonal faults are of key relevance. Local slope failures are observed adjacent to salt structures, especially on the shallower half of the

interval. Unit 3 exhibits two main thickness trends between the northern and southern areas. These are represented in Figure 3.15 by the isochron map between the seafloor and horizon C4, located close to the base of the unit. To the south, maximum thicknesses are observed close to the axis of the mini-basins and thins towards flanking salt structures (fig. 3.15, exhibiting onlapping reflection configurations (fig. 3.7). This lateral thinning can be symmetric, as in MB7, or markedly asymmetric. On the northern domain, the thickness of Unit 3 is lower near the axis of the mini-basins and increased towards the salt structures, often creating significant localised thickening within grabens (fig. 3.15).

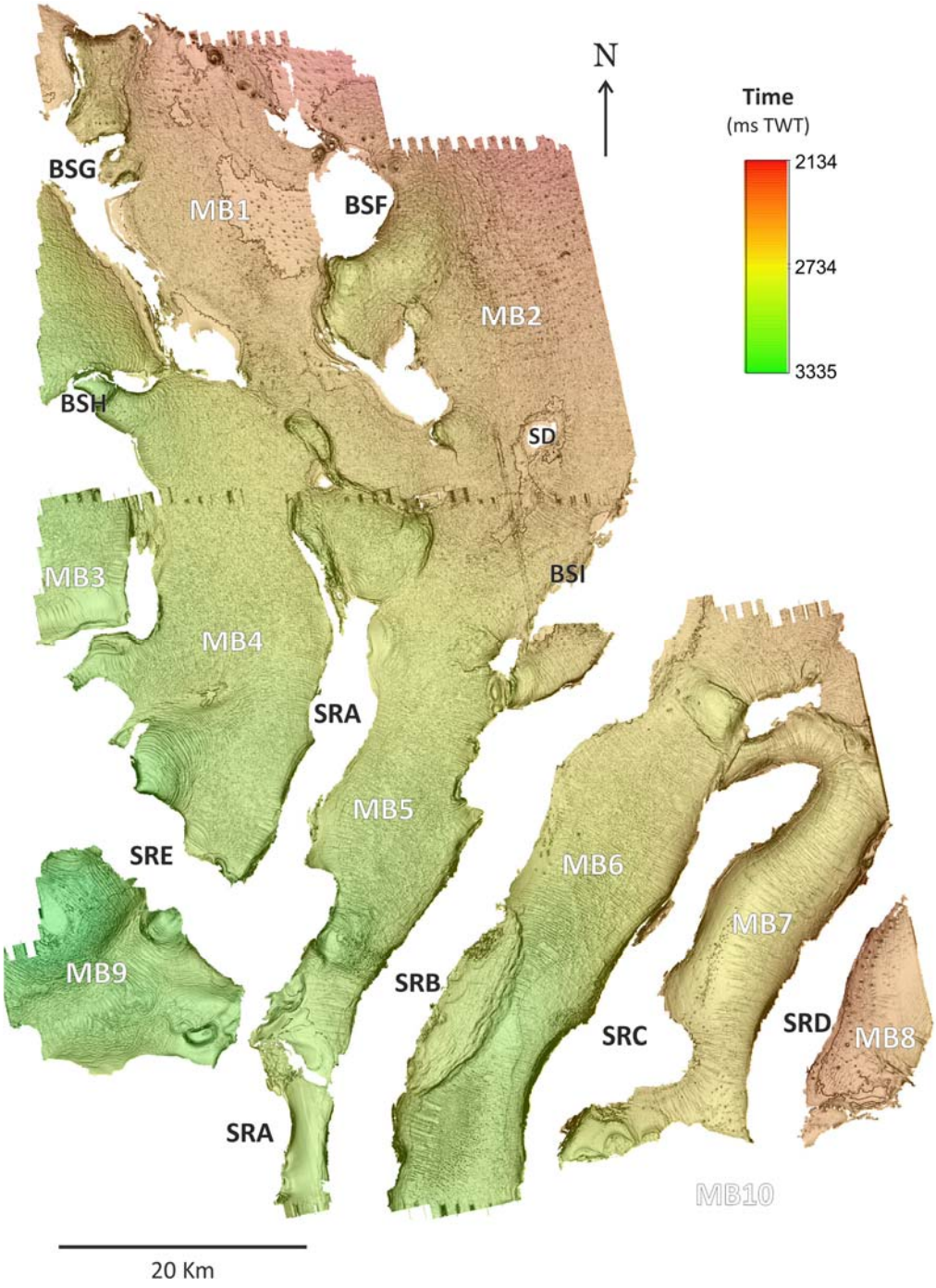

Figure 3.11. Regional time-structure map of horizon **C1**. This horizon is interpreted as the top of the polygonal fault tier, within Unit 3. Variable fault patterns are observed in each mini-basin. Typical polygonal fault patterns occur in the central regions of the mini-basins. Polarised polygonal faults developed perpendicularly to the salt structures in the regions adjacent to these. MB = mini-basin; SR = salt ridge; BS = buried salt structure; SD = salt diapir.

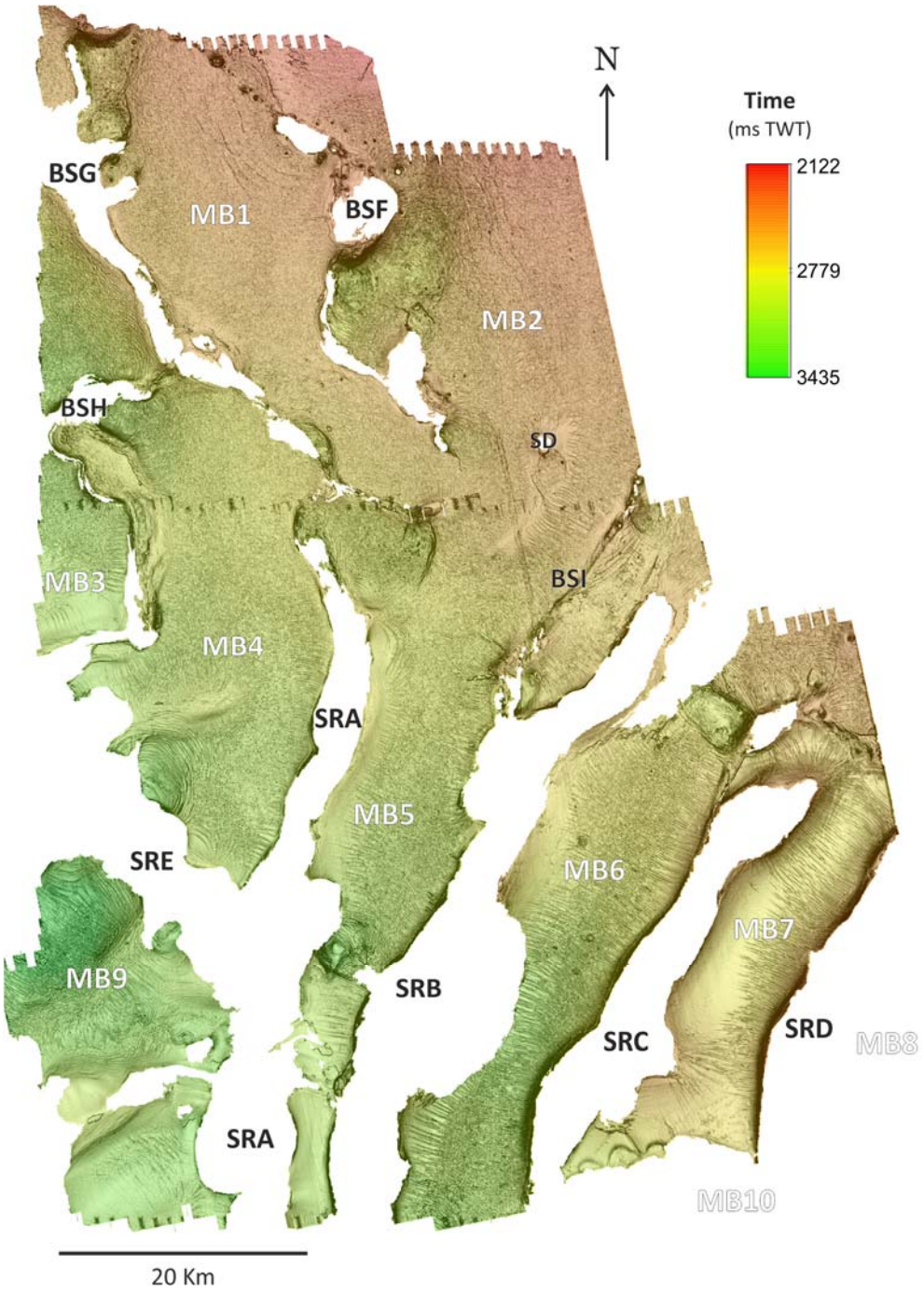

Figure 3.12, Regional time-structure map of horizon **C2**, occurring in the middle of the polygonal fault tier (Unit 3). Variable fault patterns are observed in each mini-basin. Typical polygonal fault patterns occur in the central regions of the mini-basins. Polarised polygonal faults developed perpendicularly to the salt structures in the regions adjacent to these. MB = mini-basin; SR = salt ridge; BS = buried salt structure; SD = salt diapir.

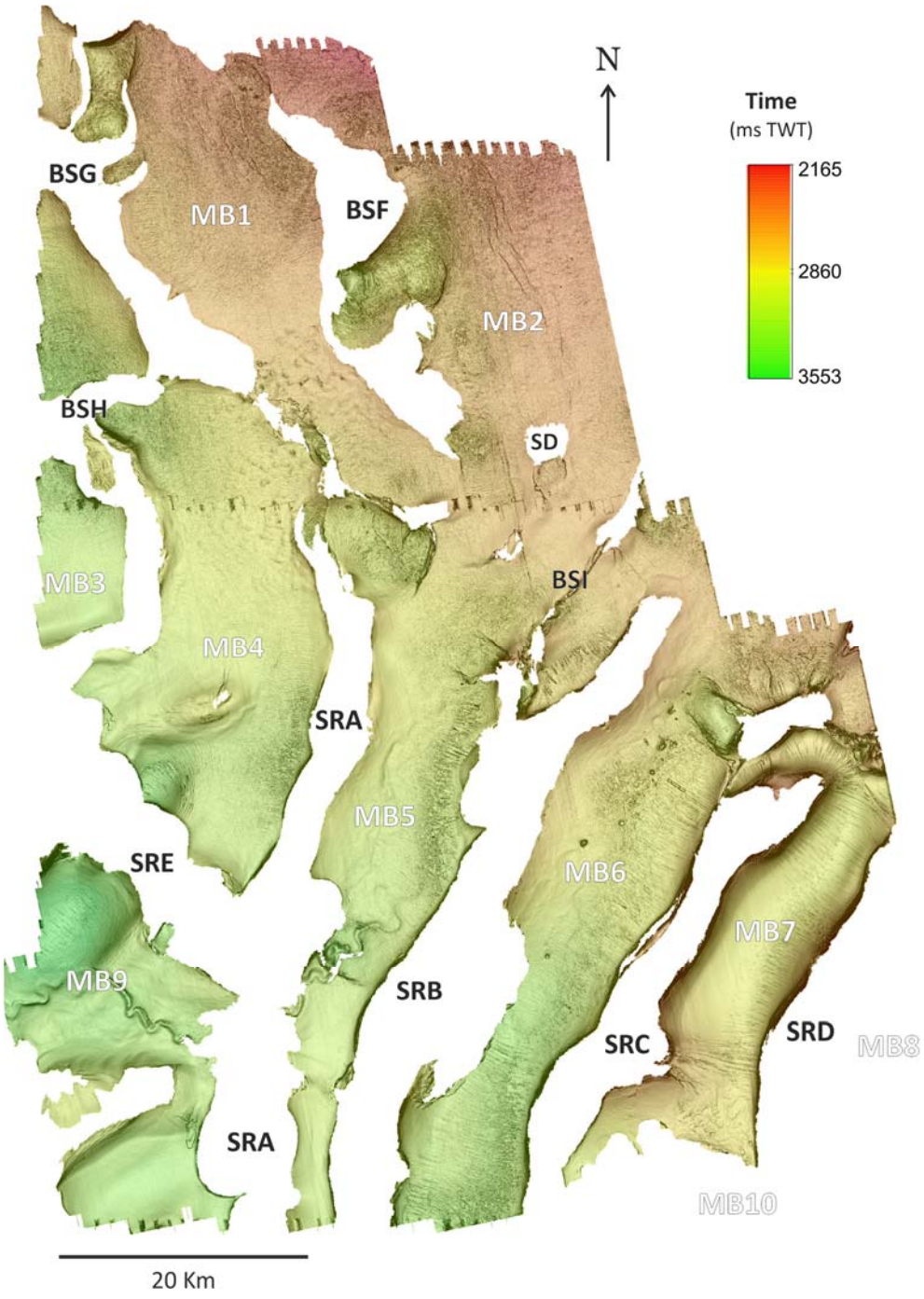

Figure 3.13. Regional time-structure map of horizon **C3**, the base of the polygonal fault tier (Unit 3). Variable fault patterns are observed in each mini-basin. Typical polygonal fault patterns occur in the central regions of the mini-basins. Polarised polygonal faults developed perpendicularly to the salt structures in the regions adjacent to these. However, fault relief on **C3** morphology is fainter than on horizons **C1** and **C2** (figs. 3.11 and 3.12), and becomes less observable south-westwards. MB = mini-basin; SR = salt ridge; BS = buried salt structure; SD = salt diapir.

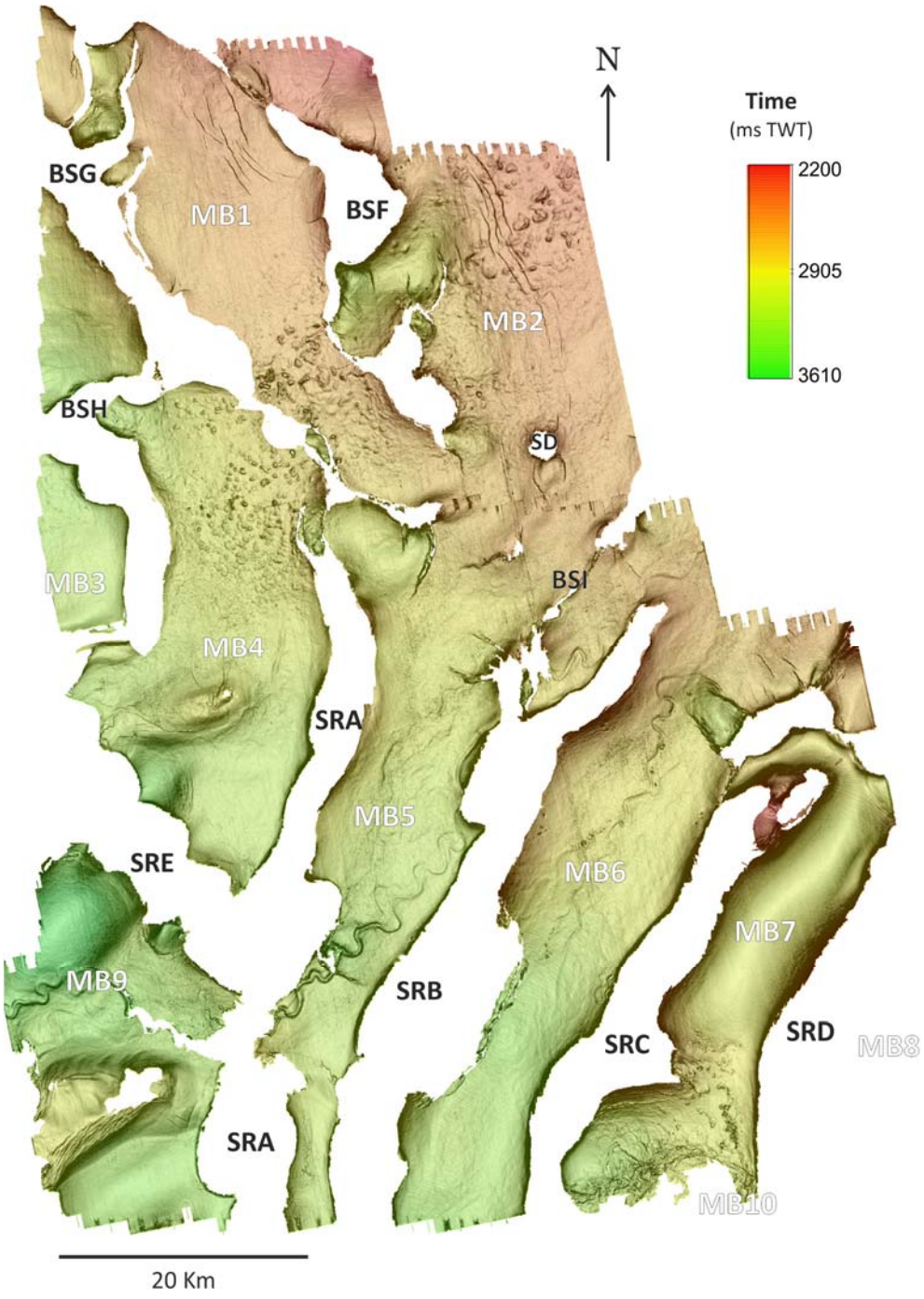

Figure 3.14. Regional time-structure map of horizon **C4**. Patterns associated with polygonal faults are absent. Long NW-oriented faults occur in MB1 and MB2, parallel to BSF. The horizon shows the imprint of underlying sinuous submarine channels on the southern area and of the irregular relief morphology of a large MTD on the north. MB = mini-basin; SR = salt ridge; BS = buried salt structure; SD = salt diapir.

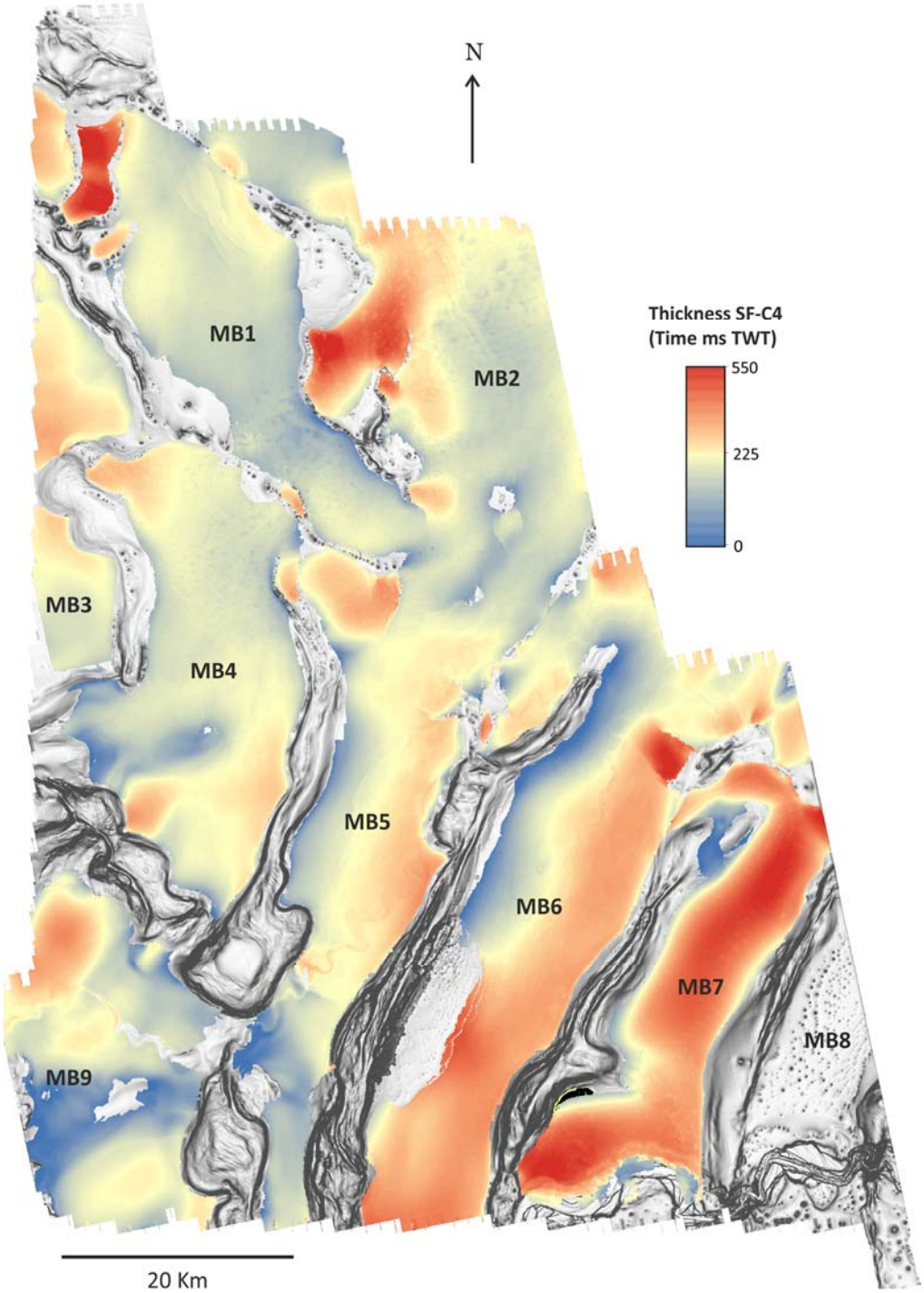

Figure 3.15. TWT-thickness map calculated between the seafloor and horizon **C4**, representing the thickness trends of Unit 3, overlaid on dip map of the seafloor. This interval is thicker in the southeast mini-basins, decreasing towards the west-northwest. Local thicker areas of this interval occur adjacent to salt structures to the north. MB = mini-basin.

Layer-bound faults in Unit 3

Strata within the middle interval of Unit 3 are pervasively deformed by small normal faults (fig. 3.10). These faults exhibit a wide range of planform geometries in the mini-basins (figs. 3.11 to 3.17). A polygonal arrangement is mapped in the central regions of the mini-basins where faults strike at a variety of azimuths, defining a network of polygons made of short fault segments up to 640 m in length. In cross-section the layer-bound faults are generally planar and very steep (with dips ranging from 50° to 70°). They are confined vertically in their extent to the strata between horizons **C1** and **C3** (fig. 3.10 and 3.7), hence being interpreted as layer-bound faults. Maps of horizon **C4** show no presence of polygonal faults at the deeper levels of Unit 3 (fig. 3.14). The highest displacements are concentrated in the central sections of the fault surfaces, reaching up to 21m. The faulted interval exhibits variable thickness, up to 345ms TWT (290m) (fig 3.16). The thicker intervals occur along the length of mini-basins MB6 and MB7 to the south, and local structure-bounded areas in MB1 and MB2. The fault tier has a wedge geometry and thins towards the basin rims, where the majority of the constituent faults dip upslope (towards the thin end of the wedge; fig. 3.7). The upper limit of the interval is marked by the same reflection in all mini-basins, i.e. horizon C1 (fig. 3.10). This is interpreted to represent the time at which the layer-bound faulting system became inactive. The base of the interval gradually decreases in depth as it thins towards the flanks of the mini-basins (fig. 3.12 and 3.15).

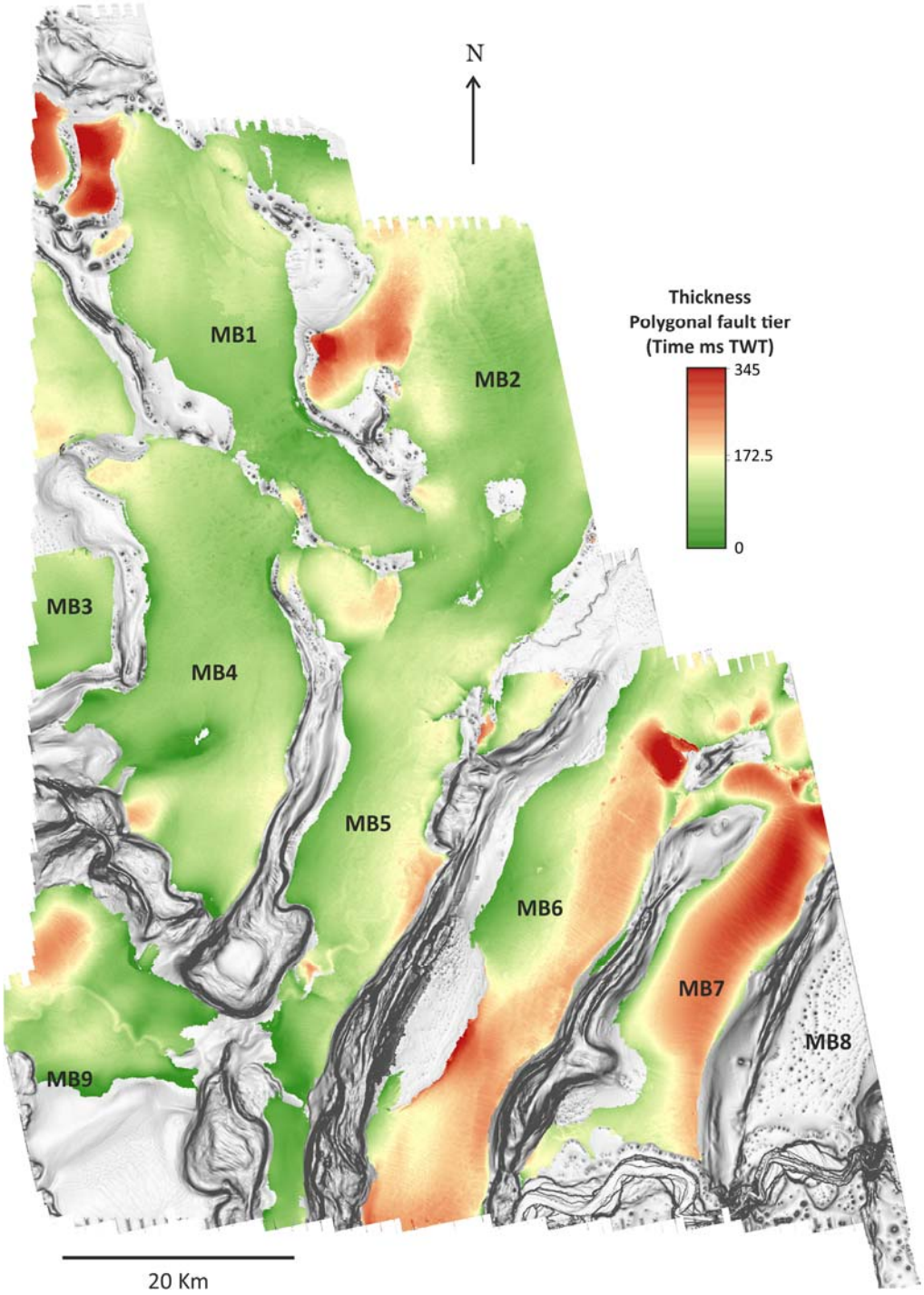

Figure 3.16. TWT-thickness map of the polygonal fault tier bounded by horizons **C1** and **C3**. This tier is thicker in the southeast mini-basins, decreasing towards the west-northwest. Local thicker areas of this interval occur adjacent to salt structures to the north. MB = mini-basin.

The layer-bound fault system exhibits many of the characteristics of polygonal fault systems, albeit with some considerable deviations from what could be regarded as the norm for these systems worldwide (Cartwright and Dewhurst, 1998). The classical polygonal pattern is observed in central areas of several mini-basins (figs. 3.11 and 3.12). However, this pattern changes quite dramatically towards the salt structures at the margins of the mini-basins. The distinctive polygonal character is abruptly lost in the proximity to salt bodies, where faults strike orthogonal to these structures and exhibit longer traces, up to 3400m in length (fig. 3.11 and 3.12). This is well represented by the fault pattern in mini-basin MB7, which is dominated by strong alignments of fault strikes orthogonal to the margins, and an almost uni-directional pattern across the basin axis (fig. 3.12). In the central areas of this mini-basin, adjacent fault segments commonly interact to form relay ramps. Similar fault patterns were recognised by Carruthers et al. (2013), who describe polygonal fault systems polarised into strongly radial faults around salt diapirs. Carruthers et al. (2013) argued that the radial and polygonal discontinuities are the same fault set but affected by local stress polarisation. Therefore, by analogy, the orthogonal orientation of the faults described in this study may result from local stress field perturbations either related to salt emplacement/growth or consequent changes in topographic gradient (or a combination of both). We refer to these fault arrays as polarised polygonal faults (PPFs). PPFs occur in regions surrounding salt walls that are affected by local anisotropic stress fields, confined to areas inside a transition boundary of 1315-3170m radii (average = 2350m radii). Polygonal faults occur in areas outside the transition boundary, where the horizontal stress field is isotropic (Carruthers et al., 2013; Cartwright, 2011). Due to the close proximity of two adjacent salt structures,

the transition boundaries of the limiting salt walls of mini-basin MB7 overlap, preventing the development of polygonal fault arrays, and instead resulting in a unidirectional fault pattern. This is also partially observed on mini-basin MB2, west of structure BSI.

One notable feature of the distribution of the PPF system is that it is absent in a region along the western rim of mini-basin MB7 (fig. 3.17), as PPFs die out laterally where a change in seismic amplitudes is observed. This change in amplitude response and fault behaviour may be due to lateral lithological variations, such as deposition of coarser sediments or subtle changes in mineralogy, which may not be suitable for polygonal faulting formation (Cartwright, 2011). Thinning of the basal strata of the tier observed in this part of the mini-basin could also prevent fault nucleation and propagation, if polygonal faulting is initiated within this package. However, it is possible that in this region (polarised) polygonal faulting is of a magnitude that the faults are not imaged, i.e. below the seismic resolution limit.

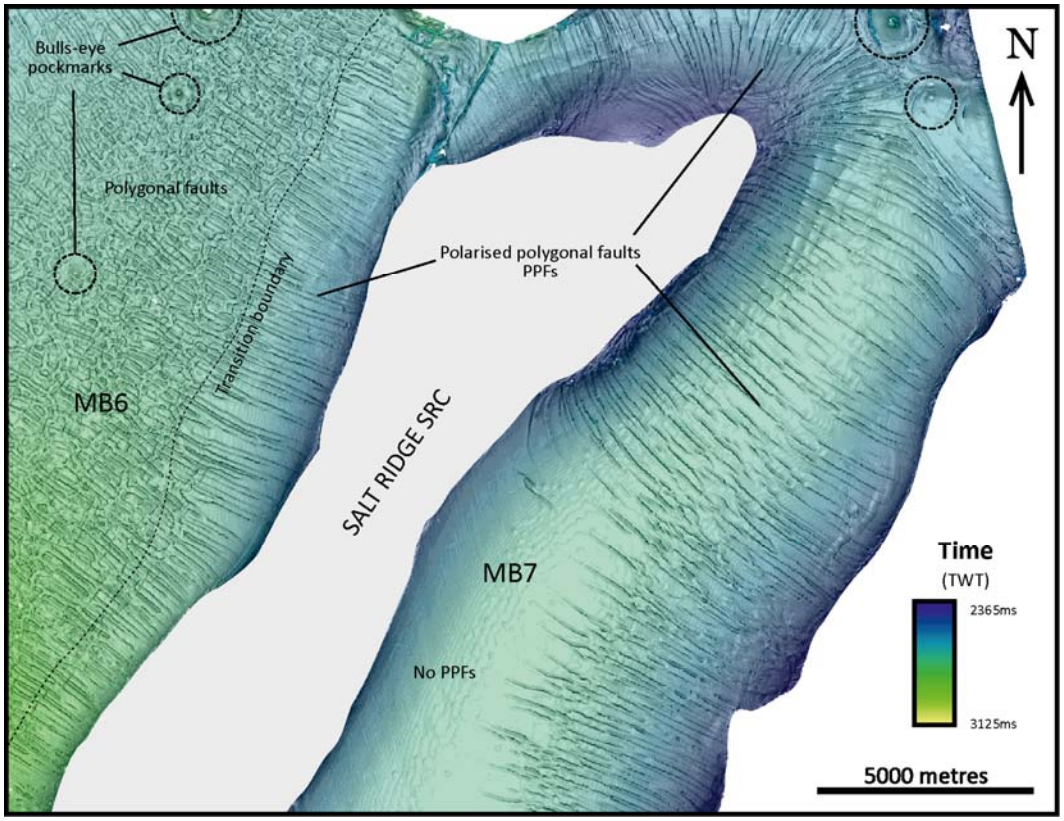

Figure 3.17. Structure and dip map of seismic horizon **C2**. Note the contrast between polygonal fault arrangements in different areas – the central region of mini-basin MB6 exhibits a typical polygonal pattern, whereas mini-basin MB7 and salt margins of MB6 present polarised faults striking perpendicular to salt structures. Although MB6 is pervasively affected by polygonal faulting, there are regions of MB7 absent of seismically resolvable discontinuities (ex., the south-western rim of MB7 depicted here).

3.2.3. Salt structural styles in the study area

The salt structures observed on the study area result from a variety of extensional and contractional regional deformation associated with halokinesis widely documented on the Angola margin (Duval et al., 1992; Fort et al., 2004; Hudec and Jackson, 2011; Rouby et al., 2005). The separation between the northern and southern domains of the study area and the contrasting structural architecture follows a rough ENE-WSW boundary (fig. 3.6). This limit is roughly parallel to the Luanda Transfer Zone and others on

the margin (fig. 3.18), suggesting an influence of deeper basement structures on salt deformation (Hudec and Jackson, 2002; Lentini et al., 2010).

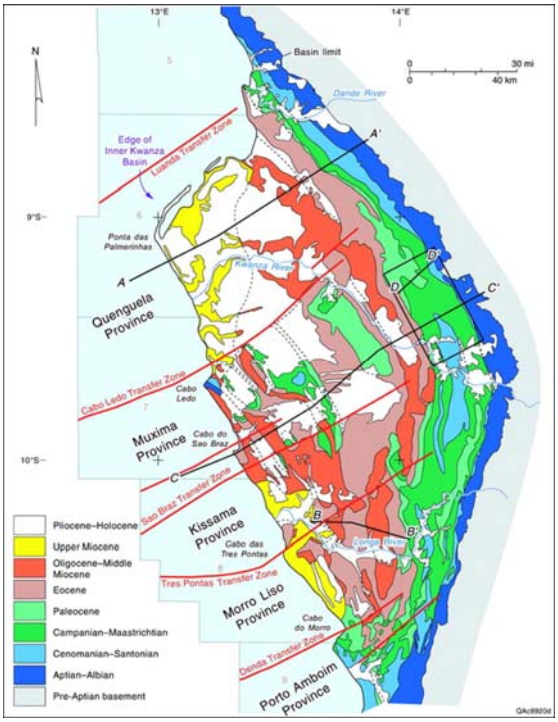

Figure 3.18. Map showing the NE-SW trends of the Luanda Transfer Zone and other main transfer zones on the Angola margin (from Hudec and Jackson, 2002).

Salt structures on the northern domain consist of laterally discontinuous buried ridges and diapirs that strike along a northwest-southeast direction, following the shelf break morphology/coast line north of Luanda. Structures in this domain indicate preferential extensional regimes represented by numerous normal faults and diapirs (figs. 3.19 to 3.24). Wide grabens reaching over 5km are bound by N-S faults adjacent to the salt ridges and deeply rooted in the salt source levels. Fault offset reaches as much as 500ms TWT, significantly displacing the Miocene Unit 2, but these are drastically lower in Unit 3 in the order of 10's of ms TWT. Deep antiform structures are observed in MB1 and MB2 (fig. 3.21 and 3.24), associated with

either passive diapir fall and creation of mock-turtle anticlines bound by regional synthetic and antithetic roller faults or early buckling (Duval et al, 1992; Hudec and Jackson, 2011). The deep salt structures are not covered by the 3D seismic data so it is not possible to properly visualise the core of the anticlines. The subsurface salt bodies show variable geometries. Rounded to flat-topped diapirs, often more than 3000m wide, have limited to no seafloor expression and are bordered by strata growth packages suggesting passive growth phases (figs. 3.21C and 3.24C). Diapir inversion and rejuvenation has also occurred, represented by a few subsurface triangular salt bodies. The apex of each of these can be located at different depths, but all show characteristics of reactive diapirism (sensu Vendeville, 2005) with numerous normal faults dipping towards the salt crest (figs. 3.21D, 3.24D, 3.24E). Positive seafloor relief associated with the northern salt structures is observed in MB1 (fig. 3.21), possible associated with diapir shortening and active growth pulses (Hudec and Jackson, 2011).

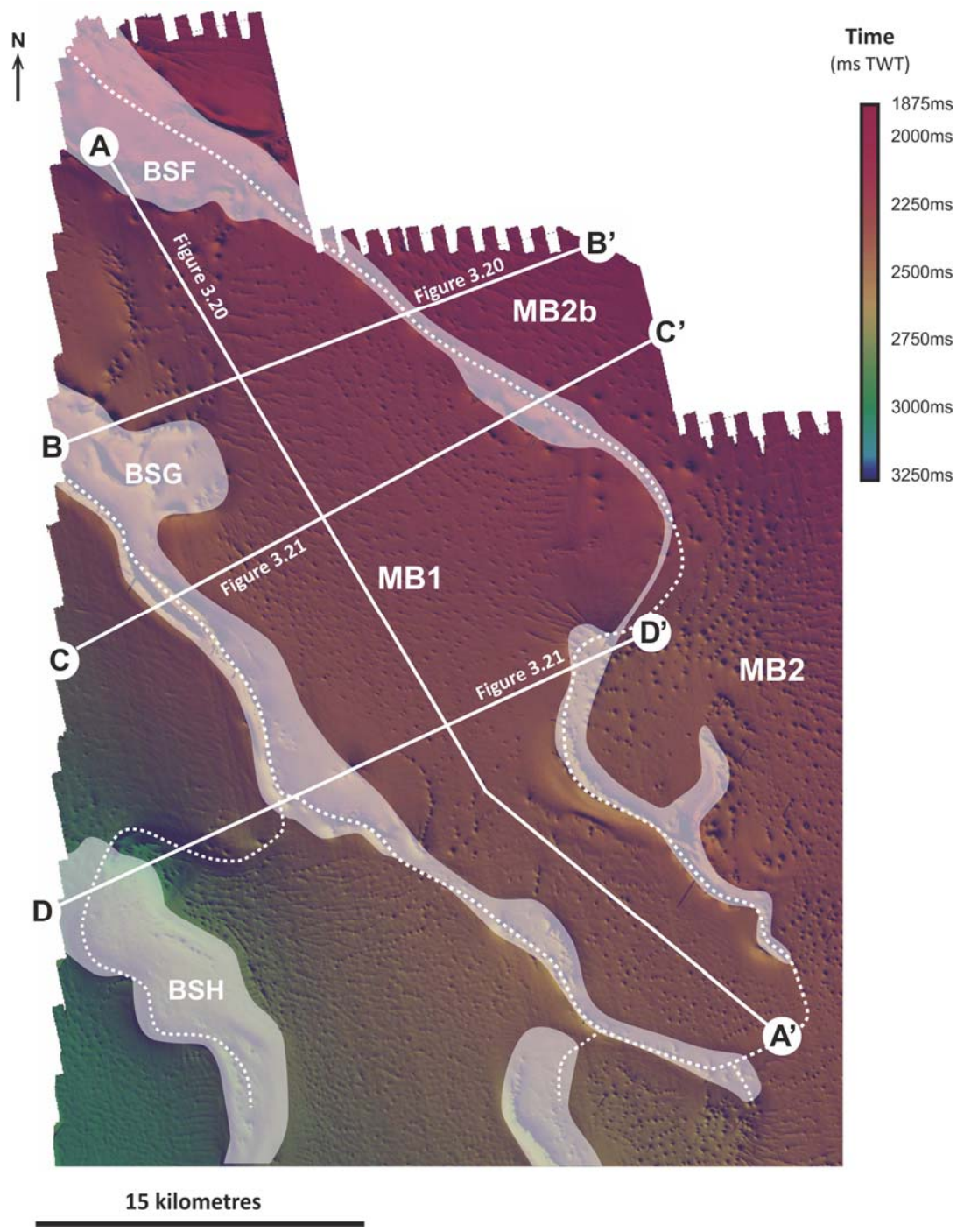

Figure 3.19. Seafloor map of minibasin MB1 and outline of bordering salt structures (white shadows). White lines indicate the locations of the cross-sections shown in figures 3.19 and 3.20. MB = mini-basin; SR = salt ridge; BS = buried salt structure; white shadow = salt structure; dashed white line = mini-basin limit.

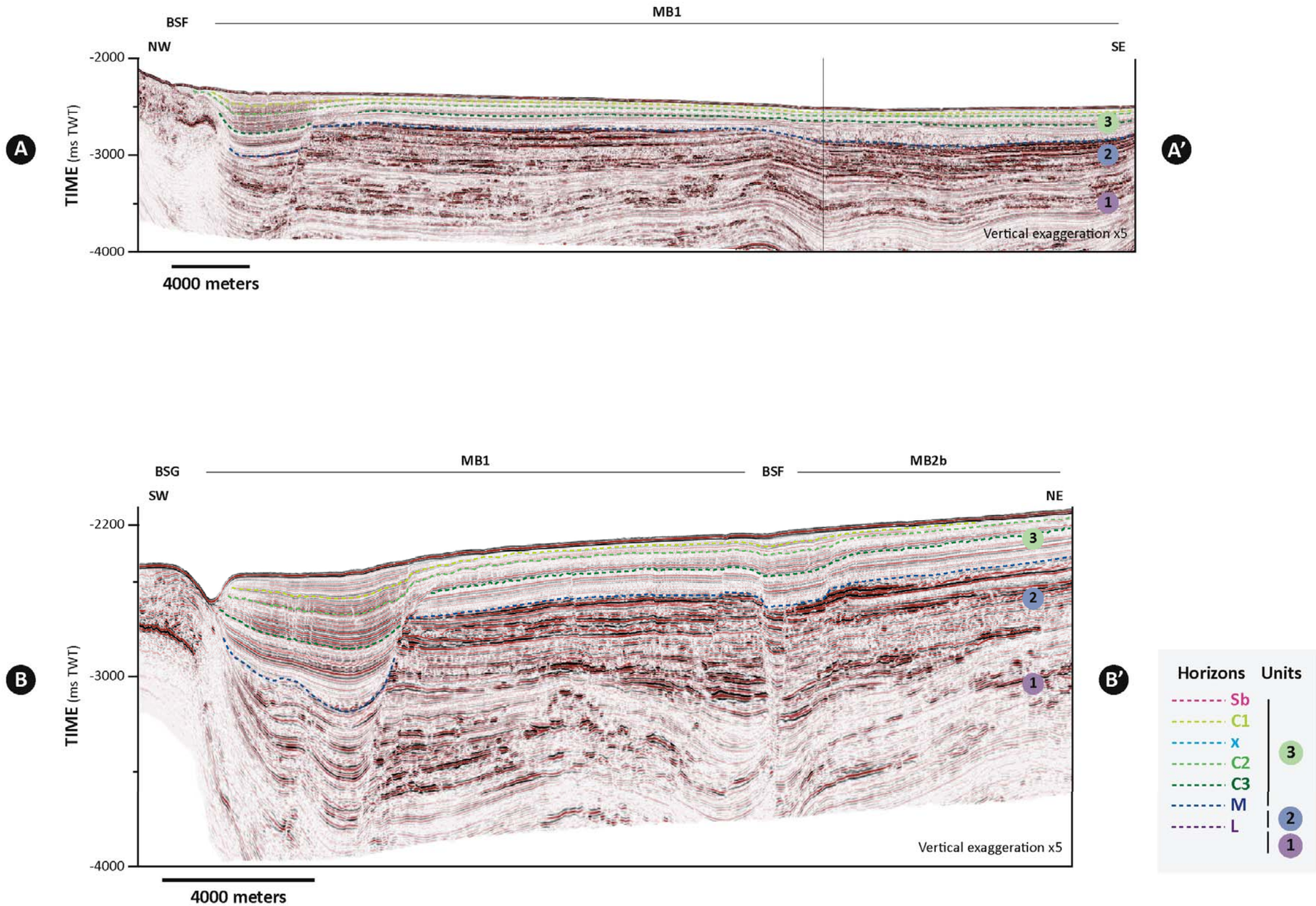

Figure 3.20. Seismic profiles intersecting mini-basin MB1. Fault-bounded grabens are observed close to the vertical salt structure. A deep anticline if visible in section B. MB = mini-basin; SR = salt ridge; BS = buried salt structure. Seismic sections locations in figure 3.19. (Seismic courtesy of PGS.)

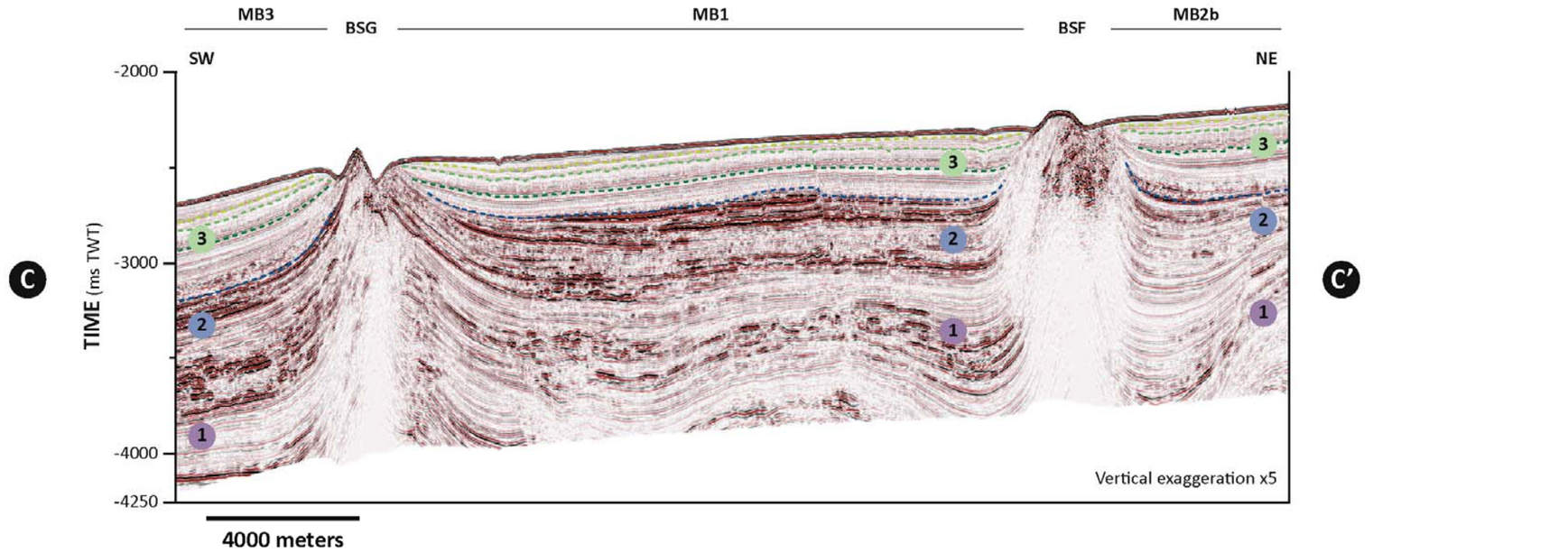

Figure 3.21. Seismic sections across MB1. Seafloor relief in section C is created by rising diapirs is interpreted to result from their rejuvenation. A deep fold is present along the axis of MB1. Section D shows different diapir geometries. Wide, flatter tops are associated with passive diapirism while the triangular shapes are associated with rejuvenated reactive diapirism. MB = mini-basin; SR = salt ridge; BS = buried salt structure. Seismic sections locations in figure 3.19. (Seismic courtesy of PGS.)

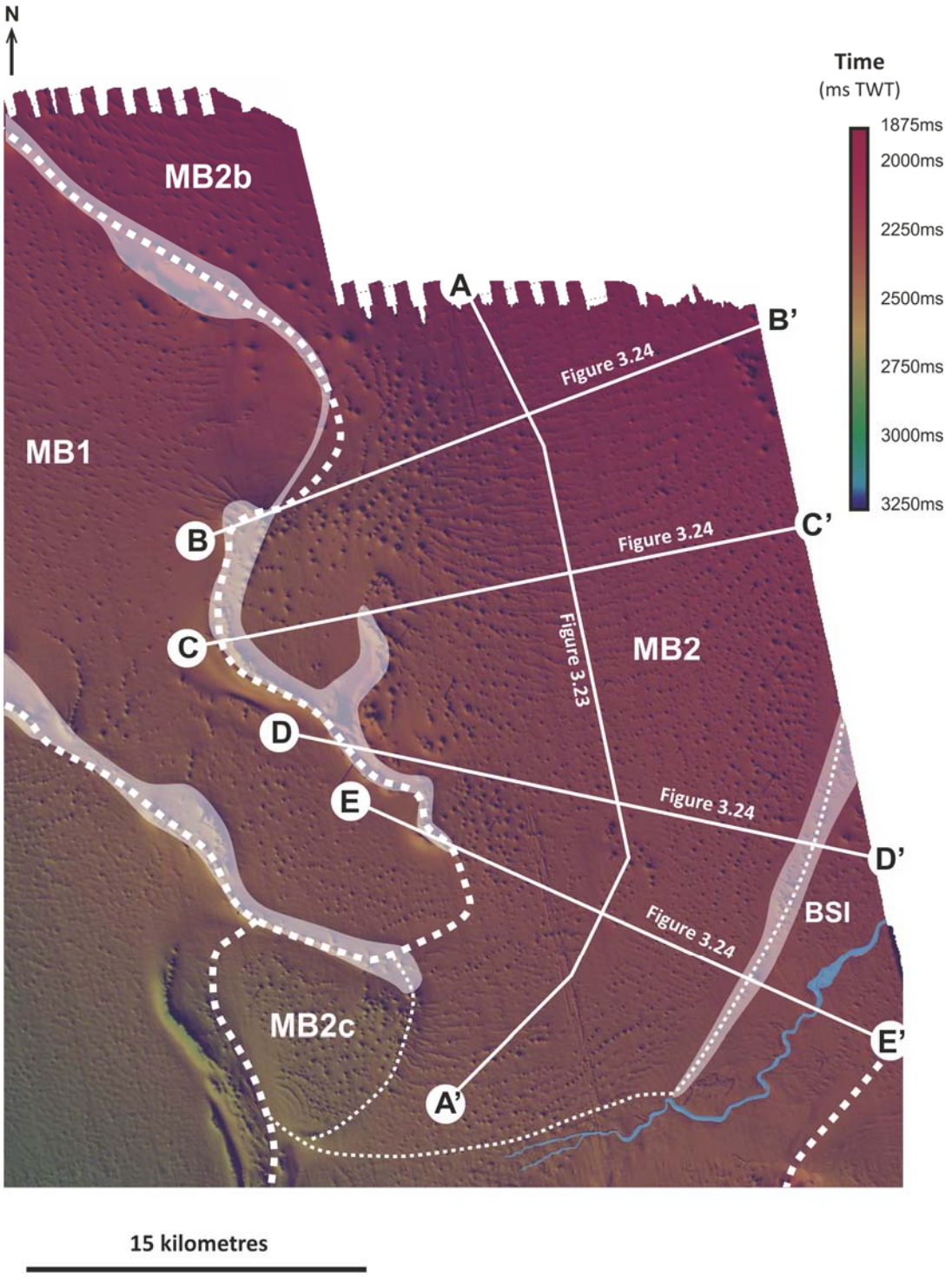

Figure 3.22. Seafloor map of basin MB2. Numerous pockmarks are observed here, with a distinctive arcuate pattern at the axis. White lines indicate the locations of the cross-sections shown in figures 3.22 and 3.23. MB = mini-basin; SR = salt ridge; BS = buried salt structure; white shadow = salt structure; dashed white line = mini-basin limit.

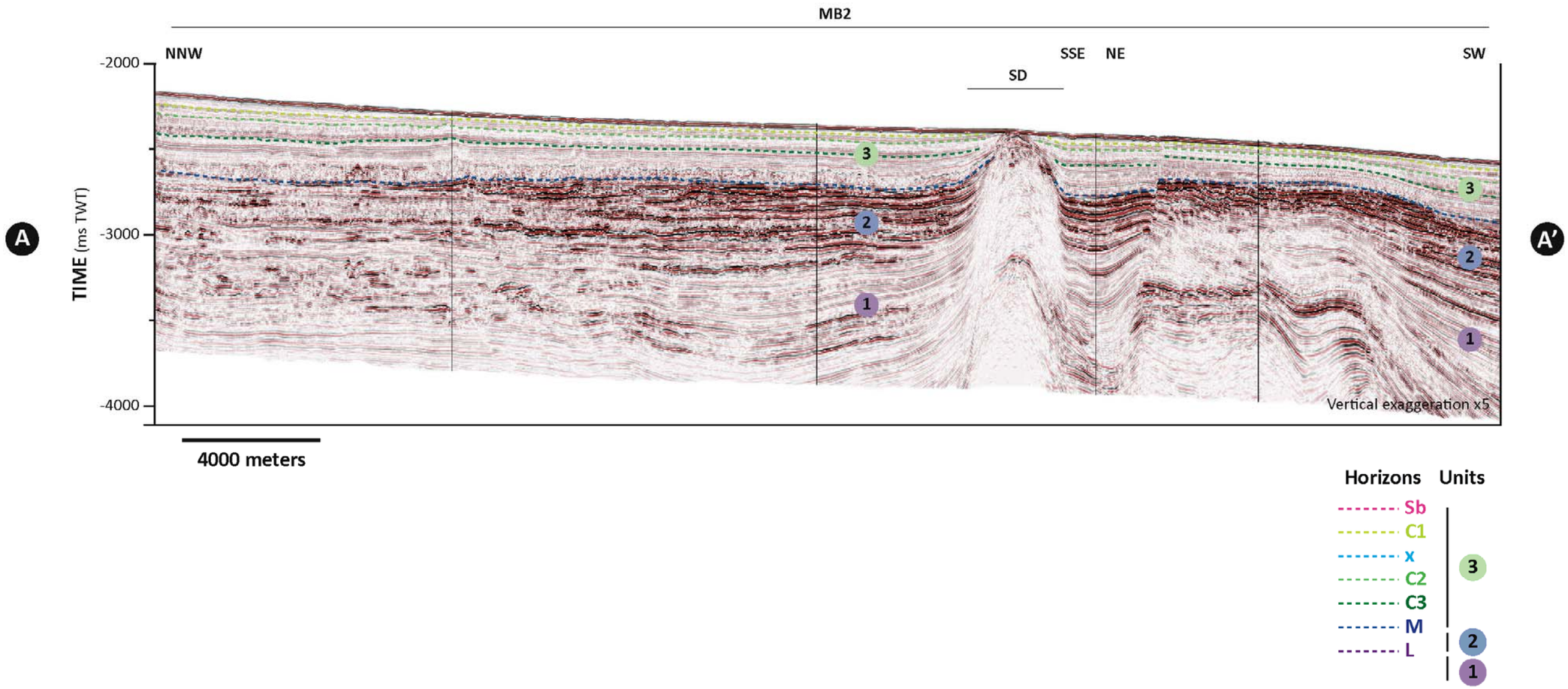

Figure 3.23. Seismic section along the axis of MB2. Rising salt structures are absent on the northern half, but relevant towards the south. MB = mini-basin; SR = salt ridge; BS = buried salt structure; SD = salt diapir. Seismic section location in figure 3.22. (Seismic courtesy of PGS.)

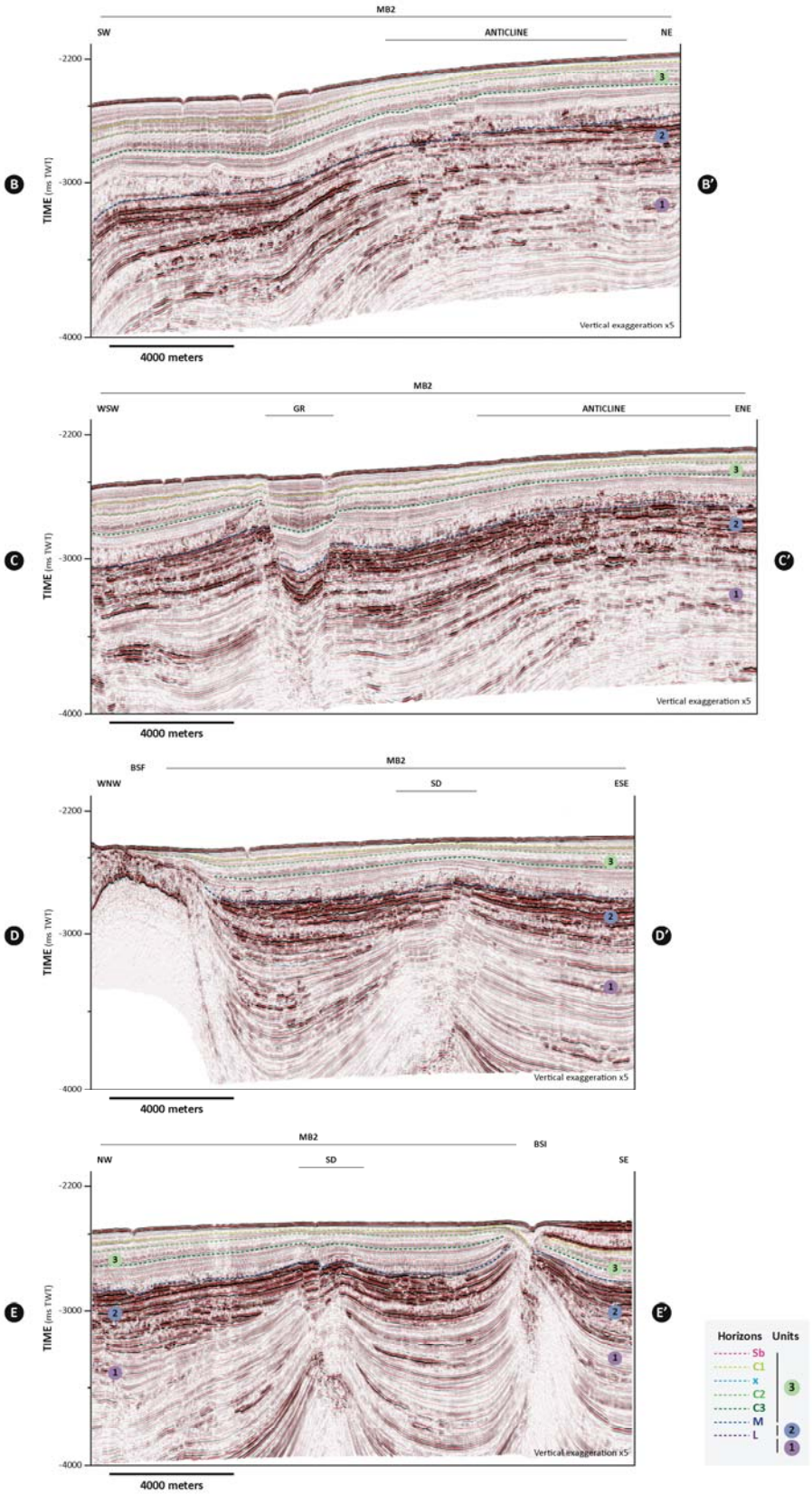

Figure 3.24. Seismic sections across MB2. A wide deep anticline is seen in B and C. Buried reactive diapirs are observed in sections D and E. MB = mini-basin; SR = salt ridge; BS = buried salt structure; SD = salt diapir. Seismic sections locations in figure 3.22. (Seismic courtesy of PGS.)

The southern region of the area is characterised by northeast-southwest striking extensive salt walls creating positive relief on the seafloor. These are created by the squeeze of buried salt units by gravitational downslope translation, thus the compressional thrust architecture presented by most of them (figs. 3.25 to 3.35). The orientation of these features may be inherited from syn-rift and basement structures (not visualised in the data available), possibly associated to a rifting segment oblique to the main South Atlantic spreading axis, similarly to what is described by Ashby (2013) for the conjugate Santos-Kwanza basins. The morphology of the compressed salt bodies is fairly uniform, represented by sub-vertical to east-dipping cores (fig. 3.31). Sections of the salt ridges often have preserved segments of strata over arched tops (Fig. 3.31). This may be associated with alternating episodes of salt deflation and sediment deposition on the sag, followed by rejuvenation and shortening leading to the deformation and uplift of the salt and overlying sediments, thus creating relief on the seafloor. The inter-ridge space on the southern area is characterised by elongated synclines accommodating sediments from Units 2 and 3. Low amplitude anticlines are only observed at depth, but have limited effect on the geometry of Unit 3 (figs. 3.29, 3.31 and 3.32). The exception is in mini-basin MB9 where a large antiform exhumes Unit 1 nearly to the seafloor (fig. 3.34). The large structure has controlled the sedimentation in Unit 2 and 3 on this mini-basin.

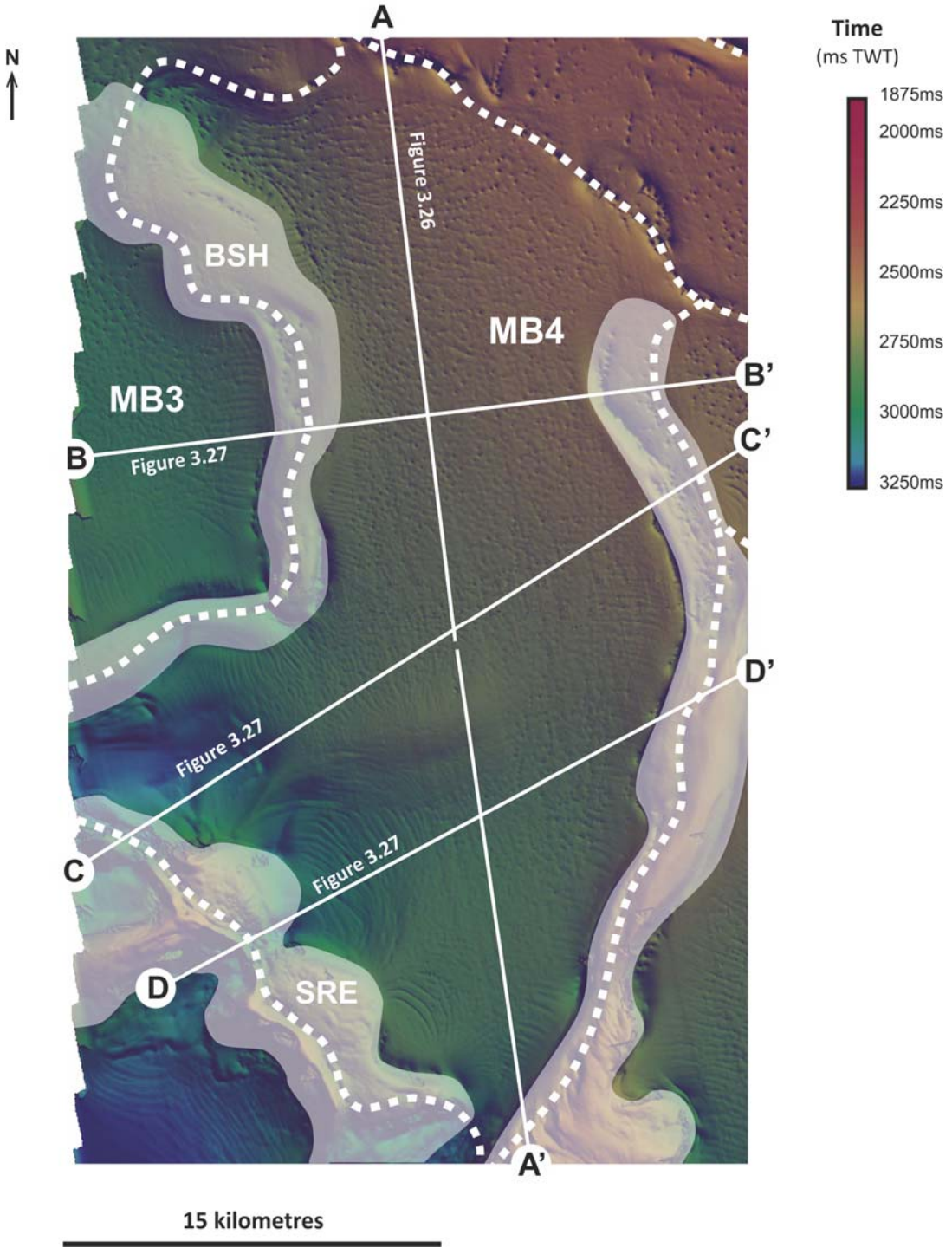

Figure 3.25. Seafloor map of mini-basin MB4. This mini-basin is bordered by N-S structures along the length, but by E-W structures along its the northern and southern limits. White lines indicate the locations of the cross-sections shown in figures 3.25 and 3.26. MB = mini-basin; SR = salt ridge; BS = buried salt structure; white shadow = salt structure; dashed white line = mini-basin limit.

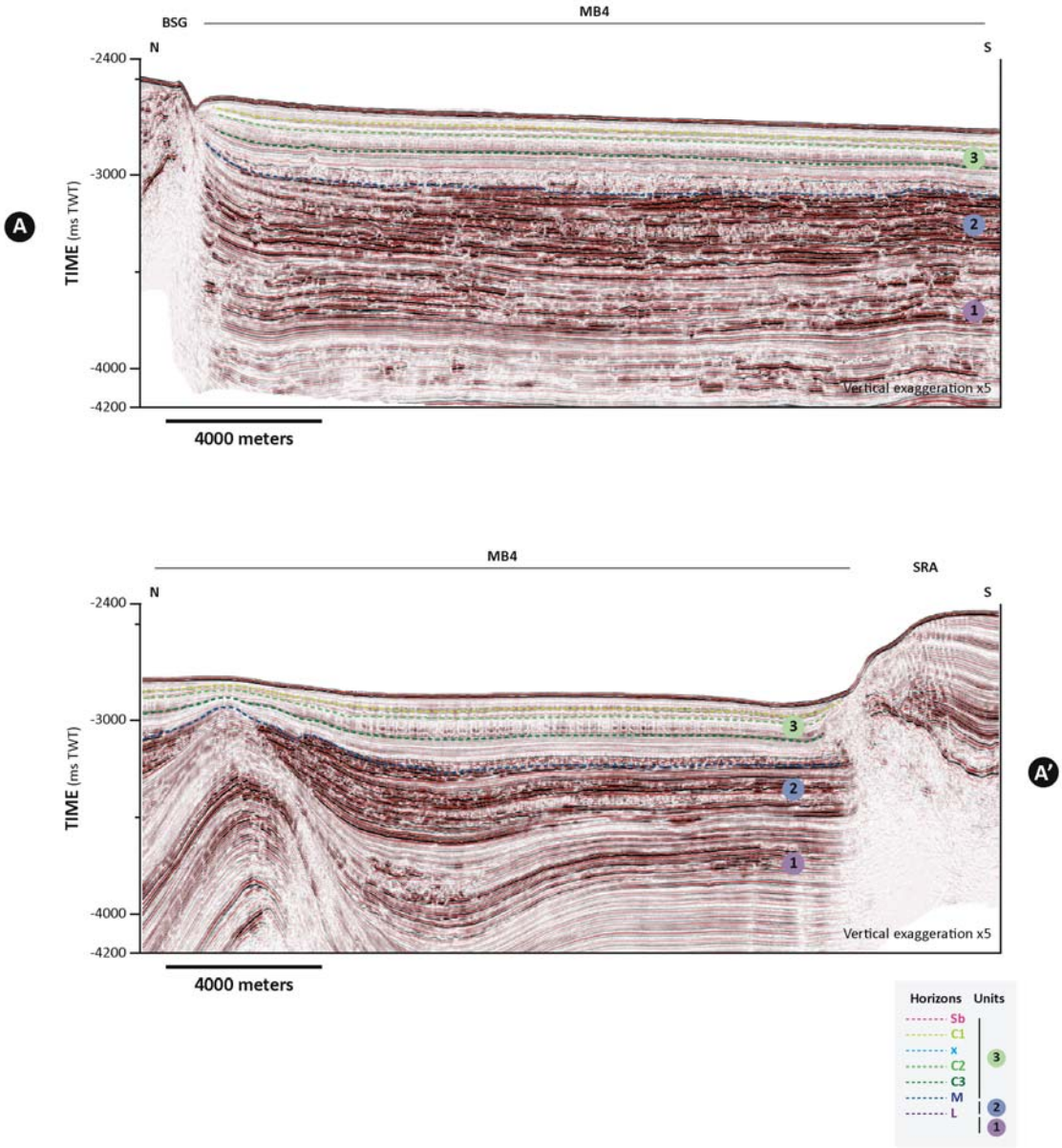

Figure 3.26. Seismic sections along MB4. A buried structure limits it to the north, but to the south marked seafloor relief is created by rising salt ridge SRA. A buried tight anticline (or rising diapir?) near the mini-basin centre influences the sedimentary thickness of Unit 3 and interfered with the polygonal fault tier. MB = mini-basin; SR = salt ridge; BS = buried salt structure. Seismic sections locations in figure 3.25. (Seismic courtesy of PGS.)

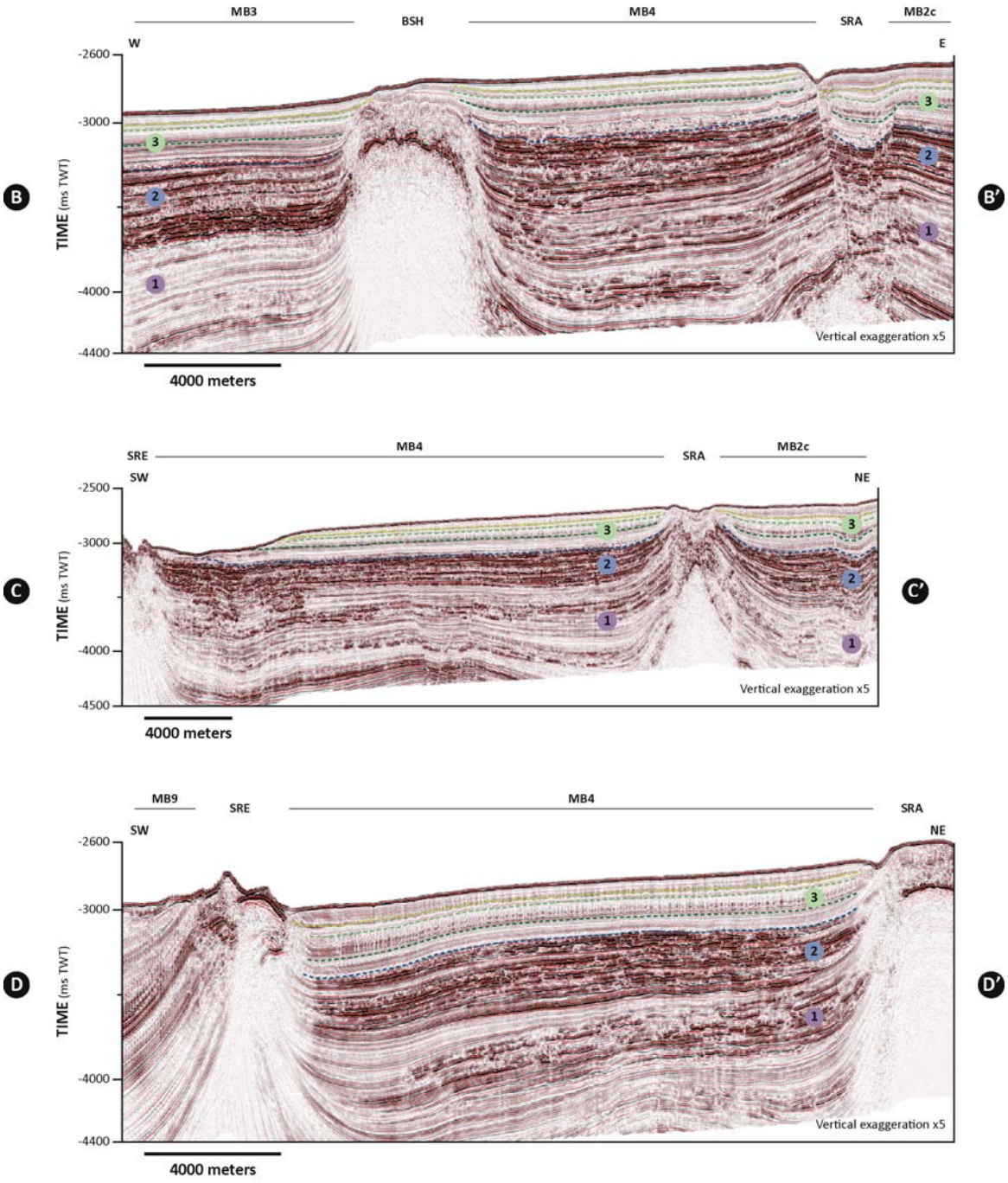

Figure 3.27. Seismic sections across mini-basin MB4. Note the shallowing of salt ridge SRA and change in the geometry of top salt from north to south, i.e. from section B to D. MB = mini-basin; SR = salt ridge; BS = buried salt structure. Legend of stratigraphy in figure 3.25. Seismic sections locations in figure 3.25. (Seismic courtesy of PGS.)

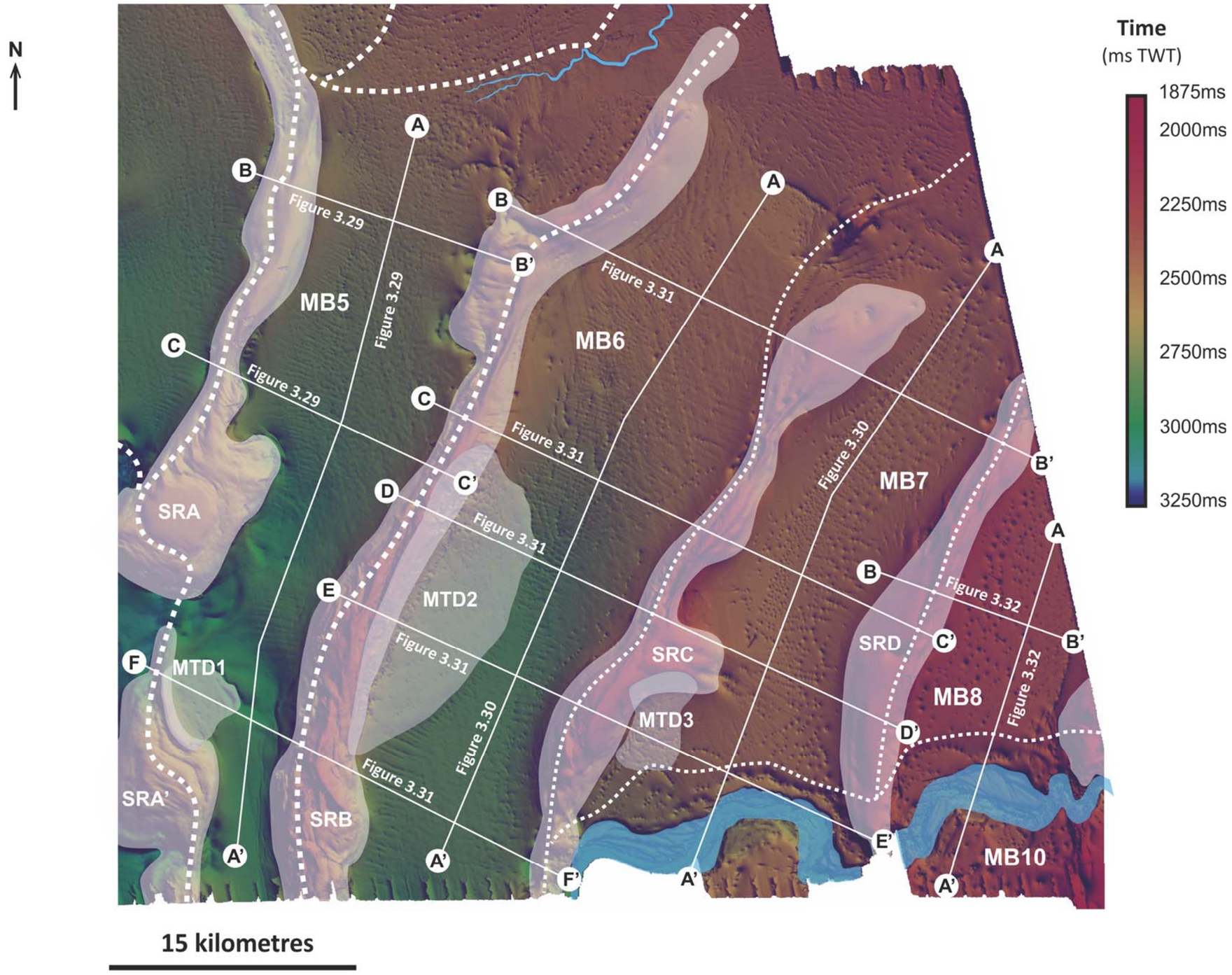

Figure 3.28. Seafloor map showing mini-basins MB5, MB6, MB7 and MB8, and bordering salt ridges. The large channel 2 incised on the south of MB7 and MB8. Three mass-transport deposits (MTDs 1, 2 and 3) occur adjacent to ridge flanks. White lines indicate the locations of the cross-sections shown in figures 3.28, 3.29, 3.30, and 3.31. MB = mini-basin; SR = salt ridge; BS = buried salt structure; white shadow = salt structure; blue shadow = submarine channel; dashed white line = mini-basin limit.

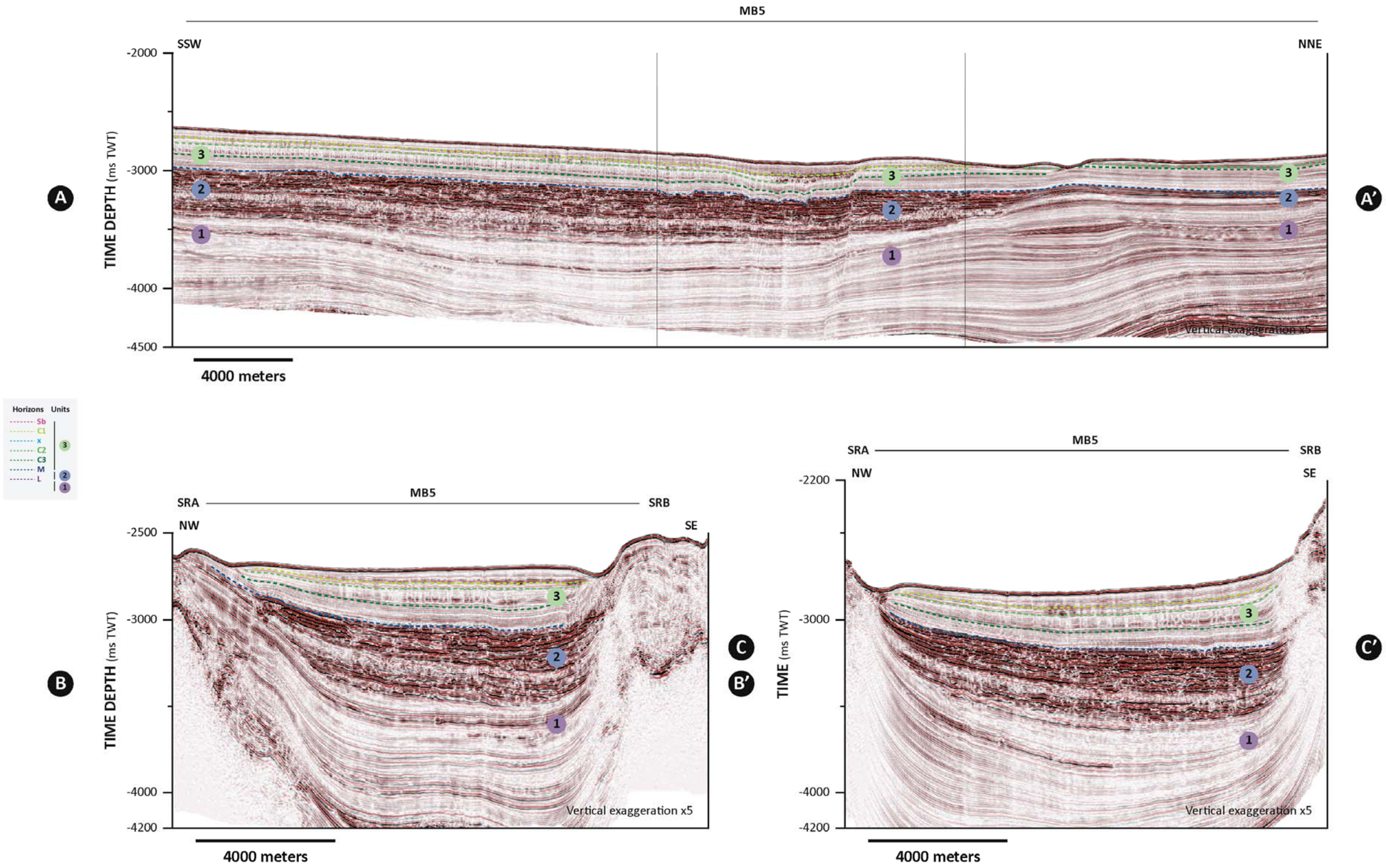

Figure 3.29. Seismic sections along and across mini-basin MB5. NW-SE sections show the general synform architecture of the mini-basin. MB = mini-basin; SR = salt ridge; BS = buried salt structure. Seismic sections locations in figure 3.28. (Seismic courtesy of PGS.)

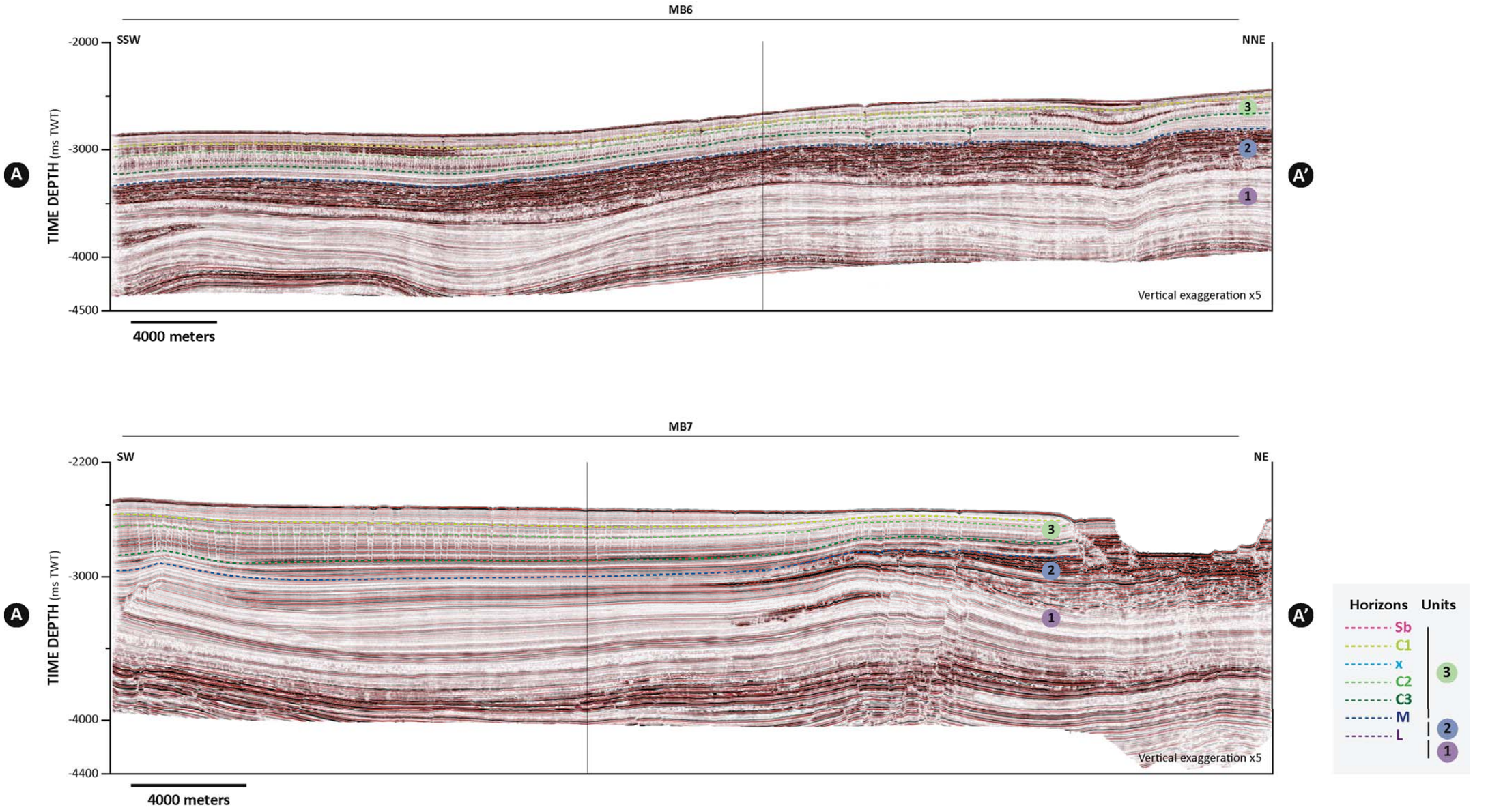

Figure 3.30. Seismic sections along mini-basins MB6 and MB7. Note the limited to absent high-amplitude reflections of Unit 2 in MB7. Seismic sections locations in figure 3.28. (Seismic courtesy of PGS.)

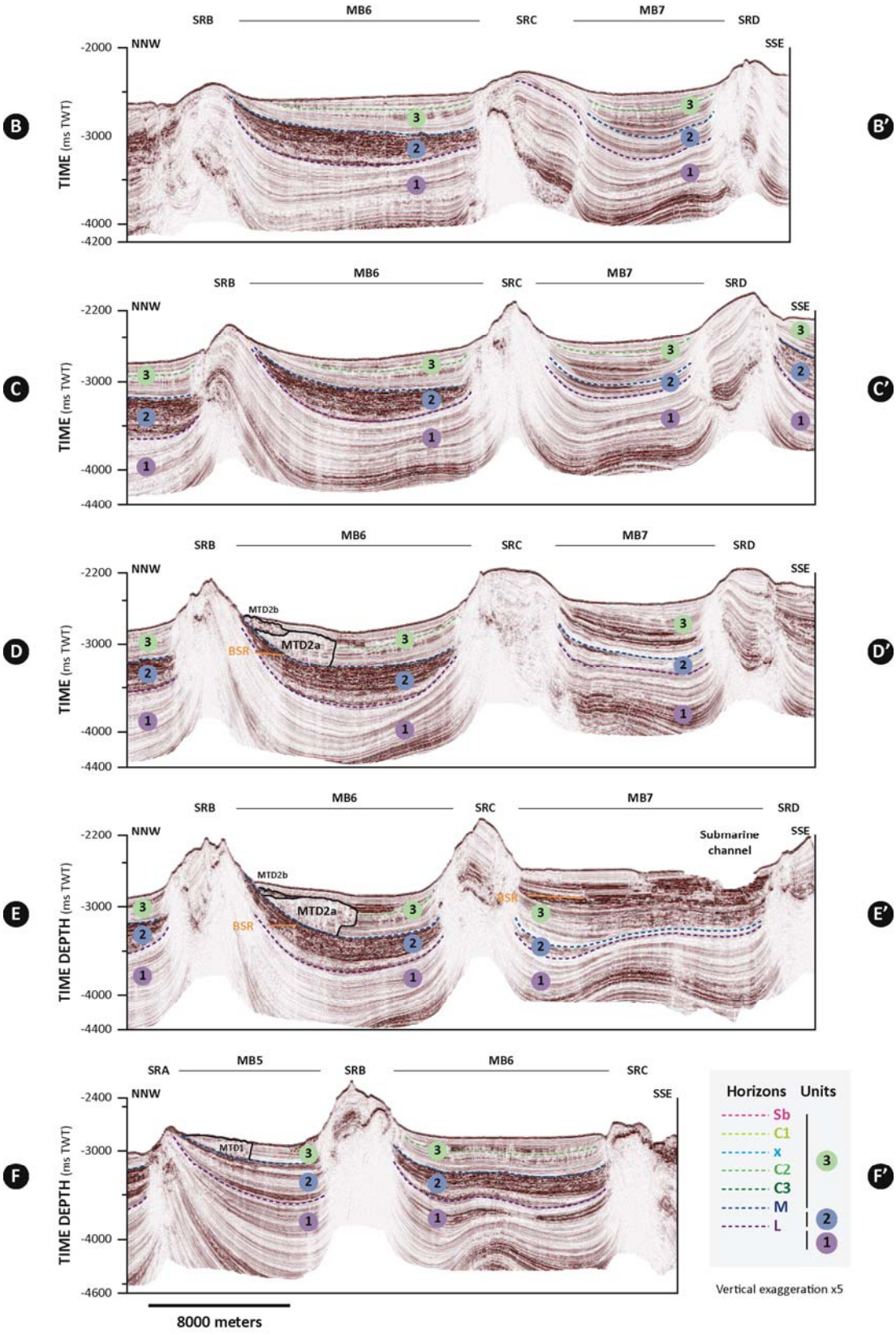

Figure 3.31. Seismic sections across the width of mini-basins MB6 and MB7. Preserved fragments of stratified reflections are observed above sagged salt tops in SRD, possibly associated with passive deflation and sediment accommodation in the diapir top sag and later uplift by contraction and salt ridge rise. MB = mini-basin; SR = salt ridge; BS = buried salt structure. Seismic sections locations in figure 3.28. (Seismic courtesy of PGS.)

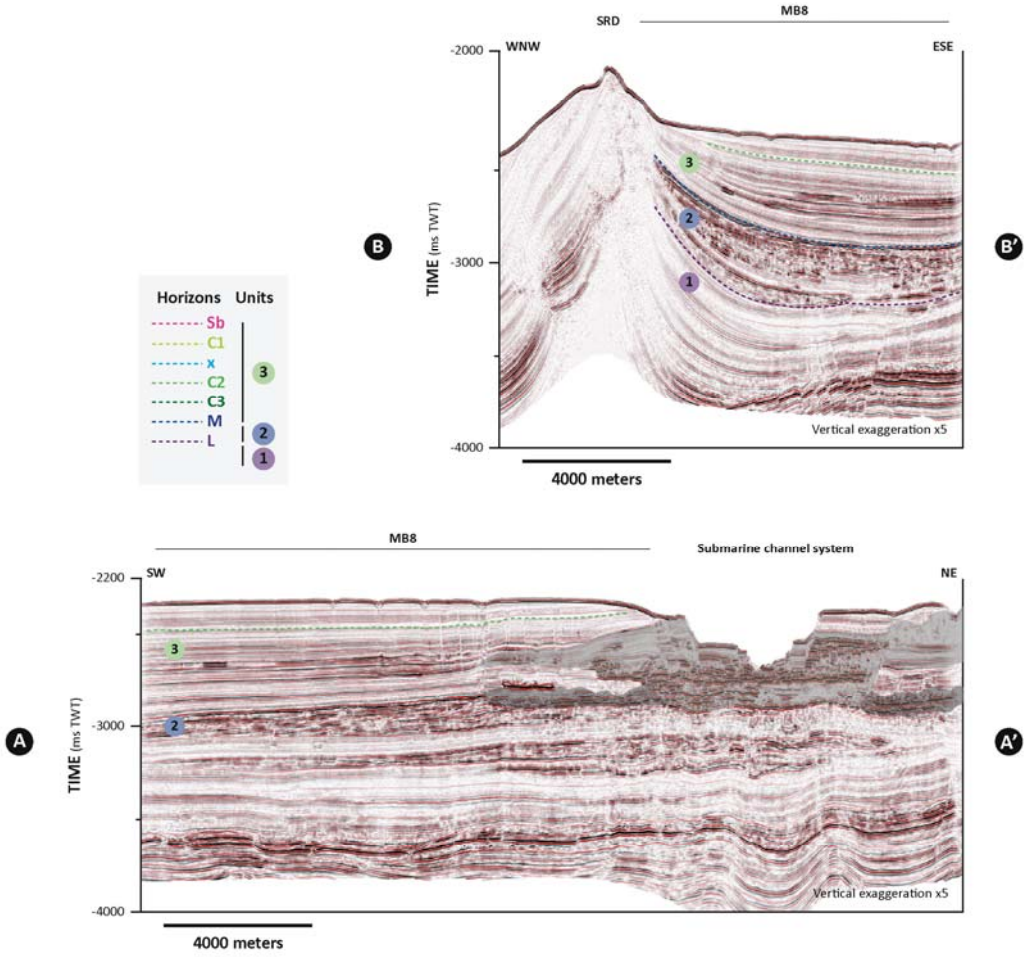

Figure 3.32. Seismic sections in mini-basin MB8. Channel 2 to the south is a deep incision with several terraces. Seismic sections locations in figure 3.28. (Seismic courtesy of PGS.)

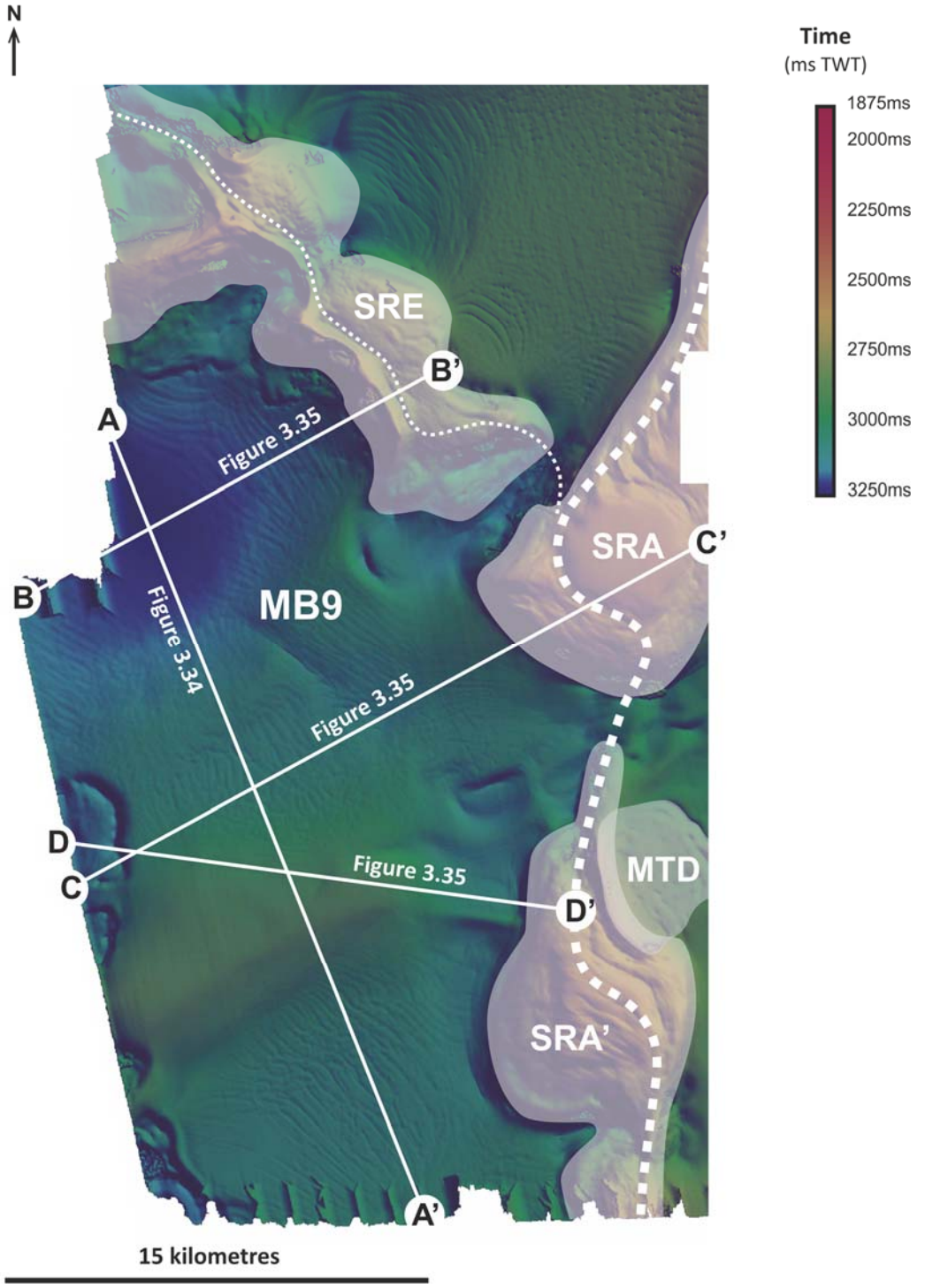

Figure 3.33. Seafloor map of mini-basin MB9, showing polygonal fault patterns. White lines indicate the locations of the cross-sections shown in figures 3.33 and 3.34. MB = mini-basin; SR = salt ridge; BS = buried salt structure; white shadow = salt structure; dashed white line = mini-basin limit.

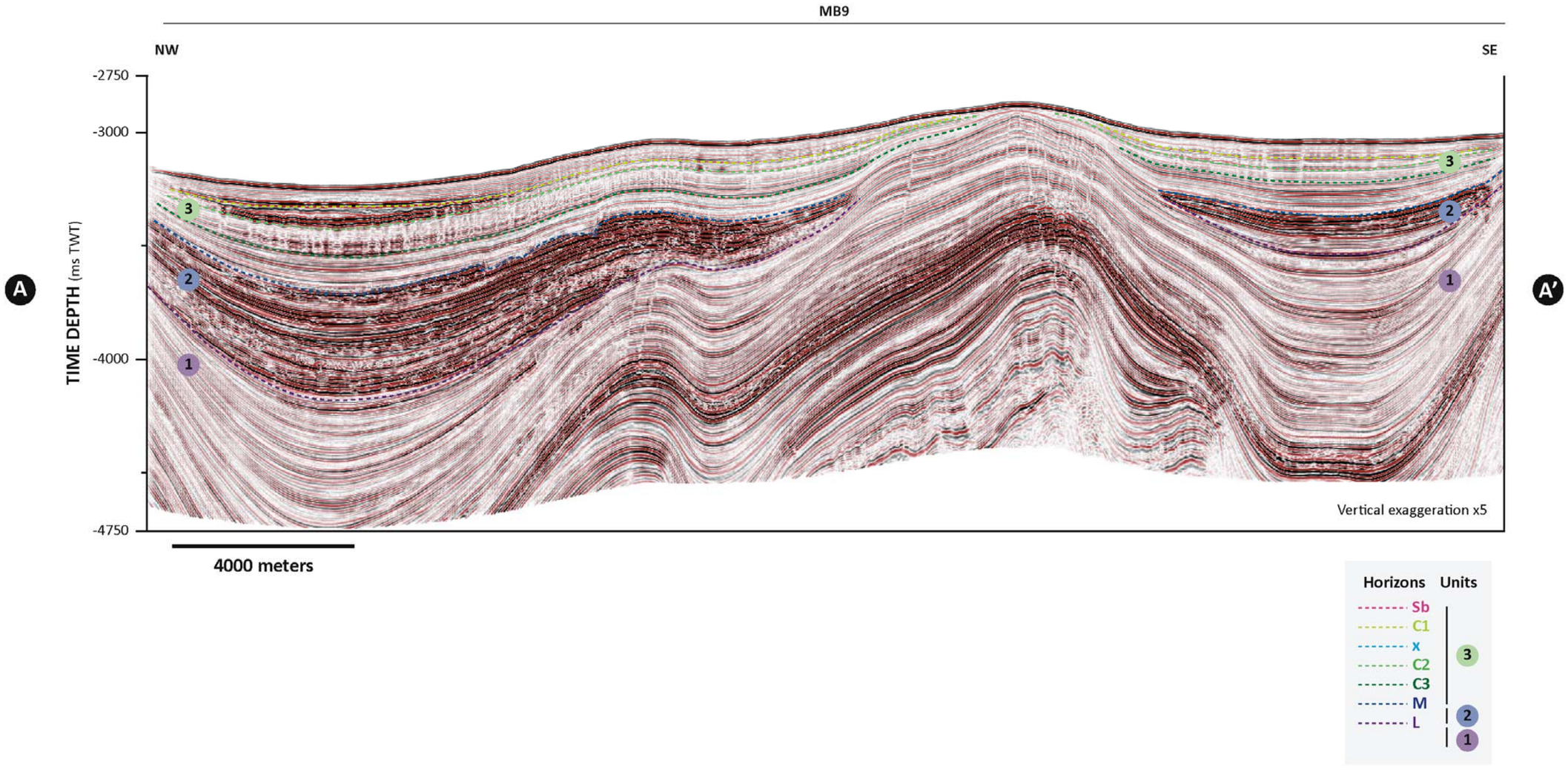

Figure 3.34. North-south seismic section along MB9. Unit 1 is uplifted to shallow levels above a deep structure, which controls sedimentation in Units 2 and 3. A shallow lens of high-amplitude reflections is observed within Unit 3 towards the NW. Seismic section location in figure 3.33. (Seismic courtesy of PGS.)

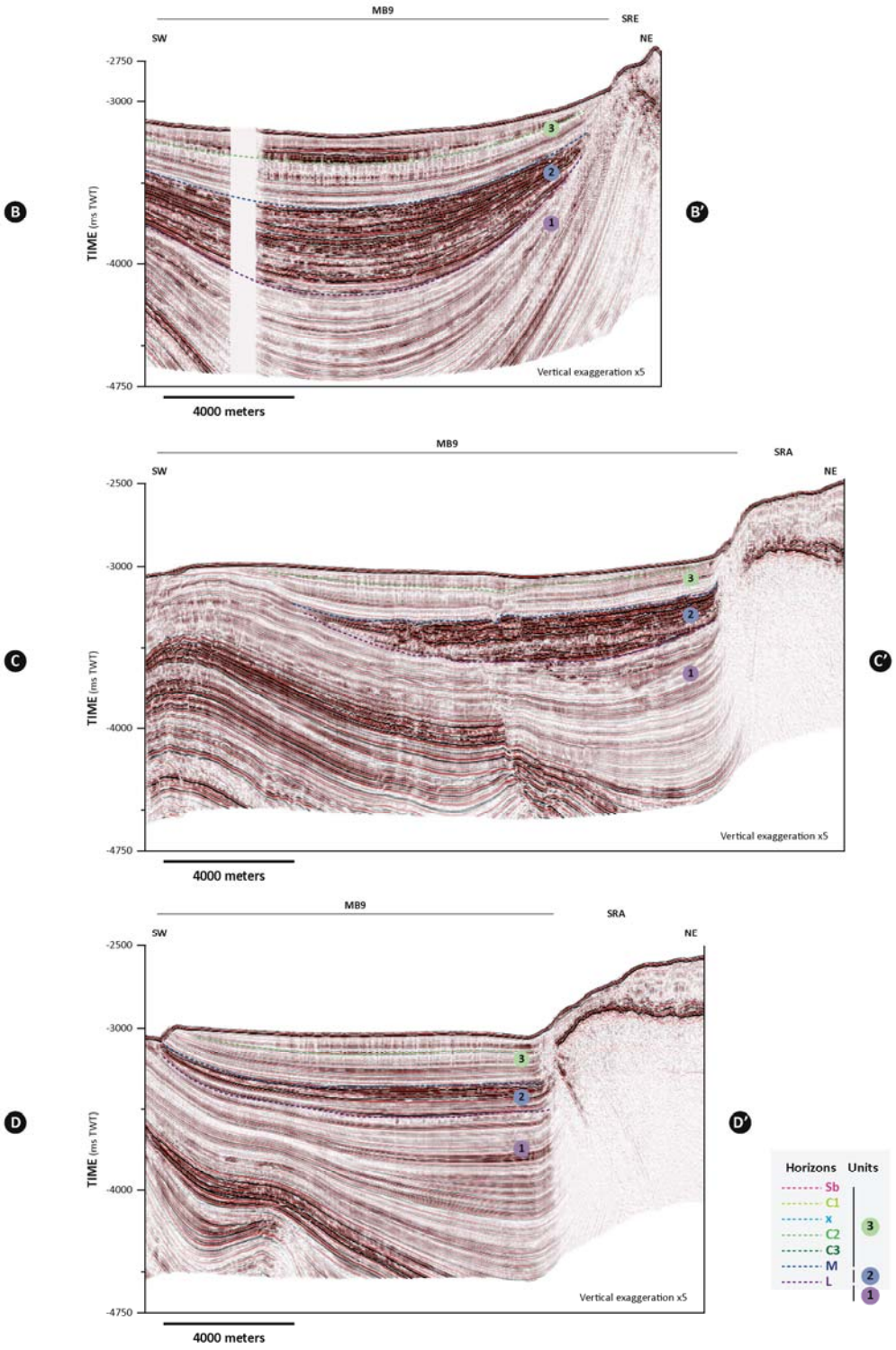

Figure 3.35. Seismic sections across mini-basin MB9. Seismic sections locations in figure 3.33. (Seismic courtesy of PGS.)

On average, salt wall height and gradient tend to decrease downslope, whereas width becomes greater (table 3.1). Their spacing also increases seaward, in agreement to what is described for gravity-driven extension of rafted structures (Rouby et al., 2003; Vendeville, 2005). The salt ridge height and width decrease northwards, terminating against the northwest-southeast trending buried salt structures mentioned above.

Table 3.1. Morphology of salt ridges in the study area.

Ridge	Length (km)	Average height (m)	Average width (m)	Average gradient (°)	
SRA	60.0	320	6689	2.74	Downslope
SRB	57.5	435	4051	6.13	^
SRC	47.5	455	3421	7.58	^
SRD	30.0	460	3267	8.02	Upslope

3.2.4. Seismic-stratigraphic correlation between salt mini-basins

Although the seismic stratigraphy of the study area can be summarised by the three distinct units described above (Units 1, 2 and 3), each mini-basin shows variations in the sedimentation style throughout time due to different topographic confinements produced by the salt structures. However, in most cases it is possible to correlate the top and base Unit reflectors and horizons **C1**, **C2**, **C3** and **C4** between adjacent salt mini-basins (figs. 3.36 and 3.37).

The use of seismic packages (sequences of reflectors with a specific seismic character) is crucial on the identification and mapping of the units throughout the entire study area. The presence of unambiguous seismic packages within a certain unit significantly aids on the determination of top and bottom reflectors of that unit, providing a higher mapping confidence.

Seismic packages are particularly important when the correlation of individual reflectors is impractical, and mapping is only viable by tracking groups of seismic reflectors. This method proved extremely useful on the subdivision of Unit 3, as following a single reflector within the polygonaly faulted interval is often challenging due to the pronounced lateral discontinuity produced by pervasive faulting.

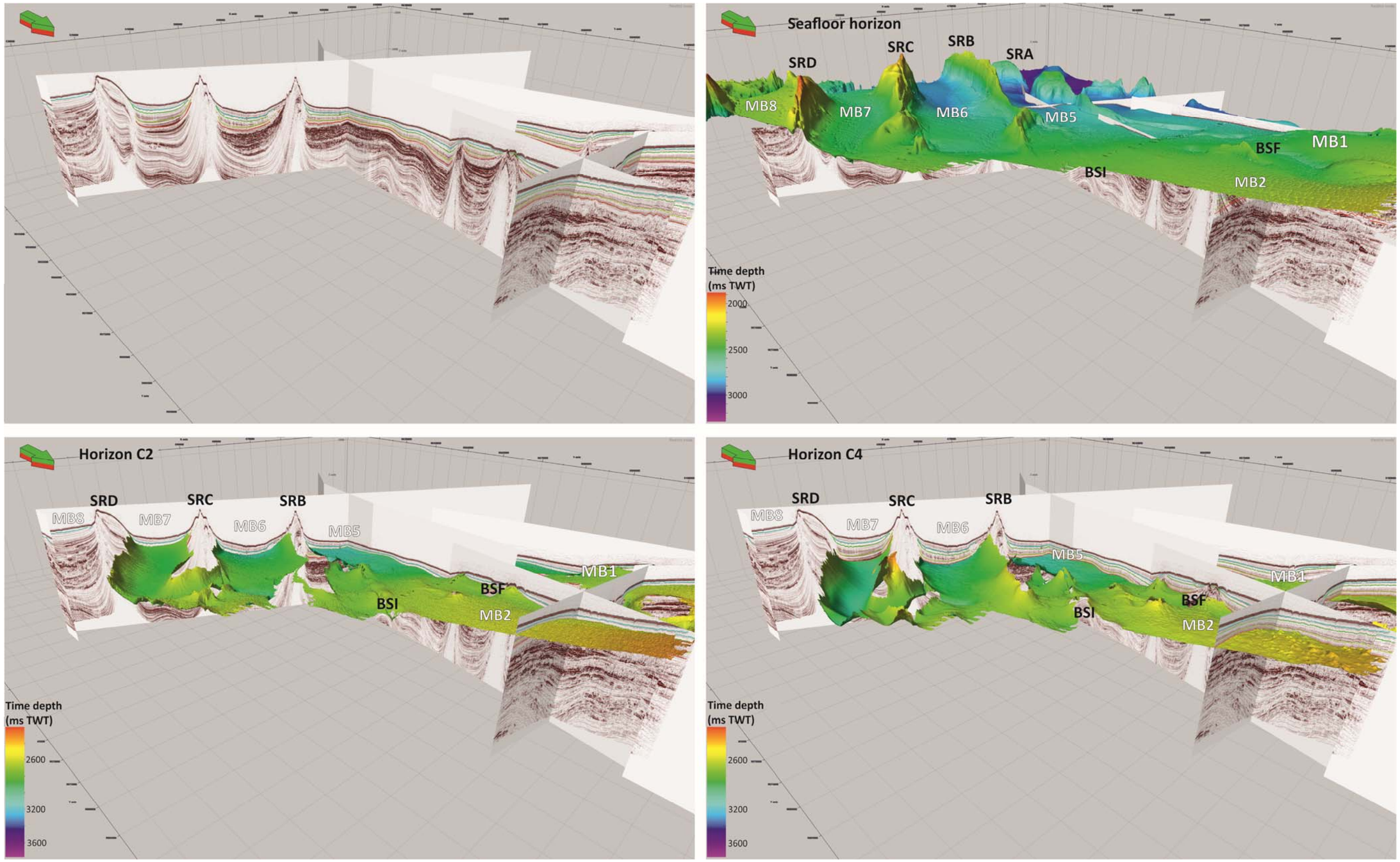

Figure 3.36. 3D perspective view of seismic sections and horizons from a northeast perspective. All the horizons are correlatable between the different mini-basins. MB = mini-basin; SR = salt ridge; BS = buried salt structure. (Seismic courtesy of PGS.)

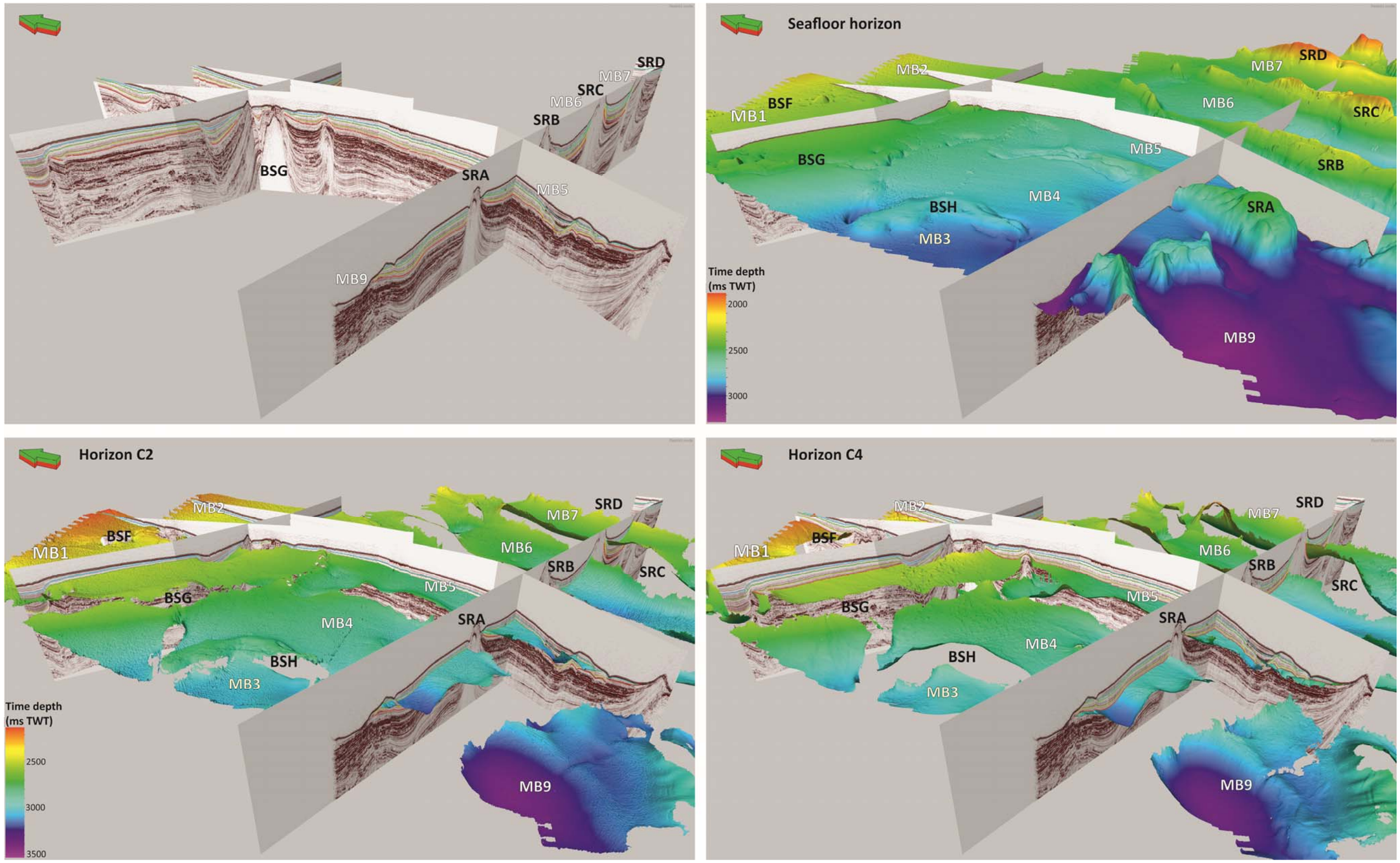

Figure 3.37. 3D perspective view of seismic sections and horizons from a southwest perspective. All the horizons are correlatable between the different mini-basins. MB = mini-basin; SR = salt ridge; BS = buried salt structure. (Seismic courtesy of PGS.)

Chapter 4

POCKMARK DISTRIBUTIONS AND
THE ROLE OF POLYGONAL FAULTS

4. Pockmark distributions and the role of polygonal faults

Abstract

This chapter describes and analyses a large array of pockmarks at the modern seabed of the Lower Congo Basin (offshore Angola), in order to understand the fluid migration routes and shallow plumbing system of the study area. The 3D seismic visualization of feeding conduits (pipes) allowed the identification of the source interval for the fluids expelled during pockmark formation. The source interval is interpreted to be a shallow depth reservoir. Spatial statistics are used to show the relationship between the underlying (polarised) polygonal fault (PPFs) patterns and seabed pockmark distributions. The results show PPFs control the linear arrangement of pockmarks and feeder pipes along fault strike, but faults do not act as conduits. Spatial statistics also revealed pockmark occurrence is not considered to be random, especially at short distances to nearest neighbours (<200m) where anti-clustering distributions suggest the presence of an exclusion zone around each pockmark in which no other pockmark will form. The results of this study are relevant for the understanding of shallow fluid plumbing systems in offshore settings, with implications for our current knowledge on shallow (<500mbsf) fluid flow systems in hydrocarbon-rich continental margins.

Keywords: pockmark distributions; polygonal faults; spatial statistics; shallow plumbing systems; Lower Congo Basin.

4.1. Introduction

Pockmarks are evidence of highly focused fluid flow, and constitute one of the best-documented expressions of seabed fluid escape, occurring at a wide variety of marine environments (Judd and Hovland, 2007). They are shallow depressions on the seafloor, generally circular to elliptical in shape, with a

diameter ranging from a few metres to hundreds of metres. Pockmarks are most commonly developed in soft, fine-grained sediments, which are remobilized or eroded by the expulsion of fluids of variable composition such as biogenic or thermogenic gas (methane), pore water, fresh water, and even oil (Berndt, 2005; Gay et al., 2006b; Judd and Hovland, 2007).

The latest advances in subsurface imaging technology have led to the discovery of numerous pockmark arrays, particularly in the Pleistocene (Andresen and Huuse, 2011; Gay et al., 2007; Gay et al., 2006b; Hovland and Judd, 1988). The vast majority of pockmark studies describe a wide range of spatial distributions, from single isolated craters to large pockmark fields (Andresen and Huuse, 2011; Gay et al., 2006b; Judd and Hovland, 2007; Moss and Cartwright, 2010), reflecting the influence of underlying seal bypass systems. Pilcher and Argent (2007) and Gay et al. (2007) have presented descriptions of linear pockmark alignments related to structural features such as normal faults, suggesting that fluid migration through these discontinuities is favoured over a more pervasive flow through the sedimentary matrix. Gay (2006a) and Davies (2003) interpret channel sand bodies as the shallow reservoirs supplying fluids to produce curvilinear pockmark trails. However, very few previous studies have explicitly identified the source layer(s) for the fluids involved during pockmark formation.

A large extraordinary array of pockmarks is described here, formed at the modern seabed, offshore Angola, and based on a high-resolution 3D seismic survey. Two distinctive pockmark populations are compared and contrasted: one which is characterised by a semi-regular distribution, and one which shows pronounced alignments of pockmarks. By comparing these two

sets and the feeder pipes that underlie some of the individual pockmarks, it is possible to describe in detail the shallow plumbing system of the studied area. It is shown that the linear alignments are entirely due to shallow normal faults. However, in contrast with previous studies, it is further demonstrated that preferential alignment of pockmarks along fault strike is not due to flow focusing on the fault surface or the action of fault planes as conduits, but it is due to fault control of the position of feeder pipes that act as conduits for focused fluid escape during pockmark formation.

The main aim of this study is to explore the insights that pockmark distributions can bring on the question of source, timing, triggers, origin of fluids, and fluid migration routes, in order to improve our understanding of shallow plumbing systems in sedimentary basins.

4.2. Local setting

4.2.1. Study area

The work presented in this chapter is focused on the distributions of pipes and pockmarks of mini-basins MB6 and MB7, delimited by the salt-related structures SRB, SRC, and SRD. This case study covers an area of approximately 1600km^2 in water depths ranging from 1425m (1900ms TWT) to 2440m (3250ms TWT).

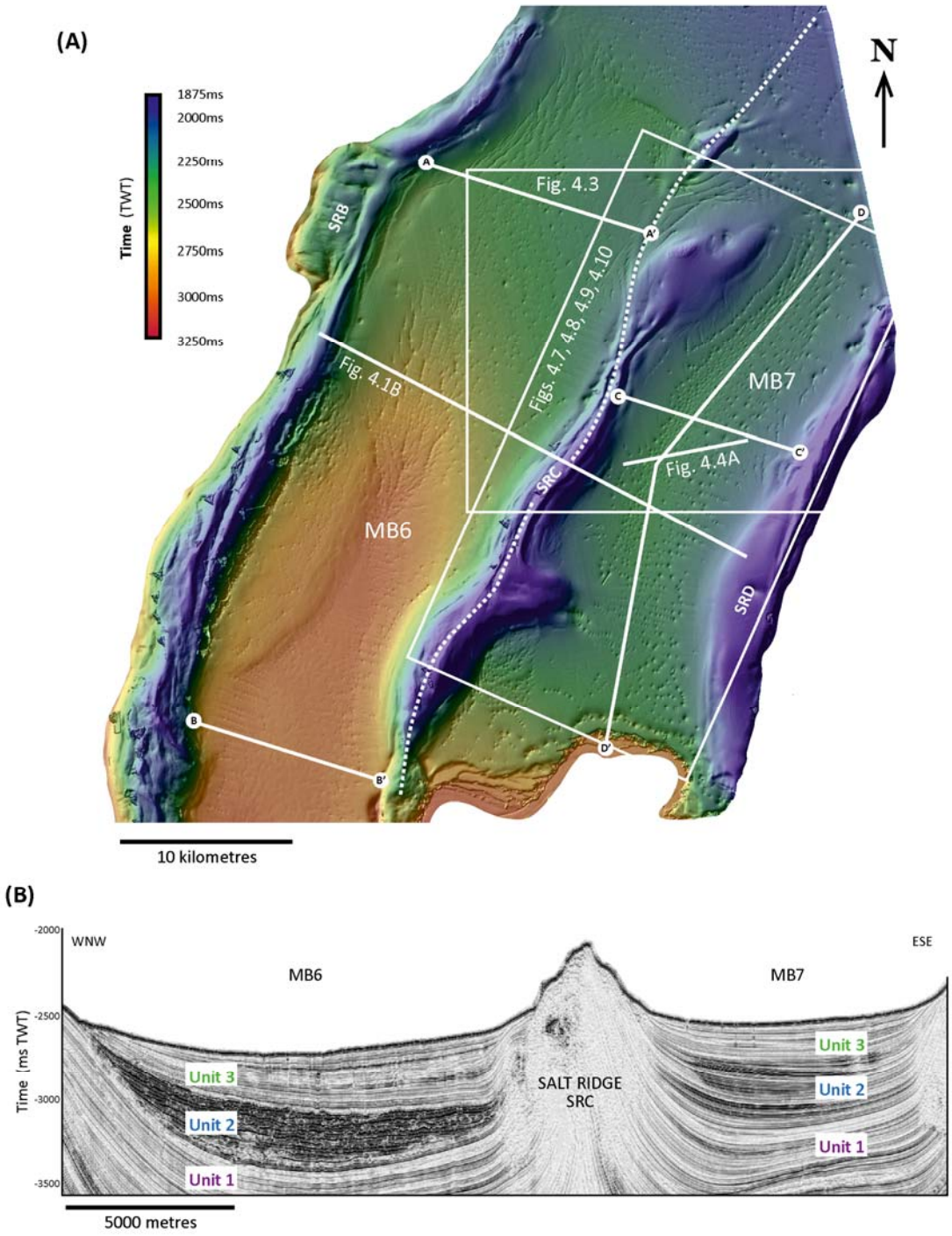

Figure 4.1. (A) Structure map of the seafloor of the study area, and location of figures 4.1B, 4.3, 4.4A, 4.7, 4.9, 4.10 and 4.11. Mini-basins MB6 and MB7 are delimited by NNE-SSW salt ridges. Seabed pockmarks are observed as circular depressions distributed throughout the mini-basins. **(B)** WNW-ESE seismic cross-section intersecting mini-basins MB6 and MB7, and the salt ridge that separates them. Units 1, 2 and 3 are shown having distinct seismic characters (see section 3.2.2). (Seismic courtesy of PGS.)

4.2.2. Shallow seismic stratigraphy

The seismic stratigraphy of the study area is divided into three main seismic-stratigraphic units: 1, 2, and 3 (figs. 4.1b, 4.2, and 3.10). The stratigraphic interval of interest for this study covers the shallow-most seismic Units 2 and 3 (fig. 4.2), which correlate to the successions of Oligocene-Miocene and Pliocene-Holocene age, respectively.

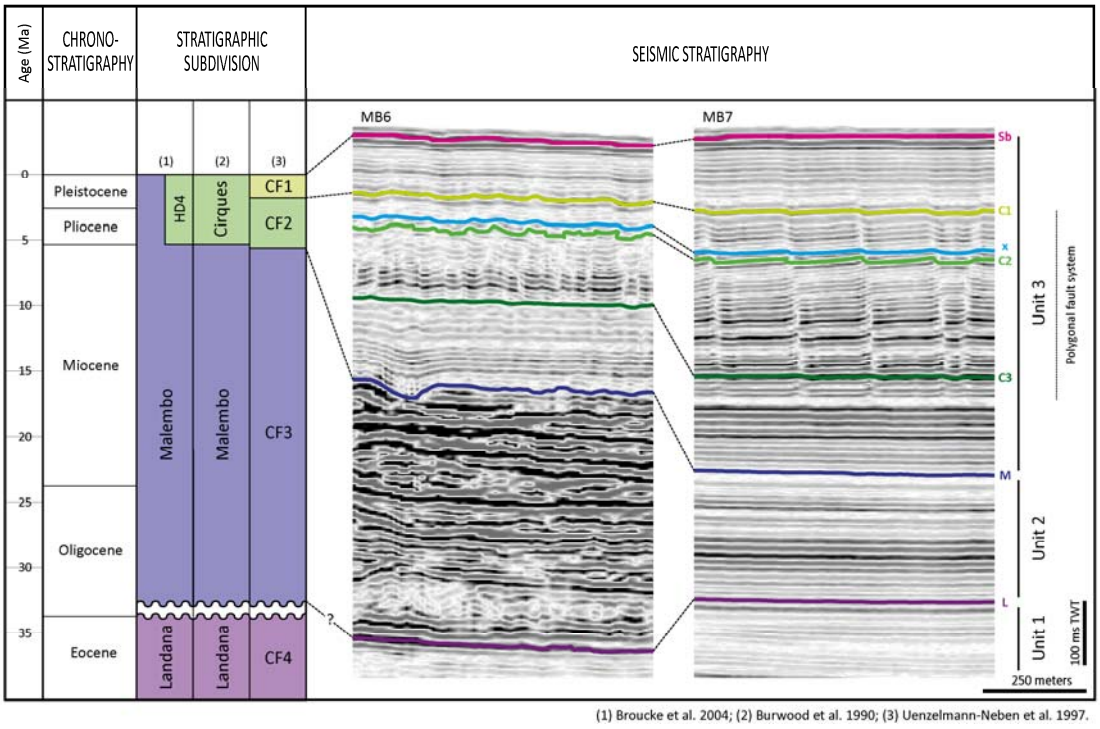

Figure 4.2. Seismic stratigraphy of mini-basin MB6 and MB7. **Sb** = seabed (top of Unit 3); **C1** = top of polygonal fault tier; **x** = estimated source layer; **C2** = reflection at middle of polygonal fault tier; **C3** = base of polygonal fault tier; **M** = top of Unit 2; **L** = top of Unit 1 (see fig. 3.10). (Seismic courtesy of PGS.)

Unit 1 is characterised by laterally continuous, sub-parallel to parallel reflections of very low to moderate amplitude, which is mostly associated with fine-grained deposits. Occasional reflections of higher amplitude may indicate deposition of coarser sediments. Local wavy reflections of low sinuosity

represent sediment waves with upslope migration. This unit is interpreted to comprise hemipelagic deposits intercalated with minor turbiditic lobes and sparse contourite drifts, confined within the mini-basins. The contact with Unit 2 above is an erosional unconformity.

Unit 2 is characterised by sub-parallel to chaotic reflections of moderate to very high amplitude. It is generally thicker along the mini-basins axis, thinning and onlapping towards the flanking salt structures (fig. 4.1b). Moderate to low amplitude chaotic reflections present at the bottom of this unit are associated with mass-transport deposits which are intercalated with thin laterally continuous turbidites (moderately high amplitude reflections). The top succession of Unit 2 exhibits continuous high to very high amplitude reflections related to axial submarine channels and less confined clastic deposition (including channel levees), interbedded with hemipelagic intervals (figs. 4.1b and 4.2).

Unit 3 is characterised by laterally continuous and parallel reflections of very low to moderate amplitude, representative of fine-grained hemipelagic deposition. Reflections of slightly higher amplitude in this succession may be associated with the deposition of coarser grain size material (Gay et al., 2007), possibly related to laterally continuous turbidites. Similarly to Unit 2, Unit 3 has maximum thicknesses along the axis of the mini-basins and thins towards the flanking salt structures, exhibiting onlapping reflection configurations (fig. 4.1b).

Although the shallow seismic stratigraphy of the Lower Congo Basin can be summarised by the units described above, the mini-basins presented in this

study show variations in the sedimentation style throughout time due to different topographic confinements produced by the salt structures. The mass-flow channels that are generally described in the literature for the Oligocene-Miocene succession (Unit 2) (Anka et al., 2013) are absent in mini-basin MB7 (fig. 4.2). In fact, the whole shallow stratigraphy of mini-basin MB6 is characterised by hemipelagic deposition, covering the entire time span between late Paleocene (top of Unit 1) to the present day (modern seabed). However it is possible to correlate the top and base reflection markers of seismic-stratigraphic Unit 2 between the adjacent mini-basins, where the dividing salt ridge does not pierce the entire overburden (NE limit of the study area). There is no marked transition between Units 2 and 3, although some reflections exhibit enhanced amplitude along the basin axis and are interpreted as possible unconfined turbidites.

4.2.2.1. Layer-bound faults in Unit 3

Strata within the middle interval of Unit 3 are pervasively deformed by small normal faults. These faults exhibit a wide range of planform geometries in mini-basins MB6 and MB7. A polygonal arrangement is mapped in the central regions of mini-basin MB6 where faults strike at a variety of azimuths, defining a network of polygons made of short fault segments up to 640 m in length (fig. 4.3). However, this pattern changes quite dramatically towards the margins of the mini-basins. The distinctive polygonal character is abruptly lost in the proximity to salt bodies, where faults strike orthogonally to these structures and exhibit longer traces up to 3400m in length (fig. 4.3). This fault

behaviour corresponds to that seen more widely in the study area and described in section 3.2.2.

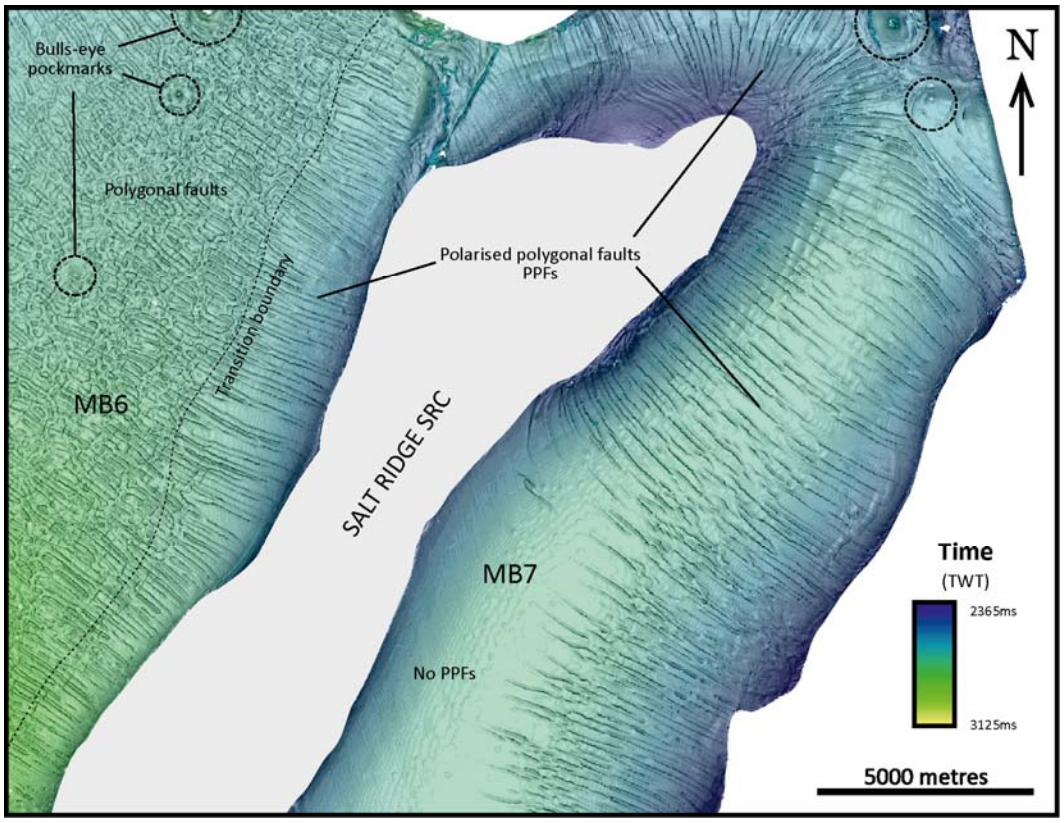

Figure 4.3.(A) Structure and dip map of seismic horizon **C2**. Note the contrast between polygonal fault arrangements in different areas – the central region of mini-basin MB6 exhibits a typical polygonal pattern, whereas mini-basin MB7 and salt margins of MB6 present polarised faults striking perpendicular to salt structures. Although MB6 is pervasively affected by polygonal faulting, there are regions of MB7 absent of seismically resolvable discontinuities (ex., the south-western rim of MB7 depicted here).

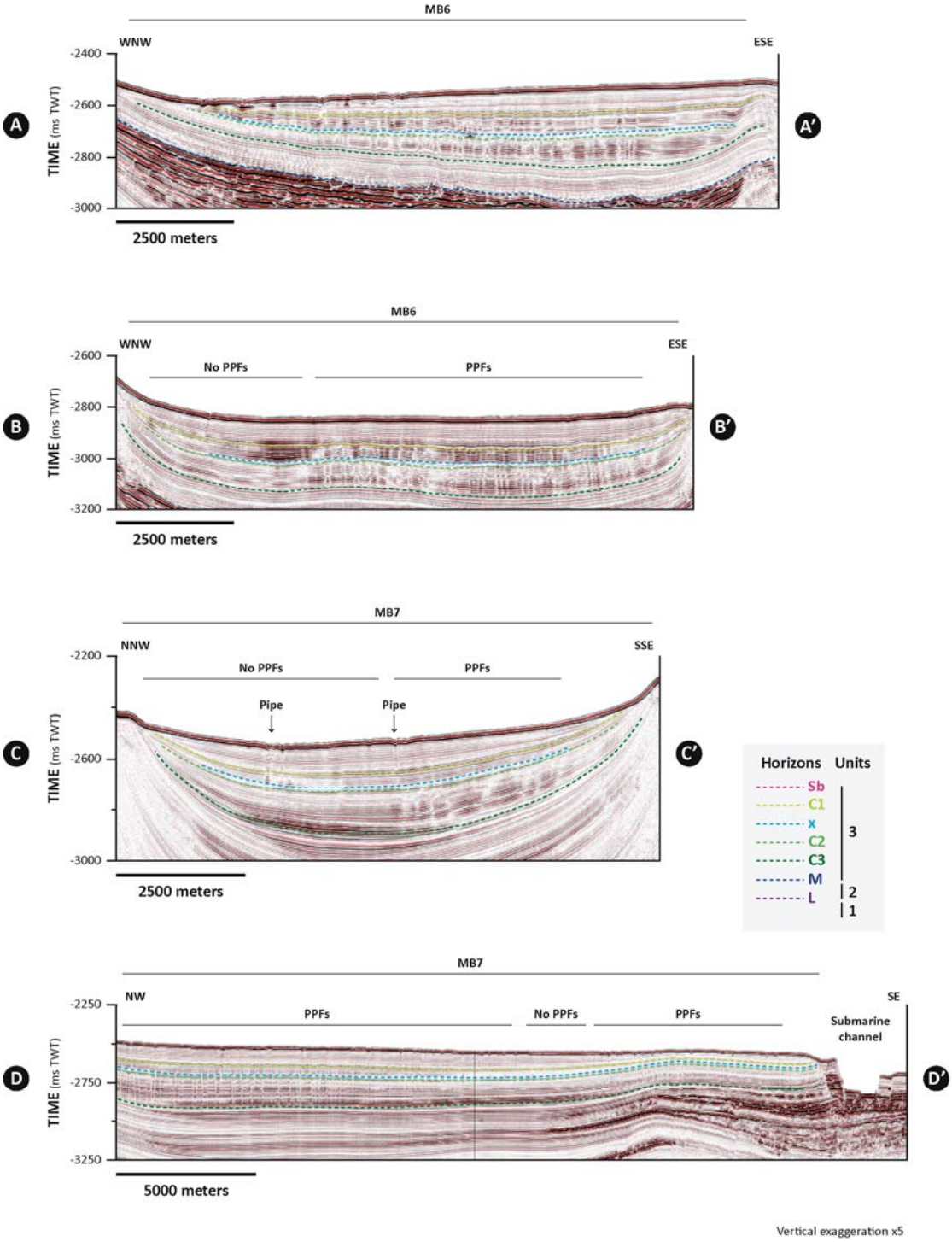

Figure 4.3. (B) Seismic sections along MB6 (A-A' and B-B') and MB7 (C-C' and D-D') showing the polygonal faulted tier in both mini-basins. Locations of these sections are on figure 4.1. (Seismic courtesy of PGS.)

The fault pattern in mini-basin MB7 is dominated by strong alignment of fault strikes orthogonal to the margins, and an almost uni-directional pattern across the mini-basin axis (fig. 4.3). In the central areas of this mini-basin, adjacent fault segments commonly interact to form relay ramps. In cross-section the layer-bound faults of mini-basins MB6 and MB7 are generally planar and very steep (with dips ranging from 50° to 70°). They are confined vertically in their extent to the strata between horizons **C1** and **C3** (fig. 4.3 and 4.4a), hence being interpreted as layer-bound faults. The highest displacements are concentrated in the central sections of the fault surfaces, reaching up to 21m. The faulted interval exhibits variable thickness, ranging between 26 and 240m (31ms and 285ms TWT). It has a wedge geometry and thins towards the basin rims, where the majority of the constituent faults dip upslope (towards the thin end of the wedge). The upper limit of the interval is marked by the same reflection in both mini-basins, i.e. horizon **C1** (fig. 4.3). This is interpreted to represent the time at which the layer-bound faulting system became inactive. The base of the interval gradually decreases in depth as it thins towards the flanks of the mini-basins (figs. 4.3 and 4.4a).

As mentioned in Chapter 3, the layer-bound fault system exhibits many of the characteristics of polygonal fault systems. The classical polygonal pattern is observed in central areas of mini-basin MB6, but on its rims the faults are strongly polarised in their strikes and approximately orthogonal to salt structures. By analogy with polygonal fault systems that occur around salt diapirs (Carruthers et al., 2013), the orthogonal orientation of the faults described in this study may result from local stress field perturbations either related to salt emplacement/growth or consequent changes in topographic gradient (or a combination of both). These fault arrays are referred here to as

polarised polygonal faults (PPFs). PPFs occur in regions surrounding salt walls, confined to areas inside a transition boundary of 1315-3170m radii. Polygonal faults occur in areas outside the transition boundary. Due to the close proximity of two adjacent salt structures, the transition boundaries of the limiting salt walls of mini-basin MB7 overlap, preventing the development of polygonal fault arrays, and instead resulting in a unidirectional fault array.

One notable feature of the distribution of the PPF system is that it is absent in a region along the western rim of mini-basin MB7, as PPFs die out laterally where a slight decrease in seismic amplitudes is observed. This change in amplitude response and fault behaviour may be due to lateral lithological variations, such as deposition of coarser sediments or subtle changes in mineralogy, which may not be suitable for polygonal faulting formation (Cartwright, 2011). Thinning of the basal strata of the tier observed in this part of the mini-basin could also prevent fault nucleation and propagation, if polygonal faulting is initiated within this package. However, it is possible that in this region (polarised) polygonal faulting is of a magnitude that the faults are not imaged, i.e. below the seismic resolution limit.

4.3. Fluid flow features

A variety of fluid flow features were developed within the shallowest hemipelagic sediments of Unit 3. In the study area, vertically focused fluid flow features include pockmarks and pipes. More laterally extensive fluid flow processes are represented by bottom simulating reflections (BSRs) associated with gas hydrates, and isolated high amplitude reflections (bright spots).

4.3.1. Pockmarks

The seafloor of the surveyed region is populated by pockmarks, with 5% of its area (approx. 80km^2) occupied by 3410 of these fluid expulsion features. Seabed pockmarks occur within a wide range of water depths, from 1830m to 2250m below sea-level. They are recognized as circular to elongated depressions related to erosion of underlying reflections (Judd and Hovland, 2007). Seabed pockmarks occur mostly within the salt mini-basins, with densities ranging between <1 and 17 pockmarks per km^2. Few pockmarks are observed above salt ridges. Pockmark size ranges from 45m to 665m in diameter (length of long axis; average = 185m), and from a few meters to 36m in depth (average ≈ 5m depth) (fig. 4.5). No seismically resolvable onlap or drape infill has been observed for the seabed pockmarks.

Buried pockmarks representing paleo fluid expulsion events are sporadically observed within mini-basin MB6. Their stratigraphic occurrence is limited to certain seismic reflections within the polygonal-faulted interval of Unit 3 (fig. 4.4b). They occur in spatial associations of vertically stacked paleo-pockmarks separated by intervals of drape and onlap fill, and are located at the centre of polygonal fault cells. The pockmark morphology, stratigraphic occurrence, and spatial relationship to polygonal faults which concentrically surround a pockmark depression are similar to those previously described as 'bulls-eye' pockmarks by Andresen and Huuse (2011), and which were the subject of a recent structural analytical study (Morgan et al., 2015). The formation process, timing and source of fluids for the genesis of the paleo-pockmarks are thoroughly discussed by these authors. Our observations

support the interpretation that these paleo-pockmarks predate the formation of the polygonal fault system affecting the surrounding strata. For the present study however, only the latest episode of fluid expulsion is considered, focusing on understanding the distribution of seabed pockmarks.

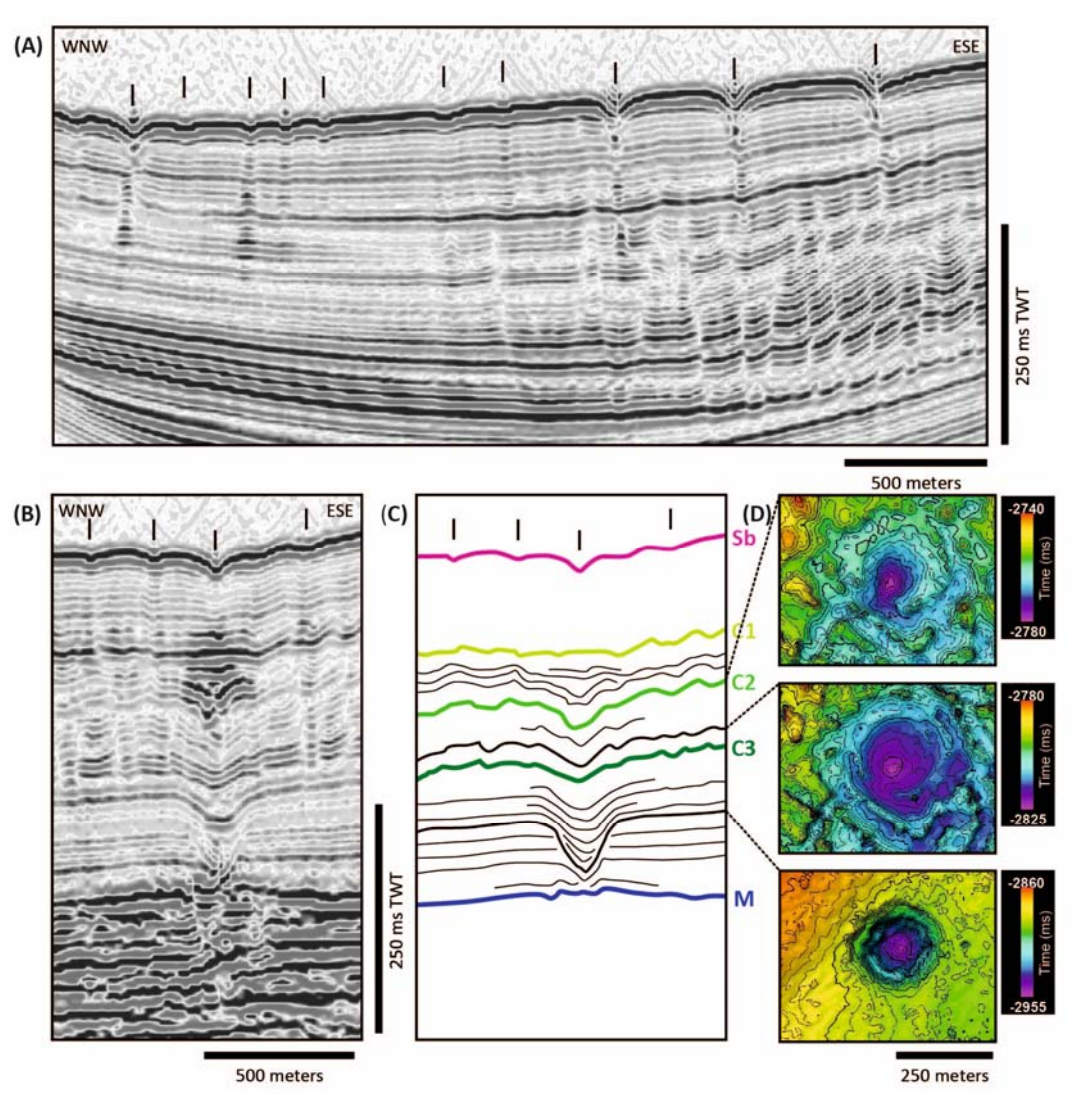

Figure 4.4. Seabed pockmarks versus sub-surface bulls-eye pockmarks – seismic profiles and maps at event reflections. **(A)** Seismic section across mini-basin MB7, showing seabed pockmarks, feeding pipes and the polygonal fault system within Unit 3. Arrows point to seabed pockmarks. Location of seismic section is in Fig. 4.1A. **(B)** Seismic section intersecting a sub-surface bulls-eye pockmark and several seabed pockmarks (black arrows) in mini-basin MB6. **(C)** Interpretation of seismic section shown in (B). **(D)** Maps of reflections within the bulls-eye pockmark, showing its internal structure and variation with depth. (Seismic courtesy of PGS.)

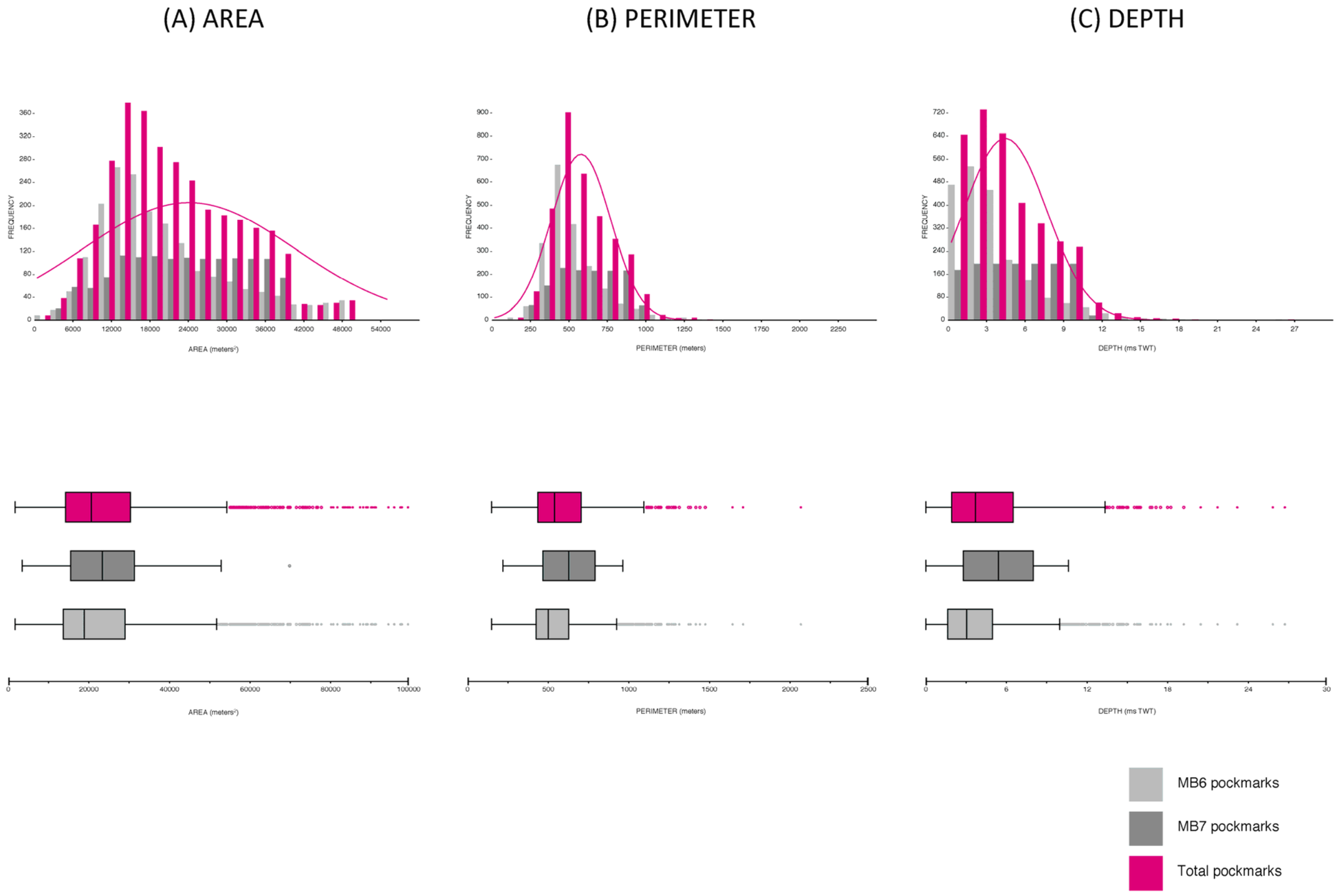

Figure 4.5A-C. Statistical distributions for pockmark morphological parameters in mini-basins MB6 and MB7: area (A), perimeter (B), and depth (C). Pink line = best fit Gaussian curve (normal distribution).

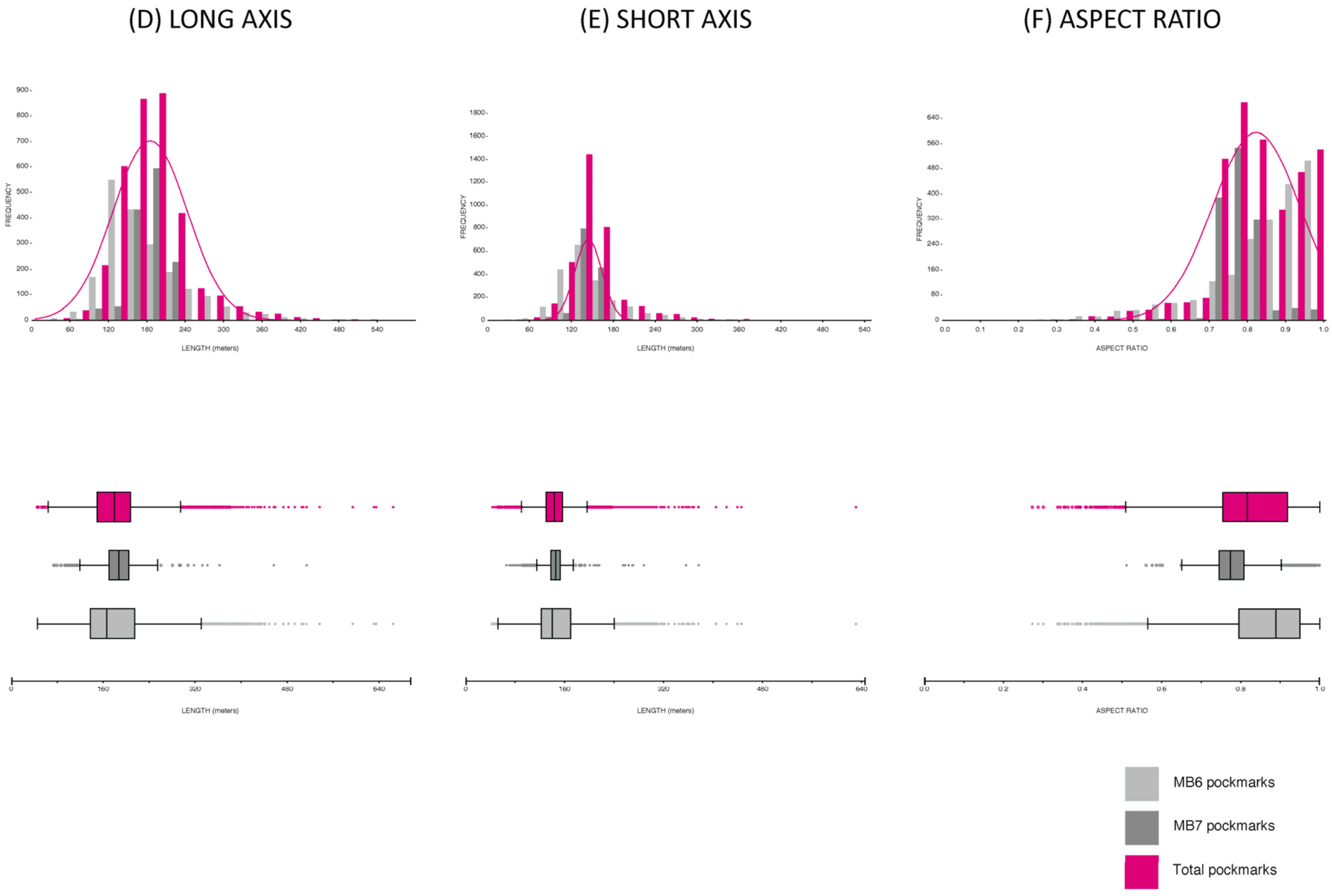

Figure 4.5D-F. Statistical distributions for pockmark morphological parameters in mini-basins MB6 and MB7: long axis (D), short axis (E), and aspect ratio (F). Pink line = best fit Gaussian curve (normal distribution).

(G) AZIMUTH OF LONG AXIS

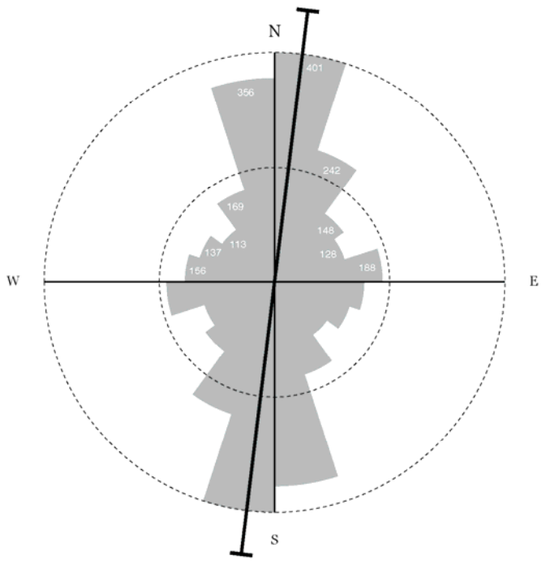

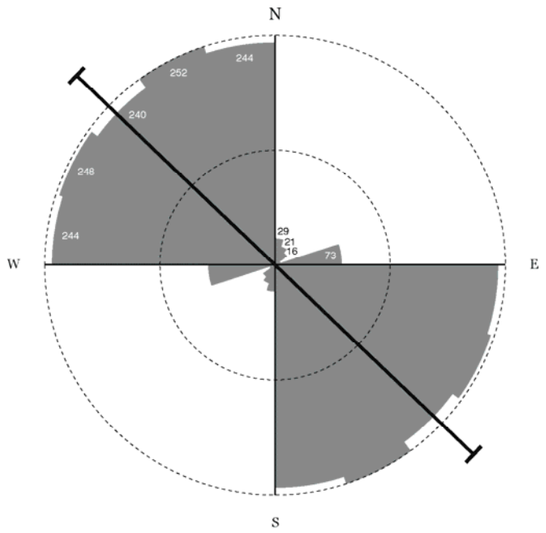

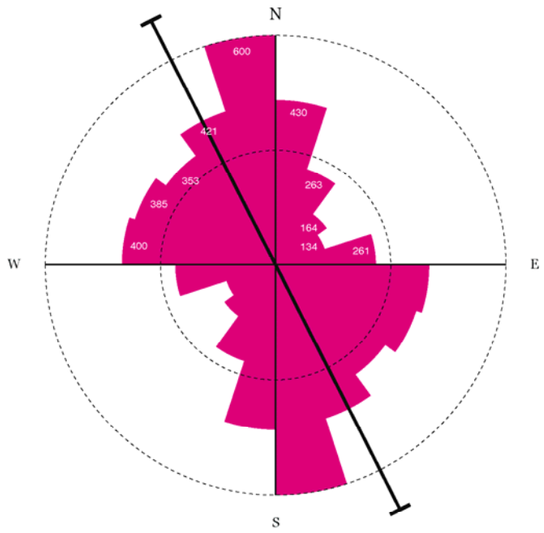

(H) POCKMARK MORPHOLOGY GENERAL STATISTICS

	AREA meters^2	PERIMETER meters	DEPTH ms TWT	LONG AXIS meters	SHORT AXIS meters	ASPECT RATIO	AZIMUTH degrees	COUNT
MINIMUM	1642.2	148.3	< 0.1	45.4	43.3	0.27	0.0	
MAXIMUM	331497.4	2067.0	30.3	664.5	630.9	1.00	179.8	
MEAN	24681.8	546.5	3.8	184.8	152.3	0.85	78.6	2038
STANDARD DEVIATION	19934.6	188.0	3.2	70.8	50.2	0.13	59.8	
MINIMUM	3449.8	218.4	< 0.1	73.9	65.9	0.51	0.0	
MAXIMUM	69822.9	962.1	10.6	514.1	376.6	1.0	177.5	
MEAN	23217.2	625.6	5.4	185.8	144.4	0.78	125.2	1373
STANDARD DEVIATION	9575.4	191.3	3.0	30.4	19.4	0.06	0.06	
MINIMUM	1642.2	148.3	< 0.1	45.4	43.3	0.27	0.0	
MAXIMUM	331497.4	2067.0	30.3	664.5	630.9	1.00	179.8	
MEAN	24092.2	578.4	4.5	185.2	149.1	0.82	97.3	3411
STANDARD DEVIATION	16576.8	193.3	3.2	58.0	40.9	0.11	56.7	

MB6 pockmarks
MB7 pockmarks
Total pockmarks

Figure 4.5G-H. Statistical distributions for pockmark morphological parameters in mini-basins MB6 and MB7: azimuth of long axis (G). A table summary of the general statistics for pockmark morphology in shown in panel H.

4.3.2. Pipes

Seabed pockmarks are often associated with pipes, consisting of narrow zones of vertically stacked high amplitude anomalies, occasionally exhibiting disrupted internal reflections (fig. 4.6). Considered as seal bypass systems, pipes occur at leak-off points for overpressured pore fluids and promote cross-stratal focused fluid flow (Cartwright et al., 2007; Løseth et al., 2009; Cartwright and Santamarina, 2015). In the study area pipes are mostly observed in mini-basin MB7 and are stratigraphically restricted to Unit 3. In total, 570 vertically stacked amplitude anomalies were identified in mini-basin MB7, representing the largest array of pipes yet identified in a single geological province (fig. 4.7). Their vertical extent varies between 38m and 170m (average 110m height) (fig. 4.8). In planform pipes are generally circular, with diameters ranging from 57m to 145m (average 95m wide). Slenderness ratios (height/diameter; Cartwright and Santamarina, 2015) vary from 0.49 to 2.44.

The reflection amplitudes within pipes are generally higher than the background reflectivity of the hosting sediments, and localised amplitude anomalies are generally marked by abrupt lateral changes of amplitude. The lower reflections within pipes commonly display upward convex geometries, up to the top of the polygonaly-faulted tier (horizon **C1**; figs. 4.6 and 4.9). Above this and towards the seabed, pipes exhibit a sag geometry with downward (concave) deflection of reflections. All pipes are observed to terminate upwards at seabed pockmarks. However, internal structures are better imaged and resolved in pipes with diameters wider than the limit of seismic resolution (>25m). The widest pipes reach up to 144m in diameter and

often exhibit disrupted internal reflections and loss of coherency towards the top, with sharp 'sags' delimiting the lateral margins. Narrow pipes have gently curving deflections.

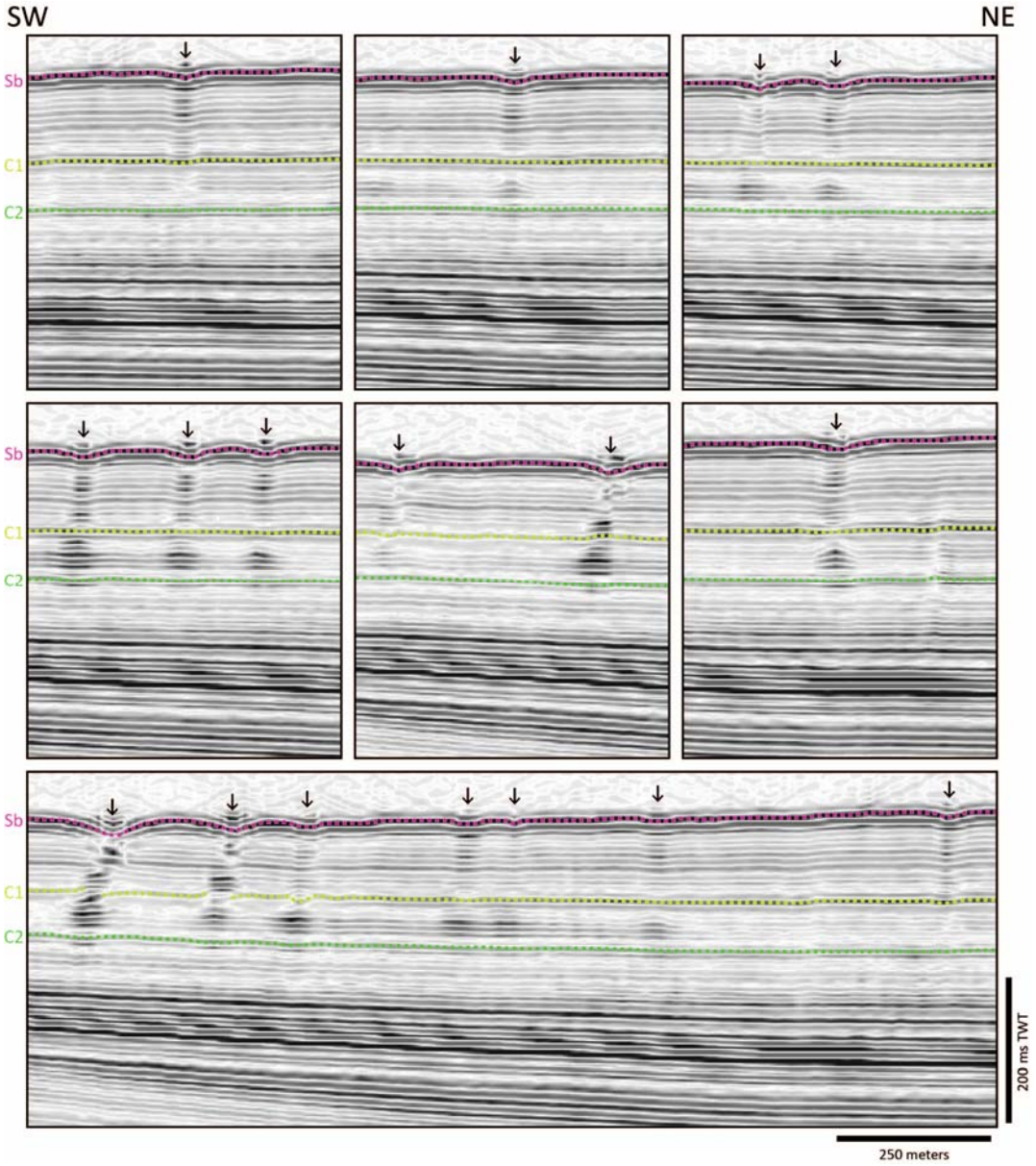

Figure 4.6. Seismic profiles of pipes present in a non-polygonaly faulted area of mini-basin MB7, occurring without being associated to any seismically resolvable discontinuity. Pipe defined as columnar zone of enhanced amplitude (vertically stacked amplitude anomalies), occasionally presenting disrupted internal reflections. (Seismic courtesy of PGS.)

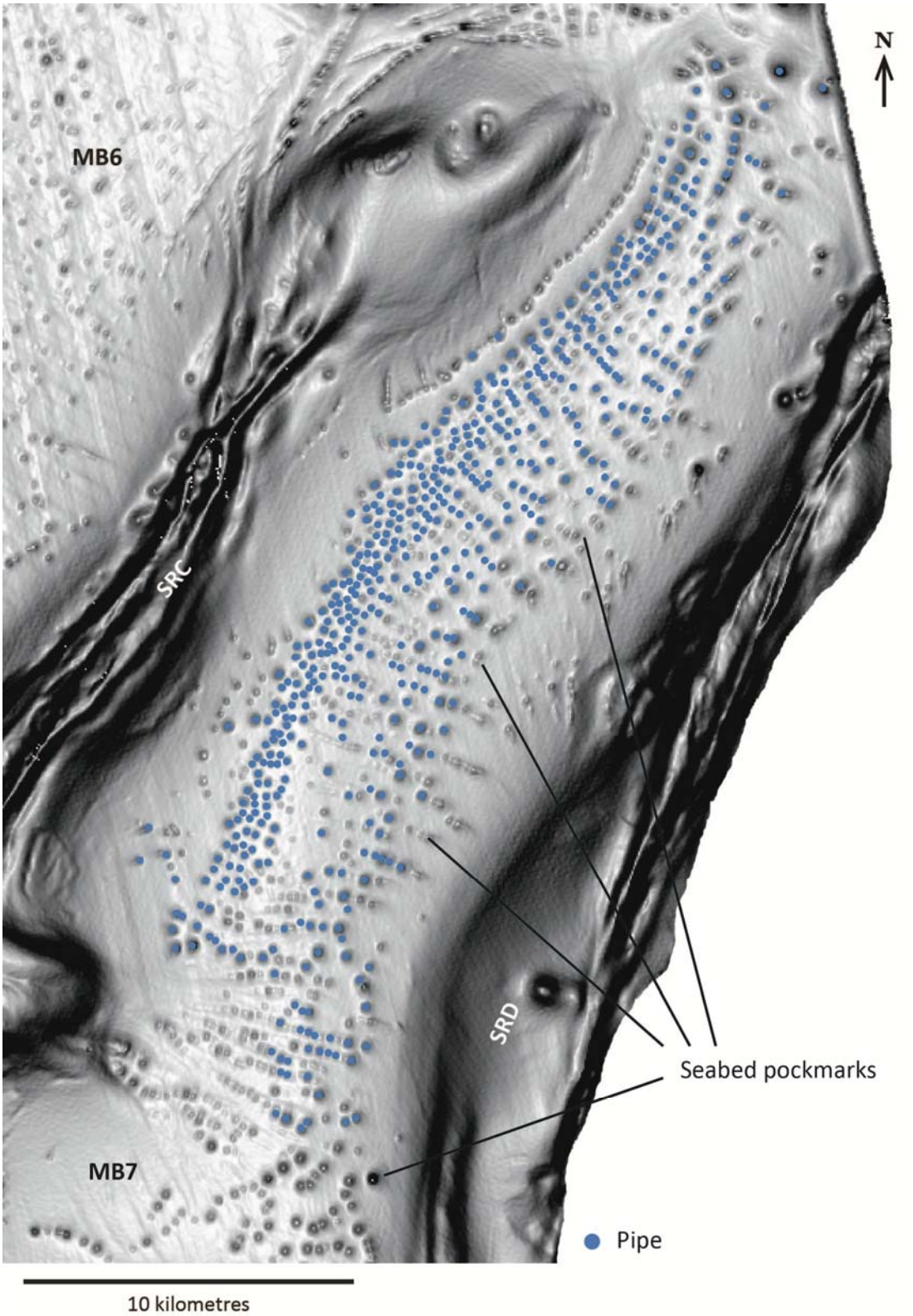

Figure 4.7. Seabed TWT dip-map showing the location of the 570 pipes (blue dots) identified in mini-basin MB7, and their relation to seabed pockmarks.

Recognition of the basal structure of pipes is crucial for constraining the location of the source of fluids (Moss & Cartwright, 2010). It is interpreted here that the base of stacked amplitude anomalies marks the horizon from which pipes emanate. Based on this, an histogram was constructed of the stratigraphic position of the base of the 570 pipes identified in mini-basin MB7 (fig. 4.9). At least ten reflections with Unit 3 were correlated in their entirety throughout MB7. Each reflection in MB7 was consecutively numbered from seabed (**Sb**) downwards to horizon **C3**. The ten main horizons identified and used for this analysis are: **r1**, **C1**, **r2**, **x**, **C2**, **r3**, **r4**, **r5**, **r6**, and **C3**. The frequency histogram displays the number of pipes that rise from a particular horizon (pipe amplitude anomaly base). The vast majority of pipes (46.0% of measured pipes) originate within the seismic interval between horizons **x** (17 to 113mbsf, 20-135ms TWT bsf) and **C2** (42 to 172mbsf, 50-205ms TWT bsf), up to 32m (38ms TWT) thick. Seismic horizon **x** is characterised by a soft reflection (decrease in acoustic impedance) whose amplitude and lateral continuity is highly variable. The remaining columnar amplitude anomalies (54.0%) originate at various levels within an interval up to 207ms TWT thick, 3 to 204m below the seabed. Amplitude anomalies rooted below the interval **x-C2** (between horizons **r3** and **r6**) comprise 29.3% of measured pipes, and shallower pipes rising above horizon **x** (between horizons **r1** and **r2**) compose 24.7% of total pipe population. In general, pipes are identified where the highest amplitudes are observed for their basal reflections. Beneath horizon **r6** there is no disruption or amplitude enhancement that may be attributed to the presence of focused fluid flow features. Pipes terminate at the seabed at the centre of their associated pockmark depression. The bases of pipes are much harder to define in the region where polarised polygonal faults are observed.

Imaging problems associated with faults introduce local amplitude variations, and these can be sometimes confused with pipe-related anomalies. This issue is especially pertinent for pipes apparently rooted below reflection **C2**: the source of these pipes may be in fact at shallower intervals, as the close proximity of amplitude anomalies associated to PPFs cannot be distinguished from the pipe base anomaly. For pipes rooted above reflection **C2**, the positions are considered to be accurate to ±2 seismic reflections. The occurrence of pipes apparently rooted below reflection **C2** may be associated with seismic artefacts induced by fault proximity.

Although composed of stacked amplitude anomalies (c.f. Ho et al., 2012), pipes are rarely strictly vertical (90°) features. Instead most pipes exhibit a slight angle with the vertical, typically quasi-perpendicular to the slope/seafloor. In MB7, pipes that occur on the western side of the mini-basin dip 45° to 86° towards W-NW, whereas pipes on the eastern side dip 40° to 86° towards E-SE. The opposite dipping direction of pipes in opposite sides of the mini-basin and their angle with the seafloor suggest that pipes were rotated after they formed, most probably by basin tilting due to recent salt growth. However, it is possible that overpressured fluids were expelled via a non-vertical migration path, exploiting pre-existing sub-seismic discontinuities in the hosting stratigraphy.

A critical observation of pipe distribution is that pipe occurrence is spatially mostly limited to the area of MB7 where the interval between horizons **x** and **C2** is present. Similarly, seabed pockmarks are not observed outside the area covered by this interval. Remarkably, the longest pockmark alignment in the study area (10km length, composed of 35 seabed pockmarks) is vertically

above the pinch-out of the same interval (fig. 4.10), where fluids are most likely to accumulate (by lateral and vertical migration). Together with the results obtained from the pipe base histogram (fig. 4.9), these observations imply that the interval **x-C2** within Unit 3 is the sedimentary package from which the fluids involved in pockmark formation were stored prior to their expulsion at the modern seabed.

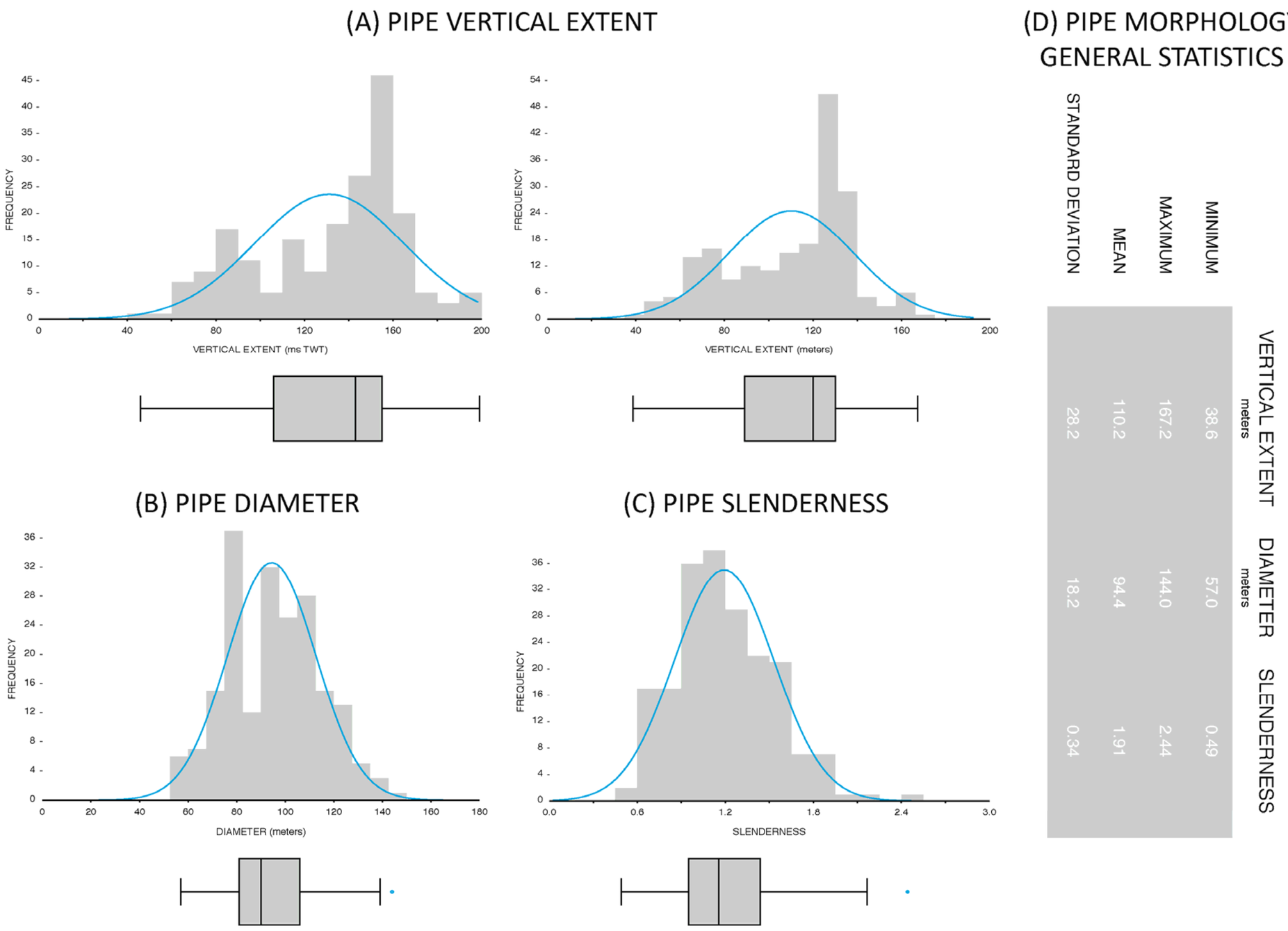

Figure 4.8. Statistical distributions for pipe morphological parameters in mini-basin MB7: vertical extent (A), diameter (B), and slenderness (C). Blue line = best fit Gaussian curve (normal distribution). A table summary of the general statistics for pipe morphology in shown in panel D.

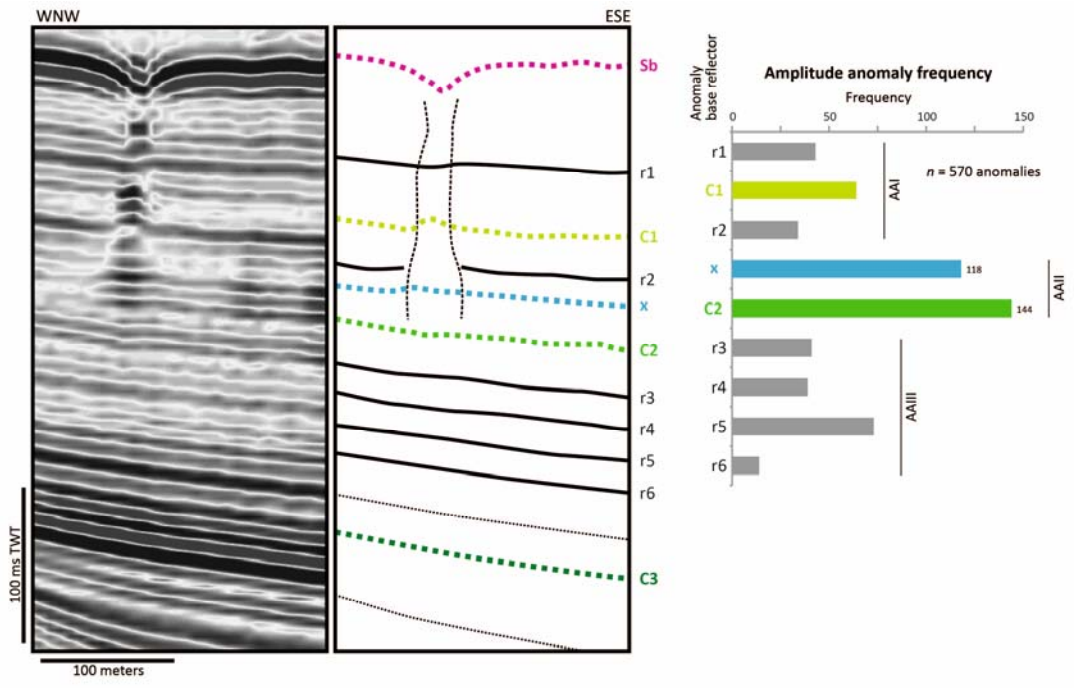

Figure 4.9. Pipe amplitude anomaly base reflection frequency. Each reflection in mini-basin MB7 was consecutively numbered from seabed (**Sb**) downwards (horizons **r1**, **C1**, **r2**, **x**, **C2**, **r3**, **r4**, **r5**, **r6**, and **C3**). The frequency histogram displays the number of pipes that rise from a particular horizon (pipe amplitude anomaly base). Most pipe bases are located between horizons **x** and **C2** (46% pipes). Data collected for 570 pipes in mini-basin MB7. Pipe shown in seismic section is located in the non-polygonaly faulted area of MB7, and rises from reflection **C2**. (Seismic courtesy of PGS.)

The pinch-out of this interval is characterised by low amplitude (almost transparent) internal reflections onlapping onto the base of horizon **x**. It is possible therefore that this specific low amplitude package may be composed of sediments that were involved in supplying the fluids for the pockmark formation process.

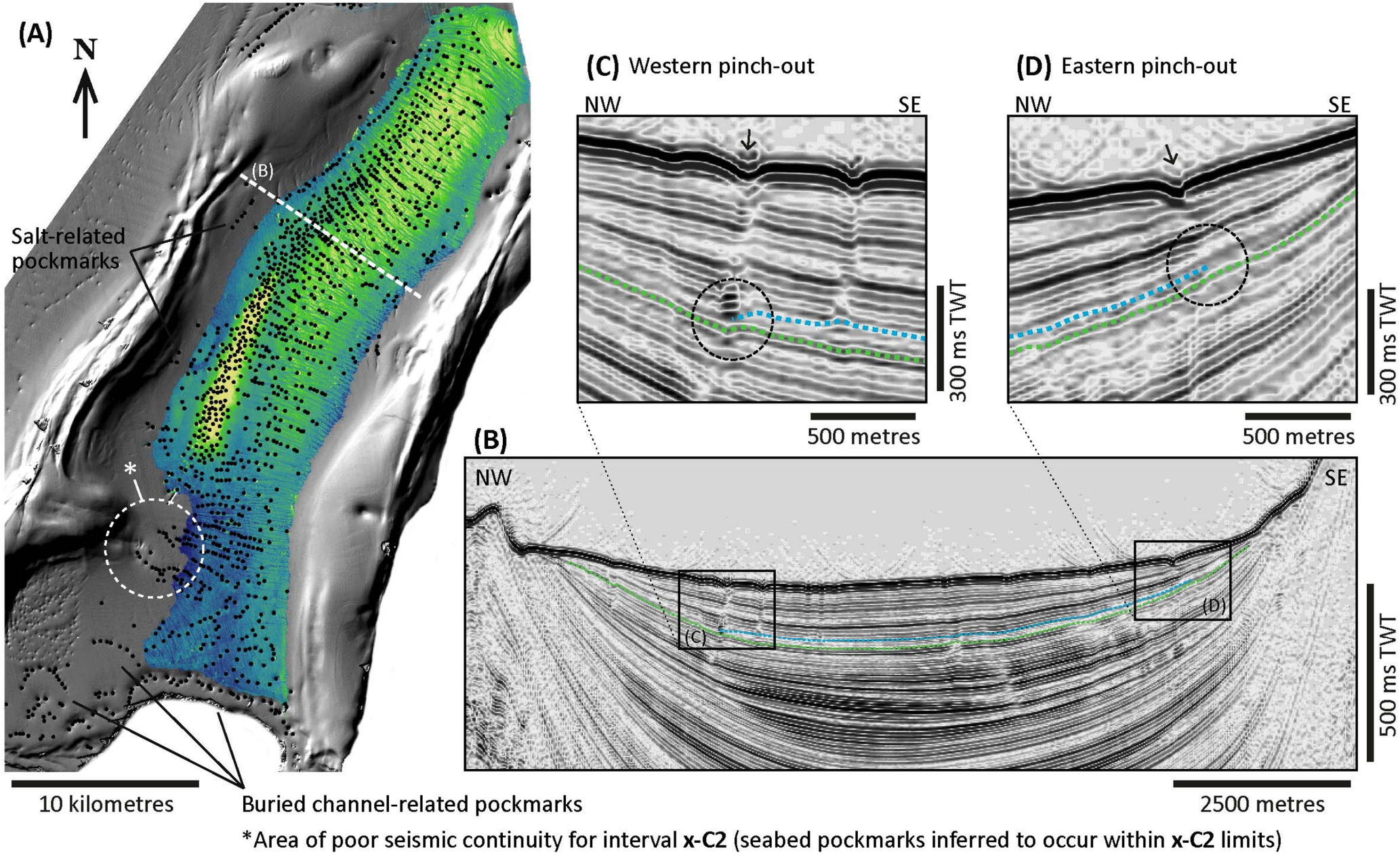

Figure 4.10. (A) RMS amplitude map of the seismic interval between reflections **x-C2**, and seabed pockmark distribution – pockmarks within mini-basin MB7 mostly occur in areas where the interval was not deposited. Longest pockmark alignment parallel to the salt ridge is vertically above the pinch-out of the same interval. **(B)** Transverse seismic section of mini-basin MB7, highlighting interval **x-C2**. **(C)** and **(D)** Close-up of pinch-out areas of **x-C2**, showing internal reflections and pockmark vertically above pinch-outs (turbiditic levees/confined drifts?). **x** = dashed blue line; **C2** = dashed green line; seabed pockmarks = black dots and arrows. (Seismic courtesy of PGS.)

4.3.3. BSRs and gas hydrates

Semi-continuous reflections of negative polarity and moderate to strong amplitude are observed to crosscut the shallow stratigraphy. The present day depth range of these reflections is 75-150mbsf (90-180ms TWT bsf). Their geometry and phase is consistent with bottom-simulating reflections (BSRs) associated with the base of the gas hydrate stability zone (GHSZ), as previously described for deep-water settings offshore West Africa (Cunningham and Lindholm, 2000; Gay et al., 2006b). The strength of these reflections decreases laterally, and they are difficult to identify within salt mini-basins where bedding is conformable to seabed morphology. Local brightening of BSRs and elevation of their position relative to the seafloor is observed in faulted areas of the salt anticlines, where salt is closer to the seabed, and when underlain by high-amplitude turbiditic channel deposits. Nervetheless, the presence of localised development of a gas hydrate-related BSR implies a sufficient methane flux was present at least locally in the study area.

4.4. Spatial analysis of fluid flow features

The most striking features observed on the seabed of the surveyed area are the extraordinary density and total number of pockmarks (>3410), their wide variability in size, and their remarkable distribution patterns. Seabed pockmarks are commonly arranged in a linear fashion, forming trails or alignments of up to 10km in length. The phenomenal abundance of pipes and pockmark trails in the region provides a unique opportunity to analyse their

distribution employing spatial statistical methods, which may contribute to the understanding of the migration pathways associated to this fluid flow system.

4.4.1. Pipe source distributions

To analyse the distribution of the 570 pipes observed in MB7, their spatial coordinates were taken at the centre of their basal amplitude anomaly. The total population of pipes was sub-divided into three sub-populations according to the source intervals separated by the distinctive frequency peak at the interval **x-C2** observed on the pipe source histogram (fig. 4.9). Pipe groups **AAI**, **AAII** and **AAIII** comprise conduits rising from intervals **r1-r2**, **x-C2**, and **r3-r6**, respectively. Amplitude anomalies rooted within interval **r3-r6** (**AAIII**) occur exclusively in faulted areas, whereas pipes **AI** and **AAII** (intervals **r1-r2** and **x-C2**) are distributed throughout the mini-basin, regardless of the presence or absence of seismically resolvable layer-bound faults (PPFs) (51.1% of pipes **AAII** occur in non-faulted areas, and the remaining 48.9% on faulted regions). Average nearest neighbour analysis (see section 2.3) conducted on the total population of pipes and on each of the three sub-populations show that the distribution of pipes is considered clustered at the 99% statistical significance level (see table 4.1). These results however do not shed light on if (and how) the source and position of individual pipes is related to other neighbouring pipes.

Table 4.1. Spatial distribution analysis of amplitude anomalies in MB7. Average nearest neighbour test results shown for 99% of statistical significance. AA = amplitude anomaly; ANN = average nearest neighbour (Rn); z = *z* score.

Reflector	AA freq.	%		ANN		ANN	
r1	43	7.5		CLUSTERED	Rn=0.73; z=-3.33		
C1	64	11.2	24.7	CLUSTERED	Rn=0.81; z=-2.84	CLUSTERED	Rn=0.79; z=-4.86
r2	34	6.0		RANDOM	Rn=0.91; z=-0.978		
x	118	20.7	46.0	CLUSTERED	Rn=0.83; z=-3.47	CLUSTERED	Rn=0.82; z=-5.55
C2	144	25.3		CLUSTERED	Rn=0.64; z=-8.32		
r3	41	7.2		CLUSTERED	Rn=0.70; z=-3.71		
r4	39	6.8	29.3	RANDOM	Rn=0.98; z=-0.23	CLUSTERED	Rn=0.74; z=-6.31
r5	73	12.8		CLUSTERED	Rn=0.76; z=-3.84		
r6	14	2.5		DISPERSED	Rn=1.97; z=6.95		
Total	570	100.0	100.0	CLUSTERED	Rn=0.91; z=-4.00	CLUSTERED	Rn=0.91; z=-4.00

Moss and Cartwright (2010) used Anselin Local Moran's I cluster and outlier analysis to statistically assess the spatial distribution of pipe formation in distinct time phases. The same approach is used here (see section 2.3), but adapted in order to determine whether pipes with a base in a particular source interval are preferentially surrounded by pipes sourced either from the same or from a different interval. Pipes that are considered statistically significant outliers (i.e., pipes that have a statistically significant different source value from their neighbours) and clusters (pipes surrounded by others with a statistically similar source) have a local Moran's I (*Ii*) *Z* scores <-2 or >2, respectively. Pipes that are not statistically significant (non-outliers) hold *Ii Z* scores between -1 and 1. The results obtained from this method are shown in figure 4.11. Statistically significant outliers (dark blue circles) and clusters (red circles) occur almost exclusively in faulted areas, whereas pipes with no statistically significant source value are most observed in non-faulted regions (green circles). The null hypothesis that there is no systematic pattern to the spatial distribution of pipe sources is rejected at the >95% confidence level for

faulted domains, but not for the non-faulted corridor. The results from the Moran's I spatial analysis suggest pipe source distribution is influenced by the presence or absence of PPFs. Taking into account imaging problems induced by faults (see section 4.3.2), pipes apparently rooted below reflection **C2** may be associated with seismic artefacts. As such, the identification of the pipe source interval is more reliable in non-faulted areas, which the data suggests to be interval **x-C2**.

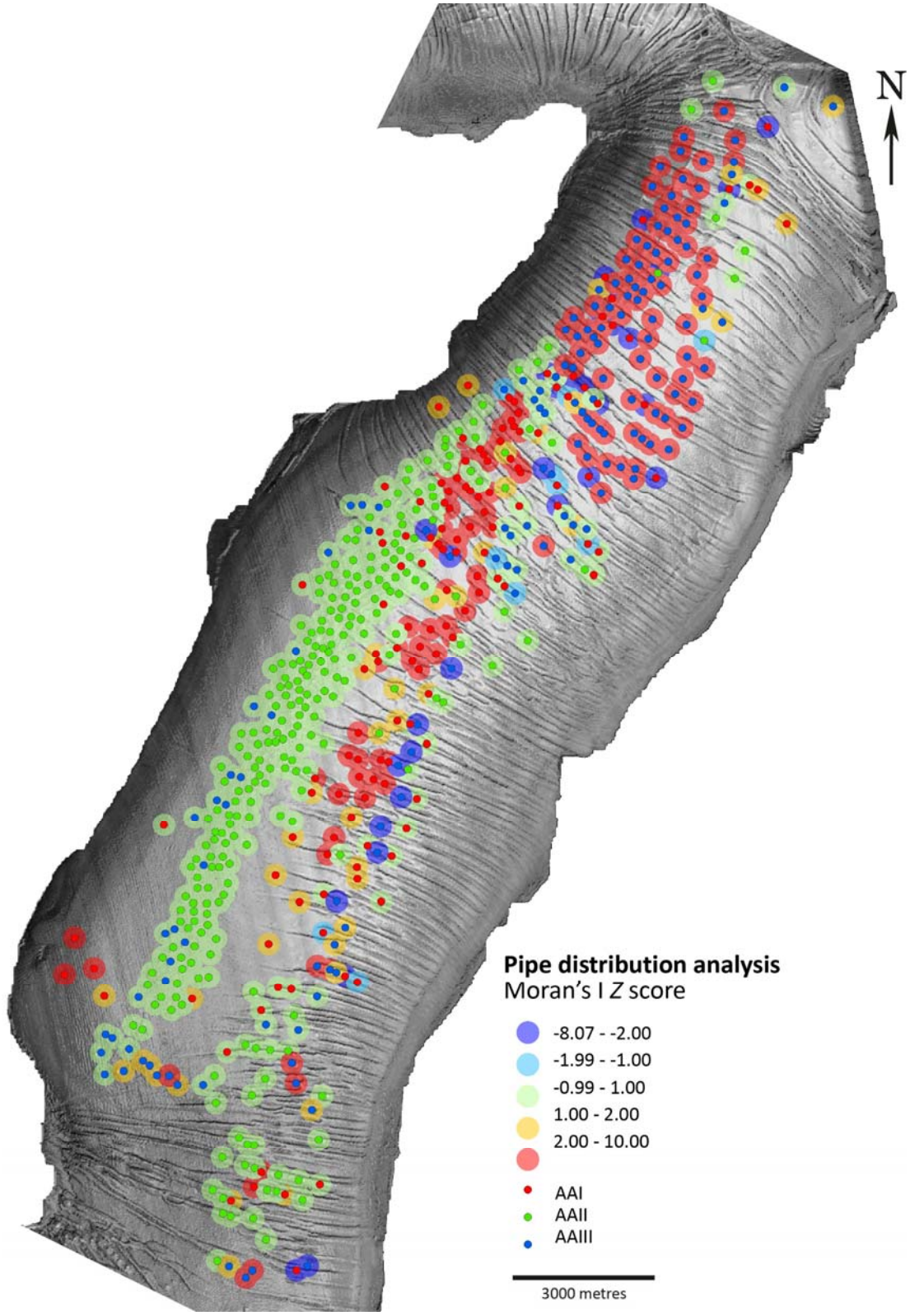

Figure 4.11. Spatial distribution of pipes within mini-basin MB7, and their relation to underlying polarised polygonal faults (see text for explanation).

4.4.2. Pockmark distributions

The statistical detection of point alignments employed in this study (the continuous sector method of Hammer, 2009) is used to numerically corroborate the pockmark patterns that stand out to the eye, and to determine whether these result from random chance or are in fact controlled by underlying discontinuities, as implied by the results of the pipe source spatial analysis above.

All seabed pockmarks observed in mini-basin MB7 were mapped (comprising a total of 1086 pockmarks), and the spatial coordinates of their centre were taken at the deepest point within each depression.

By overlaying the centre points of seabed pockmarks to a dip map of horizon **C2**, it is possible to compare the spatial distribution of these pockmarks with the underlying polarised polygonal faults (fig. 4.12). Two sets of pockmarks were defined according to where they occur in relation to faults: set A (283 pockmarks, green dots) includes pockmarks located in areas not affected by any seismic resolvable discontinuity, and set B (803 pockmarks, pink dots) comprises pockmarks that occur within faulted regions. Visually, set B pockmarks tend to be arranged in a linear fashion striking parallel to the underlying faults, whereas the distribution of set A pockmarks appears to be more erratic (fig. 4.12a).

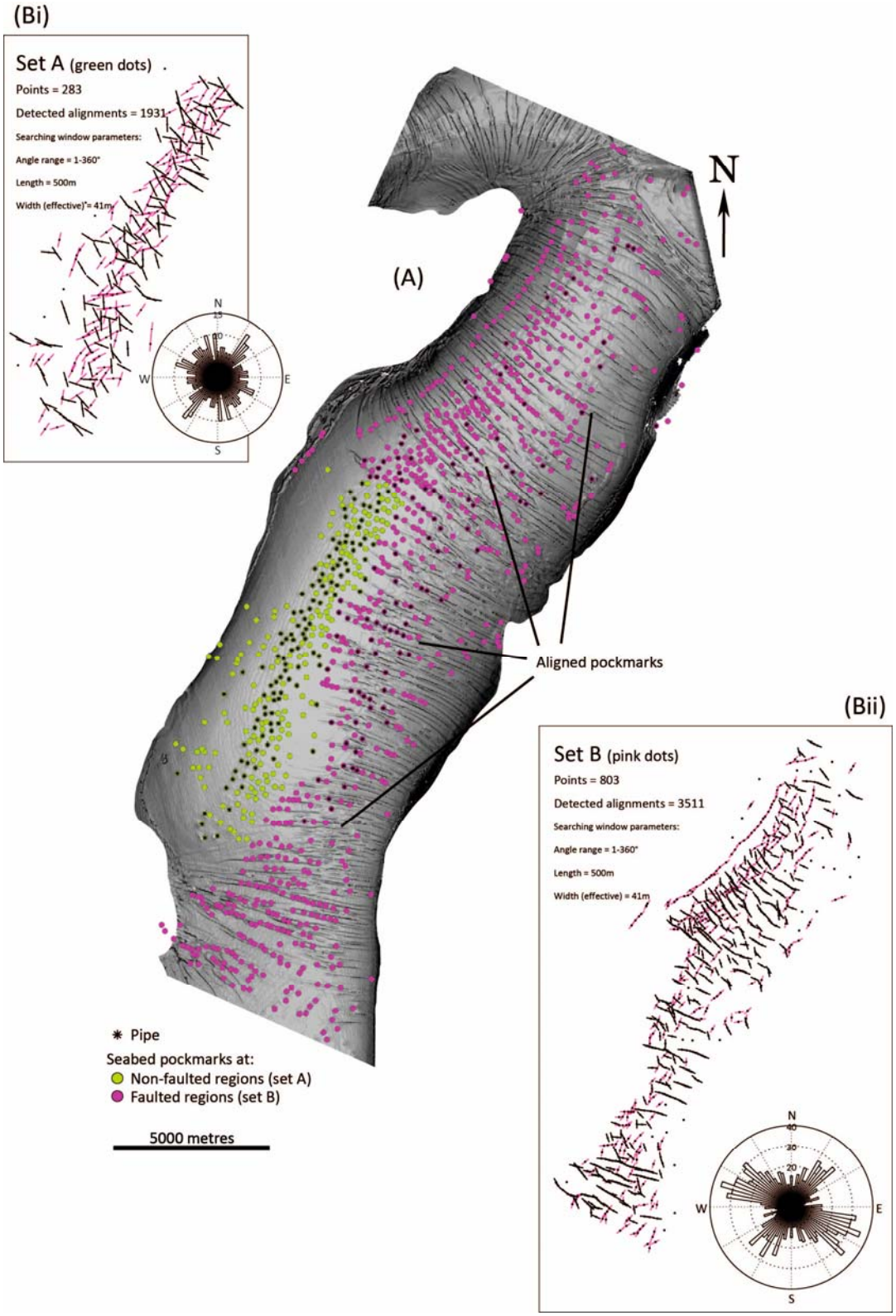

Figure 4.12. (A) Spatial distribution of seabed pockmarks and pipes of mini-basin MB7, and their relation to underlying hybrid polygonal faults. Two sets of pockmarks were defined: set A (green dots) – pockmarks not associated to any seismic resolvable discontinuity; set B (pink dots) – pockmarks occurring at faulted regions. Visually, set B pockmarks tend to be arranged in a linear fashion, striking parallel to underlying faults, whereas set A pockmark distribution appears to be more erratic. **(B)** Seabed pockmark alignment detection. *i*) Alignment detection for set A. *ii*) Alignment for set B.

The results of the alignment detection by the continuous sector method (Hammer, 2009) employed for sets A and B are shown in figures 4.12b*i* and 4.12b*ii*, respectively (see section 2.3). To perform this test, a circular zone around each point of 500m radius (*r*, radial length) was chosen, as this value detected the largest amount of point alignments for the two sets of pockmarks. With r = 500m, this method extracted 30 aligned segments amongst set A pockmarks, and 322 aligned segments for set B (at a significance level of $p < 0.5$) (values of r <500m or >500m did not detected as many alignments). The rose diagrams in these figures show the orientation of the aligned segments obtained for both sets (fig. 4.12b). A Rayleigh test on the extracted alignments shows no preferred direction of set A alignments ($p = 0.74$), whereas set B exhibits a highly significant and marked preferred direction NNW-SSE (mean direction = 156.34°) ($p < 0.001$). Using the Watson-Williams (equal mean) and Mardia-Watson-Wheeler (equal distribution) tests for analysing the distributions of two samples of directional data (Mardia, 1972 *in* Hammer et al., 2001; see section 2.3), the calculated preferred orientation of set B pockmark alignments was compared to the strikes of the 601 underlying polarised polygonal faults. A highly significant p value ($p << 0.001$) was calculated on both tests, supporting the inference that there is a genuine spatial relationship between seabed pockmark distributions and polarised polygonal fault patterns.

First order spatial statistics (average nearest neighbour) at the 99% significance level applied to set A pockmarks show a tendency towards a dispersed distribution (Rn = 1.10, z = 3.20), whereas set B pockmarks are considered clustered (Rn = 0.75, z = -15.16). However, this method only

provides a general distribution overview based on average values with a single search radius, which is not precise enough to assess pipe distributions at the basin scale.

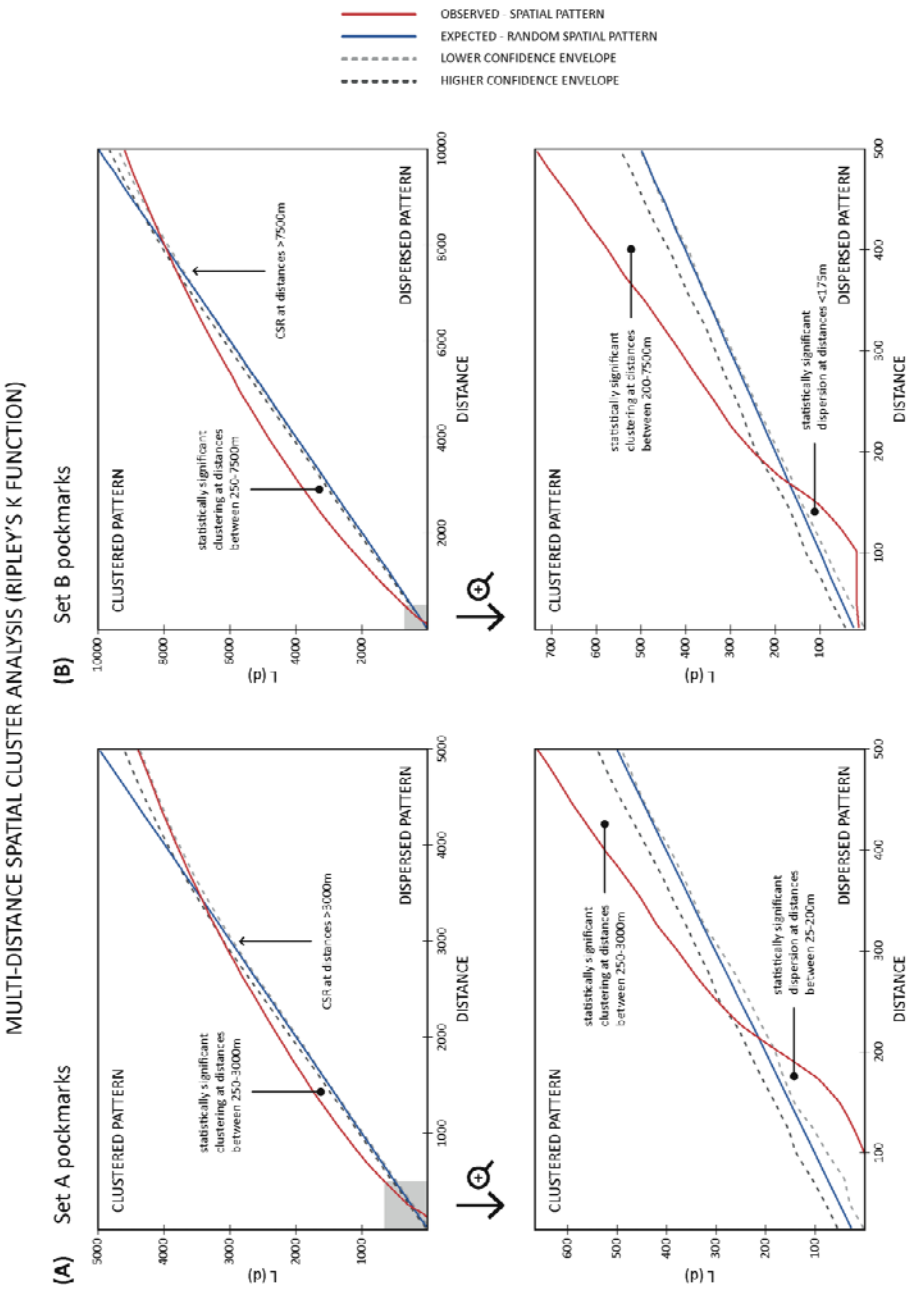

Figure 4.13. Graphical representation of the multi-distance spatial cluster analysis (Ripley's K function) for **(A)** set A and **(B)** set B pockmarks. The bottom plots show the results obtain for small distances between nearest neighbouring pockmarks (corresponding to the grey shaded areas of the plots on the top). CSR = complete spatial randomness.

To examine patterns at multiple search radii, the more robust Multi-distance spatial cluster analysis (Ripley's K Function) is employed (see section 2.3). Ripley's statistics (*L(d)*) applied to set A pockmarks revealed a tendency towards dispersion or anti-clustering between 25-200m of distance between nearest neighbours, tending to be clustered for distances between 250-3000m (fig. 4.13a). The same analysis showed a lateral inhibition (dispersion) of set B pockmarks up to a distance of 175m, and a tendency towards clustering for distances larger than 200m (fig. 4.13b). These results suggest an exclusion zone of <200m around each pockmark where no other pockmark will form, which may reflect the existence of a fluid drainage area – the area around the base of each feeding pipe in which the source interval was depleted of fluids to produce a pockmark. This is in agreement to the "pockmark drainage cell" described by Moss and Cartwright (Moss, 2010; Moss and Cartwright, 2010).

From ca. 3000m onwards, *L(d)* falls below the high confidence interval, becoming flattened in the manner expected from complete spatial randomness (CSR). As such, for distances greater than 3000m, the position of a given pockmark has no influence on the location at which a new pockmark will form.

4.4.3. Pockmark-pipe-fault relationship

In cross-sections orthogonal to pockmark alignments of set B it is possible to observe the geometrical relationship between feeding pipes and PPFs (fig. 4.14). Invariably these pipes occur on the hanging wall blocks of PPFs, the majority of which rise from where faults intersect the strata between reflections **x** and **C2**. Although there are some amplitude anomalies adjacent to faults, pipes and faults are separate features. If PPFs were to serve as

migration pathways for the fluids involved in pockmark formation, pipes might be expected to rise from the upper tips of these faults. Instead, pipes form and develop where the interval **x-C2** is intersected by fault surfaces, explaining the offset observed between PPF traces and pockmark alignments. Thus, pockmarks lie above the footwall cut-offs of the inferred stratal position of the source package.

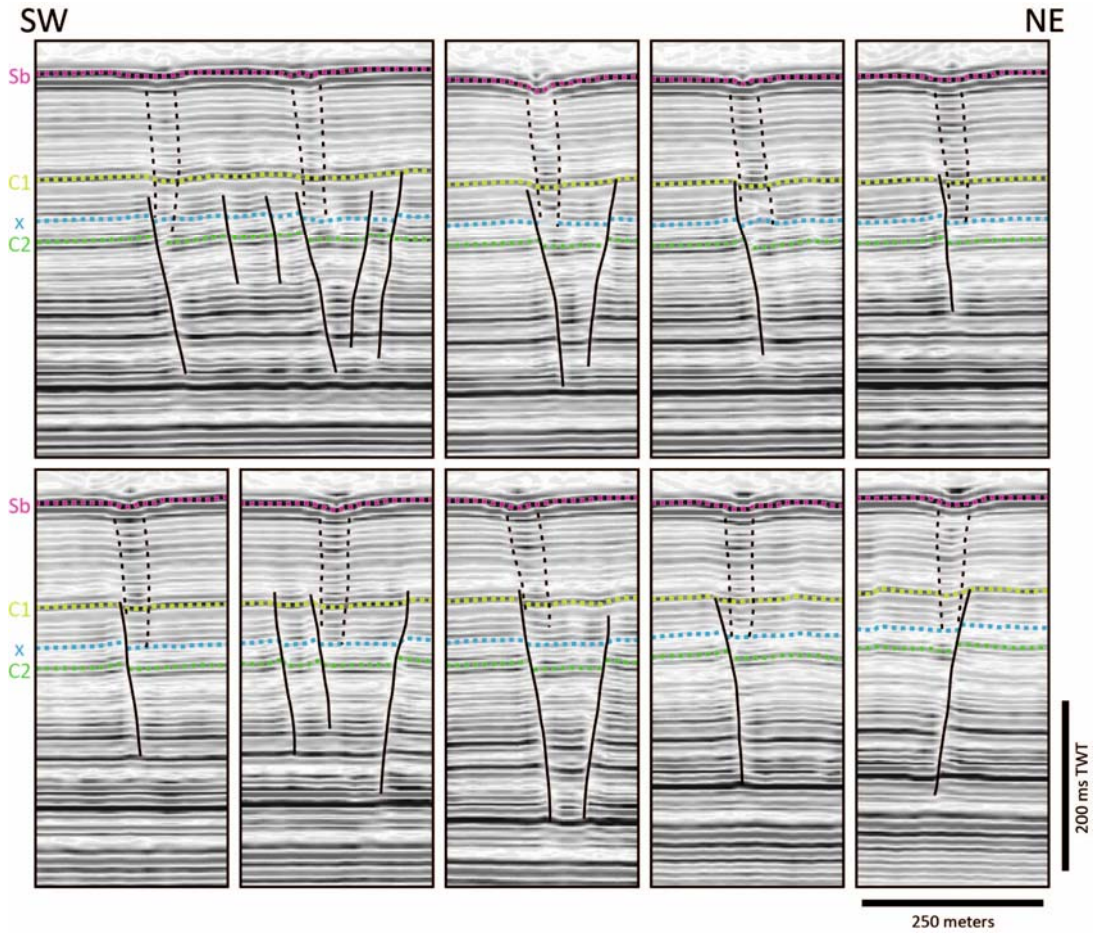

Figure 4.14. Seismic profiles showing pipe position in relation to polarised polygonal fault planes in mini-basin MB7 – invariably, pipes occur on hanging wall blocks, rising from where faults intersect the interval between reflections **x** and **C2** (fluid source interval). (Seismic courtesy of PGS.)

4.5. Discussion – structural controls on pockmark alignments

Having established the nature of the pockmark distributions in the study area, an underlying aim of this discussion is to examine how these alignments can be used to develop a model for plumbing systems as a whole. The next sections address the following issues:

1) Fluid migration routes: what types of conduit are present in the near shallow sub-surface?

2) Source and type of fluids responsible for pockmark formation: is it gas or pore fluid and is it sourced shallow or deep from within the mini-basin fills?

3) Controls on pockmark spacing along alignments: does this give clues as to the plumbing system?

4) Driving and trigger mechanisms: what caused this episode of focused fluid expulsion, and what is the significance of the timing of pockmark formation for the underlying causal mechanism?

4.5.1. Fluid conduits

Pockmarks result from the expulsion of fluids at the seabed, and it is widely assumed that the ascending fluids are focused along a columnar conduit below (Cartwright et al., 2007; Ho et al., 2012; Judd and Hovland, 2007; Løseth et al., 2009; Løseth et al., 2011; Moss and Cartwright, 2010). The seismic expression of the pathways used for these fluids to migrate through the sedimentary succession can vary greatly. Most seabed pockmarks in the study area show no underlying amplitude anomalies that could be related to the

presence of a feeding conduit. However, all pipes identified within MB7 terminate at the centre of a seabed pockmark. The spatial relationship observed between these two fluid flow features imply that pipes are the conduits for the fluids expelled at the seabed during pockmark formation. As such, every seabed pockmark may reasonably be expected to be associated with an underlying feeding pipe. Pipes with clear seismic imaging as columnar zones of distorted reflections combined with stacked amplitude anomalies may reflect local cementation or deformation of strata during fluid flow, or be evidence of presently stored fluid within them (Andresen, 2012; Ho et al. 2012). The absence of a pipe below a pockmark is suggested here to be the result of the resolution limitations of the 3D seismic data. In cases where no pipe is imaged, it is suggested that pipe width must fall well below the limit of seismic resolution, or the physical properties of the material inside the pipe do not yield acoustic impedances that contrast with the hosting sediments (Løseth et al., 2011).

The pipes observed in the study area are similar (though generally smaller) to many previous examples of pipes interpreted from 3D seismic data (see Cartwright and Santamarina (2015) for review) in which a mechanism of fracture driven, cross-stratal migration of methane is implicated in their formation. The presence of methane in the fluids that first transited to the seabed via the pipe conduits is thus consistent with their seismic expression in the study area. Note that this does not exclude a significant contribution from ascending pore fluids.

4.5.2. Source and type of fluids

In the present-day fluid flow regime of the Lower Congo Basin (expressed by seabed pockmarks), hydrocarbon fluids are typically considered to be sourced from reservoirs within the turbiditic fans of Oligocene-Miocene age (Gay et al., 2006a), or to be focused flow of thermogenic fluids along salt flanks (Andresen and Huuse, 2011; Gay et al., 2007). However, such a deep source of potentially thermogenic hydrocarbons is unlikely to explain seabed pockmark distributions of the type and extent presented in this study. The seabed of both salt mini-basins presented here is highly populated with pockmarks, being almost entirely covered by these depressions. The large extent of these pockmark fields implies a laterally continuous reservoir of relatively uniform physical properties, which stored the fluids that were to be intimately involved in their formation process. Such a laterally continuous extensive reservoir could be expected to be located at shallow depths. More deeply-sourced fluids would have more likelihood of being focused along complex migration pathways within the sedimentary succession, exploiting in their ascent a combination of stratal and structural permeable pathways, and thus might be expected to yield more localised distributions. The most likely deeper reservoirs for the seabed pockmarks would be expected to be the deep-water channelized units of Unit 2 that can be seen within some of the mini-basin fills in the area (e.g. in MB6, fig. 4.2) but their absence in MB7 where large numbers of pipes and pockmarks are observed argues against this unit acting as the principal immediate source for the pockmarks. The absence of pockmarks directly above salt ridges and along the mini-basin rims also argues against a deeper source (c.f. Andresen and Huuse, 2011).

Pipes that fed the seabed pockmarks are observed to be stratigraphically limited to the shallowest seismic Unit 3 (fig. 4.9), strongly supporting the interpretation of a shallow reservoir within part or all of this unit. The histogram of pipe root horizons (fig. 4.9) shows that pipes root at several levels within Unit 3, but with a majority in the interval between horizons **x** and **C2**. By overlying pockmark loci with the amplitude map of interval **x-C2**, it is clear that seabed pockmarks occur mostly within the limits of the area where this layer was deposited (fig. 4.10). It is also interesting to note that, non-faulted regions of MB7 closely match areas of enhanced amplitudes and more chaotic reflections within this interval. These amplitudes may be related to deposition of coarser sediments (possibly sands), which may act to inhibit the nucleation and initial propagation of polygonal faults (Cartwright, 2011). This corridor of enhanced amplitudes/possible sand may be related to confinement of coarser sediments transported by turbidity currents. It could also result from bottom-current sorting at the time of deposition, especially taking into account the concave shape of MB7 (higher velocity bottom-currents near the central parts of the mini-basin where fine sediments are washed away, with settling of coarser fractions to be deposited in low velocity areas (mini-basin steeper rims)).

An intriguing observation is that all the BSRs observed in salt anticline flanks occur at depths similar to the depth range of reflection **x**, suggesting a possible connection between the hydrate stability zone (present day) and the most likely source interval for the fluids responsible for pockmark formation. Identification of any putative BSR within the mini-basin MB7 is difficult because the hemipelagic fill is concordant to the seafloor. Nevertheless, it is

plausible that reflection **x** coincides with the base of the gas hydrate stability zone (GHSZ). If so, then it is conceivable that pockmark formation may be associated with gas hydrate dissociation and/or expulsion of free gas beneath the GHSZ. Methane produced from the dissociation of gas hydrates could then be considered as the main fluid involved in seabed pockmark formation. Although speculative, the dissociation of gas hydrates and subsequent gas expulsion may have been triggered by alterations of the PT regime (shifting away from hydrate stability conditions) caused by salt growth and ensuing topographic changes. Since there was no geochemical data available for this thesis, it is not possible to interpret the origin of the gas that is involved in the development of a BSR in this area, but in nearby areas both biogenic and thermogenic sources have been inferred for the gas trapped in the hydrate layer (Andresen and Huuse, 2011).

The ubiquitous presence of pockmarks on the seafloor and buried in Pliocene-Pleistocene sediments of the Lower Congo Basin and the neighbouring Kwanza Basin have been linked to changes in hydrostatic pressure due to rapid sea-level changes since the Pliocene (Andresen and Huuse, 2011; Serié et al., 2016). Varying eustatic conditions caused by glacial-interglacial fluctuations have been argued to impact subsurface pore pressures and gas hydrate stability (Liu and Flemings, 2009; Bertoni et al., 2013; Hermanrud et al., 2013). In particular, sea-level drops may lead to the expulsion of fluids (water and gas) from shallow sediments. Thus, it is also plausible that a reduction of pressure by a rapid sea-level drop could either have triggered gas release from hydrates or from solution in pore fluids in the source interval (Hermanrud et al., 2013; Riboulot et al., 2013).

4.5.3. Controls on pockmark distribution – the role of polarised polygonal faults

Seabed pockmarks have been commonly observed to be aligned in a linear fashion, forming trails up to 10km in length. Linear pockmark arrays have been shown to reflect the distribution of underlying structural or stratigraphic discontinuities controlling the establishment of pathways for upward fluid migration (structural discontinuities: Gay et al., 2007; Pinet et al., 2009; stratigraphic discontinuities Gay et al., 2006a*;* Pilcher and Argent, 2007).

The structural controls on pockmark alignments described in this study add to the previous examples of pockmark alignments noted above, with the novel aspect here being the inter-relationship between polarised polygonal faults and pockmarks (fig. 4.15). In contrast to some previous studies, however, there is no evidence that the polygonal faults acted as conduits. The spatial alignment is instead interpreted here as a control by the fault plane on the nucleation position of the pipe feeding the pockmark (figs. 4.11 and 4.12), with the critical locus being at the intersection of the fault plane with the likely fluid source interval. This argument is supported by the recognition that seabed pockmark formation is not specifically linked to the polygonal fault system, simply because pockmarks are also present in areas not affected by polygonal faulting. Also, there is a considerable time-period (estimated to be between 192k.y. – 1.15M.a.) between the end of the active period of polygonal faulting and the timing of pockmark formation, as evidenced by the 135ms TWT (115m) thick hemipelagic succession deposited above the top tier of the polygonaly faulted interval (reflection **C1**).

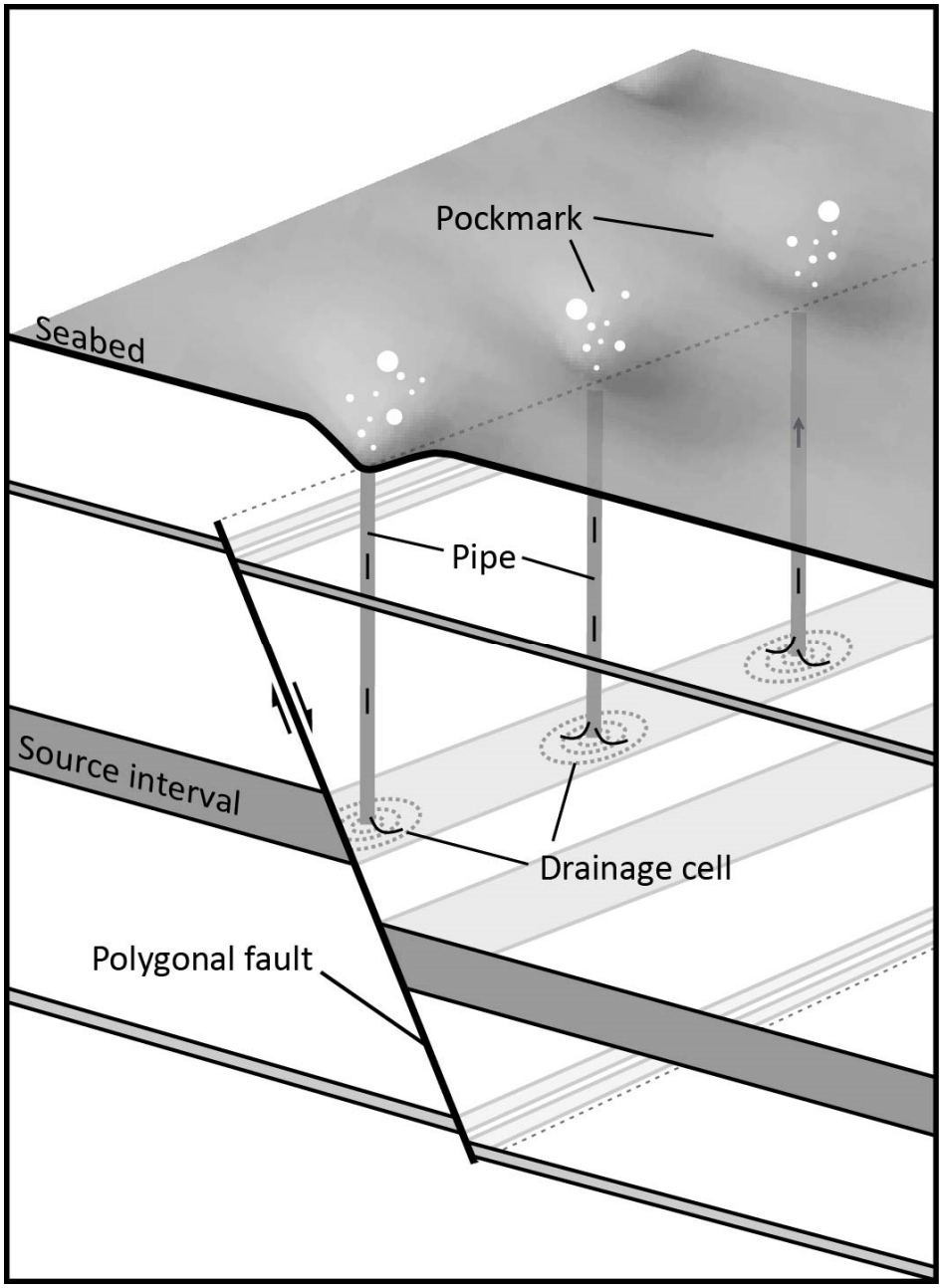

Figure 4.15. Shallow fluid flow system – model schematics. (Polarised) polygonal faults formed in shallow Unit 3 hemipelagic sediments intersect an interval with the capacity to retain fluids (including gas, most likely of biogenic origin). Over time, fluid pressure inside the source interval builds up. Overpressure is focused along the intersection of the fault plane with the source layer. With seal integrity compromised at this level due to the presence of pre-existing discontinuities (faults), changes to the local P-T regime enable seal breaching. Spatial focusing of overpressure within drainage cells promote seal failure and the upward migration of fluids along a vertical conduit (pipe). Pipes are formed on the hanging wall block, following the strike of the underlying fault. Fluids are expelled at the seabed, with the remobilisation of fine unconsolidated sediments to form linear pockmark trails. Pockmarks lie above the footwall cut-offs of the inferred stratal position of the source package. (Polarised) polygonal faults are seal features.

4.5.4. Implications for the shallow plumbing system

Based on the evidence derived from the seismic interpretation and statistical analysis, it is suggested the following evolutionary model for the seabed pockmarks in the study area:

1. Pockmark formation in mini-basins MB6 and MB7 occurred within the past few thousand years, since all the pockmarks have a clear expression at the seafloor, and none of the pockmarks show any resolvable signs of being buried by recent sediments.

2. The statistical data on distribution is consistent with this being a single episode of fluid expulsion, since there is clear evidence for an exclusion zone whereby the formation of one pockmark inhibits neighbouring pockmarks from forming within the exclusion zone. This in turn suggests a period of fluid expulsion whose duration was short enough to prevent any resetting of the hydrodynamic boundary conditions that led to the venting.

3. The source of the fluids involved in pockmark formation in this event was most probably from within Unit 3, and from the pinch-out relationship was most likely located stratigraphically between reflections **x** and **C2**. The seismically resolved conduits between the source and the seabed pockmarks are pipe-like structures similar to fluid escape pipes observed in many other basins. From their stacked amplitude anomaly patterns of these conduits, the fluids transported through these conduits most probably included free gas, which is consistent with standard models for pockmark formation.

4. The trigger for the fluid expulsion event is unknown, but from the coincidence between the observed depth to reflection **x** and the BSR observed on the mini-basin flanks, it is suggested that gas hydrate dissociation may have been involved in liberating methane and its focused expulsion to the seabed led to the formation of the pockmarks. Hydrate dissociation may have been triggered by the dramatic change in sea level at the end of the last glacial maximum (c.f. Sultan et al., 2004).

5. The alignments of pockmarks and pipes in the area of MB7 affected by polarised polygonal faults is seen here as an exploitative relationship, whereby the locus of pipe formation was at the intersection of the fault plane with the fluid source layer. There is no evidence that the faults acted as conduits, which is supported by the systematic offset between pockmark positions and the upper tip positions of the fault planes.

4.6. Conclusions

- 3410 seabed pockmarks have been mapped in two salt-related mini-basins (MB6 and MB7) in the Lower Congo Basin, offshore Angola. Their diameters range from 45 to 665m, and they have an average spacing of 300m. Of these, 570 pockmarks are underlain and fed via pipe-like conduits that are clearly imaged on the 3D seismic data.

- The pockmarks exhibit interesting local alignments in their distribution that can be clearly shown to be related to polarised polygonal faults. The

uniformity of their statistical distribution argues for a shallow depth below the seabed for the source interval that supplied the fluids forming the pockmarks.

- The distribution of the pockmarks in MB7 suggests that the primary storage interval is the sedimentary package **x-C2**.

- The stacked amplitude anomalies associated with the seismically imaged pipes is linked to fluid (gas) migration. The composition and ultimate origin of the fluids are unknown.

- Spatial statistics analysis of seabed pockmarks distributions revealed that pockmark occurrence is not considered to be random at short distances to their nearest neighbours. In faulted areas of mini-basin MB7, seabed pockmarks are clustered and form alignments along a preferred NNW-SSE direction, which are controlled by the underlying polarised polygonal fault patterns.

- In non-faulted areas of mini-basin MB7, seabed pockmarks do not form alignments, and their spatial distribution is considered random at distances >3000m to their nearest neighbours.

- 2nd order spatial statistics revealed that seabed pockmarks distributions (both in faulted and non-faulted areas) tend to be dispersed or anti-clustered at short distances (<200m) to their nearest neighbours. This result suggests there is an exclusion zone of <200m around each pockmark in which no other pockmark will occur.

- Although the spatial distribution of seabed pockmarks is controlled by underlying PPFs, pockmark formation is not linked to the polygonal fault

system. Pipes invariably occur on hanging-wall blocks, rising vertically from where fault planes intersect the estimated source interval - fluids at the source exploit the discontinuity, producing linear pockmark arrangements parallel to the faults.

- Pockmark formation occurred in the last few thousand years, possibly related to gas hydrate dissociation linked to variations on the P-T regime caused by sea level changes or salt growth.

Chapter 5

POCKMARK DISTRIBUTIONS
ASSOCIATED WITH MTDs

5. Pockmark distributions associated with MTDs

Abstract

The modern seafloor of the Lower Congo Basin (offshore West Africa) is covered by extraordinary arrays of pockmarks, some of which were formed directly above deposits generated by slope failure and mass movements (mass-transport deposits, MTDs). The linear arrangement of these pockmarks coincides with underlying discontinuities within the MTD material, revealing that the collapse-induced extensional and compressional faults and fractures control the distribution of fluid migration pathways. The stratigraphic position of the MTDs in relation to the seabed provides clues on the timing of pockmark formation relative to slope failure events. Seabed pockmark formation was not synchronous to the slope failure events, as evidenced by packages of hemipelagic sediments (up to 80m thick) deposited above the MTDs. The analysis of amplitude anomalies and feeding pipes associated with pockmarks allows the identification of the most likely fluid source interval, and shows that fluids were stored within the MTD sediments prior to their expulsion at the seabed. Bottom-simulating reflectors (BSR) are observed in salt anticline flanks at similar depths to the estimated source interval, suggesting a possible connection to the present day gas hydrate stability zone (GHSZ). As such, it is possible that pockmark formation may be linked to gas hydrate dissociation and/or expulsion of free gas beneath the GHSZ.

This chapter shows indisputable evidences of 1) storage and migration of fluids within mass-transport deposits (MTDs), and 2) the local influence of MTDs on subsurface fluid drainage networks. The results have important implications for our current knowledge of permeability and storage capacity of MTDs, and are relevant for the understanding of shallow fluid plumbing systems in offshore settings and overall fluid flow systems in hydrocarbon-rich continental margins.

Keywords: pockmark distributions; mass-transport deposits; spatial statistics; shallow plumbing systems; Lower Congo Basin.

5.1. Introduction

Fluid flow systems in deep-water continental margins have been the focus of many studies in the past decades as they are an integral part of the evolution of sedimentary basins (Andresen, 2012; Berndt, 2005; Cartwright et al., 2007; Hovland and Judd, 1988a). The understanding of fluid flow processes is crucial in the petroleum exploration, submarine geohazards and ecosystems. Pockmarks have been given special attention, as they are evidence of highly focused fluid flow expelled at the seafloor in a wide range of geological settings (Andresen and Huuse, 2011; Cartwright and Santamarina, 2015; Gay et al., 2007; Judd and Hovland, 2007; Moss and Cartwright, 2010). Pockmarks are shallow circular to elliptical depressions developed in soft, fine-grained sediments, which are remobilized by the expulsion at the seabed of fluids of variable composition, such as biogenic and thermogenic gas (methane), and pore water. Their spatial distribution is controlled by the conditions of the underlying sediments and pore fluid pressure, and are preferentially associated with discontinuities that act as seal bypass systems (Cartwright et al., 2007; Judd and Hovland, 2007; Riboulot et al., 2013). In 3D seismic data, pockmarks are frequently observed directly above columns of acoustic amplitude anomalies (pipes or chimneys), interpreted to be the conduits along which fluids vertically ascend from their transient reservoir units to be expelled at the seafloor (Gay and Berndt, 2007; Judd and Hovland, 2007; Løseth et al., 2009; Maia et al., 2016; Marcon et al., 2014; Moss and Cartwright, 2010). The spatial analysis of the distribution of pockmark and their feeding pipes provides clues to the location of source intervals, origin of fluids, timing and triggers for fluid expulsion events, and migration pathways,

in order to improve our understanding of shallow plumbing system in sedimentary basins (Antonellini and Aydin, 1995; Hovland et al., 2002; Maia et al., 2016; Moss and Cartwright, 2010).

The occurrence of submarine slope failures significantly alters the stratigraphic organization of deep-marine sedimentary basins. The resulting mass-transport deposits (MTDs) can affect areas of several square kilometres and show a spectrum of increasing internal deformation, ranging from poorly-deformed internal strata preserved as blocks, to faulting and folding due to brittle and plastic deformation, culminating in completely disaggregated strata (Bull et al., 2009; Hampton et al., 1996; Posamentier and Walker, 2011). The sedimentary composition of MTDs is prone to great uncertainty. The deposits can either be fairly homogeneous, often composed by fine-grained material, or markedly heterogeneous where fine- and coarse-grained sediments occur (Meckel III, 2011; Posamentier, 2004; Tripsanas et al., 2008).

MTDs have been considered as generally impermeable features constituting sealing units for vertically ascending fluids (Shipp et al., 2004). However, this view has been disputed by growing evidences of fluid migration or retention in MTDs, controlled by their architectural and compositional heterogeneities (Meckel III, 2011; Riboulot et al., 2013; Welbon et al., 2007). Arrays of pockmarks overlying MTDs tend to show linear and/or arcuate organized patterns. Such distributions are frequently coincident not only with the outer limits of the MTDs but also with the orientation of their extensional or compressional internal faults (Maia et al., 2015). Thus, MTDs are not fully impermeable units and can influence the migration pathways of fluids ascending through them (Gamboa et al., 2011; Gamboa and Alves, 2015;

Riboulot et al., 2013). Less known is the capacity of MTDs to store relevant volumes of fluids and act as viable reservoirs. This is highly dependent upon the presence and preservation of laterally continuous permeable strata in the MTDs (Meckel III, 2011). Low-remobilization MTDs have a higher potential to preserve these, especially if large blocks and slabs are present, consequently increasing the retention capacity of fluids (Gamboa et al., 2011; Welbon et al., 2007). It has also been postulated that organic matter can also be present within MTDs, increasing their potential to act as fluid sources and storage units, if the appropriate conditions are met (Haughton et al., 2003). However, no indisputable proof of this has been previously shown until now.

The occurrence of pockmarks associated with mass-transport deposits offshore Angola is described here, based on the interpretation of high-resolution 3D seismic data. Three MTDs adjacent to salt ridges are analysed using seismic attributes to assess their internal discontinuities (fig. 5.1). It is shown that there is a direct control of overlying seabed pockmark distributions by MTD heterogeneities, which is markedly distinct from pockmark distribution in areas without MTDs. Furthermore, by assessing the timing of fluid escape and the MTD event, it is demonstrated that the remobilized strata may be permeable and capable of fluid storage and migration within themselves.

The main aim of this chapter is to explore the role of mass-transport deposits on the structural and stratigraphic organization of the subsurface, and how slope failures can impact the fluid retention capacity and the drainage pattern of shallow plumbing systems in offshore sedimentary basins.

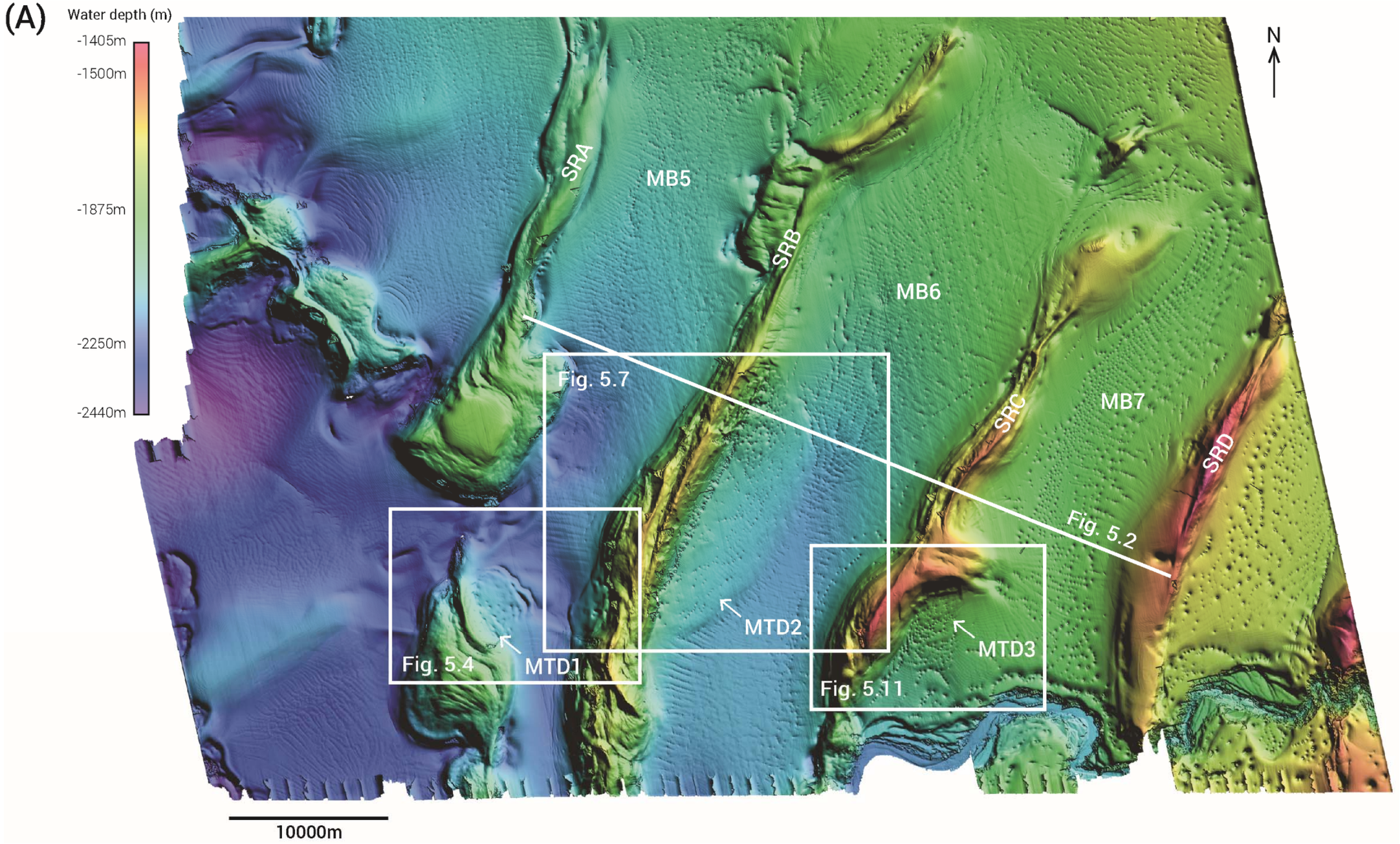

Figure 5.1. Seafloor map of the study area for this chapter evidencing the salt mini-basins and numerous pockmarks, some of which formed directly above MTDs. MB = mini-basin; SR = salt ridge; MTD = mass-transport deposit.

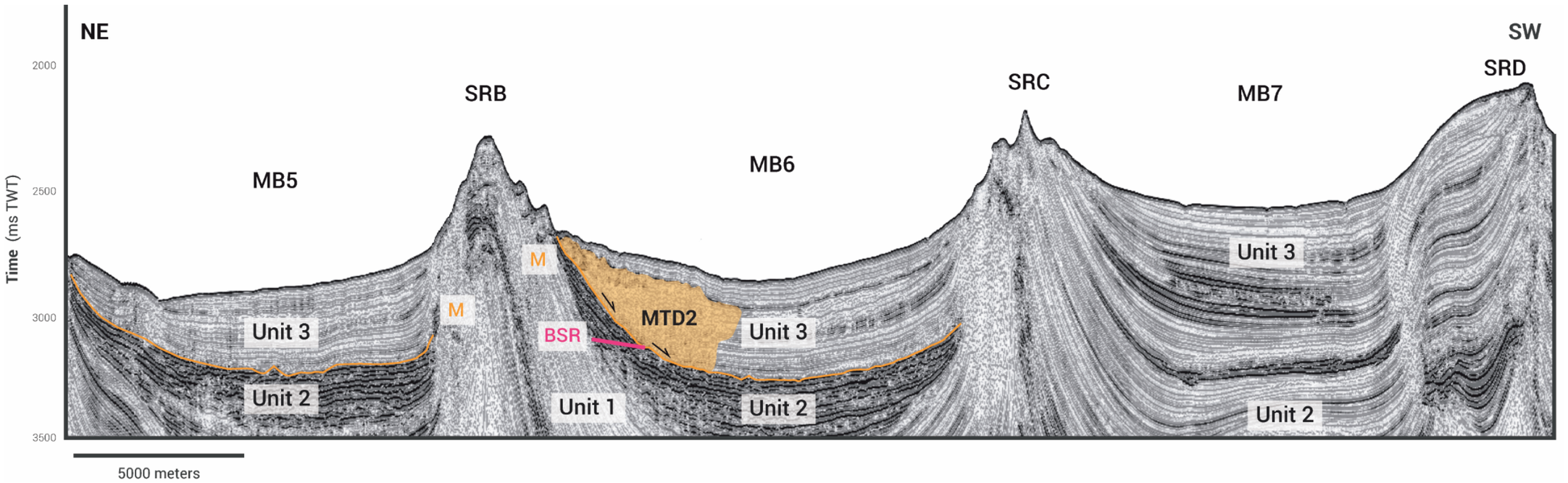

Figure 5.2. Seismic cross-section showing the general structure of the study area for this chapter. Location is shown in figure 5.1. Compressional salt ridges delimit mini-basins MB5, MB6 and MB7. Each mini-basin has its own shallow stratigraphy architecture, but generally the post-salt sequence has three main distinct seismic units (Units 1, 2 and 3), correlatable between mini-basins. The unconformity between Units 2 and 3 is often exploited as the basal shear interval for MTDs. (Seismic courtesy of PGS.)

5.2 Seismic geomorphology of MTDs

Submarine slope failures are prone to remobilise variable amounts of sediment which can reach high volumes, in order of the hundreds or thousands of cubic kilometres (Moscardelli and Wood, 2016; Weimer and Shipp, 2004). These often include a variety of deformation features, having led to the establishment of a deformation continuum that correlates the degree of internal disaggregation with the remobilisation distance (Bull et al., 2009; Posamentier and Martinsen, 2011; Shanmugam, 2006; Varnes, 1978). Mass-failures that preserve large portions of the internal stratigraphy are commonly described as slides (Masson et al., 2006; Weimer and Slatt, 2004). The preserved sections of strata are generally represented as blocks (Alves, 2015) or slabs (O'Leary, 1991), which are shown on seismic data as laterally limited features with continuous parallel reflections, and are comparable in character to the surrounding strata in place. The disaggregated, debritic material surrounding the blocks is generally represented by chaotic, discontinuous reflections of low seismic amplitude (Weimer and Shipp, 2004). Next on the deformation continuum are deposits deformed by plastic and ductile processes, defined as slumps (Bull and Cartwright, 2010; Frey-Martínez et al., 2006; Weimer and Shipp, 2004). Slump facies commonly exhibit moderate to high-amplitude folded or imbricate reflections, which facilitates their recognition on the seismic data. Outcrop-scale examples of slumps commonly mimic the features observed on the seismic data (Posamentier and Martinsen, 2011). On the far end of the spectrum are debris-flows, which include mass-failures with the highest internal disaggregation and little or no preservation

of internal structures. On seismic data, these are identified as seismic packages of low to moderate amplitude with a very chaotic character, with no resoluble internal stratification (Hampton et al., 1996; Posamentier and Walker, 2006).

Given this variability of deformation styles, which are often not fully represented on seismic data due to limitation of data resolution, the term mass-transport complex (MTC) was introduced (Weimer and Shipp, 2004). This is used as an umbrella term to refer to large volume remobilised strata produced by slope failure processes that can only be visualised at seismic scales, thus encompassing associated deformational processes that include creep, sliding, slumping, and debritic flows (Bull and Cartwright, 2010; Posamentier, 2004; Strachan, 2008; Tripsanas et al., 2008; Weimer, 1990; Weimer and Shipp, 2004). Mass-transport complexes where thus defined as presenting various reflection configurations on 3D seismic data, bounded by clear top and base surfaces. Regardless of their internal character, MTCs are underlain by a variable basal surface that can be planar (Posamentier, 2004; Posamentier and Martinsen, 2011), have irregular relief and/or present a stepped morphology (Frey-Martínez et al., 2011; Gamboa et al., 2012; Gee et al., 2005). On map sections, these basal surfaces can show elongated scours of variable sizes (Gee et al., 2005). Relevant shear deformation occurs at the base of MTDs, especially when observed at outcrop scales, which led to the consideration to refer to this as a basal shear interval instead of a single surface (Alves and Lourenço, 2010; Gamboa and Alves, 2015). The MTC upper surface if generally irregular, representing the post-failure bathymetry. However, this aspect can be altered by later erosion and reworking of sediment by channels or contour currents, or occurrence of overlying MTCs (Bull et al., 2009;

Weimer and Shipp, 2004). The internal character of the MTCs can be highly variable and include the whole range of low to high deformation of strata. However, it is common to observe a zonation in deformation styles within MTCs. Extensional deformation features occur closer to the headwall and rotated/gliding blocks of preserved strata occur. This domain transitions downslope to pressure ridges and thrusted blocks towards the toe domains as compressional stresses are created due to the flow arrest (Frey-Martinez et al., 2005; Gamboa and Alves, 2016; Hampton et al., 1996; Posamentier and Martinsen, 2011; Weimer and Shipp, 2004). The term has meanwhile evolved to create a distinction between mass-transport complexes (MTC) and deposits (MTDs) (Pickering and Hiscott, 2015). Although still often interchangeable, their criteria of identification are still based on the visualisation of disrupted seismic packages bounded by a base and top surface. However, MTDs are used to describe discrete deposits while MTCs are used to describe complexes with recurrent stacked or offset MTDs (Pickering and Hiscott, 2015; Posamentier and Martinsen, 2011).

In the study area, past submarine mass-failures are observed as discrete seismic packages of disrupted and chaotic reflections. Thus, the term mass-transport deposit (MTD) is the better suited to use when describing these sediment units.

The modern seafloor of the Lower Congo Basin is covered by many pockmark arrays (fig. 5.1), some of which were formed directly above mass-transport deposits (MTDs). This is exemplified by MTDs 1, 2, and 3, which were generated by slope failure and remobilization of Unit 3 sediments, induced by salt growth (fig. 5.2). The unconformity between Units 2 and 3 (horizon **M,** figs. 5.2 and 5.3) is exploited as the basal shear interval for MTDs 1 and 2 (fig. 5.2).

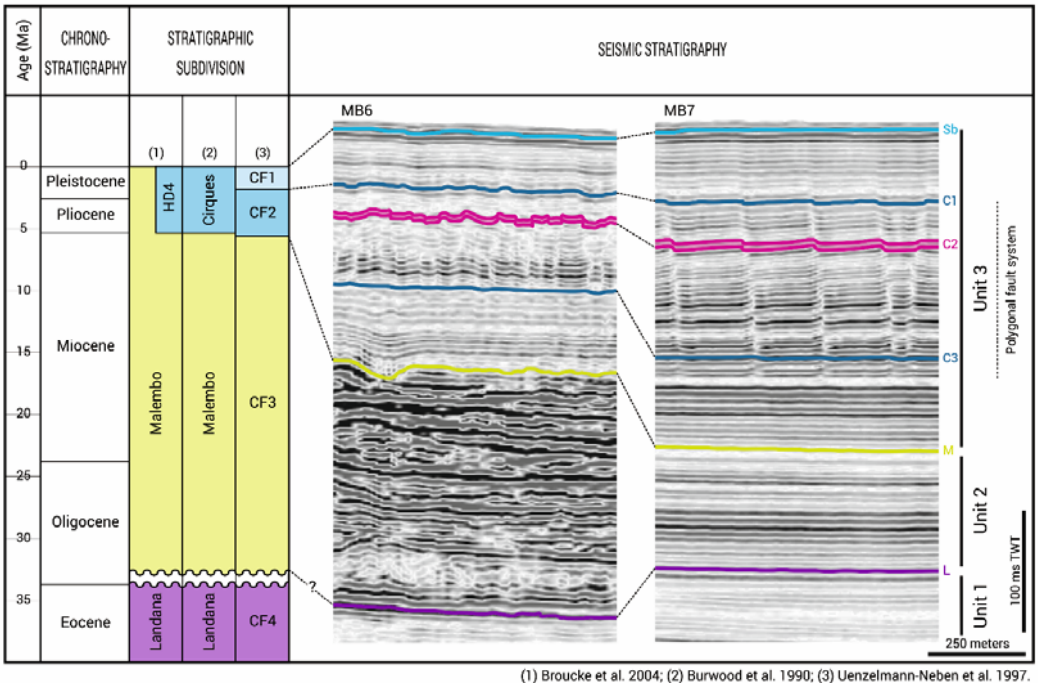

Figure 5.3. Stratigraphic framework of the shallow stratigraphy of mini-basins MB6 and MB7 (as described previously in Chapters 3 and 4). The key stratigraphic horizons are traceable between the distinct mini-basins. (Seismic courtesy of PGS.)

MTD1

MTD1 is located at the seafloor of mini-basin MB5 (fig. 5.4). It is bounded to the southwest by salt ridge SRA and confined northeastwards by

stratified, continuous sediments of Unit 3 (figs. 5.4 and 5.5). MTD1 has an elongate lobate morphology resultant from a northeast-directed slope failure, covering an area of 16.10km^2, and measuring 4.20km of maximum length and 3.80km of maximum width (fig. 5.4). MTD1 gradually thickens along a SW-NE direction, reaching a maximum thickness of 210m (250ms TWT) at its toe. Most of the MTD base interval detaches within the top levels of Unit 2 (fig.5.5a). Extensional faulting at the headwall domain and compressional thrusts at the toe domain are well evidenced within the high seismic amplitude strata at the base of the MTD (fig. 5.5a). The ramp at the base of MTD1 controls the development of internal thrusts. This ramp likely shifted the main detachment horizon from within the upper strata of Unit 2 to the interface between the latter and Unit 3 (fig. 5.5b). Deformation structures are less evident within the low-amplitude strata of Unit 3, especially towards its top, yet evidence that it occurred is indicated by the rugged morphology of the MTD at the seafloor (figs. 5.4 and 5.5). This is clear in the toe domain where arcuate pressure ridges cross the whole width of MTD1, generated by frontal shortening during downslope movement (fig. 5.4).

The internal complexity of MTD1 is further revealed by variance slices (fig. 5.6). Marked internal heterogeneities occur along its length and width. Linear discontinuities are created by internal extensional and compressional faults, with a clearer expression towards the southern and central areas of MTD1. These faults follow a general NW-SE orientation, parallel to the orientation of the MTD headwall. However, localized shifts in fault orientation are observed towards the MTD lateral boundaries due to drag effects during downslope movement. A significant portion of the toe domain of MTD1 shows

low variance volumes, indicative of increased preservation of internal strata at such locations (fig. 5.6). This aspect is exemplified by a continuous low variance elongated block up to 3000m long that crosses the full width of MTD1. Higher variance values are observed at the transitional and headwall domains, indicative of more stratal disruption (fig. 5.6). The spacing and length of the internal discontinuities is also lower in these areas. Less defined variance patterns are observed on the northern section of MTD1, possibly due to weaker internal amplitude and reflection resolution. Yet, internal lineaments are identifiable.

The character of MTD1 indicates it had a general NE-ward movement, with limited spread due to its frontal and lateral confinement (figs. 5.4b and 5.6). The strata preservation at the toe domain may represent a decrease in distal flow movement (fig. 5.5), increasing preservation potential.

Overlying MTD1 is a sediment cover up to 42m (50ms TWT) thick, which corresponds to the shallow-most layers of Unit 3. It covers the entire MTD area and preserves its morphology on the seafloor. It is characterized by parallel and continuous reflections, of moderate to high amplitude (fig. 5.5).

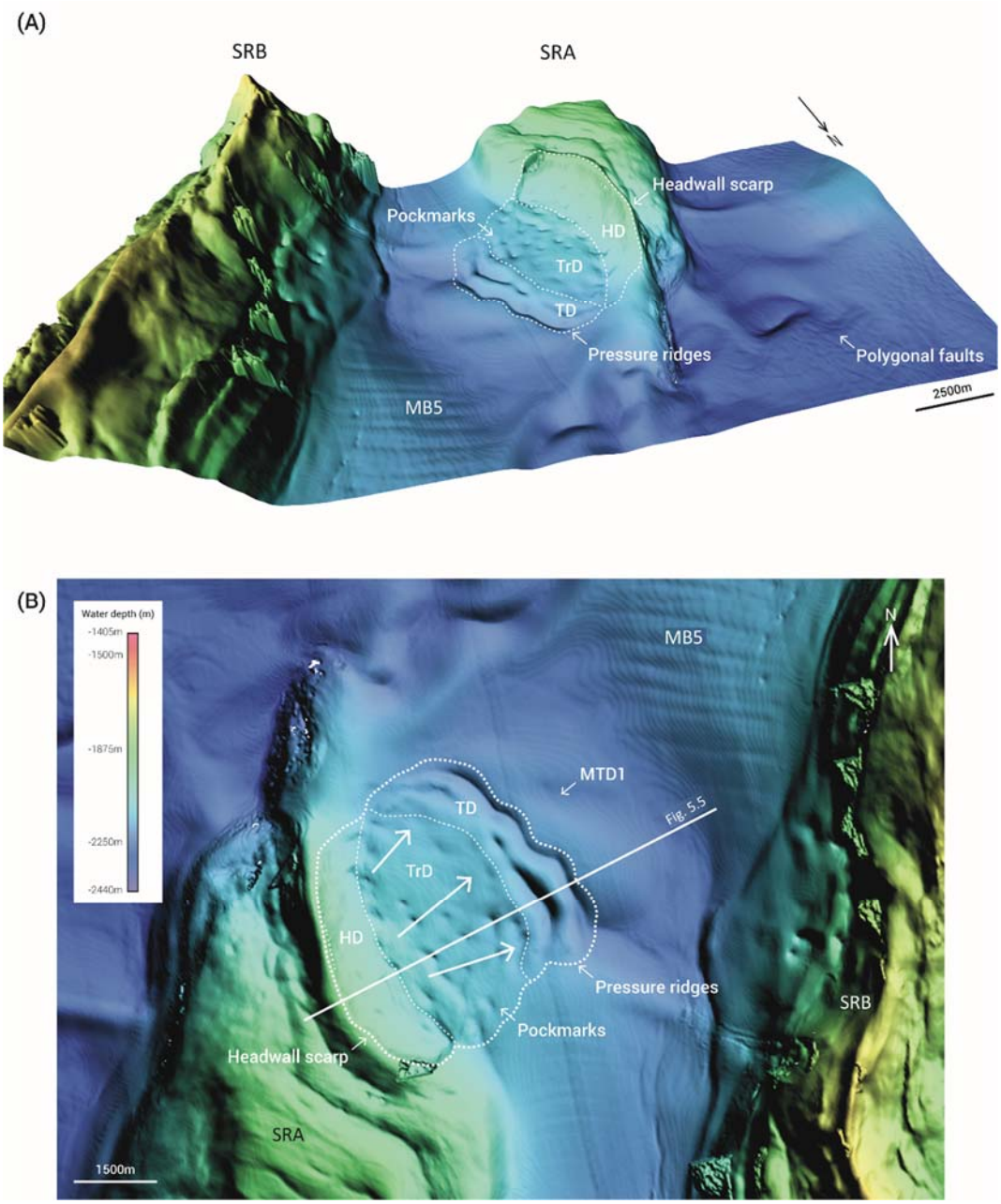

Figure 5.4. **(A)** Three-dimensional and **(B)** map view of the seafloor expression of MTD1. Location shown in figure 5.1. Marked topographic irregularities are observed at the MTD toe. Several pockmarks occur within the MTD limits, but are mostly absent elsewhere in the mini-basin. Arrows show the MTD direction of movement. HD = headwall domain; TrD = transitional domain; TD = toe domain.

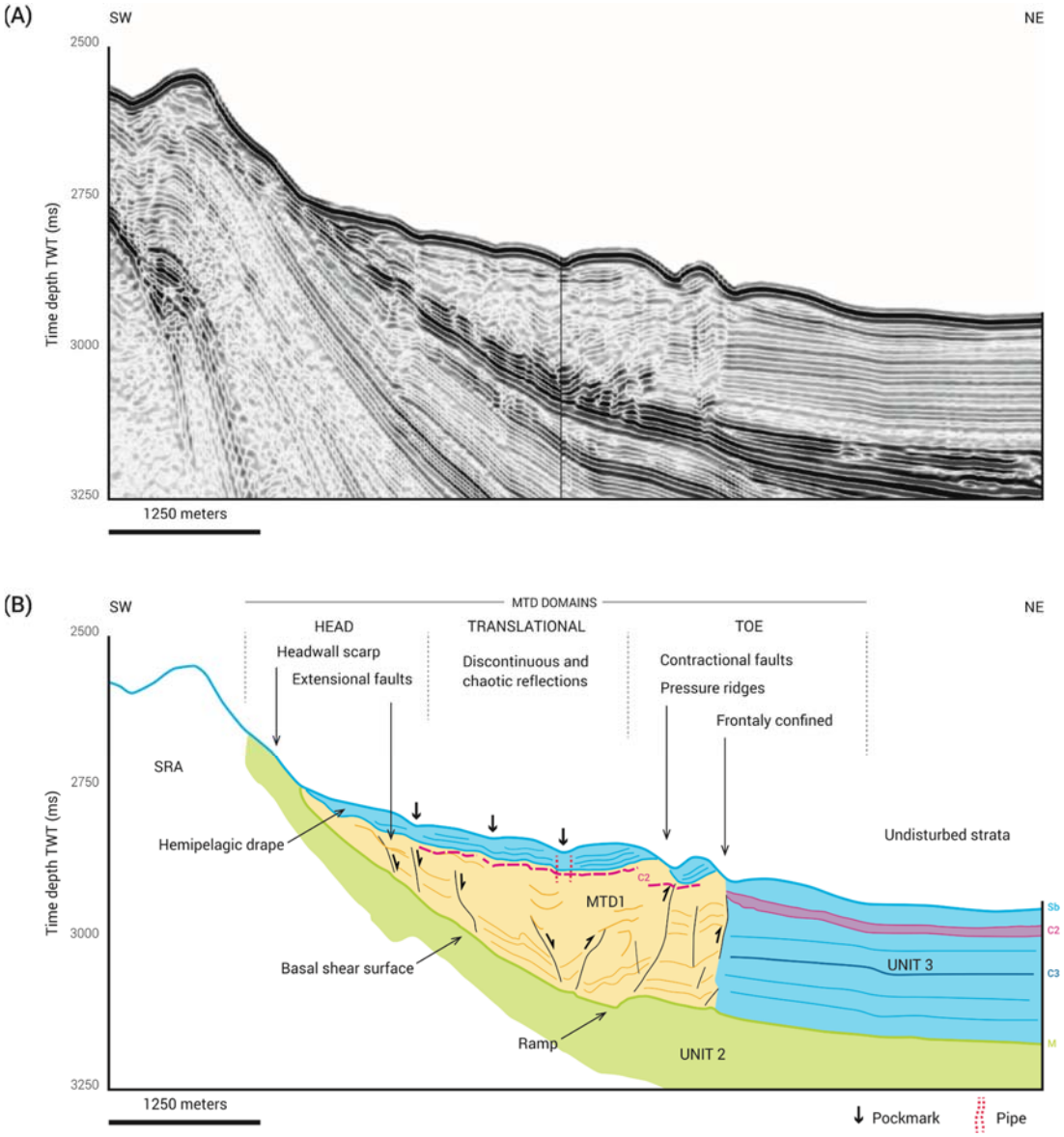

Figure 5.5. (A) Seismic profile and **(B)** interpreted section across MTD1. Location shown in figure 5.4. MTD1 has a wedge shape, pinching out against the salt ridge. Contractional and extensional faults occur in the MTD. A thin sedimentary cover overlies MTD1. Green = Unit t 2; blue = Unit 3; yellow = MTD; pink = interval **x-C2**; dashed pink line = interpreted **C**2 reflection inside MTD. (Seismic courtesy of PGS.)

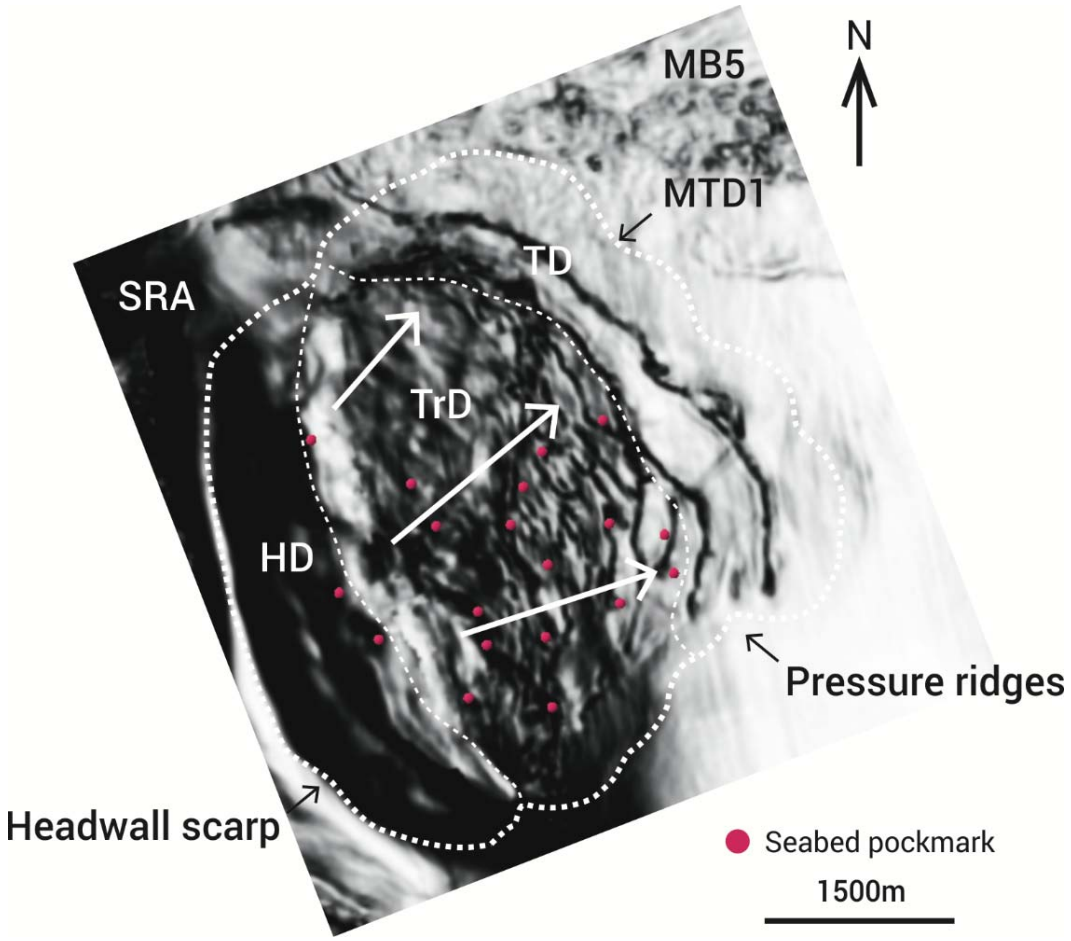

Figure 5.6. Variance slice parallel to the basal surface of MTD1, 50ms TWT above it. Continuous high-variance lines (dark colours) represent internal faults. Large sections with low variance (light colours) at the MTD toe represent semi-preserved strata. This contrasts with the low variance at the headwall and transitional domains, where strata deformation is higher. Red dots represent seabed pockmarks overlying the MTD, which are spatially close to the intra-MTD faults and discontinuities. HD = headwall domain; TrD = transitional domain; TD = toe domain. Dark colours represent higher variance values.

MTD2

MTD2 is located in mini-basin MB6, and it is comprised of two sub-deposits – MTD2a and MTD2b (fig. 5.7 and 5.8). It has a northeast-striking headwall along salt ridge SRB, and it is confined east-southeastwards by stratified, continuous sediments (fig. 5.9). MTD2a has an elongate lobate morphology, covering an area of 82.00km^2. It is 17.25km wide (parallel to the

NE-SW salt ridge SRB) and 5.80km in length, which is measured along its direction of movement. The morphology of the MTD2 top surface is variable along and across its area. The transitional domains of MTD2a show relatively smooth surface, while elongated ridges are present along the width of the toe domain. In contrast, MTD2b has a markedly irregular top morphology close to the headwall area, gradually becoming smoother towards its outer limit (fig. 5.8). Additional subtle lobate morphologies are identifiable along the upslope limit of the headwall domain of MTD2. MTD2a gradually thickens along a NW-SE direction, reaching a maximum thickness of 335m (400ms TWT) at the toe domain (fig. 5.8). Its head scarp has a 10° inclination, following the upslope steepening of the basal shear surface. Seismic reflections within MTD2a have lower amplitudes than the generally parallel to subparallel, unremobilised surrounding stratigraphy (fig. 5.9). Chaotic and discontinuous reflections of low amplitude predominate in the middle and top sections of this MTD. The base and the edges of MTD2a are characterized by low amplitude reflections of parallel and continuous geometry within fault-bounded elongated blocks (fig. 5.9).

Within the headwall domain, there are sections of continuous parallel reflections, indicative of limited disaggregation, bounded by extensional faults (fig. 5.9). The translational domain of MTD2a shows increasingly reworked material represented by lower strata continuity and amplitude. The toe domain is the most distal part and shows the greatest thickness. However, MTD2a thins slightly towards its frontal limit due to pronounced frontal ramps that create a stepped basal shear interval. This area is characterized by thrust-folded strata and elongated blocks, bounded by contractional faults (fig. 5.9).

Seismic variance slices (fig. 5.10) reveal these as parallel to subparallel arcuate features with a NE-SW orientation, perpendicular to the direction of movement (pop-up blocks; fig. 5.10). The larger, better preserved blocks tend to occur closer to the MTD2 frontal ramp but their width gradually decreases upwards (figs. 5.8 and 5.9). The linear features are also well expressed at the translational domain, although with relatively smaller spacing and lateral extent. Towards the headwall domain, fault-related discontinuities are less clear as increasingly mottled variance patterns predominate (fig. 5.9). MTD2a is interpreted to be a slump caused by slope failure of Unit 3 sediments adjacent to SRB. Its transport direction is NW-SE, perpendicular to the salt ridge SRB, with a relatively short remobilization distance forced by the stepped frontal ramp.

The smaller-sized MTD2b derived from ridge SRB is observed directly above the northern part of MTD2a (fig. 5.7 and 5.8). MTD2b is characterized by relatively higher amplitude chaotic reflections, measures 7.05km x 3.97km, and has a thickness of up to 122m (132ms TWT) (fig. 5.9). Because no stratified sediments are visible between them, MTD2b could have occurred shortly after the event that originated MTD2a, also as a result of slope failure of Unit 3 sediments adjacent to the salt ridge.

Hemipelagic sediments up to 80m (95ms TWT) thick drape MTD2a and MTD2b, preserving their morphology on the seafloor. This drape succession corresponds to the shallow-most strata of Unit 3, characterized by parallel and continuous reflections of moderate to high amplitude (fig. 5.9).

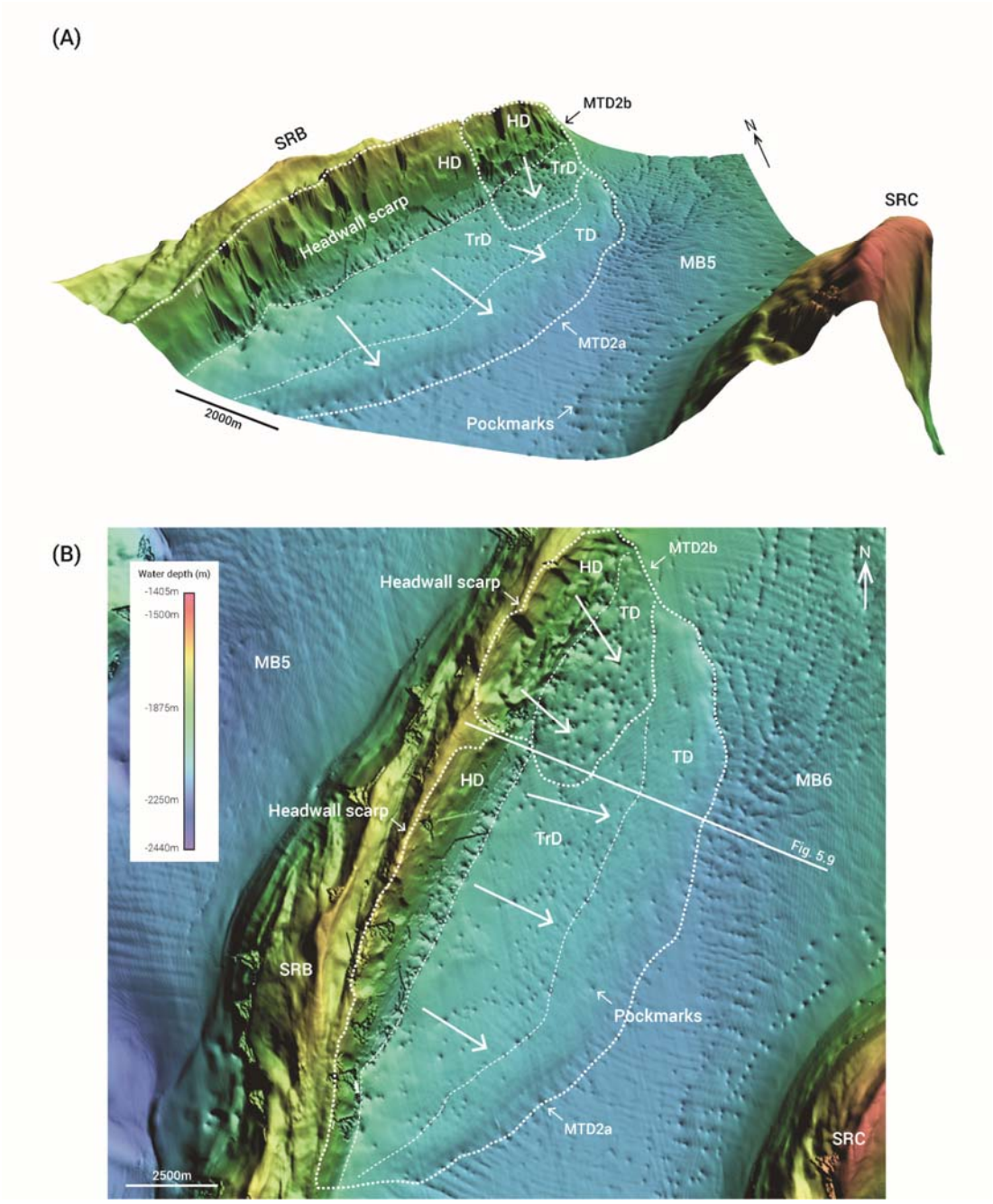

Figure 5.7. (A) Three-dimensional and **(B)** map view of the seafloor expression of MTD2. Location shown in figure 5.1. The deposit is adjacent to salt ridge SRB, and has a short length (parallel to the movement direction) comparatively to the large width. Numerous seafloor pockmarks show variable distribution patterns. MTD2 is sub-divided in MTD2a and MTD2b, each showing distinct pockmark patterns. Large arrows show the transport direction downslope. HD = headwall domain; TrD = transitional domain; TD = toe domain.

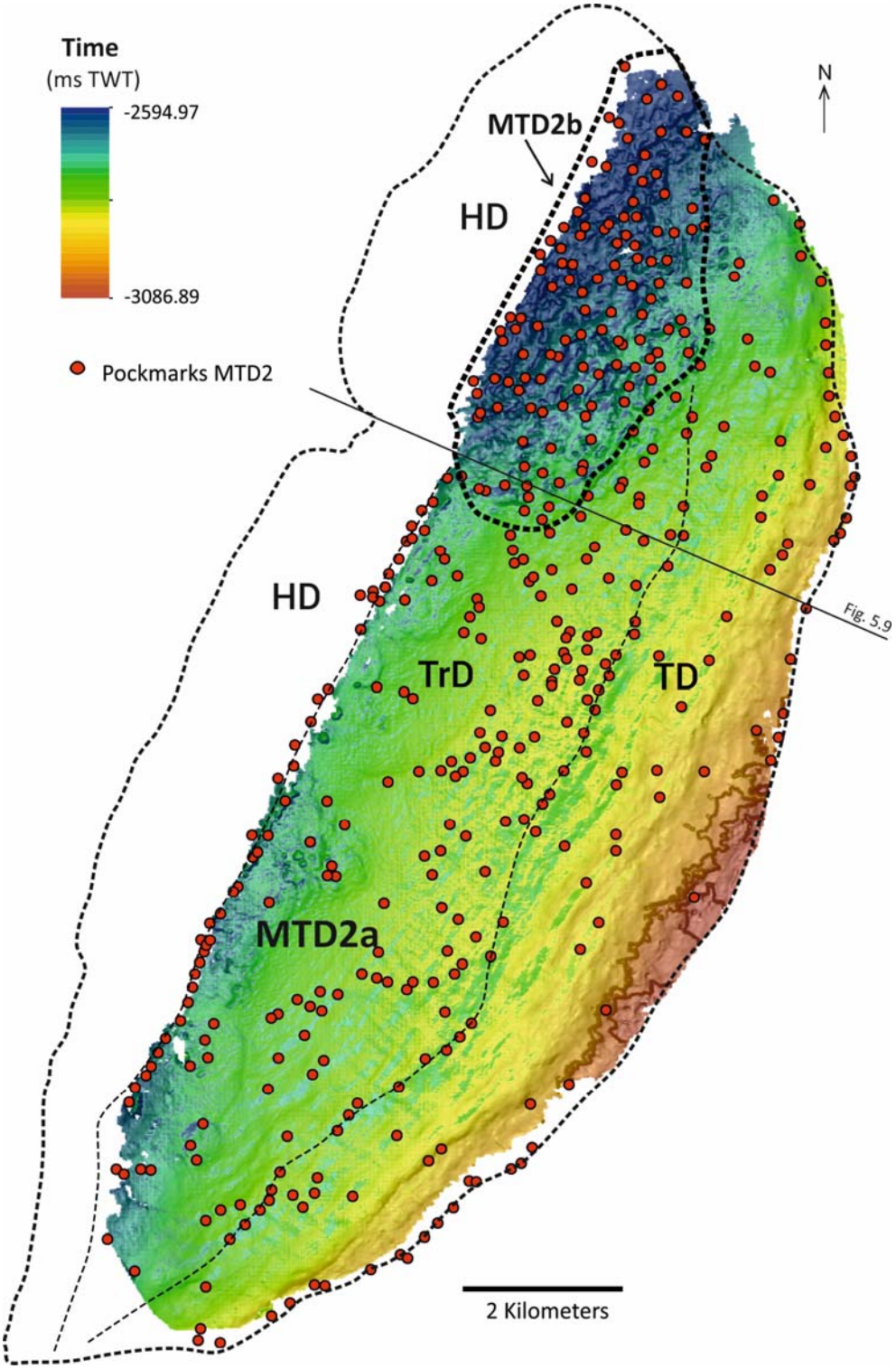

Figure 5.8. Morphology of MTD2 top surface. Elongated ridges are observable along the toe domain of MTD2a. MTD2b has a markedly irregular morphology when compared to the other areas of MTD2.

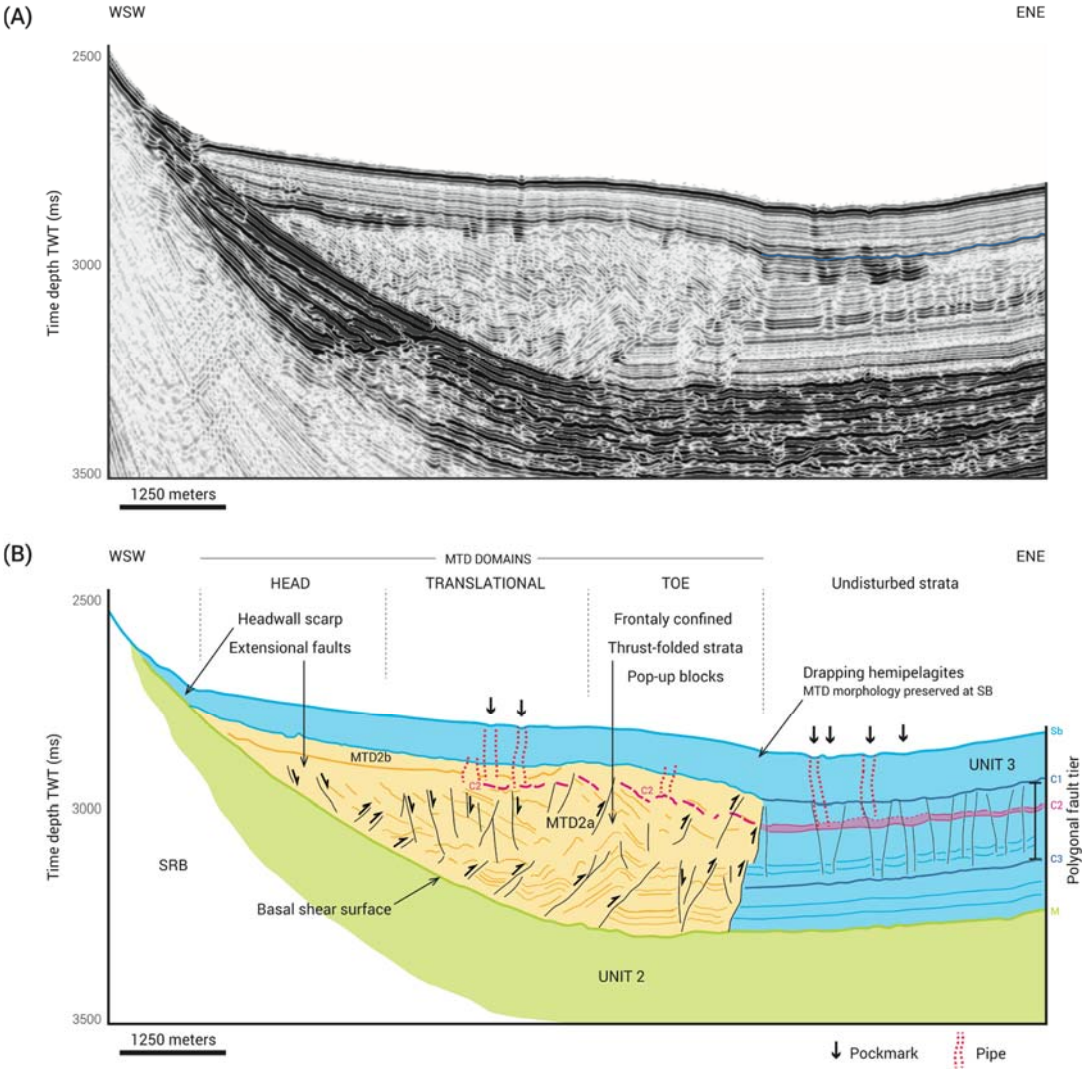

Figure 5.9. (A) Seismic profile and **(B)** interpreted section of MTD2. Location in figure 5.7. The deposit pinches out agains the salt ridge, and is the thickest in the toe domain. Segmented seismic reflections predominate within the MTD, but fairly large blocks occur in the toe domain. Numerous thrust structures are observed close to the base and toe of MTD2a. The deposit is draped by a continuous hemipelagic package. Pipes associated with seafloor pockmarks propagate from the upper MTD strata. This suggests the MTD was able to store fluid which was later released during the fluid espace episodes. Green = Unit 2; blue = Unit 3; yellow = MTD; pink = interval **x-C2**; dashed pink line = interpreted **C2** reflection inside MTD. (Seismic courtesy of PGS.)

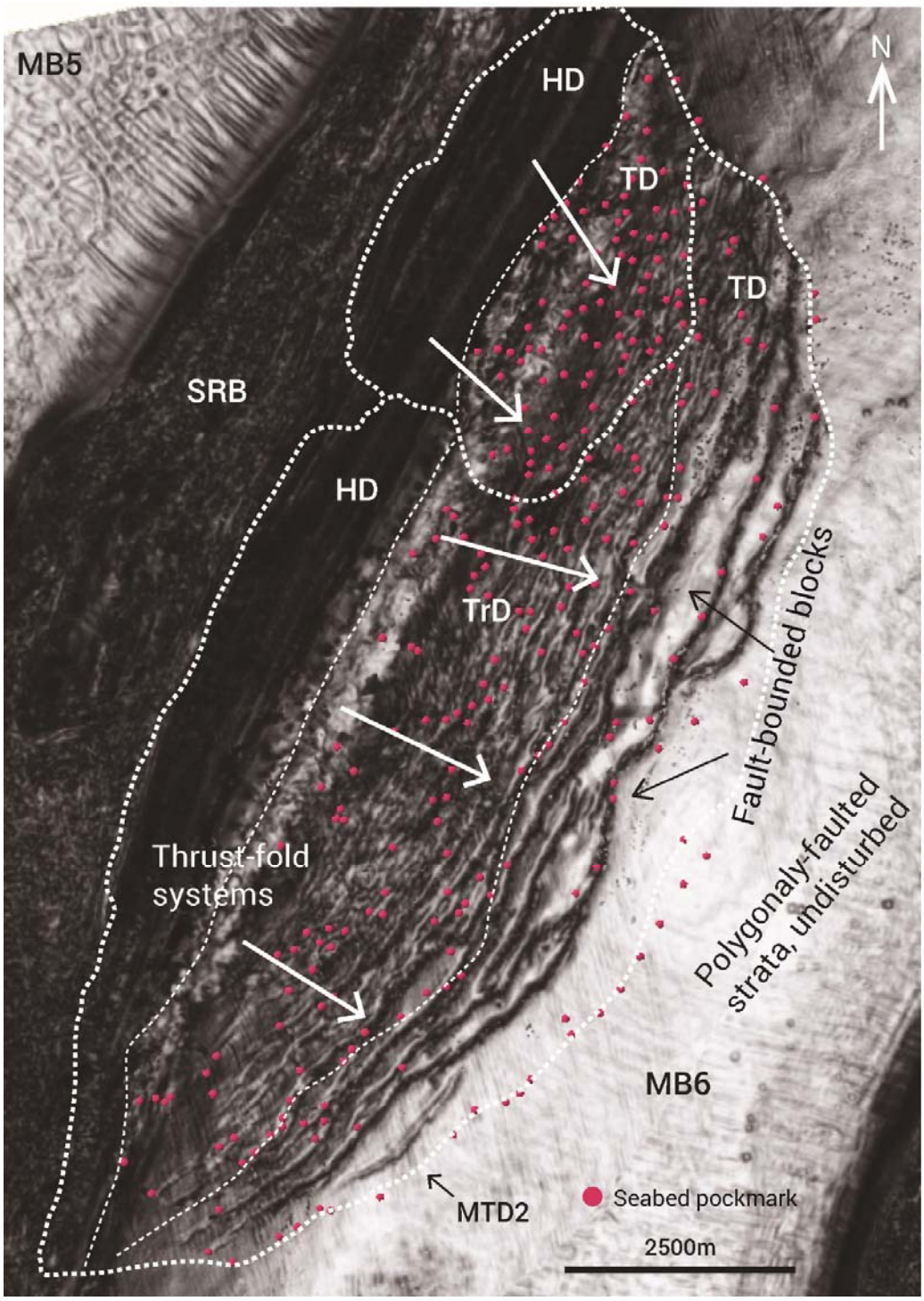

Figure 5.10. Variance slice parallel to the base of MTD2, intersecting the deposit and surrounding area of MB6. The map shows the MTD internal discontinuities and allows the identification of its domains. Long fault-bounded blocks occur within the toe domain. Numerous seafloor pockmarks follow alignments coincident with the internal discontinuities of MTD2a. The pockmark distribution over MTD2b is less organised. HD = headwall domain; TrD = transitional domain; TD = toe domain. Dark colours represent higher variance values.

MTD3

MTD3 is located at the seabed of mini-basin MB7 (figs. 5.2 and 5.11). It is bound to the north and west by salt ridge SRC and frontally confined southwards by stratified sediments of Unit 3 (fig. 5.12). MTD3 has an elongate lobate morphology, covering an area of 14.20km^2, and measuring 5.00km of maximum length and 3.25km of maximum width. MTD3 gradually thickens southwards, reaching a maximum thickness of 165m (196ms TWT). Contrasting with the previous MTDs, the base of MTD3 detaches along horizon **C3**, located at intermediate levels of Unit 3 (fig. 5.12). The higher seismic amplitudes observed along and below horizon **C3** suggest that lithology played a role on the location of the detachment interval. MTD3 shows a heterogeneous internal character marked by disrupted low-amplitude seismic reflections.

Partially preserved blocks of strata occur near the bottom levels of the transitional and toe domains (figs. 5.12 and 5.13). Extensional faults predominate within the headwall and transitional domains, and contractional features at the toe domain. However, the latter do not form protuberant ridges on top of MTD3 (figs. 5.11 and 5.12), contrasting with the marked ones observed at the toe of MTD1 (fig. 5.4).

Despite the generally moderate/low amplitudes observable on the seismic profiles (fig. 5.12), variance and amplitude attributes reveal a marked internal heterogeneity between the upslope and downslope domains (figs. 5.13 and 5.14c). Variance values in the headwall and translational domain are generally lower, and numerous closely spaced discontinuities are observed (fig. 5.13). A contrasting pattern is identified in the distal half of MTD3, marked by

large low variance segments up to 500m wide and lengths exceeding 2000m (fig. 5.13). These are interpreted as blocks of semi-preserved strata which are bound by arcuate E-W lineations associated with internal faulting. Two high variance, ENE-WSW oriented bands are observed crossing the width of MTD3. These may relate to the boundaries between the different MTD domains.

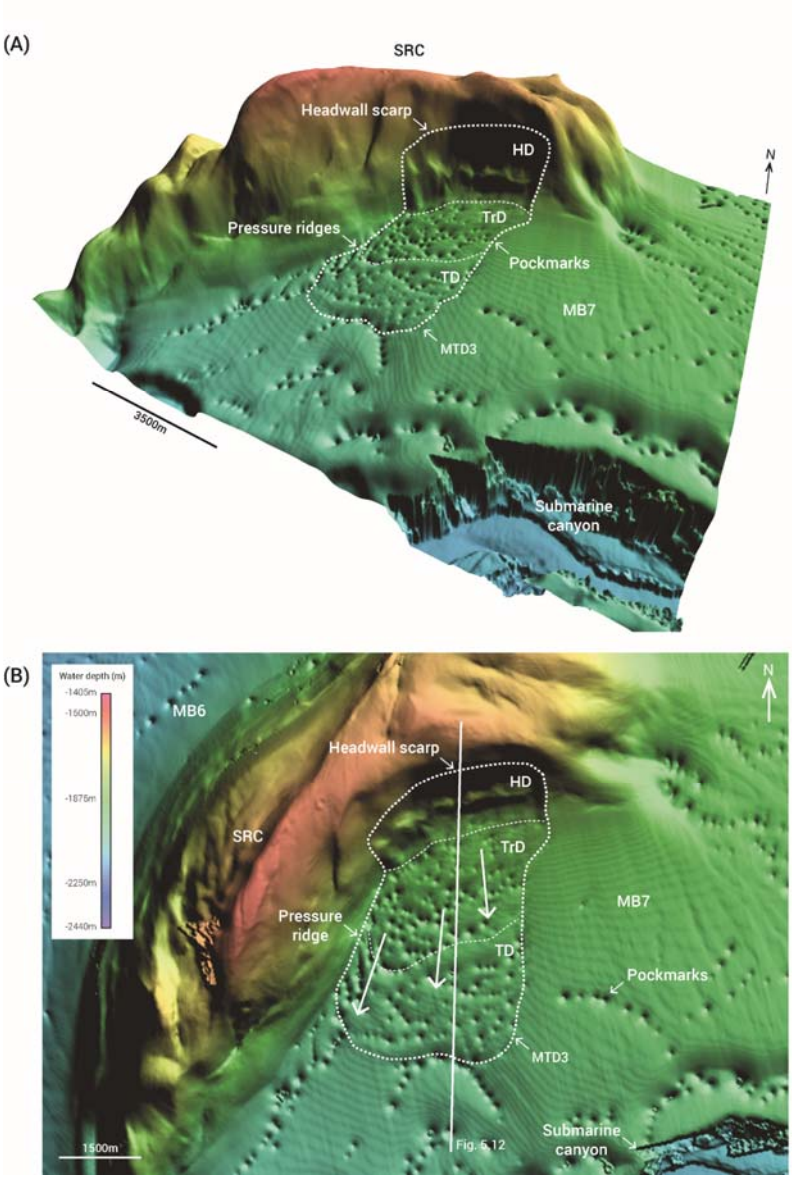

Figure 5.11. (A) 3D view and **(B)** map view of MTD3 at the seafloor. Location shown in figure 5.1. The MTD is bound at the headwall and western flank by salt ridge SRC. It has limited morphological expression on the seafloor. Numerous pockmarks occur within the whole area of MTD3 with very distinct patterns compared to other zones of mini-basin MB7. Arrows show the direction of transport. HD = headwall domain; TrD = transitional domain; TD = toe domain.

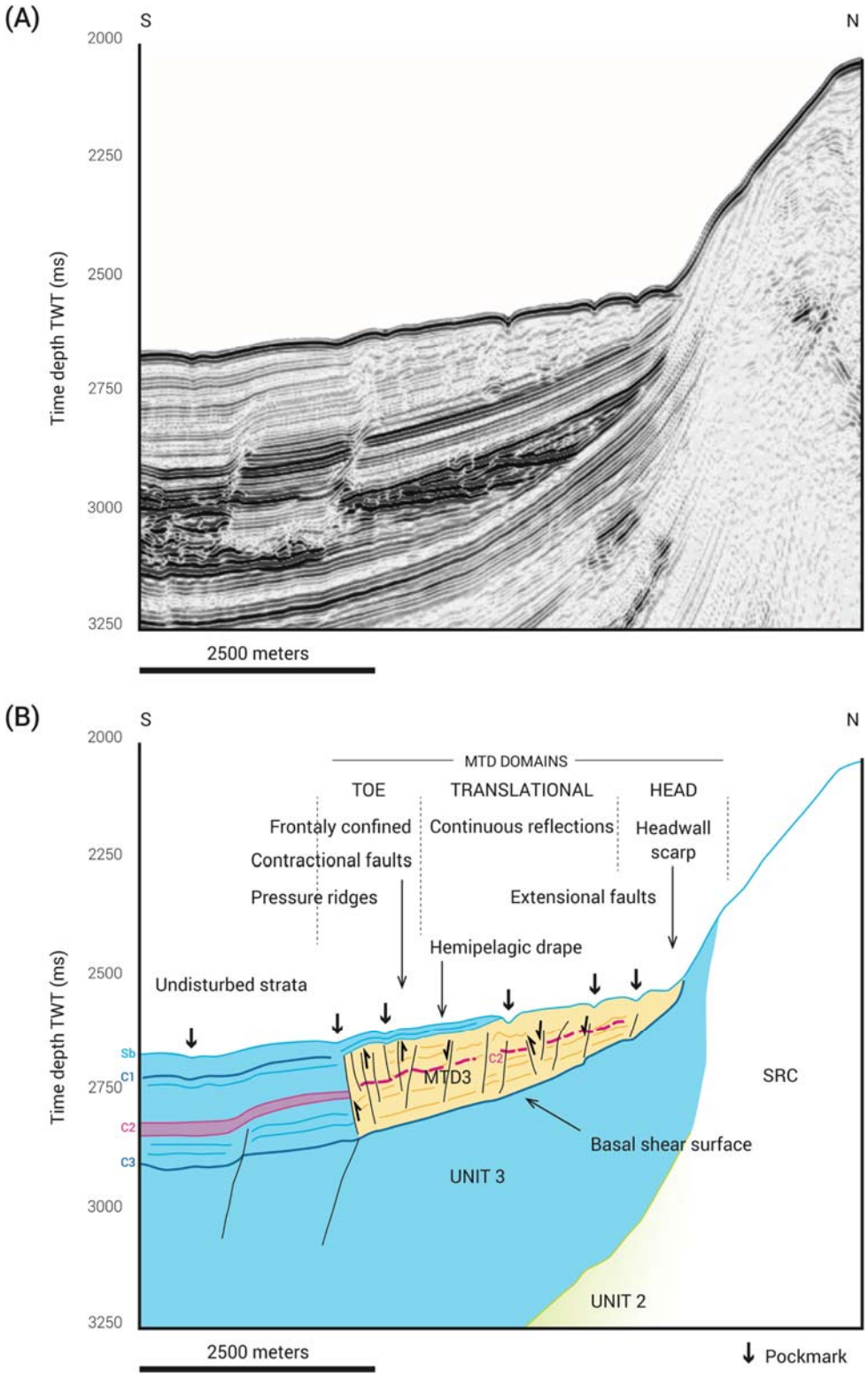

Figure 5.12. (A) Seismic profile and **(B)** interpreted section across MTD3. Location shown in figure 5.11. MTD3 detaches along horizon **C3** within Unit 3, which is much thicker in MB7 due to the presence of the large channel system. MTD 3 has generally low amplitude, with blocks of preserved strata present at the toe domain. A thin hemipelagic interval covers the toe and part of the transitional domains of MTD3. Green = Unit 2; blue = Unit 3; yellow = MTD; pink = interval **x-C2**; dashed pink line = interpreted **C2** reflection inside MTD. (Seismic courtesy of PGS.)

MTD3 is partially covered by Unit 3 sediments. This sediment cover, up to 50m (60ms TWT) in thickness, overlies the most distal domains of MTD3 and it is characterized by parallel and continuous reflections of moderate to high amplitude (fig. 5.12).

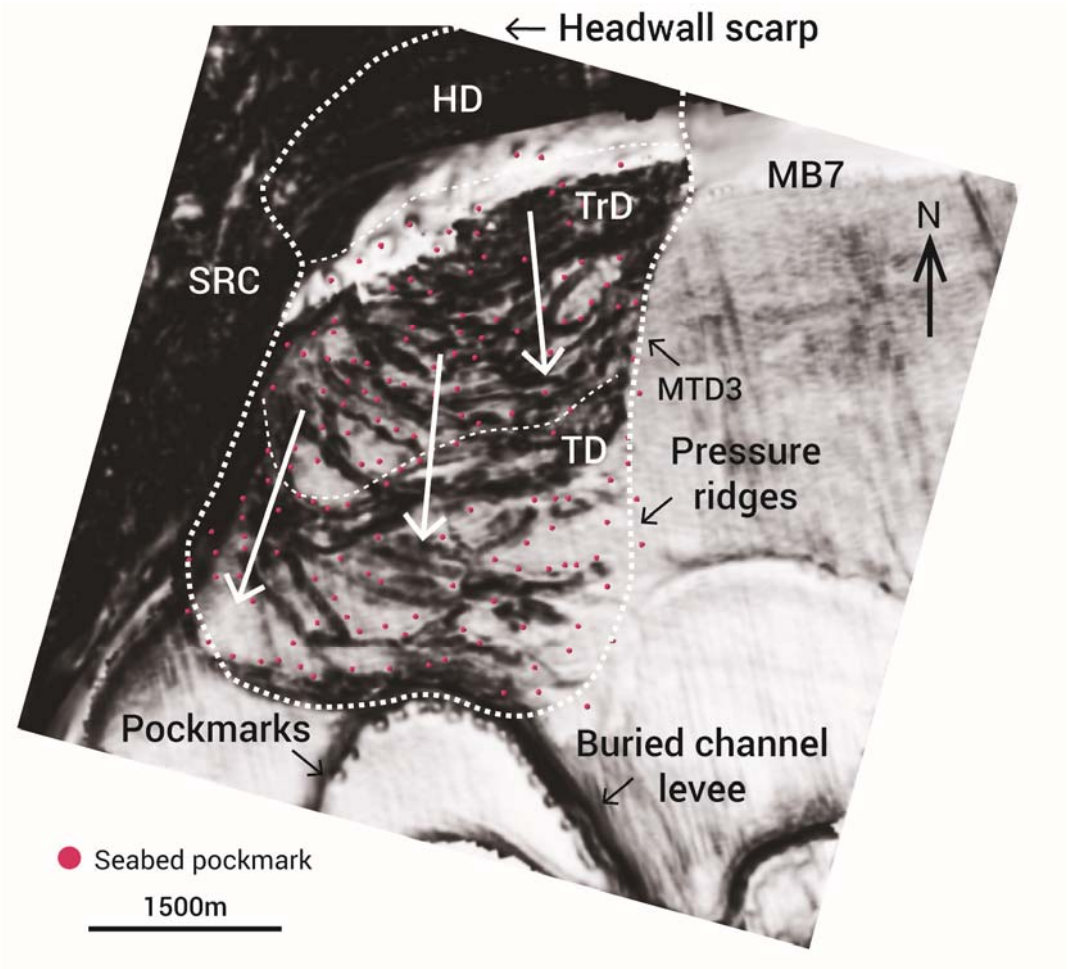

Figure 5.13. Variance slice parallel to the basal surface of MTD3. Lobate fault-bounded blocks with low variance predominate in the toe domain, gradually decreasing in size upslope. The higher variance in the headwall domain indicates higher disaggregation upslope. The distribution of pockmarks overlying MTD3 is influenced by its internal discontinuities. This is particularly evident around the larger blocks neart the toe. HD = headwall domain; TrD = transitional domain; TD = toe domain. Dark colours represent higher variance values.

5.3. Fluid flow-related features associated with MTDs

5.3.1. Amplitude anomalies within MTDs

Marked variations in seismic amplitude values occur due to changes in subsurface lithologies, the presence of fluids (especially when pipes and pockmarks are present), or a combination of both. Maximum amplitude maps computed within the MTDs show significant amplitude heterogeneities in the deposits (fig. 5.14).

The internal maximum amplitude of MTD1 (fig. 5.14b) shows marked internal discontinuities correlatable with the variance slice in figure 5.6. The highest amplitude values are coincident with the NW-SE discontinuities created by internal faults. Small SW-NE faults at the toe domain are also observed in amplitude maps. These are interpreted to result from limited lateral spreading during downslope movement, laterally segmenting the strata at the MTD toe (fig. 5.14b). Areas of low to moderate amplitudes in MTD1 coincide with lower variance values (fig. 5.6). These are interpreted to represent higher strata preservation, which tend to occur at the transitional and toe domains. In contrast, lower amplitudes predominate in the headwall domain where strata disaggregation is higher.

The maximum amplitude map of MTD2a highlights internal contrasts (fig. 5.14a). Similarly to MTD1, the disaggregated strata tend to show low amplitude values. Thus, amplitude patterns also reflect the internal strata organization, especially when compared to variance values (fig. 5.10). The banded alternation of lower to higher amplitudes downslope expresses

increased stratal preservation, especially towards the toe of MTD2a. Numerous elongated moderate-amplitude patches occur here, representing the blocks (fig. 5.14a). The highest maximum amplitude values are observed along the elongated MTD discontinuities coincident with internal faults. Other large areas of high amplitude occur along the MTD headwall, likely due to an effect of the basal interval on the MTD intersecting the high-amplitude strata of Unit 2.

The maximum amplitude maps of MTD3 show its highest values generally occur in the downslope domains (fig. 5.14c), where seismic variance is lower (fig. 5.13) and strata disaggregation is less intense. The peak amplitude values are observed along the arcuate discontinuities associated with internal faults, especially within the distal domains. A marked high amplitude band is observed near the boundary of the translational and toe domain which coincides with high variance values (fig. 5.13). This may represent marked deformation at the transition between the two domains.

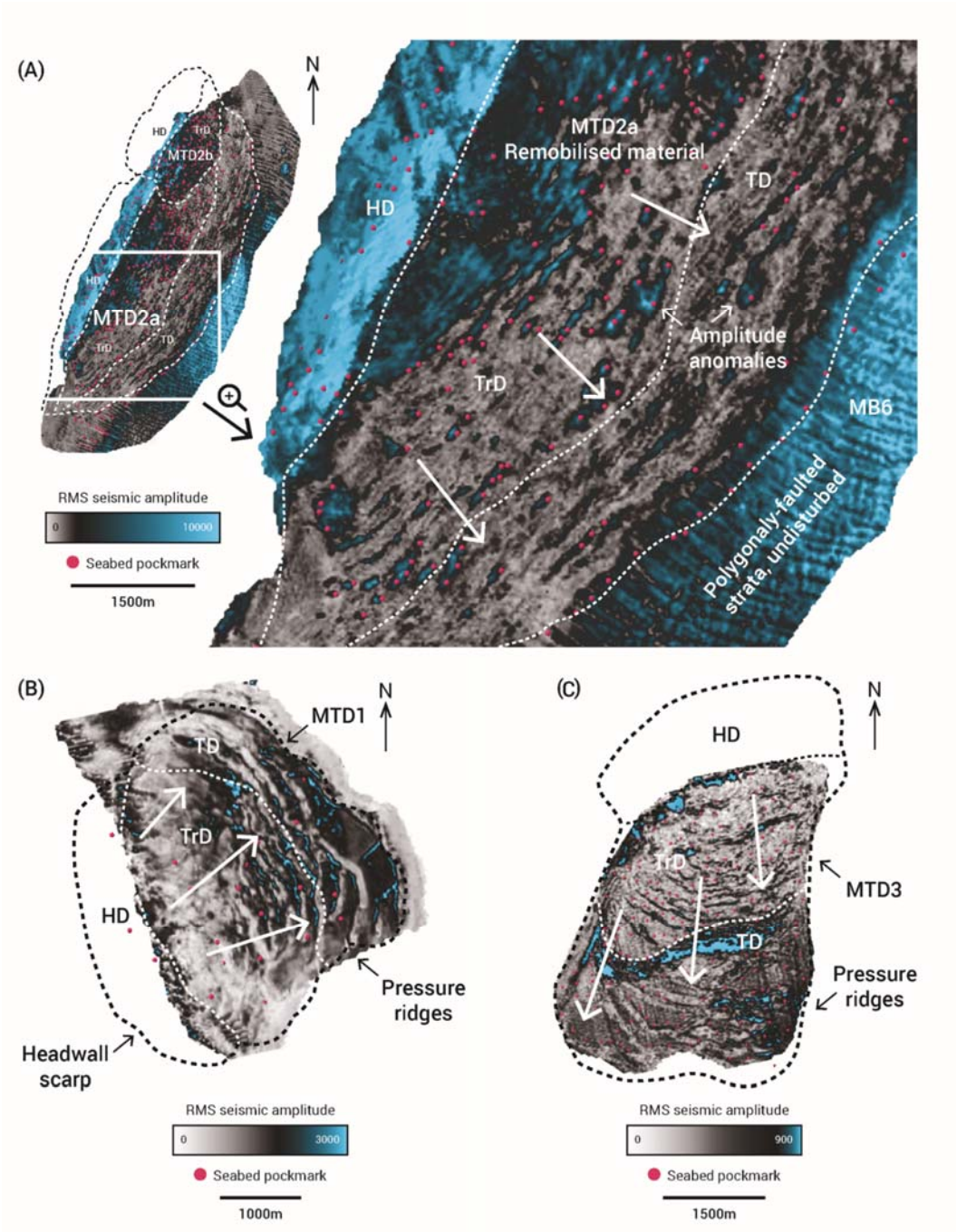

Figure 5.14. Maximum seismic amplitude maps of the MTDs, with seabed pockmark locations. **(A)** MTD2a has a low amplitude compared to the surrounding strata of MB6. Elongated high-amplitude patches occur within it, coincident with the internal faults and seabed pockmark alignments. These overlaps suggest the internal high amplitudes could be associated with fluid, or coarser permeable sediment that allows fluid movement. **(B)** MTD1 has low to moderate amplitudes. The highest values higlight internal faults, and are spatially coincident with seabed pockmarks. **(C)** The highest amplitudes in MTD3 are observed along the internal discontinuities. High-amplitude lineaments underlie pockmark trails. The marked high-amplitude band at mid-MTD locations may delimit different internal deformation domains. HD = headwall domain; TrD = transitional domain; TD = toe domain.

5.3.2. Pockmarks

The seafloor of the study area is covered with thousands of pockmarks, occurring generally within the salt-withdrawal mini-basins. Most seabed pockmarks are observed to be distributed in linear arrays, which reflect the structural and stratigraphical controls imposed on the underlying fluid plumbing system. Generally, pockmark alignments within the mini-basins are commonly perpendicular to the salt ridges, and the large majority are interpreted to be controlled by the orientation of the underlying polarized polygonal faults (see Chapter 4, Maia et. al., 2016). However, seabed pockmarks located above mass-transport deposits exhibit distinct distribution patterns from the ones formed in non-remobilized areas of the mini-basins.

5.3.2.1. Pockmarks over MTD1

Sixteen (16) pockmarks are observed at the seabed above MTD1 (figs. 5.4 and 5.6). Pockmark size ranges from 120m to 200m in diameter (length of long axis; average = 155m), and from a few meters to 10m in depth. Pockmark density above this MTD is 1 pockmark/km^2. No seismically resoluble onlap or infill has been observed within these depressions (fig. 5.5). The 16 pockmarks overlying MTD1 occur above the central and southern areas of the deposit and show a good spatial correlation with its internal discontinuities, as shown is variance and amplitude maps (figs. 5.6 and 5.14b). Upslope pockmarks are found along the lineament created by the headwall scar, and along an internal lineament that can be interpreted as the boundary of the transitional domain. MTD1 shows a gradual thickness increase downslope, ranging from 25ms TWT near the headwall to 275ms TWT at the central section of the toe (fig. 5.15).

Nearest neighbour analysis (see section 2.3) indicates fairly high distances between most neighbouring pockmarks, between 360 and 640m, for a mean distance of 447m (table 5.1 and Fig. 5.16). This value is significantly larger than the expected distance of 253m predicted by the model. The tests indicate a statistically significant overdispersion. This is also suggested by the Ripley's K test that indicates point dispersion for the pockmark distance ranges observed (fig. 5.16b). As pockmarks are scarce and fairly evenly spaced over MTD1, no significant relationship of their alignments can be obtained from this example. No pockmarks occur over the thicker sections of the deposit (fig. 5.15).

The spatial coincidence of the pockmarks and MTD faults (fig. 5.5 and 5.14) in the southern area suggests that the internal discontinuities played a key role in fluid migration. The partially disaggregated MTD1 strata of Unit 3 may preserve its limited permeability, so the internal faults constitute focus surfaces for fluids and enhance their upward migration. Pockmarks are remarkably absent on the northern area of MTD1 (fig. 5.6). This may be due to less developed internal faults and fractures, which alongside the partial sediment cover of MTD1 (fig. 5.5) hindered the development of a fluid plumbing and escape system.

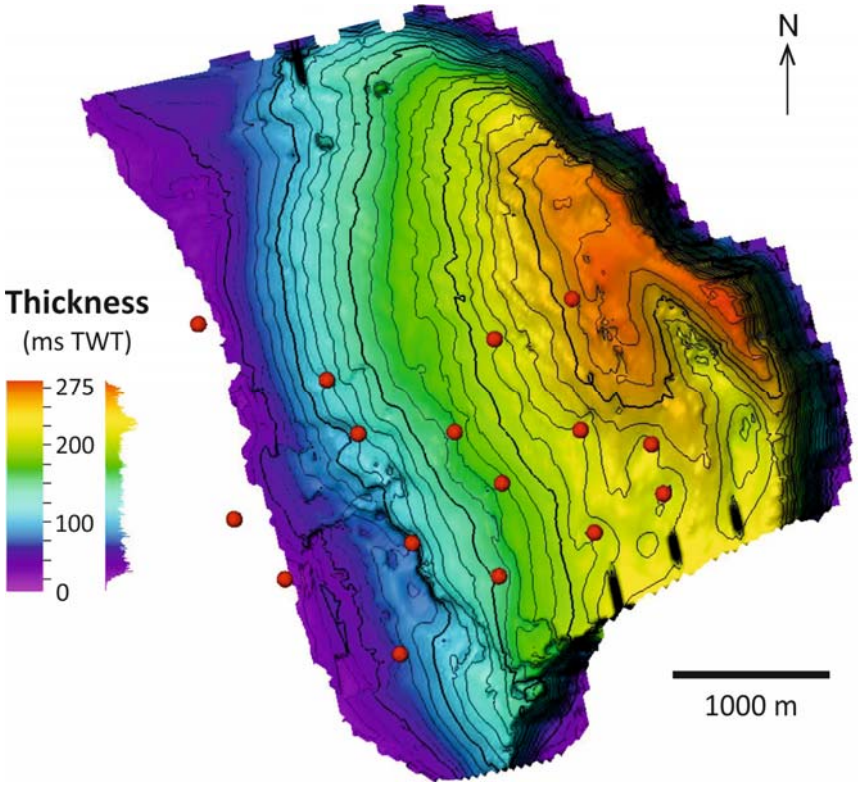

Figure 5.15. Thickness map of MTD1. The deposit shows a gradual thickness increase along its length, with the higher values adjacent to the frontal limit.

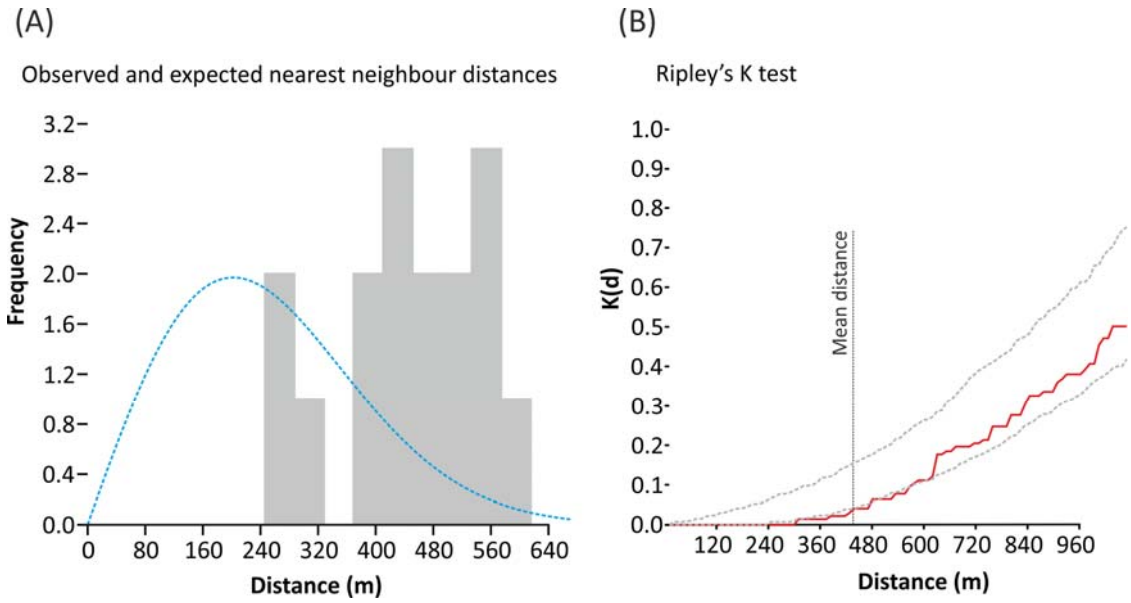

Figure 5.16. (A) Average nearest neighbour analysis for pockmarks overlying MTD1. The observed distance frequencies show a low match with the expected distance model. Most pockmarks are between 370 m to 620 m apart. Blue line = expected nearest neighbour distances. **(B)** Ripley's K test for pockmark distribution patterns. The plot indicates dispersed patterns within the range of distance values recorded for MTD1 pockmarks. Red line = observed spatial pattern K(d); dashed grey lines = confidence interval limits.

5.3.2.2. Pockmarks over MTD2

At the seafloor overlying MTD2, a total of 422 pockmarks are observed (MTD2a = 308 pockmarks, MTD2b = 114 pockmarks) (figs. 5.7 and 5.10). Pockmark size ranges from 70m to 180m in diameter (length of long axis; average = 115m), and from a few meters to 10m in depth. General pockmark densities above MTD2a and MTD2b are 2.24 and 5.21 pockmarks/km^2, respectively. No seismically resoluble onlap or infill has been observed within these depressions (fig. 5.9). Within the hemipelagic drape above MTD2a and MTD2b, 106 narrow columns of vertically stacked high amplitude anomalies are observed (5.9). These are interpreted to be pipes – the conduits along which pore fluids migrated upwards to be expelled at the seafloor, above which sub-circular pockmarks have formed. These pipes have a vertical extent varying between 109m and 248m (average 177m height), and their circular diameters range from 41m to 170m (average 87m wide).

The distribution of the pipes and pockmarks has a close relationship with the geometry of MTD2. A first control is imposed by its limits (figs. 5.7 and 5.10). Well-defined pockmark alignments follow the headwall scarp and the lobate frontal limits of MTD2a (figs. 5.7). Internal controls are inferred by the overlay of pockmark locations with fault-related discontinuities in the translational and toe domains of MTD2a, which often show the highest amplitude and variance values (figs. 5.10 and 5.14a). A few lineaments oblique to the main fault orientation, with corresponding pockmark alignments, are also observed (fig. 5.7). These may represent internal transfer zones poorly resolvable on seismic data, yet play an important role on the drainage network.

Statistical analysis of the pockmark distributions and the fault trends further support their close relationship (figs. 5.17 and 5.18). The automatic point alignment detection test (see section 2.3) clearly shows a preferential orientation of the detected features along a NE-SW orientation (fig. 5.17a and 5.19). Some evident alignments towards E-W orientations were also detected in lower frequencies. Note that not all alignments were identified by the automatic operations.

The map patterns of Kernel density of pockmarks indicate a main NE-SW orientation trend (fig. 5.17b). The plot also highlights the zones with higher pockmark density as occurring over MTD2b (fig. 5.17b). The nearest neighbour analysis calculated a mean distance between pockmarks across the whole MTD of 237.17m, slightly higher than the expected distance of 223.63m (table 5.1 and fig. 5.18a). The distribution plot shows that the majority of pockmarks occurs within a distance radius between 200 and 300m, with only a few located over 1000m apart. The spatial analysis tests indicate a tendency for overdispersion, which is associated with clustering patterns at distances over 140m as indicated by the Ripley's K test (fig. 5.18b).

Table 5.1. Synthesis table of the average nearest neighbour tests for pockmark distributions above MTDs 1, 2 and 3.

Feature	Nr. of points	Mean distance	Expected distance	R	Z	p (random)
MTD1	16	447.12	253.27	1.7654	5.857	4.71E-09
MTD2 - no headwall	343	252.16	238.06	1.0592	2.986	0.035856
MTD2	422	237.17	223.63	1.0605	2.378	0.017407
MTD2a - no headwall	217	271.67	264.96	1.0253	0.7196	0.47587
MTD2b	114	210.94	156.27	1.3499	7.1465	8.90E-13
MTD3	152	180.23	134.45	1.3405	8.0298	9.76E-16
Pockmarks outside MTD2	528	249.21	282.64	0.8817	-5.198	2.00E-07

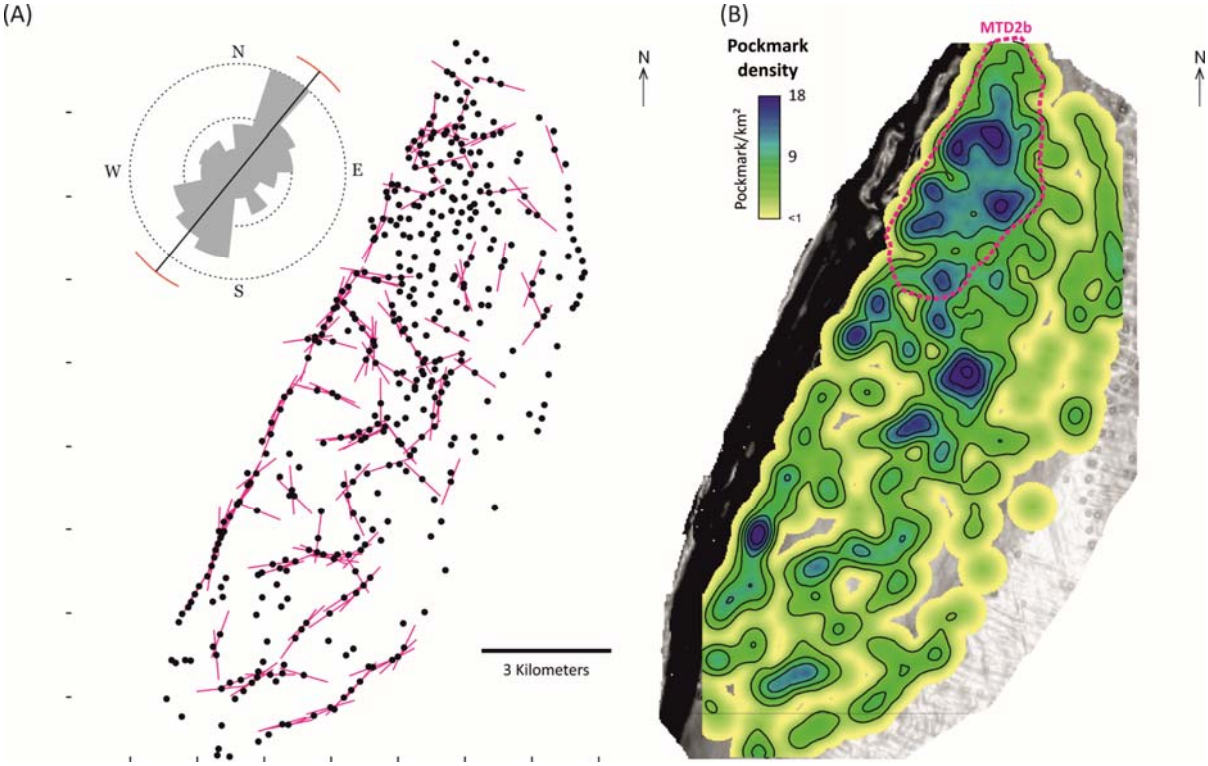

Figure 5.17. (A) Map representation of the automatic pockmark alignment detection for MTD2. The rose plot shows a predominance of NE-oriented alignements. However, relevant numbers of E-NE alignements are recorded. **(B)** Kernel density map of pockmarks overlying MTD2 Generally higher densities are observed on the north, within the limits of MTD2b. Elongated, NE-oriented density patterns predominate within the area of MTD2a.

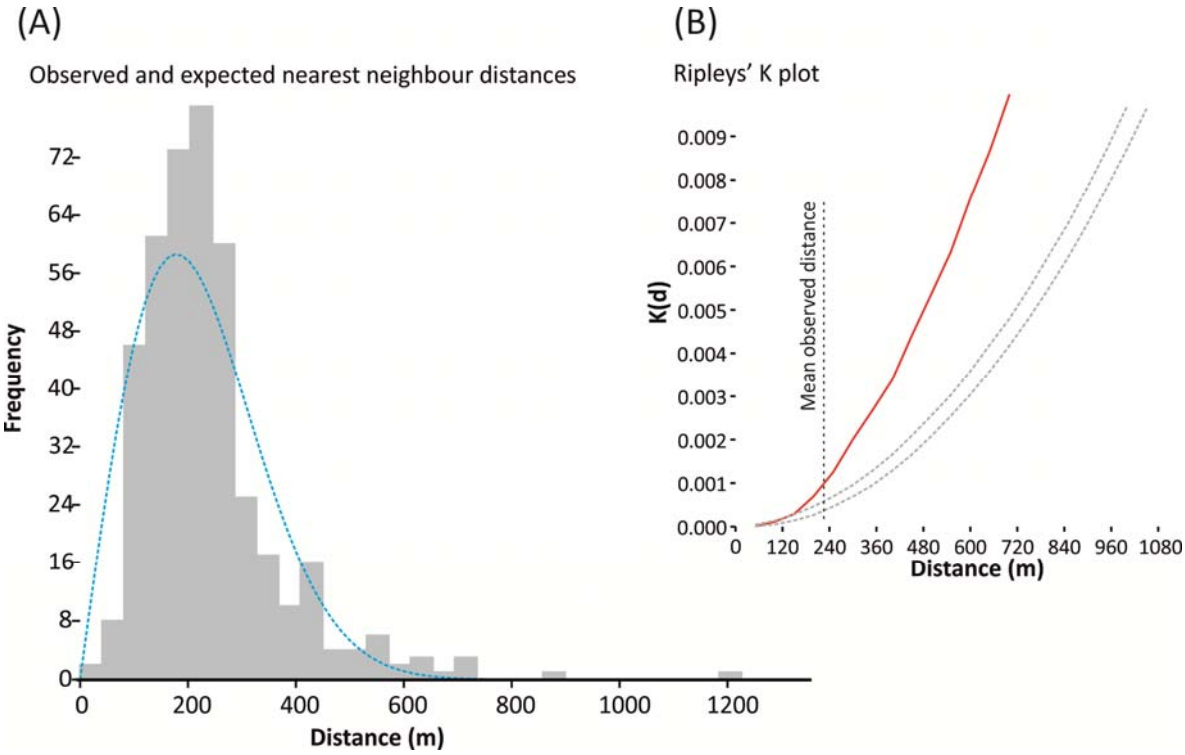

Figure 5.18. (A) Average nearest neighbour analysis for pockmarks overlying MTD2. The observed distance frequencies show a good match with the expected distance. Most pockmarks show spacings between 100m to 350m. Blue line = expected nearest neighbour distances. **(B)** Ripley's K test for pockmark distribution. Random distributions area valid for distances below 120m, but above this there are clustered patterns. Red line = observed spatial pattern K(d); dashed grey lines = confidence interval limits.

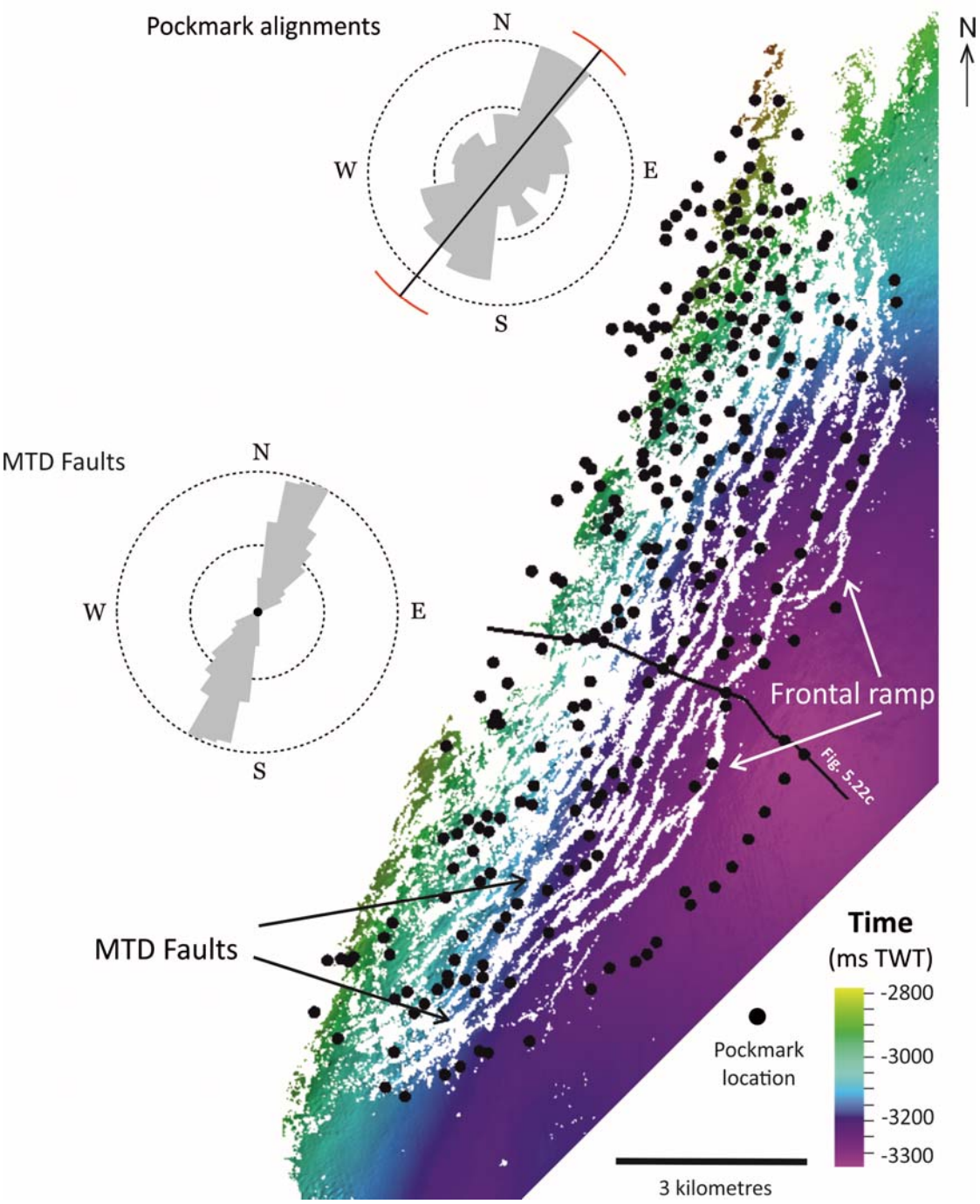

Figure 5.19. Seismic horizon **C5** confidently tracked in MB6 and within MTD2 (see fig. 5.2 for reference). The interpretation gaps correspond to intra-MTD2 faults. This horizon shows the well-preserved, elongated blocks towards the MTD2 lower levels. As previously shown, the seafloor pockmarks frequently overlie the gaps created by the internal discontinuities of MTD2. The pockmarks delimiting the MTD frontal limit are not directly influenced by the lower ramp in the basal detachment level. Rose diagrams of pockmark alignments and faults show a matching predominance of NE-directed orientation for both features.

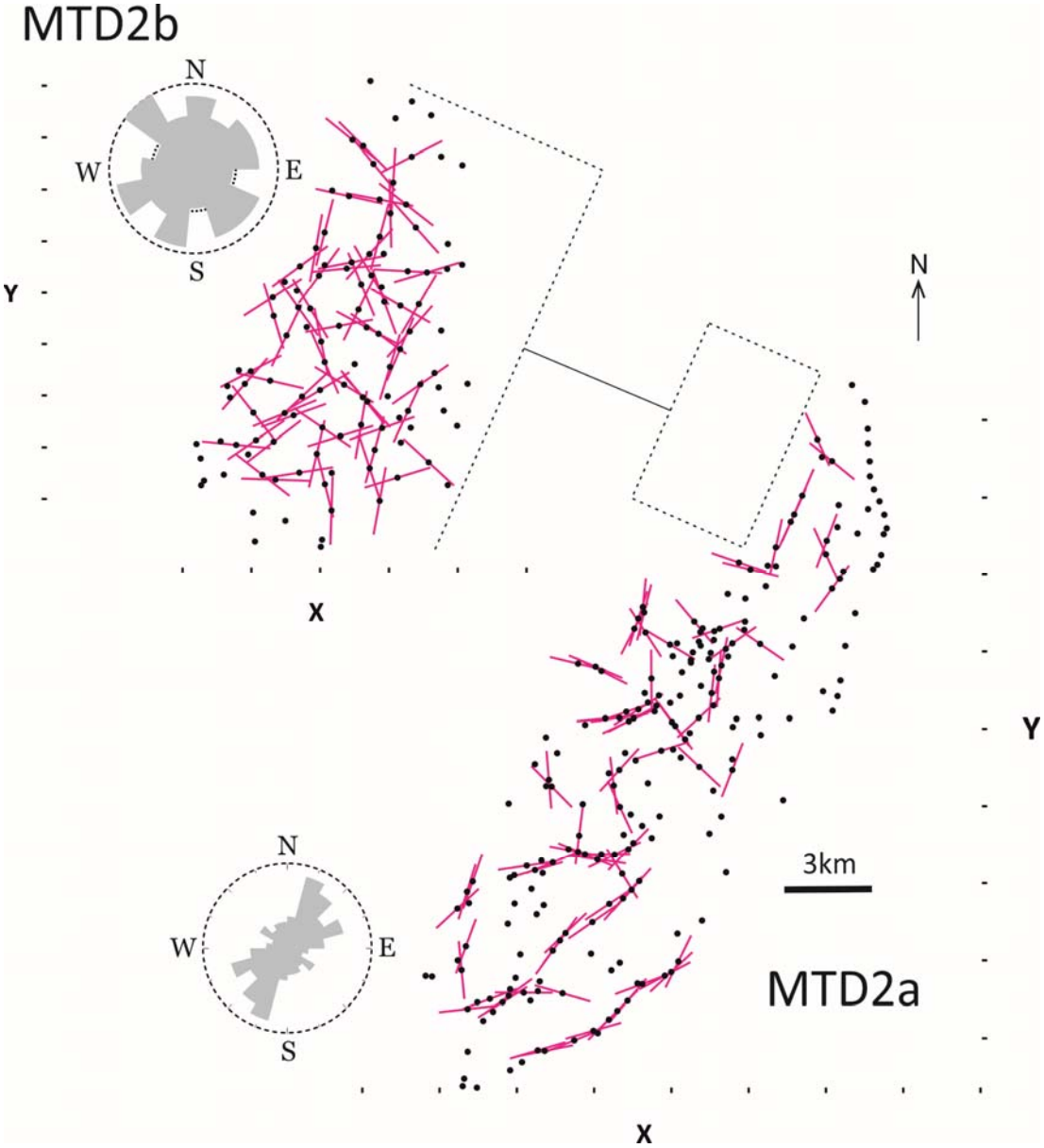

Figure 5.20. Comparison of pockmark alignment patterns between MTD2a and MTD2b, excluding the headwall pockmarks. MTD2a shows the predominance of general NE orientations, sub-parallel to the fault orientations. MTD2b shows a markedly contrasting pattern, with fairly numerous frequencies for all quadrants. However, a NW-SE orientation stands out, parallel to the direction of movement of MTD2b. This may be influenced by internal MTD discontinuities hard to visualise at the seismic scale.

To compare the orientation of pockmark alignments and intra-MTD faults, seismically-visible discontinuities within MTD2 were mapped and measured, and their spatial distribution was analysed (fig. 5.19). The calculated mean orientation of pockmark alignments and intra-MTD2 discontinuities are very similar, suggesting a very close relationship between them. This resemblance is highlighted by the overlay of pockmark locations and MTD attribute maps (figs. 5.10 and 5.14a) and intra-MTD horizons with good continuity to be reliably tracked within the mass-failure (fig. 5.19). The block-bounding gaps created by the internal faults are often spatially coincident with the pockmark alignments, especially towards the distal area (fig. 5.19). The main trends of faults and pockmark alignments follow a NE-SW direction, although the main orientation of MTD faults is predominantly below N45°E. A secondary orientation of circa N60°E is observed in alignments of seabed pockmarks. Internal faults with identical orientations are present within MTD2 (fig. 5.19). These discontinuities tend to terminate against the main N30°E ones, suggesting they may derived from the linkage of the main intra-MTD deformation structures. A relevant aspect is the slight orientation offset between the MTD faults and pockmark alignments. These could be due to the influence of the discontinuities on the location of the pockmarks which do not act as fluid conduits, a similar mechanism to the one established in Chapter 4 for polarised polygonal faults. Nevertheless, the close spatial relationship between both supports the case of the MTD deformation influencing the pockmark distribution.

A further breakdown of the pockmark patterns was made by separately analysing their distribution over MTD2a and MTD2b. As these sub-deposits

show marked contrasts in internal character and amplitude patterns (figs 5.9, 5.14a), they could influence the seabed pockmark scattering patterns within relatively close areas. The alignment detection tests for pockmarks over MTD2a show a NNE-SSW orientation (fig. 5.20), very similar to the orientations measured for the internal faults (fig. 5.19). In fact, these two orientations – MTD2a pockmarks and MTD2a faults – have much closer trends around N30°E than the ones comparing internal discontinuities to the total pockmark alignments over MTD2b (~N45°E) (fig. 5.17 and 5.20). Nearest-neighbour analysis for pockmarks overlying MTD2a (headwall pockmarks excluded) indicate a mean distance of 271m between points, very similar to an expected 265m (table 5.1 and fig. 5.21). The plot indicates the highest spacing frequency to be in the order of 200-300m, and the distribution density fits within the predicted curve (fig. 5.21a). These trends are similar to the ones obtained for the full pockmark population overlying MTD2 (fig. 5.18).

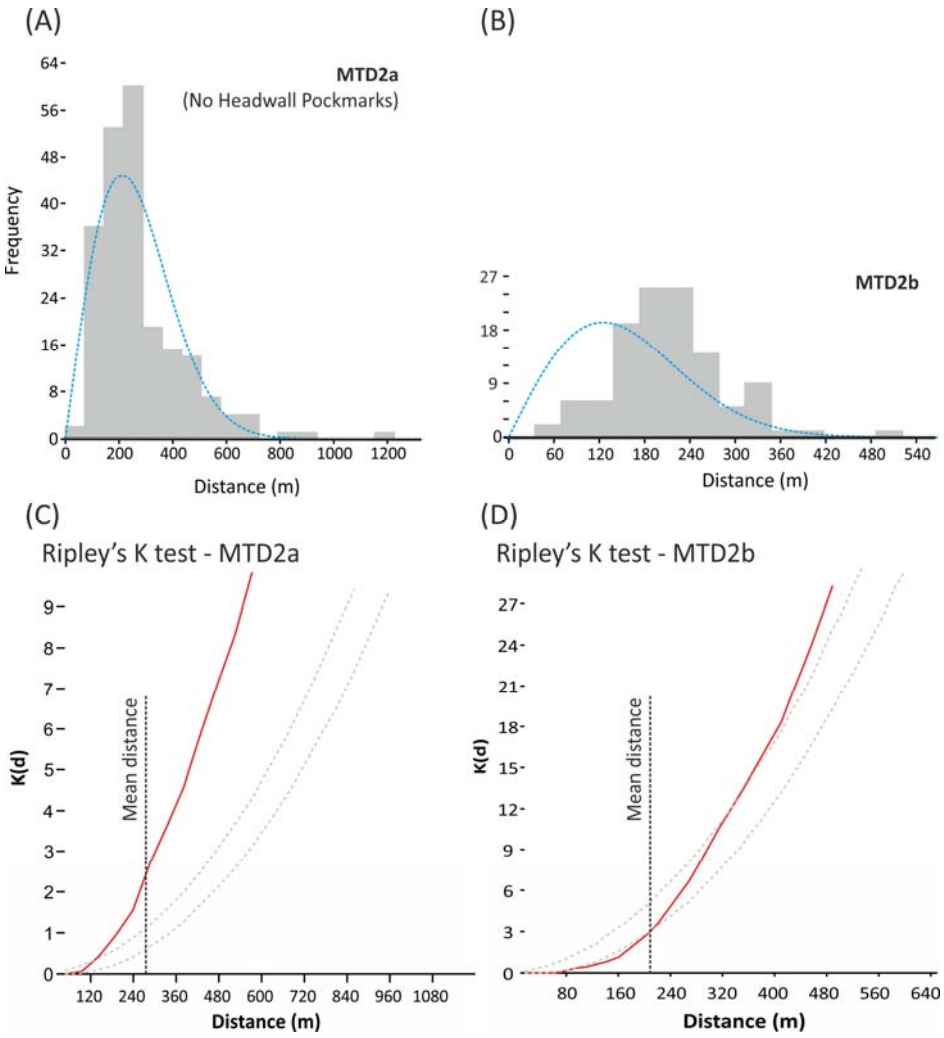

Figure 5.21. Average nearest neighbour plots for pockmark distance in **(A)** MTD2a and **(B)** MTD2b. Both sub-deposits show the higher frequencies for distance values to be around 180m to 240m. The observed frequencies in MTD2a have a close fit to the model prediction, but this is not the case in MTD2b. Blue line = expected nearest neighbour distances. **(C)** The Ripley's K test for MTD2a indicates a random point distribution at distances below 130m, for which there are very low frequencies, and clustered patterns for distances over 130m. **(D)** Ripley's K test for MTD2b pockmarks indicating a dispersed for distances up to 170m, and random distributions from the latter value to 350m. Clustered patterns occur for distances above 350m. Red line = observed spatial pattern (K(d); dashed grey lines = confidence interval limits.

The alignment orientations over MTD2b differ from the ones within MTD2a (fig. 5.20). There is a main trend detected along a NW-SE orientation, but various other orientations were also found with high frequencies. This less organised distribution of pockmarks is considered to result from the arrangement of intra-MTD2b discontinuities and morphology. A main

orientation observed, around N50°W to N30°W, is parallel to the direction of MTD2b movement. Nearest neighbour analysis calculated the mean point spacing as 211m for an expected distance of 156m (table 5.1 and fig. 5.21b). The highest frequency of pockmark spacing is between 180 and 240m, lower than the values obtained for MTD2a. Pockmarks spaced at relatively low distances (i.e. below 140m) are more frequent in MTD2b comparatively to MTD2a. The observed frequency in MTD2b is markedly offset from the expected frequency curve, further evidencing different distribution patterns between pockmarks overlying MTD2a and MTD2b (fig. 5.21). This also supports the interpretation of the contrasting intra-MTD deformation structures influencing pockmark distributions over MTD2.

The pockmark distribution relates to the thickness patterns of MTD2 (fig. 5.22a and 5.23b). This is the thickest of the mass-transport deposits analysed in this chapter, being over twice the value of the other examples. It increases from low thickness values below 42m (50ms TWT) along the headwall pinch-out to thicknesses of circa 336m (400ms TWT) at the toe domain. Excluding the headwall pockmarks, most of the remaining fluid-escape features occur in areas where MTD2 is 75 to 315m (90 to 375ms TWT) thick, coincident with the extensional and transitional upslope domains (fig. 5.22a). The presence of MTD2b towards the north does not seem to affect the overall thickness patterns of the full MTD2. However, the thickness patterns of the localised MTD2b are markedly distinct from MTD2a (fig. 5.23b).

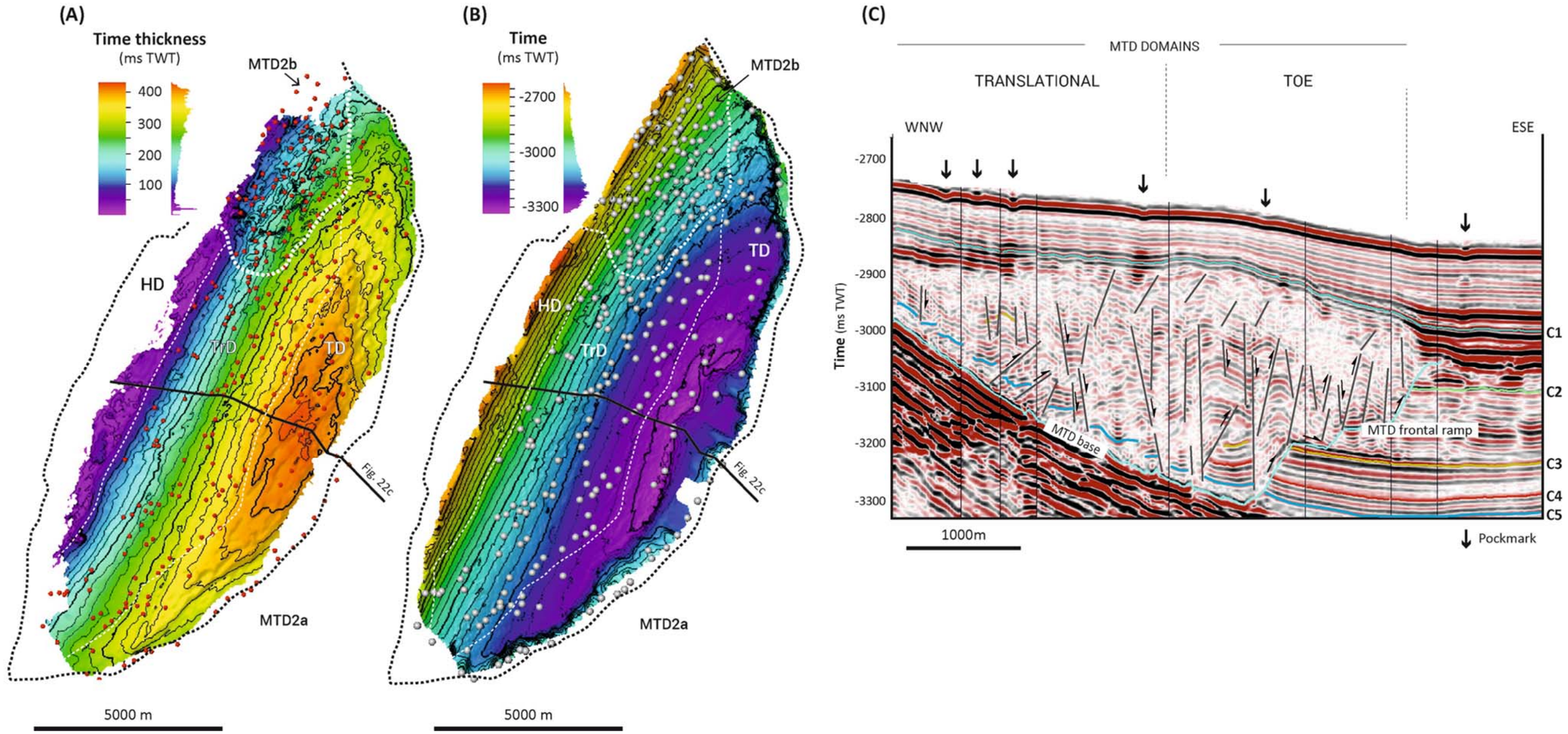

Figure 5.22. (A) Thickness map of MTD2, overlain by the location of seabed pockmarks. Pockmarks are more numerous within areas 100ms TWT to 350ms TWT thick. The thicker areas corresponding to the toe domain show a relatively lower number of pockmarks. **(B)** Morphological map of the basal surface of MTD2. Its stepped morphology and corresponding frontal ramps are suggested to influence the location of seabed pockmarks. **(C)** Seismic section of MTD2 intersecting pockmarks along its length. The spacing of pockmarks is lower in the headwall and transitional domains. The pockmark within the toe domain has a fainter seafloor expression comparatively to the marked depressions in the remaining areas. The lowermost basal ramp is interpreted to influence the development of extensional and compressional faults directly underlying the pockmarks in the toe domain.

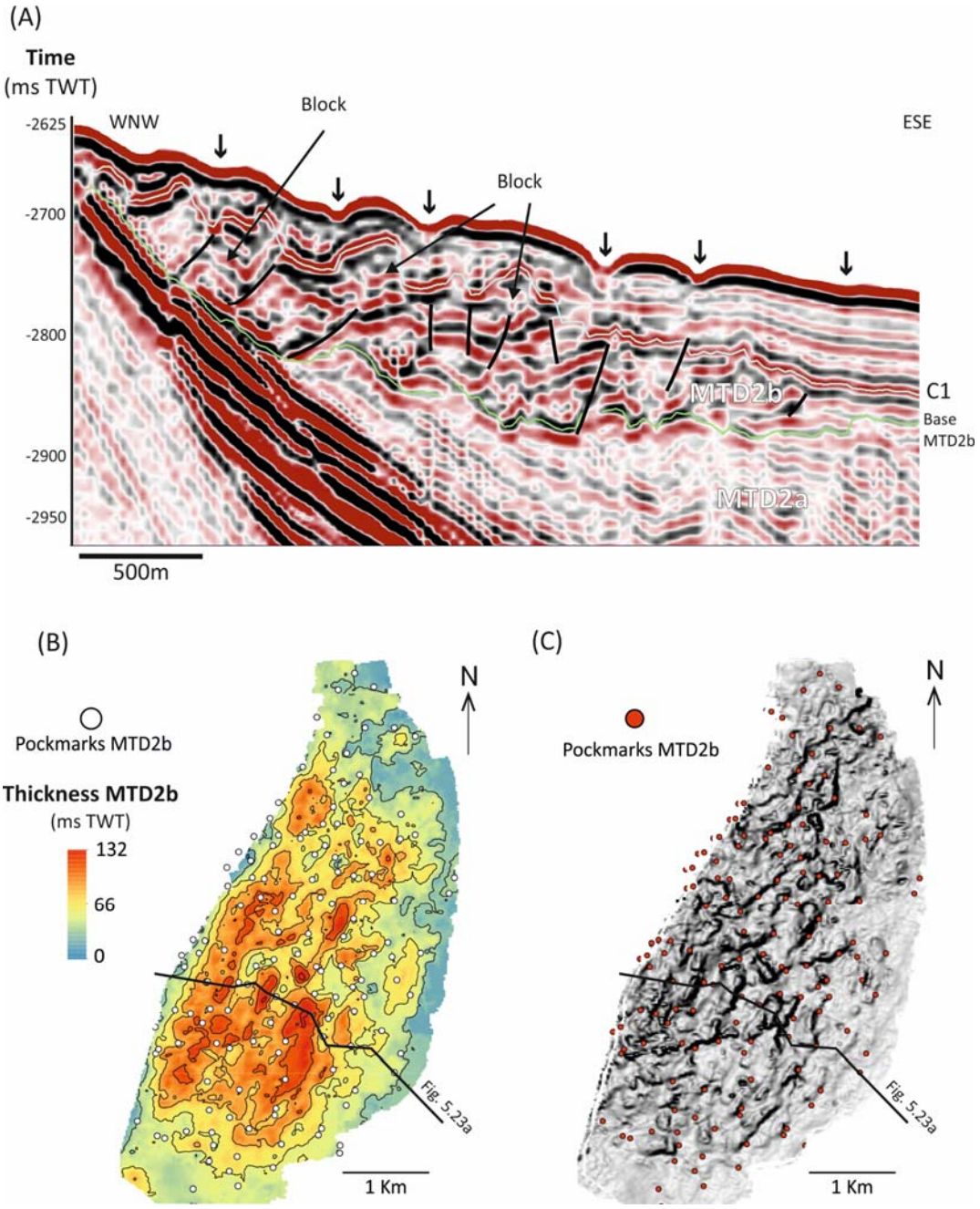

Figure 5.23. (A) Seismic section across MTD2b. The top surface is markedly irregular due to the presence of blocks. The deposit is characterised by high amplitudes, contrasting with the general character of MTD2a. **(B)** Thickness map of MTD2b. Pockmarks do not overlie the thicker areas of the deposit. **(C)** Dipmap of the top surface of MTD2b. High dips correspond to the flanks of blocks and ridges. Pockmarks often overlie the high-dip lineaments.

The compressional toe domain of MTD2a is characterised by an elongated domed area delimited by the 375ms TWT isochore line (fig. 5.22a). Pockmark number is lower within this delimited area, and various ones line up along the edge of the thickness contour lines. These are also sub-parallel to the

orientation of intra-MTD faults. This relationship between MTD thickness and pockmark presence is supported by seismic profiles (fig. 5.22c). A path selected to intersect pockmarks along the length of MTD2a shows the majority of seafloor depressions, pipes and acoustic anomalies along the area where the MTD2a top surface is concave upwards, and also immediately at the MTD2a frontal limit (fig. 5.22c). Within the thickened bulge, in which thrusts and compressional faults occur, the fluid flow indicators are less frequent to absent (fig. 5.22c).

The morphology of the stepped basal surface of MTD2 is considered to influence the location of a few pockmarks overlying the toe of the deposit (fig. 5.22b). Maps of the morphology of the MTD base and the seabed pockmarks show a clear superposition of the latter over the sharp depth decrease imposed by the frontal ramp (fig. 5.22b). The ramp is also associated with compression-induced faults that propagate vertically through most of the MTD, up to the fluid source interval estimated for mini-basins MB6 and MB7 (interval **x-C2**; see Chapter 4). Pockmarks within the thickened toe domains are influenced by faults associated with the frontal ramp of MTD2. Marked folding occurs in the strata directly overlying the lowermost ramp segment. However, the pockmarks overlie a secondary normal fault antithetic to the main thrusts, suggesting the control of localised extension on fluid escape within the compressional domain of MTD2a (fig. 5.22c).

The thickness patterns of MTD2b are relatable to the distribution of the seabed pockmarks overlying it (fig. 5.23). Seismic profiles show pockmarks located above local depressions of the top surface of MTD2b (fig. 5.23a). These are adjacent to elongated NE-SW oriented pinnacles associated to ridges and

blocks, represented on isochrone maps as the thickest areas of MTD2b. No seabed pockmarks overlie these thicker features, instead they are located over the depressions adjacent to them (fig 5.23b). In addition, pockmarks often overlie lineaments of high dip along the steep edge of blocks and ridges, suggesting their influence on pockmark distribution. The limited length and continuity of these topographic highs creates NW-SE oriented thinner gaps above which pockmarks have developed (fig 5.23b).

Pockmarks in mini-basin MB6 outside MTD2

Numerous pockmarks occur in mini-basin MB6 outside the area affected by MTD2. Identical orientation analysis and point lineament detection tests were made to compare the pockmark distribution patterns observed (fig. 5.24). As mentioned in Chapter 4, polarised polygonal faults (PFFs) deform mini-basin MB6, occurring in the vicinities of MTD2. PFFs are sub-perpendicular to the salt ridges and show a clear NW-SE orientation (figs. 5.24a and 5.24b). This direction is sub-perpendicular to the one of intra-MTD2 faults. Small faults of very limited extent and perpendicular to the PFFs occur in low numbers. The pockmark alignments outside MTD2 show two very clear orientations: one parallel to the mini-basin faults and one sub-perpendicular to it (fig. 5.24c). Based on the results from Chapter 4 and the overlay of pockmark and fault locations, it is clear that the WNW-ESE pockmark alignments are controlled by the PFFs. The NE-SW pockmarks in non-MTD areas are likely controlled by a combination of factors (fig. 5.24d). A main controlling factor is the presence of the MTD and its associated relief. This

develops pockmark alignments along the MTD2 border. The topographic influence of the MTD extends beyond its limits, and pockmark alignments parallel to it are observed near the northern flank (figs. 5.24c and 5.24d). Further NE-SW pockmark alignments are observed along the flank of salt ridge SRC. These are interpreted to be structurally influenced by the salt ridge.

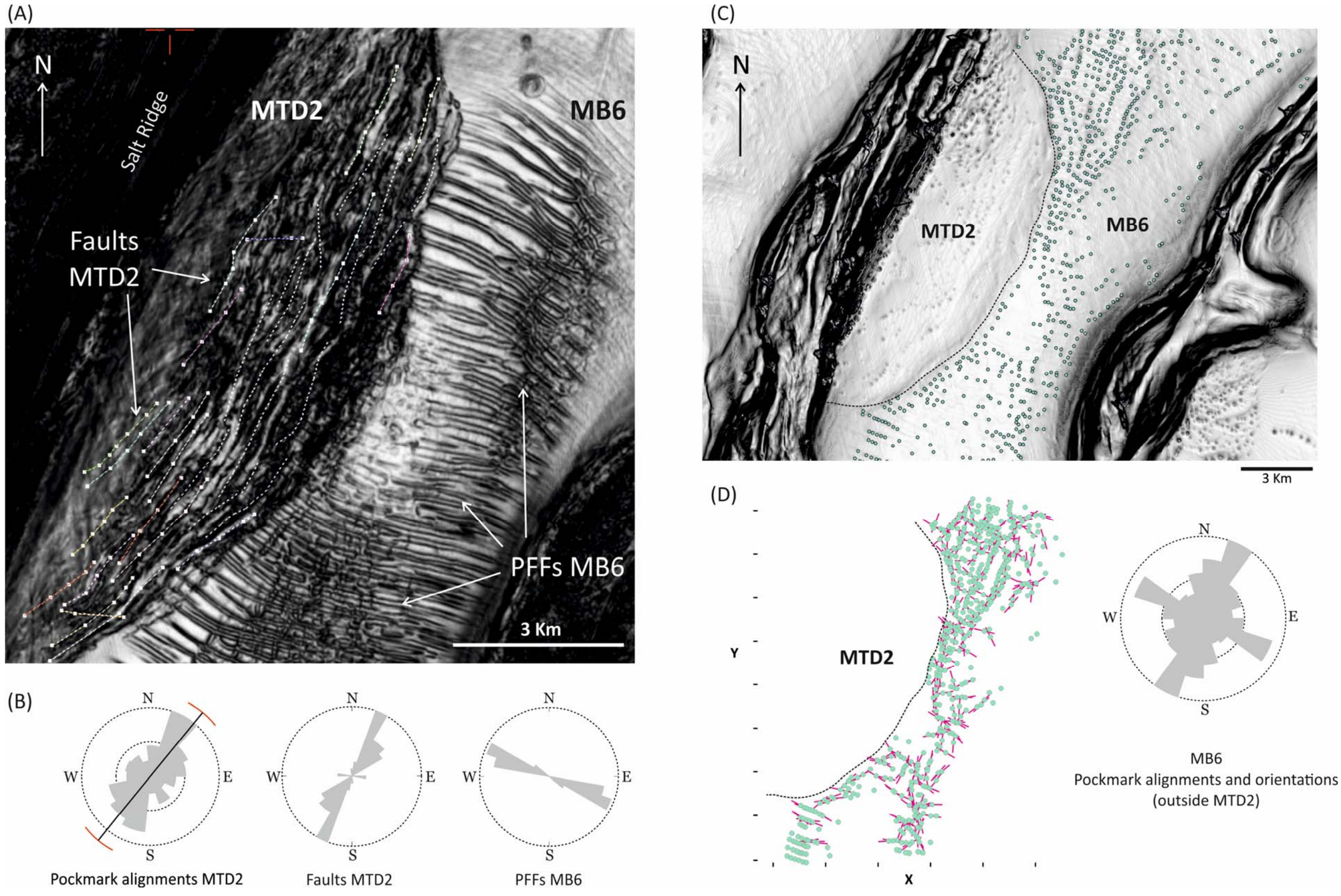

Figure 5.24. (A) Variance slice evidencing intra-MTD2 faults and the general high variance patterns of MTD2. This contrasts with the lower variance patterns of MB6 strata outside the MTD, where numerous NW-SE polarysed polygonal faults (PFFs) are visible. **(B)** Rose diagrams representing the orientations of pockmark alignements over MTD2, intra-MTD2 faults and PFFs outside the MTD. The latter shows markedlly contrasting orientations, sub-perpendicular to the MTD-related features. **(C)** Seafloor dipmap of MB6 showing the location of seafloor pockmarks outside MTD 2 (green dots). **(D)** Pockmark alignment diagram and corresponding rose diagram. Two major orientations are identified: a NW-SE direction parallel to the orientation of PFFs, and a NE-SW direction perpendicular to the PFFs.

5.3.2.3. Pockmarks over MTD3

The seabed above MTD3 is highly saturated in pockmarks (fig. 5.11), with 149 circular depressions identified (corresponding to a density of 10.49 pockmarks/km^2). Pockmark size ranges from 65m to 180m in diameter (length of long axis; average = 110m), and from a few meters to 15m in depth. No seismically resoluble onlap or infill has been observed within these depressions. The number and distribution of pockmarks has some relationship with the thickness patterns of MTD3: pockmarks are more numerous and are closer-spaced within the transitional domains, where thickness is lower than 135m (160ms TWT) (fig. 5.25a). The highest spacing is observed on the thicker areas of the deposit. However, pockmark density patterns are not uniform within each domain (fig 5.25b and 5.26). The highest densities are present on the western section of the MTD, adjacent to the salt ridge limit. The density map also highlights the contrast of pockmark spacing between the transitional and toe domains, with lower density patterns in the latter. Generally, pockmark density appears to increase with decreasing MTD thickness. The transition between domains is represented by a NW-oriented band of low pockmark density (fig. 5.25b).

The pockmark distribution patterns and spacing are most likely controlled by the MTD internal faults (figs. 5.13, 5.25a and 5.26). Similarly to MTD2, the discontinuities in the headwall and toe of MTD3 seem to control fluid expulsion alignments. The MTD3 flanks also control pockmark lineaments: on the west they are forced by the salt structure, and on the east they are controlled by the MTD3 limit (figs. 5.12, 5.14 and 5.26b). The internal

distribution is controlled by the spacing, extent and curvature of the fault-related discontinuities (figs. 5.13, 5.26b). Pockmarks over the translational domain tend to be closer-spaced. In contrast, pockmarks in the toe domain have higher distances between lineaments with pronounced arching influenced by wider fault-bounded blocks. The pockmarks overlie high amplitude discontinuities throughout the MTD (fig. 5.13c).

The nearest neighbour analysis show an offset between the observed and modelled frequencies (table 5.1 and fig. 5.27). Mean distances of 180m exceed the expected values of 134m. The nearest neighbour analysis indicates a tendency for general overdispersion, but the Ripley's K plot shows a varied distribution (fig. 5.27b). There is a tendency for dispersion below distances of 190m (within which most of the pockmarks occur) and randomised patterns between 200 to 300m. Clustering is expected at distances exceeding 350m, but such cases are rare within the observed spacing frequencies (fig. 5.27).

The directional analysis for pockmarks alignments over MTD3 shows a predominant E-W orientation, perpendicular to the direction of movement of MTD3 (fig. 5.26c), subparallel to the main MTD3 faults (fig. 5.26b). Secondary orientations are observed, with relevance for NE-SW alignments. These are mostly observed upslope and close to the west flank of MTD3. In summary, the pockmark distribution and internal faults of MTD3 show spatial and directional correlation. Pockmark spacing is also identical to the spacing between the internal faults, especially towards the MTD toe.

5.3.2.3. Pockmarks surrounding MTD3

The area surrounding MTD3 shows a low number of pockmarks (fig. 5.26a and 5.28). These non-MTD pockmarks are grouped together in two distinct control types. Pockmarks aligned along the border of the salt ridge have a clear control by the structure. Other seafloor pockmarks grouped within arcuate alignments are controlled by the architecture of the adjacent canyon system. These are organised along markedly curvilinear shapes found in the vicinities of the active channel conduit (figs. 5.28 and 5.1). Furthermore, the canyon-controlled pockmark arrays have a south-facing concavity while the MTD curved alignments are less marked north-facing concavities. PFF-influenced pockmarks are also present in the area, but these occur at distances of at least 5000m eastwards of MTD3 (fig. 5.28a). Remarkably, the area where pockmarks are absent does not show any evident subsurface discontinuities that could promote the generation of fluid migration pathways, i.e. it does not show disturbance by MTDs, channel-related elements or PFFs (fig. 5.28b)

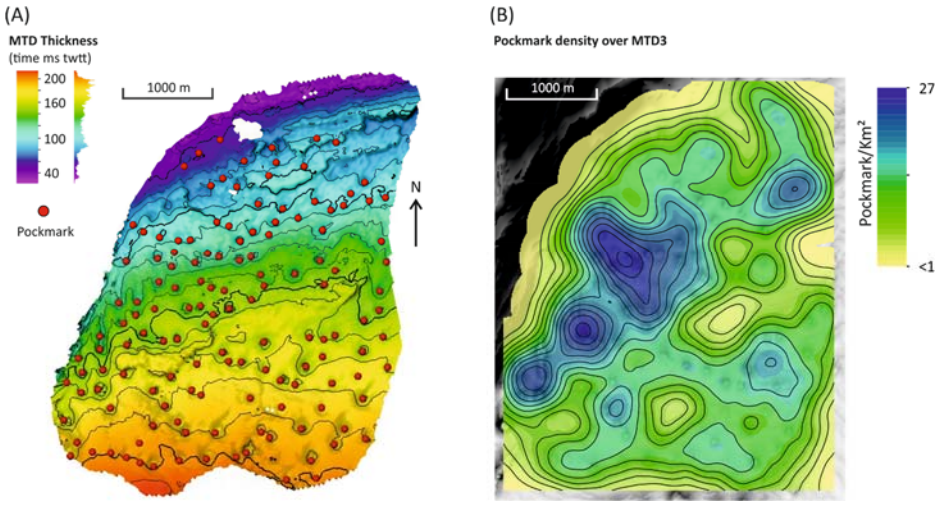

Figure 5.25. (A) Thickness map of MTD3, showing a gradual increase towards the toe domain. **(B)** Pockmark density over MTD3. The highest densities are observed towards the western flank of the deposit in areas adjacent to the salt ridge.

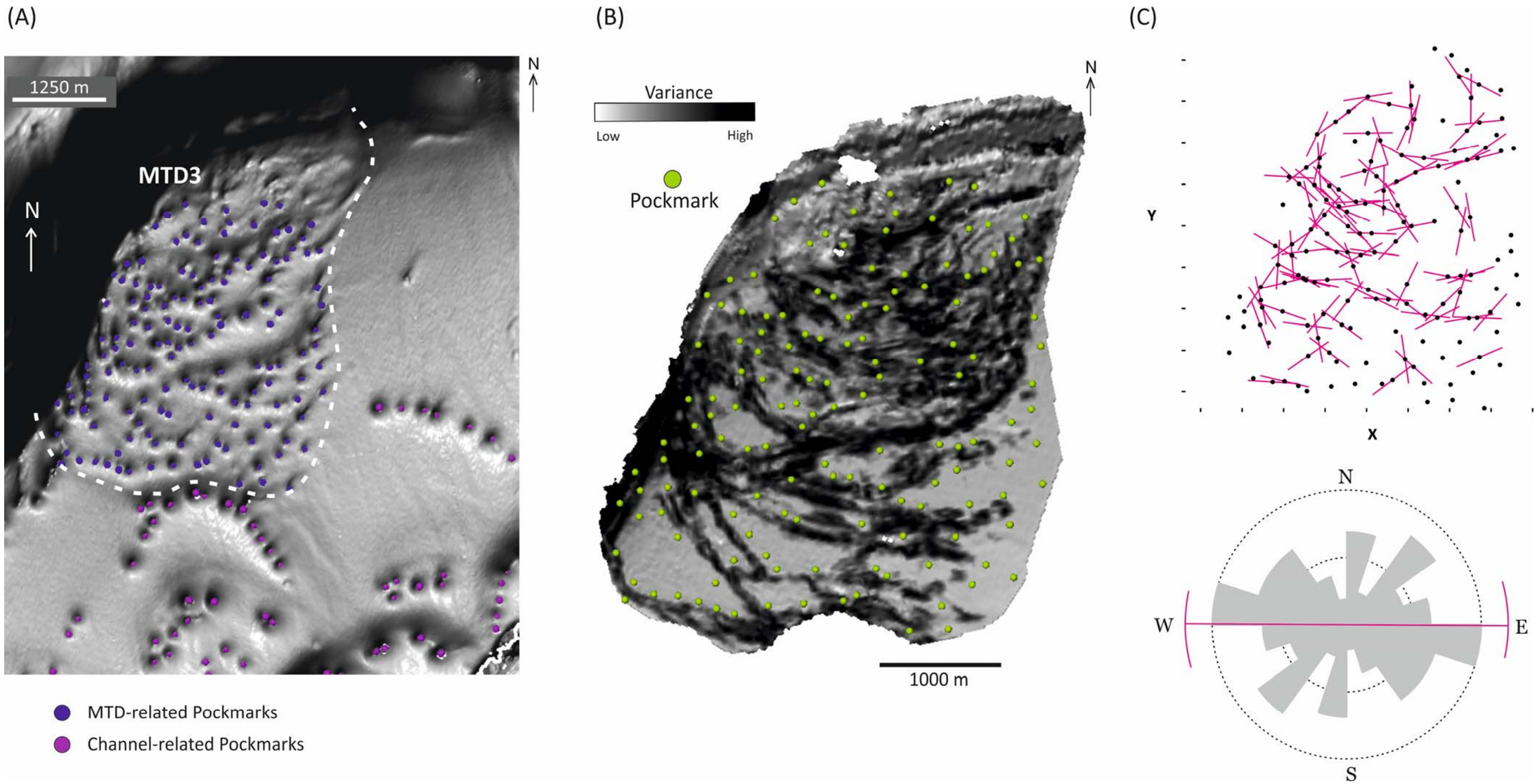

Figure 5.26. (A) Seafloor dip-map of the area around MTD3. Blue dots represent the numerous pockmarks overlying the MTD, whereas purple dots represent the pockmarks associated with the geometry of the nearby channel system. Pockmarks are mostly absent elsewhere in the figure. **(B)** Variance slice parallel to the basal surface of MTD3. Wide fault-bounded blocks are frequenct in the toe domain, separated by low variance E-W faults. E-W faults and discontinuities are also discernible within the headwall and transitional domains. The seabed pockmarks (green dots) have close proximity to the intra-MTD faults. **(C)** Pockmark alignment diagram and corresponding rose plot. Two main trends are observed: an E-W one, sub-parallel to the MTD discontinuities, and an NNE-SSW parallel to the movement direction. The E-W alignments are interpreted to be influenced by the internal faults. The NNE-SSW ones are interpreted to result from the control of the structure along the western flank of MTD3, and possible intra-MTD interfaces related with downslope movement.

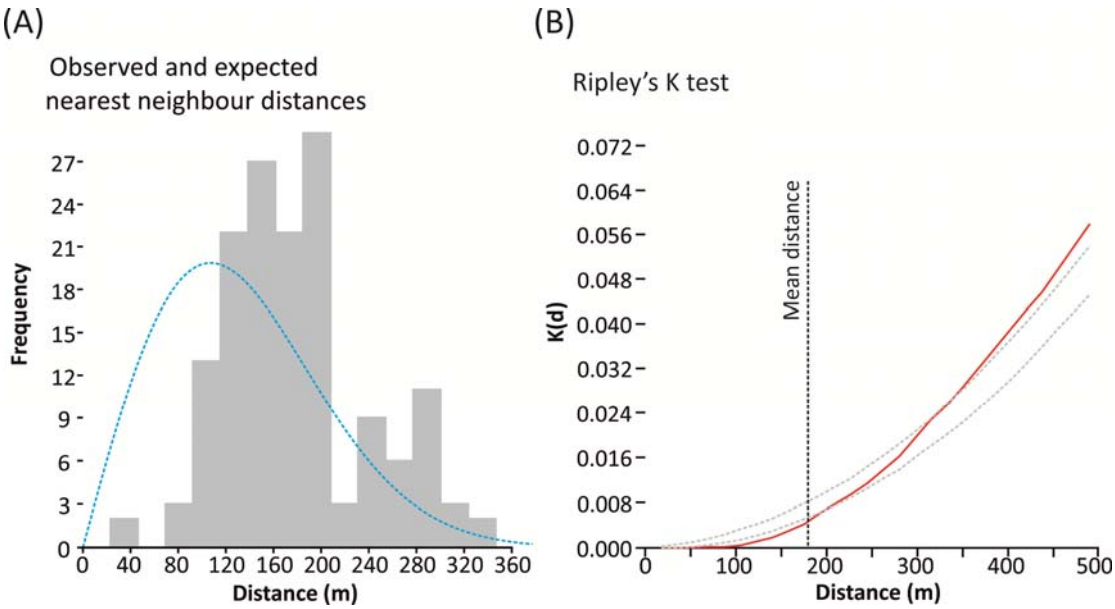

Figure 5.27. **(A)** Average nearest neighbour histogram for pockmarks over MTD3 showing the higher frequencies for distances between 120m and 220m. Blue line = expected nearest neighbour distances. **(B)** Ripley's K test diagram indicating a tendency for dispersed patterns for distances below 200m, within which the majority of pockmarks occur. Randomised distribution patterns are expected for distances between 200m and 350m. Red line = observed spatial pattern (K(d); dashed grey lines = confidence interval limits.

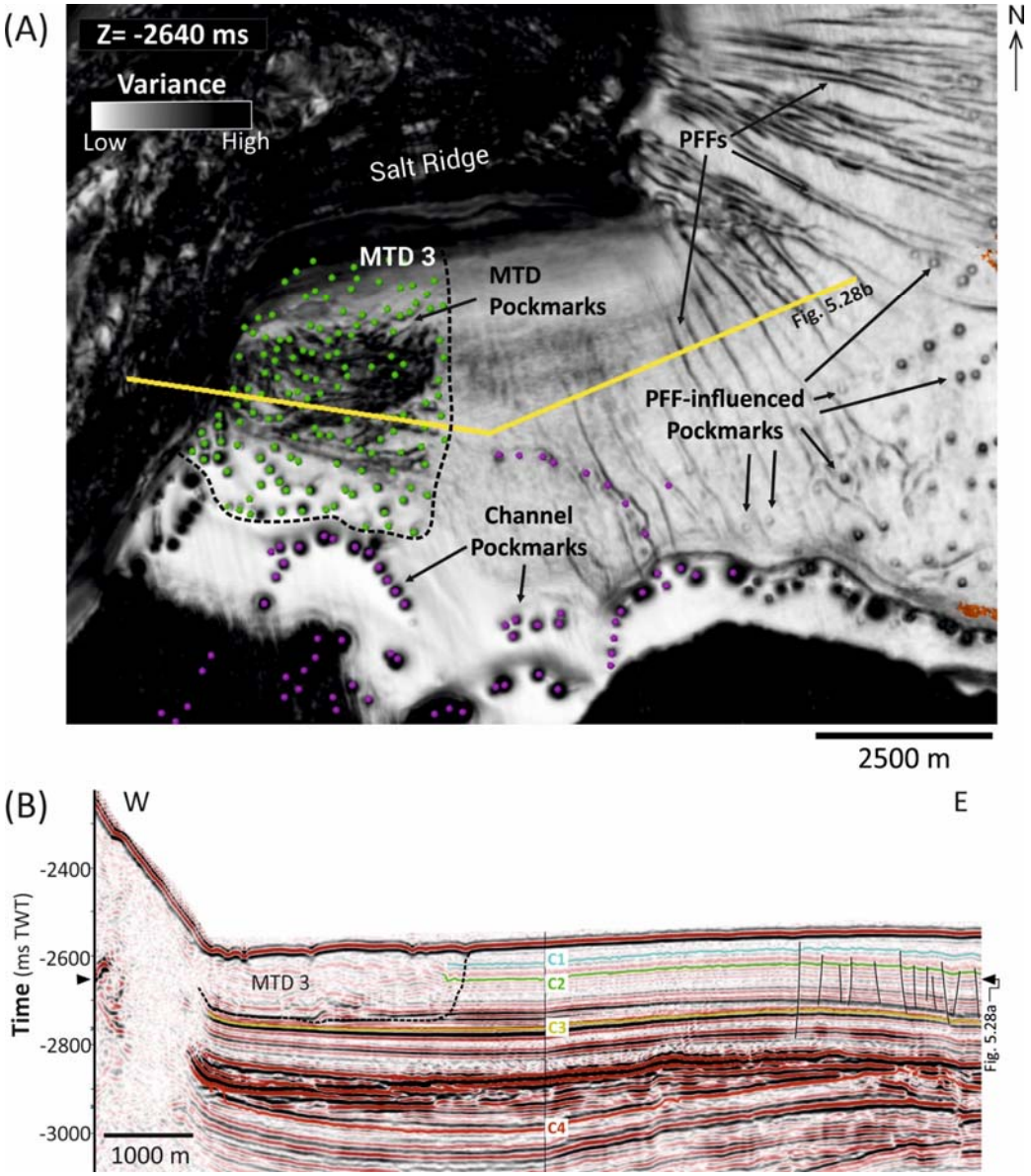

Figure 5.28. (A) Variance slice at -2640ms intersecting various features nearby MTD3. Of relevance is the absence of faults and pockmarks in the immediate 2km east of the deposit. PFFs start to be prevalent from this distance, influencing the presence of pockmarks, as described in Chapter 4. **(B)** Seismic profile intersecting MTD3 and the surrounding stratigraphy. PFFs occur towards the east, predominantly tier-bound between horizons **C2** and **C3**. (Seismic courtesy of PGS.)

5.3.3. Bottom-simulating reflectors

Bottom-simulating reflectors (BSRs) are observed in the salt anticline flanks (fig. 5.29). The BSRs are represented as semi-continuous reflections of negative polarity and moderate to strong amplitude that crosscut the shallow stratigraphy. They occur at similar depths to the estimated source interval **x-**

C2 (fig. 5.3) (see Chapter 4), suggesting a possible connection with the base of the gas hydrate stability zone (GHSZ), as previously described for deepwater settings offshore West Africa (Cunningham and Lindholm, 2000; Gay et al., 2006b; Serié et al., 2016). The strength of these reflections decreases laterally, and they are not observed within salt withdrawal mini-basins where bedding is conformable to seabed morphology. The development of a gas hydrate-related BSR would imply a sufficient methane flux was present at least locally in the study area.

BSRs were identified underlying MTDs 2a and 3, but not MTD1. The BSR underneath MTD2a is identified by a stratigraphy-crossing linear feature identifiable by a marked amplitude contrast in Unit 2 strata, but no uniform reflection is created (fig 5.29a). This feature systematically terminates against the MTD2a base surface and is not observed in the remobilized strata. The elongated BSR shows a relatively uniform width of 1500m and is parallel to the salt ridge (fig. 5.29b). It underlies the full length of MTD2a, but only within the intermediate domains. The spatial coincidence between the BSR and MTD2a indicates that gas may have played a role in triggering the mass failure.

The BSR underlying MTD3 is a wedge-shaped package of high-amplitude reflections, expressed by a strong stratigraphy-crossing reflection perpendicular to the salt ridge (fig. 5.29c and 5.29d). The BSR is over 150 ms TWT below MTD3, so a direct relationship between both features is unlikely. However, as the presence of the BSR indicates the presence of gas in the area, there is also the possibility of fluids contributing to the shallow slope failure.

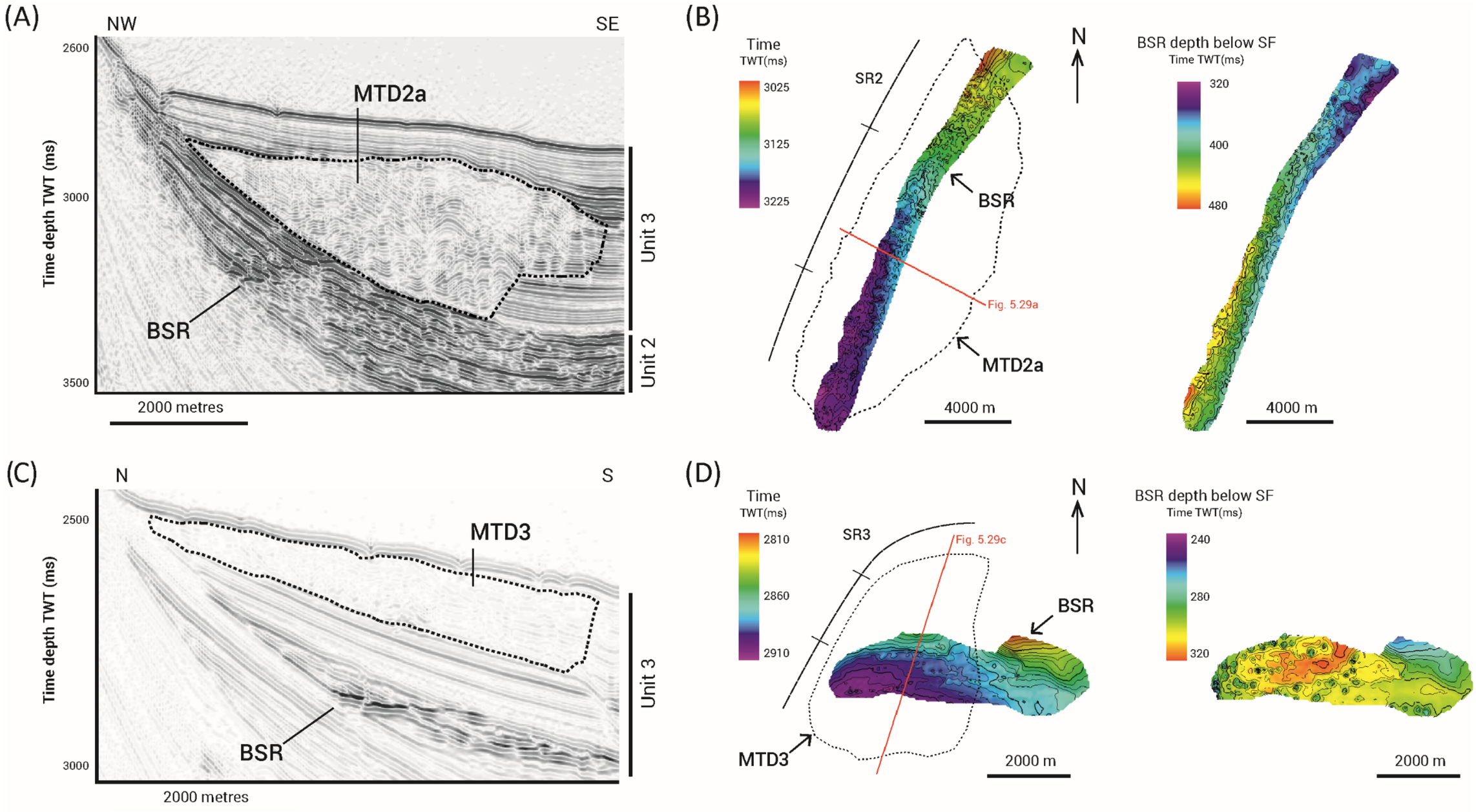

Figure 5.29. (A) Seismic profile showing the interpreted BSR underlying the upslope domains of MTD2. This BSR dips westward towards the salt ridge, cross-cutting the high-amplitude strata of Unit 2. **(B)** Total time map (left) and time interval below the seafloor (right) of the BSR associated with MTD 2. Both maps show a tendency for a SW increase of BSR depth. **(C)** Seismic profile showing MTD3 and the underlying BSR. These two elements do not intersect at any point. This BSR developed in high-amplitude strata of Unit 3 associated with the nearby channel system. **(D**) Total depth map (left) and depth below the seafloor (right) of the BSR associated with MTD3. The time map shows a relatively flat BSR with only a 20 ms TWT increase in depth southwestwards. (Seismic courtesy of PGS.)

5.4. Discussion - Fluid storage and leakage within MTDs

5.4.1. Source of fluids

The West African margin is rich in fluid-accumulation units distributed within the Cenozoic interval (Danforth et al., 1997; Emery et al., 1975; Fort and Brun, 2005). Of these, Miocene sand-prone turbidite channels of the Malembo formation (Fig. 5.3) are particularly important as they store gas and constitute main reservoirs on the margin (Abreu et al., 2003; Anderson et al., 2000; Gay et al., 2006). Leakage from these turbiditic units feeds seabed pockmarks offshore Angola (Andresen and Huuse, 2011; Gay et al., 2006; Ho et al., 2012). In the study area, these correspond to the high amplitude strata of Unit 2 where the presence of strata-crossing BSRs indicate the presence of free gas in these sediments. To constrain the location of the source of fluids expelled during pockmark formation, it is crucial to identify any related fluid-flow indicators and the basal structure of their feeding pipes (Berndt, 2005; Maia et al., 2016; Moss and Cartwright, 2010). It is interpreted here that the base of stacked amplitude anomalies marks the horizon from which pipes emanate (see Chapter 4). Based on this criteria, the analysis of amplitude anomalies and feeding pipes associated to pockmarks elsewhere in mini-basins MB6 and MB7 allowed the identification of a shallow fluid source interval as an up to 25m-thick package within Unit 3 (interval **x-C2** in Figs. 5.3, 5.5b and 5.9b) (Maia et al., 2016; Chapter 4).

The MTDs analysed in this chapter variably interact with the estimated fluid sources in Units 2 and 3. A common aspect is that all the deposits

analysed intersect interval **C2**, incorporating it in the sediments remobilized during slope failure (figs. 5.5, 5.9 and 5.12). This led to folding, and extensional and compressional faulting of **C2** during the MTD movement. Evidence that fluids emanate from within the MTD is shown by the bases of pipes located within sediments of MTD2. Pipes in mini-basin MB6 occurring in strata close to, but not affected by, MTD2 are clearly rooted in **C2** (fig. 5.9). The mass deformation limits the recognition of the exact strata level from which these pipes rise from. However, tracing interval **C2** within the remobilised mass shows a vertical proximity between its location and the base of the pipes rising from MTD2. In addition, the pipes are close to intra-MTD faults that offset interval **C2** (fig. 5.9a). This same process is replicated for MTDs 1 and 3, which show the faulted and folded remnants of interval **C2** within their deposits (fig. 5.5 and 5.12). However, a clear presence of pipes is absent from these examples. This is likely due to the lack of a thick and continuous hemipelagic drape section like the one covering MTD2.

Fluid inputs from the turbidite-rich Unit 2 cannot be discarded as MTDs 1 and 2 have their basal detachment interval at the stratigraphic interface between it and Units 3. The mechanical contrast between the strata in both stratigraphic intervals could itself be a precursor to induce slope failure (Bünz et al., 2005; Hampton et al., 1996), especially when on the flank of a salt ridge. In addition, the BSR underlying part of MTD2 (figs. 5.29a and 5.29b) indicates the presence of free gas in Unit 2, a common observation on the Angola margin (Gay et al., 2006). Gas in this unit thus tends to migrate updip along the tilted turbidite strata at the flanks of the ridges. Gas build-up is often a relevant factor in slope instability (Berndt et al., 2012; Hampton et al., 1996;

Masson et al., 2006) and could have contributed to the triggering of the MTDs. This is relevant for MTD2, which is underlain by a BSR along its full width (fig. 5.29b). However, the same is not true for MTD3. Despite being underlain by a BSR in sand-prone sediments in Unit 3, there is no clear indication of visible fluid escape features to clearly establish a link between the underlying gas and MTD3 (fig. 5.29c). Gas migrating from Unit 2 probably played a more influential role on the development of pockmarks along the headwall or sidewall limits of MTDs adjacent to the salt ridges (figs. 5.6, 5.7b, 5.8, 5.17a). In such cases, gas may have migrated up flank along the basal interface of MTDs. Intra-MTD thrusts clearly intersecting the top levels of Unit 2 are observed near the base of MTD1 (fig. 5.5). This situation may favour the entrainment and escape of gas or other fluids derived from Unit 2 along the faults and discontinuities created by the mass-movements. This may raise the question if pockmarks in MB5 are created by gas migrating from areas where Unit 2 was only disturbed by MTD1, with interval **C2** being too shallow to either generate gas or sufficient overpressure to trigger expulsion.

In summary, it is considered that the source of the fluids involved in the majority of MTD-related pockmark formation was most likely from within Unit 3, especially in cases where they occur in higher densities. Additional fluids may have been supplied from Unit 2, with higher relevance towards distal domains. The stacked amplitude anomaly patterns of the feeding pipes mean the fluids migrating through these conduits most probably included free gas, which is consistent with standard models for pockmark formation (Cathles et al., 2010; Hovland and Judd, 1988b). The bottom-simulating reflectors that are observed underlying MTD2a suggest a possible connection

to the present day gas hydrate stability zone (GHSZ). As such, it is possible that pockmark formation may be linked to gas hydrate dissociation and/or expulsion of free gas beneath the GHSZ (Sultan et al., 2010). However, it may also be the case that gas came out of solution from pore fluids (exsolution), and water is in fact the main driving fluid to form pockmarks.

5.4.2. Controls on pockmark distributions

5.4.2.1. Pockmarks overlying MTDs

Pockmarks are distributed throughout all MTD domains, overlying extensional and compressional internal discontinuities (figs. 5.5, 5.9, 5.11, 5.14). These observations show the importance of MTDs on the local disturbance of gas-rich units and how their heterogeneities control the immediate fluid expulsion paths.

The distribution of the pockmarks above MTD1 correlate with its internal heterogeneities, showing alignments parallel to, and overlying, its internal faults (figs. 5.6 and 5.14b). These predominate on the upslope domain, possibly due to internal extension that facilitated fluid ascension. Pockmarks are absent towards the front of the MTD1. Strikingly, the pockmark-free area overlies the area where internal strata disaggregation is lower and the basal surface detaches along the interface between Units 2 and 3. Contrasting with the remaining mini-basins, very scarce pockmarks are observed outside the MTD1 area (fig. 5.4b) and the shallow strata is not deformed by polygonal fault tiers (fig. 5.5a), strengthening the premise of pockmark-related fluid expulsion being controlled by the MTD.

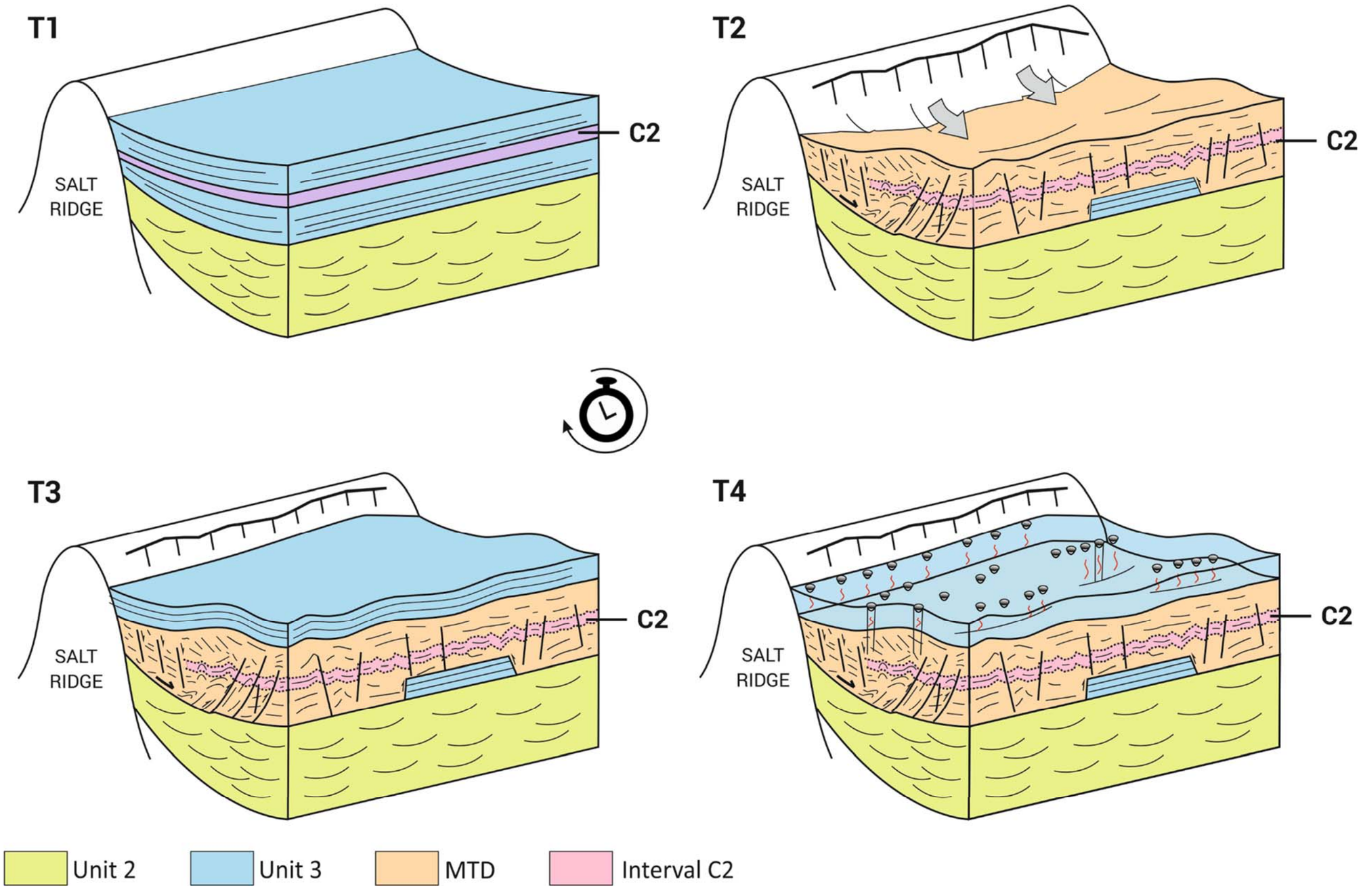

Figure 5.30. Schematic diagram of the relationship between MTDs flanking salt ridges and fluid expulsion. T1- deposition of Unit 2 and Unit 3 sediment. **C2** corresponds to the fluid source interval in the examples studied. T2- instability along the salt ridge and triggering of slope collapse. Sedimentary units become locally deformed by internal faults, also deforming the fluid source interval. T3- hemipelagic sediment draping over the MTD. The thickness of this cover can be variable and influenced by erosion and sedimentation rates. T4- fluid expulsion event releasing the fluids trapped, or generated, within the disturbed fluid source interval. The fluid escape pathways are influenced by the internal MTD faults and discontinuities created during downslope movement.

Pockmarks are distributed throughout all MTD2a domains along extensional and compressional discontinuities (figs. 5.9, 5.10, 5.14a, 5.22). The linear arrangement of the pockmarks coincides with underlying discontinuities within the MTD2a material, revealing that collapse-induced extensional and compressional faults and fractures control the distribution of intra-MTD fluid migration pathways (fig. 5.10, 5.14, 5.19). The orientation analysis of MTD2a faults and pockmark alignments also supports this interpretation as both features show predominant NE-SW orientations (fig. 5.19). Pockmark density is relatively lower within the toe domain (fig. 5.17b), possibly due to the strata thickening and predominance of thrusts and compressive stresses that may limit genesis of fluid escape paths (fig. 5.9, 5.22a and 5.22c). However, the presence of pockmarks in these compressional areas is evidence that such pathways are not completely sealed. Internal compression is possibly less intense towards the top of MTD2a where interval **C2** is estimated to be present, thus mitigating but not impeding the escape of fluids from this source level.

The distribution of pockmarks overlying MTD2b is marked by different alignment organisation when compared to MTD2a (figs. 5.10, 5.17, 5.19). The pockmark density patterns are more uniform in MTD2b (fig. 5.17) and its alignment orientations are more uniform, with a broad range of orientations (fig. 5.20). This is due to the distinct internal organization of MTD2b, where the chaotic reflection patterns and amplitude variations are associated with markedly irregular top and base morphologies created by thickened blocks and ridges with limited lateral extent (fig 5.23). Thus, the higher frequency of NW-SE oriented alignments observed in MTD2b (sub-parallel to the direction of

the mass movement) is interpreted to relate to lateral gaps between these blocks and ridges (fig. 5.19 and 5.23). The thinner accumulations in gaps between them may be the expression of boundaries between MTD compartments with different downslope movement rates and lateral spreading (e.g. Gamboa and Alves, 2016). The heterogeneities of MTD2b suggest that fluid migration paths through this deposit tend to develop along thinned accumulations of sediment possibly related to sediment either less compacted or with higher disaggregation, especially when close to internal discontinuities and faults (fig. 5.23).

Similarly, the distribution of the pockmarks overlying MTD3 is strongly controlled by its internal discontinuities. Pockmarks are scarcer immediately near the headwall (figs. 5.11, 5.13 and 5.26). The translational domain shows the higher number of occurrences, where other less organized pockmarks occur besides the linear distribution pattern. Contrasting with MTD1, numerous pockmarks on the toe domain of MTD3 are organized along arcuate lineaments pointing south-southeastwards (fig. 5.26). This organization is linked to the pressure ridges created during the divergent frontal flow of MTD3. A relevant aspect to consider is that, despite the well-evidenced control of the general E-W MTD faults, the automatic detection of pockmark alignments shows a relatively broader spectrum of orientations (fig. 5.26c). This is due to the arcuate shape of the internal features, characteristic of mass-flows, and the limitations of the mathematical method. As the algorithm detection uses straight lines between points, this produces additional small alignments with shifting orientations to fit the curved shape. Similarly to

MTD2a, the pockmark distribution and internal faults of MTD3 show a close spatial and directional relationship.

Overlapping pockmark locations with amplitude and variance maps of the MTDs indicates a relationship between all these features (figs. 5.10, 5.14 and 5.19). As high amplitudes are commonly associated with the presence of fluid escape features such as pipes and these are very abundant in the study area, it is interpreted that the high amplitudes along the MTD faults and discontinuities are related to fluids. This gains relevance as the high-amplitude features directly underlie pockmark alignments (fig. 5.14). These observations imply that MTD internal discontinuities control the position of pipes and pockmarks. However, it is difficult to ascertain whether or not these discontinuities act as conduits themselves, as there is no seismic evidence that indicate that pipes rise from the upper tips of MTD faults. It may be the case that the leak-off point develops where the fluid source interval within the MTD is intersected by its internal discontinuities (as observed elsewhere in the study area; Chapter 4; Maia et al., 2016).

Pockmark densities associated to the MTDs described here vary quite significantly in the three distinct mini-basins, decreasing from 10.49 pockmarks/km2 (MTD3) to 0.99 pockmarks/km2 (MTD1) towards the distal parts of the slope. It is argued that this variation may result of different sedimentation rates in different confined mini-basins. In the Lower Congo Basin, sedimentation rates decrease with distance to shore (ODP Leg 175; Pufahl et al., 1998). Proximity to upslope source of sediments (terrigenous input) and organic matter promotes higher porosities (due to coarser-sized sediments), higher generation of biogenic gas, and overpressure build-up due

to a thicker overburden. This is especially pertinent in the case of MTD3, which is located nearby a submarine channel system (Channel 1) that causes a marked thickening of Unit 3 in the southern areas of MB7 (figs. 5.10 and 5.11).

5.4.2.2. Pockmarks outside MTD areas

A relevant point of discussion is the local effect of MTDs on pockmark distributions comparatively to the surrounding basin areas, with stark contrasts between such patterns having been demonstrated in this work. The most evident example occurs in mini-basin MB6, where MTD2 occurs (figs. 5.7 and 5.23). The analysis undertaken shows intra-MTD2 faults and overlying pockmarks to follow NE-SW alignments, with scarce frequencies of other orientations (fig. 5.24a). In contrast, polarised polygonal faults (PFFs) in mini-basin MB6 follow WNW-ESE orientations, with minor sub-perpendicular ones linking the large segments (fig 5.24b). As demonstrated in Chapter 4 and shown in figure 5.24d, PFFs exert a key control on the distribution of WNW-ESE pockmark alignments. Other predominant NE-SW pockmark alignments in MB6 are observed but lack a very clear fault control like the ones described above. These are suggested to be influenced by the proximity to salt ridge SRC towards the eastern flank of MB6, and by a local distress and topographic effect of MTD2 in surrounding strata.

Statistical analysis also demonstrate these contrasts. Pockmark distributions in areas outside MTD2 show statistically significant clustering, whereas within MTD2 they show a statistically significant overdispersion. The

latter is associated with serial clustering and heterogeneous distributions, occurring when the observed variance is larger than the one predicted for Poisson distributions as a result of a non-constant probability within the analysed cells (Bolker, 2008; Crawley, 2012). In geological terms it can be interpreted as a less predictable distribution pattern of MTD-related pockmarks. This can be associated with the deformation heterogeneities developed by downslope movement which are rarely uniform due to variable composition, thickness or even remobilisation distance of MTDs or their internal elements. In contrast, pockmark distributions along basin faults are probabilistically more predictable as they are controlled by larger-scale processes. These are here expressed by structure-controlled pockmark alignments close to salt ridges or the evenly-spaced PFFs in the mini-basins (fig. 5.24).

This comparison is simpler for MTD1 and MTD3. The area of MB1 surrounding MTD 1 is completely void of pockmarks (fig. 5.7). The closer occurrences are over 3000m away, near salt ridge SRB. This suggests that the presence of MTD1 is a predominant factor for the development of pockmarks in the distal area. The area of mini-basin MB7 near MTD3 has more varied controls on pockmark genesis and distributions (fig. 5.28). The higher numbers and proximity are unmistakably over the MTD3. The closer ones outside it are due to seepage along stratigraphic discontinuities created by paleo-meanders of the nearby Channel 1, a phenomena that has been previously observed on this margin (Gay et al., 2007). Further east, pockmarks start to be more frequent where PFFs develop (fig. 5.28a). The lack of pockmarks and faults immediately east of MTD3 suggests that, if it wouldn't

have formed, there would be no pockmark formation on the location occupied by the deposit. Instead, the slope failure created significant disturbances within a limited region that induced pockmark distributions completely distinct to the ones in the nearby basin.

The analysis undertaken in this thesis show the importance on deep-water MTDs on the local re-arrangement of the fluid drainage network at a mini-basin (or larger margin) scale. Not only such deposits and intrinsic deformation structures can modify flow paths of fluid migrating from the deep subsurface (Riboulot et al., 2013), they induce important disruption on otherwise undisturbed (i.e., not affected by PPFs) storage levels like the one here represented by **C2** (figs. 5.5, 5.9, and 5.12). This disruption leads to newly formed faults able to influence fluid leakage when pressure conditions exceed the seal retaining capacity.

5.4.3. Timing of fluid expulsion relative to MTD event

Despite all MTDs described in the study area having a marked seabed expression, they are fully or partially buried underneath a sediment cover of variable thickness. Pockmarks associated to these MTDs occur at the seabed, above the hemipelagic drape over MTD2 or the sediment over MTDs 1 and 3 (figs. 5.5, 5.9, 5.12 and 5.30).

Although is it possible that sediment remobilization would promote pore fluids within the pre-mass movement material to be expelled at the seabed, there are no seismically observable evidences of fluid expulsion

synchronous to MTD events. If there was no visible cover above the MTDs or if fluid escape features (pockmarks) occurred directly above these deposits (at the base of the hemipelagic succession), fluid expulsion most likely would have occurred during or shortly after sediment remobilization.

However, the presence of a hemipelagic drape above MTD2 implies that the seabed fluid expulsion event (pockmark formation) occurred after sediment remobilization (MTD event) and the deposition of sediment (fig. 5.30). Assuming that all seabed pockmarks in the area most likely formed at the same time (they all occur at the same event horizon), the interval of time between seabed fluid expulsion and each MTD event can be estimated as the time it took to deposit the hemipelagic drape. As such, pockmarks formation was posterior to sediment remobilization (fig. 5.30).

It is argued that fluids and overpressure for seabed fluid expulsion were most likely generated after the mass-transport event and retained within these sediments, otherwise fluids would have been expelled synchronously to sediment remobilization. Considering the high organic content estimated to be present in Unit 3 sediments (Pufahl et al., 1998), this implies that MTD sediments have enough storage capacity (porosity) to retain fluids for a significant amount of time, until overpressure build up exceeds lithostatic pressure, or a shift in P-T conditions occurs. These results are relevant to understand the role of MTDs in fluid storage in the subsurface. Traditionally considered as sealing/baffle (Sun et al., 2017; Weimer and Shipp, 2004) or bypassing units (Riboulot et al., 2013), sandy MTDs with capacity to act as reservoirs have also been recognised (Beaubouef and Abreu, 2010; Meckel III, 2011). The examples here presented show further proof that MTDs are able to

constitute viable storage units if the right conditions, and opens new perspectives on their influence on shallow and deep subsurface plumbing systems.

5.5. Conclusions

- The analyses of amplitude anomalies and feeding pipes associated to pockmarks allows the identification of the most likely fluid source interval to be within MTD sediments (remobilized Unit 3 strata). Pockmark formation may be linked to gas hydrate dissociation and/or expulsion of free gas beneath the GHSZ, or to gas exsolution from pore fluids in the source interval.

- Fluid expulsion at the seabed (formation of pockmarks) occurred posterior to the mass-transport events, indicating fluids were stored within MTD material prior to their expulsion. Pockmarks and their feeding pipes occur directly above the internal discontinuities of the MTDs, implying an intra-MTD structural control of these heterogeneities on seabed pockmark location.

- Statistical analysis of pockmark distribution patterns overlying MTDs comparatively to surrounding areas demonstrate important local modifications of the fluid plumbing network imposed by the mass-movements. MTD-induced distributions of pockmarks are less predictable due to flow and deformation heterogeneities.

- The amount of pockmarks formed at the seabed is likely to be influenced by the proximity to the shore source of sediments and organic matter – higher

sedimentation rates in proximal basin locations promote higher amount of pockmarks.

- This case study shows evidence of storage and migration of fluids within MTDs. These results have profound implications on our current knowledge of permeability and storage capacity of MTDs, and are relevant for the understating of shallow fluid plumbing systems in offshore settings and overall fluid flow systems in hydrocarbon-rich continental margins.

Chapter 6

POCKMARKS IN MINI-BASIN MB2:
EFFECTS OF SHALLOW GRAVITATIONAL SLIDING
AND FLUID SOURCE DEPTH

6. Pockmarks in Mini-Basin MB2:

Effects of shallow gravitational sliding and fluid source depth

Abstract

In marine geological settings, pockmarks are evidence of highly focused fluid expulsion at the seabed. The modern seafloor of the Lower Congo Basin (LCB, offshore West Africa) is covered by densely packed arrays of thousands of pockmarks, whose distribution reflects in part the spatial organization of underlying seal bypass features. From the analysis of the spatial distribution of seabed pockmarks, it is possible to infer sub-surface processes that control the fluid migration routes and the overall shallow plumbing system of the basin. Several different control mechanisms (structural and/or stratigraphic) have been described to influence the position where a pockmark forms. However, these previously cited mechanisms fail to explain a set of strongly arcuate alignments that occur within a salt-withdrawal mini-basin in the Lower Congo Basin. These alignments are the subject of this case study. A new type of shallow fluid flow control is inferred, operating at a sub-seismic scale. It is suggested that the shallowest sediments of the study area have been gliding downslope, in a process of incipient low strain gravitational sliding, driven by gravitational forces. This mechanism may produce sub-seismic discontinuities that ultimately influence the spatial arrangement of seabed pockmarks. Furthermore, from the wide variability of pockmark sizes present in the area and the local geomorphology, it is possible to conclude that pockmark size is related 1) to the sub-surface depth at which the fluid source interval occurs and 2) to lateral variations of the degree of overpressure.

Keywords: pockmark distributions; spatial statistics; gravitational sliding; pockmark size-source depth scaling; shallow plumbing systems; Lower Congo Basin.

6.1. Introduction

From all the mini-basins in the study area, mini-basin MB2 exhibits the most extraordinary array of seabed pockmarks, with linear arrangements unique to this sub-area and never described before in the literature. This chapter focuses on the distribution of seabed pockmarks present in MB2 and the fluid flow controls that can be inferred by their spatial arrangement and morphological variations at seismic scale. The chapter is divided into two main sections – 6.2 and 6.3. Section 6.2 focuses on mechanisms that control the spatial distribution of pockmarks, promoting the development of arcuate alignments of seabed pockmarks. Section 6.3 analyses the morphological variability of seabed pockmarks and its relation to fluid source depth in MB2. To simplify the readability of this chapter, each section has its own separate discussion of results and interpretations. The concluding section comprises all conclusions gathered from this study.

6.1.1 Mini-basin MB2 and its shallow seismic stratigraphy

Mini-basin MB2 is located in the north of the general thesis study area. Figure 6.1 shows the time-dip map of the mini-basin seafloor surface, locations of seabed pockmarks (fig. 6.1b), and Figure 6.2 its main structural features. MB2 comprises a large-scale elongated anticline at its centre (coincident with the MB2 axis), and is delimited by two buried salt walls (BSF and BSI). These structures were the result of salt tectonic activity in the area, the main process of structural deformation in the Lower Congo Basin. The general

geomorphology and structure of MB2 is described in more detail in section 6.2.2.1. (Salt tectonic deformation).

The seismic stratigraphy of mini-basin MB2 is divided into four main seismic-stratigraphic units: 1, 2, MTD, and 3 (figs. 6.3, 6.4 and 6.5). The stratigraphic interval of interest for this study covers the shallowest seismic Unit 3 (which correlate to the succession of Pliocene-Holocene age) and the underlying MTD. Despite some variations in the sedimentation style due to different topographic confinements produced by salt tectonics, the units described above can be correlated to the seismic stratigraphy of neighbouring mini-basins, as discussed in Chapter 3. Key seismic horizons identified in mini-basins MB5, MB6 and MB7 are also observed and were mapped in MB2, including the estimated fluid source interval for seabed pockmark formation (interval **x-C2**; see Chapter 4).

Unit 1 is characterised by laterally continuous, sub-parallel to parallel reflections of very low to moderate amplitude, which is mostly associated with fine-grained deposits (fig. 6.3 and 6.4). Occasional reflections of higher amplitude may indicate deposition of coarser sediments. This unit is interpreted to comprise hemipelagic deposits intercalated with minor turbiditic lobes and sparse contourite drifts (c.f. Chapter 3). The contact with Unit 2 above is interpreted as an erosional unconformity, based on reflection termination geometries (Mitchum et al., 1977).

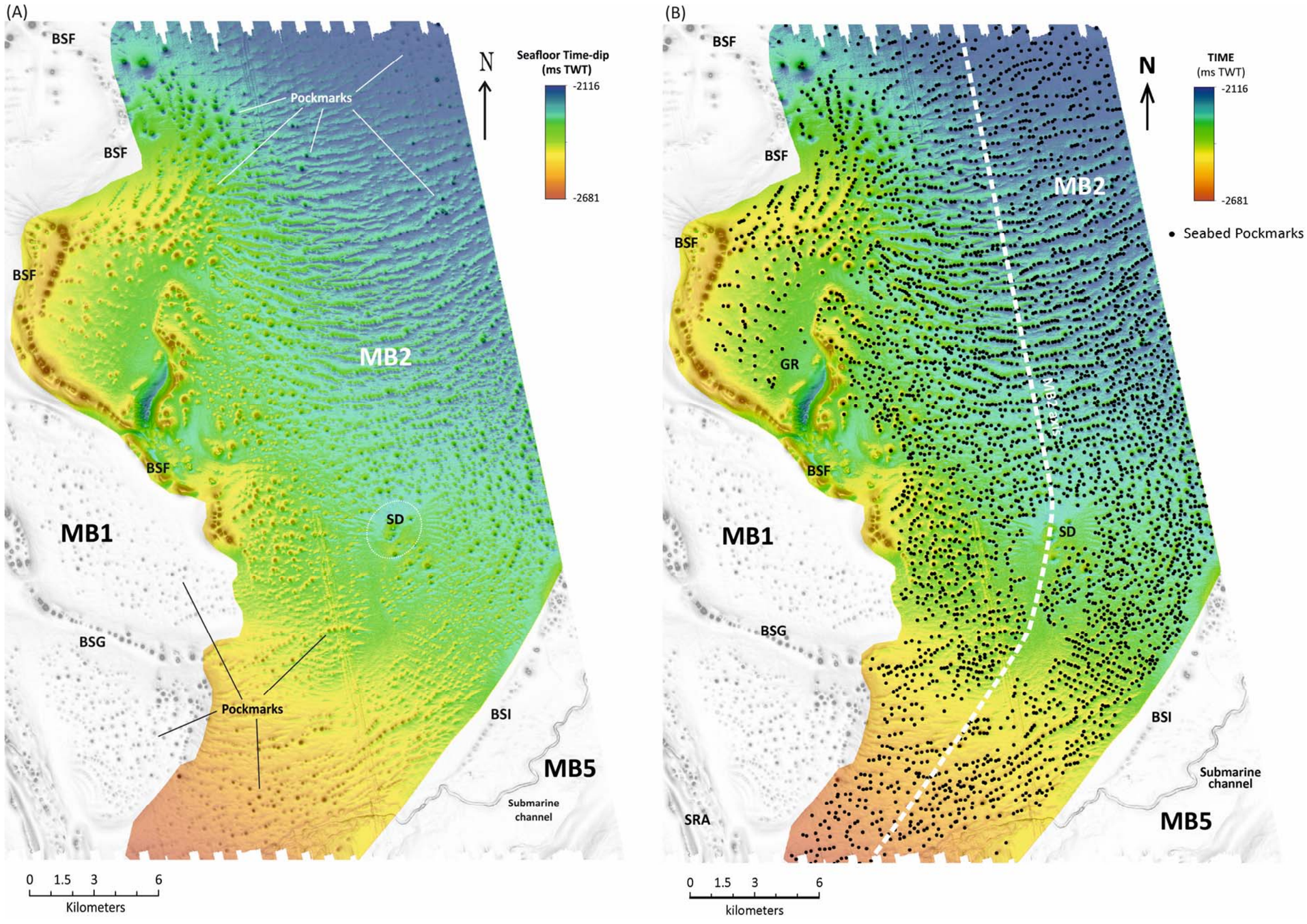

Figure 6.1. **(A)** Seafloor time-dip maps of the seafloor of mini-basin MB2. Numerous sub-circular pockmarks with variable size and distribution patterns are observed. **(B)** Seafloor map of MB2 highlighting mapped pockmarks. MB = mini-basin; SR = salt ridge; BS = buried salt structure; SD = salt diapir; GR = graben.

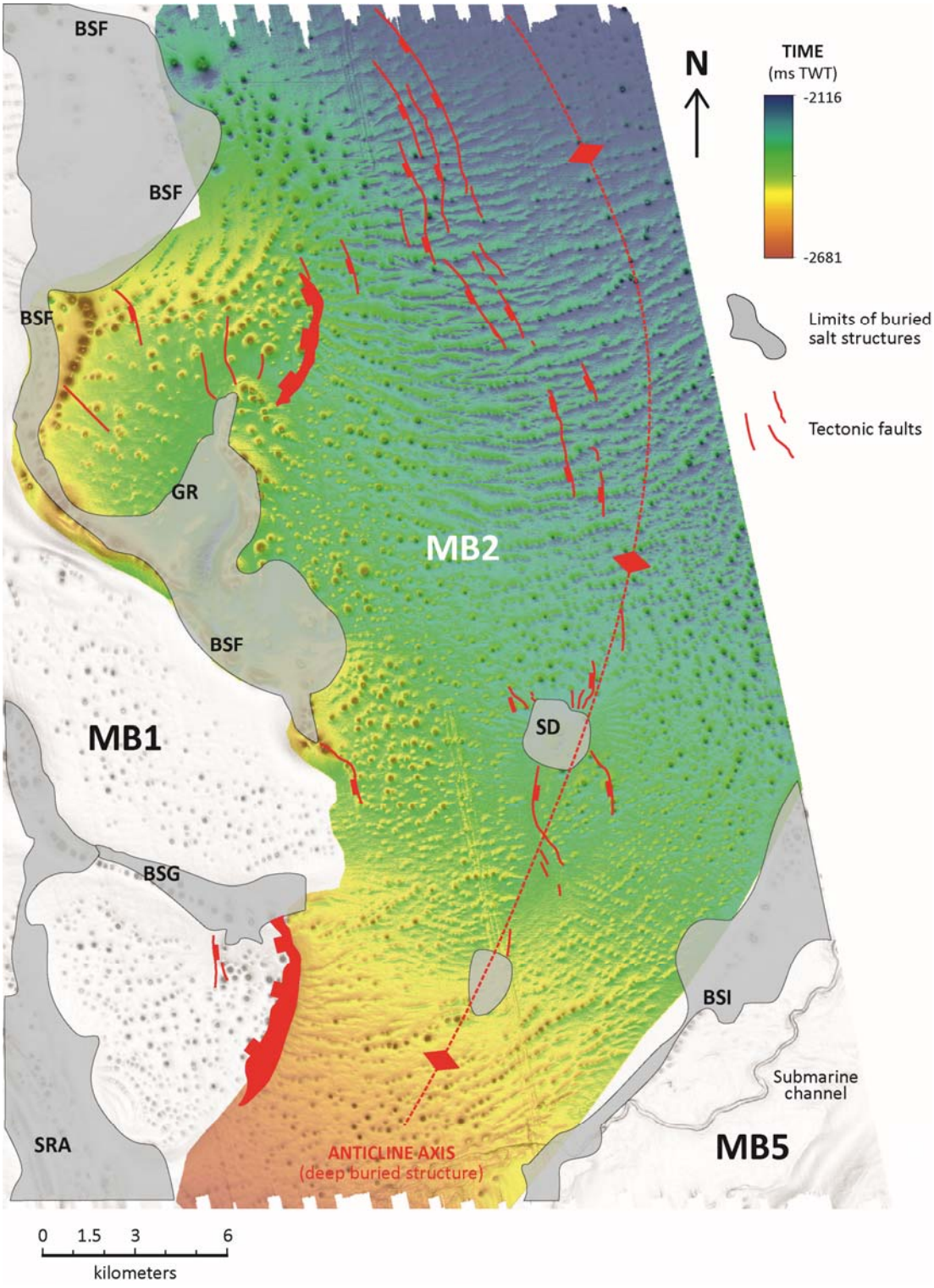

Figure 6.2. Seafloor map of MB2 highlighting interpreted tectonics features, namely the deeply buried anticline axis and larger deep-rooted faults. MB = mini-basin; SR = salt ridge; BS = buried salt structure; SD = salt diapir; GR = graben.

Unit 2 is characterised by sub-parallel to chaotic reflections of moderate to very high amplitude. It is generally thinner along the mini-basin axis, thickening towards the flanking salt structures (fig. 6.3 and 6.4). Moderate to low amplitude chaotic reflections present at the bottom of this unit are associated with mass-transport deposits which are intercalated with thin laterally continuous turbidites (moderately high amplitude reflections) (c.f. Chapter 3). The topmost succession of Unit 2 exhibits continuous high to very high amplitude reflections related to submarine channels and less confined clastic deposition, interbedded with hemipelagic intervals (fig. 6.4).

Between seismic Units 2 and 3 lies an extensive mass-transport deposit (MTD), which is not present in the mini-basins analysed in Chapters 4 and 5. The interpretation of this unit as an MTD is based on standard criteria as outlined by Frey Martinez et al. (2006) and Bull et al. (2009) (see Chapter 5). The contact with Unit 2 below is an erosional unconformity, whereas Unit 3 sediments conform to the morphology of the top surface of the MTD (fig. 6.4). The MTD unit is described in more detail in section 6.2.2.3.

Unit 3 is characterised by laterally continuous and parallel reflections of very low to moderate amplitude, representative of fine-grained hemipelagic deposition. Reflections of slightly higher amplitude in this succession may be associated with the deposition of coarser grain size material (Gay et al., 2007), possibly related to laterally continuous turbidites. Unit 3 has minimum thicknesses along the axis of MB2 and thickens towards the flanking salt structures (fig. 6.4).

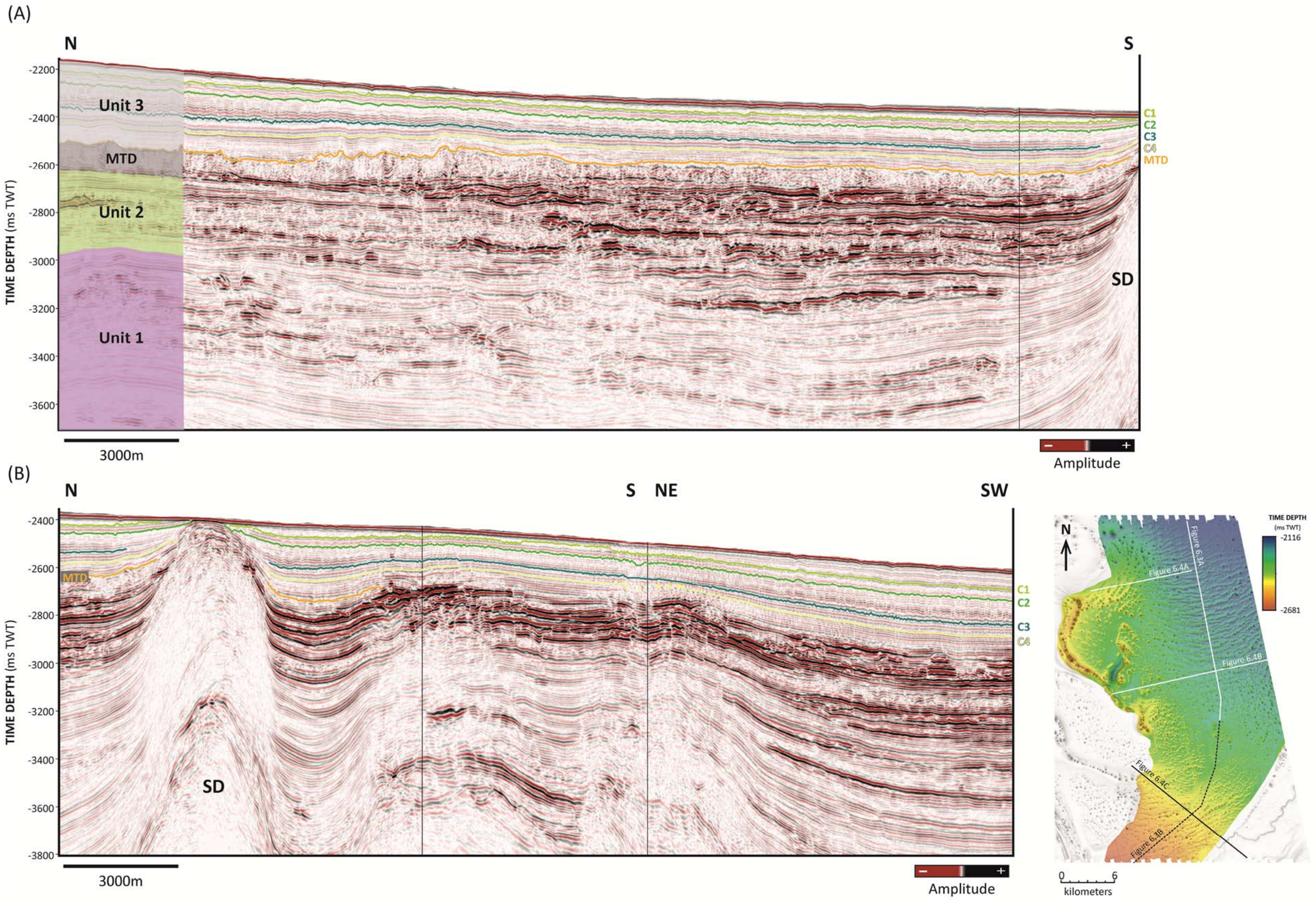

Figure 6.3. Seismic profiles along the axis of MB2 depicting the mini-basin architecture on **(A)** the northern half and **(B)** the southern half. Subsurface diapirs and salt-related deformation at the central basin areas is more significant southwards. SD = salt diapir. (Seismic courtesy of PGS.)

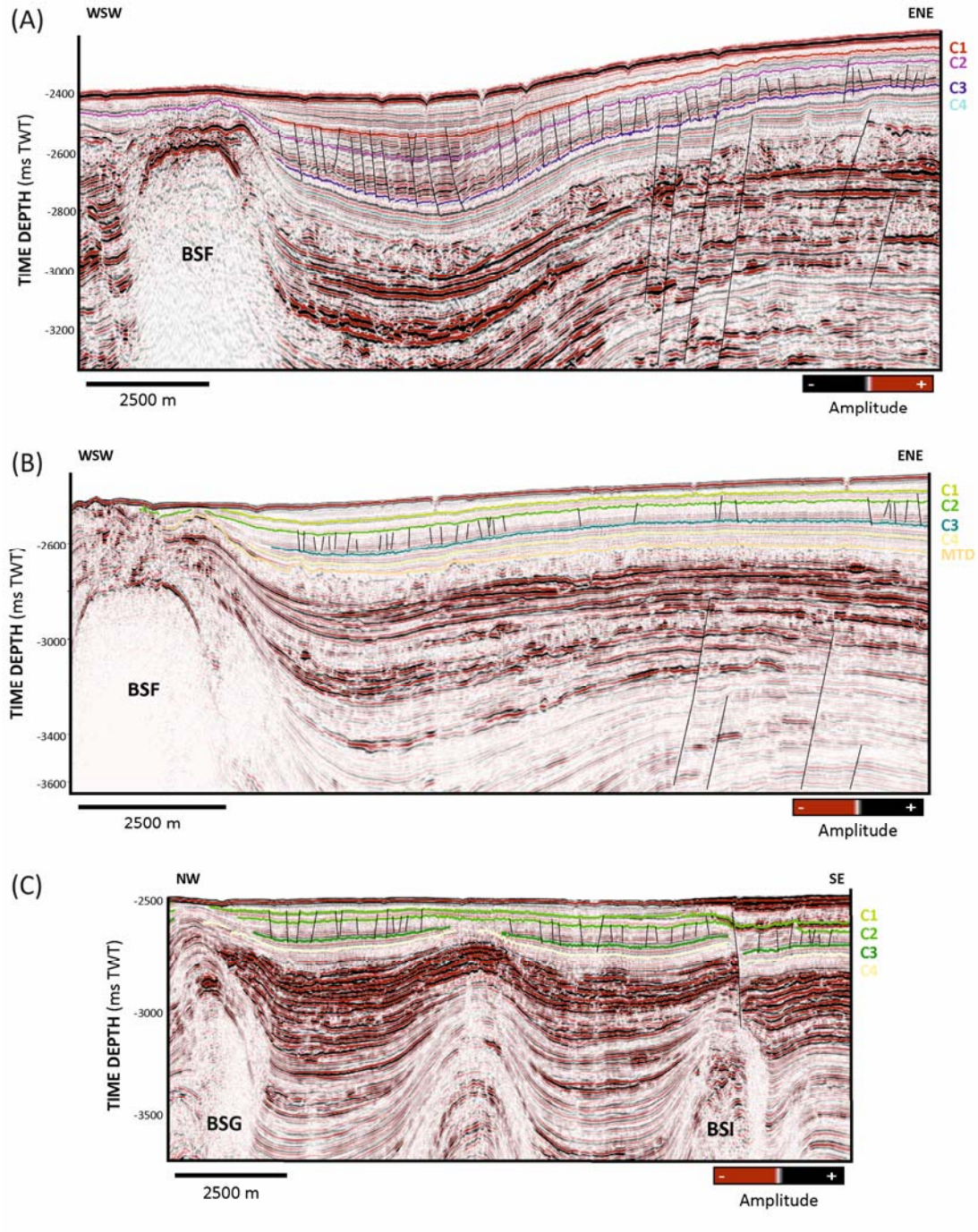

Figure 6.4. Seismic sections perpendicular to the axis of MB2. Locations shown in figure 6.5. **(A)** and **(B)** evidence the axial buried antiform and the mini-basin-bordering salt structures to the west. **(C)** Section depicting rising salt structures central to MB2 in addition to the bordering BSG and BSI. SR = salt ridge; BS = buried salt structure; SD = salt diapir; GR = graben. (Seismic courtesy of PGS.)

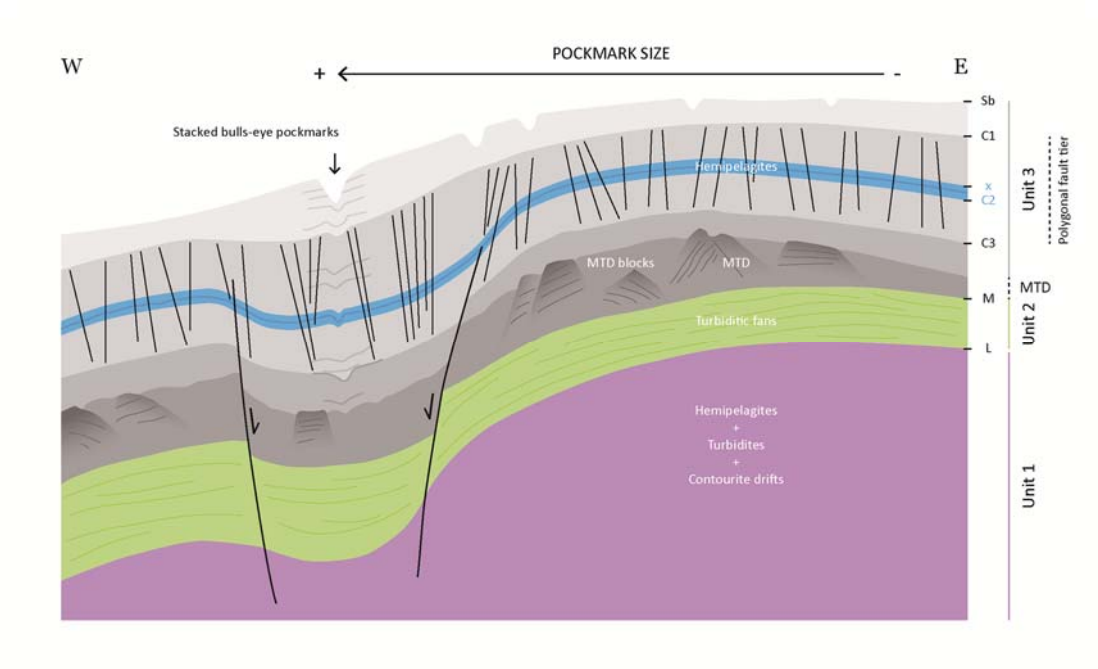

Figure 6.5. Diagram explaining the general structure and seismic stratigraphy of MB2, along a E-W section.

6.1.2. Initial considerations for pockmarks in MB2

The great majority of pockmarks present in MB2 occur at the seafloor within the mini-basin. These are shallow circular to sub-circular depressions of various sizes, created by fluid expulsion at the seafloor along with remobilisation of the shallowest unconsolidated fine-grained sediments (fig. 6.6a). Their occurrence at the present-day seafloor with no seismically observable infill indicate these were formed during a very recent fluid expulsion episode. As such, it is interpreted that MB2 seabed pockmarks were formed during the same event that led to the formation of the seabed pockmarks elsewhere in the study area (see Chapters 4 and 5). Fluid conduits below seabed pockmarks are rarely observed in this mini-basin, and do not show the same seismic character as the feeding pipes described in MB6 and MB7. The pipes identified in MB2 are typically vertical columns of low

amplitude and show disruption of seismic reflectors (fig. 6.6b). Similarly to pipes in other mini-basins, feeding conduits observed below a MB2 pockmark are stratigraphically limited to Unit 3 sediments and rooted between the interval between horizons **x** and **C2** (fig. 6.6c). As such, for the purpose of this study, it is assumed that the source of fluids involved in the generation of MB2 seabed pockmarks was most likely located stratigraphically between reflectors **x** and **C2** (see also Chapters 4 and 5).

Rare vertically-stacked paleo-pockmarks are identified within the polygonal-faulted interval of Unit 3. These stacked paleo-pockmarks are separated by intervals of drape and onlap fill, and are located at the centre of polygonal fault cells (fig. 6.6b). As such, these buried pockmarks are interpreted to be 'bulls-eye' pockmarks (Andresen and Huuse, 2011), and represent past events of fluid expulsion, predating the formation of the polygonal fault system affecting the surrounding strata. In MB2, bulls-eye pockmarks occur at the lateral margins of the mini-basin, near the limiting salt structures. Observations of MB2 bulls-eye pockmarks are similar to the ones described for MB6 (see Chapter 4), and are in agreement to the formation process, timing and source of fluids for the genesis of bulls-eye pockmarks discussed by Andresen and Huuse (2011) and Morgan et al. (2015).

Large-sized pockmarks are also observed at the seafloor above the buried salt structures present in MB2 (fig. 6.1 and 6.7). Due to the spatial association with these features, it is likely that the controls on their distribution are linked to the deformation features produced by the emplacement of the salt bodies. These deformation structures include large-scale extensional faults above and around the salt, and may promote the migration of fluids from

reservoirs within the turbiditic fans of Oligocene-Miocene age (Gay et al., 2006), or focused flow of thermogenic fluids along salt flanks (Andresen and Huuse, 2011; Gay et al., 2007). However, such a deep source of potentially thermogenic hydrocarbons is unlikely to explain seabed pockmark distributions of the type and extent present in MB2. As such, salt-related pockmarks are not considered for the spatial analysis of MB2 pockmarks.

For the present study, only the latest episode of fluid expulsion is considered, focusing on the understanding of the distribution of seabed pockmarks within mini-basin MB2. The distribution of bulls-eye pockmarks and pockmarks located above salt structures will not be addressed here.

As in previous chapters, the main limitation of this study is the seismic resolution associated to the 3D seismic survey. This is particularly pertinent when inferring the presence of a mechanism operating at a smaller scale than the one allowed by the dataset (shallow gravitational sliding described in section 6.2), or assessing the morphology of pockmarks to interpret whether they are individual pockmarks or they result from the coalescence of small-size pockmarks that fall below the resolution limit (section 6.3). All qualitative and quantitative measurements, observations and interpretation are given with full appreciation of the resolution limits of the seismic survey and potential errors of the data.

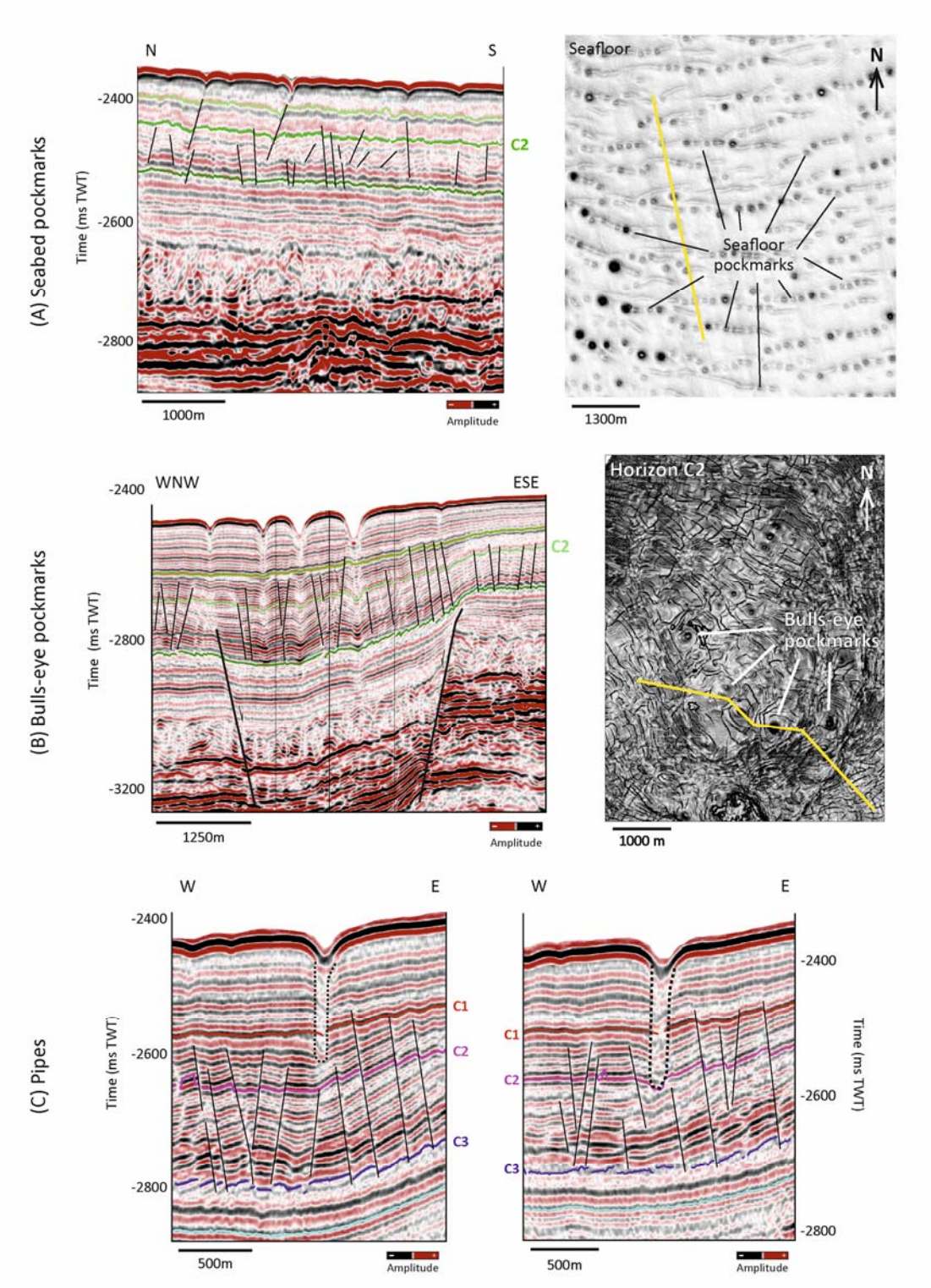

Figure 6.6. Seismic profiles and dip maps showing the character of **(A)** seafloor pockmarks, **(B)** bulls-eye pockmarks and **(C)** pipes (see main text for details). (Seismic courtesy of PGS.)

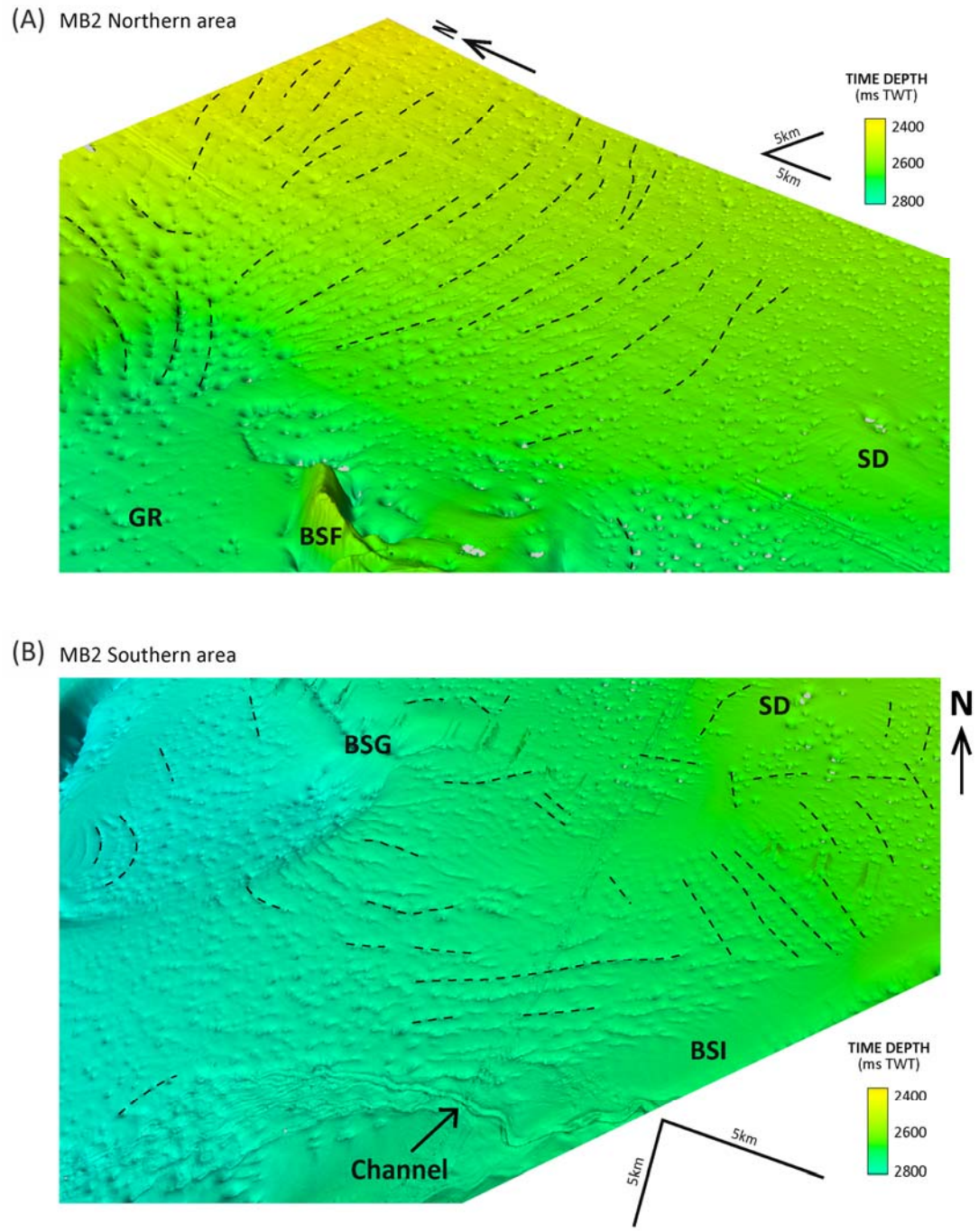

Figure 6.7. Perspective views of the **(A)** northern and **(B)** southern areas of the seabed surface of MB2. Pockmark alignments are highlighted with the dashed lines. Well organised E-W patterns are frequent to the north, but more variable to the south. Note the presence of linear alignments perpendicular to BSG towards the southeast. SR = salt ridge; BS = buried salt structure; SD = salt diapir; GR = graben.

6.2. Pockmark distributions in MB2

The spatial distribution of pockmarks can be closely linked to the presence of discontinuities at depth that influence the pathways along which fluids migrate to be expelled at the seafloor, as discussed in previous chapters of this thesis. In mini-basin MB2, seabed pockmarks are distributed in long arcuate alignments perpendicular to the general slope (fig. 6.1 and 6.7) that show no spatial association with any seismically resoluble major structure at depth (figs. 6.3 and 6.4). The main aim of this section is to derive an understanding of the mechanisms that control the spatial distribution of pockmarks in MB2, promoting the development of arcuate alignments of seabed pockmarks. Seabed pockmark distributions are analysed using spatial statistics, and compared to underlying deformation features. From the analysis of this unique spatial arrangement of pockmarks, the existence of an incipient creeping or very slow gravitational sliding process of the shallow sediments is inferred to operate at the sub-seismic scale that strongly influences the fluid plumbing system in this region of the Lower Congo Basin. This will be analysed later in the chapter.

6.2.1. Spatial distribution of seabed pockmarks in MB2

MB2 exhibits 3896 seabed pockmarks of various sizes, distributed throughout the entire mini-basin (fig. 6.1). Pockmarks in MB2 are mostly arranged in linear arrays, similarly to the pockmarks present in other mini-basins. However, the typical pattern of these alignments differs from the ones described in previous chapters. MB2 pockmark alignments are generally

curvilinear and parallel to sub-parallel to each other, crossing the entire mini-basin width along an E-W strike (forming trails up to 5.25km in length) (fig. 6.1 and 6.7). These arcuate alignments are perpendicular to the general N-S slope of MB2, and their apices (points of highest curvature at the middle of the linear trail) follow the central axis of MB2 and point downslope (southwards) (figs. 6.1 and 6.7). The curvature of the alignments increases downslope, with almost straight alignments in the northern-most area of MB2 becoming progressively more arcuate towards the south. This arcuate pattern is present the northern half of MB2, and terminates in the region where a salt diapir (SD) pierces the overburden (figs. 6.1 and 6.7).

Smaller areas located in the southern half of the mini-basin and near its westernmost flanking salt structure (BSF) show different pockmark distribution patterns. In the areas immediately surrounding the buried salt diapir SD no pockmarks occur, despite a few large-sized pockmarks located vertically above it. Alignments in the southern-most region of MB2 are generally parallel to the buried NE-SW salt wall (BSI) that limits the mini-basin in the southeast, albeit a small area where pockmark alignments are perpendicular to this structure (figs. 6.1 and 6.7). Non-linear spatial arrangements are observed in two small areas near buried salt structures BSF and BSI, and within a region of subsidence (graben GR) towards the west of MB2, where pockmarks are distributed in a more arbitrary fashion.

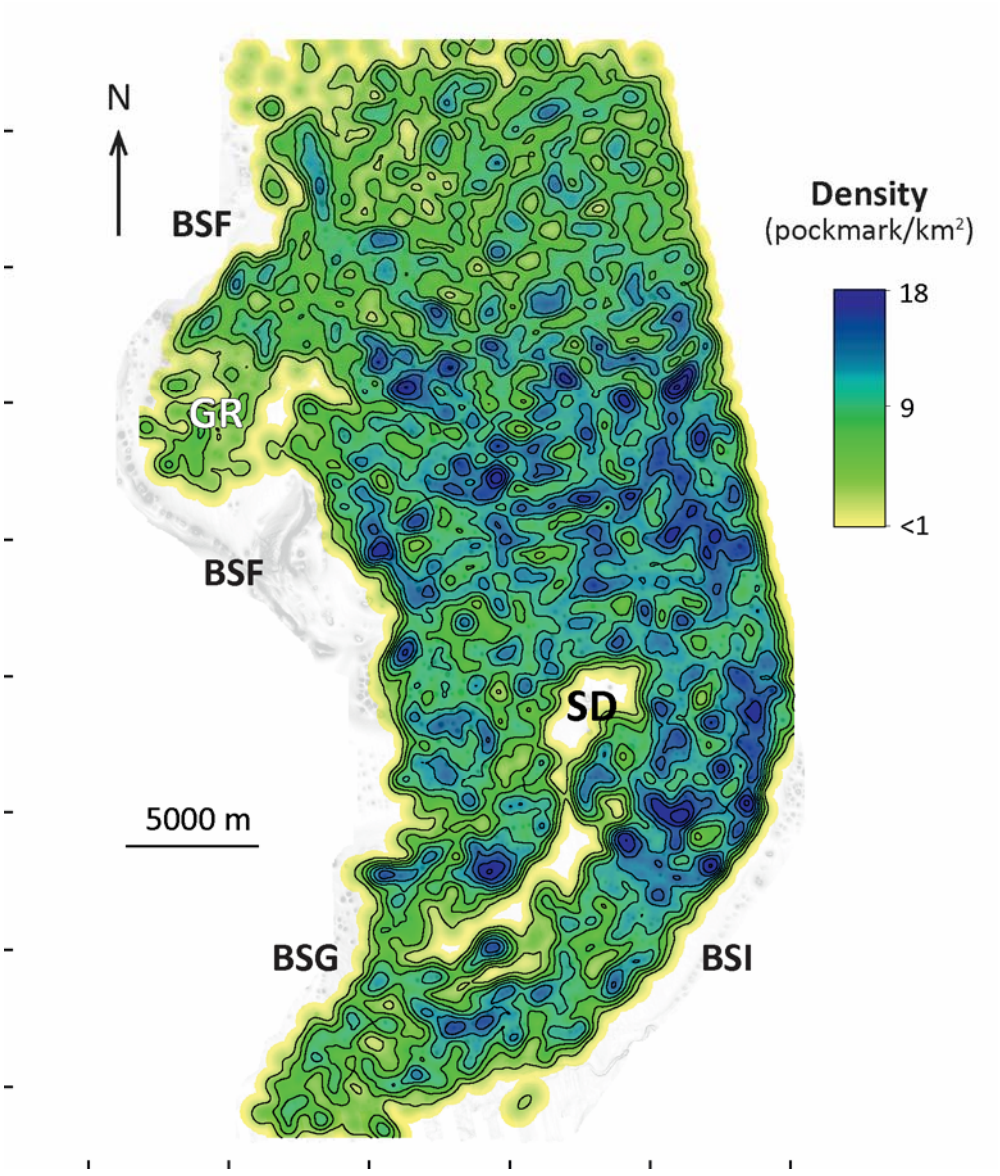

Figure 6.8. Kernel Density map for MB2 seabed pockmarks. The density patterns highlight the pockmark distribution patterns, including pockmark alignments. SR = salt ridge; BS = buried salt structure; SD = salt diapir; GR = graben.

Density maps for the pockmark distribution highlight the areas with higher occurrences (fig. 6.8). Pockmark density varies between 0 and 18 pockmarks per km^2. Low densities, comparatively to the whole value range, occur towards the north of MB2 and within the graben region (GR) that is adjacent to buried salt structures. A marked increase in pockmark density is observed in the central domains of MB2 where the south-facing arcuate alignments occur: here, high density values are locally identified surrounded

by moderate to low values (fig. 6.8). The density patterns suggest E-W banding, consistent with the pockmark alignment orientations observed on seafloor maps. On the southern half of MB2 the density patterns are more variable, with patches of moderate to low density. The minimum values are observed along the axis of basin over salt diapir SD and buried salt structures further south. The density patterns here do not show evidence of any clear preferred orientation, with the exception of the localised NW-SE oriented higher density patches perpendicular to BSI where PFFs occur.

The spatial variability of pockmark alignment orientations is best visualised using automatic point alignments operations (fig. 6.9). Two alignment detection tests were made with detections radius of 300m (fig. 6.9a) and 400m (fig. 6.9b). The general patterns detected are identical in both tests. Their most striking feature are the well evidenced E-W arcuate alignments occurring on the northern and central area of MB2, with a high frequency of alignments being identified. The ENE-WSW orientations towards the northern limit of the area are detected as well. Pockmark alignments towards the western limit of MB2 exhibit N-S to NE-SW orientations, shifting orientation closer to the salt structure BSF. Alignments between diapir SD and salt structures BGS and BSI show higher orientation variability. Alignments perpendicular to salt structure BSI are identified on a limited area near its limit. These are coincident with well visualised PPFs adjacent to the salt ridges, as observed on the mapped seismic surfaces (fig. 6.14). Towards the southern limit of MB2, where its axis shifts to a marked NE-SW orientation, alignments sub-parallel to this orientation are observed. The main contrast between both tests rests on the number of alignments detected for a radius difference of only

100m. Thus, the 400m radius detection test identified a larger number of alignments and broader range of orientations (fig. 6.9b). A key observation is the detection of more N-S alignments within the area of the E-W arcuate alignments comparatively to the 300m radius test. This is relevant for the perception of the control on pockmark spacing, suggesting that the spacing between pockmark alignments (or scattered pockmarks between them) exceeds 300m or 400m. The 400m radius test also detects higher numbers of alignments on the western flank of MB2, near the salt structure BSF. These areas show a general increase of pockmark spacing away from the axis of MB2 towards the salt ridges. The less well organised orientation patterns towards the southern half of MB2 are also better evidenced with the 400m radius, clearly delimiting a transition area between this and the well organised arcuate alignments to the north/centre of MB2 (fig. 6.9b). This is clearly observed around diapir SD, where variable orientations occur with no markedly clear trend. The exceptions to this pattern are the clear NW-SE alignments perpendicular to BGI, controlled by the PFFs, and the SW-NE alignments already described above.

The rose plot of the alignments orientations show the large majority of detected features following ENE-WSW trends, with average orientation of N88°E obtained for both detection tests using the 300m and 400m radius (fig. 6.9). This orientation is mostly influenced by the large number or arcuate alignments occurring on the north-central areas of MB2. In both cases, the lower frequencies of NW-SE and N-S alignments are either due to their occurrence close to the salt structures, or detections between different E-W alignments in central MB2.

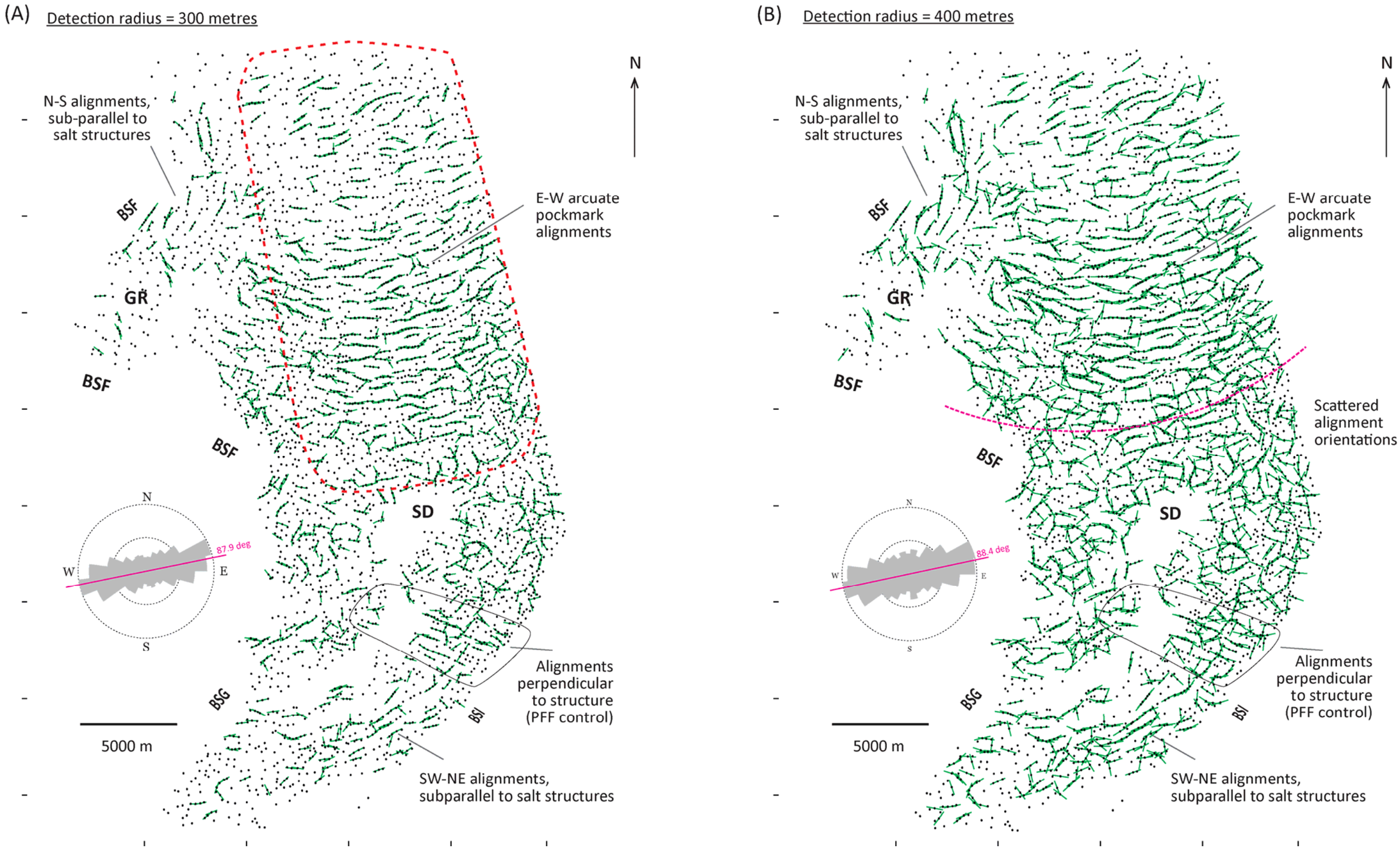

Figure 6.9. Alignment detection tests for MB2 pockmark alignments, performed with **(A)** search radius = 300m, and **(B)** search radius = 400m. Rose diagrams show results for all data points in MB2. SR = salt ridge; BS = buried salt structure; SD = salt diapir; GR = graben.

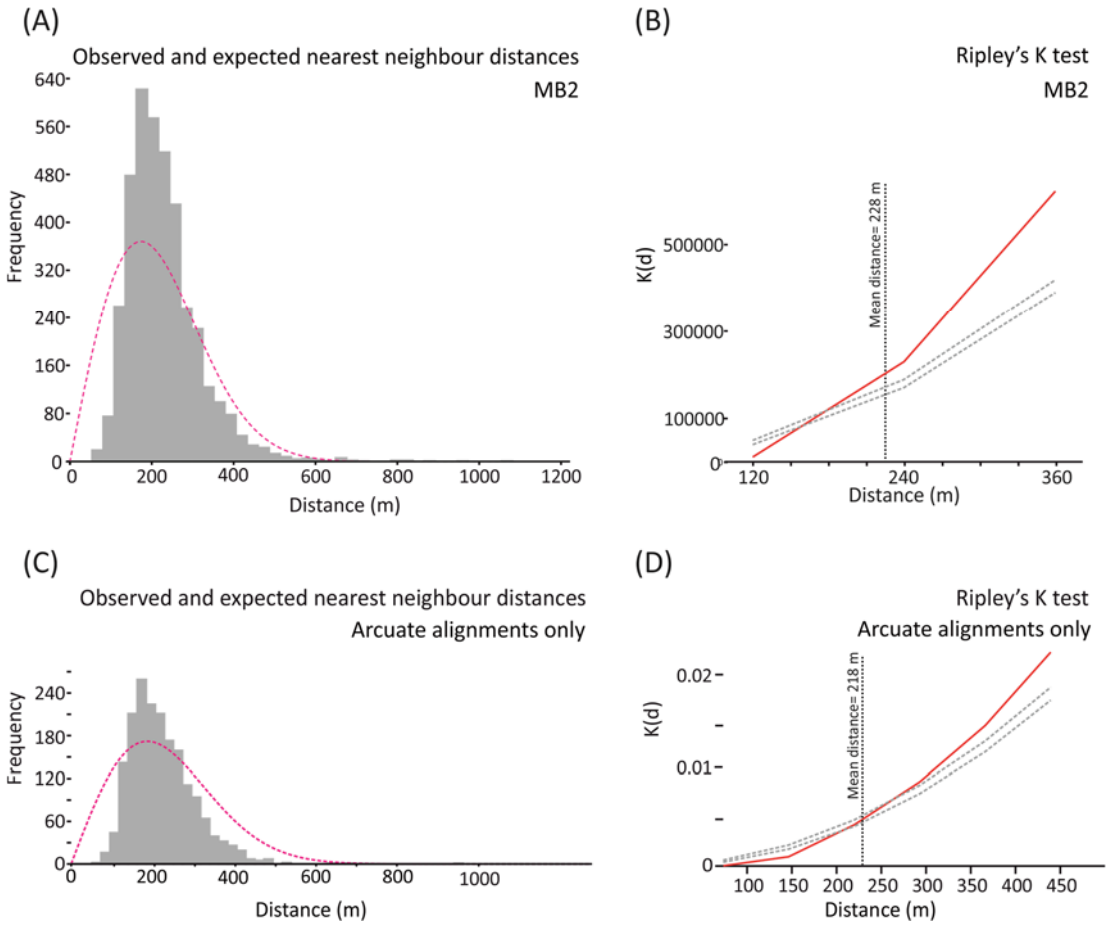

Figure 6.10. Average nearest neighbour and Ripley's K analysis for MB2 seabed pockmarks. **(A)** Average nearest neighbour analysis for all MB2 pockmarks. **(B)** Ripley's K analysis for all MB2 pockmarks. **(C)** Average nearest neighbour analysis for MB2 pockmark arcuate alignments. **(D)** Ripley's K analysis for MB2 pockmark arcuate alignments. Dashed pink line = expected nearest neighbour distances; Red line = observed spatial pattern K(d); dashed grey lines = confidence interval limits.

The nearest neighbour analysis for seabed pockmarks in MB2 indicates that most pockmarks are spaced between 120 and 300 metres, for an overall mean distance of 228m from an expected 217m (fig. 6.10a). Pockmark spacing over 600m occurs in very low frequencies in MB2. This test indicates a statistically significant point over-dispersion. The Ripley's K test for the full pockmark population of MB2 shows statistically significant dispersion for distances below 160m, consistent with the over-dispersion returned by the nearest neighbour, which are well below the mean observed distance and the majority of spacing values obtained (fig. 6.10b).

A separate analysis of pockmark distribution (radius = 300m) was undertaken for the sub-population of E-W arcuate alignments (fig. 6.11). These are delimited by the dashed red polygon in figure 6.9a. Similarly to described above, alignments towards the north have more marked NE-SW trends. Pockmark spacing in here is higher as well. Southwards, the ENE-WSW alignments predominate and spacing between the points is shorter, which also allows the detection of higher alignments numbers. Towards the south of this subset, the preferential E-W orientation is disturbed by a higher number of N-S trending alignments due to the proximity of the diapir SD. The rose plot shows similar trends to the main ones of MB2, with the larger majority of features following the general E-W orientation. The nearest neighbour analysis returns a statistically significant over-dispersion (fig. 6.10c). The mean pockmark distance is 218m, for an expected distance of 183m, and the highest spacing frequencies are observed between 150 and 300m. Within these value ranges, the Ripley's K test shows variable distribution patterns (fig. 6.10d). For distances up to 200m, it indicates point dispersion. Between 200m and 270m, the test values fall within the expected for random distribution patterns, also including the mean distance observed. Clustered distributions occur above 270m. The indication of dispersal and spatial randomness returned by the Ripley's K test seems to contradict the clear organised patterns shown by the alignments, and the over-dispersion pattern returned by the nearest neighbour analysis. This variability may be due to small point agglomerations observed within the organised alignments, and to the perturbation of the distribution patterns towards the vicinity of existing structures.

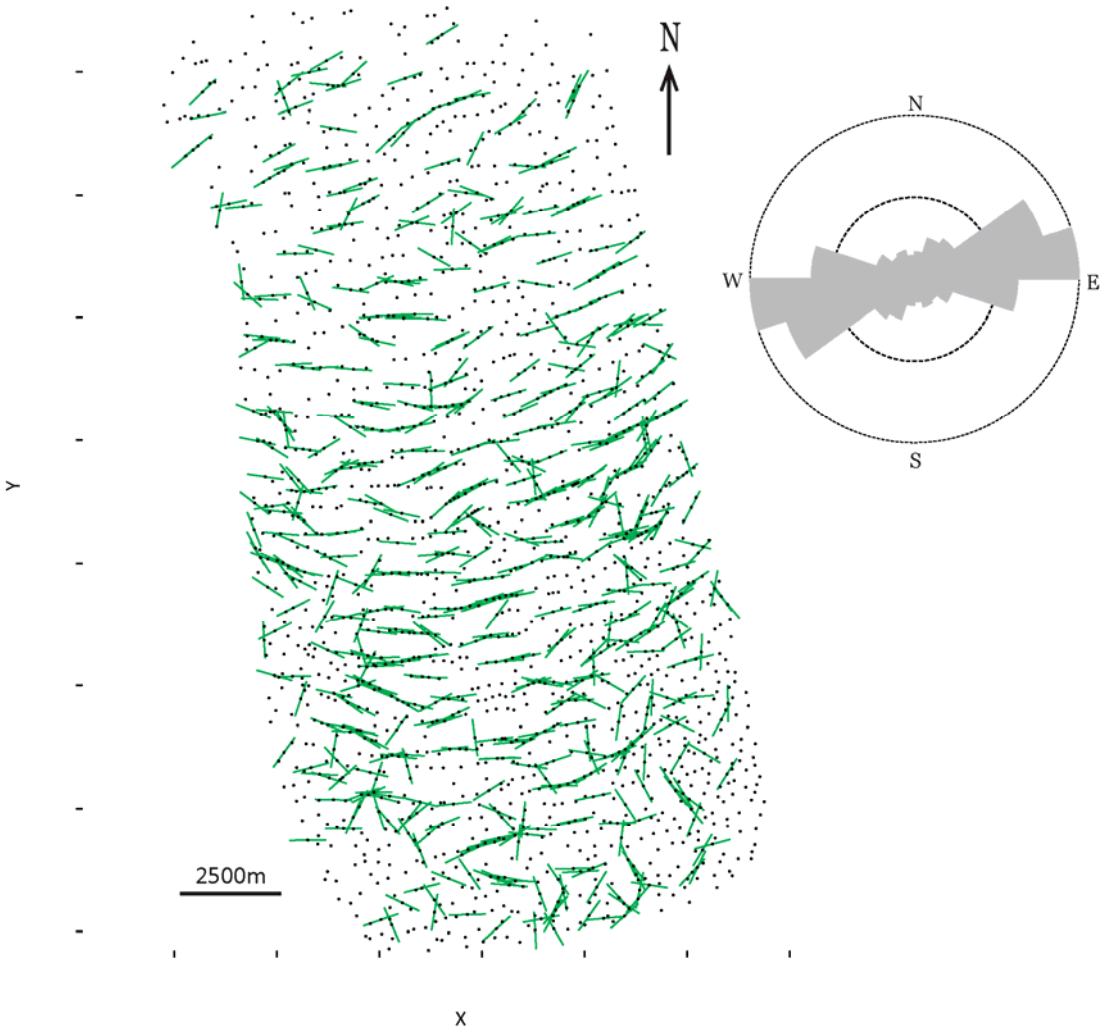

Figure 6.11. Alignment detection results for MB2 arcuate pockmark alignments.

As discussed in previous chapters, differences in the spatial distributions of seabed pockmarks may reflect different seal bypass mechanisms in the underlying strata. As such, the difference in pockmark patterns from the north and south regions of MB2 may result from different controls on the shallow fluid flow of the mini-basin. To understand the controls that affect fluid migration routes, it is critical to compare the pockmark patterns observed at the seafloor with structural and depositional deformation features present at depth.

6.2.2. Deformation features affecting MB2 overburden

Mini-basin MB2 exhibits several deformation features that affect the post-salt sediments. Structural deformation is associated to salt tectonic activity in the area, resulting in the diapirism of salt bodies, major tectonic faults, and folding of the overburden. Non-tectonic deformation processes include slope failure evident by extensive mass-transport deposits, and polygonal faulting of the shallowest Unit 3 sediments. In this section, all the seismically visible discontinuities produced by these deformation events are described, to be compared with the spatial distribution of seabed pockmarks, as an attempt to explain the local controls on the shallow plumbing system and fluid expulsion.

6.2.2.1. Salt tectonic deformation

Salt tectonics produced major structural deformation of the Lower Congo Basin. In mini-basin MB2, this is evidenced by large-scale folding and faulting of post-salt sediments from salt withdrawal and diapirism (figs. 6.3, 6.4 and 6.5). The deformation styles observed are predominantly extensional, leading to the development of normal faults and grabens. This contrasts with mini-basins MB6 and MB7, analysed in the previous chapters, as they were bordered by contractional salt structures. The full visualisation of the deep salt structures bordering MB2 is not possible due to the limited lateral and depth coverage of the 3D seismic data. However, the visualised features and comparison with published models from the Angola margin allow an assessment of the main features.

Mini-basin MB2 is delimited by two buried salt walls (BSF and BSI), whose growth conditioned the tectono-stratigraphic evolution of the entire mini-basin (fig. 6.1). Different salt structures and geometries are observed along the mini-basin axis. On the northern half, the main geomorphological feature observed is a large-scale anticline located in the centre of MB2 (fig. 6.4a). The crest of this elongated anticline follows a general N-S strike, plunges southwards, and coincides with the MB2 axis (figs. 6.3 and 6.4). It is bound to the west by BSF, and to the east by what would be inferred as the northward continuation of BSI (fig. 6.2). Regions of subsidence border the anticline in the proximity of salt walls BSF and BSI, interpreted to result from salt withdrawal at depth to form the adjacent salt structures. The latter regions are characterised by syncline folding of the overburden, and sediment thickening (fig. 6.4). Several major tectonic faults on the flank of the antiform (keystone faults) extend up the Pliocene interval, being sub-parallel to BSF, and are rooted deeper than the vertical extent covered by the seismic survey (figs. 6.2 and 6.4). They are up to 7350m in length and >1250ms TWT height, and strike along a NNW-SSE direction. The fault planes are planar and very steep, dipping west. All faults exhibit a normal displacement, and are located along the crest and west flank of the buried anticline. These faults are interpreted to result from subsidence of the north-west margin of MB2 due to salt withdrawal. Vertical salt structures of the BSF to the north have flattened tops (fig. 6.4a), indicating cessation of growth and burial of a passive diapir (Hudec and Jackson, 2011). The passive diapirism and extensional setting suggest that the anticline can be part of a mock-turtle structure, commonly observed on this margin (Duval et al., 1992; Rouby et al., 2005). Alternatively, the folding could be created by late buckling and diapir rejuvenation (Hudec and Jackson, 2011).

The transition to the southern halokinetic structures in MB2 is marked by salt diapir (SD), which pierces the entire overburden sediments in the central region of MB2 (fig. 6.3). Its top sits near the seafloor, and the lack of seafloor expression and thickening of the flanking strata indicates passive growth. The growth of this diapir controls the local stress field, which produced folding of the surrounding strata and several radial faults. Around the salt diapir, Unit 3 reflections near the seabed onlap older reflections suggesting a recent salt growth episode. However, truncation of the shallowest reflections (sediments younger than **C1**) by the seabed reflector above the diapir implies erosion. As such, locally the seafloor is an erosional surface. This is further supported by the lack of topographic relief created by the diapir at the seafloor. South of diapir SD two buried diapirs are observed along the axis of MB2 (fig. 6.3b and 6.4c). The thick, constant thickness over the buried structures indicate diapir rejuvenation created by shortening (Hudec and Jackson, 2011). Reactive diapirism and anticline breaching has occurred along BSI (fig. 6.4c, see also Chapter 3).

Comparisons between the seafloor pockmark distribution and discontinuities within MB2 produced by salt deformation do not suggest any spatial correlation between fluid escape patterns and these major features.

6.2.2.2. Polygonal faults

A single polygonal fault tier affects the entire extent of MB2, deforming Unit 3 sediments between horizons **C1** and **C3** (figs. 6.3, 6.4, and 6.13). In

planform, this tier exhibits the typical pattern expected for a polygonal fault system where faults strike at a variety of azimuths, defining a network of polygons made of short fault segments up to 750m in length. Variations to this pattern are only observed in close proximity to the salt structures that border MB2 (BSF and BSI) and surrounding the salt diapir SD (figs. 6.14 and 6.17). In these areas, the polygonal faults become polarised in the same manner described in Chapter 4 for the polarised polygonal fault (PPF) system, with fault orientations developing preferably perpendicular to the salt structures. In these polarised regions, these faults do not exceed 4650m in length.

In cross-section, the polygonal faults in MB2 are generally planar and very steep (with dips ranging from 50° to 70°). They are confined vertically in their extent to the strata between horizons **C1** and **C3** (figs. 6.4 and 6.19), hence being interpreted as layer-bound faults. The faulted interval exhibits variable thickness, ranging between <10ms and 307ms TWT. It has a slight wedge geometry, thickening towards the basin rims. The upper limit of the interval is marked by the same reflection as in mini-basins MB6 and MB7, i.e. horizon **C1** (fig. 6.19). This is interpreted to represent the time at which the layer-bound faulting system became inactive, which is consistent to the observations made in Chapter 4. The base of the interval is horizon **C3** and it gradually increases in depth as it thickens towards the flanks of the mini-basin (fig. 6.4).

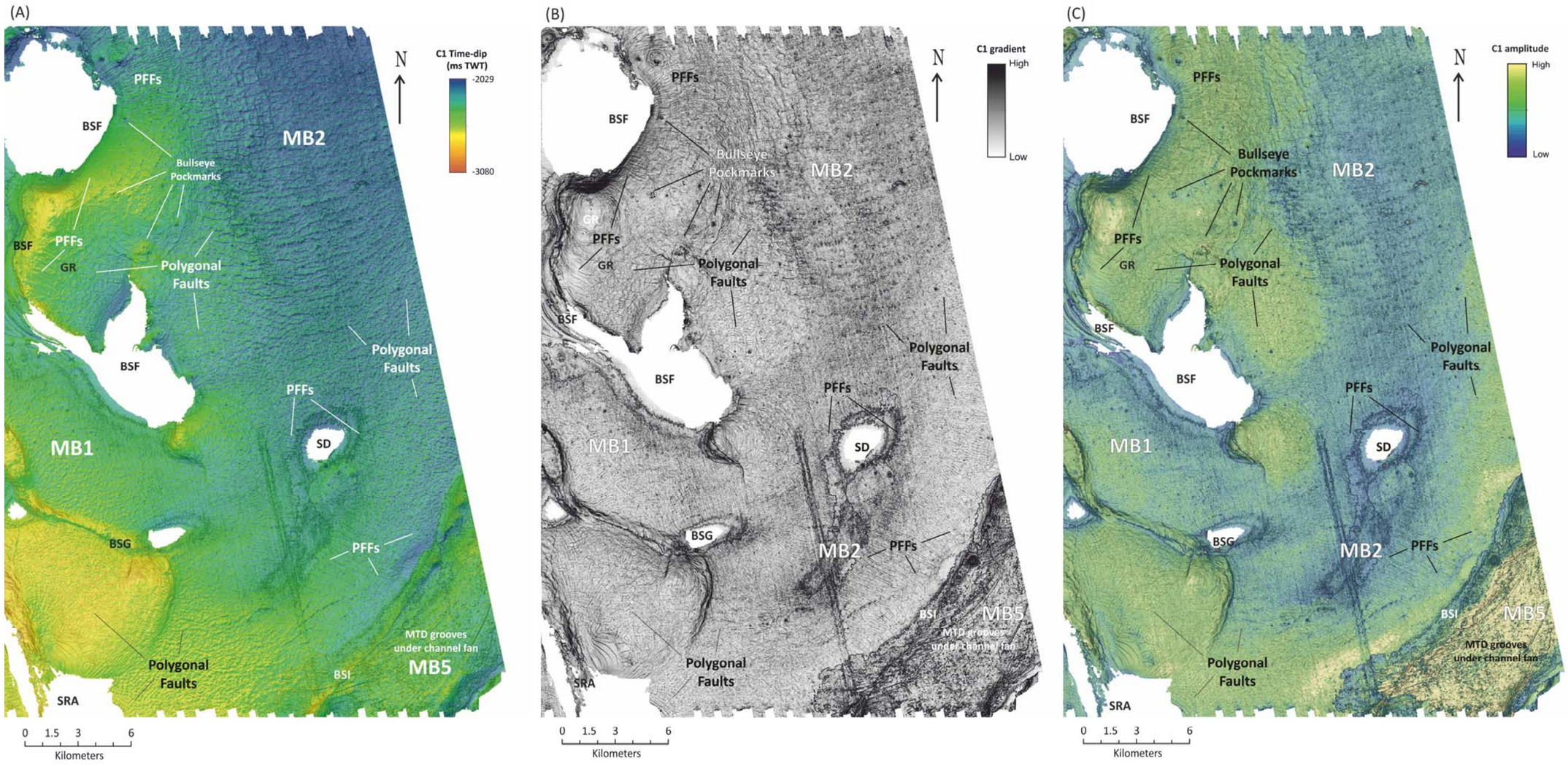

Figure 6.12. (A) Time-dip map of seismic horizon **C1** in MB2. **(B)** Dip map of seismic horizon **C1** in MB2. **(C)** Amplitude map of seismic horizon **C1** in MB2. SR = salt ridge; BS = buried salt structure; SD = salt diapir; GR = graben.

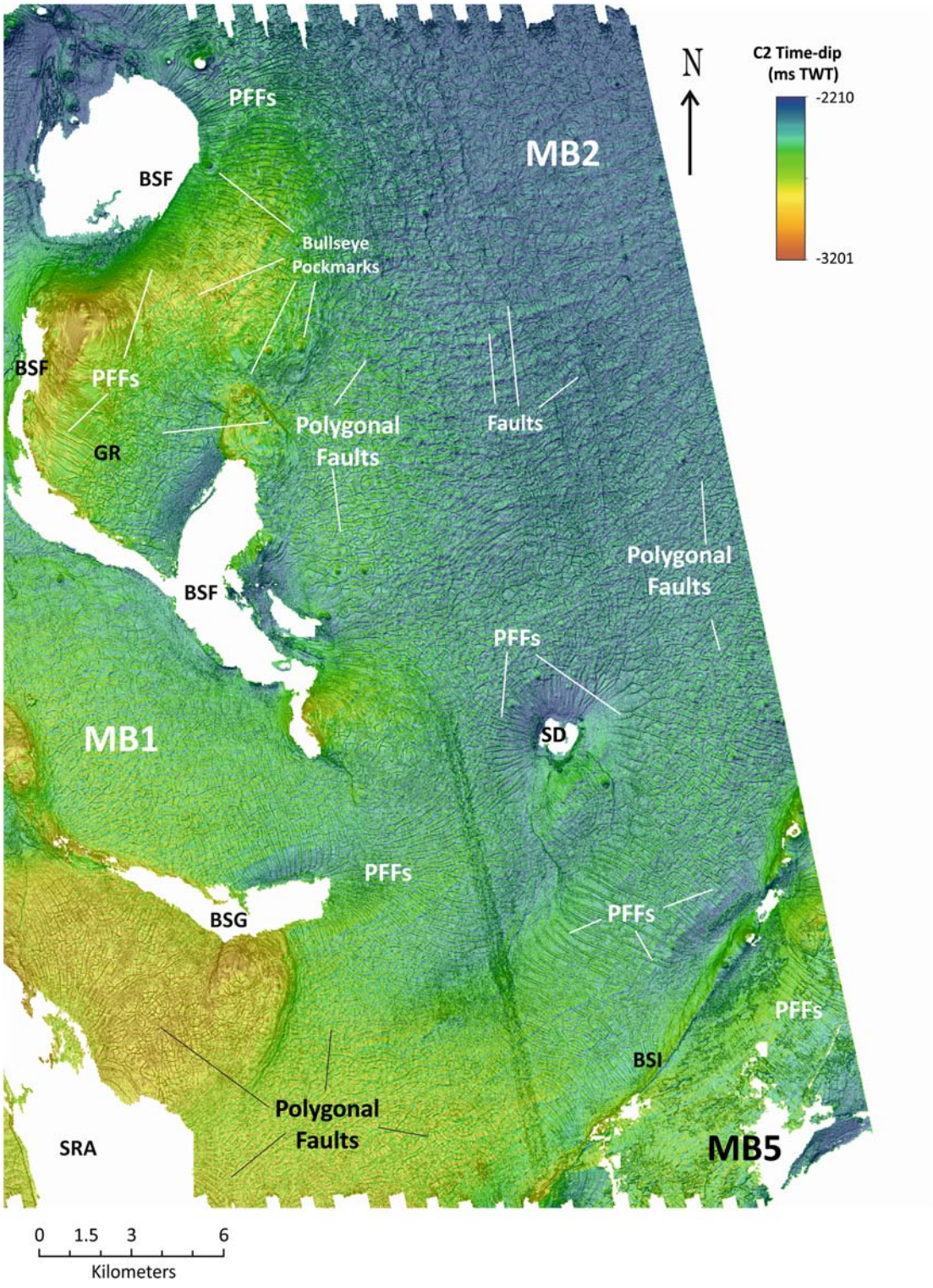

Figure 6.13. Time-dip map of seismic horizon **C2** in MB2. SR = salt ridge; BS = buried salt structure; SD = salt diapir; GR = graben.

As discussed in Chapter 4, the orthogonal orientation of the PPFs observed near salt structures in this mini-basin is also interpreted to result from local stress field perturbations either related to salt emplacement/growth or consequent changes in topographic gradient (or a combination of both). PPFs occur in regions surrounding salt walls that are affected by local anisotropic stress fields, confined to areas inside a transition boundary of 900-3350m radii. Polygonal faults occur in areas outside the transition boundary, where the horizontal stress field is interpreted to be isotropic (Carruthers, 2012; Cartwright, 2011). Towards the south of MB2, there is a small region where the fault pattern is dominated by strong alignments of fault strikes orthogonal to the mini-basin margin, and an almost uni-directional pattern across the basin axis (figs. 6.14a and 6.17). Due to the proximity of two adjacent salt structures, the transition boundaries of the limiting salt bodies of this region overlap, which is interpreted to prevent the development of polygonal fault arrays, and instead resulting in a unidirectional fault array, as observed in MB7 (see Chapter 4).

Amplitude maps of horizons **C1**, **C2** and **C3** further highlight lithological variations and discontinuities within the sediments that comprise the polygonal fault tier (figs. 6.12c, 6.15, and 6.17c). In general, lower amplitudes are observed in the central regions of MB2, and high amplitudes at the margins of the mini-basin. This lateral variation of amplitude may reflect a lateral change in lithology or a variation in pore fluid content. Polygonal faulting affects these sediments equally in areas of low and high amplitude, which suggests that a lateral lithological variation is unlikely (fine-grained sediments are generally the dominant lithology in layers (tiers) of polygonal

faulting). As such, the amplitude variations observed here are most likely the result of differences in gas content within pore fluids, with areas of higher amplitude containing higher amounts of gas.

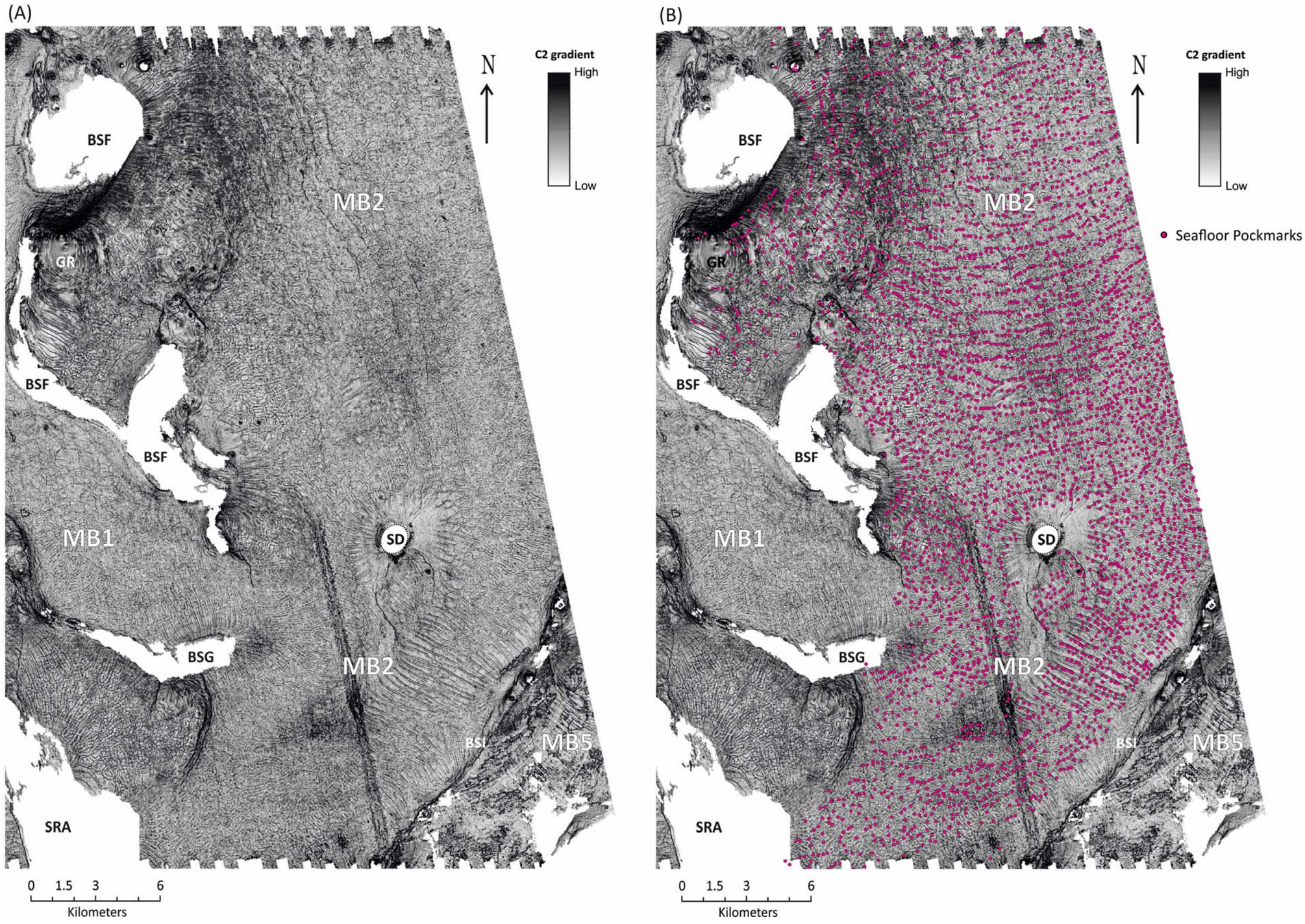

Figure 6.14. (A) Dip map of seismic horizon **C2** in MB2. **(B)** Dip map of seismic horizon **C2** in MB2 with seafloor pockmark locations. SR = salt ridge; BS = buried salt structure; SD = salt diapir; GR = graben.

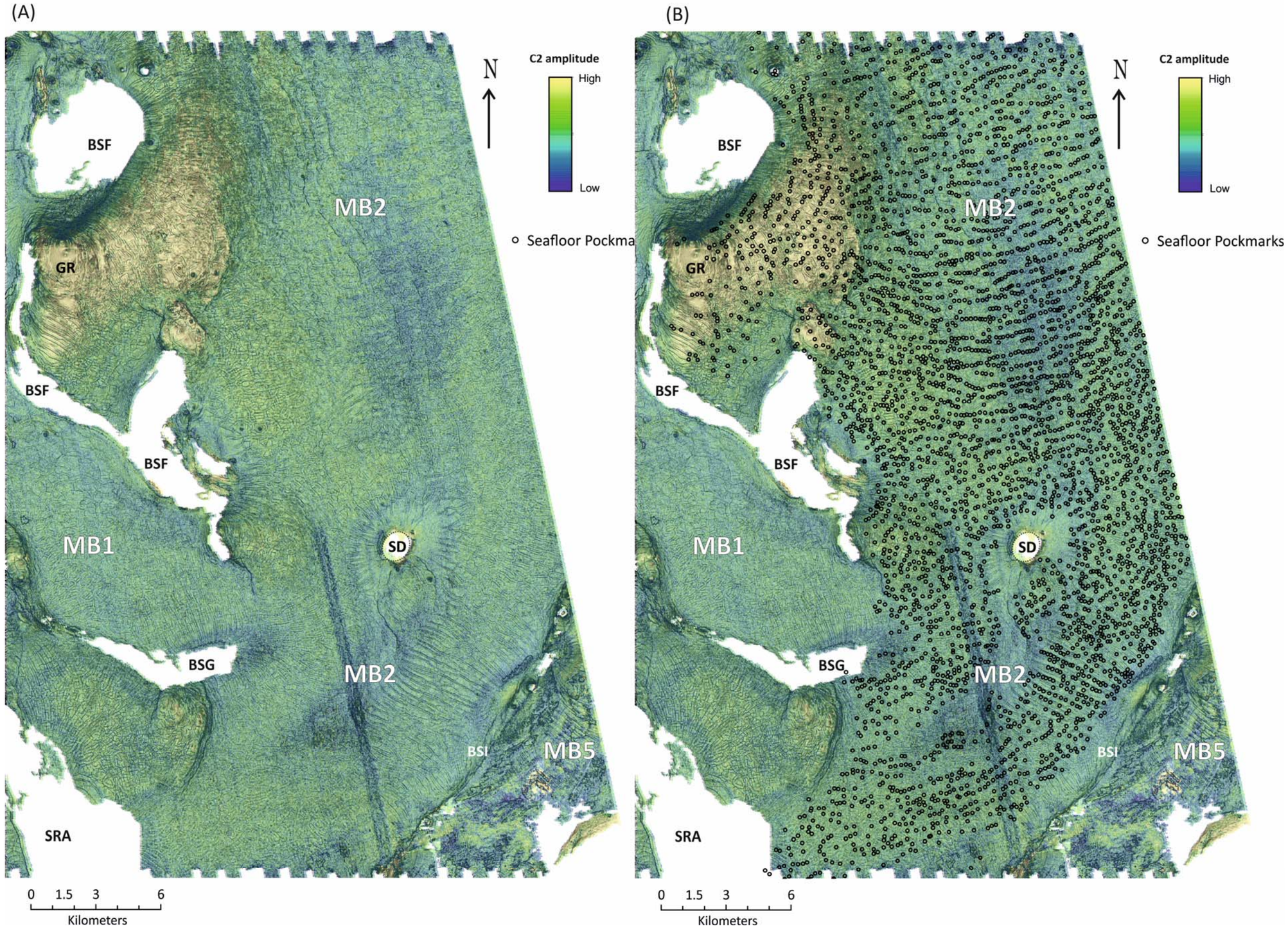

Figure 6.15. (A) Amplitude map of seismic horizon **C2** in MB2. **(B)** Amplitude map of seismic horizon **C2** in MB2 with seabed pockmark locations. SR = salt ridge; BS = buried salt structure; SD = salt diapir; GR = graben.

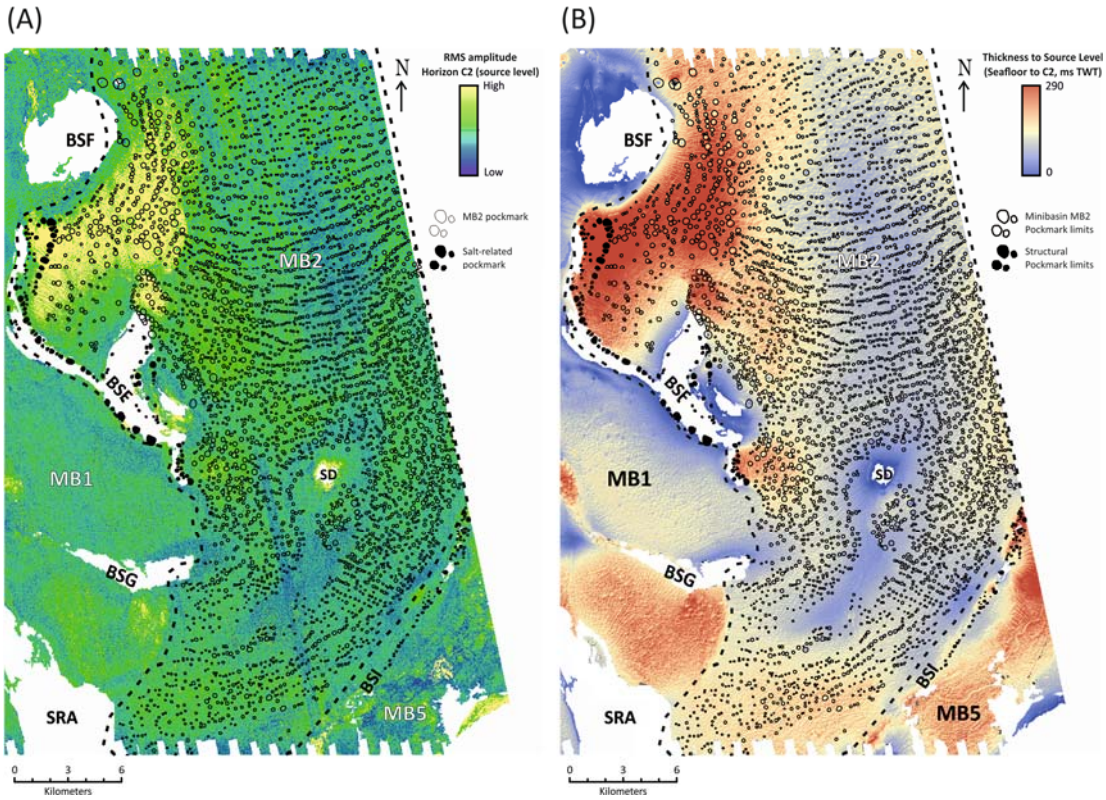

Figure 6.16. (A) RMS amplitude map of estimated fluid source interval **x-C2** in MB2 with seabed pockmark locations. **(B)** Thickness map of the interval seabed-**C2** in MB2 with seabed pockmark locations. SR = salt ridge; BS = buried salt structure; SD = salt diapir; GR = graben.

Minor local variations in amplitude are observed in the central region of the northern half of MB2. These are better identified in the amplitude map of horizon **C3** (fig. 6.17c). Short linear trails of low amplitude cross this region, following a general E-W strike (perpendicular to MB2 axis). These low amplitude lineaments are parallel to each other, and closely resemble the pockmark alignments observed at the seabed. These low amplitude trails are the only features within the polygonal fault tier that share the same spatial distribution as pockmarks, and may be linked to what is controlling the pockmark patterns.

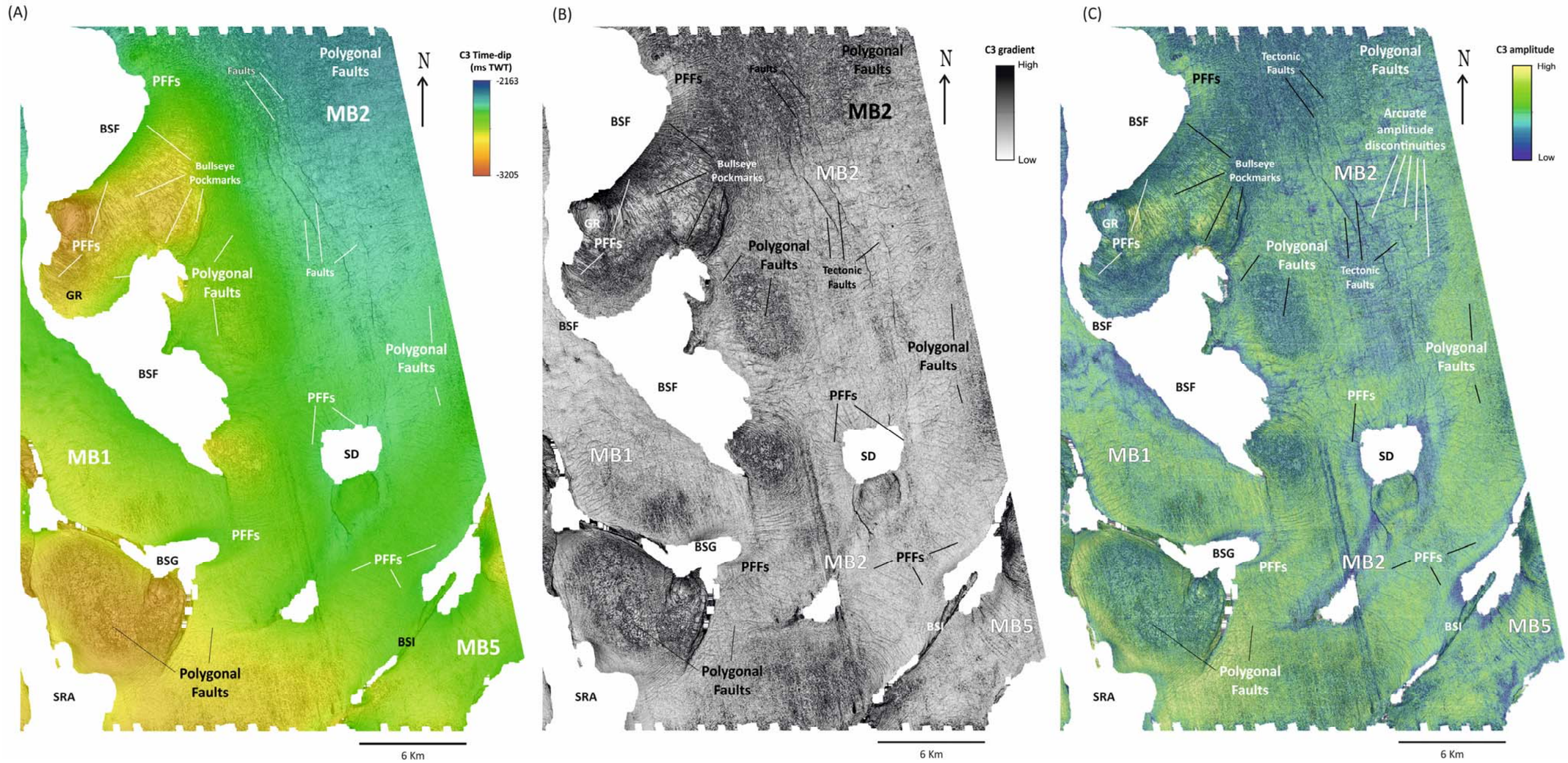

Figure 6.17. (A) Time-dip map of seismic horizon **C3** in MB2**. (B)** Dip map of seismic horizon **C3** in MB2. **(C)** Amplitude map of seismic horizon **C3** in MB2. SR = salt ridge; BS = buried salt structure; SD = salt diapir; GR = graben.

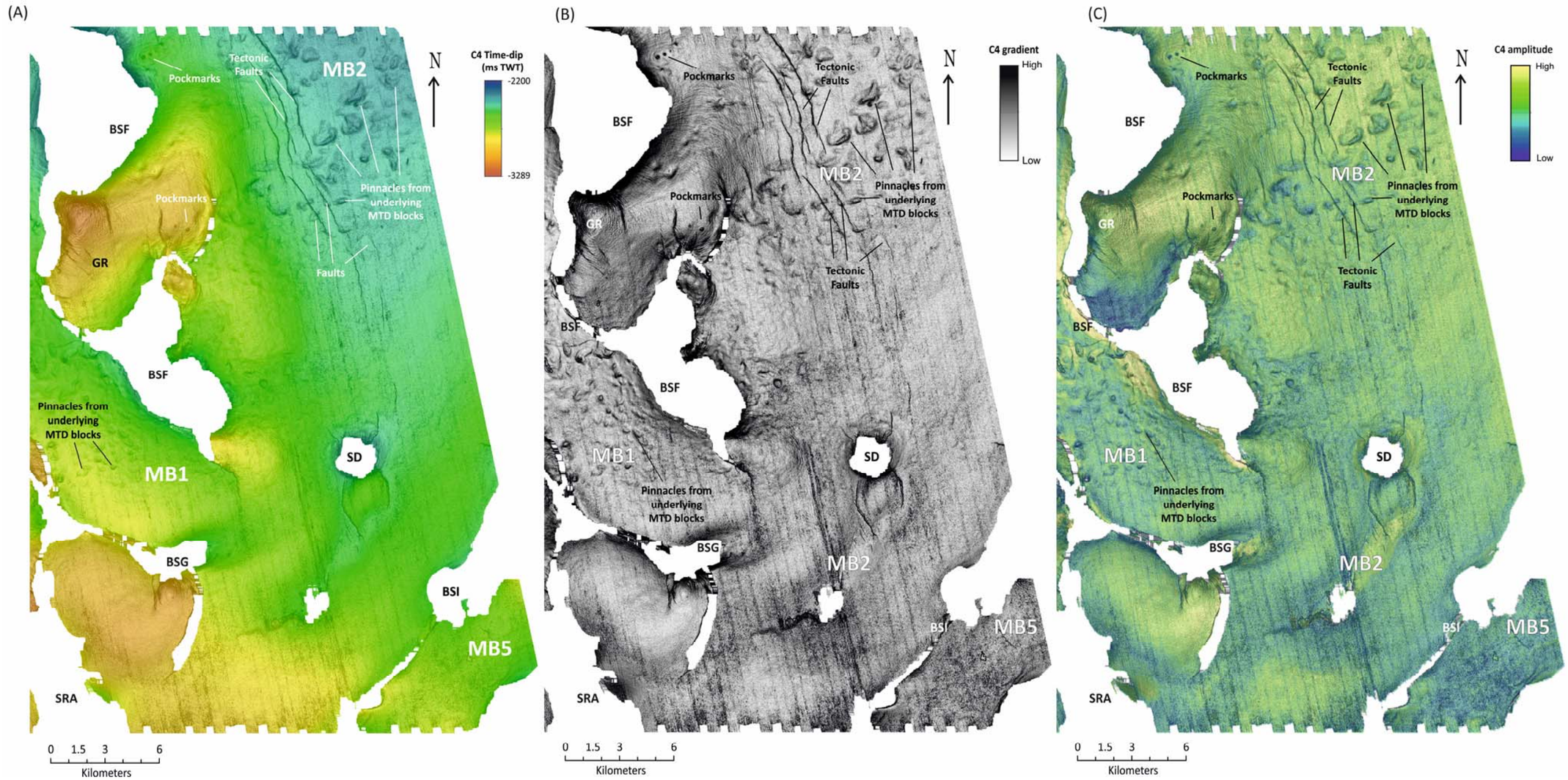

Figure 6.18. (A) Time-dip map of seismic horizon **C4** in MB2**. (B)** Dip map of seismic horizon **C4** in MB2**. (C)** Amplitude map of seismic horizon **C4** in MB2. SR = salt ridge; BS = buried salt structure; SD = salt diapir; GR = graben.

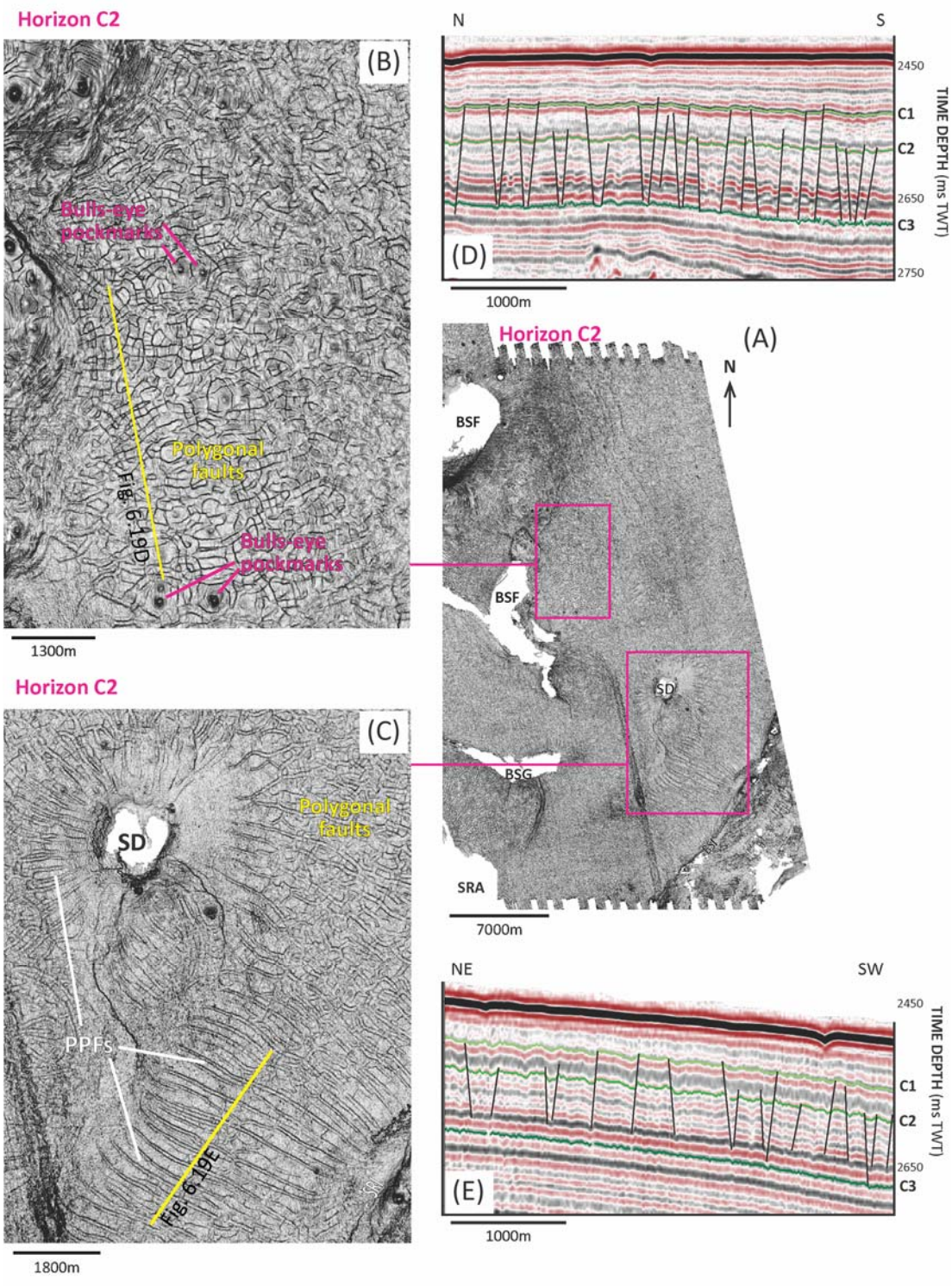

Figure 6.19. Dip maps and seismic sections showing the geometry of polygonal faults and of polarised polygonal faults (PPFs). SR = salt ridge; BS = buried salt structure; SD = salt diapir; GR = graben. (Seismic courtesy of PGS.)

6.2.2.3. MTD

Above Unit 2 sediments, an extensive MTD with an area of 990km^2 is observed. It is 49km long following a NE-SW oriented axis, and 38km wide (figs. 6.4 and 6.20). The true length of the deposit is unknown as it extends NE beyond the limits of the seismic survey. The deposit is up to 250ms TWT thick and has a southward-thinning trend (fig. 6.21). The thicker accumulations occur on the northern half of mini-basin MB2, showing NE-SW elongated patterns that mimic the movement of the MTD. The thicker patches on the map correspond to large blocks remobilised within the mass-flow. Thickness values on the southern half of MB2 are more uniform and do not exceed 80ms TWT. The base of the MTD is interpreted along a continuous reflection that underlies the mottled amplitude reflections of the deposit (fig. 6.4). This delimits the MTD from the high-amplitude reflections of the underlying Unit 2.

The MTD has marked lateral heterogeneities represented by variation in amplitude (fig. 6.22). Mottled reflections of the MTD deformed matrix have low to moderate amplitudes. This pattern is locally interrupted by stacks of high-amplitude reflections of limited extent that indicate the presence of blocks. Blocks are also easily identifiable on seismic profiles by the localised topographic highs on the MTD top surface (fig. 6.4). RMS amplitude maps taken 30ms TWT below the MTD top surface highlight the marked internal amplitude contrasts in the deposit (fig. 6.22). The highest variabilities are located on the northern half of mini-basin MB2. The RMS amplitude higher value forms elongated patterns along the NE-SW orientation, mimicking the orientation of the flow movement. Isolated high-amplitude patches in this area often indicate the presence of blocks, but not strictly. Towards the central

domains of mini-basin MB2, the overall RMS amplitude decreases. Individualised patches of higher amplitude associated with MTD blocks, often with geometric shapes, are clear in here. Very high-amplitude broad areas are observed on the southern areas of the map, but these patterns are due to the decreased thickness of the MTD – i.e. where it is thinner than 30ms TWT the RMS window computation captures the high-amplitude values of the turbiditic deposits of Unit 2. This also applies to very high amplitudes observed on the flank of the salt ridges (fig. 6.17). Comparisons between the thickness and RMS maps of the MTD do not show a constant correlation between both (figs. 6.21 and 6.22, respectively).

This MTD is covered by Unit 3 sediments. The effects of the geomorphology of the buried MTD in the overlying hemipelagic drape (Unit 3) are not observed in sediments shallower than horizon **C3** (figs. 6.3, 6.4, 6.15 and 6.17). Below **C3**, the stratigraphy mimics the morphology of the top of the MTD, with the geometry of blocks being clearly preserved up until horizon **C4** (fig. 6.18). This horizon can be used as a reliable marker to assess the notable irregularities on the MTD top surface. Between horizons **C4** and **C3**, the effect of MTD morphology is attenuated upwards (figs. 6.3 and 6.4). However, it can still interact with the base of the polygonal fault tier. This causes local disturbances of the fault pattern that are replicated upwards to shallower horizons such as **C2** (fig. 6.14).

Comparisons between the seafloor pockmark distribution and the MTD morphology, thickness or internal amplitude do not suggest any general correlation between fluid escape patterns and the buried deposit (figs. 6.21 and 6.22).

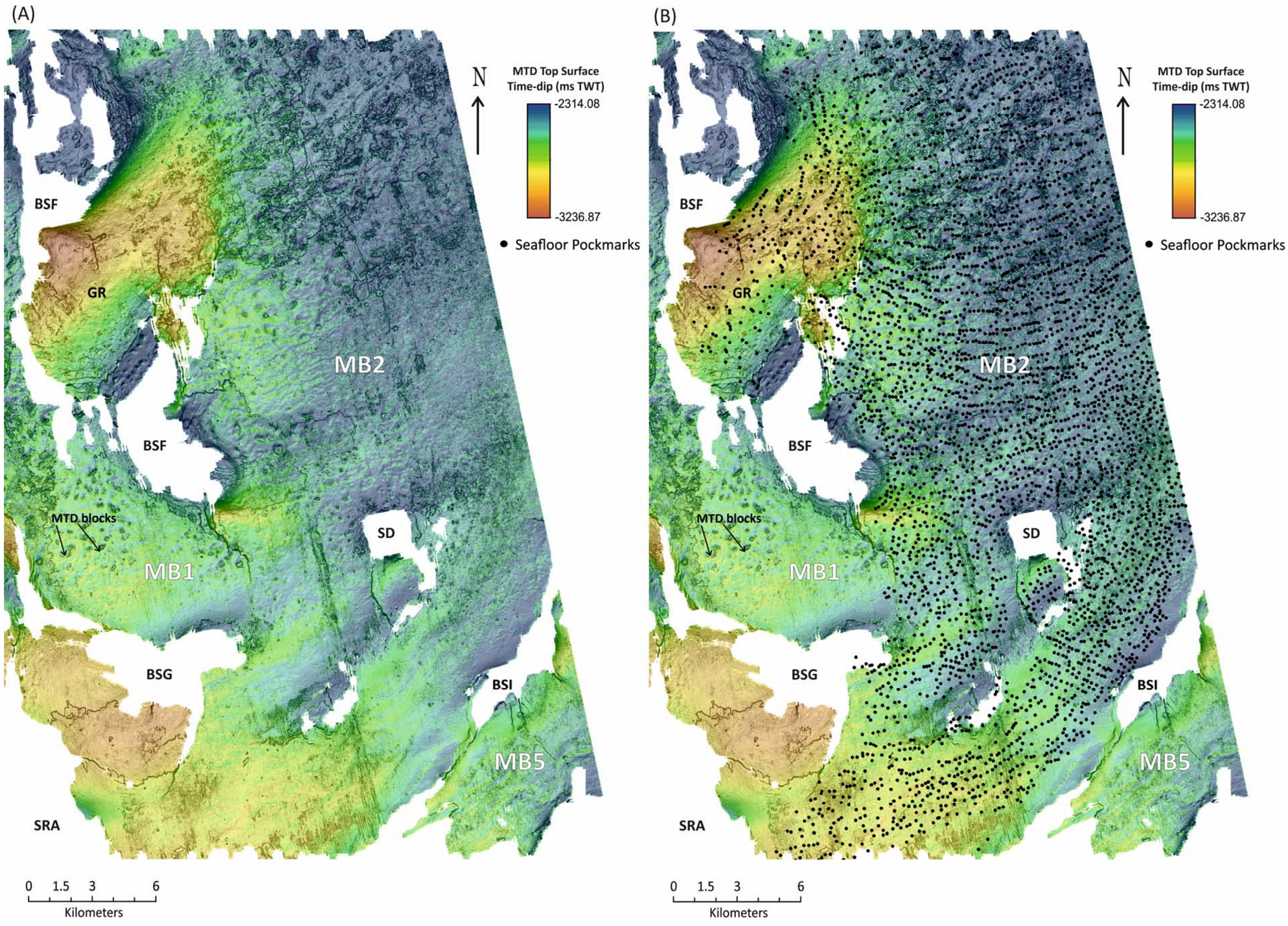

Figure 6.20. (A) Time-dip map of the MTD top surface in MB2. **(B)** Time-dip map of the MTD top surface in MB2 with seabed pockmark locations. SR = salt ridge; BS = buried salt structure; SD = salt diapir; GR = graben.

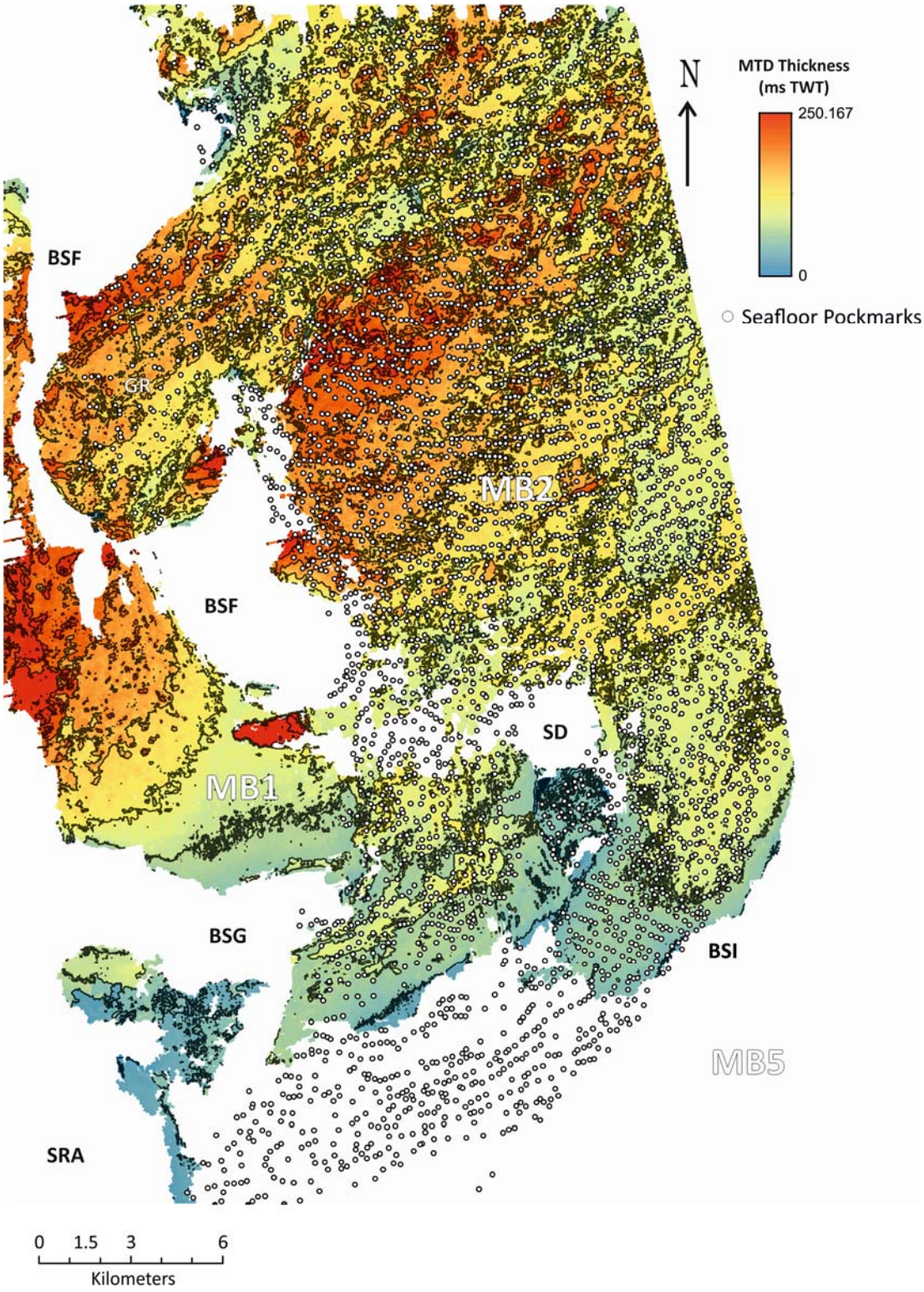

Figure 6.21. Thickness map of the MTD in MB2 with seabed pockmark locations. SR = salt ridge; BS = buried salt structure; SD = salt diapir; GR = graben.

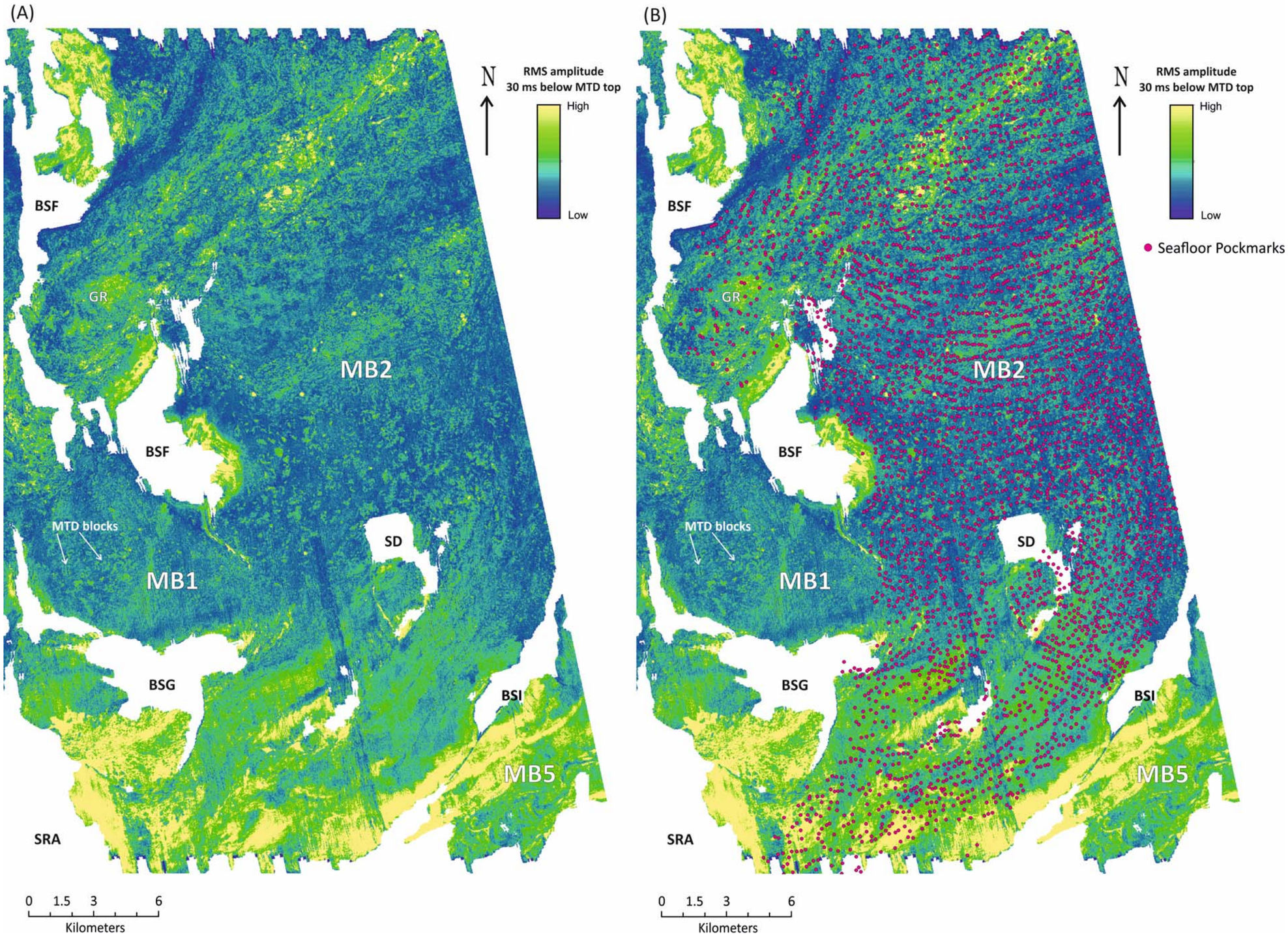

Figure 6.22. (A) RMS amplitude map of the top 30ms TWT MTD of MB2. **(B)** Amplitude map of the MTD shown in (A) with seabed pockmark locations. SR = salt ridge; BS = buried salt structure; SD = salt diapir; GR = graben.

6.2.3. Shallow gravitational sliding as a control on pockmark spatial distribution – discussion

6.2.3.1. Arcuate pockmark alignments in MB2 north region

When compared to seismic amplitude and dip maps of horizons **C1**, **C2**, **C3**, top and base of the MTD, the distribution of arcuate pockmark alignments in MB2 shows no spatial association to the discontinuities identified at depth. There are no seismically observable features, on vertical seismic profiles, in the northern half of MB2 that may explain the curvilinear arrangement of seabed pockmark trails. The only exception is the spatial resemblance between low amplitude lineaments within the polygonal fault tier (within the interval **C2-C3**; figs. 6.15c and 6.17c) and the seabed pockmarks in a small central area of MB2 (6.7a), suggesting that there may be a controlling mechanism acting within the shallowest sediments.

The lack of seismically visible evidence (such as discontinuities) that explain arcuate pockmark patterns at the seabed suggests that the mechanism that controls the distribution of fluid migration pathways may operate at small scales, close and below the limit of seismic resolution. Despite the limited seismic evidence, it is possible to infer possible causes for this pockmark distribution from its curvilinear arrangement and the geomorphology of the area. The geometry of the arcuate alignments (perpendicular to general N-S slope of MB2, with their apices pointing downslope) resembles compressional features observed at the toe domain of mass-transport deposits or involved in gravitational tectonics (fig. 6.23). Considering this analogy, it

is proposed that an incipient mass movement of the shallowest sediments of Unit 3 may be occurring in MB2, driven by gravitational forces acting downslope. This low strain movement or gravity slide may produce sub-seismic internal deformation of the sediments near the seabed, which may constitute seal bypass features for fluids to be expelled at the seafloor. Pore fluid expulsion may be promoted by downslope compression of shallow sediments as pervasive dewatering may occur due to shortening (downslope contraction) and horizontal compaction (as discussed by Morley et al., 2017).

In gravitational sliding, slow intergranular friction occurs, with the translation of coherent mass of sediments on slope-parallel slip planes, with minor internal deformation. The slow sliding process is controlled by sediment compaction parallel to the slope, and requires pore pressures in excess of the hydrostatic fluid pressure columns (Mandl and Crans, 1981). Excess pore pressures in fine-grained sediments reduce the effective overburden weight, which is carried by intergranular contact pressures (the source of frictional shearing strength). In a downslope compressional regime, small-scale flow fabrics may develop, producing parallel to sub-parallel, arcuate discontinuities perpendicular to the mass flow (to which the maximum compressive stress will develop), and convex in the downdip direction. These flow fabrics are of limited topographic relief, and are not likely to be visible in seismic surveys (Masson et al., 1993; Bull, 2009). In the lateral margins, friction between the moving mass and the stationary strata laterally constraining the flow may produce minor discontinuities parallel to the gross flow direction, associated with strike-slip movement. This phenomena would explain downdip convex arcuate lineaments perpendicular to the slope in the centre of MB2, becoming more parallel to the lateral

margins near the limiting salt structures (BSF and BSI). Sub-seismic discontinuities within the shallowest sediments of Unit 3 would follow these orientations. These discontinuities may affect the fluid source layer **x-C2** (estimated from previous chapters, since the seismic stratigraphy is correlatable between the mini-basins of this study area), promoting the establishment of pathways for upward fluid migration (fig. 6.24a).

The main driving mechanism for the gravitational sliding of shallow sediments may be the slope topography created by subsidence of the northern region of MB2, accompanying the salt withdrawal related to diapir SD growth that started prior to the deposition of the MTD. This is evident by the thickening of pre-MTD sediments observed towards the south of MB2 (figs. 6.3, 6.25 and 6.26). Pockmark alignments become arcuate from the point where Unit 2 sediments thicken, and this character is discontinued in the vicinity of diapir SD, where there is significant thinning of the overburden (figs. 6.3 and 6.25). No other mini-basin of the study area has the same structural characteristics of MB2; as such, this mechanism and its influence on the shallow plumbing system does not elsewhere.

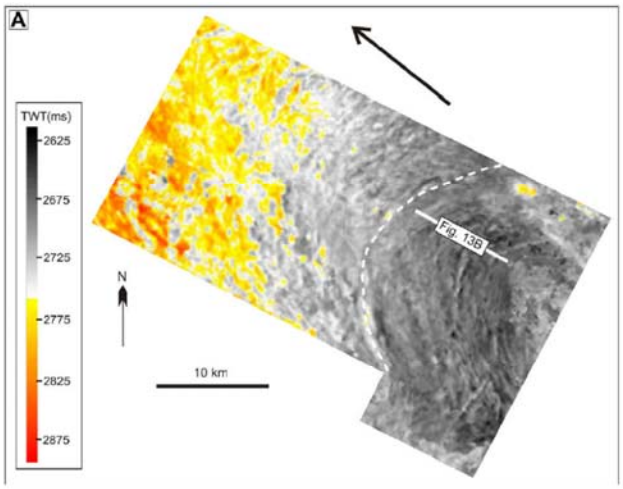

(modified from Bull *et al.*, 2009)

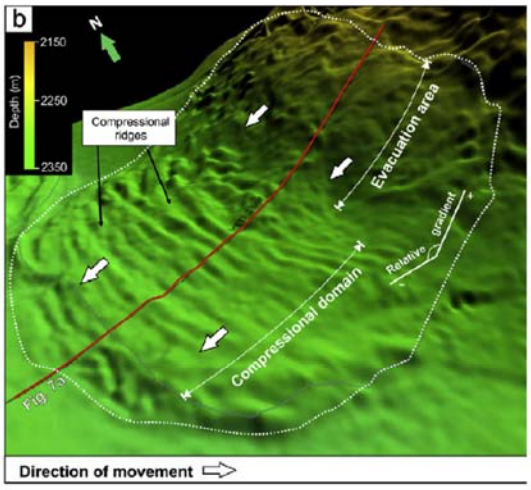

(modified from Gamboa and Alves, 2016)

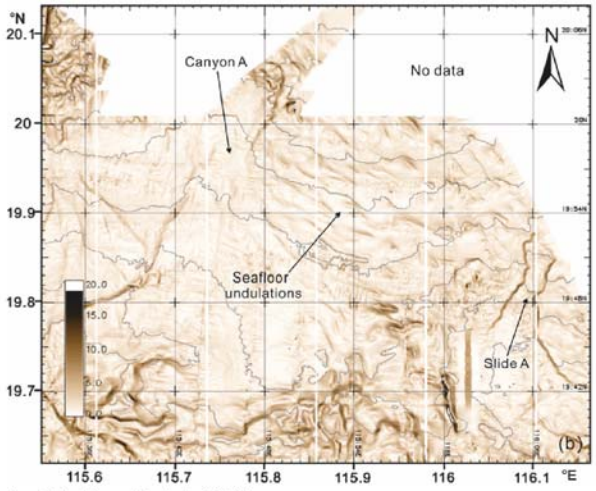

(modified from Li *et al.*, 2016)

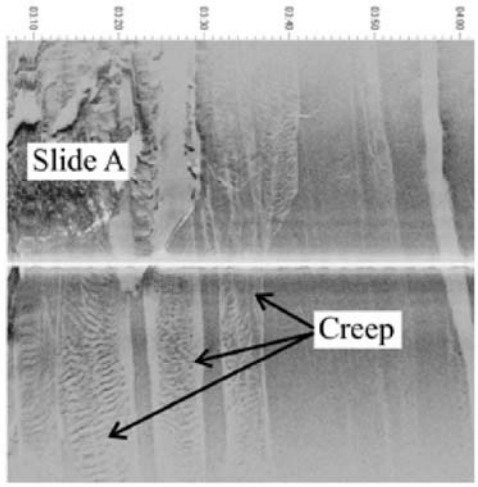

(from http://www.ig.uit.no/Loslope)

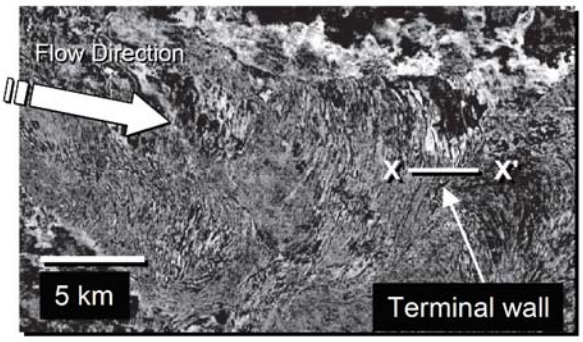

(modified from Posamentier and Martinsen, 2011)

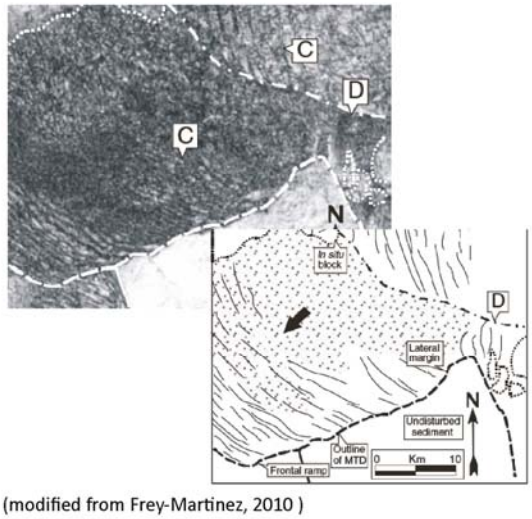

(modified from Frey-Martinez, 2010)

Figure 6.23. Examples of arcuate structures associated with creep and compressional deformation in deep marine sediments.

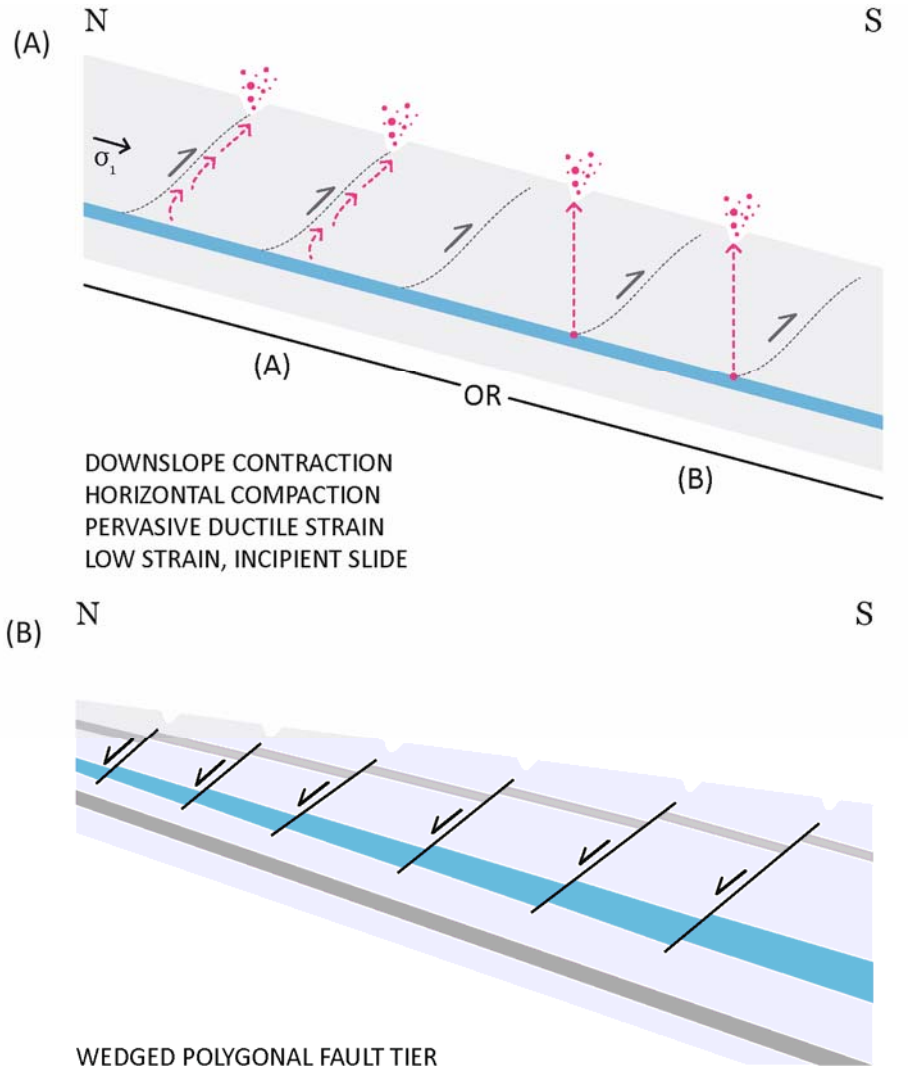

Figure 6.24. (A) Diagram explaining the incipient shallow gravitational sliding process that may be occurring in MB2. In segment (a) sub-seismic discontinuities may act as conduits for fluid migration; whereas in segment (b) sub-seismic discontinuities only influence the location where a vertical fluid conduit forms, by promoting seal leakage where the discontinuity intersects the source interval. **(B)** Diagram explaining a wedged polygonal fault tier.

Figure 6.25 compares seismic sections and maps from amplitude and variance volumes of MB2. The seismic amplitude cross-section shows southward thinning and decreasing reflection organisation between horizons **C2** and **C3** (fig. 6.25a). This change in seismic character within the **C2-C3** interval is marked by a sharp lateral

boundary coincident with the transition from linear to arcuate pockmark alignments on the seafloor, and the pinch-out of high-amplitude turbidites near the top of Unit 2 (fig. 6.26). On variance profiles, horizon **C2** intersects a thin moderate to high variance level within the area of the arcuate alignments (fig. 6.25b). The variance of **C2** markedly decreases on the northern areas. These changes in variance represent a change in sediment cohesion, with a boundary established at the transition from the linear to arcuate alignments. The variance time slice 64ms above **C3,** which intersects the disrupted areas of **C2**, highlights the presence of E-W arcuate low variance features within the dark very high variance surroundings (fig. 6.25c). Areas with polygonal faults are intersected by this time slice towards the west and north. The variance time slice 32ms above horizon **C3** shows lower variances, but clear and long high variance E-W features are observed. These underlie the area of occurrence of the arcuate seabed pockmark alignments. Numerous polygonal faults and PFFs are observed at this level but do now show the E-W trends. The variance slice along horizon **C3** – the base of the polygonal fault tier – has general low variance (fig. 6.25.c). Numerous polygonal faults and the axial large salt-related faults are observed. There is no clear evidence of E-W oriented features at this level. These observations suggest that 1) the high variance values around and below horizon **C2** are indicative of increased stratal disturbance, rooted at a level between it and **C3** and 2) the seabed pockmark alignments may relate to structural disturbances affecting the **x-C2** interval interpreted as the shallow fluid source.

It may also be argued that the arcuate pockmark alignments are associated to discontinuities present in the polygonal fault tier. If so, pockmark alignments may be spatially controlled by one preferential polygonal fault orientation (generally oriented

perpendicular to the slope), despite the typical arrangement of the polygonal faults in MB2. This may be due to the extensional movement of polygonal faults and the geomorphology of the buried southwards-plunging anticline, probably combined with an incipient gravitational sliding of shallow sediments. The buried structure may cause short segments of normal faults to be deflected from a general E-W strike (perpendicular to slope) to NW-SE or NE-SW orientations towards the flanks of the anticline, creating an overall arcuate pattern of discontinuities facing downslope (southwards). As discussed in Chapter 4, the fluid expulsion event that originated the seabed pockmarks is not linked or synchronous to the polygonal fault system. It is probable that at the time of seabed pockmark formation, overpressured pore fluids may have exploited the pre-existing structural disruption at their source interval (created by pre-existing polygonal faults) to bypass the seal and migrate upwards along a preferential locus oriented perpendicular to MB2 axis, likely aided by a process of low strain creeping or gravitational sliding of the shallowest sediments.

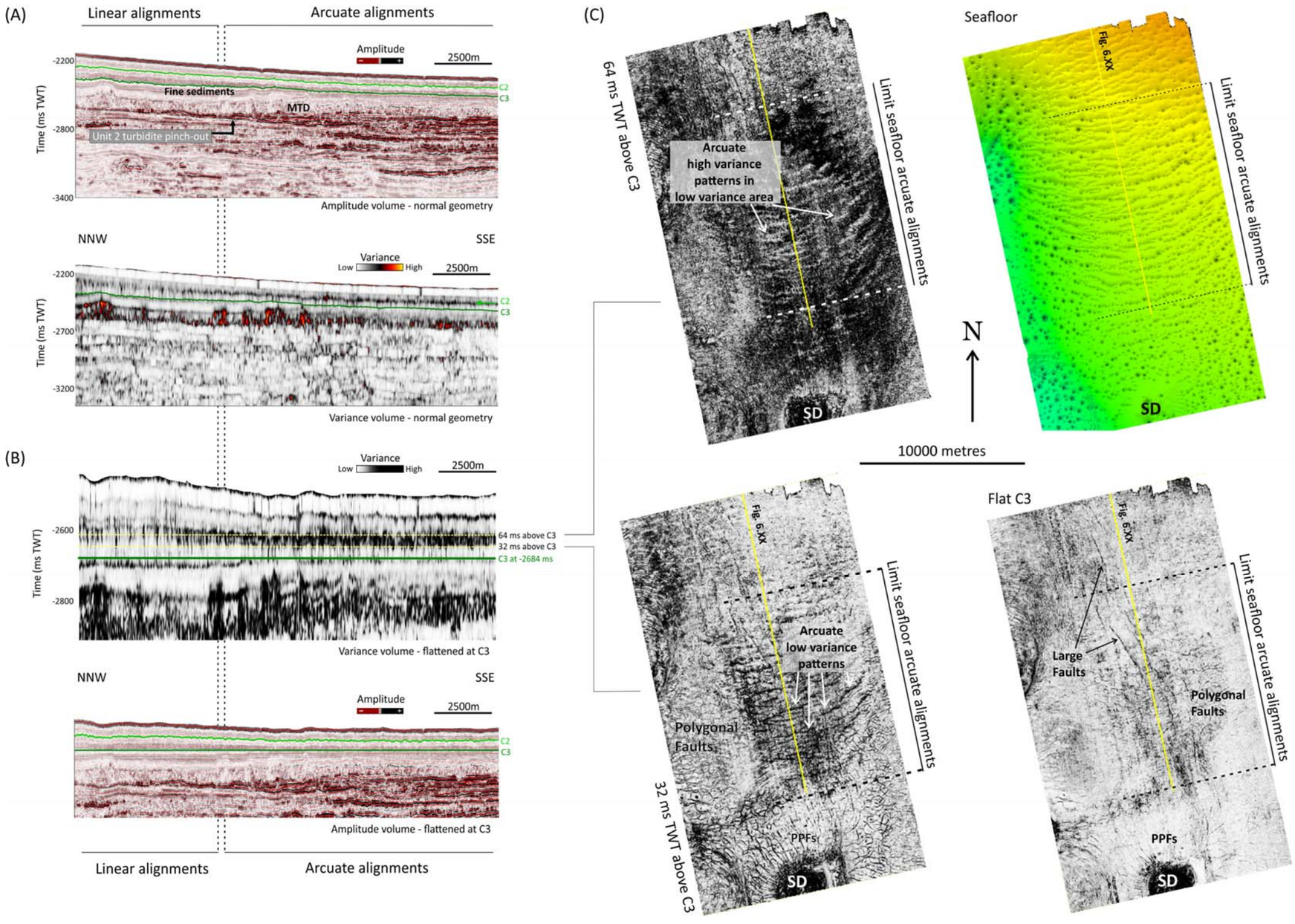

Figure 6.25. (A) Normal geometry seismic profiles from amplitude and variance volumes. The amplitude section shows southward thinning and decreasing reflection organization between horizons **C2** and **C3**. This change in seismic character within the **C2-C3** interval is marked by a sharp lateral boundary coincident with the transition from linear to arcuate pockmark alignments on the seafloor, and the pinch-out of high-amplitude turbidites near the top of Unit 2. On variance profiles, horizon **C2** intersects a thin moderate to high variance level within the area of the arcuate alignments. The variance of **C2** markedly decreases on the northern areas. **(B)** Sections of variance and amplitude volume flattened along horizon **C3**. The variance profile show the location of the flattened **C3** and of the level of two time-slices 32ms and 64ms above it. These two slices intersect the top and bottom of the high variance dark band in which **C2** is included. **(C)** Map sections of the seafloor and variance time slides covering the area of arcuate alignments in MB2, deepening anti-clockwise from the top right. The seafloor tip-dip map shows the reference area with the arcuate pockmark alignments. SR = salt ridge; BS = buried salt structure; SD = salt diapir; GR = graben. (Seismic courtesy of PGS.)

.

The mechanisms discussed above differ on the nature of the discontinuities exploited for pockmark formation and the general stress regime imposed by the slope geomorphology. Gravitational sliding of shallow sediments in a downslope compressional regime could produce seismic to sub-seismic north-dipping compressional discontinuities, if no pre-existing deformation features were present (fig. 6.24a). However, pre-existing extensional discontinuities developed by the polygonal fault system may be exploited by a shallow gravitational sliding process, on an overall downslope extensional regime (fig. 6.24b). Both hypothetical mechanisms are plausible explanations for the downslope-facing arcuate alignments of seabed pockmarks observed in MB2. However, due to the lack of seismic evidence, it is not possible to discern which of these processes occurred in reality. In any case, it is interpreted here that an incipient gravitational sliding of shallow sediments took place, either producing or exploiting pre-existing discontinuities that control upward fluid migration to form arcuate seabed pockmark alignments in MB2. The locus for the formation of fluid conduits for pockmarks was most likely at the intersection of discontinuity planes with the likely fluid source interval (**x-C2**), in a similar process to the way PPFs control the pockmark alignments described in Chapter 4. There is no seismic evidence that these discontinuities acted as conduits themselves.

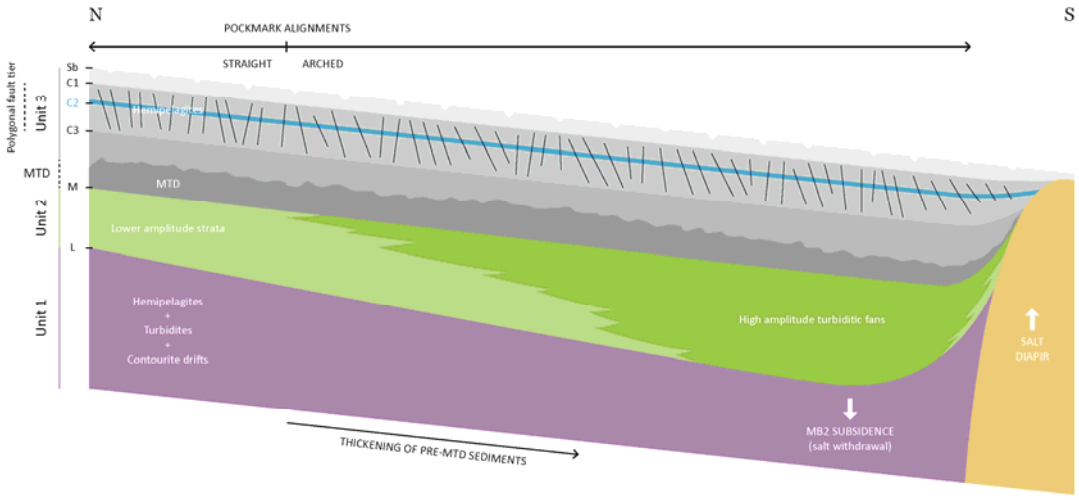

Figure 6.26 . Diagram explaining the general structure and seismic stratigraphy of MB2 along a N-S section.

6.2.3.2. Local exceptions to the arcuate pattern

Southwards of salt diapir SD, there is a small area where seabed pockmarks form linear trails perpendicular to salt ridge BSI, along a WNW-ESE strike (figs. 6.14 and 6.17). These alignments have the same orientation and length as the underlying polarised polygonal faults (PPFs). As such, it is interpreted that the seabed pockmark distribution in this area is spatially controlled by the PPF system, in the same manner as discussed in Chapter 4. The pre-existing arrangement of PPFs set the discontinuity pattern along which the location of pockmark feeding conduits was established – fault planes control the nucleation position of feeding pipes, with the critical locus being at the intersection of the fault with the estimated fluid source interval.

6.3. Pockmark morphology – size-source depth scaling

The size of individual pockmarks in any given area varies greatly. It is well established that pockmarks are erosional features and that their size depends on the amount of seabed sediment material remobilised during their formation. However, few published studies have undertaken any analysis of the spatial distribution of pockmark size and elucidate the physical processes that control this size variability.

Judd and Hovland (2007) argue that pockmark size is influenced by the sediment type in which pockmarks are formed. In general, pockmark size decreases with increasing grain size. However, this assumption fails to explain pockmark fields exhibiting a wide range of sizes (distributed in clusters of similar size) in areas where seabed sediment composition shows no lateral lithological variation. This is the case of the seabed pockmark field in mini-basin MB2. Furthermore, Van Rensbergen et al. (2007) suggest that the initial size of a pockmark is dependent on the eruptive force of the fluids being expelled at the seabed. This eruptive force may in turn be related to the degree of overpressure and depth of the fluid source. The distribution patterns of pockmark size in MB2 provide an excellent opportunity to assess these factors.

The main aim of this section is to understand what controls the morphological variability of MB2 seabed pockmarks, and to investigate its relation to the fluid source depth. The spatial distribution of pockmark sizes is analysed and contrasted with the geomorphological structure of MB2, using a multi-parameter comparison approach. The results from this study indicate that there is a relationship between pockmark size and the depth of the fluid

source layer, most likely linked to the pressure at which pore fluids are stored prior to their expulsion.

6.3.1. Morphological description of MB2 pockmarks

The seafloor of mini-basin MB2 is highly saturated in pockmarks, with 3896 shallow depressions identified within its limits (fig. 6.1). Seabed pockmarks occur at water depths between 1645m to 2075m below sea-level. Pockmark density varies between 0 and 18 pockmarks per km^2 (fig. 6.8). Pockmark size ranges from 45m to 564m in diameter (length of long axis; average = 155m), and from a few meters to 77ms TWT (~60m) in depth (average = 8ms TWT = ~6.5m) (fig. 6.27). From observations of time and dip maps of MB2 seafloor, seabed pockmarks are considered to be individual pockmarks, regardless of their size. The smooth circular to sub-circular outer border of large sized pockmarks (with no indentations visible within the limits of the seismic resolution) and the occurrence of a single depression at their centre (fig. 6.6a) suggest these are not the result of coalescence of small-sized pockmarks. As such, for all the spatial analysis and interpretations presented here, it is assumed that all seabed pockmarks of MB2 are individual pockmarks formed by fluid expulsion at a single venting point or area. No seismically resoluble onlap or drape has been observed for the seabed pockmarks.

A quantitative analysis was undertaken for the vast number of mapped pockmarks. The analysis focused on parameters such as pockmark area and depth, water depth of their central point, pockmark width, length, and circularity. This section describes frequency histograms for each of these

parameters, and does a comparative analysis of multiple parameters to assess any relevant trends.

Pockmark morphology histograms

Histogram plots provide quick overviews of the predominant values for each pockmark characteristic (figs. 6.27 to 6.29). The pockmark area histogram shows a predominance of low values, with most pockmarks exhibiting areas below 0.05km^2 (fig. 6.27). The highest frequencies are observed for areas between 0.010 and 0.012km^2, for over 2000 pockmarks in MB2. Low numbers are observed for pockmarks exceeding 0.05km^2 in area. The pockmark depth histogram shows identical trends, with the higher frequencies observed for low depth values (fig. 6.27). Thus, the majority of seabed pockmarks in MB2 have depths below 10ms TWT, with the highest frequency peak observed for values of 2.5ms TWT. Values exceeding 15ms TWT gradually decrease in occurrence, with the highest values recorded being represented by single elements.

The pockmark circularity histogram shows a markedly skewed distribution pattern (fig. 6.28). This parameter indicates the proximity of the pockmark shape to a perfect circle, represented by values of 1 (one), using a calculation based on its area and perimeter. The vast majority of pockmarks are circular to sub-circular, as they show circularity values between 0.9 and 1. A few hundred pockmarks have circularity values between 0.9 and 0.8, indicative of slightly elongated forms. Pockmarks with circularity values below 0.8 occur in very low frequencies, with a minimum value of 0.53 observed for a single element.

The water depth at which seabed pockmarks occur has a more even distribution (fig. 6.29). The highest numbers are found between water depths of -2325ms TWT to -2500ms TWT. Despite the limited information provided by this 2D plot, comparisons between the plot depth values with seafloor time-depth maps and pockmark density maps indicate that the peak values correspond to pockmarks along the axial areas of MB2. The lower frequency values on the water depth plot predominantly correspond to the northern and southern limits of MB2.

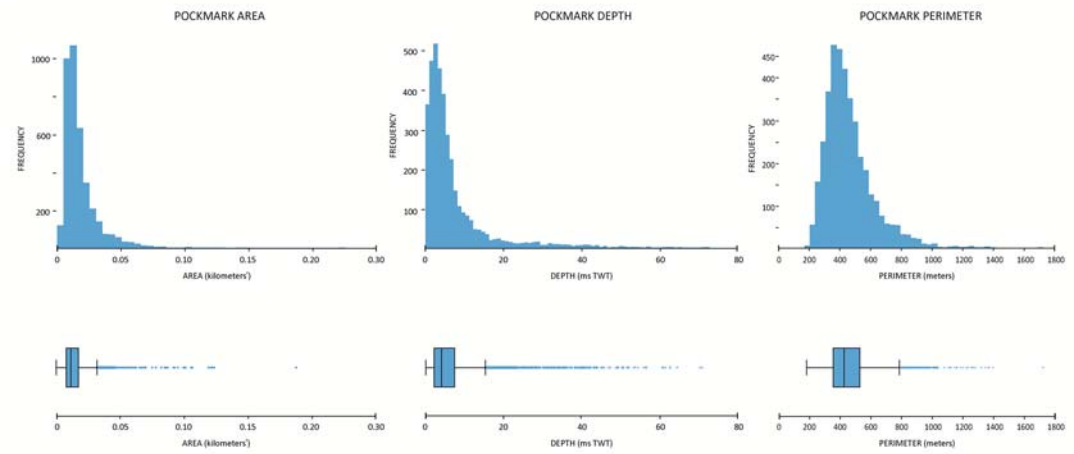

Figure 6.27. General statistics for the morphology characteristics of MB2 seabed pockmarks.

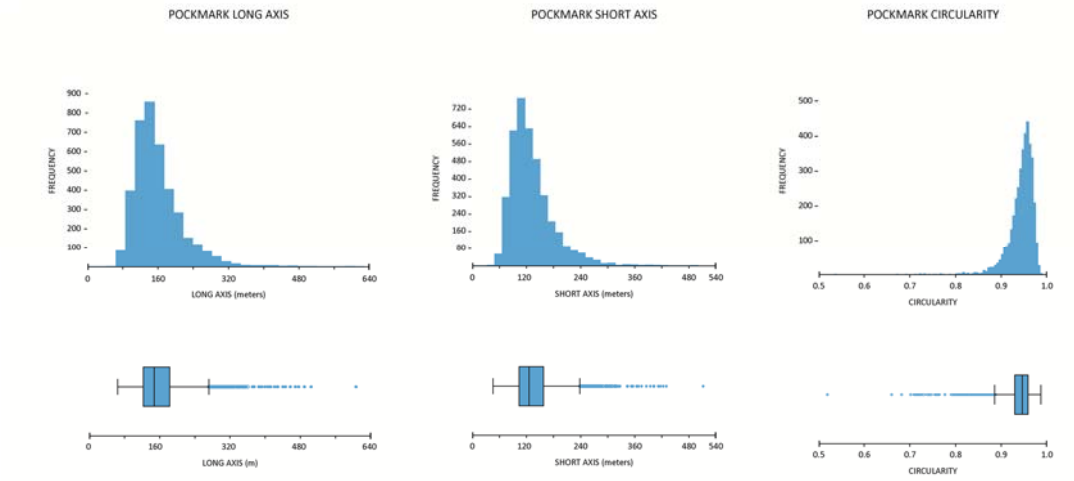

Figure 6.28. General statistics for axis size and circularity of MB2 seabed pockmarks

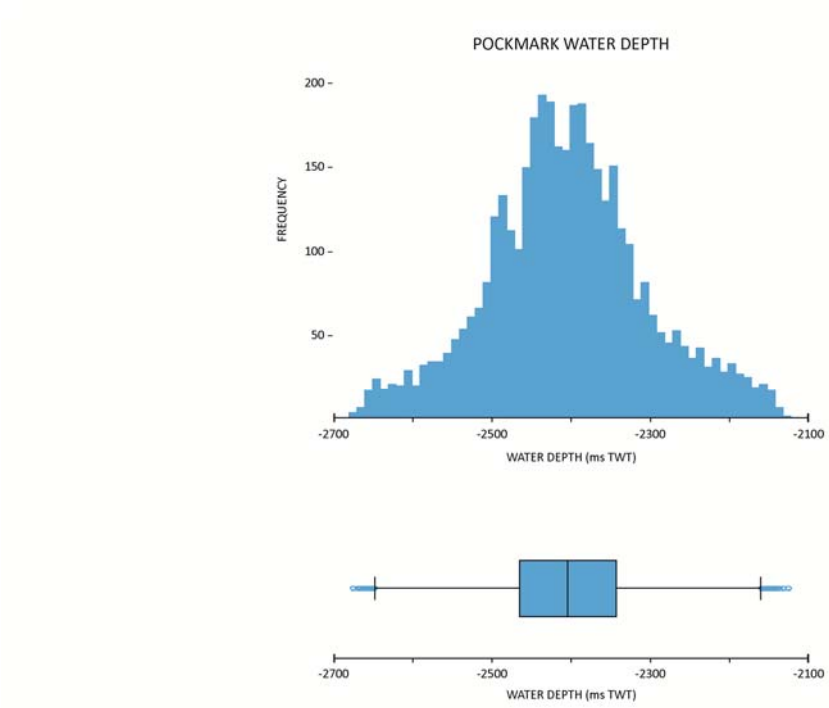

POCKMARK MORPHOLOGY - GENERAL STATISTICS

	AREA meters²	PERIMETER meters	DEPTH ms TWT	LONG AXIS meters	SHORT AXIS meters	CIRCULARITY	WATER DEPTH ms TWT	COUNT
MINIMUM	2287.2	180.2	< 0.1	64.5	43.1	0.54	-2677.2	3896
MAXIMUM	224910.8	1721.3	71.1	606.5	497.0	0.99	-2125.8	
MEAN	17853.5	460.3	6.8	158.9	131.6	0.94	-2403.4	
STANDARD DEVIATION	14663.3	157.2	8.5	53.5	47.2	0.03	101.4	

Figure 6.29. Water depth statistics for the analysed pockmarks, and summary statistical table.

Pockmark morphology scatter plots

Comparisons between various pockmark parameters were made to identify any significant trends between them (fig. 6.30). The closer relationship observed relates the area and depth of seabed pockmarks (fig. 6.30a). The data shows a close increasing relationship between both parameters. The steeper increasing trend is observed for areas up to 0.07km^2

and depths up to 50-60ms TWT. A less steep trend is inferred for areas over 0.1km^2, where depth values range between 40 and 75ms TWT. The levelling of the higher pockmark depth values (to 50-70ms TWT) while the pockmark area increases may suggest the presence of factors limiting their depth increase but not their widening, maybe through pockmark coalescence or sub-surface gas expulsion/expansion conditions.

The comparison of the pockmark width and length shows a very close relationship and a tendency for the presence of sub-circular pockmarks (fig. 6.30b), which had already been confirmed by the pockmark circularity histogram (fig. 6.28). This is shown by the gradual conjugate increase of pockmark width and length, with most values plotting close to the aspect ratio (length/width) = 1 trend, represented on the plot by the black zero-intersecting line (fig. 6.30b). Very few pockmarks plot away from the major trend, with only six showing length values exceeding 2 to 3.5 times their width.

The pockmark area variability and the water depth at which they occur in MB2 has some but limited relationship (fig. 6.30c). Most pockmarks have areas below 0.05km^2 and scatter greatly within the range of water depths recorded, especially for values between -2300 and -2500ms TWT. However, the wide water depth range indicates that small pockmarks are likely to occur anywhere in the basin. A trend does arise for larger pockmark areas (generally above 0.05km^2), indicating that these tend to develop towards deeper locations. Comparing these observations with the seafloor maps, the larger ones occur in regions further away from the axis of MB2. The analysis comparing the pockmark depth and water depth shows a similar pattern to the area-water depth plot (fig. 6.30d). Most pockmarks with depths below 10ms

TWT are scattered throughout the entire range of water depth values. Again, the highest concentration of pockmarks is found between water depths of -2300 and -2500ms TWT. Pockmarks with depths over 20ms TWT show an increasing trend to occur towards deeper water levels. There is also a gradual increase in water depths at which the larger sized pockmarks occur.

The length/width ratio (LW) of the measured pockmarks was compared to both their areas and depths (fig. 6.30e). Both plots show similar patterns and are here described together. The vast majority of pockmarks shows aspect ratios between 1 and 1.7. The highest density of plotted points within this aspect ratio range corresponds to pockmarks on water depths up to 20ms TWT and areas below 0.03km^2. Pockmarks deeper than 20ms TWT have a more limited range of aspect ratios, not exceeding 1.4. In contrast, the highest number of elongated pockmarks is less than 10ms TWT deep. Similarly, pockmarks with larger areas have a lower range of aspect ratios, under 1.5. Only smaller pockmarks with areas below 0.03km^2 show frequent occurrences of aspect ratios above 1.5. These comparisons between the pockmark aspect ratio, area and depth suggest that the larger ones tend to have more circular shapes.

To summarise, the data show that, almost always, larger pockmarks are deeper. These larger, deeper pockmarks also tend to be more perfectly circular than the smaller, shallower ones. These latter types show aspect ratios ranging from circular to mildly sub-circular.

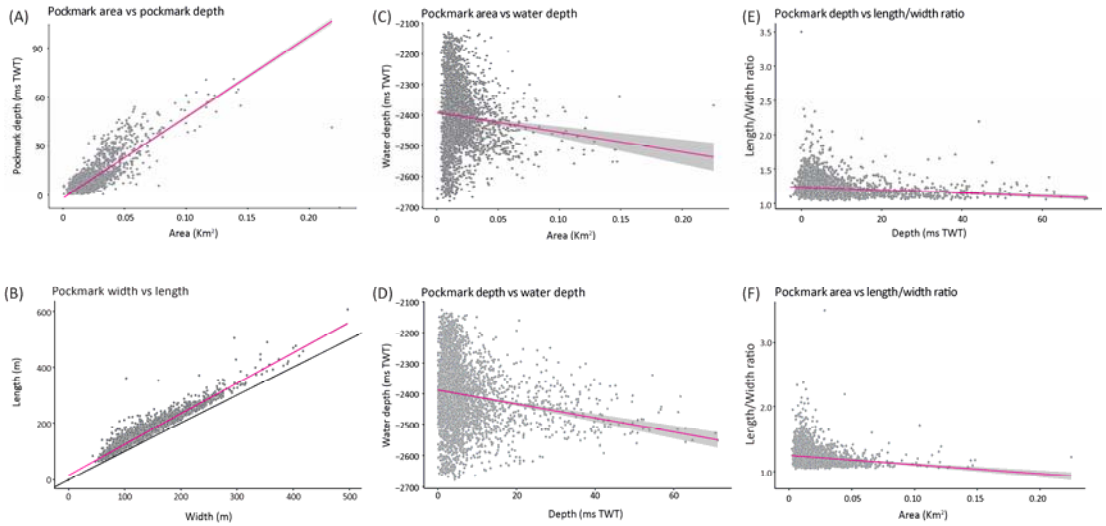

Figure 6.30. Scatter plots relating different morphology characteristics of MB2 seabed pockmarks.

6.3.2. Geomorphology of Unit 3 and pockmark size variability

MB2 pockmarks exhibit the widest range of size and depth of the entire study area. However, the distribution of pockmark size throughout the mini-basin appears to be not arbitrary. Initial observations indicate that the smallest pockmarks are located within the central regions of MB2, whereas large-sized ones occur predominantly along mini-basin rims, in the areas near the limiting salt structures. To understand what controls this lateral sorting of pockmark size, it is necessary to compare size distribution with the geomorphological behaviour of underlying geological features, focusing especially on the estimated fluid source interval (**x-C2**).

6.3.2.1. Unit 3 geomorphology

Three main structural features are associated with mini-basin MB2: the salt ridges on each of its flanks (BSF, BSG, SRA to the west, and BGS to the East), and the central south-plunging anticline with a wide crest coincident

with the axial domains of MB2. The movement of the salt structures and associated faults influences the depositional patterns of Unit 3. To assess this, Unit 3 is sub-divided into four intervals to produce isochron maps bounded by the seafloor surface and horizons **C1**, **C2**, **C3** and **C4** (figs. 6.31 and 6.32).

The interval thickness between the seafloor and horizon **C1** has a range of 200ms TWT, with its lower values along the axis length of MB2 (fig. 6.31a). The minimum thickness (near zero) is observed in the vicinities of diapir SD, with low values also observed further south of it. These patterns are likely due to recent salt growth pulses of SD that deform **C1**. The thickness along the axial central and northern areas of MB2 is predominantly lower than 70ms TWT, but evident increases towards the flanks of the central anticline are observed. Thickness values towards the east do not exceed 90ms TWT, but this is constrained by the 3D survey limits. Thickness increase towards the western flank are more evident due to the steeper gradient of the flank here. These patterns are not uniform as regions up to 5km wide and 100 to 120ms TWT thick can cover about a third of the basin width in central MB2. Towards the north this same range of thickness values is constrained to a thin band less than 2km wide limiting the graben GR to the northwest. The graben GR has the thickest accumulations between **C1** and the seafloor with values between 150 and 200ms TWT. A thicker patch with about 4km width located west of diapir SD suggests the influence of a smaller structure causing localised subsidence. Towards the southern edge of MB2 the interval has uniform thickness values across its width. The seafloor pockmarks scattered on the basin locally influence the isochron thickness patterns on the map, being represented by low values comparatively to their immediate surroundings.

These also clearly highlight the pockmark distribution patterns, with relevance for the arcuate E-W alignments in the central basin, shown as fainter lower thickness lines, and the larger pockmarks within the graben GR standing out as marked localised thinning over 50ms TWT. This effect caused by the pockmarks decreases towards the south, likely due to their smaller size and seafloor expression.

The interval between **C1** and **C2** has a similar thickness range to the overlying one, of about 210ms TWT, and identical areal thickening trends (fig. 6.31b). However, the central domains show a more constrained thickness range of 10ms TWT along the axis. The thinner accumulations are evident along the axis of MB2, coincident with the anticline axis. Thickness values towards the NW of MB2 increase to >200ms TWT. The highest values are recorded within the graben GR, but the lateral thickness increase is less pronounced when compared to the seafloor-**C1** interval. Other localised thickened areas towards the centre and south occur adjacent to the salt structures. The isochron map shows quite distinctively the presence of polygonal faults, especially in the areas with higher thickness values. The presence of pockmarks influencing the thickness patterns is less evident, although isolated peak thickness values within the areas where polygonal faults are well visualised can correspond to 'bulls-eye' pockmarks.

The isochron map between horizons **C2** and **C3** shows that marked thickness contrasts are more localised when compared to the overlying interval, and has the largest thickness range observed, reaching 236ms TWT (fig. 6.21c). However, the main trends are still maintained due to the influence of the central anticline, with the thinner accumulations observed along the axis

of the mini-basin. The highest thickness values occur within the graben GR, located to the NW of MB2. Eastwards of the graben there is a general thickness decrease, but there are sharp drops of thickness (exceeding 100ms TWT) near faults. More gradual thickness changes occur where structures are smoother. Similarly to the interval above, the isochron maps highlight the fault patterns in the area. Polygonal faults are widespread, and PPFs are identifiable in the thick sequences within the graben GR. On the central area, wide E-W arcuate lines with comparatively lower thickness than their surroundings are discernible. These are coincident with the arcuate pockmarks alignments at the seafloor, possibly indicating a control factor is present between **C2** and **C3** (as discussed in section 6.2). The isochron map also shows a series of long, NW-SE trending faults along the axis of the mini-basin. These occur as three main alignments of normal fault segments of variable sizes, but not exceeding 6km in length. These large faults have arcuate shapes with the concavity facing west, towards structure BSF. Two N-S faults linked to the southern flank of diapir SD are also highlighted on the ischron map. These show marked arcuate shapes, with the two fault concavities facing each other, and are interpreted as radial faults.

The isochron patterns between horizons **C3** and **C4** differ in some aspects from the overlying intervals, and have a smaller range of 140ms TWT (fig. 6.31d). A key feature is that the axial thinning identified towards the shallow levels is less evident. The southern edge of MB2, which was predominantly thicker on overlying intervals, either has the same or lower thickness when compared to the central domains of the mini-basin. The thicker accumulations are found within the graben GR, but with lower values

and a limited extend. Contrasting with the above intervals, where thickness within the graben was systematically the highest, between **C3** and **C4** the thinner accumulations occur within the structure. The northern section of MB2 shows a widespread thickening of this package with values in the order of 70 to 80ms TWT. Polygonal fault patterns are not observed, and this interval is located below the polygonal faulted tier. However, the NW-SE faults and the diapir-attached faults are well evidenced between **C3** and **C4**. The isochron map also evidences numerous and dispersed sub-circular to elongated features characterised by low thickness values. These correspond to the pinnacles of rafted blocks included in the MTD underlying horizon **C4** (see section 6.3.1). As these features constitute marked topographic highs on the MTD top surface, they influence the depositional morphology of horizon **C4** and the accommodation space between it and **C3**. Furthermore, differential compaction may increase the local deformation of **C4** caused by the underlying blocks.

The distribution of the seafloor pockmark sizes can be broadly associated to the isochron thickness patterns observed for the sub-intervals of Unit 3 (fig. 6.32). The larger ones occur closer to the salt structures and where the thickness is higher, such as within the graben GR and the thicker area west of diapir SD. The E-W arcuate pockmark alignments in the axial domains of MB2 overlie the areas where the interval thickness is lower, and coincident with the anticline axis. Strikingly, the shift of orientation of the E-W alignments towards the flanks of the mini-basin is generally coincident with areas where stratal thickening is observed. This shift of orientation and stratal thickening is also broadly associated with increasing pockmark size.

Pockmarks are absent along the elongated area south of diapir SD that is characterised by low thickness values in all intervals.

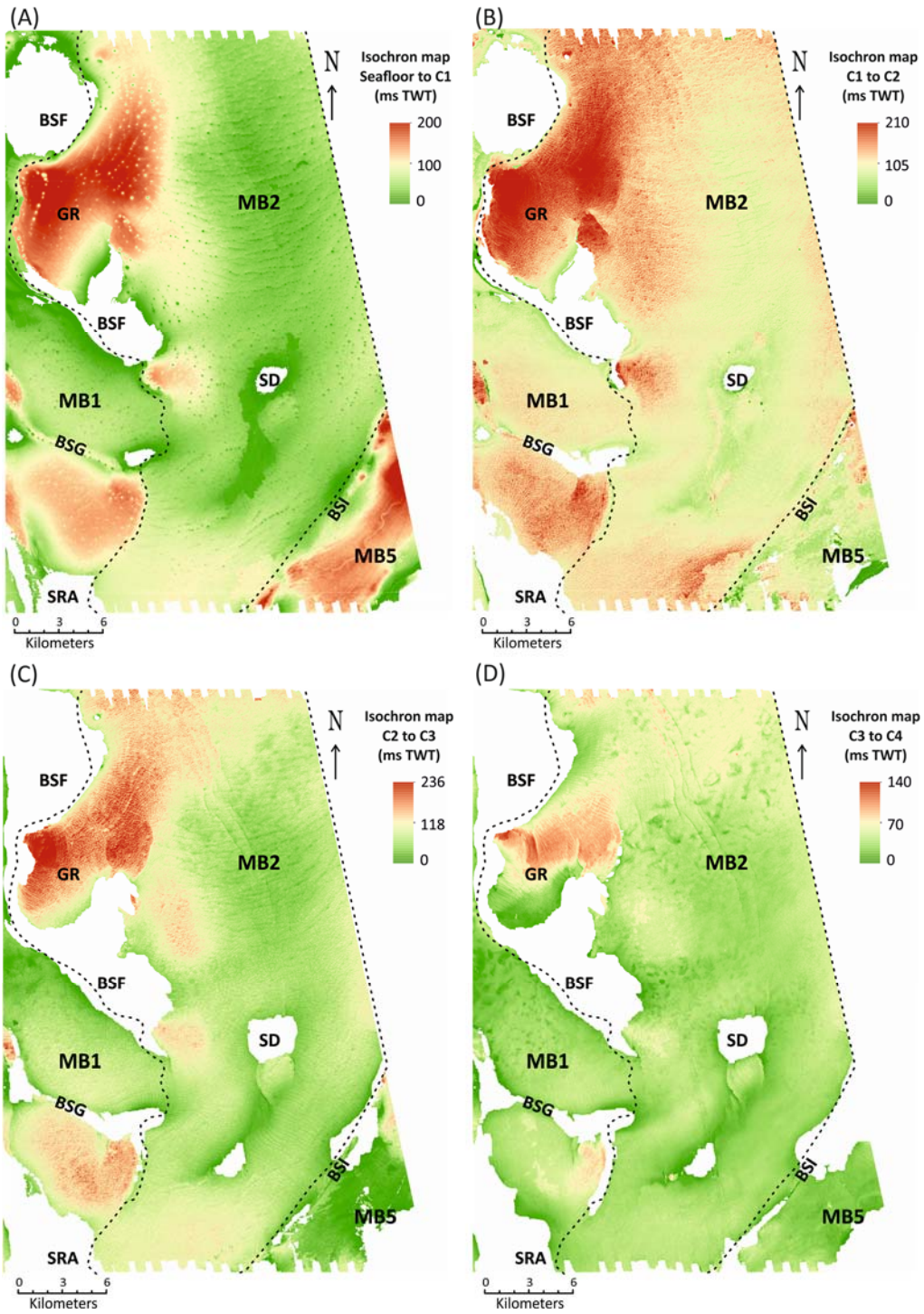

Figure 6.31. Isochron maps for the seismic intervals **(A)** seafloor-**C1**, **(B) C1-C2**, **(C) C2-C3**, and **(D) C3-C4**. SR = salt ridge; BS = buried salt structure; SD = salt diapir; GR = graben; dashed line = MB2 limit.

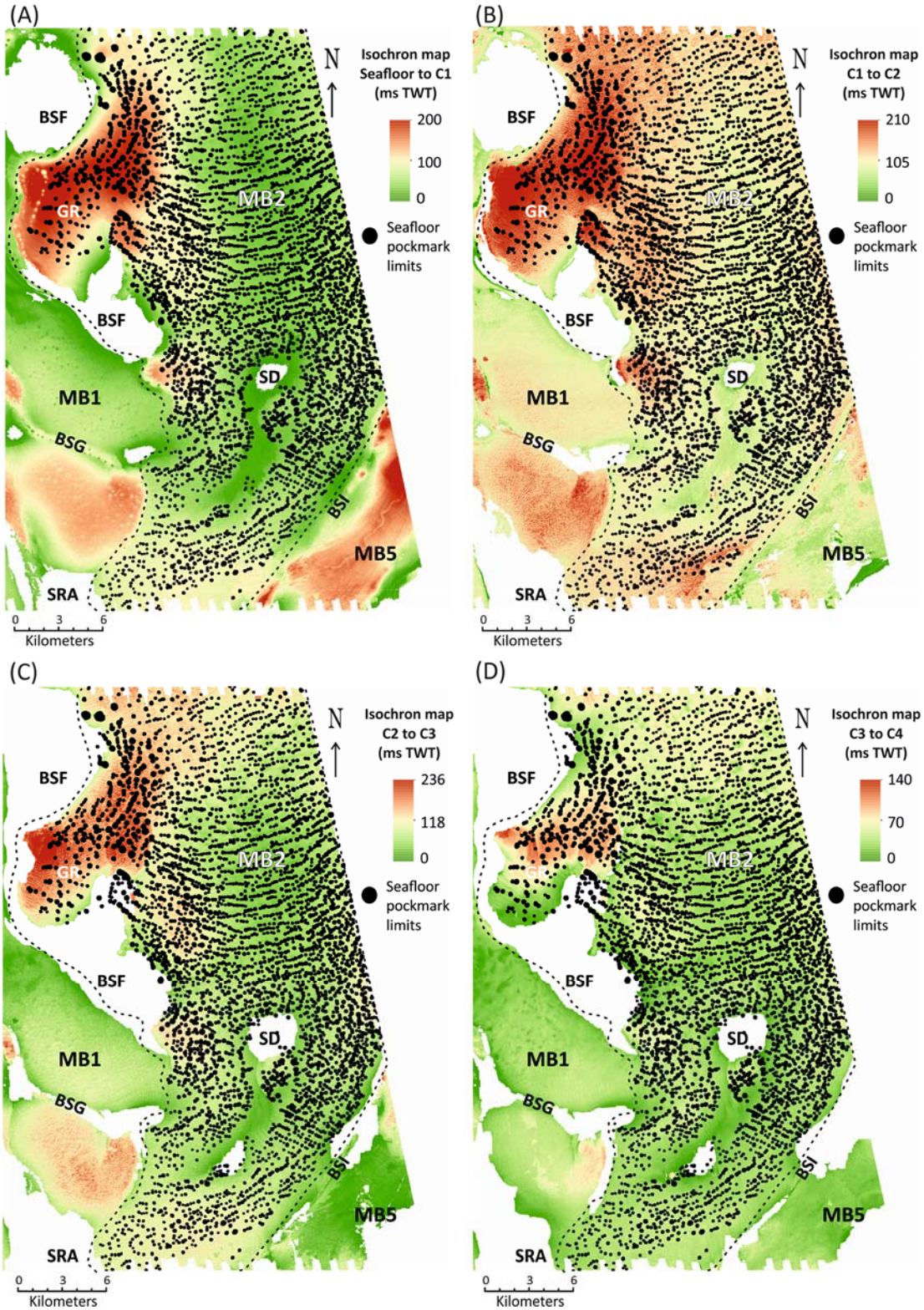

Figure 6.32. Isochron maps for the seismic intervals **(A)** seafloor-**C1**, **(B) C1-C2**, **(C) C2-C3**, and **(D) C3-C4**, showing seabed pockmark locations. SR = salt ridge; BS = buried salt structure; SD = salt diapir; GR = graben; dashed line = MB2 limit.

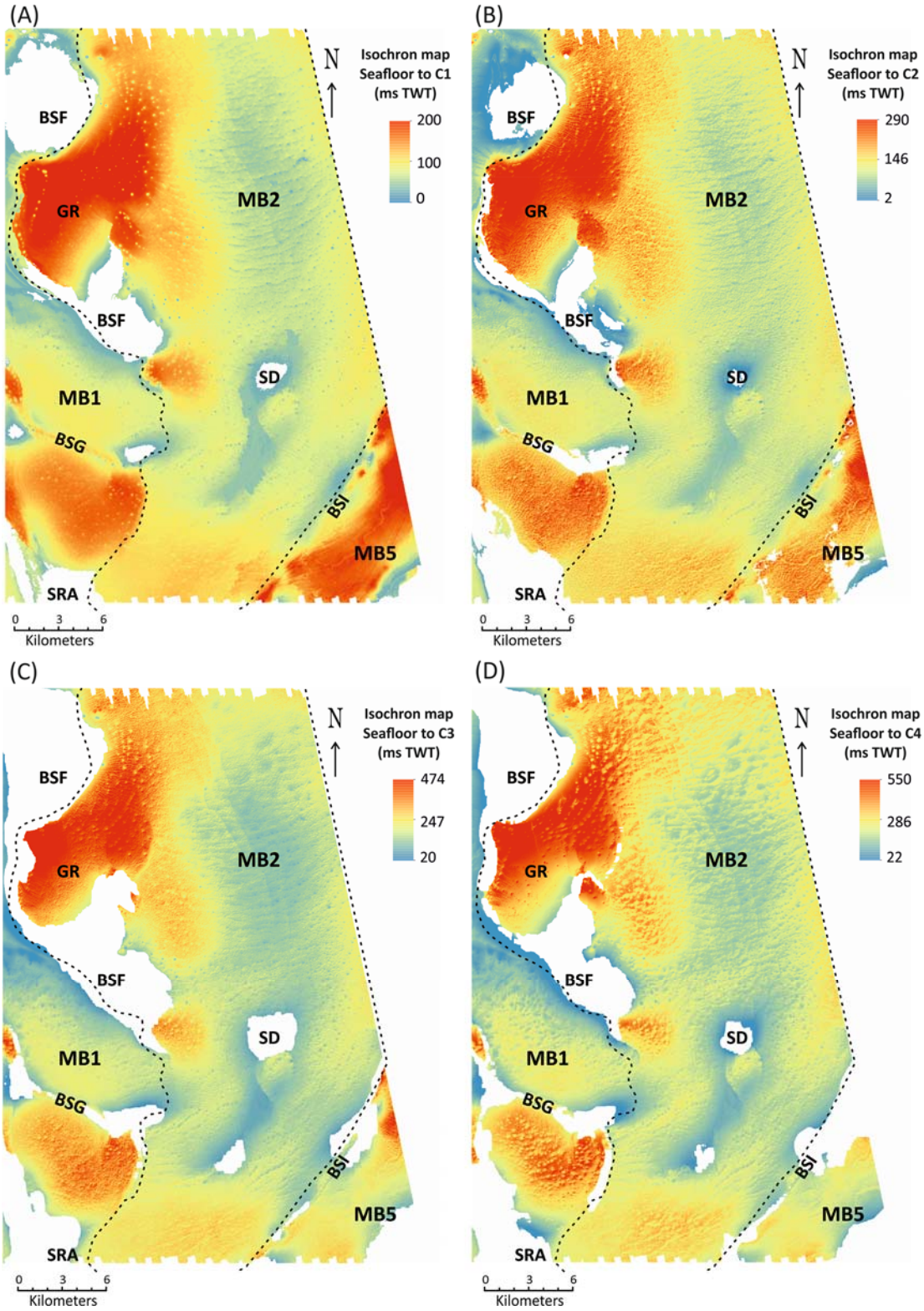

Figure 6.33. Isochron maps for the seismic intervals **(A)** seafloor-**C1**, **(B)** seafloor-**C2**, **(C)** seafloor-**C3**, and **(D)** seafloor-**C4**. SR = salt ridge; BS = buried salt structure; SD = salt diapir; GR = graben; dashed line = MB2 limit.

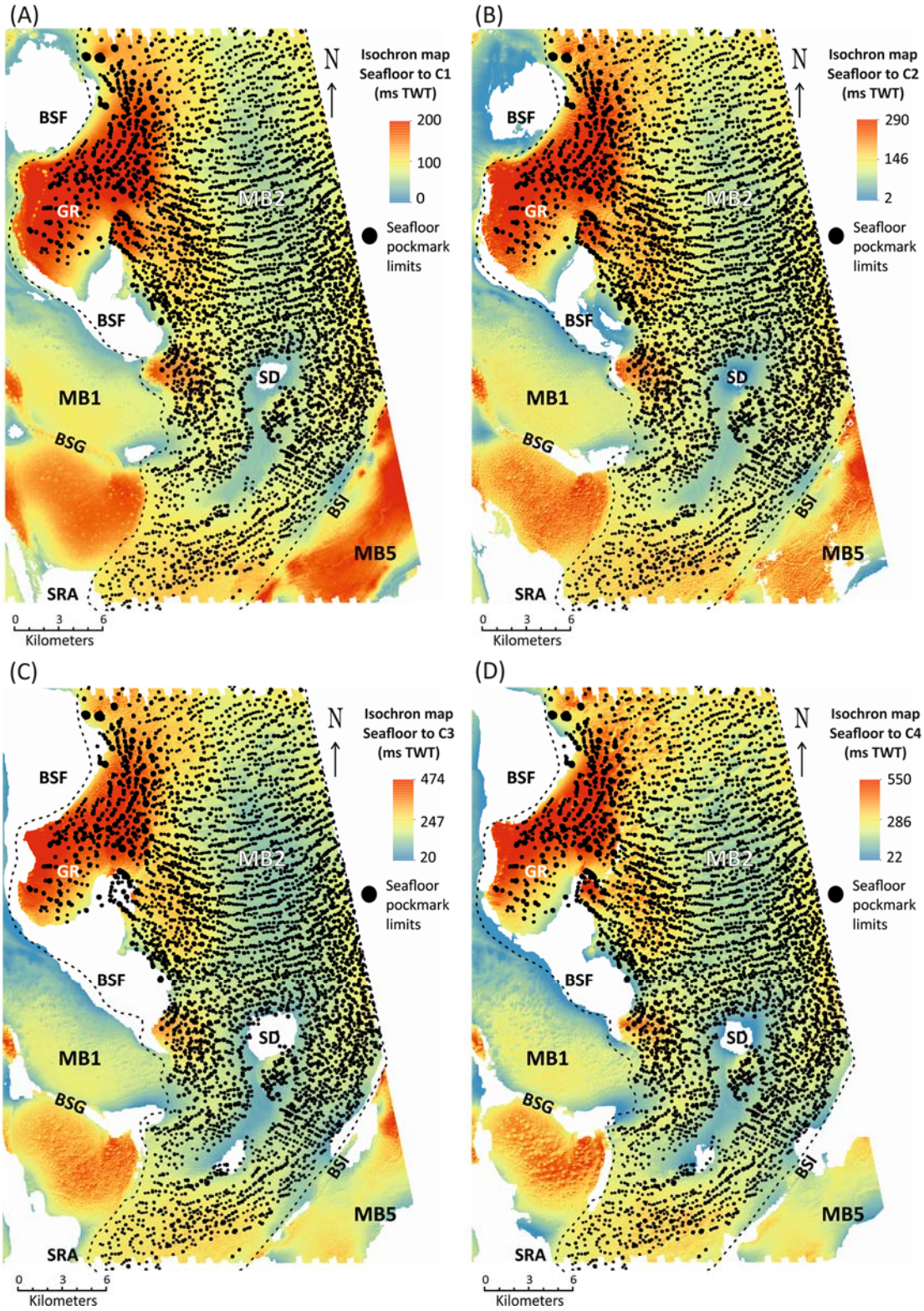

Figure 6.34. Isochron maps for the seismic intervals **(A)** seafloor-**C1**, **(B)** seafloor-**C2**, **(C)** seafloor-**C3**, and **(D)** seafloor-**C4**, showing seabed pockmark locations. SR = salt ridge; BS = buried salt structure; SD = salt diapir; GR = graben; dashed line = MB2 limit.

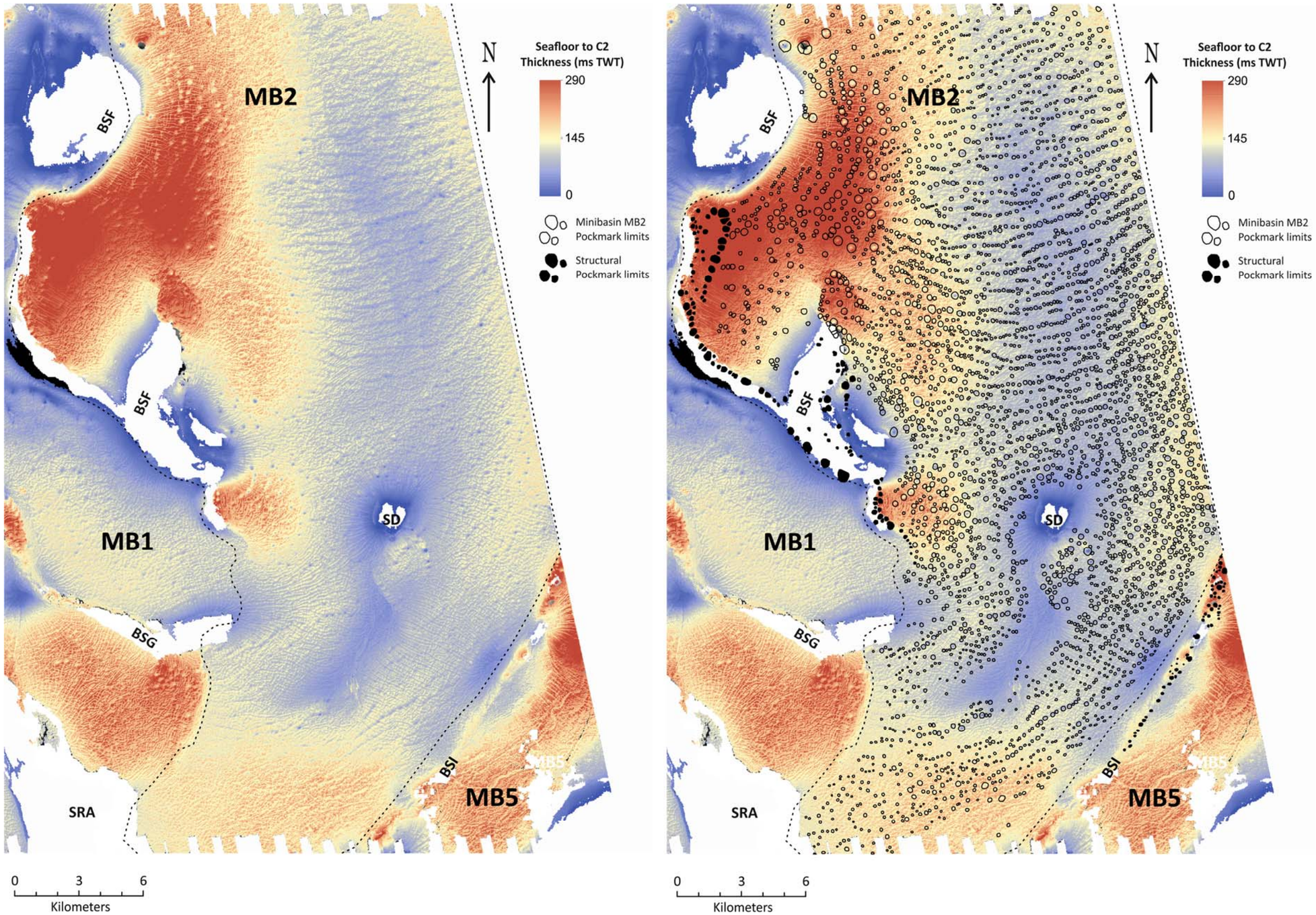

Figure 6.35. Isochron maps for the seismic interval seafloor-**C2** (A) without and (B) with the overlay of pockmark-bounding polygons. Salt-related pockmark limits are shown filled in black for comparison with shallow-sourced pockmark morphology. SR = salt ridge; BS = buried salt structure; SD = salt diapir; GR = graben; dashed line = MB2 limit.

6.3.2.2. Size distribution of seabed pockmarks

This section focuses on the statistical analysis of the characteristics of seabed pockmarks and their relationship to the position relative to the axis of mini-basin MB2 (which corresponds to the axis of the buried anticline structure) and the depth to horizon **C2**, interpreted as the base of the estimated fluid source interval (figs. 6.33 to 6.35).

Pockmark size distribution histograms

The frequency analysis relating the pockmark position in the mini-basin relative to its axial region indicates that 71% (2788 of a total of 3896) occur within a distance of 5000m from the MB2 axis (fig. 6.36). The histogram plot shows a gradual decrease in frequency for distances between 5000 and 10000 metres. Above the latter value, the plot trend flattens and pockmarks occur in relatively low frequencies for the distances >10000m away from MB2 axis.

The histogram of depth from seabed pockmark to horizon **C2** (interpreted to represent the base of the fluid source level) shows most pockmarks occur within source depth values of 65 and 100ms TWT (fig. 6.36). Comparing these values with the seabed depth to **C2** isochron map (fig. 6.35), the peak frequencies observed on the histogram correspond to pockmarks present within the axial domains of MB2. A gradually decreasing number of pockmarks have depths to **C2** between 100 and 150ms TWT, representing the gradual increase in depth of **C2** and the decreasing number of pockmarks away

from the axis of MB2. Low numbers of pockmarks have depths to **C2** over 200ms TWT, being present towards the flanks of the mini-basin.

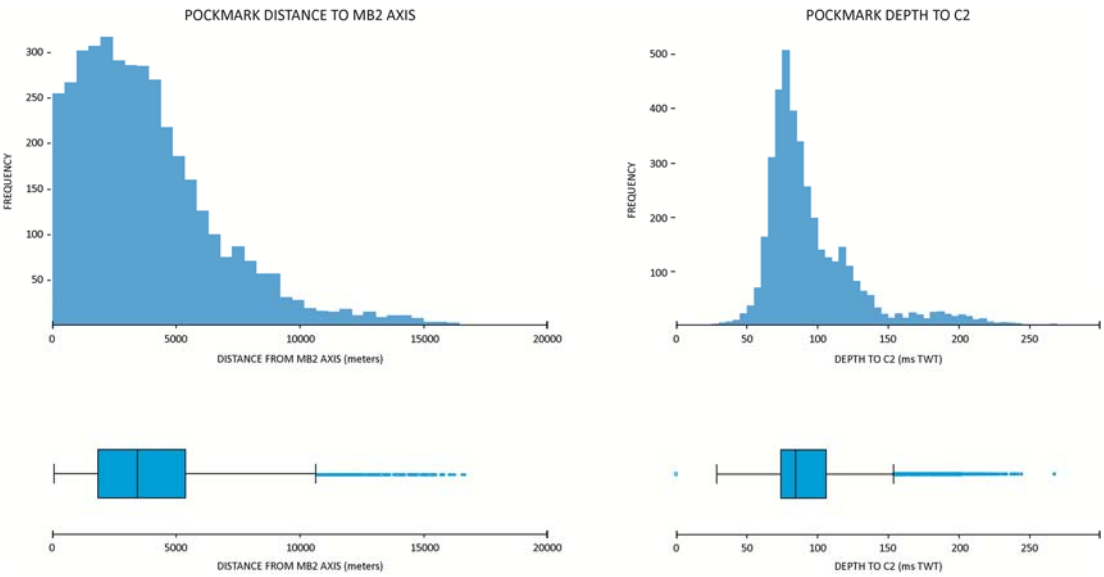

Figure 6.36. General statistics for the pockmark distance to MB2 axis and pockmark sub-seabed depth to **C2**.

Pockmark size distribution scatter plots

A scatter plot relating pockmark area and its corresponding depth to source layer (**C2**) shows marked data dispersal (fig. 6.37a). The highest concentration of points indicates most pockmarks with areas below 0.05km^2 occur above 60 to 150ms TWT from their source. Apart from this, the remaining points are scattered within the data ranges observed. As pockmarks with the same area (large or small) can occur at the same depth from horizon **C2**, there is no clear relationship between these parameters evidenced by this scatter plot.

The pockmark depth and the depth to **C2** scatter plot also show limited correlation between these parameters (fig. 6.37b). There is a dense cluster of points for pockmark depth up to 10ms TWT tending to occur between depths to **C2** between 50 and 100ms TWT. However, and similarly to what is described for the pockmark area, the pockmark depths and their corresponding depths to **C2** have scattered distributions.

The scatter plot relating depth to **C2** and the water depth of the pockmarks indicates that a relationship can be established, but values can scatter significantly from the trend (fig. 6.37c). The marked dispersal occurs for depth to **C2** values between 50 and 150ms TWT, which have corresponding pockmark water depths within the whole range of values recorded (2100 to 2650ms TWT). Comparing this to the thickness seabed-**C2** maps, this spread pattern corresponds to the higher number of pockmarks along the axis of MB2. The relationship becomes clearer towards the higher depths to **C2**, which show a correlation to increasing pockmark water depths.

Pockmark morphological parameters were contrasted to their distance to the axis of mini-basin MB2 (figs. 6.37d and 6.37e). Pockmark area and depth variations have identical increasing trends with distance from the MB2 axis, and most features occur within <7500 metres. Within this interval, the large majority of pockmark area and depth values are of 0.05km^2 and 20ms TWT, respectively. For distances between 7500 and 10000m, there is an increased scattering of the higher values. Pockmarks have areas up to 0.17km^2, although an isolated value of 0.23km^2 was recorded. Pockmark depth also increases with distance to MB2 axis, with numerous occurrences between 20 and 70ms TWT. For distances between 10000m and 15000m, the pockmark area and depth

values are less scattered (areas up to 0,05km^2 and depth up to 20ms TWT), although a few large values for both parameters were recorded. Both pockmark area and depth tend to increase with distance away from the axis of MB2, but correlation may be limited due to high data scattering with increasing distance. The scatter plot relating the depth of pockmark to source interval (**C2**) shows increasing depth values with distance away from the mini-basin axis (fig. 6.37f). This is expected as it follows the morphology of horizon **C2**, which mimics the buried anticline structure. Of relevance is the marked increase of **C2** depth from distances >7500m onward, where many of the pockmarks occur within the graben area (GR) where horizon **C2** is deeper when compared to the remaining areas of the mini-basin. Furthermore, this increase in **C2** depth between 7000m and 10000m is coincident with the distance from axis where increases in the overall pockmark size (i.e., area and depth) are observed.

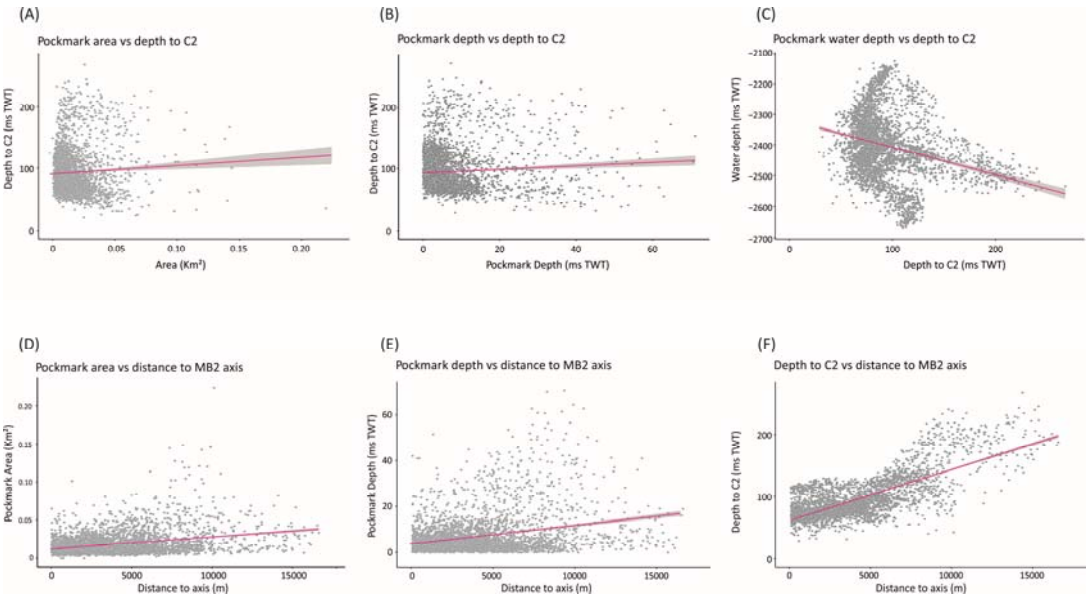

Figure 6.37. Scatter plots relating different morphology characteristics of MB2 seabed pockmarks with **(A, B, C)** sub-seabed depth of **C2**, **(D, E, F)** and distance to MB2 axis.

Multi-parameter comparative plots for pockmark size distribution

The scatter plots have a limited capacity to illustrate the spatial variability of pockmark parameters. Scatter bubble plots are here used for a simultaneous representation of multiple pockmark parameters and their spatial variability. Plotting the XY pockmark position, bubble size as a representation of pockmark area and bubble colour for pockmark depth. This plot provides a clearer observation of the relationship between these parameters (fig. 6.38). The axial area of MB2 has a predominance of small-sized pockmarks with depths generally below 20ms TWT, especially on the northern half of the basin. Larger axial pockmarks, commonly with higher depths, are scarce in the northern and central areas of MB2, but are more frequent in the vicinities of diapir SD and towards the southern edge of MB2. The distribution of pockmark size shows a clear increase in both pockmark area and pockmark depth towards the flanks of MB2, with the larger ones present near the salt structures. Consequently, the arcuate E-W alignments on the central domains of MB2 include increasingly larger pockmarks from the trail centre towards its eastern and western limits. The larger pockmarks on the northwest flank of MB2 often form N-S arcuate alignments parallel to the salt ridge BSF, and within the graben GR present at this location. These areas include the deepest pockmarks observed in MB2, often exceeding 50ms TWT. Despite the presence of large pockmarks, smaller sized ones also occur between them. Agglomerations of larger pockmarks are present southwards between diapir SD and the flanking salt ridges. They have depths generally below 50ms TWT. The southernmost sections of MB2 have a few larger sized pockmarks with depths between 20 to 40ms TWT, spatially coincident with a

deep buried salt structure. However, the majority of pockmarks on the southern domains of MB2 are less than 20ms TWT deep, being predominantly further apart and smaller when compared to the rest of MB2. Pockmark alignments perpendicular to BSI on the SE limit of the basin and associated to PFFs (see section 6.2) have some of the smaller sizes observed. These are often smaller than many pockmarks identified on the arcuate alignments observed in the central area of MB2.

The comparison between the distribution of pockmark areas and the depth seabed-**C2** shows a tendency for larger ones to occur in locations where **C2** is deeper (fig. 6.39). This further strengthens the influence of the basin structure on seabed pockmark size. The depth to the source is predominantly below 100ms TWT in the axial area, especially where the arcuate alignments occur. The minimum depth values observed near diapir SD are due to shallowing of **C2** along the flanks of the rising salt structure, and are mostly associated with larger pockmarks. The general increase of pockmark size with increasing depth to **C2** is clearly exemplified on the western flank of the mini-basin. This is particularly relevant within the graben GR adjacent to salt ridge BSF, which causes a deepening of horizon **C2**. This, and the proximity to salt ridge BSF, suggests a relevant influence of structural controls and deeper source levels for the development of larger pockmarks in MB2.

The compiled observations of the variation of pockmark depth and area, its distance to the source (**C2**) and the position within mini-basin MB2 show a clear relationship between them. The smaller pockmarks occur in large numbers closer to the axis of the mini-basin, where the depth to the source barely exceeds 100ms TWT. Pockmark sizes closer to the axis barely exceed

0.1km^2 and depths of 20ms TWT. As the distance from the mini-basin axis increases, the size of the pockmarks also follows a steady increase. In the example here studied, this is represented by a higher number of pockmarks deeper than 30ms TWT, and where the maximum value of 73ms TWT is reached. This is also where the depth from the seafloor to the source horizon has a marked increase.

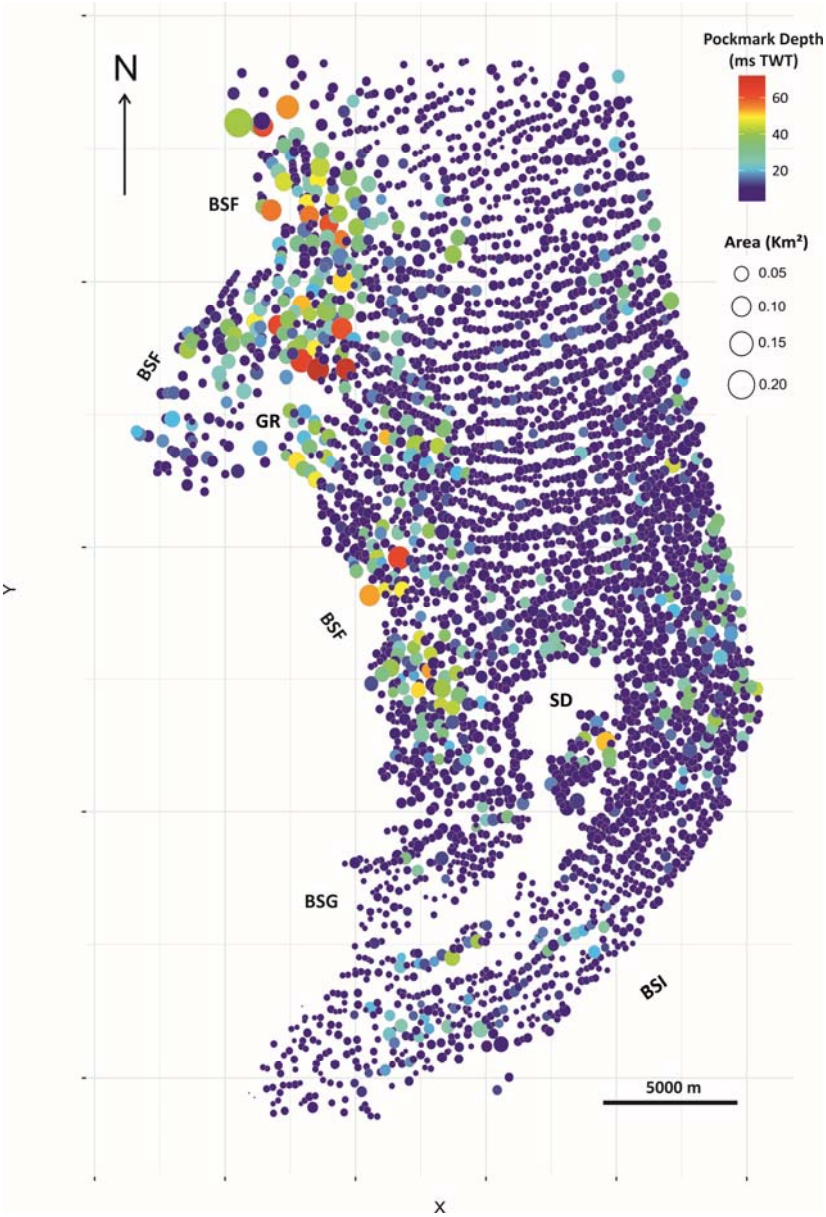

Figure 6.38. Bubble scatter plot showing seabed pockmark size distribution in MB2. Bubble size = pockmark area; bubble colour = pockmark depth. SR = salt ridge; BS = buried salt structure; SD = salt diapir; GR = graben.

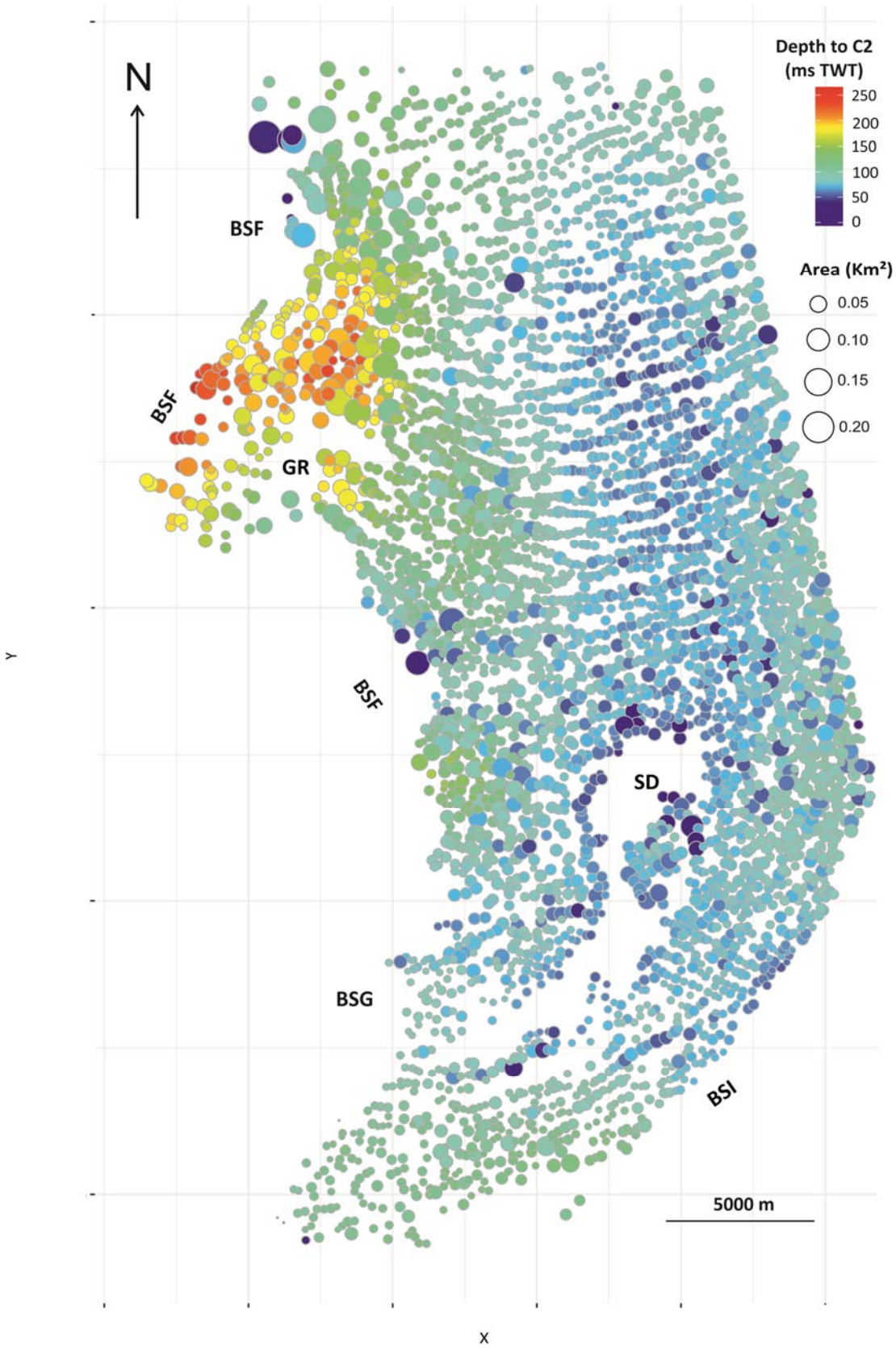

Figure 6.39. Bubble scatter plot showing seabed pockmark size distribution and depth to fluid source in MB2. Bubble size = pockmark area; bubble colour = sub-seabed depth of **C2** (base of estimated source interval). SR = salt ridge; BS = buried salt structure; SD = salt diapir; GR = graben.

6.3.3. Pockmark size variability and fluid source depth – discussion

From the analysis of the spatial distribution of pockmark sizes throughout mini-basin MB2, it is possible to deduce that the size (both depth and area) of seabed pockmarks generally increase away from the axial regions of MB2, which coincide with the crest of a large buried anticline structure (figs. 6.4 and 6.37). The hemipelagic sediments that compose Unit 3 were deposited above this structure, preserving its morphology up towards the seabed (despite a minor upward attenuation of the anticline topographic relief). As such, the thickness of Unit 3 sediments is the thinnest along the axial regions of the anticline, thickening progressively towards the flanks of the structure (in a E-W direction), where a significant mini-basin subsidence occurred. Thus, the depth below seabed of the estimated fluid source interval for pockmarks (interval **x-C2**) varies according to the geomorphology of the buried anticline: the source interval sits at deeper sub-seabed levels along the flanks of the anticline, where the highest rates of subsidence took place (fig. 6.40). As these regions correspond to the marginal areas of MB2 where the larger-sized pockmarks are observed, it is likely that there is a relationship between the depth of the fluid source interval and the size of the pockmarks fed from it.

To verify this interpretation and to provide a better understanding of the shallow plumbing system in place, a comparative analysis of pockmark size (depth and area), distance to MB2 axis and sub-seabed depth of **C2** was made, based on graphical representations of all the data acquired for MB2 pockmarks. A multi-parameter scatter bubble plot was especially created for this (fig. 6.41). The abscissae axis (x-axis) represents the distance (in meters)

at which a pockmark is located from the MB2 axis along a E-W direction, and the ordinates axis (y-axis) shows pockmark depth (in ms TWT). The bubble size is proportional to pockmark area (in km^2) and its colour represents the depth of **C2**, measured below the seabed (in ms TWT). The distribution of bubble size and colour in the plot confirms the existence of a pockmark size-source depth relationship. Smaller-sized pockmarks (small bubbles) are located preferentially in the central regions of MB2, within <5000m from the anticlinal crest, where the source interval occurs at its shallowest depths (blue-coloured bubbles). Larger-sized pockmarks (large bubbles) occur mostly within the rims of MB2 (distances >10000m from the anticline axis), where the source layer is deeper below the seabed (yellow-orange-red bubbles). From distribution of bubbles in this plot, it is possible to conclude that there is a proportional relationship between pockmark size and the depth of the fluid source. Regions where the fluid source interval is deeper below the seabed tend to exhibit larger-sized pockmarks. Thus, generally the deeper the fluid source, the larger the pockmark it will produce when fluids are expelled at the seafloor.

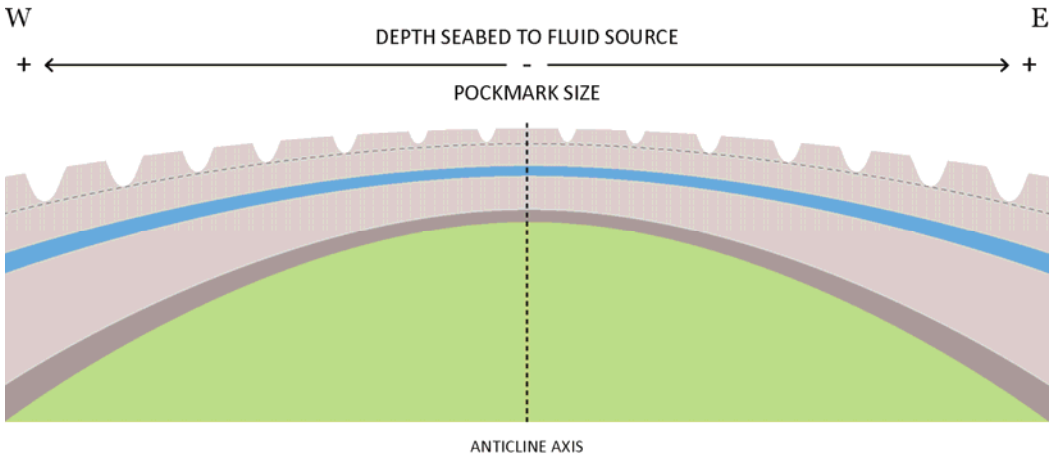

Figure 6.40. Diagram showing the general structure of MB2 axial anticline, pockmark size variation, and thickness and depth variation of seismic Unit 3 (in light grey). Estimated source interval **x-C2** represented in blue. MTD = dark grey; Unit 2 = green.

The mechanism behind this phenomenon may be related to the absolute magnitude of pore pressure in the storage layer at the source interval. Pore fluid pressure may be influenced by the source depth below seabed (fig. 6.42). As the source interval is increasingly deeper and buried under a thicker overburden, pore fluids may become more overpressured if the sedimentation rate exceeds the capacity of the permeability to drain the necessary fluids from the compacting sediments such that they become undercompacted (Magara, 1978). Higher fluid pressures may in turn promote the generation of feeding conduits of larger diameters and more seabed sediment remobilisation during pockmark formation (greater eruptive force), producing larger pockmarks. Moss (2010) argues that pipe diameter may be a function of overpressure, in which a greater degree of fluid pressure may produce a larger seal hydrofracture system. Fracture size may also be dependent on the lithological properties of the seal, such as fracture potential, sediment type and compositional heterogeneities, permeability or contextual setting. If these parameters are laterally homogeneous throughout the seal, the degree of overpressure is related to the size of the seal bypass hydrofractures and, consequently, the size of the feeding conduit (Moss, 2010). Thus, pockmark size may provide a relative proxy for overpressure at the fluid source. In MB2, pockmark size variability may result from lateral variations of fluid pressure at the source, which is a function of depth. As such, the main control on pockmark size may be the degree of overpressure given by a proxy, namely the depth of the fluid source interval.

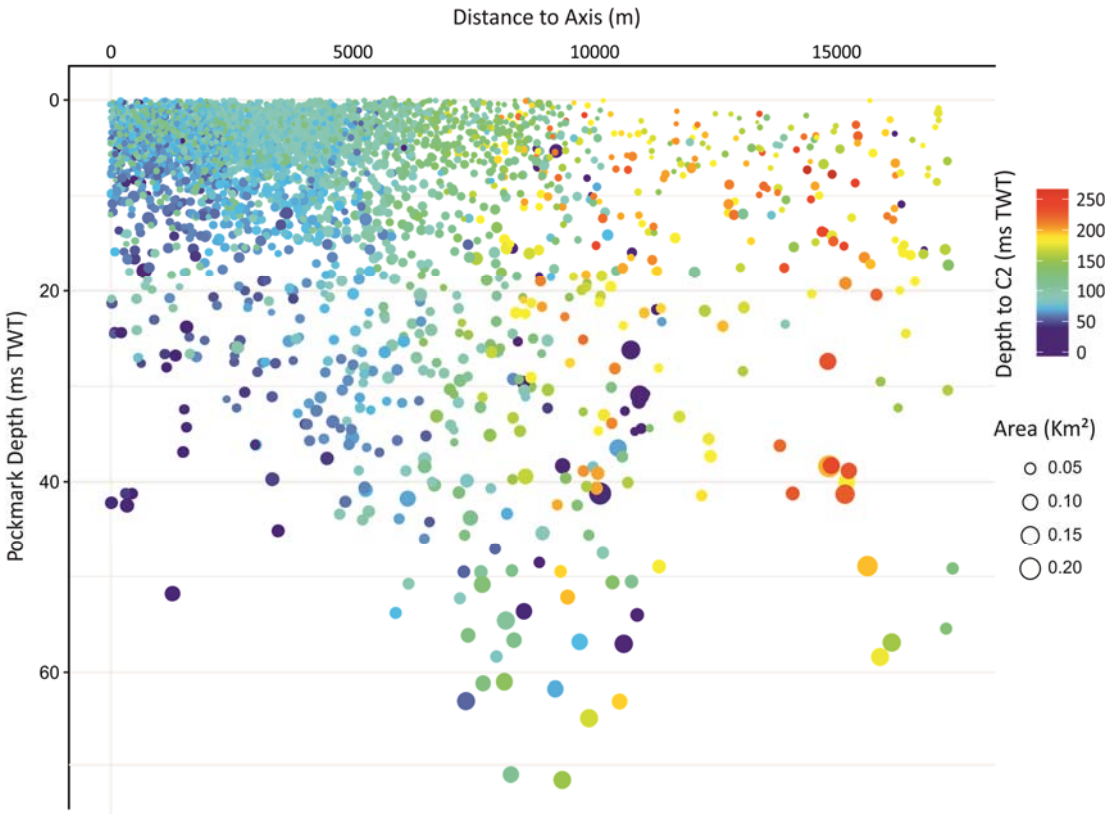

Figure 6.41. Bubble-scatter plot showing the relationship between seabed pockmark size (area and depth), sub-seabed depth of the base of the estimated source interval (**C2**), and pockmark location in relation to MB2 axis (correspondent to the buried anticline axis). X axis = distance to MB2 axis; Y axis = pockmark depth; bubble size = pockmark area; bubble colour = sub-seabed depth of horizon **C2**.

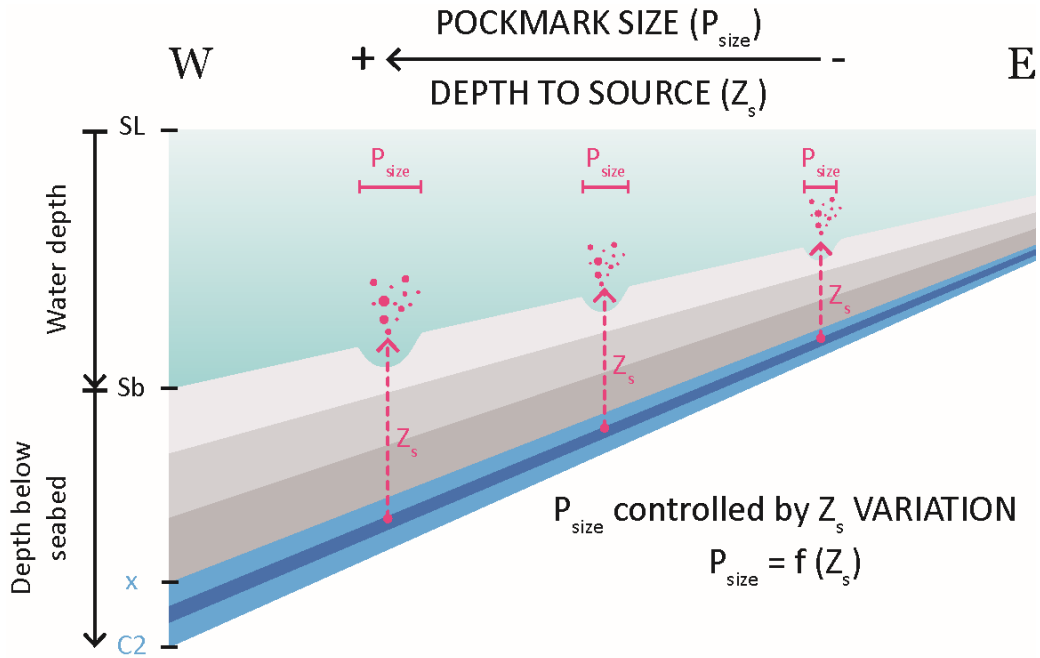

Figure 6.42. Diagram explaining the relationship between pockmark size and depth to source (see main text for explanation).

Local exception – Graben area (GR)

An exception to the above discussion is a sub-area near the west border of MB2, delimited by major extensional tectonic faults which cause subsidence of this region. Seabed pockmarks are much scarcer in this area compared to the entire MB2. Four seismic observations may explain this lower pockmark density: 1) there is lateral variation of seismic response of **C1-C2** sediments (figs. 6.14d and 6.15d); 2) increased frequency of polygonal faults; 3) presence of bulls-eye pockmarks at **C2** level; 4) occurrence of major tectonic faults. All these factors combined may cause pore fluids to be released from Unit 3 sediments prior to the last fluid expulsion event, so less fluid is stored within these to be expelled during seabed pockmark formation.

6.4. Conclusions

- 3896 individual seabed pockmarks have been mapped within salt mini-basin MB2, between -1645m to -2075m below sea-level. Pockmark size ranges from 45m to 564m in diameter (length of long axis; average = 155m), and from a few meters to ~60m in depth (average = ~6.5m).
- MB2 seabed pockmarks were most likely formed during the same event that originated the seabed pockmarks elsewhere in the study area (see Chapters 4 and 5), and were fed by fluids stored within the shallow interval **x-C2** (stratigraphically located in the hemipelagic Unit 3) prior to their expulsion.
- The seabed pockmarks in MB2 are mostly distributed in long arcuate

alignments perpendicular to the general N-S slope, striking along a E-W direction. Their apices (points of highest curvature at the middle of the linear trail) follow the central axis of MB2 and point downslope (southwards).

- These arcuate alignments show no spatial association with any seismically resoluble discontinuity at depth. The lack of seismically visible evidences (discontinuities) that explain pockmark patterns at the seabed suggests that the mechanism that controls the distribution of fluid migration pathways may operate at the sub-seismic scale (falling below the seismic vertical resolution limit).
- From the curvilinear arrangement of seabed pockmarks, it is interpreted here that an incipient gravitational sliding of shallow sediments took place, either producing or exploiting pre-existing sub-seismic discontinuities (likely related to the polygonal fault system) that control upward fluid migration to form arcuate seabed pockmark alignments in MB2.
- The incipient gravitational sliding of shallow sediments is fuelled by gravitational forces downslope. The main driving mechanism for this may be the slope topography created by subsidence of the southern region of MB2, accompanying the salt withdrawal related to diapir SD growth that started prior to the deposition of the MTD. The surface of detachment for the incipient shallow gravitational sliding process may be stratigraphically located at **C2** level.
- Pore fluid expulsion may be promoted by downslope compression of shallow sediments as pervasive dewatering may occur due to shortening (downslope contraction) and horizontal compaction.
- The locus for the formation of fluid conduits for pockmarks was most

likely at the intersection of discontinuity planes with the likely fluid source interval (**x-C2**) (similarly to the role of PPFs described in Chapter 4). There is no seismic evidence that these discontinuities acted as conduits themselves.

- Local exceptions to the arcuate distribution pattern of seabed pockmarks are interpreted to be controlled by the PPF system, in the same manner as discussed in Chapter 4. The pre-existing arrangement of PPFs set the discontinuity pattern along which the location of pockmark feeding conduits was established – fault planes control the nucleation position of feeding pipes, with the critical locus being at the intersection of the fault with the estimated fluid source interval.
- The depth and area of seabed pockmarks generally increase away from the axial regions of MB2, which coincide with the crest of a large buried anticline structure.
- From the analysis of the spatial distribution of pockmark size in MB2, it is possible to deduce a relationship between pockmark size and the depth of the fluid source layer, most likely linked to the pressure at which pore fluids are stored prior to their expulsion. Regions where the fluid source interval is deeper below the seabed tend to exhibit larger-sized pockmarks. Thus, generally the deeper the fluid source, the larger the pockmark it will produce when fluids are expelled at the seafloor.
- The pockmark size-source depth relationship may be related to the state of pressure in which the pore fluids are stored at the source. As the source interval is buried increasingly deeper and under more lithostatic load due to a thicker overburden, pore fluids become more overpressured by undercompaction. Higher fluid pressures may in turn promote the generation

of flow conduits of larger diameters and more seabed sediment remobilisation during pockmark formation, producing larger pockmarks.

- In MB2, pockmark size variability may result from lateral variations of fluid pressure at the source, which is a function of depth. Pockmark size may provide a relative proxy for overpressure at the fluid source. The main control on pockmark size may be the degree of overpressure and depth of the fluid source interval.
- Overpressure in the source would vary laterally as a function of depth if sedimentation rates and undercompaction are the primary reason for the excess pressure above hydrostatic.

Chapter 7

CONTROLS ON SEAL BREACHING INFERRED FROM THE SPATIAL ANALYSIS OF POCKMARK ARRAYS

SUMMARY AND DISCUSSION

Controls on seal breaching inferred from the spatial analysis of pockmark arrays

Summary and discussion

The aims of this chapter are 1) to summarise the observations and interpretations from Chapters 4, 5, and 6; 2) to incorporate key findings and list all control mechanisms that affect the spatial distribution and morphology of pockmarks; and 3) to discuss the implications of this research for the general shallow plumbing system of the Lower Congo Basin.

7.1. Summary

The main focuses of the research presented in this thesis are the spatial arrangement of pockmarks and its intimate link to underlying geological processes that control the distribution of seal-bypass features, and promote the migration of fluids to be expelled at the seafloor. Each main chapter analysed specific case studies within different salt-withdrawal mini-basins, each representing different controls on the spatial distribution of pockmarks. Together, these processes interact at the local and basinal scale and are an integral part of the shallow plumbing system of the Lower Congo Basin.

7.1.1. Chapter 4

Chapter 4 described and analysed a population of 3410 seabed pockmarks have been mapped in two salt-related mini-basins (MB6 and 7) in the Lower Congo Basin, offshore Angola. Of these, 570 pockmarks are underlain and fed via pipe-like conduits that are clearly imaged on the 3D seismic data. The results of this study showed seabed pockmark distribution is related to the patterns exhibited by underlying polarised polygonal faults. Pipes invariably occur on hanging-wall blocks, rising vertically from where fault planes intersect the estimated source interval - fluids at the source exploit the discontinuity, producing linear pockmark arrangements parallel to the faults. The uniformity of their statistical distribution argues for a shallow depth below the seabed for the source interval that supplied the fluids forming the pockmarks, estimated to be sedimentary package **x-C2**. The stacked amplitude anomalies associated with the pockmark-feeding pipes is linked to free gas migration, but its composition and ultimate origin is unknown.

Spatial statistics analysis of seabed pockmarks distributions revealed that pockmark occurrence is not considered to be random. In faulted areas, seabed pockmarks are clustered and form alignments along a preferred NNW-SSE direction. In non-faulted areas, seabed pockmarks do not form alignments, and their spatial distribution is considered random at distances >3000m of their nearest neighbours. Seabed pockmarks distributions tend to be dispersed or anti-clustered at short distances of their nearest neighbours,

suggesting there is an exclusion zone of <200m around each pockmark in which no other pockmark will occur.

7.1.2. Chapter 5

Chapter 5 investigates the spatial relationship between pockmarks occurring above three MTDs and their internal discontinuities. Fluid expulsion at the seabed occurred posterior to the mass-transport events, indicating fluids were stored within MTD material prior to their expulsion. Pockmarks and their feeding pipes occur directly above the internal discontinuities of the MTDs, implying an intra-MTD structural control of these heterogeneities on seabed pockmark location. Statistical analysis of pockmark distribution patterns overlying MTDs comparatively to surrounding areas demonstrate important local modifications of the fluid plumbing network impose by the mass-movements. MTD-induced distributions are less predictable due to flow and deformation heterogeneities.

7.1.3. Chapter 6

The case study of mini-basin MB2 is discussed in Chapter 6. A population of 3896 individual seabed pockmarks were mapped, and their spatial distributions were analysed and compared with underlying geological features. The seabed pockmarks in MB2 are mostly distributed in long arcuate alignments perpendicular to the general N-S slope, with their apexes pointing downslope and following the axis of a large scale buried anticline (coincident with MB2 central axis). These arcuate alignments show no spatial

association with any seismically resoluble discontinuity at depth. The lack of seismically visible evidences (discontinuities) that explain pockmark patterns at the seabed suggests that the mechanism that controls the distribution of fluid migration pathways may operate at the sub-seismic scale. From the curvilinear arrangement of seabed pockmarks, it is interpreted that an incipient gravitational sliding of shallow sediments took place, either producing or exploiting pre-existing sub-seismic discontinuities (likely related to the polygonal fault system) that control upward fluid migration to form arcuate seabed pockmark alignments in MB2. The incipient gravitational sliding of shallow sediments is fuelled by gravitational forces downslope. The main driving mechanism for this may be the slope topography created by subsidence of the southern region of MB2, accompanying the salt withdrawal related to diapir SD growth. The surface of detachment for the incipient shallow gravitational sliding process may be stratigraphically located at **C2** level. Pore fluid expulsion may be promoted by downslope compression of shallow sediments as pervasive dewatering may occur due to shortening (downslope contraction) and horizontal compaction. The locus for the formation of fluid conduits for pockmarks was most likely at the intersection of discontinuity planes with the previously estimated fluid source interval (**x-C2**) (similarly to the role of PPFs described in Chapter 4). There is no seismic evidence that these discontinuities acted as conduits themselves.

Seabed pockmarks in MB2 also show great variability in the spatial distribution of their size and depth. The depth and area of seabed pockmarks generally increase away from the crest of the large buried anticline structure.

From the analysis of the spatial distribution of pockmark size in MB2, it is possible to deduce a relationship between pockmark size and the depth of the fluid source layer, most likely linked to the pressure at which pore fluids are stored prior to their expulsion. Regions where the fluid source interval is deeper below the seabed tend to exhibit larger-sized pockmarks. Thus, generally the deeper the fluid source, the larger the pockmark it will produce when fluids are expelled at the seafloor. The pockmark size-source depth relationship may be related to the state of pressure in which the pore fluids are stored at the source. As the source interval is increasingly deeper and under more lithostatic pressure due to a thicker overburden, pore fluids become more overpressured. Higher fluid pressures may in turn promote the generation of feeding conduits of larger diameters and more seabed sediment remobilisation during pockmark formation, producing larger pockmarks. In MB2, pockmark size variability may result from lateral variations of fluid pressure at the source, which is a function of depth. Pockmark size may provide a relative proxy for overpressure at the fluid source. The main control on pockmark size may be the degree of overpressure and depth of the fluid source interval.

7.2. Controls on pockmark spatial distribution

Pockmarks are evidence of fluid escape at the seabed. Their spatial arrangements at the seabed reflect the distribution of underlying seal bypass systems. The geo-mechanical context of a certain area influences flow properties, i.e. different geological settings produce different styles of focused fluid flow and expulsion. As such, distinct hydrodynamic regimes produce different pockmark populations. These regimes are controlled by the local stress fields (stress direction and magnitude), which may deform basinal sediments, modifying the local topography and geomorphology, and generating discontinuities, fractures, and/or faults. These features will influence further sediment deposition and control fluid migration pathways, affecting the general plumbing systems of the area.

This section lists and discusses all the controls on pockmark distributions identified for the study area, from stratigraphic controls to structural controls, increasing the structural deformation affecting intra-basin sediments.

7.2.1. Stratigraphic/depositional controls

Stratigraphic or depositional controls are the primary, most simple processes that regulate the spatial arrangement of pockmarks. These controls are intimately associated with the nature of the subsurface sediments and how these are distributed within a basin. Controls produced by the post-depositional deformation of sediments are not featured in this list (see sections 7.2.2 and 7.2.3).

7.2.1.1. The suitable geological setting

The primary control that determines whether pockmarks will be formed in a certain area relates to the lithological and mechanical properties of the subsurface sedimentary strata. For a pockmark to be formed, there are specific conditions that need to be met: 1) suitable sediment type and composition of the source interval (fluid reservoir), seal package, and seabed sediments; 2) the pore fluid properties and content; 3) and temperature and pressure conditions.

The source or storage interval is a mass of sediment with storage capacity, enabling the build-up of fluid pressures (overpressures). It is the origin of the mobile components (sediments and/or fluids), and it must be a high porosity/high permeability medium sealed by an impermeable caprock, or a moderate to high porosity lithology with low permeability. In this thesis, the source is the point or place from which fluids ascend to form a pockmark (not "source rock" as fluid-generating layer). The impermeable caprock or seal is "*an assemblage of generally low-permeability lithofacies that halt or retard the flow*" of fluids towards the seafloor (Cartwright et al., 2007). For pockmarks to be formed, the basin surface must comprise soft, unconsolidated, fine-grained sediments; and the seabed must be stable, with no large-scale active erosion or deposition (Judd and Hovland, 2007). Fluid properties and availability are also major elements for pockmark formation. The fluids involved in this process may have a wide range of compositions (e.g., from groundwater to methane-rich gas, or both) and origins (shallow or deep), but they must be presented in the system, stored within the source

sediments. The temperature and pressure conditions of the system play a major role in pockmark formation, as they influence the state of pressure of pore fluids. Excess pore fluid pressures (overpressures) are necessary to drive fluid and sediment flow. Focusing of overpressure at the source is necessary for seal breaching and pockmark formation. Buoyancy pressure is also necessary for the upward migration of fluids. All these elements must be present and suitable conditions need to be established to form a pockmark at the seabed. Otherwise, if a certain sedimentary environment fails to meet these requirements, the pockmark formation process will not take place. This is exemplified in figure 4.10 (Chapter 4), where no seabed pockmarks occur where the source interval is absent (see Stratigraphic controls).

In the Lower Congo Basin, this initial control on the distribution of pockmarks is demonstrated by the spatial association between pockmark occurrence and the presence or absence of the estimated shallow source interval (interval **x-C2**; see Chapter 4). Seabed pockmarks occur almost exclusively within the areas covered by the source interval. In mini-basin regions where this interval is absent at depth, there are no visible pockmarks at the seabed (fig. 4.10, Chapter 4). Furthermore, lateral variations of the seismic character of the source interval were observed to influence seabed pockmark distribution: areas of reduced seismic amplitude yield fewer to no pockmarks, which may be related to variations of sediment type or pore fluid composition. The absence of the source layer or a variation of its seismic character in these areas indicate that, locally, the basic requirements for pockmark formation are not fulfilled at the source level.

7.2.1.2. Lithological variations

Fluid flow within a sedimentary basin may be influenced by lithological variations of the subsurface strata. The hydraulic contrast between two different rock types in contact with each other will affect the plumbing system of the area, by controlling the position of fluid migration pathways. This is especially pertinent in areas where sand-rich intervals occur within mud-dominated sediments. In the study area, lithological variations controlling the distribution of seabed pockmarks are observed in regions of significant lateral change the in the character of the source or seal intervals (as mentioned above), possibly related to deviations on the optimal sand/shale ratio for pockmark formation. Areas with different sediment successions with a mini-basin may exhibit distinct pockmark patterns (e.g., areas of presence/absence of pockmarks; fig. 4.10).

Linear stratigraphic discontinuities, such as pinch-outs and those created by submarine channels, also exert a control on pockmark distribution patterns. Fluid expulsion influenced by these features will produce linear pockmark trails. Lateral terminations of sedimentary bodies or pinch-outs may form linear stratigraphic discontinuities between distinct lithologies. Fluids expelled vertically above pinch-out interfaces may form linear pockmark arrangements, such as the ones shown in Figure 7.1 associated with a buried MTD, and the wedge pinch-outs observed in mini-basin MB7. In the examples shown in this thesis, the pinch-out and fault alignments are quite distinct on the seafloor, but in other basins this may not be the case if structure-parallel faults develop. However, the presence of pockmark

alignments associated with the pinch-outs are a clue to identify the edge of a fluid-bearing/controlling buried sedimentary body, regardless of the distribution controls elsewhere within or over it.

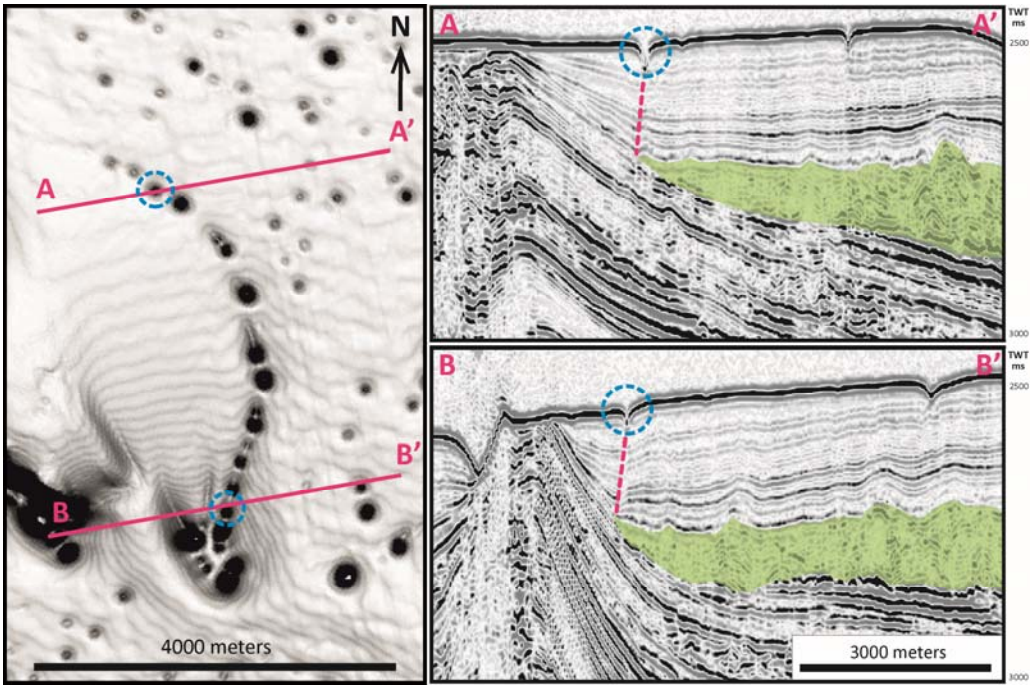

Figure 7.1. Seabed pockmark alignment vertically above MTD pinch-out in mini-basin MB1.

Coarse-grained channels buried within mud-dominated sediments constitute preferential fluid migration pathways. Sinuous pockmark alignments are indicative of fluid escape from channel sediments, and have been extensively described in the Lower Congo Basin by Gay et al. (2006a, 2006b, and 2007). Pockmarks associated to buried submarine channels may occur either along the central length of the channel, or vertically above the channel-levee interface. Both these scenarios were observed in the study area. In MB6, bulls-eye pockmarks occurring in the central region of the mini-basin were developed above a turbiditic channel within the top-most

sediments of Unit 2 (fig. 7.2). Meandering trails of seabed pockmarks are observed along the margins of the large submarine channel 1 crossing the south region of the study area (fig. 7.3a). These trails are located vertically above the channel-levee interface of buried paleo-channels and paleo-meanders. These interfaces provided a stratigraphic discontinuity exploited by fluids as a nucleation point for seal breaching, allowing their upward migration and expulsion at the seabed (fig. 7.3b). Fluids may be sourced from within the channel sediments. The distribution patterns of pockmarks associated with paleo-channels is quite distinct from other linear arrangements due to their very curved and meandering geometry. Since most hydrocarbon reservoirs in the Lower Congo Basin are within deeply buried paleo-channels, the identification of these trails at the seabed suggest the existence of weak seals and reservoir leakage, which have considerable implications for the viability of these packages for fluid storage.

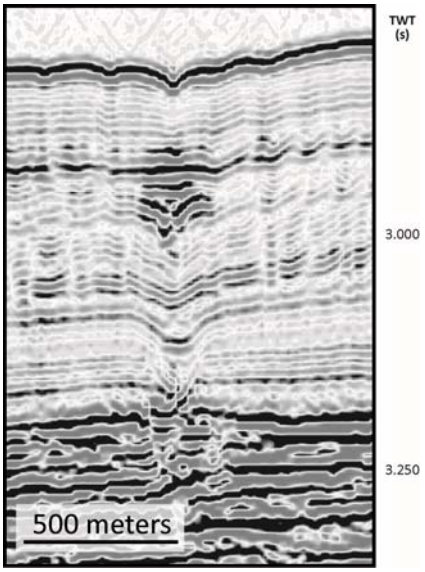

Figure 7.2 Bulls-eye pockmark vertically above Unit 2 turbiditic channel, located in mini-basin MB6. (Seismic courtesy of PGS.)

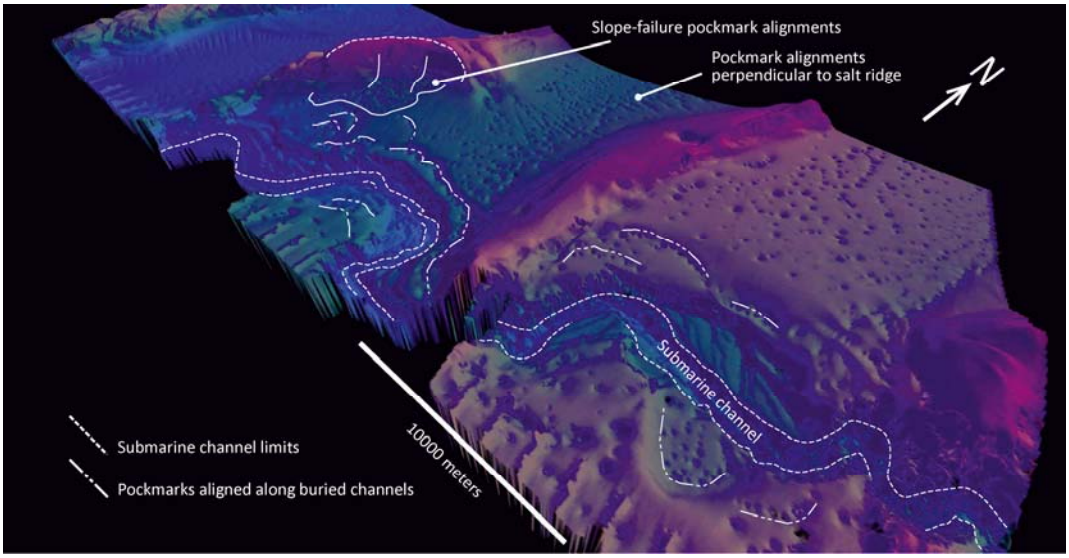

Figure 7.3. Meandering pockmark alignments at the margins of the large submarine channel 1.

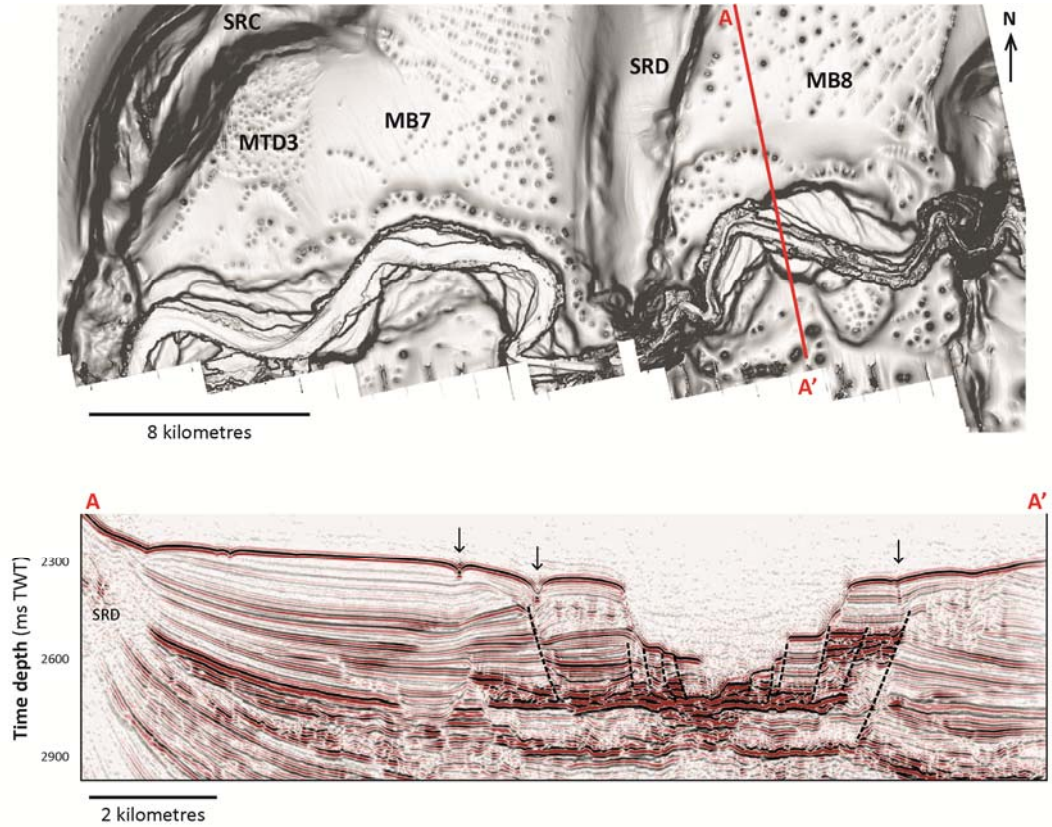

Figure 7.4. Seismic profile across the large channel indicating the pockmarks above stratigraphic interfaces associated with paleo-meanders. (Seismic courtesy of PGS.)

7.2.2. Strati-structural controls

Strati-structural controls on the formation of pockmarks refer to the influence of sediment failure and remobilisation on the distribution of fluid expulsion features. Submarine slope failures and consequent sediment remobilisation produce a series of internal deformation in the affected strata, akin to regional tectonic features. Extensional and compressional structures are generated during slope movement, and these will impact the fluid drainage patterns in the same manner as regional deformation structures, although at localised scales. The possibility of analysing fluid expulsion patterns associated with slope failures undertaken in this thesis sheds new insights on their relationship.

7.2.2.1. Shallow gravitational sliding

The distribution of pockmarks controlled by a shallow gravitational sliding mechanism is quite distinct from other spatial arrangements that have been described in published works. Pockmarks occur in long arcuate trails on inclined slopes, with their apices facing the downslope direction, resembling compressional features observed at the toe domain of mass-transport deposits or involved in gravitational tectonics. The gravitational sliding process acts within the shallowest sediments, and is a precursor to slope failure, inducing a localised change on the shallow plumbing system. This incipient (low strain) mass movement of the shallowest sediments (driven by gravitational forces acting downslope) produces minor sub-seismic internal deformation of the sediments near the seabed, which may

constitute seal bypass features for fluids to be expelled at the seafloor. Pore fluid expulsion may be promoted by downslope compression of shallow sediments, as pervasive dewatering occurs due to shortening (downslope contraction) and horizontal compaction.

This type of curvilinear arrangement of pockmarks is identified in the northern half region of mini-basin MB2, as is thoroughly discussed in Chapter 6. From the seabed pockmark patterns and the geomorphology of the area, it was interpreted that an incipient gravitational sliding of shallow sediments took place, operating at a sub-seismic scale (due to the lack of subsurface seismically-visible discontinuities that would explain the pockmark distribution). The locus for the formation of fluid conduits for pockmarks was most likely at the intersection of discontinuity planes with the likely fluid source interval (**x-C2**), in a similar process to the way PPFs control the pockmark alignments described in Chapter 4. There is no seismic evidence that these discontinuities acted as conduits themselves.

The impact of shallow gravitational sliding on the seafloor fluid venting is expressed by the increase of pockmark density in the areas of the slow movement compared to other stable ones. This may imply that the slow-moving strata induced a higher number of venting structures, possibly associated with a local increase of small expulsion episodes during movement. Recognising such seafloor pockmark patterns and contrasting them to surrounding areas could be a valid diagnostic for weaker slope regions prone to failure.

7.2.2.2. MTD internal discontinuities

In the study area, pockmarks were observed above MTDs, distributed throughout all their domains, overlying extensional and compressional internal discontinuities (see Chapter 5). These observations show the importance of MTDs on the local disturbance of gas-rich units and how their heterogeneities control the immediate fluid migration path. Their influence on fluid re-routing paths had already been recognised (e.g. Riboulot et al., 2013), but the results shown in this thesis are relevant for their capacity to retain fluids and act as reservoirs. This characteristic has been considered, but poor evidence of it has been shown so far. A direct implication of this is the uncertainty of the pressure and consolidation of fluid-bearing MTD strata, thus increasing the already high risk associated with these deposits on offshore drilling operations.

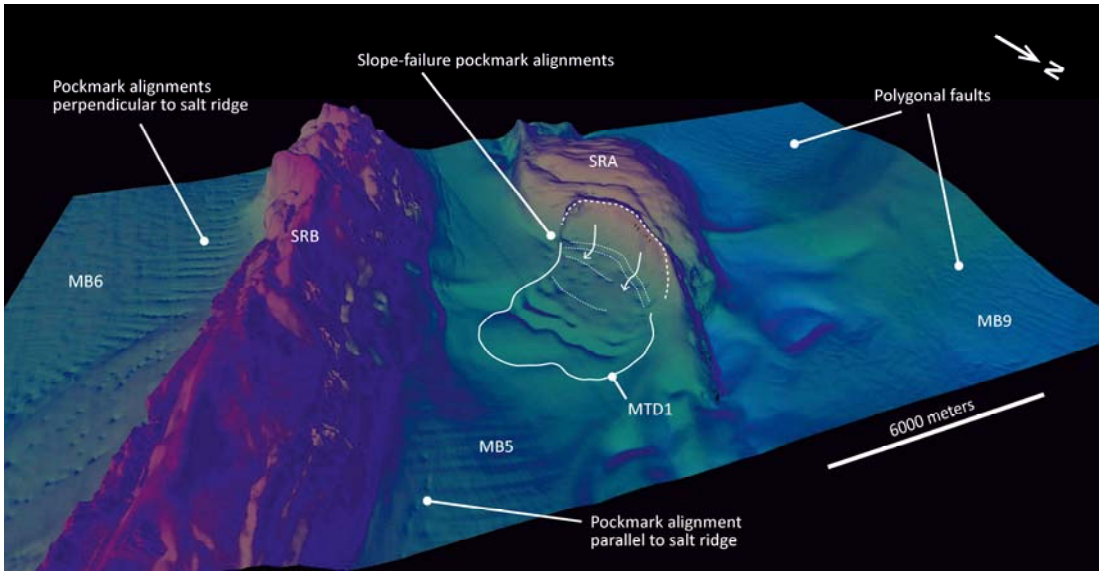

Figure 7.5. Aligned pockmarks associated to MTD1.

A key conclusion taken from the analysis of the different MTDs in the study area is that slope failure will impact the geometry of the subsurface plumbing system. This is important as it will induce marked changes in the structure and local stress that can differ significantly from the regional plumbing network inferred from the regional structures and trends. The most representative example in this thesis is MTD2, which imposes a deformation pattern controlled by NE-SW faults that is markedly different from the distributions observed on non-remobilised areas of mini-basin MB6, where the seabed pockmark arrays are controlled by E-W polarised polygonal faults. There may be also a secondary level of intra-MTD structural uncertainty derived from the interference with the polygonal fault systems. As MTD2 was formed after the genesis of the polygonal fault tier (its frontal ramp detaches along the tier base at the toe), the mass-movement affected strata that was already deformed by the evenly-spaced polarised polygonal faults perpendicular to ridge SRB. Thus, there may be remnants of the pre-existing deformation fabric not visible on the seismic data, in addition to the faults extending along the MTD width, further increasing the complexity of the subsurface drainage system. Less evident internal MTD deformation and transfer zones may also be hard to be recorded on seismic. However, the fluid escape patterns and their expression at the seabed can be indicators of their presence.

MTDs 1 and 3 play a similar role on the capacity of fluid storage. The occurrence of pockmarks on top of these mass-flow deposits, which are also associated to the MTD internal faults and discontinuities, is a direct evidence that the pre-failure strata on the salt ridge flanks were effective fluid-holding

sediment. However, this would not be clear by analysing the areas outside the MTDs, as they occur in regions not immediately surrounded by pockmarks nor by seismically resoluble polygonal faults. The pockmark-MTD relationship further strengthens the argument of the impact of slope failure on fluid escape.

MTDs also have an indirect impact on the drainage network. These deposits tend to be quite heterogeneous, especially when large blocks are present. After burial, the competence contrast between the deformed matrix and still consolidated blocks leads to differential compaction at depths, influencing the geometry of the overlying strata. This is exemplified in mini-basin MB2 by the MTD below Unit 3. The block pinnacles influence the morphology of the base level of the polygonal faults and locally alter the stress pattern, creating a concentric polygonal fault around the block location. Although in MB2 there is no evident connection between a control of the MTD topography and the pockmark distribution pattern, there is a narrow segment of MB1 where this is observable (fig. 7.5). In here, pockmarks underlain by PFFs show an organised distribution but, locally where the MTD occurs at depth, the pockmarks have a more erratic scattering due to the disturbance of the subsurface fault pattern.

A common feature for all MTDs is the modification of the pockmark statistical distribution patterns. Fluid seepage associated with the MTDs will have less predictable distribution when compared to the organised clustering patterns obtained for regional fault controls.

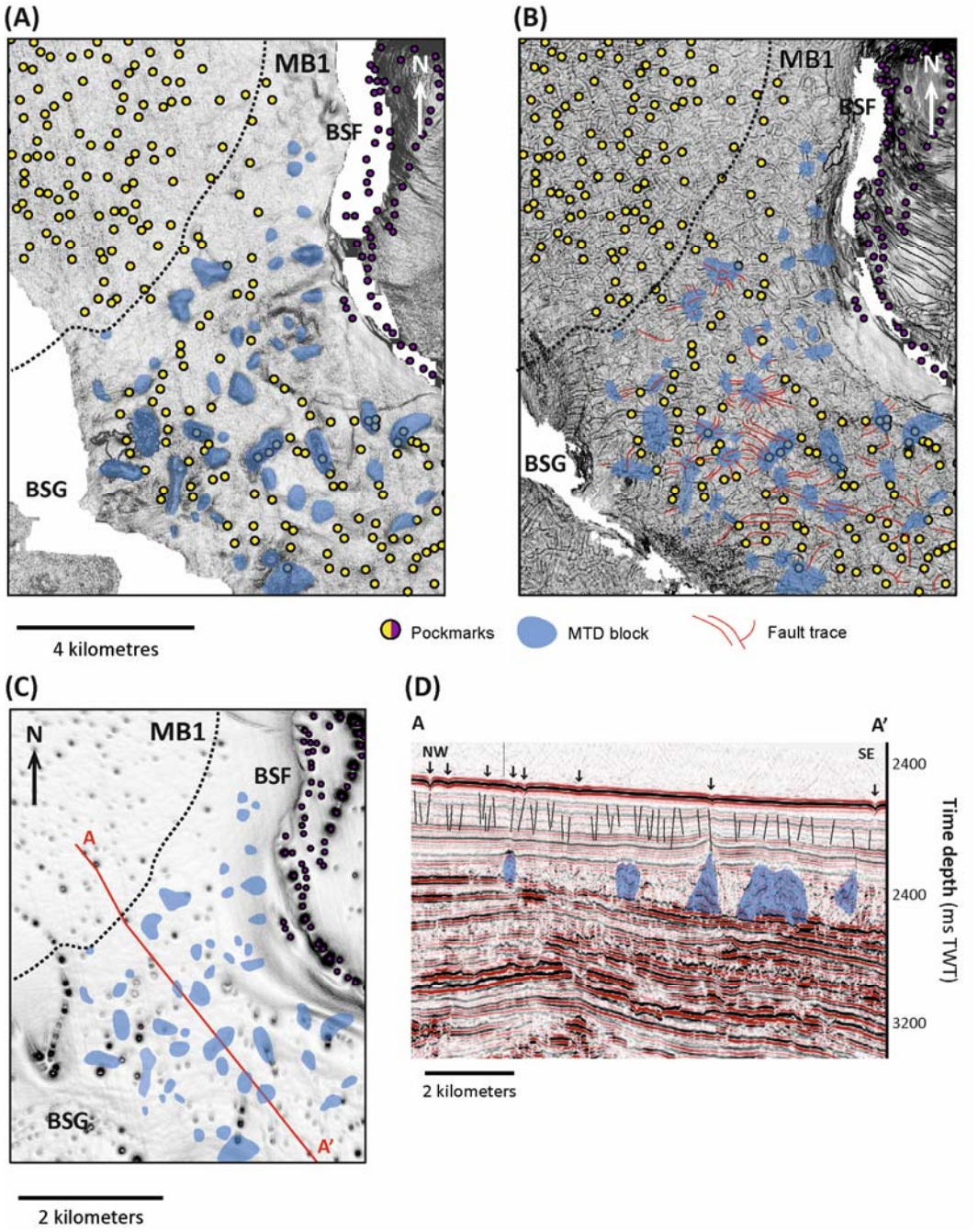

Figure 7.6 Influence of buried MTD blocks on the polygonal fault patterns in mini-basin MB1. **(A)** Dip map of horizon C4; **(B)** dip-map of horizon of C2; **(C)** dip-map of seafloor; **(D)** seismic profile A-A'. (Seismic courtesy of PGS.)

7.2.3. Structural controls

The controls on fluid flow exerted by the structural deformation of basinal sediments have been intensively researched for the understanding of plumbing systems (e.g., Cartwright et al., 2007; Sibson, 1981). Faults and fractures are known to be important as both potential conduits or barriers for fluid migration. Linear pockmark arrays have been shown to reflect the distribution of underlying faults, controlling the establishment of pathways for upward fluid migration (e.g., Gay et al., 2007; Pinet et al., 2009). In this section, it is discussed the role of these structural discontinuities on the spatial distribution of seabed pockmarks, and their implications for the shallow plumbing system of the study area.

7.2.3.1. Polygonal faults and polarised polygonal faults

In Chapter 4, the close spatial relationship between seabed pockmarks and (polarised) polygonal faults was thoroughly discussed. In MB6 and MB7, linear trails of seabed pockmarks are observed to be coincident to the trace of polarised polygonal faults, both orthogonal to the salt ridges SRB, SRC, and SRD. It was demonstrated that polarised polygonal faults control the distribution of pockmarks but, in contrast to what has been described in previous studies (Gay et al., 2006), these faults did not act as fluid conduits. The spatial alignment is instead a control by the fault plane on the nucleation position of the pipe feeding the pockmark, with the critical locus being at the intersection of the fault plane with the likely fluid source interval. There is no evidence that the faults acted as conduits, which is supported by the

systematic offset between pockmark positions and the upper tip positions of the fault planes. However, in areas where the typical polygonal fault pattern is present, seabed pockmarks exhibit a more variable distribution (hard to constrain by statistical analysis), considered to be dispersed for short distances between nearest neighbours (<200m) and clustered for distances >250m (2nd order statistics of pockmark distributions, in Chapter 4). This effect is related to the increased variability of the polygonal fault orientations. Although in the polygonaly faulted areas, the pipe-fault relationship is difficult to observe, it is expected that a control similar to the imposed by PPFs is in action, i.e. faults are not conduits for fluid migration.

7.2.3.2. Tectonic faults

It is well established that faults may constitute preferential pathways for fluid flow on the Angola margins (Berndt, 2005; Serié et al., 2017; Stover et al., 2001). In the study area, there are several pockmark alignments positioned along the strike of large subsurface tectonic faults, associated with structural deformation of mini-basins' sediments (fig. 7.6). These alignments are typically composed of larger-sized pockmarks and extend for lengths up to 20km. In seismic cross-sections, it is possible to observe that seabed pockmark alignments generally occur vertically above the fault tip (fig. 7.6). This spatial relationship is evidence that these faults were exploited as conduits for the upward fluid migration at the time of pockmark formation. In some cases, seismic amplitude anomalies are observed adjacent to the fault plane, which may be related to the presence of fluids within the surrounding sediments.

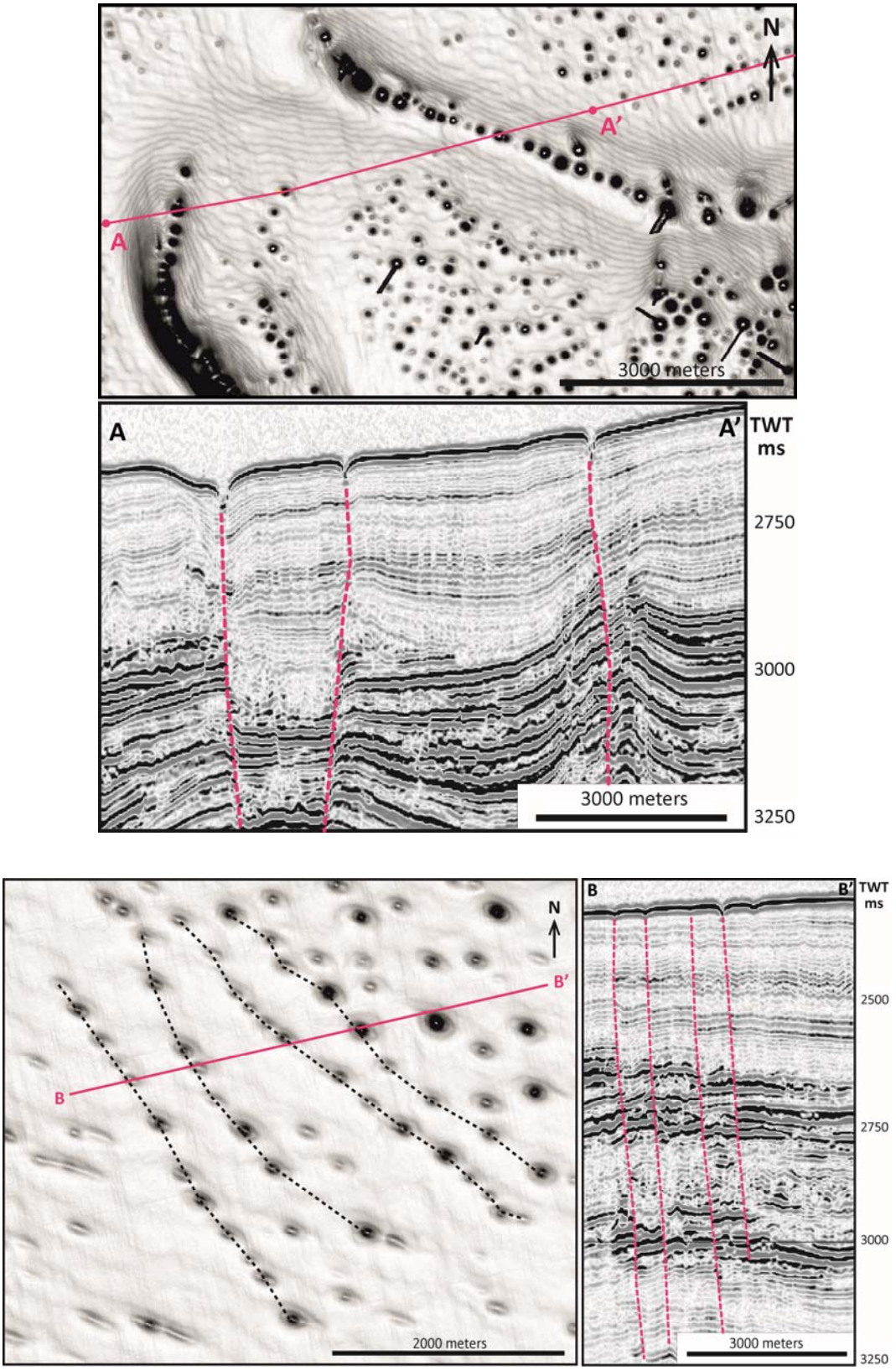

Figure 7.7 Fault-controlled seabed pockmark alignments in mini-basins **(A)** MB2c, and **(B)** MB1. (Seismic courtesy of PGS.)

The Lower Congo Basin is a tectonically active area, in which salt growth plays an important role. The large-scale faults associated with salt bodies may also serve as fluid migration pathways, connecting deep subsurface source-rocks and reservoirs to shallower levels of the basin. These faults usually develop along salt wall flanks and/or above buried edifices. Thus, pockmarks fed via these faults are expected to occur in close proximity with these structures, forming long trails following the faults' strike. In the study area, these pockmarks are distributed parallel to salt ridges (along their flanks) or vertically above buried structures (fig. 7.7).

Pockmarks associated with tectonic faults differ from pockmarks within mini-basins, as they are typically much larger in size. They may be the result of seafloor expulsion of deep-sourced fluids (possibly from within Unit 2 or deeper strata), which are likely highly overpressured and may promote more seabed sediment remobilisation (forming larger depressions), either by a short-lived strong flux expulsion event or continued fluid venting at the seabed.

Positive-relief salt bodies rarely exhibit pockmarks directly above them, only along their flanks. This near-absence of pockmarks vertically above these structures may be explained by the uplift, exhumation and erosion of shallow sediments that may serve as sealing caprocks to deep reservoirs, preventing fluid storage and, thus, pockmark formation.

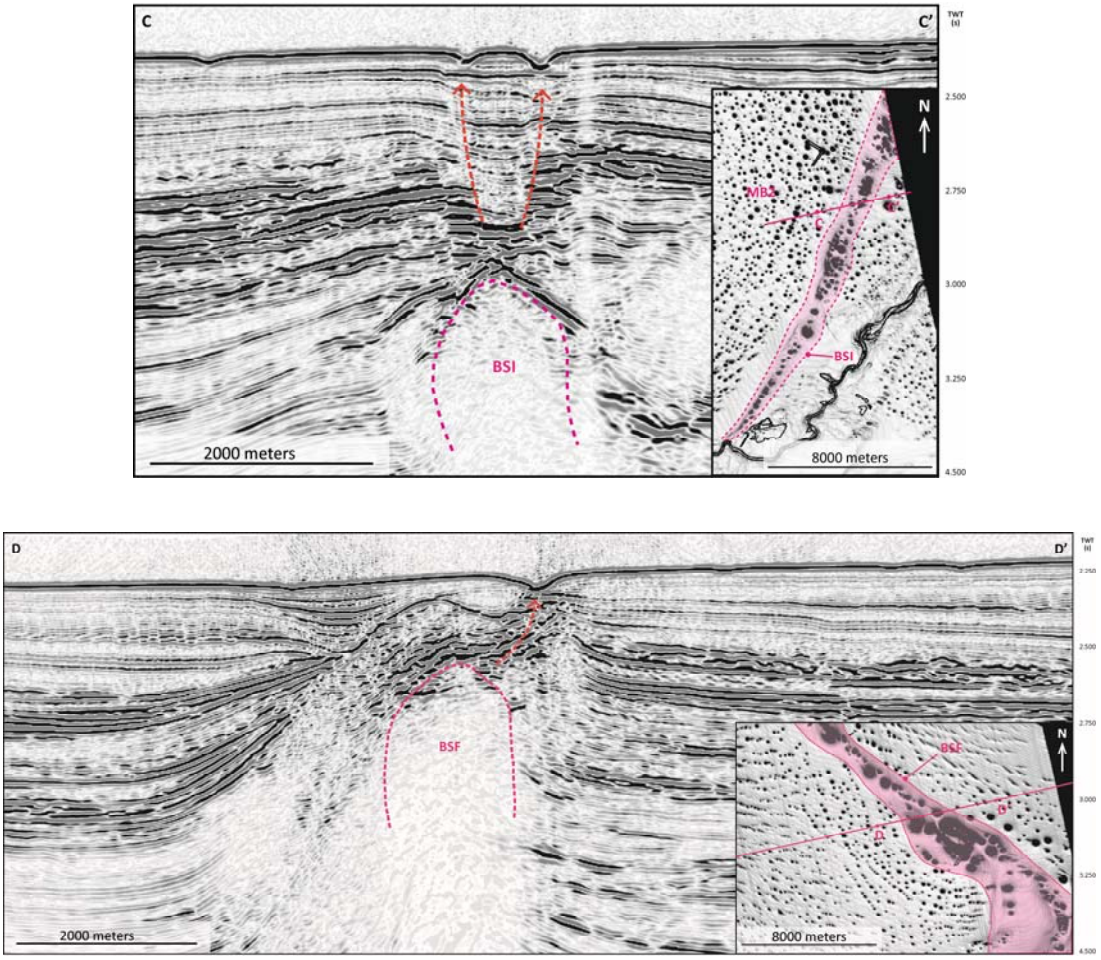

Figure 7.8 Seabed pockmark alignments vertically above buried salt structures **(C)** BSI in MB2, and **(D)** BSF in MB1. (Seismic courtesy of PGS.)

One of the main problematic issues around the subject of faulting and fluid flow is to determine whether seabed fluid escape is linked to periods of fault activity, or whether fault zones are semi-permanent for fluid migration. Are they features of enhanced permeability in seal sequences, or do these pathways heal?

The methodology to analyse fault-conduit potential has to be similar to the one applied for seal analysis, taking in to account the same parameters and fault properties. Ideally it is the integration of 3D seismic data with theoretical juxtaposition diagrams and well data, including fault kinematics

and growth history (Knipe et al., 1998). The main factors that determine fault conduit/seal behaviour are: 1) fault surface attitude; 2) fault displacement; 3) lithology and mechanical properties of offset strata; 4) burial depth; 5) juxtaposition of lithology across fault plane; 6) fault gouge, considering especially its nature and permeability; 7) dimensions of the damage zones; 8) distribution of deformation features within the damage zones; 9) stress direction and magnitude; 10) fluid properties (density, compressibility and sources); and 11) temperature and pressure conditions (Zhang *et al.*, 2010, Knipe, 1997). All these properties must be considered for accurate fault seal/conduit studies, combining datasets from different scales. In micro-scale analysis, the continuity, spatial distribution and petrophysical properties of fault rocks must be assessed and integrated with flow models (Knipe et al., 1998). In larger scales, it is necessary to evaluate pre-, syn- and post-deformation effective stress and temperature history, as they control the development of fault structures and influence fluid properties. In fault-controlled flow analysis, 3D seismic technology provides the means for a better and more complete understanding of the relationship between fluid distribution and fault architecture and evolution (Huuse et al., 2010). Hydrocarbon-related amplitude anomalies are identified and analysed according to their position, geometry and spatial distribution. Faults are mapped and classified, followed by a quantitative kinematic evaluation, including growth and movement history. The results from this first structural analysis must be integrated with lithological and petrophysical information collected in wells drilled in the study area, in order to associate fluid flow to physical properties.

Unfortunately, the research presented in this thesis is limited to the available 3D seismic data. As such, an in-depth fault-conduit analysis is not possible to be performed. However, from the seismic observations made, it is attempted to answer the questions above in the context of the study area.

As mentioned previously, discontinuities formed by polygonal faulting did not act as conduits. Seabed pockmark formation is not specifically linked to the polygonal fault system, simply because pockmarks are also present in areas not affected by polygonal faulting. There is a considerable time-period between the end of the active period of polygonal faulting and the timing of pockmark formation, as evidenced by hemipelagic succession deposited above the top tier of the polygonaly faulted interval (reflector **C1**). Thus, polygonal faults are considered to be sealant discontinuities embedded in fine-grained sediments.

As for the tectonic faults present in the study area, the observation that seabed pockmark alignments occur vertically above fault tips is evidence that these discontinuities were permeable pathways for fluid flow, at least during the fluid expulsion event that originated the seabed pockmarks. Occurring at the seabed with no evidence of prior fluid expulsion (no paleo-pockmarks below the seabed) and no sediment infill, it is assumed that these pockmarks were formed during the same fluid expulsion event as the seabed pockmarks within the mini-basins. As such, the trigger for pockmark formation must be the same for all seabed pockmarks in the study area, and it is unlikely that these fault-controlled pockmarks were formed by fluid escape during a seismic-slip event.

In the very rare cases where stacked paleo-pockmarks occur below fault-controlled seabed pockmarks, it is plausible that the several paleo-episodes of fluid expulsion may be linked to periods of fault activity. As such, these faults may be permeable fluid pathways when displacement occurs (possibly associated with episodes of salt deformation), but barriers for fluid migration when dormant.

7.2.4. Summary of controls on pockmark distributions

To summarise all the controls on pockmark distributions identified for the study area, a visual graphic was created, listing in a hierarchic order of complexity the processes involved and the type of pockmark spatial arrangements they produce (fig. 7.8). The style of control is listed from top to bottom, from stratigraphic controls to structural controls, increasing the structural deformation affecting intra-basin sediments. The complexity of each control style increases from left to right. As such, the simplest control mechanism is shown in the top-left area of the diagram (suitable setting – presence vs. absence of the source layer), and the most structurally complex is on the bottom-right corner (tectonic faults associated to salt deformation). The visual graphic is a simplistic way of showing how all these mechanisms work, and each of them is explained occurring as a single process. However, it is noted that several controls may be acting simultaneously, increasing even further the complexity of the shallow plumbing system.

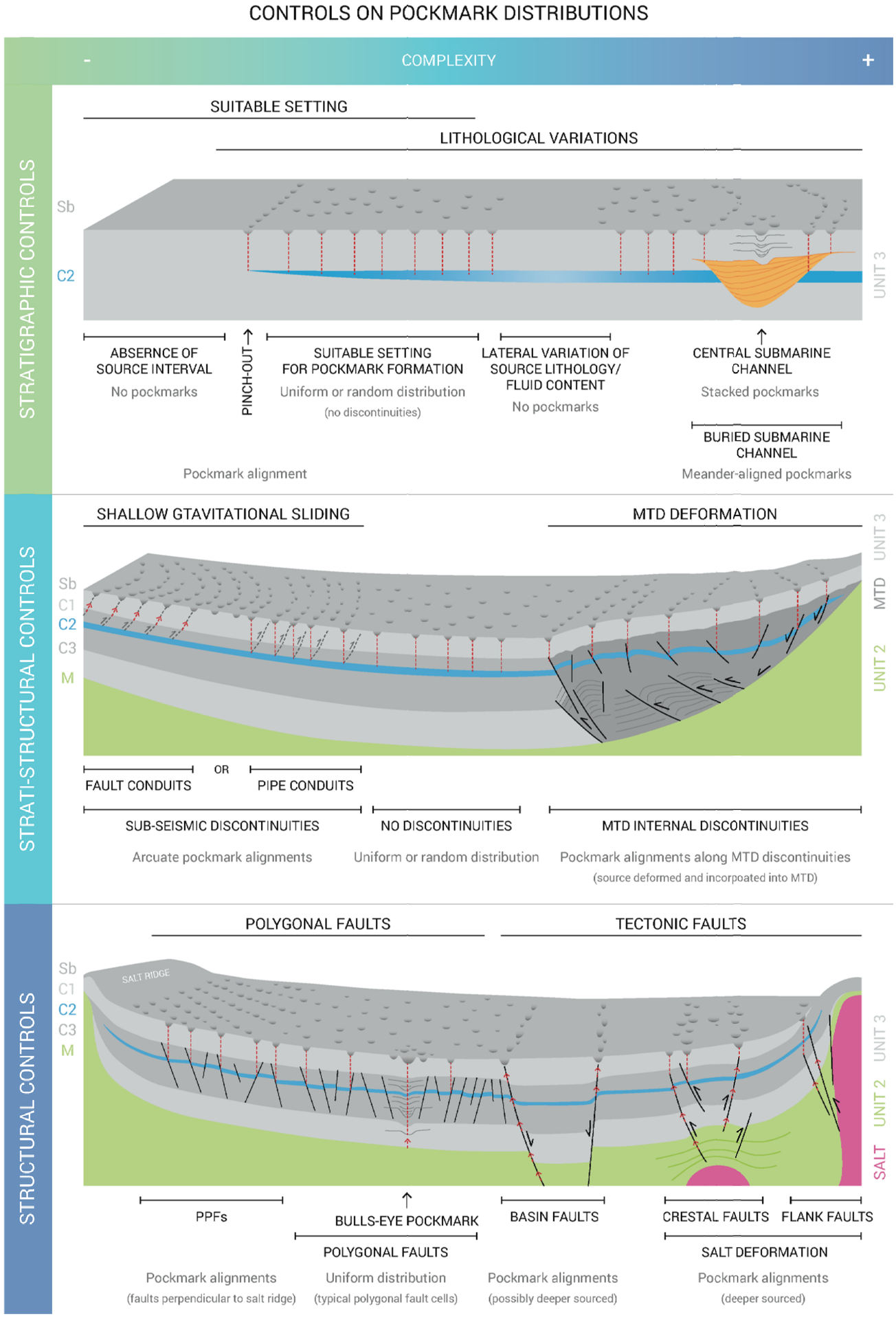

Figure 7.9. Summary of controls on pockmark distributions.

7.2.5. Pockmark spacing and drainage cell

Moss and Cartwright (2010) and Moss (2010) proposed the existence of a "pockmark drainage cell", defined as the area around the base of a feeding pipe in which the source interval is depleted of fluids to produce a pockmark. This conceptual model implies the presence of an exclusion zone around each pockmark in which no other pockmark occurs or will be formed. In spatial statistics, this "exclusion zone" may be defined as an anti-clustering pattern – "*the decreased likelihood of finding neighbours within a close distance of any point*" (Cartwright et al., 2011). The 2nd order spatial statistical tests applied to seabed pockmarks in mini-basins MB6 and MB7 showed that their distributions tend to be dispersed or anti-clustered at short distances (<200m) of their nearest neighbours, both in faulted and non-faulted areas (see Chapter 4). This result suggests there is indeed an exclusion zone of <200m around each pockmark in which no other pockmark was formed. Thus, it is plausible that a drainage cell mechanism was in action in the study area, and may be responsible for the spatial focusing of overpressure required for seal failure and pockmark formation. However, further statistical analysis of the pockmark populations would need to be undertaken to confirm this hypothesis, taking special consideration of the spacing between pockmarks of variable sizes. Furthermore, the drainage cell model was first discussed for an area where no structural control is evident on the distribution of pockmarks. Pre-existing discontinuities (such as faults) may affect this mechanism and "polarise" the drainage cell. This effect could

be analysed by studying the spacing between pockmarks along the same fault-controlled alignment, and it is proposed to be done in a future research.

7.3. Modifiers to pockmark size and shape

7.3.1. Depth of fluid source

In Chapter 6, from the analysis of the spatial distribution of variable pockmark sizes throughout mini-basin MB2, it was inferred that the size of pockmarks is proportionally related to the subsurface depth at which the fluid source interval occurs. Regions where the fluid source interval is deeper below the seabed tend to exhibit larger-sized pockmarks. Thus, generally the deeper the fluid source, the larger the pockmark it will produce when fluids are expelled at the seafloor. The mechanism behind this phenomenon may be related to the absolute magnitude of pore pressure in the storage layer at the source interval, which is influenced by the source depth below seabed. As the source interval is increasingly deeper and buried under a thicker overburden, pore fluids may become more overpressured. Higher fluid pressures may in turn promote the generation of feeding conduits of larger diameters (if the lithological properties of the seal are laterally homogenous) by producing a larger seal hydrofracture system. Higher fluid pressures and fluxes yield greater eruptive forces, which promote more seabed sediment remobilisation during pockmark formation, producing larger depressions. As such, pockmark size may provide a relative proxy for overpressure at the fluid source. In the study area, pockmark size variability is interpreted to result from lateral variations of fluid pressure at the source, which is a function of

depth. Thus, the main control on the initial pockmark size may be the degree of overpressure, estimated by the depth of the fluid source interval.

7.3.2. Shape of the vent

The initial morphology of a pockmark depends on the shape of the venting structure. Although the shape of these features was not the focus of the work presented in this thesis, it is acknowledged that it plays a significant role in determining the geometry of fluid expulsion depressions.

Focused fluid flow and sediment remobilisation from a point vent will produce circular pockmarks (Hovland et al., 2002). In the study area, the fluid conduits feeding seabed pockmarks are observed as high amplitude pipes of circular to sub-circular planforms (see Chapter 4). The mechanism behind the initiation of a pipe is generally considered to result from failure of a capillary seal by hydrofracturing (Cathles et al., 2010; Løseth et al., 2001; Moss and Cartwright, 2010). Hydrofracturing of seal sediments develops fractures perpendicular to the direction of minimum stress, induced by overpressure at the root zone. The following processes of pipe formation are still under debate, but may be related to flow localization and erosive fluidization, amplified by capillary effects (Cartwright and Santamarina, 2015). Regardless of the mechanism of pipe genesis (which is not in the scope of this thesis), pipes are typically circular in planform, and produce circular pockmarks. However, if fluids are expelled through linear conduits (e.g., faults), pockmarks may develop elliptical shapes, parallel to the orientation

of the linear vent (Dandapath et al., 2010). In extreme cases, these may even be identified as linear furrows, as the ones described by Gay et al. (2004).

The great majority of the seabed pockmarks in the study area is circular to sub-circular in planform. This geometry is in agreement to what is expected for pockmarks fed by pipes, such as the ones observed throughout mini-basin MB7. This circular shape is not affected by the different underlying linear discontinuities controlling the distribution patterns of the seabed pockmarks; i.e., fault-controlled pockmarks still exhibit circular morphologies. This was maintained even under such distinct linear controls such as the ones imposed by 1) polygonal and polarised polygonal faults (see Chapters 4 and 6), 2) faults and fractures in MTDs resultant from localised slope failure (see Chapter 5), 3) larger tectonic faults rooted deeper in the basin, or 4) inferred linear discontinuities associated with shallow gravitational sliding (see Chapter 6). In addition, the circular shape was prevalent regardless of an interpreted extensional or contractional stress, as exemplified by the different domains of the MTDs. As such, in the study area, the main control on pockmark shape is the circular geometry of the feeding pipes. A small population of elliptical pockmarks is observed in mini-basin MB1, but their shape may be explained by late seabed erosion, as discussed in the section below (section 7.4.3).

7.3.3. Modification posterior to fluid expulsion

The morphology of a pockmark may be modified from its original shape by the action of bottom-currents (Hovland et al., 2002). This modification turns circular to sub-circular pockmarks into elongated depressions through scouring and bottom-current erosion, ultimately originating furrows at the seabed. Bottom-currents may also prevent the deposition of sediments over pockmarks. This process occurs especially in areas of steeper slope. Bottom-currents may also have and important role on the evolution of stacked pockmarks, formed by multiphase fluid expulsion. This process is described by Ho et al. (2012) as advancing pockmark arrays, occurring preferentially on inclined slopes. Migration of the stacked pockmarks occurs in the downslope direction, controlled by the interaction of local bottom-currents with sediment deposition and pre-existing pockmark topography.

Advancing pockmark arrays are not observed in the study area, but their presence elsewhere in the Lower Congo Basin indicates bottom-currents may be an important control on the shape and size of the seabed pockmarks analysed here. As mentioned above, the great majority of the pockmarks studied are circular to sub-circular, which suggest bottom-currents have had little to no influence on their shape. The only clear examples of bottom-current action are observed in MB1, in a region of steeper slope (fig. 7.9). Pockmarks become progressively elongated as the slope inclination increases, forming linear furrows in the steepest slope area. In these pockmarks, the deepest point of the depression is located off centre

and towards the upslope, interpreted to be the point of fluid venting. The elongated scour downslope of this point is the result of local bottom-current erosion.

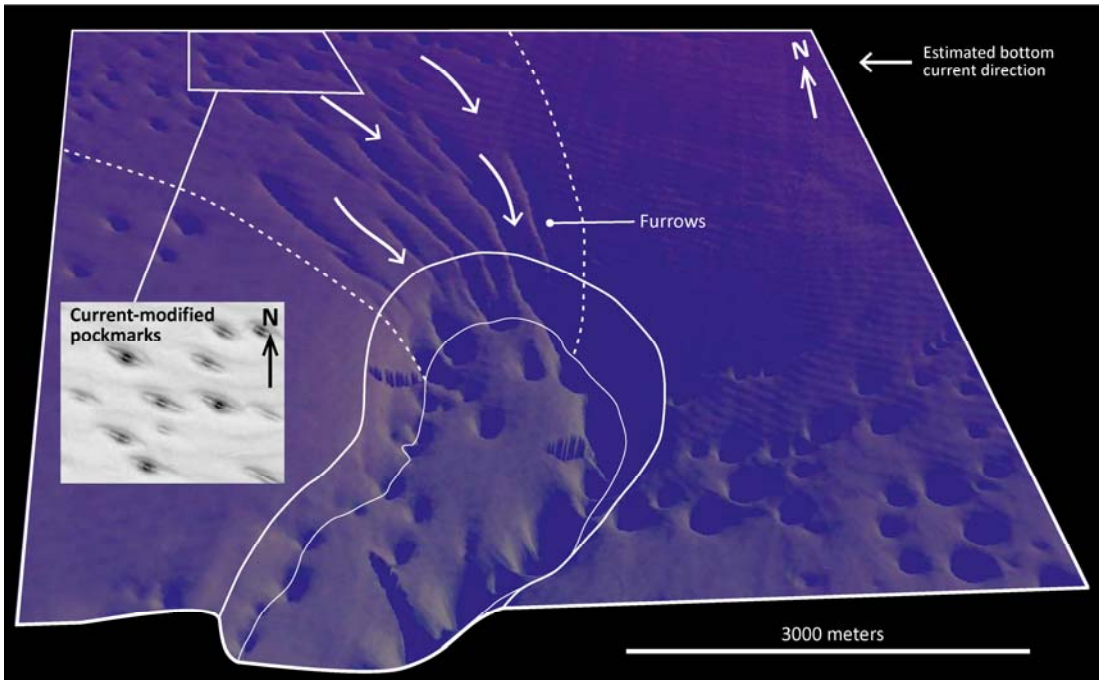

Figure 7.10 Current-modified seabed pockmarks in MB1.

7.4. Seabed pockmark formation in the Lower Congo Basin

7.4.1. Source and type of fluids

The source and type of fluids involved in the formation of the seabed pockmarks analysed here was discussed in Chapter 4 (section 4.5.2.). From the results of this study, it is interpreted that the source of the fluids was from within Unit 3, most likely located stratigraphically between reflectors **x** and **C2**. The seismically resolved conduits between the source and the seabed

pockmarks are pipe-like structures, similar to fluid escape pipes observed in many other basins. From the stacked amplitude anomaly patterns of these conduits, the fluids transported through these pathways most probably included free gas.

It is conceivable that pockmark formation may be associated with gas hydrate dissociation and/or expulsion of free gas beneath the GHSZ. Methane produced from the dissociation of gas hydrates could then be considered as the main fluid involved in seabed pockmark formation. Since no geochemical data was available for this thesis, it is not possible to interpret the origin of the gas that is involved in in this process, but it is acknowledged that in nearby areas both biogenic and thermogenic sources have been inferred for the gas trapped in the hydrate layer (Andresen and Huuse, 2011). However, it is likely that the fluids expelled at the seafloor may result from pore-water and biogenic gas derived from early sediment compaction and decomposition of organic-rich sediments, as discussed by Serié et al. (2017).

7.4.2. Pockmark age

To date the pockmark formation event, it is crucial to identify the erosional base of pockmarks. In this thesis, only the last episode of fluid expulsion is analysed in detail, corresponding to the pockmarks occurring at the present-day seafloor of the study area, assuming that all of them most likely formed at the same time (all occur at the same event horizon). It is interpreted here that the last episode of pockmark formation occurred within the past few thousand years, since all the pockmarks have a clear expression

at the seafloor, and the great majority of the pockmarks do not show any resolvable signs of being buried by recent sediments. The presence of a small set of very elongated pockmarks and linear furrows in MB1 (fig. 7.9) suggests erosion of these pockmarks by bottom-currents, most likely posterior to their generation. Also, few seabed pockmarks infilled with sediments occur near the small submarine channel 2, southwards of MB2 (fig. 7.10). These observations (although minor relative to the other thousands of seabed pockmarks throughout the study area) indicate that some time has passed since the last fluid expulsion event. However, since the effects of these phenomena (bottom-current erosion and sedimentation associated to submarine channels) can take place very rapidly in a geological time-scale, it is still feasible that pockmark formation occurred in the past few thousands of years.

Absolute dating of pockmark formation was not possible, but through seismic stratigraphic relationships the timing of the fluid expulsion episode relative to deformation of basinal sediments can be established. Because of the wide range of spatial arrangements exhibited by seabed pockmarks, it is clear that all controls on their distribution were already in place prior to pockmark formation. As such, pockmark formation occurred posteriorly to all the structural deformation affecting the Lower Congo Basin (i.e., salt tectonic deformation, slope failure, and shallow polygonal faulting).

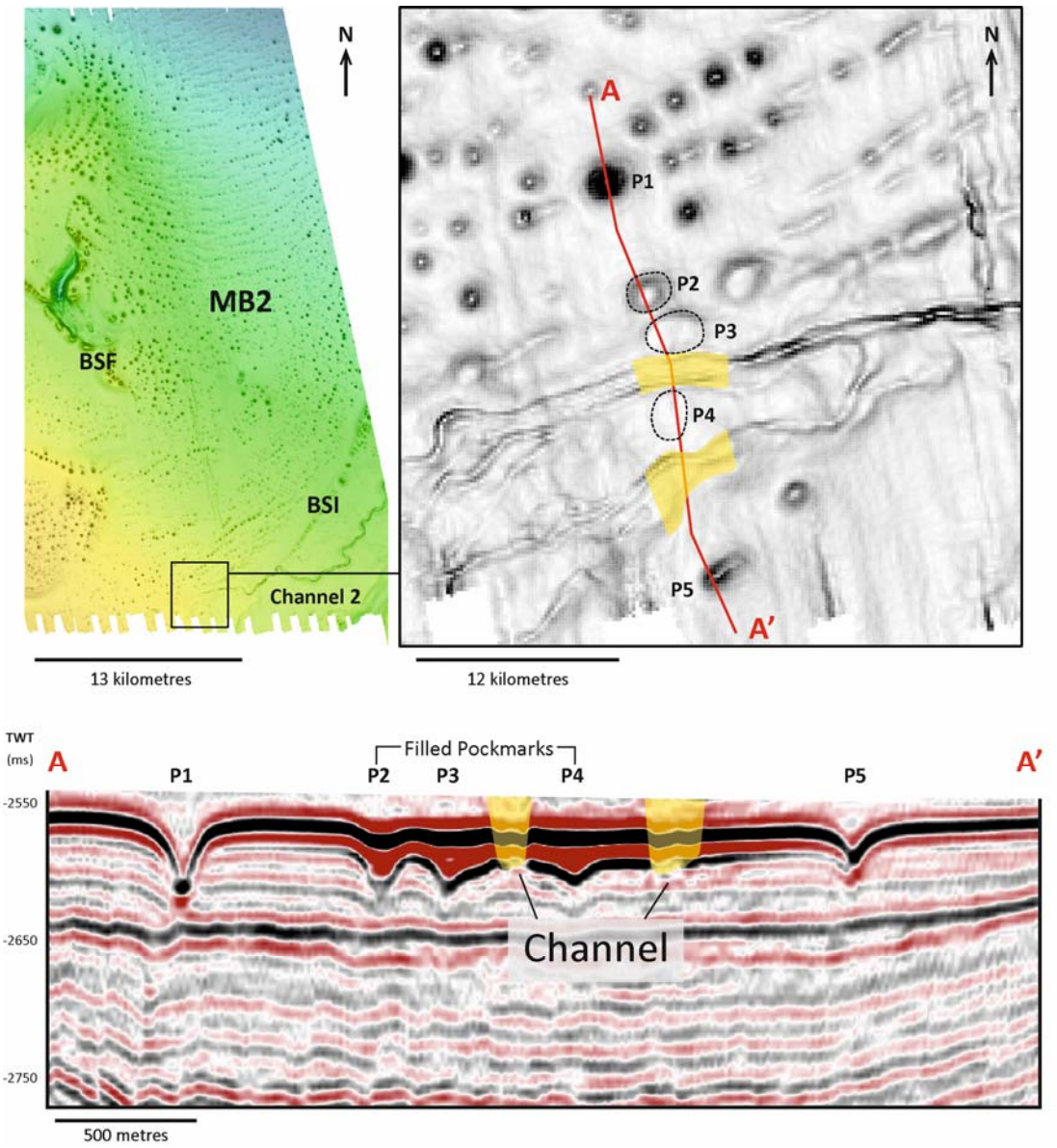

Figure 7.11. Seabed pockmarks infilled with Channel 2 sediments. (Seismic courtesy of PGS.)

7.4.3. Triggers for the fluid expulsion event

As mentioned previously, because all seabed pockmarks occur at the same event horizon, they most likely formed at the same time. The statistical data on pockmark distribution is consistent with this being a single episode of fluid expulsion, since there is clear evidence for an exclusion zone whereby the formation of one pockmark inhibits neighbouring pockmarks from

forming within the exclusion zone. This in turn suggests a period of fluid expulsion whose duration was short enough to prevent any resetting of the hydrodynamic boundary conditions that led to the venting.

Seabed pockmarks saturation and spacing suggest homogeneity of the pore space on the immediate seal. Thus, to form such an extensive field of pockmarks at the same time, the trigger for the fluid expulsion event must have acted at a large scale. This trigger is unknown, but from the coincidence between the observed depth to reflector **x** and the BSR observed on the mini-basin flanks (MB6 and MB7, see Chapters 4 and 5), it is suggested that gas hydrate dissociation may have been involved in liberating methane and its focused expulsion to the seabed led to the formation of the pockmarks. Although speculative, the dissociation of gas hydrates and subsequent gas expulsion may have been triggered by alterations of the pressure-temperature regime, shifting away from hydrate stability conditions. These changes may have been caused by salt growth and ensuing topographic changes, or triggered by a dramatic change in eustatic sea level, or a combination of both. The timing of seabed pockmark formation may coincide with a period of varying eustatic conditions due to glacial-interglacial fluctuations (Judd and Hovland, 2007; Miller et al., 2005), as discussed for pockmarks in nearby areas (Serié et al., 2017; Andresen, 2012). As such, it is possible that the rapid change in sea level at the end of the last glacial maximum may have produced changes in hydrostatic pressure of the area (c.f. Sultan et al., 2004), promoting gas release from hydrates or from solution in pore fluids in the shallow source interval (Hermanrud et al., 2013; Riboulot et al., 2013).

7.5. Limitations of the research

The work presented in this thesis was possible by the availability of high quality of 3D seismic data, which allowed a very good visualisation and interpretation of the facies and structures present in the studied area. The major limitations of this study reside on the geographical coverage and the minimum resolution scales possible to be obtained from the 3D seismic dataset. Despite the good geographical data coverage, the assessment of the true extent of geological features (such as halokinetic features and mini-basin full structures) is compromised. This implies that the quantitative studies undertaken may be unable to represent the geological reality in its fullness, especially when considering the spatial statistical analysis of pockmarks near the limits of the dataset.

The major constrain in this research is the minimum resolution available from the 3D seismic data. The horizontal resolution of the data is 25 metres, which is sufficient for the general assessment of the lateral extent of the stratigraphic, structural and fluid flow features, at the scales required for deep-marine exploration. The main resolution limitation resides on the vertical scale of the analysed features. The seismic resolution is of circa 11 metres for the shallowest units. Although this is still sufficient to highlight shallow features at the limit of seismic resolution on attribute maps, there are strong limitations on the visualisation of geological features at a sub-seismic scale that can have important small-scale controls on the shallow plumbing system of the area. Such is expected to influence the correct assessment of

small fault and fractures networks, and consequently their impact of the fluid flow paths in the shallow strata.

This research would also have greatly beneficiated from information provided by well data, but this was not available. The information provided by drilled wells in the Lower Congo Basin would have allowed a more detailed characterisation of the composition and age of the stratigraphic units analysed, minimising the errors from the literature-based assumptions undertaken. The availability of well data would also have allowed a more detailed characterisation of the composition and thickness of key sediment packages, particularly at sub-seismic scales.

7.6. Future work

3D seismic conduit analysis in only valid if the processes by which faults act as conduits for fluid migration are understood and correctly identified for each case study. Although it is clear that faults play a major role in fluid distribution in the Earth's crust, there are still questions that need to be addressed to complement the ongoing research of fault-controlled fluid migration. Future studies must consider the following problematic topics:

1) Constant vs. episodic leakage – Is it only active faults that control fluid flow, or can inactive faults also be vertical conduits? Do faults cease their flow potential by progressive cementation or can they be semi-permanent open pathways?

2) Does the geo-mechanical context influence flow properties? Do different geological settings produce different styles of fault-controlled flow? If so, how? What are the processes involved?

3) "What are the typical fluid/rock ratios, flow rates, and discharges for fault zones acting as fluid conduits" (Hickman et al., 1995)? What impact do they have on primary and secondary hydrocarbon migration?

Future work on fault-controlled hydrocarbon migration using 3D seismic data must combine structural analysis, fault motion history, geometrical and contextual analysis with hydrocarbon distribution. To minimise the "scale" limitations of using 3D seismic data, well data should be available. The research would great benefit from observations made during field work, cover this gap on sub-seismic features and to validate the observations made at larger scale in seismic data.

Evidences for fault-related flow come from the most diverse areas, but few studies combine different geological settings in a comparative analysis, thus failing to establish a wider theoretical context. Several areas from different sedimentary basin types should be analysed and compared, to maximise the variability in the main condition boundaries and integrate them in an extended theoretical model.

The increasing number of studies on the geochemistry of seafloor seeps is providing new insights on the composition and sources of fluids being released to the seafloor. Despite the limitations implied with such

methods, their availability to complement the information provided by the 3D seismic data is relevant for the full understanding of the whole plumbing system.

Chapter 8

CONTROLS ON SHALLOW PLUMBING SYSTEMS INFERRED FROM THE SPATIAL ANALYSIS OF POCKMARK ARRAYS

THESIS CONCLUSIONS

Controls on shallow plumbing systems inferred from the spatial analysis of pockmark arrays

Conclusions

8. Thesis conclusions

The research work presented in this thesis is of extreme importance to understand the controls on seal breaching of slope sediments. Seal bypass features distributed above fluid reservoirs are often associated to “leaky” traps, which may have a significant impact on the exploration of hydrocarbon fields. Identifying these features and understanding how and where they are formed is crucial to avoid drilling hazards, especially those related to shallow gas.

The research presented in this thesis attempted to answer the following questions:

I. What are the controls on seal breaching and pockmark distribution?

The main controls on seal breaching and pockmark distribution identified in the study area are related to the local conditions of overpressure and buoyancy, the stress field (stress direction and magnitude), and pre-existing deformation features. The local stress field will determine the deformation patterns of the basin, modifying the local topography and geomorphology, and generating discontinuities, fractures, and/or faults.

These features will influence further sediment deposition and control fluid migration pathways, affecting the general plumbing systems of the area. Seal failure of the shallow sediments occurs at the point of maximum overpressure, focused by pre-existing discontinuities and sub-seismic heterogeneities in the seal. Thus, different geological settings produce different styles of focused fluid flow and expulsion.

Three main types of fluid flow controls were recognised in the study area, related to a wide spectrum of deformation styles: 1) stratigraphic/depositional controls; 2) strati-structural controls; and 3) structural controls. Stratigraphic or depositional controls are the primary, most simple processes that regulate the spatial arrangement of pockmarks, and are intimately associated with the nature of the subsurface sediments and how these are distributed within a basin. These controls are associated to the small window of special conditions in which pockmarks form (i.e., the suitable geological setting), and lithological variations either resultant from the contact of different sedimentary bodies (e.g., pinch-outs; interface submarine channel-hosting sediments) or from lateral variations of the properties of a particular interval. Strati-structural controls refer to the influence of sediment failure on the distribution of pockmarks. Submarine slope failure and consequent sediment remobilisation produce internal deformation of the affected strata. The scale of this deformation depends on the type of shallow sediment failure, ranging from incipient gravitational gliding that produces minor sub-seismic discontinuities to large-scale mass-transport deposits that completely rework the internal fabric of the affected sediments. The deformation structures generated during slope failure will

impact the local fluid drainage patterns in a similar manner as regional processes. The most complex set of controls on seal breaching and pockmark formation are associated to the structural deformation of sediments, in which faults and fractures are the main controlling features. Structural controls comprise the effects of polygonal faults, tectonic faults and halokinetic structures on the distribution of fluid migration pathways. Faults were observed to be both conduits (tectonic faults) and barriers (polarised polygonal faults) for fluid flow, depending on their geo-mechanical setting. Either way, faults do influence the position of fluid migration pathways and have a significant impact on the shallow plumbing system.

II. What impacts seal bypass features formed during early burial have on potential caprocks?

The impact of seal bypass features on potential caprocks depends on the type of feature and its hosting sediments. Early burial discontinuities such as polygonal faults may influence the location where seal failure will take place, but still be impermeable barriers for fluid migration. Other discontinuities may be preferential pathways for repeated and future seal failure, as exemplified by vertically stacked pockmarks and bulls-eye pockmarks observed in the study area. These features are evidence that the same migration pathway was re-used multiple times to produce paleo- and seabed pockmarks. However, it is possible that if the pockmark drainage cell mechanism is in place, there is an exclusion area around each pipe or pockmark in which no other seal bypass feature will be formed. As such, even

though the main feeding pipe may be exploited multiple times, the immediate surrounding sealing sediments (within the exclusion zone distance) may retain its integrity whilst the local stress field is stable.

The results from this thesis show that it is possible to infer and distinguish stratigraphic and structural controls on the shallow plumbing system of a certain basin based on the distribution patterns of pockmark arrays.

Chapter 9

REFERENCES

9. References

Abreu, V., Sullivan, M., Pirmez, C. and Mohrig, D., 2003. Lateral accretion packages (LAPs): an important reservoir element in deep water sinuous channels. Marine and Petroleum Geology, 20(6-8): 631-648.

Alsop, G., Brown, J., Davison, I. and Gibling, M., 2000. The geometry of drag zones adjacent to salt diapirs. Journal of the Geological Society, 157(5): 1019.

Anderson, J.E., Cartwright, J., Drysdall, S.J. and Vivian, N., 2000. Controls on turbidite sand deposition during gravity-driven extension of a passive margin: examples from Miocene sediments in Block 4, Angola. Marine and Petroleum Geology, 17(10): 1165-1203.

Andresen, K.J., 2012. Fluid flow features in hydrocarbon plumbing systems: What do they tell us about the basin evolution? Marine Geology, 332: 89-108.

Andresen, K.J. and Huuse, M., 2011. Bulls-eye' pockmarks and polygonal faulting in the Lower Congo Basin: Relative timing and implications for fluid expulsion during shallow burial. Marine Geology, 279(1-4): 111-127.

Anka, Z., Ondrak, R., Kowitz, A. and Schødt, N., 2013. Identification and numerical modelling of hydrocarbon leakage in the Lower Congo Basin: Implications on the genesis of km-wide seafloor mounded structures. Tectonophysics, 604: 153-171.

Anka, Z. and Séranne, M., 2004. Reconnaissance study of the ancient Zaire (Congo) deep-sea fan. (ZaiAngo Project). Marine Geology, 209(1-4): 223-244.

Anka, Z., Séranne, M., Lopez, M., Scheck-Wenderoth, M. and Savoye, B., 2009. The long-term evolution of the Congo deep-sea fan: A basin-wide view of the interaction between a giant submarine fan and a mature passive margin (ZaiAngo project). Tectonophysics, 470(1–2): 42-56.

Antonellini, M. and Aydin, A., 1995. Effect of faulting on fluid flow in porous sandstones; geometry and spatial distribution. AAPG Bulletin, 79(5): 642-671.

Ashby, D., 2013. Influences on continental margin development: a case study from the Santos Basin, South-eastern Brazil, PhD Thesis, Durham University.

Bacon, M., Simm, R. and Redshaw, T., 2003. 3-D seismic interpretation. Cambridge Univ Pr, 209 pp.

Beaubouef, R.T. and Abreu, V., 2010. MTCs of the Brazos-Trinity Slope System; Thoughts on the Sequence Stratigraphy of MTCs and Their Possible Roles in Shaping Hydrocarbon Traps. In: D.C. Mosher et al. (Eds.), Submarine Mass Movements and Their Consequences. Springer, pp. 475-490.

Berg, R.R., 1975. Capillary pressures in stratigraphic traps. AAPG Bulletin, 59(6): 939-956.

Berger, W., Wefer, G., Richter, C., Lange, C., Giraudeau, J. and Hermelin, O., 1998. The Angola-Benguela upwelling system: Paleoceanographic synthesis of shipboard results from Leg 175, Proceedings of the Ocean Drilling Program. Initial reports. Ocean Drilling Program, pp. 505-531.

Berndt, C., 2005. Focused fluid flow in passive continental margins. Philosophical Transactions of the Royal Society A: Mathematical, Physical and Engineering Sciences, 363(1837): 2855.

Berndt, C., Costa, S., Canals, M., Camerlenghi, A., de Mol, B. and Saunders, M., 2012. Repeated slope failure linked to fluid migration: the Ana submarine landslide complex, Eivissa Channel, Western Mediterranean Sea. Earth and Planetary Science Letters, 319: 65-74.

Bertoni, C., Cartwright, J. and Hermanrud, C., 2013. Evidence for large-scale methane venting due to rapid drawdown of sea level during the Messinian Salinity Crisis. Geology, 41(3): 371-374.

Blanpied, M.L., Lockner, D.A. and Byerlee, J.D., 1992. An earthquake mechanism based on rapid sealing of faults. Nature, 358(6387): 574-576.

Boles, J.R., Eichhubl, P., Garven, G. and Chen, J., 2004. Evolution of an hydrocarbon migration pathway along basin-bounding faults: Evidence from fault cement. AAPG Bulletin, 88: 947-970.

Bolker, B.M., 2008. Ecological models and data in R. Princeton University Press, 408 pp.

Bolli, H., Ryan, W., Foresman, J., Hottman, W., Kagami, H., Longoria, J., McKnight, B., Melguen, M., Natland, J. and Proto-Decima, F., 1978. Angola continental margin—Sites 364 and 365. Initial Reports of the Deep Sea Drilling Project, 40: 357-390.

Broucke, O., Temple, F., Rouby, D., Robin, C., Calassou, S., Nalpas, T. and Guillocheau, F., 2004. The role of deformation processes on the geometry of mud-dominated turbiditic systems, Oligocene and Lower-Middle Miocene of the Lower Congo basin (West African Margin). Marine and Petroleum Geology, 21(3): 327-348.

Brown, A.R., 2004. Interpretation of Three-Dimensional Seismic Data, sixth ed. AAPG Memoir, 42. American Association of Petroleum Geologists, Memoir 42, Tulsa, 534 pp.

Brownfield, M.E. and Charpentier, R.R., 2006. Geology and Total Petroleum Systems of the West-Central Coastal Province (7203), West Africa. USGS Bulletin 2207-B.

Brun, J.-P. and Fort, X., 2011. Salt tectonics at passive margins: Geology versus models. Marine and Petroleum Geology, 28(6): 1123-1145.

Brüning, M., Sahling, H., MacDonald, I.R., Ding, F. and Bohrmann, G., 2010. Origin, distribution, and alteration of asphalts at Chapopote Knoll, Southern Gulf of Mexico. Marine and Petroleum Geology, 27(5): 1093-1106.

Bull, S., Cartwright, J. and Huuse, M., 2009. A review of kinematic indicators from mass-transport complexes using 3D seismic data. Marine and Petroleum Geology, 26(7): 1132-1151.

Bünz, S., Mienert, J., Bryn, P. and Berg, K., 2005. Fluid flow impact on slope failure from 3D seismic data: a case study in the Storegga Slide. Basin Research, 17(1): 109-122.

Burwood, R., 1999. Angola: source rock control for Lower Congo Coastal and Kwanza Basin petroleum systems. In: N.R. Cameron, R.H. Bate and V.S. Clure (Eds.), The Oil and Gas Habitats of the South Atlantic. Geological Society, London, Special Publications 153

pp. 181-194.

Burwood, R., Cornet, P.J., Jacobs, L. and Paulet, J., 1990. Organofacies variation control on hydrocarbon generation: A Lower Congo Coastal Basin (Angola) case history. Organic Geochemistry, 16(1): 325-338.

Byerlee, J., 1990. Friction, overpressure and fault normal compression. Geophysical Research Letters, 17(12): 2109-2112.

Byerlee, J., 1993. Model for episodic flow of high-pressure water in fault zones before earthquakes. Geology, 21(4): 303-306.

Carruthers, D., 2012. Interaction of polygonal fault systems with salt diapirs, PhD Thesis, Cardiff University.

Carruthers, D., Cartwright, J., Jackson, M.P. and Schutjens, P., 2013a. Origin and timing of layer-bound radial faulting around North Sea salt stocks: New insights into the evolving stress state around rising diapirs. Marine and Petroleum Geology, 48: 130-148.

Carruthers, D., Cartwright, J., Jackson, M.P.A. and Schutjens, P., 2013b. Origin and timing of layer-bound radial faulting around North Sea salt stocks: New insights into the evolving stress state around rising diapirs. Marine and Petroleum Geology, 48: 130-148.

Cartwright, A., Moss, J. and Cartwright, J., 2011. New statistical methods for investigating submarine pockmarks. Computers & geosciences, 37(10): 1595-1601.

Cartwright, J., 2007. The impact of 3D seismic data on the understanding of compaction, fluid flow and diagenesis in sedimentary basins. Journal of the Geological Society, 164(5): 881-893.

Cartwright, J., 2011. Diagenetically induced shear failure of fine-grained sediments and the development of polygonal fault systems. Marine and Petroleum Geology, 28(9): 1593-1610.

Cartwright, J. and Dewhurst, D., 1998a. Layer-bound compaction faults in fine-grained sediments. Geological Society of America Bulletin, 110(10): 1242-1257.

Cartwright, J. and Huuse, M., 2005. 3D seismic technology: the geological 'Hubble'. Basin Research, 17(1): 1-20.

Cartwright, J., Huuse, M. and Aplin, A., 2007. Seal bypass systems. American Association of Petroleum Geologists Bulletin, 91(8): 1141-1166.

Cartwright, J., James, D. and Bolton, A., 2003. The genesis of polygonal fault systems: a review. Geological Society London Special Publications, 216(1): 223.

Cartwright, J. and Santamarina, C., 2015. Seismic characteristics of fluid escape pipes in sedimentary basins: implications for pipe genesis. Marine and Petroleum Geology, 65: 126-140.

Cartwright, J.t. and Dewhurst, D., 1998b. Layer-bound compaction faults in fine-grained sediments. Geological Society of America Bulletin, 110(10): 1242-1257.

Cathles, L.M., Su, Z. and Chen, D., 2010. The physics of gas chimney and pockmark formation, with implications for assessment of seafloor hazards and gas sequestration. Marine and Petroleum Geology, 27(1): 82-91.

Chopra, S. and Marfurt, K.J., 2005. Seismic attributes—A historical perspective. Geophysics, 70(5): 3SO-28SO.

Clark, I.R. and Cartwright, J.A., 2011. Key controls on submarine channel development in structurally active settings. Marine and Petroleum Geology, 28(7): 1333-1349.

Cole, G., Requejo, A., Ormerod, D., Yu, Z. and Clifford, A., 2000. Petroleum Geochemical Assessment of the Lower Congo Basin. In: M.R. Mello and B.J. Katz (Eds.), Petroleum Systems of the South Atlantic Margins. AAPG Memoir 73, pp. 352-339.

Coward, M.P., Purdy, E.G., Ries, A.C. and Smith, D.G., 1999. The distribution of petroleum reserves in basins of the South Atlantic margins, Geological Society Special Publication, pp. 101-131.

Cramez, C. and Jackson, M.P.A., 2000. Superposed deformation straddling the continental-oceanic transition in deep-water Angola. Marine and Petroleum Geology, 17(10): 1095-1109.

Crawley, M.J., 2012. The R book. John Wiley & Sons.

Crutchley, G.J., Gorman, A.R., Pecher, I.A., Toulmin, S. and Henrys, S.A., Geological controls on focused fluid flow through the gas hydrate stability zone on the southern Hikurangi Margin of New Zealand, evidenced from multi-channel seismic data. Marine and Petroleum Geology, In Press, Accepted Manuscript.

Cunningham, R. and Lindholm, R., 2000. Seismic evidence for widespread gas hydrate formation, offshore West Africa, Petroleum Systems of South Atlantic margins. AAPG Memoir 73, pp. 93-105.

Dandapath, S., Chakraborty, B., Karisiddaiah, S.M., Menezes, A., Ranade, G., Fernandes, W., Naik, D.K. and Prudhvi Raju, K.N., 2010. Morphology of pockmarks

along the western continental margin of India: Employing multibeam bathymetry and backscatter data. Marine and Petroleum Geology, In Press, Corrected Proof.

Danforth, A., Koning, T. and de Deus, O., 1997. Petroleum Systems of the Coastal Kwanza and Benguela Basins, Angola, Hedberg AAPG/ABGP Joint Research Sympoxium "Petroleum System of the South Atlantic Margin", Rio de Janeiro, Brazil.

Davies, R.J., Cartwright, J.A., Stewart, S.A., Underhill, J.R. and Lappin, M., 2004. 3D Seismic Technology: Application to the Exploration of Sedimentary Basins. Geological Society London Memoir, 29.

Davies, R.J. and Stewart, S.A., 2005. Emplacement of giant mud volcanoes in the South Caspian Basin: 3D seismic reflection imaging of their root zones. Journal of the Geological Society, 162(1): 1-4.

Davis, J.C., 2002. Statistics and Data Analysis in Geology, 3rd Edition. Wiley, New York.

Davison, I., Alsop, G.I., Evans, N.G. and Safaricz, M., 2000a. Overburden deformation patterns and mechanisms of salt diapir penetration in the Central Graben, North Sea. Marine and Petroleum Geology, 17(5): 601-618.

Davison, I., Alsop, I., Birch, P., Elders, C., Evans, N., Nicholson, H., Rorison, P., Wade, D., Woodward, J. and Young, M., 2000b. Geometry and late-stage structural evolution of Central Graben salt diapirs, North Sea. Marine and Petroleum Geology, 17(4): 499-522.

de Boer, J.Z., Hale, J.R. and Chanton, J., 2001. New evidence for the geological origins of the ancient Delphic oracle (Greece). Geology, 29(8): 707-710.

Deptuck, M.E., Steffens, G.S., Barton, M. and Pirmez, C., 2003. Architecture and evolution of upper fan channel-belts on the Niger Delta slope and in the Arabian Sea. Marine and Petroleum Geology, 20(6-8): 649-676.

Deptuck, M.E., Sylvester, Z., Pirmez, C. and O'Byrne, C., 2007. Migration-aggradation history and 3-D seismic geomorphology of submarine channels in the Pleistocene Benin-major Canyon, western Niger Delta slope. Marine and Petroleum Geology, 24(6-9): 406-433.

Dimitrov, L.I., 2002. Mud volcanoes—the most important pathway for degassing deeply buried sediments. Earth-Science Reviews, 59(1): 49-76.

Dooley, T.P., Jackson, M.P.A. and Hudec, M.R., 2009. Inflation and deflation of deeply buried salt stocks during lateral shortening. Journal of Structural Geology, 31(6): 582-600.

Duval, B., Cramez, C. and Jackson, M.P.A., 1992. Raft tectonics in the Kwanza Basin, Angola. Marine and Petroleum Geology, 9(4): 389-404.

Emery, K.O., Uchupi, E., Phillips, J., Bowin, C. and Mascle, J., 1975. Continental margin off western Africa: Angola to Sierra Leone. AAPG Bulletin, 59(12): 2209-2265.

Ercilla, G., 1996. Gas-charged sediments and large pockmark-like features on the Gulf of Cadiz slope (SW Spain). Marine and Petroleum Geology, 13(2): 253-261.

Etiope, G., 2015. Natural Gas Seepage: The Earth's Hydrocarbon Degassing. Springer.

Evans, R., 1978. Origin and significance of evaporites in basins around Atlantic margin. AAPG Bulletin, 62(2): 223-234.

Fort, X., Brun, J.-P. and Chauvel, F., 2004. Salt tectonics on the Angolan margin, synsedimentary deformation processes. AAPG Bulletin, 88(11): 1523-1544.

Fort, X. and Brun, J.P., 2005. Deformation induced pathways for hydrocarbon migration through the Aptian salt level in the Angolan margin. GCSSEPM Foundation 25th Annual Bob F. Perkins ...: 1-17.

Fossen, H., 2016. Structural geology. Cambridge University Press.

Fowles, J. and Burley, S., 1994. Textural and permeability characteristics of faulted, high porosity sandstones. Marine and Petroleum Geology, 11(5): 608-623.

Frey-Martínez, J., 2010. 3D Seismic interpretation of mass transport deposits: implications for basin analysis and geohazard evaluation, Submarine Mass Movements and Their Consequences. Springer, pp. 553-568.

Frey-Martinez, J., Cartwright, J. and Hall, B., 2005. 3D seismic interpretation of slump complexes: examples from the continental margin of Israel. Basin Research, 17(1): 83-108.

Frey-Martínez, J., Cartwright, J. and James, D., 2006. Frontally confined versus frontally emergent submarine landslides: A 3D seismic characterisation. Marine and Petroleum Geology, 23(5): 585-604.

Gamboa, D., Alves, T. and Cartwright, J., 2011. Distribution and characterization of failed (mega) blocks along salt ridges, southeast Brazil: Implications for vertical fluid flow on continental margins. Journal of Geophysical Research, 116(B8): B08103.

Gamboa, D. and Alves, T.M., 2015. Three-dimensional fault meshes and multi-layer shear in mass-transport blocks: Implications for fluid flow on continental margins. Tectonophysics, 647–648(0): 21-32.

Gamboa, D. and Alves, T.M., 2016. Bi-modal deformation styles in confined mass-transport deposits: Examples from a salt minibasin in SE Brazil. Marine Geology, 379: 176-193.

Gartrell, A., Zhang, Y., Lisk, M. and Dewhurst, D., 2004. Fault intersections as critical hydrocarbon leakage zones: integrated field study and numerical modelling of an example from the Timor Sea, Australia. Marine and Petroleum Geology, 21(9): 1165-1179.

Gay, A. and Berndt, C., 2007. Cessation/reactivation of polygonal faulting and effects on fluid flow in the Vøring Basin, Norwegian Margin. Journal of the Geological Society, 164(1): 129-141.

Gay, A., Lopez, M., Berndt, C. and Séranne, M., 2007. Geological controls on focused fluid flow associated with seafloor seeps in the Lower Congo Basin. Marine Geology, 244(1-4): 68-92.

Gay, A., Lopez, M., Cochonat, P., Levaché, D., Sermondadaz, G. and Seranne, M., 2006a. Evidences of early to late fluid migration from an upper Miocene turbiditic channel revealed by 3D seismic coupled to geochemical sampling within seafloor pockmarks, Lower Congo Basin. Marine and Petroleum Geology, 23(3): 387-399.

Gay, A., Lopez, M., Cochonat, P., Séranne, M., Levaché, D. and Sermondadaz, G., 2006b. Isolated seafloor pockmarks linked to BSRs, fluid chimneys, polygonal

faults and stacked Oligocene-Miocene turbiditic palaeochannels in the Lower Congo Basin. Marine Geology, 226(1-2): 25-40.

Gay, A., Lopez, M., Cochonat, P. and Sermondadaz, G., 2004. Polygonal faults-furrows system related to early stages of compaction – upper Miocene to recent sediments of the Lower Congo Basin. Basin Research, 16(1): 101-116.

Gay, A., Lopez, M., Ondreas, H., Charlou, J.L., Sermondadaz, G. and Cochonat, P., 2006c. Seafloor facies related to upward methane flux within a Giant Pockmark of the Lower Congo Basin. Marine Geology, 226(1-2): 81-95.

Gee, M.J.R., Gawthorpe, R.L. and Friedmann, J.S., 2005. Giant striations at the base of a submarine landslide. Marine Geology, 214(1-3): 287-294.

Giavarini, C. and Hester, K., 2011. Gas hydrates: Immense energy potential and environmental challenges. Springer Science & Business Media.

Gluyas, J. and Swarbrick, R., 2013. Petroleum geoscience. John Wiley & Sons.

Graue, K., 2000. Mud volcanoes in deepwater Nigeria. Marine and Petroleum Geology, 17(8): 959-974.

Hammer, Ø., Harper, D. and Ryan, P., 2001. PAST: Paleontological Statistics Software Package for Education and Data Analysis Palaeontol. Electronica 4: 1–9.

Hammer, Ø., Webb, K.E. and Depreiter, D., 2009. Numerical simulation of upwelling currents in pockmarks, and data from the Inner Oslofjord, Norway. Geo-Marine Letters, 29(4): 269-275.

Hampton, M.A., Lee, H.J. and Locat, J., 1996. Submarine Landslides. Review of Geophysics, 34(1): 33-59.

Hart, B.S., 1999. Definition of subsurface stratigraphy, structure and rock properties from 3-D seismic data. Earth-Science Reviews, 47(3-4): 189-218.

Haughton, P.D.W., Barker, S.P. and McCaffrey, W.D., 2003. 'Linked' debrites in sand-rich turbidite systems - origin and significance. Sedimentology, 50(3): 459-482.

Hedberg, H.D., 1974. Relation of methane generation to undercompacted shales, shale diapirs, and mud volcanoes. AAPG Bulletin, 58(4): 661-673.

Heggland, R., 1998. Gas seepage as an indicator of deeper prospective reservoirs. A study based on exploration 3D seismic data. Marine and Petroleum Geology, 15(1): 1-9.

Hempton, M., Rosen, M., Coughlin, R., Scardina, A., Hagen, E. and Nordstrom, D., 1990. The geology of west Africa—a regional review. American Association Petroleum Geologists Bulletin, 75: 583.

Hempton, M., Rosen, M., Coughlin, R., Scardina, A., Hagen, E. and Nordstrom, P., 1991. Regional paleogeographic evolution of west Africa: Implications for hydrocarbon exploration. AAPG Bulletin, 75(CONF-910403--).

Hermanrud, C., Venstad, J.M., Cartwright, J., Rennan, L., Hermanrud, K. and Bolås, H.M.N., 2013. Consequences of water level drops for soft sediment deformation and vertical fluid leakage. Mathematical Geosciences, 45(1): 1-30.

Hernández-Molina, F., Llave, E. and Stow, D., 2008. Continental slope contourites. Developments in Sedimentology, 60: 379-408.

Hickman, S., Sibson, R. and Bruhn, R., 1995. Introduction to special section: mechanical involvement of fluids in faulting. Journal of Geophysical Research, 100(B7): 12831.

Hillman, J.I.T., Klaucke, I., Bialas, J., Feldman, H., Drexler, T., Awwiller, D., Atgin, O. and Çifçi, G., 2018. Gas migration pathways and slope failures in the Danube Fan, Black Sea. Marine and Petroleum Geology.

Ho, S., Cartwright, J. and Imbert, P., 2012. Vertical evolution of fluid venting structures in relation to gas flux, in the Neogene-Quaternary of the Lower Congo Basin, Offshore Angola. Marine Geology, 332: 40-55.

Hooper, E.C.D., 1991. Fluid Migration along Growth Faults in Compacting Sediments. Journal of Petroleum Geology, 14: 161-180.

Hovland, M., 2003. Geomorphological, geophysical, and geochemical evidence of fluid flow through the seabed. Journal of Geochemical Exploration, 78-79: 287-291.

Hovland, M., Gardner, J.V. and Judd, A.G., 2002. The significance of pockmarks to understanding fluid flow processes and geohazards. Geofluids, 2(2): 127-136.

Hovland, M. and Judd, A.G., 1988a. Seabed Pockmarks and Seepage. Graham and Trotman, London.

Hovland, M. and Judd, A.G., 1988b. Seabed pockmarks and seepages: impact on geology, biology, and the marine environment. Springer.

Hudec, M.R. and Jackson, M.P.A., 2002. Structural segmentation, inversion, and salt tectonics on a passive margin: Evolution of the Inner Kwanza Basin, Angola. Geological Society of America Bulletin, 114(10): 1222-1244.

Hudec, M.R. and Jackson, M.P.A., 2007. Terra infirma: Understanding salt tectonics. Earth-Science Reviews, 82(1-2): 1-28.

Hudec, M.R. and Jackson, M.P.A., 2011. The salt mine: A digital atlas of salt tectonics. The University of Texas at Austin, Bureau of Economic Geology, Udden Book Series No 5; AAPG Memoir 99, 305 pp.

Huuse, M., Jackson, C.A.L., Van Rensbergen, P., Davies, R.J., Flemings, P.B. and Dixon, R.J., 2010. Subsurface sediment remobilization and fluid flow in sedimentary basins: an overview. Basin Research, 22(4): 342-360.

Ivakhnenko, O.P. and Potter, D.K., 2004. Magnetic susceptibility of petroleum reservoir fluids. Physics and Chemistry of the Earth, Parts A/B/C, 29(13-14): 899-907.

Jackson, M.P.A., 1995. Retrospective salt tectonics. In: M.P.A. Jackson, D.G. Roberts and S. Snelson (Eds.), Salt Tectonics: a global perspective. AAPG Memoir 65, pp. 1-28.

Jackson, M.P.A., Vendeville, B. and Schultz-Ela, D.D., 1994. Structural Dynamics of Salt Systems. Annual Review Of Earth And Planetary Sciences, 22: 93-117.

Jackson, M.P.A. and Vendeville, B.C., 1994. Regional extension as a geologic trigger for diapirism. Geological Society of America Bulletin, 106(1): 57-73.

James, D., 1997. Discussion on a model for the structure and development of fault zones. Journal of the Geological Society, 154(2): 366-368.

Jolivet, J., Bonnin, J., Beuzart, P. and Auzende, J.-M., 1984. Cinématique de l'Atlantique nord et central. Publications du CNEXO Série Rapports scientifiques et techniques, 54: 1-108.

Jolley, S.J., Barr, D., Walsh, J.J. and Knipe, R.J., 2007. Structurally complex reservoirs: an introduction. Geological Society, London, Special Publications, 292(1): 1-24.

Judd, A.G. and Hovland, M., 2007. Seabed Fluid Flow. Cambridge University Press, 492 pp.

Karner, G.D., Driscoll, N.W., McGinnis, J.P., Brumbaugh, W.D. and Cameron, N.R., 1997. Tectonic significance of syn-rift sediment packages across the Gabon-Cabinda continental margin. Marine and Petroleum Geology, 14(7): 973-1000.

Kearey, P., Brooks, M. and Hill, I., 2002. An introduction to geophysical exploration. Wiley-Blackwell, 268 pp.

King, L.H. and MacLEAN, B., 1970. Pockmarks on the Scotian shelf. Geological Society of America Bulletin, 81(10): 3141-3148.

Knipe, R.J., 1997. Juxtaposition and seal diagrams to help analyze fault seals in hydrocarbon reservoirs. AAPG Bulletin, 81(2): 187-195.

Knipe, R.J., Jones, G. and Fisher, Q.J., 1998. Faulting, fault sealing and fluid flow in hydrocarbon reservoirs: an introduction. In: G. Jones, Q.J. Fisher and R.J.

Knipe (Eds.), Faulting, Fault Sealing and Fluid Flow in Hydrocarbon Reservoirs. Geological Society, London, Special Publications, 147, pp. vii-xxi.

Kolla, V., Bourges, P., Urruty, J.M. and Safa, P., 2001. Evolution of deep-water Tertiary sinuous channels offshore Angola (west Africa) and implications for reservoir architecture. American Association of Petroleum Geologists Bulletin, 85(8): 1373-1405.

Kopf, A.J., 2002. Significance of mud volcanism. Rev. Geophys., 40(2): 1005.

Kumar, M.B., 1977. Geothermal and geopressure patterns of Bayou Carlin-Lake Sand area, South Louisiana; implications. AAPG Bulletin, 61(1): 65-78.

Lachenbruch, A., 1980. Frictional heating, fluid pressure, and the resistance to fault motion. Journal of Geophysical Research, 85(B11): 6097-6112.

Lentini, M.R., Fraser, S.I., Sumner, H.S. and Davies, R.J., 2010. Geodynamics of the central South Atlantic conjugate margins: implications for hydrocarbon potential. Petroleum Geoscience, 16(3): 217-229.

Lerche, I., 2013. Dynamical geology of salt and related structures. Elsevier.

Leyden, R., Asmus, H., Zembruscki, S. and Bryan, G., 1976. South Atlantic diapiric structures. AAPG Bulletin, 60(2): 196-212.

Li, W., Alves, T.M., Wu, S., Rebesco, M., Zhao, F., Mi, L. and Ma, B., 2016. A giant, submarine creep zone as a precursor of large-scale slope instability offshore the Dongsha Islands (South China Sea). Earth and Planetary Science Letters, 451: 272-284.

Ligtenberg, J.H., 2005. Detection of fluid migration pathways in seismic data: implications for fault seal analysis. Basin Research, 17(1): 141-153.

Liu, X. and Flemings, P., 2009. Dynamic response of oceanic hydrates to sea level drop. Geophysical Research Letters, 36(17).

Loncke, L., Mascle, J. and Parties, F.S., 2004. Mud volcanoes, gas chimneys, pockmarks and mounds in the Nile deep-sea fan (Eastern Mediterranean): geophysical evidences. Marine and Petroleum Geology, 21(6): 669-689.

López, D. and Smith, L., 1995. Fluid flow in fault zones: Analysis of the interplay of convective circulation and topographically driven groundwater flow. Water Resources Research, 31(6): 1489-1503.

Løseth, H., Gading, M. and Wensaas, L., 2009. Hydrocarbon leakage interpreted on seismic data. Marine and Petroleum Geology, 26(7): 1304-1319.

Løseth, H., Wensaas, L., Arntsen, B., Hanken, N., Basire, C. and Graue, K., 2001. 1000 m long gas blow-out pipes, 63rd EAGE Conference & Exhibition.

Lundin, E.R., 1992. Thin-skinned extensional tectonics on a salt detachment, northern Kwanza Basin, Angola. Marine and Petroleum Geology, 9(4): 405-411.

Magara, K., 1978. The significance of the expulsion of water in oil-phase primary migration. Bulletin of Canadian Petroleum Geology, 26(1): 123-131.

Maia, A.R., Cartwright, J. and Andersen, E., 2016. Shallow plumbing systems inferred from spatial analysis of pockmark arrays. Marine and Petroleum Geology, 77: 865-881.

Maia, A.R., Cartwright, J., Andersen, E. and Gamboa, D., 2015. Fluid flow within MTDs: Evidences of fluid storage and leakage from 3D seismic data, offshore West Africa, 7th International Symposium Submarine Mass Movements and Their Consequences, Wellington, New Zealand.

Mandl, G., 1988. Mechanics of tectonic faulting: models and basic concepts. Elsevier, Amsterdam, 407 pp.

Mandl, G. and Crans, W., 1981. Gravitational gliding in deltas. Geological Society, London, Special Publications, 9(1): 41-54.

Marcon, Y., Ondréas, H., Sahling, H., Bohrmann, G. and Olu, K., 2014. Fluid flow regimes and growth of a giant pockmark. Geology, 42(1): 63-66.

Mardia, K.V., 1972. Statistics of directional data. Journal of the Royal Statistical Society. Series B (Methodological): 349-393.

Masson, D., Huggett, Q. and Brunsden, D., 1993. The surface texture of the Saharan debris flow deposit and some speculations on submarine debris flow processes. Sedimentology, 40(3): 583-598.

Masson, D.G., Harbitz, C.B., Wynn, R.B., Pedersen, G. and Løvholt, F., 2006. Submarine landslides: Processes, triggers and hazard prediction. Philosophical Transactions: Mathematical, Physical and Engineering Sciences (Series A), 364(1845): 2009-2039.

Matthäi, S. and Roberts, S., 1997. Transient versus continuous fluid flow in seismically active faults: an investigation by electric analogue and numerical modelling. Fluid Flow and Transport in Rocks. Mechanisms and Effects: 263–95.

Mayall, M., Jones, E. and Casey, M., 2006. Turbidite channel reservoirs--Key elements in facies prediction and effective development. Marine and Petroleum Geology, 23(8): 821-841.

Meckel III, L.D., 2011. Reservoir characteristics and classification of sand-prone submarine mass-transport deposits. In: C. Shipp, P. Weimer and H. Posamentier (Eds.), Mass-transport deposits in deepwater settings. SEPM Special Publication 96, pp. 423-450.

Meckel III, L.D., Angelatos, M., Bonnie, J., McGarva, R., Almond, T., Marshall, N.F., Bourdon, L. and Ausrich, K., 2011. Reservoir characterization of sand-prone mass-transport deposits within slope canyons. In: C. Shipp, P. Weimer and H. Posamentier (Eds.), Mass-transport deposits in deepwater settings. SEPM Special Publication 96, pp. 391-422.

Meyers, P., 1998. Microbial gases in sediments from the southwest African margin, Proceedings of the Ocean Drilling Program. Initial reports. Ocean Drilling Program, pp. 555-560.

Miller, K.G., Kominz, M.A., Browning, J.V., Wright, J.D., Mountain, G.S., Katz, M.E., Sugarman, P.J., Cramer, B.S., Christie-Blick, N. and Pekar, S.F., 2005. The Phanerozoic record of global sea-level change. science, 310(5752): 1293-1298.

Mitchum, R.M., Jr., Vail, P.R. and Sangree, J.B., 1977. Seismic stratigraphy and global changes of sea level, part 6: Stratigraphic interpretation of seismic reflection patterns in depositional sequences. In: C.E. Payton (Ed.), Seismic stratigraphy - applications to hydrocarbon exploration. AAPG Memoir 26, Tulsa, Ok, pp. 117-133.

Morgan, D., Cartwright, J. and Imbert, P., 2015. Perturbation of polygonal fault propagation by buried pockmarks and the implications for the development of polygonal fault systems. Marine and Petroleum Geology, 65: 157-171.

Morley, C., Maczak, A., Rungprom, T., Ghosh, J., Cartwright, J., Bertoni, C. and Panpichityota, N., 2017. New style of honeycomb structures revealed on 3D seismic data indicate widespread diagenesis offshore Great South Basin, New Zealand. Marine and Petroleum Geology, 86: 140-154.

Moss, J. and Cartwright, J., 2010a. 3D seismic expression of km-scale fluid escape pipes from offshore Namibia. Basin Research, 22(4): 481-501.

Moss, J.L., 2010. The spatial and temporal distribution of pipe and pockmark formation. PhD Thesis, PhD Thesis, Cardiff University, 314 pp.

Moss, J.L. and Cartwright, J., 2010b. 3D seismic expression of km-scale fluid escape pipes from offshore Namibia. Basin Research, 22(4): 481-501.

Moulin, M., Aslanian, D., Olivet, J.-L., Contrucci, I., Matias, L., Géli, L., Klingelhoefer, F., Nouzé, H., Réhault, J.-P. and Unternehr, P., 2005. Geological constraints on the evolution of the Angolan margin based on reflection and refraction seismic data (ZaïAngo project). Geophysical Journal International, 162(3): 793-810.

Muir Wood, R., 1994. Earthquakes, strain-cycling and the mobilization of fluids. Geofluids: origin, migration and evolution of fluids in sedimentary basins: 85-98.

National Research Council, 1996. Committee on Fracture Characterization and Fluid Flow. Rock fractures and fluid flow: contemporary understanding and applications, 316.

Nourollah, H., Keetley, J. and O'Brien, G., 2010. Gas chimney identification through seismic attribute analysis in the Gippsland Basin, Australia. The Leading Edge, 29: 896.

O'Brien, G.W., Cowley, R., Quaife, P. and Morse, M. (Eds.), 2002. Characterizing hydrocarbon migration and fault-seal integrety in Australia's Timor Sea via multiple, integrated remote-sensing technologies. Surface Exploration Case Histories: Applications of Geochemistry, Magnetics and Remote Sensing, 48. AAPG Studies in Geology.

O'Brien, G.W. and Woods, E.P., 2005. Hydrocarbon-related diagenetic zones (HRDZs) in the Vulcan Subbasin, Timor Sea: recognition and exploration implications. APPEA Journal, 35(1): 220-252.

Oluboyo, A., Gawthorpe, R., Bakke, K. and Hadler-Jacobsen, F., 2014. Salt tectonic controls on deep-water turbidite depositional systems: Miocene, southwestern Lower Congo Basin, offshore Angola. Basin Research, 26(4): 597-620.

Parnell, J. and Schwab, A., 2003. Seismic Evidence for the Distribution and Migration of Fluids in Sedimentary Basins. Geofluids, 3(4): 213-217.

Pichel, L.M., Huuse, M. and Finch, E., 2016. Salt tectonics and fluid flow on morocco offshore: Insights from seismic interpretation and discrete-element modelling, International Conference and Exhibition, Barcelona, Spain, 3-6 April 2016.

Society of Exploration Geophysicists and American Association of Petroleum Geologists, pp. 33-33.

Pilcher, R. and Argent, J., 2007. Mega-pockmarks and linear pockmark trains on the West African continental margin. Marine Geology, 244(1-4): 15-32.

Pinet, N., Duchesne, M. and Lavoie, D., 2009. Linking a linear pockmark train with a buried Palaeozoic structure: a case study from the St. Lawrence Estuary. Geo-Marine Letters: 1-6.

Posamentier, H., 2004. Stratigraphy and geomorphology of deep-water mass transport complexes based on 3D seismic data, Offshore Technology Conference, Houston, TX.

Posamentier, H. and Martinsen, O.J., 2011. The character and genesis of submarine mass-transport deposits: insights from outcrop and 3D seismic data. In: C. Shipp, P. Weimer and H. Posamentier (Eds.), Mass-transport deposits in deepwater settings. SEPM Special Publication 96, pp. 7-38.

Posamentier, H.W., Davies, R.J., Cartwright, J.A. and Wood, L., 2007. Seismic geomorphology - an overview. Geological Society, London, Special Publications, 277(1): 1-14.

Posamentier, H.W. and Walker, R.G., 2011. Deep-Water Turbidites and Submarine Fans, Facies Models Revisited. SEPM (Society for Sedimentary Geology), pp. 399-520.

Pufahl, P., Maslin, M., Anderson, L., Brüchert, V., Jansen, F., Lin, H., Perez, M., Vidal, L. and Party10, S.S., 1998. 18. Lithostratigraphic summary for LEG 175: Angola-

Benguela upwelling system, Proceedings Ocean Drilling Program, Initial Reports, pp. 533-542.

Reed, D.L., Silver, E.A., Tagudin, J.E., Shipley, T.H. and Vrolijk, P., 1990. Relations between mud volcanoes, thrust deformation, slope sedimentation, and gas hydrate, offshore north Panama. Marine and Petroleum Geology, 7(1): 44-54.

Reusch, A., Loher, M., Bouffard, D., Moernaut, J., Hellmich, F., Anselmetti, F.S., Bernasconi, S.M., Hilbe, M., Kopf, A., Lilley, M.D., Meinecke, G. and Strasser, M., 2015. Giant lacustrine pockmarks with subaqueous groundwater discharge and subsurface sediment mobilization. Geophysical Research Letters, 42(9): 3465-3473.

Riboulot, V., Cattaneo, A., Sultan, N., Garziglia, S., Ker, S., Imbert, P. and Voisset, M., 2013. Sea-level change and free gas occurrence influencing a submarine landslide and pockmark formation and distribution in deepwater Nigeria. Earth and Planetary Science Letters, 375: 78-91.

Rice, D.D., 1992. Controls, habitat, and resource potential of ancient bacterial gas. Bacterial Gas: 91-118.

Rouby, D., Guillocheau, F., Robin, C., Bouroullec, R., Raillard, S., Castelltort, S. and Nalpas, T., 2003. Rates of deformation of an extensional growth fault/raft system (offshore Congo, West African margin) from combined accommodation measurements and 3-D restoration. Basin Research, 15(2): 183-200.

Rouby, D., Raillard, S., Guillocheau, F., Bouroullec, R. and Nalpas, T., 2002. Kinematics of a growth fault/raft system on the West African margin using 3-D restoration. Journal of Structural Geology, 24(4): 783-796.

Saffer, D.M. and Tobin, H.J., 2011. Hydrogeology and mechanics of subduction zone forearcs: Fluid flow and pore pressure. Annual Review Of Earth And Planetary Sciences, 39: 157-186.

Séranne, M., 1999. Early Oligocene stratigraphic turnover on the west Africa continental margin: a signature of the Tertiary greenhouse-to-icehouse transition? Terra Nova, 11(4): 135-140.

Serié, C., Huuse, M., Schødt, N.H., Brooks, J.M. and Williams, A., 2017. Subsurface fluid flow in the deep-water Kwanza Basin, offshore Angola. Basin Research, 29(2): 149-179.

Sheriff, R.E. and Geldart, L.P., 1995. Exploration Seismology. Cambridge University Press, second edition, 592 pp.

Shipp, C., Nott, J.A. and Newlin, J.A., 2004. Physical characteristics and impact of mass transport complexes on deepwater jetted conductors and suction anchor piles, Offshore Technology Conference, Houston, Texas.

Sibson, R., 1995. Selective fault reactivation during basin inversion: potential for fluid redistribution through fault-valve action. Geological Society, Special Publications, 88: 3-19.

Sibson, R.H., 1981. Fluid flow accompanying faulting: field evidence and models. Earthquake prediction: 593-603.

Sibson, R.H., 1985. Stopping of earthquake ruptures at dilational fault jogs. Nature, 316(6025): 248-251.

Sibson, R.H., 1990. Conditions for fault-valve behaviour. Geological Society, London, Special Publications, 54(1): 15-28.

Sibson, R.H., 1994. Crustal stress, faulting and fluid flow. Geological Society, London, Special Publications, 78(1): 69-84.

Sibson, R.H., 1996. Structural permeability of fluid-driven fault-fracture meshes. Journal of Structural Geology, 18(8): 1031-1042.

Sibson, R.H., Moore, J.M.M. and Rankin, A.H., 1975. Seismic pumping--a hydrothermal fluid transport mechanism. Journal of the Geological Society, 131(6): 653-659.

Smith, D.A., 1980. Sealing and nonsealing faults in Louisiana Gulf Coast salt basin. AAPG Bulletin, 64(2): 145-172.

Spathopoulos, F., 1996. An insight on salt tectonics in the Angola Basin, South Atlantic. Geological Society, London, Special Publications, 100(1): 153-174.

Stewart, S.A., 2006. Implications of passive salt diapir kinematics for reservoir segmentation by radial and concentric faults. Marine and Petroleum Geology, 23(8): 843-853.

Stover, S.C., Ge, S., Weimer, P. and McBride, B.C., 2001. The effects of salt evolution, structural development, and fault propagation on Late Mesozoic-Cenozoic oil migration: A two-dimensional fluid-flow study along a megaregional profile in the northern Gulf of Mexico Basin. AAPG Bulletin, 85(11): 1945-1966.

Stow, D.A.V., Alam, M. and Piper, D.J.W., 1984. Sedimentology of the Halifax Formation, Nova Scotia: Lower Palaeozoic fine-grained turbidites. In: D.A.V. Stow and

D.J.W. Piper (Eds.), Fine-grained sediments: Deep-water processes and facies. Geological Society, London, Special Publications 15, pp. 127-144.

Sultan, N., Cochonat, P., Canals, M., Cattaneo, A., Dennielou, B., Haflidason, H., Laberg, J., Long, D., Mienert, J. and Trincardi, F., 2004. Triggering mechanisms of slope instability processes and sediment failures on continental margins: a geotechnical approach. Marine Geology, 213(1): 291-321.

Sultan, N., Marsset, B., Ker, S., Marsset, T., Voisset, M., Vernant, A.M., Bayon, G., Cauquil, E., Adamy, J., Colliat, J.L. and Drapeau, D., 2010. Hydrate dissolution as a potential mechanism for pockmark formation in the Niger delta. Journal of Geophysical Research: Solid Earth, 115(B8): n/a-n/a.

Sun, Q., Alves, T., Xie, X., He, J., Li, W. and Ni, X., 2017. Free gas accumulations in basal shear zones of mass-transport deposits (Pearl River Mouth Basin, South China Sea): An important geohazard on continental slope basins. Marine and Petroleum Geology, 81: 17-32.

Talukder, A.R., 2012. Review of submarine cold seep plumbing systems: leakage to seepage and venting. Terra Nova, 24(4): 255-272.

Taylor, M., Dillon, W.P. and Pecher, I., 2000. Trapping and migration of methane associated with the gas hydrate stability zone at the Blake Ridge Diapir: new insights from seismic data. Marine Geology, 164(1): 79-89.

Tripsanas, E.K., Piper, D.J.W. and Campbell, D.C., 2008. Evolution and depositional structure of earthquake-induced mass movements and gravity flows: Southwest Orphan Basin, Labrador Sea. Marine and Petroleum Geology, 25(7): 645-662.

Tueckmantel, C., Fisher, Q.J., Knipe, R.J., Lickorish, H. and Khalil, S.M., 2010. Fault seal prediction of seismic-scale normal faults in porous sandstone: A case study from the eastern Gulf of Suez rift, Egypt. Marine and Petroleum Geology, 27(2): 334-350.

Valle, P.J., Gjelberg, J.G. and Helland-Hansen, W., 2001. Tectonostratigraphic development in the eastern Lower Congo Basin, offshore Angola, west Africa. Marine and Petroleum Geology, 18(8): 909-927.

Van Rensbergen, P., Rabaute, A., Colpaert, A., Ghislain, T.S., Mathijs, M. and Bruggeman, A., 2007. Fluid migration and fluid seepage in the Connemara Field, Porcupine Basin interpreted from industrial 3D seismic and well data combined with high-resolution site survey data. International Journal of Earth Sciences, 96(1): 185-197.

Veeken, P.C.H., 2007. Seismic stratigraphy, basin analysis and reservoir characterisation, 37. Elsevier Science, 509 pp.

Vendeville, B., 2002. A new interpretation of Trusheim's classic model of salt-diapir growth. Gulf Coast Association of Geological Societies Transactions, 52: 943-952.

Vendeville, B.C., 2005. Salt tectonics driven by sediment progradation: Part I--Mechanics and kinematics. AAPG Bulletin, 89(8): 1071-1079.

Vendeville, B.C. and Jackson, M.P.A., 1992a. The fall of diapirs during thin-skinned extension. Marine and Petroleum Geology, 9(4): 354-371.

Vendeville, B.C. and Jackson, M.P.A., 1992b. The rise of diapirs during thin-skinned extension. Marine and Petroleum Geology, 9(4): 331-353.

Venkatachalapathy, R., Veerasingam, S., Basavaiah, N. and Ramkumar, T., 2010. Comparison between petroleum hydrocarbon concentrations and magnetic properties in Chennai coastal sediments, Bay of Bengal, INDIA. Marine and Petroleum Geology, 27(9): 1927-1935.

Von Huene, R., Ranero, C.R. and Vannucchi, P., 2004. Generic model of subduction erosion. Geology, 32(10): 913-916.

von Nicolai, C., Scheck-Wenderoth, M., Warsitzka, M., Schødt, N. and Andersen, J., 2013. The deep structure of the South Atlantic Kwanza Basin — Insights from 3D structural and gravimetric modelling. Tectonophysics, 604(0): 139-152.

Walderhaug, O., 1996. Kinetic modeling of quartz cementation and porosity loss in deeply buried sandstone reservoirs. AAPG Bulletin, 80(5): 731-745.

Weimer, P. and Shipp, C., 2004. Mass transport complex: musing on the past uses and suggestions for future directions, Offshore Technology Conference, Houston, Texas.

Weimer, P. and Slatt, R.M., 2004. Petroleum systems of deepwater settings, 7. Society of Exploration Geophysicists / European Association of Geoscientists & Engineers Short Course, 465 pp.

Welbon, A.I.F., Brockbank, P.J., Brunsden, D. and Olsen, T.S., 2007. Characterizing and producing from reservoirs in landslides: challenges and opportunities. In: S.J. Jolley, D. Barr, J.J. Walsh and R.J. Knipe (Eds.), Structurally Complex Reservoirs. Geological Society London, Special Publications 292, pp. 49-74.

Yilmaz, Ö., 2001. Seismic data analysis, Vol. II. Investigations in Geophysics No. 10. Society of Exploration Geophysicists, 1050 pp.

Zhang, L., Luo, X., Liao, Q., Yang, W., Vasseur, G., Yu, C., Su, J., Yuan, S., Xiao, D. and Wang, Z., 2010. Quantitative evaluation of synsedimentary fault opening and sealing properties using hydrocarbon connection probability assessment. AAPG Bulletin, 94(9): 1379-1399.